EPA REGION 8'S RESPONSE TO PETITION FOR REVIEW

# Attachment Q

Administrative Record Document No. 54

Final Report: 2013 Uinta Basin Winter Ozone Study, Full Document

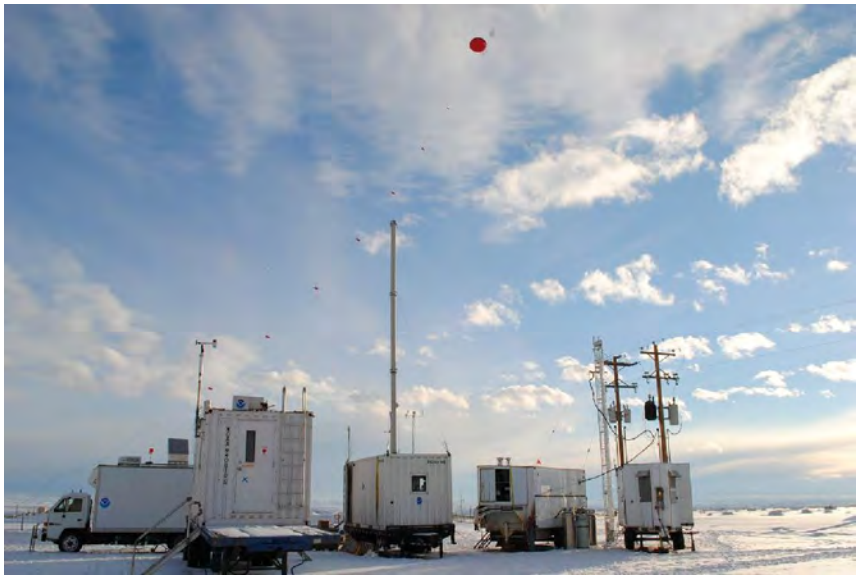

# Final Report
# 2013 Uinta Basin Winter Ozone Study


Prepared for:
Brock LeBaron
Utah Division of Air Quality
1950 West 150 North
Salt Lake City, UT 84116

Edited by:
Till Stoeckenius
ENVIRON International Corporation
and
Dennis McNally
Alpine Geophysics

ENVIRON International Corporation
773 San Marin Drive, Suite 2115
Novato, California, 94998
www.environcorp.com
P-415-899-0700
F-415-899-0707


March 2014

ENVIRON

00614

This page left intentionally blank.

# CONTENTS

**TABLES**

**FIGURES**

# EXECUTIVE SUMMARY

*Background*

The Uinta Basin is a rural area of northeastern Utah where the majority of the state's oil and gas production occurs. Ozone concentrations in excess of the current national air quality standard have been measured in the Basin during the winter. These high ozone levels are only observed in the Basin during winter inversion periods when the ground is covered by snow; ozone levels outside of these periods have remained below the air quality standard and conditions resulting in exceedances of the standard do not occur every year.

In the first quarter of 2012, a multi-phased study (the Uinta Basin Ozone Study, UBOS) was begun to identify the emissions sources and the unique photochemical processes that cause elevated winter ozone concentrations, and to identify the most effective strategies to reduce winter ozone. UBOS 2012 included measurements of ozone and ozone precursor concentrations and meteorological conditions throughout the Basin. Meteorological conditions during UBOS 2012 were not conducive to ozone formation due to a lack of snow cover; no exceedances of the 8-hour average 75 parts per billion (ppb) National Ambient Air Quality Standard (NAAQS) were observed during UBOS 2012. Key findings from UBOS 2012 are described in a summary report (Final Report: 2012 Uinta Basin Winter Ozone and Air Quality Study; available at http://www.deq.utah.gov/locations/uintahbasin/studies/2012study.htm.)

UBOS 2013 took place between January and March 2013. In contrast to UBOS 2012, conditions during UBOS 2013 were favorable to ozone formation and numerous exceedances of the NAAQS were observed. Results from UBOS 2013, in combination with those from UBOS 2012, provide a wealth of information about the meteorological conditions and atmospheric chemistry associated with winter ozone episodes in the Uinta Basin.

This important work is made possible by funding and in-kind support from the following: Uintah Impact Mitigation Special Service District (UIMSSD), Western Energy Alliance, Questar Energy Products, Bureau of Land Management (BLM), National Oceanic and Atmospheric Administration (NOAA), Environmental Protection Agency (EPA), Utah Department of Environmental Quality (UDEQ), Utah Science Technology and Research Initiative (USTAR), and Utah School and Institutional Trust Lands Administration (SITLA). Work on UBOS 2013 was conducted by researchers from Utah State University (USU); National Oceanic and Atmospheric Administration (NOAA); Utah Department of Environmental Quality (UDEQ); University of Utah (UU); University of Colorado, Boulder (CU); University of Wyoming (U of WY); University of California Los Angeles (UCLA); and University of Washington (UW).

*Findings*

Key findings from UBOS 2013 are summarized below:

I. Air Quality
   a. Maximum 8-hour average ozone concentrations measured at Ouray, which typically has among the highest readings in the Basin, reached 142 ppb during the December 2012 – March 2013 winter study, exceeding the EPA 8-hour

standard (75 ppb) by 89%. Exceedances of the standard (i.e., a daily maximum 8-hour average in excess of 75 ppb) occurred at 17 of the 20 monitoring sites operating during the study. Monitors in the major Basin population centers exceeded the standard on a total of 22 days at Vernal and 29 days at Roosevelt during 2013 with all of the exceedances occurring between January 9$^{th}$ and March 6$^{th}$. Note that the occurrence of an exceedance does not by itself constitute a *violation* of the EPA standard; a violation only occurs when the three year average of the annual fourth highest daily maximum 8-hour average is greater than 75 ppb. Exceedances occurred in the Basin during seven separate multi-day ozone episodes which were separated by periods of lower ozone levels coinciding with the passage of storm systems. These observations are in sharp contrast to conditions during the 2011-2012 winter study, when daytime 8-hour average ozone levels did not exceed 63 ppb.

b. Individual ozone episodes ranged from 3 to nearly 15 days in length, with ozone concentrations generally increasing from one day to the next during each episode, indicating a lack of ventilation.
c. Daytime ozone concentrations at locations close to but outside of the Uinta Basin, at the time of high surface ozone events inside the basin, ranged from 40 to 60 ppb. Ozone concentrations measured inside the Basin above the temperature inversion during these periods were also in the 40 to 60 ppb range. These facts, combined with observations of winds around the Basin, confirms that high surface ozone concentrations within the basin are not influenced to any significant extent by transport of ozone or precursors from outside of the Basin.
d. Days with high ozone in the Basin coincide with elevated levels of methane, volatile organic compounds (VOC) and odd nitrogen species ($NO_y$). Alkane hydrocarbons constitute the main fraction of identified VOC. VOC and $NO_x$ are the primary chemical precursors of ozone. A review of all emissions sources within the Basin (based on WRAP Phase III and UDAQ triennial inventories) indicates that activities associated with oil and gas exploration and production are the predominant sources of ozone precursors.
e. VOC concentrations in the Basin are extremely high during ozone episodes due to large amounts of VOC emissions and limited ventilation under a strong temperature inversion. Average VOC levels at Horsepool in 2013 were 1,684 ppbC (based on C2 – C7 non-methane hydrocarbons) as compared to 232 ppbC in 2012 when inversions were not present and there was more mixing.
f. Vertical profiles show that the polluted air mass associated with ozone episodes is confined to a shallow boundary layer that varies in height from 70 – 400 m (230 – 1,300 ft) above ground level.
g. The Bonanza power plant plume does not appear to contribute any significant amount of nitrogen oxides or other contaminants to the polluted boundary layer during ozone episodes; the thermally buoyant Bonanza plume was observed to rise upwards from the 183 m (600 ft) stack and penetrates through the temperature inversion layer. As a result, emissions from the Bonanza plant are

effectively isolated from the boundary layer in which the high ozone concentrations occur.

II. Meteorology

a. Observations made during the 2013 winter study confirmed that high winter ozone in the Uinta basin only occurs when the ground is covered with snow and weather conditions promote the formation of a strong temperature inversion which traps a layer of cold, stable air (a "cold pool") within the basin. In the absence of any snow cover, warming of the earth's surface by the sun causes too much convective mixing for a cold pool to form.

b. Chemical reactions resulting in ozone formation are driven by the illumination of the atmosphere from direct, reflected and scattered ultraviolet solar radiation. Reflection of light from the snow surface significantly increases (by roughly 50%) the total flux of ultraviolet radiation and thus the rate of ozone formation.

c. Ozone episodes in the Basin are characterized by complex, diurnally varying patterns of light winds which have the potential to produce gradual but significant intra-basin transport of ozone and precursors. Factors driving winds within the polluted boundary layer include differential daytime heating producing upslope flows (which can be modified by variations in snow cover), nighttime drainage flows resulting in convergence along the river valleys at the lowest Basin elevations, and spatial perturbations of the depth of the cold pool air mass by winds blowing over the mountains surrounding the Basin. These forcing factors appear to produce oscillations or an east-west "sloshing" of air within the basin that further contributes to intra-basin mixing. These processes result in transport of ozone and ozone precursors from one part of the Basin to another but are not strong enough to mechanically breakdown the temperature inversion.

d. Initial attempts at modeling meteorological conditions during episodes indicate that obtaining accurate results with current modeling techniques will be very challenging. Additional data collection and model development and testing will be required to produce a good working model suitable for evaluating alternative regulatory strategies.

III. Chemistry

a. Unique features of the chemical reactions involved in ozone production were observed during the 2013 winter ozone episodes which make these episodes very different from summer ozone episodes in urban areas. Nitrous acid (HONO) and formaldehyde rather than ozone photolysis were found to be the biggest contributors to the pool of chemical radicals responsible for ozone formation. A daytime HONO source at the snow surface appears to be primarily responsible for the contribution of HONO to the radical pool. However, the magnitude of the contribution of HONO to the radical pool is uncertain at this time due to the limited vertical extent of HONO measurements made during the 2013 study. There are also questions about the accuracy of these measurements, which were made using a single method, resulting in a significant amount of uncertainty in modeling the chemistry of ozone formation.

b. Uncertainties remain regarding the likely impact of nitrogen oxides ($NO_x$) and, to a lesser extent, volatile organic compound (VOC) emission controls on ozone levels:
    i. Analysis of data from 2012 (when elevated ozone did not occur) suggests that the limited amount of ozone production that did occur was VOC limited, i.e., VOC reductions would produce ozone reductions whereas marginal $NO_x$ reductions may result in increases in ozone. However, conditions with low ozone in 2012 cannot be used to predict ozone sensitivity to precursors during winter inversion conditions with snow cover, and further analysis is needed to assess ozone sensitivity during the 2013 episodes.
    ii. The effectiveness of $NO_x$ controls will also be impacted by the extent to which unreactive $NO_z$ species (including $HNO_3$ and organic nitrates) are being recycled back into reactive $NO_x$ by heterogeneous chemistry in snow and on particulates. Details of these potential heterogeneous reactions are not yet understood well enough to be included in photochemical models needed for evaluation of control strategies.
    iii. Measurements made during 2013 suggest that VOC reactions in the snow may contribute to ozone chemistry within the layer of air just above the snow surface (the mixed layer). The potential implications of this finding on the efficacy of VOC and $NO_x$ controls are not yet known and further study is needed.
    iv. Oxidation of VOCs is a key step in ozone accumulation. While the reactivity of VOCs varies widely, the relative contribution of individual VOC species to ozone formation depends on their abundance as well as their reactivity. Measurements made during 2012 and 2013 indicate that alkanes (including propane, iso- and n-butane and iso- and n-pentane), are much more abundant and as a result likely contribute more to ozone formation in the Basin than the more reactive but less abundant aromatic VOCs (including toluene and xylene). Nevertheless, small reductions in emissions of aromatics may be as effective as larger reductions in emissions of alkanes given the greater reactivity of aromatics. There do not appear to be large sources of other highly reactive VOCs (alkenes) in the Basin as alkene concentrations were very low relative to alkanes and aromatics.

IV. Emissions

a. Some important progress has been made on developing emission inventories for the Basin but the available data remain incomplete. Several groups, including the Utah Division of Air Quality, EPA Region VIII, and Federal Land Managers (through the Utah Air Resource Management Strategy project and the "3-States" and "West Jump" air quality modeling studies) are currently working on inventories for the Basin. Progress would be enhanced by more formal coordination of effort between these groups and the energy producers.

b. Field measurements of emissions from produced water ponds were conducted during the winter of 2012-2013 which showed that, while wintertime pond emissions comprise a small part of total VOC emissions in the Uinta Basin, VOC emitted from produced water ponds tend to be enriched in reactive VOC.
c. Field measurements made by the NOAA mobile laboratory during UBOS 2012 show significant differences in VOC emission composition depending on well and equipment types and are broadly consistent with VOC emission profiles applied to different source categories (venting, flashing, dehydrators, etc.) in the 2008 Western Regional Air Partnership (WRAP) inventory.
d. Obtaining comprehensive emissions data for the Basin is made difficult in part due to a mixture of private, federal, state and Indian surface and mineral rights ownership which results in complex regulatory jurisdictions and inconsistent reporting requirements.
e. Inventory data specific to the winter ozone season are needed as emissions from some types of sources (such as evaporation ponds and methanol use) have large seasonal variations.
f. Additional information is needed on sources of formaldehyde (which is a highly reactive volatile organic compound (VOC) that accelerates the formation of ozone), including methanol use and degree of contamination with formaldehyde and operation of dehydrators.
g. Important components of the inventory that need to be more carefully quantified include emissions of VOCs from oil, condensate and produced water storage tanks, as well as fugitive emissions from leaking components and other sources and from venting, blowdowns and other intermittent events.

V. Recommendations for Future Analyses

a. Additional field data collection and analysis are needed to improve our understanding of several key features of the winter episodes to the point where meteorological and photochemical models suitable for analyzing alternative regulatory scenarios can be developed. Two areas of particular importance were identified:
    i. The highest priority studies would focus on improved, more robust measurements of HONO concentrations and related species, their vertical distribution and temporal variations. The response of ozone to changes in VOC and $NO_x$ emissions is highly sensitive to HONO, so a clear understanding of HONO formation and removal mechanisms is critical.
    ii. Development of a comprehensive and accurate winter emission inventory for the Basin suitable for modeling applications (i.e., including sufficient speciation of chemical compounds and spatial and temporal detail) remains a critical requirement. There is a need to prioritize and coordinate efforts among the various groups that are currently developing inventories. In addition, work on “top-down” evaluation of inventories using available air quality observations is needed.
b. Several other data collection and analysis needs were identified by the UBOS research team; these are described in Section 2.6.

VI. Implications for Control Strategies

a. Ozone levels in excess of the EPA 8-hour standard are only observed during winter inversion periods; ozone levels on the majority of days during the year are below the EPA standard and exceedances of the standard do not occur every year. This suggests that episodic or seasonal controls may be a useful component of an overall air quality management strategy for the Basin.
b. Emission reductions at the Bonanza power plant are unlikely to have any effect on winter ozone episodes.
c. Reductions in all VOC emissions will be beneficial; reductions in the more reactive VOC species, such as formaldehyde and aromatic VOC, will be more beneficial on a per ton basis but less reactive VOCs dominate emissions, and therefore ozone production, in the Basin. Glycol dehydrators and produced water are two important sources of aromatic VOC.
d. Ozone response to $NO_x$ reductions is less certain. $NO_x$ control strategies will tend to be less effective if unreactive $NO_z$ is converted to reactive $NO_x$ by heterogeneous chemistry on snow or particulates, e.g., the conversion of $HNO_3$ to HONO in snow.
e. Reducing formaldehyde would be an effective way to reduce ozone, but it is not clear at this time which sources of formaldehyde (direct emissions from fuel combustion and use of methanol contaminated with formaldehyde or secondary formation of formaldehyde from VOC precursors) are most important.
f. Uncertainty in HONO sources and source strength (direct emissions or secondary formation from nitrogen precursors via several potential reaction pathways) makes it difficult to predict how responsive ozone will be to reductions in VOC and $NO_x$ emissions.

# 1.0 PREFACE, CONTRIBUTORS AND ACKNOWLEDGEMENTS

## 1.1 Preface

This report supersedes the UBOS 2012 report and includes most of the relevant background information and results from the 2012 study. While some references to specific material in the 2012 study are retained, this is intended to be a stand-alone report presenting findings from both the UBOS 2012 and 2013 studies.

## 1.2 Contributors

This report represents the contributions of a large number of dedicated scientists from federal and state government departments and agencies as well as several research universities. Primary authors are listed by section below. In most cases, a number of other UBOS participants provided detailed and helpful comments which greatly improved the initial drafts prepared by the primary authors. Affiliations of all authors are listed in the author list at the beginning of Sections 2 - 10.

Executive Summary: Till Stoeckenius, Brock LeBaron, Gail Tonnesen and Jim Roberts.

1.0 Preface, Contributors and Acknowledgements: Till Stoeckenius.

2.0 Synthesis of Results: Till Stoeckenius and Dennis McNally (parts of Section 2.1 contributed by Seth Lyman and Howard Shorthill).

3.0 Long-Term and Distributed Monitoring of Ozone, Precursors and Meteorology:

Sections 3.1 and 3.4: Seth Lyman, Marc Mansfield, Howard Shorthill, Randy Anderson, Chad Mangum, Jordan Evans, and Tate Shorthill;

Section 3.2: John Horel, Erik Crosman, and Erik Neemann;

Section 3.3: Michael Christiansen, Trevor O'Neil, and Seth Lyman.

4.0 Aircraft Observations: Anna Karion, Sam Oltmans, Gaby Petron, Colm Sweeney and Russ Schnell.

5.0 Intensive Chemical Measurements at Horsepool: James M. Roberts, Patrick R. Veres, Bin Yuan, Carsten Warneke, Felix Geiger, Peter M. Edwards, Robert Wild, William Dube, Gabrielle Petron, Jonathan Kofler, Andreas Zahn, Steven S. Brown, Martin Graus, Jessica Gilman, Brian Lerner, Jeff Peischl, Joost A. de Gouw, Rui Li, Timothy Bates, Patricia Quinn, Abigail Koss, Shao-Meng Li, David D. Parrish, Christoph J. Senff, Andrew O. Langford, Robert Banta, Randall Martin, Robert Zamora, Shane Murphy, Jeff Soltis, Robert Field.

6.0 Balloon-Borne Vertical Profiles of Ozone, Methane, Non-Methane Hydrocarbons, Nitrogen Oxides and Meteorological Parameters: Detlev Helmig, Chelsea Stephens, Jeong-Hoo Park, Jacques Hueber, Patrick Boylan, Jason Evans.

7.0 Ozone Deposition Velocity During Snow-Covered and Non-Snow-Covered Periods by Eddy Covariance: Detlev Helmig, Chelsea Stephens, Jeong-Hoo Park, Jacques Hueber, Patrick Boylan, Jason Evans.

8.0 Tethered Ozonesonde and Surface Ozone Measurements in the Uinta Basin, Winter 2013: Russ Schnell, Bryan Johnson, Patrick Cullis, Chance Sterling, Emrys Hall, Rob Albee, Allen Jordan, Jim Wendell, Samuel Oltmans, Gabrielle Petron and Colm Sweeney.

9.0 Ozone Precursor Emissions in the Uinta Basin:

9.1 Uinta Basin Emissions Inventory: Patrick Barickman;

9.2 Wintertime Emissions of Hydrocarbons from Produced Water Evaporation Facilities: Seth Lyman, Marc Mansfield, Howard Shorthill, Randy Anderson, Jordan Evans, Chad Mangum, Tate Shorthill;

10.0 Numerical Modeling of a Thermal Inversion in the Uinta Basin, Utah, January 26-30, 2013: Trang Tran, Marc Mansfield, Seth Lyman.

## 1.3 Acknowledgements: Funding Agencies

The Uinta Basin Ozone Studies for 2012 and 2013 were made possible by the combined contributions of several private and public sector organizations. The 2013 study was funded by and provided in-kind support by the: Uintah Impact Mitigation Special Service District (UIMSSD), Western Energy Alliance, QEP Resources, Inc., Bureau of Land Management (BLM), National Oceanic and Atmospheric Administration (NOAA), Environmental Protection Agency (EPA), Utah Department of Environmental Quality (UDEQ) and Utah Science Technology and Research Initiative (USTAR), and Utah School and Institutional Trust Lands Administration (SITLA).

# 2.0 SYNTHESIS OF RESULTS

## 2.1 Introduction

*Background*

The Uinta Basin is an enclosed basin that lies in the northeast corner of Utah and is part of a larger area known as the Colorado Plateau. The Basin is bounded on the north by the Uinta Mountain range, on the south by the Book and Roan Cliffs, on the west by the Wasatch Range and on the east by elevated terrain separating it from the Piceance Basin in Colorado. The Green River runs through the Basin from northeast to southwest, exiting through the Book Cliffs via Desolation Canyon. The floor of the Basin is at approximately 4800 feet above sea level with significant local topography on the order of tens to hundreds of feet.

Duchesne and Uintah Counties make up essentially the entire Basin. The Uintah and Ouray Indian Reservations cover a significant portion of the Basin (Figure 2-1). EPA and the Ute Tribe have jurisdiction over air quality management on the reservations and in Indian Country.

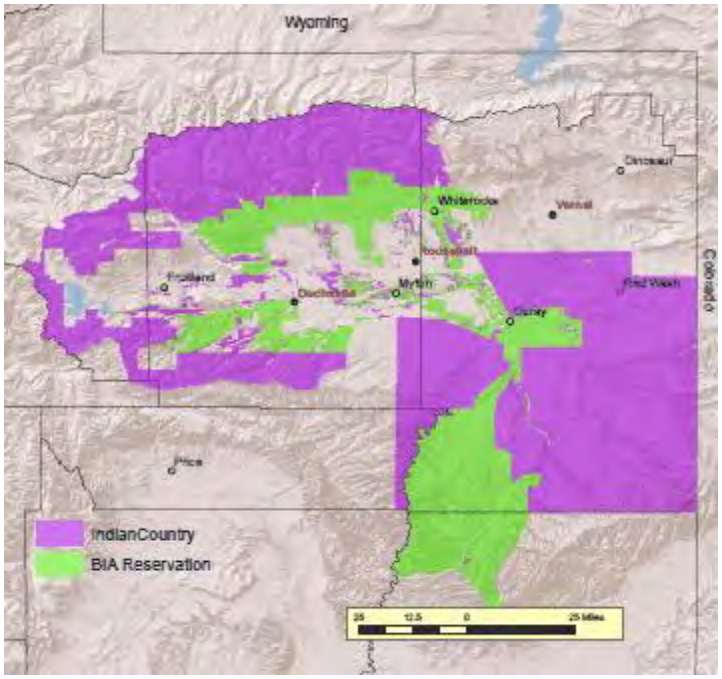


**Figure 2-1. Uinta Basin and surrounding region.**

The Basin is rural with a population of about fifty thousand people primarily located in three main towns (Duchesne, Roosevelt, and Vernal) which lie along the east-west State Highway 40 corridor. The economy of the Basin is driven by energy production from vast petroleum resources. Oil and gas development (approximately 10,000 producing wells) is widely scattered throughout the Basin (Figure 2-2) with associated drilling, processing, compression and pipeline facilities. A 500 megawatt coal fired power plant (Bonanza) operates in the Basin. There is also

some agricultural production in the Basin, primarily alfalfa and corn along with other hay and grain crops.

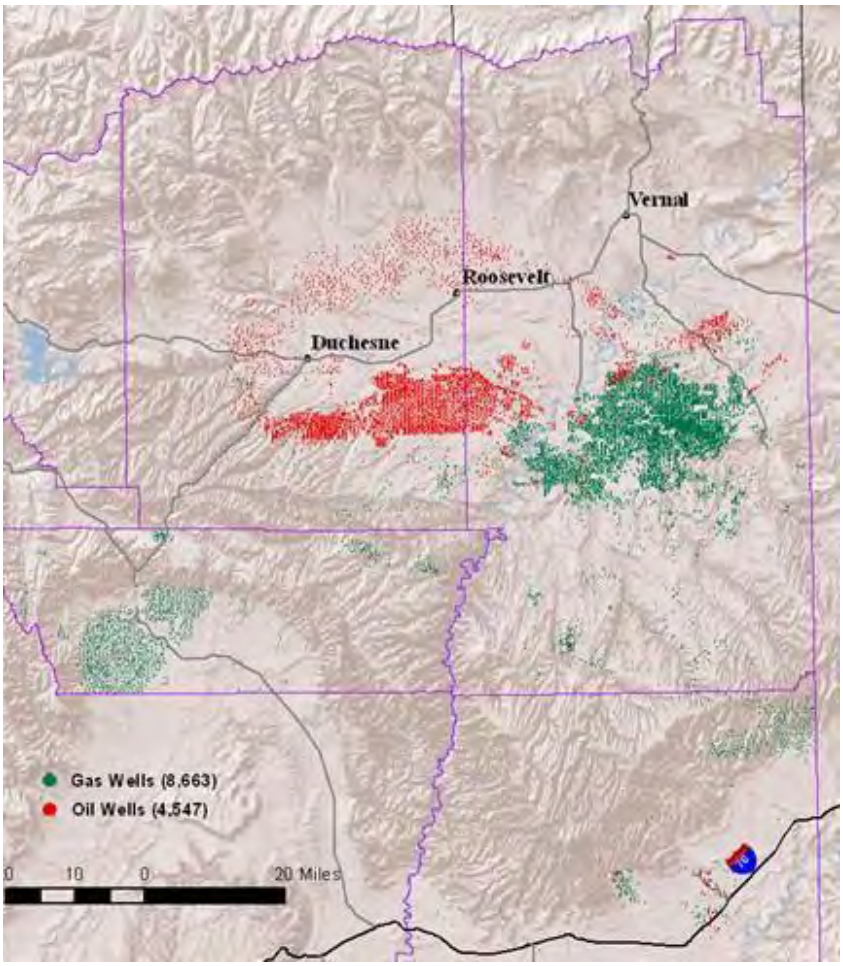


**Figure 2-2. Oil and gas well sites in Utah as of 2010.**

Air quality monitoring in the Basin began in 2006 when the Utah Department of Air Quality (UDAQ) installed monitors in Vernal to measure fine particulate ($PM_{2.5}$), ozone ($O_3$) and oxides of nitrogen ($NO_x$). Data were collected from February 2006 through December 2007. Highest 8-hour ozone averages reaching 81 ppb were found in the summer. No concentrations exceeding the 85 ppb National Ambient Air Quality Standard (NAAQS) then in affect were recorded and no elevated ozone was noted in the winter months. Two additional special studies were conducted during the winters of 2007-08 and 2008-09, but these were focused on $PM_{2.5}$ since no elevated winter ozone values had been observed in 2006-2007.

In the spring of 2009, EPA used consent decree funding to establish two monitoring sites at Ouray and Redwash in the oil and gas production area of the Basin. These sites were instrumented to measure $PM_{2.5}$, $NO_x$, $O_3$, and meteorological parameters year-round. In sharp contrast to the low ozone values found in the winter of 2006-2007, the winter of 2009-10

experienced very high ozone levels, with the highest 8-hour average of 124 ppb being measured at the Ouray site.

Utah State University (USU) conducted a special study in the winter of 2010-11 to confirm the presence of high winter ozone concentrations and map out the spatial extent of elevated ozone levels. Results from the 2010-11 study showed that ozone values were elevated throughout the Basin, with the highest concentrations tending to occur at lower elevations in the center of the Basin. The highest 8-hour ozone value measured at Ouray was 139 ppb. The data also showed that elevated ozone correlated highly with the presence of snow-covered ground and a strong temperature inversion, and that elevated ozone values did not occur absent of these conditions. A full report on results of the 2010-2011 study is available (Martin et al., 2011) and can be found at http://rd.usu.edu/files/uploads/edl_2010-11_report_ozone_final.pdf.

*2011 – 2012 Uinta Basin Ozone Study*

A full field campaign was mounted in the winter of 2011-12 to gain a more complete understanding of factors contributing to high wintertime ozone in the Basin. This campaign was part of a multi-phased study designed to identify the emissions sources and potentially unique photochemical processes that produce elevated winter ozone concentrations and assist in determining the most effective mitigation strategies. The Uinta Basin Ozone Study for the 2011-2012 winter season (UBOS 2012) consisted of six components carried out by several research organizations. Key results from each research group's work were presented at a meeting of study participants held 3 - 4 June 2012 in Vernal. A full report of the study results obtained by each research group along with a synthesis of results across all groups and a unified set of key results and conclusions accessible to a wider audience was subsequently prepared and made publically available (Lyman and Shorthill, 2013; referred to hereafter as the 2012 Synthesis Report or 2012SR).

*2012-2013 Uinta Basin Ozone Study*

Motivated by the lack of ozone conducive conditions during the 2011-2012 study, a second round of field monitoring was undertaken in the Uinta Basin during January – March 2013. Recognizing the possibility that the 2012-2013 winter could also turn out to have minimal snow and no ozone episodes, UBOS 2013 was designed to minimize upfront investment of labor and materials required to conduct an intensive measurement program unless and until such time as there was a reasonable certainty that snow cover sufficient to produce ozone conducive conditions would occur during the January – February study window. As it turned out, storms during December and early January produced a good snow pack in the Basin, and by mid-January it was obvious that conditions during UBOS 2013 would be favorable for ozone formation, prompting the decision to proceed with the intensive measurement program. Numerous exceedances of the NAAQS were subsequently observed as detailed in this report. As in the 2011-2012 study, researchers from the National Oceanic and Atmospheric Administration (NOAA) and several universities conducted extensive ground-based and airborne measurements of ozone and other key air quality and meteorological parameters and the Horsepool site was again chosen as the location to conduct a series of intensive

measurements of meteorology, ozone, ozone precursors and particulate matter. Instrumentation in 2013 differed somewhat from that used in 2012: some measurements were not available but a new set of measurements were added in 2013 to examine ozone deposition to the snow surface and chemical reactions within the snow pack which may play a role in winter ozone formation.

*Organization of the UBOS 2013 Synthesis Report*

In this *Synthesis of Results* section, we present an update to the 2011-2012 field study final report which reflects the significant amount of new information obtained from the 2013 study. As such, it represents a melding of the findings and conclusions from both the 2011-2012 and 2013 studies. Relevant material from the 2011-2012 report is carried over into this update and new or revised findings and conclusions are described.

As was the case for the 2011-2012 study, each research group participating in the 2013 winter field study prepared a final report describing in detail their individual data collection and analysis methods. These reports are included here in Sections 3 – 10 as listed in Table 2-1. Researcher's results from the 2011-2012 studies were included in the UBOS 2012 Synthesis Report (2012SR; Lyman and Shorthill, 2013). While relevant results, summaries, and conclusions from the 2012SR are included in this report, frequent references are made to the 2012SR to avoid unnecessary duplication of material and improve readability. A copy of the 2012SR is available for download at http://www.deq.utah.gov/locations/uintahbasin/docs/2014/03Mar/ubos_2011-12_final_report.pdf.

**Table 2-1. UBOS 2013 Study Components, associated research groups and the section of this report in which the final report(s) for the Study Component can be found.**

| Study Component | Research Group (Principal Investigator) | Summary Report in Section |
|---|---|---|
| Long-Term and Distributed Monitoring of Ozone, Precursors and Meteorology | Utah State Univ. (S. Lyman) | 3 |
| Aircraft Observations | NOAA/GMD | 4 |
| Intensive Chemical Measurements at Horsepool | NOAA/CIRES (J. Roberts) | 5 |
| Balloon-Borne Vertical Profiles of Ozone, Methane, Non-Methane Hydrocarbons, Nitrogen Oxides and Meteorological Parameters | Univ. Colorado, Boulder (D. Helmig) | 6 |
| Ozone Deposition Velocity During Snow-Covered and Non-Snow-Covered Periods by Eddy Covariance | Univ. Colorado, Boulder (D. Helmig) | 7 |
| Tethered Ozonesonde and Surface Ozone Measurements in the Uinta Basin, Winter 2013 | NOAA GMD (R. Schnell) | 8 |
| Ozone Precursor Emissions: Uinta Basin Emissions Inventory | P. Barickman | 9.1 |
| Ozone Precursor Emissions: Produced Water Evaporation Facilities | S. Lyman | 9.2 |
| Numerical Modeling of a Thermal Inversion in the Uinta Basin | M. Mansfield | 10 |

To present the synthesis of results in an efficient manner, this section has been written as a series of relatively short responses to a set of key questions focused on the ultimate study objectives as listed below. For each response, a brief background discussion explaining the significance of the question is provided along with a list of the field study elements that are used to address the question. This is followed by a set of *findings* that answer the question in different ways. Each response ends with a short conclusion summarizing the main points of the *findings*. Questions are grouped as to subject area as follows:

A. Physical Characteristics

*A.1: What are the key characteristics of meteorological conditions associated with ozone exceedances in the Basin?*

*A.2: Were the high levels of wintertime ozone observed during the winters of 2009-2010, 2010-2011, and 2012-2013 a result of meteorology or changes in precursor emissions?A.3: What is the climatological frequency of meteorological conditions that are conducive to ozone formation in the Uinta Basin?*

*A.4: What role does transport of ozone or ozone precursors into the Basin play in generating elevated ozone concentrations?*

*A.5: What similarities and differences are there between the Uinta Basin and the Upper Green River Basin in Wyoming?*

*A.6: Is there significant vertical stratification of precursors and if so, what role does this play in ozone formation?*

B. Atmospheric Chemistry of Ozone Formation

*B.1: Do VOC speciation and reactivity in the Basin have unique characteristics that contribute to wintertime ozone production?*

*B.2: Do pathways for ozone production exist that are unique to wintertime ozone events?*

C. Sources of Ozone Precursor Emissions

*C.1: What are the primary sources of ozone precursor emissions in the Basin? What is the spatial distribution of precursor sources?*

*C.2: Do ambient measurements and emission inventories agree for ozone precursor emissions in the Basin?*

D. Mitigation Strategies

*D.1: What possible mitigation strategies should be considered for adoption in the Uinta Basin?*

E. Additional Information Needs and Modeling Issues

*E.1: What special challenges does the basin pose for meteorological modeling?*

*E.2: Can the formulation of existing 1-D box and more complex transport and chemical models represent the observed phenomena in the Basin? If not, what are the most urgent measurement needs for improving the model representation?*

*E.3: What are the main issues regarding winter ozone formation that should be the focus of future studies?*

## 2.2 Part A: Physical Characteristics and Meteorology

***A.1: What are the key characteristics of meteorological conditions associated with ozone exceedances in the Basin?***

*Background*

Ozone levels in excess of the EPA 75 ppb 8-hour standard were observed in the Uinta Basin during the winters of 2009-2010, 2010-2011 and 2012-2013 but not during 2011-2012. Results from these four winter monitoring periods provide key insights into the meteorological conditions associated with the presence (or absence) of high winter ozone concentrations. Additional insight is provided by data collected in the Upper Green River Basin (UGRB) of southwestern Wyoming where exceedances of the ozone standard were first observed in February, 2005. The UGRB is a large oil and gas producing mountain basin located 250 km north of the Uinta Basin. Climatological conditions in the two basins are similar although the Upper Green River basin is higher in elevation (see Question A.5 below). Analyses of data from the Upper Green River Winter Ozone Study (UGWOS) indicated that ozone episodes occurred under clear skies during strong temperature inversions and in the presence of extensive snow cover (ENVIRON, 2008; Schnell et al., 2009; Stoeckenius and Ma, 2010). Comparisons of data collected in the UGRB during different winter seasons in which snow cover was and was not present indicate that snow cover is the key requirement for ozone formation. Box modeling of a winter ozone event based on UGWOS data (Nopmongcol et al., 2010; Carter and Seinfeld, 2012) indicate that the high UV albedo of the snow is one of the key drivers of ozone formation. In addition, it is hypothesized that snow cover promotes retention of the strong nocturnal surface temperature inversion during the day, thus trapping pollutants near the surface and increasing ozone precursor concentrations and ozone production rates. The snow surface could also influence the production and loss of chemical radical species necessary for ozone formation.

*Finding A.1.1: Snow cover and strong inversions with low mixed layer heights are required for formation of elevated winter ozone concentrations in the Uinta Basin. Meteorological conditions during the low ozone 2012 UBOS period differed from those in the previous two winters and during the 2013 UBOS period (all of which had high ozone) in that snow cover was not present.*

Ozone monitoring in the Uinta Basin first began during the 2009-2010 winter season and levels of ozone exceeding the 75 ppb 8-hour National Ambient Air Quality Standard were observed. Ozone exceedances were again recorded during January - March 2011 (Martin et al., 2011). In all cases, the ozone exceedances occurred during so-called “cold pool” events when stagnant weather conditions combined with extensive snow cover resulted in an extremely shallow

temperature inversion over the Basin which trapped pollutants near the surface (*ibid*). Similar conditions were observed during January – March 2013: several cold pool events with snow cover occurred during this period and these events coincided with strong temperature inversions and elevated ozone levels. Daily maximum 8-hour average ozone concentrations in the Basin during the 2013 UBOS period reached as high as 142 ppb at the Ouray monitor (which has among the highest readings in the Basin) as described in Section 3 below. In contrast, snow cover was nearly absent during the 2012 UBOS period, no exceedances of the 8-hour ozone NAAQS were observed and daily maximum 8-hour average ozone concentrations ranged from 47 to 63 ppb (2012SR, Figure 3). A comparison of ozone concentration, snow cover, and surface temperature and wind speed for January – March 2012 with the same period in 2013 shows the marked difference between these two years (Figure 2-3).

Mansfield and Hall (2012SR, Ch. VII) constructed pseudo temperature profiles by examining surface temperature readings from stations within and along the edge of the Basin located at different altitudes. This analysis showed that inversion conditions which occurred during 2011 were not present in 2012. Mansfield and Hall also performed a regression analysis based on ozone and meteorological data from 2009 – 2012 which confirmed the role of temperature inversions and snow depth in ozone formation. Their model also showed the influence of overnight carryover of ozone and ozone precursors: longer multi-day periods with inversions and snow cover are characterized by higher ozone levels than shorter periods. This is consistent with the build-up of ozone over multi-day episodes observed in 2013 (see Section 3, Figure 3-1).

*Finding A.1.2: High ozone episodes typically occur between January and March, with episodes occurring most frequently during February.*

Analysis of the 2009 – 2012 data by Mansfield and Hall (2012SR, Ch. VII) shows that, while the frequency and strength of temperature inversions in the Basin peaks in January, high ozone episodes appear to be most common in February (based on the limited observational record). Measurements made 1 November – 15 March 2013 are consistent with this pattern with no exceedance days prior to 7 January, 18 days exceeding the 8-hour standard at one or more sites in January vs. 22 days in February and 7 days in March. Mansfield and Hall hypothesize that this pattern is due to the rapid decrease in noon solar zenith angles following the winter solstice; angles do not become small enough to strongly drive the photochemical reactions until February. A similar effect was noted in the UGRB by Stoeckenius and Ma (2010). It should be noted, however, that preliminary data from winter 2013-14 show exceedances of the ozone standard at several monitors throughout the second half of December, indicating that high ozone levels can occur even when the solar zenith angle approaches its maximum at the winter solstice, so long as conditions are otherwise favorable. Analyses of indicator species ratios and other data show a trend towards higher ozone formation efficiency from December to March as solar zenith angles decrease and hours of daylight increase. This can impact total ozone production and the effectiveness of different emissions control strategies, as described in Section 3.1.3.5

*Conclusions*

Observations made during January – March in 2011, 2012 and 2013 clearly demonstrate that snow cover is a necessary condition for formation of winter ozone episodes in the Uinta Basin. Data from the 2011 and 2013 high ozone episodes and data from studies performed in the Upper Green River Basin show that ozone episodes are associated with snow cover, light winds, and strong temperature inversions, and are most common in February when the noon solar zenith angle has decreased sufficiently from its winter solstice maximum but snow cover is still more likely to be present.

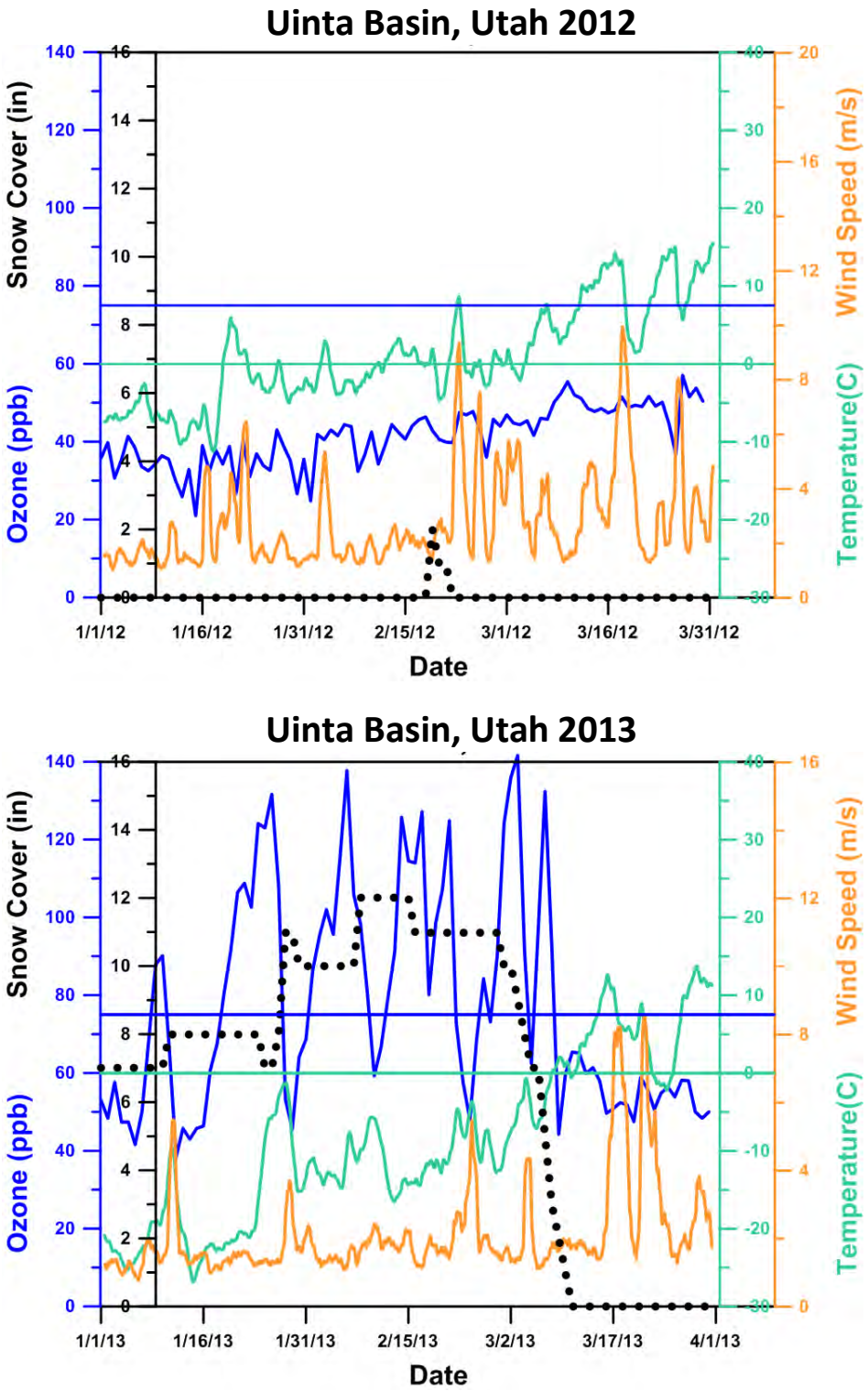


**Figure 2-3. Comparison of maximum daily 8-hr average ozone mixing ratio (MDA8) in ppb (blue), smoothed temperature (green) and wind speed (orange), and daily snow depth (black dots) from the EPA monitoring site at Ouray, Uinta Basin for January – March: 2012 (top) and 2013 (bottom); horizontal blue line represents 75 ppb ozone; horizontal green line represents 0 deg. C (Section 8).**

### *A.2: Were the high levels of wintertime ozone observed during the winters of 2009-2010, 2010-2011 and 2012-2013 a result of meteorology or changes in precursor emissions?*

*Background*

Day-to-day variations of ozone concentrations in most urban air basins have been shown to be dominated by meteorological factors (e.g., Solomon et al., 2000; NRC, 1991). Large oil and gas production areas such as exist in the Uinta basin consist of thousands of wells, all in varying phases of the production cycle (well pad construction, drilling, completion, production, recompletion, closure), each of which involve release of ozone precursor emissions that go on more or less regardless of meteorological conditions (aside from seasonal use of heaters and methanol to avoid freeze-ups). Thus, on a basin-wide level, day-to-day variations in emissions are expected to be small (with some important exceptions) and, as in the more extensively studied urban air basins, day to day variations in ozone concentrations are driven by meteorological conditions.

In rural areas where precursor emissions are dominated by oil and gas production and exploration activities, the level of certain key oil and gas production activities (most notably drilling and completions) can vary significantly from one year to the next in response to market forces. This can create significant fluctuations in precursor emissions and potentially lead to variations in ozone levels. Activity fluctuations on shorter time scales (monthly or seasonal) may also be significant. It must be noted, however, that ozone formation is a result of nonlinear chemical reactions between precursors and that, at high ratios of $NO_x$/VOC, NOx reductions can sometime cause increases in ozone. Therefore reductions (or increases) in $NO_x$ precursor emissions do not necessarily lead to reductions (or increases) in ozone concentrations.

*Finding A.2.1: While changes in precursor emissions between 2009 and 2013 in the Uinta Basin have not been quantified, the drop off in ozone concentrations in 2012 was not associated with a significant decrease in oil and gas production activities.*

Ozone precursor emission inventories representative of the 2010 - 2013 mid-winter seasons are not currently available. However, drilling and production data from the Utah Department of Natural Resources suggest that activity in in the Uinta Basin has held relatively steady and may actually have increased somewhat between 2010 and 2013 (Figure 2-4). Furthermore, no significant new emission control measures were introduced during this period. Given the overall level of oil and gas exploration and production activity in the basin, it is unlikely that the emission inventory would have changed so significantly as to account for the drop in ozone levels observed in 2012. On the other hand, the ozone differences between 2011 or 2013 and 2012 match closely with the occurrence of meteorological conditions (snow cover, strong temperature inversions, and light surface winds) found to be conducive to ozone formation as discussed under Question A.1 above.

*Conclusions*

Meteorological conditions are the primary driving factor behind the recent inter-annual variations in Uinta Basin ozone concentrations.

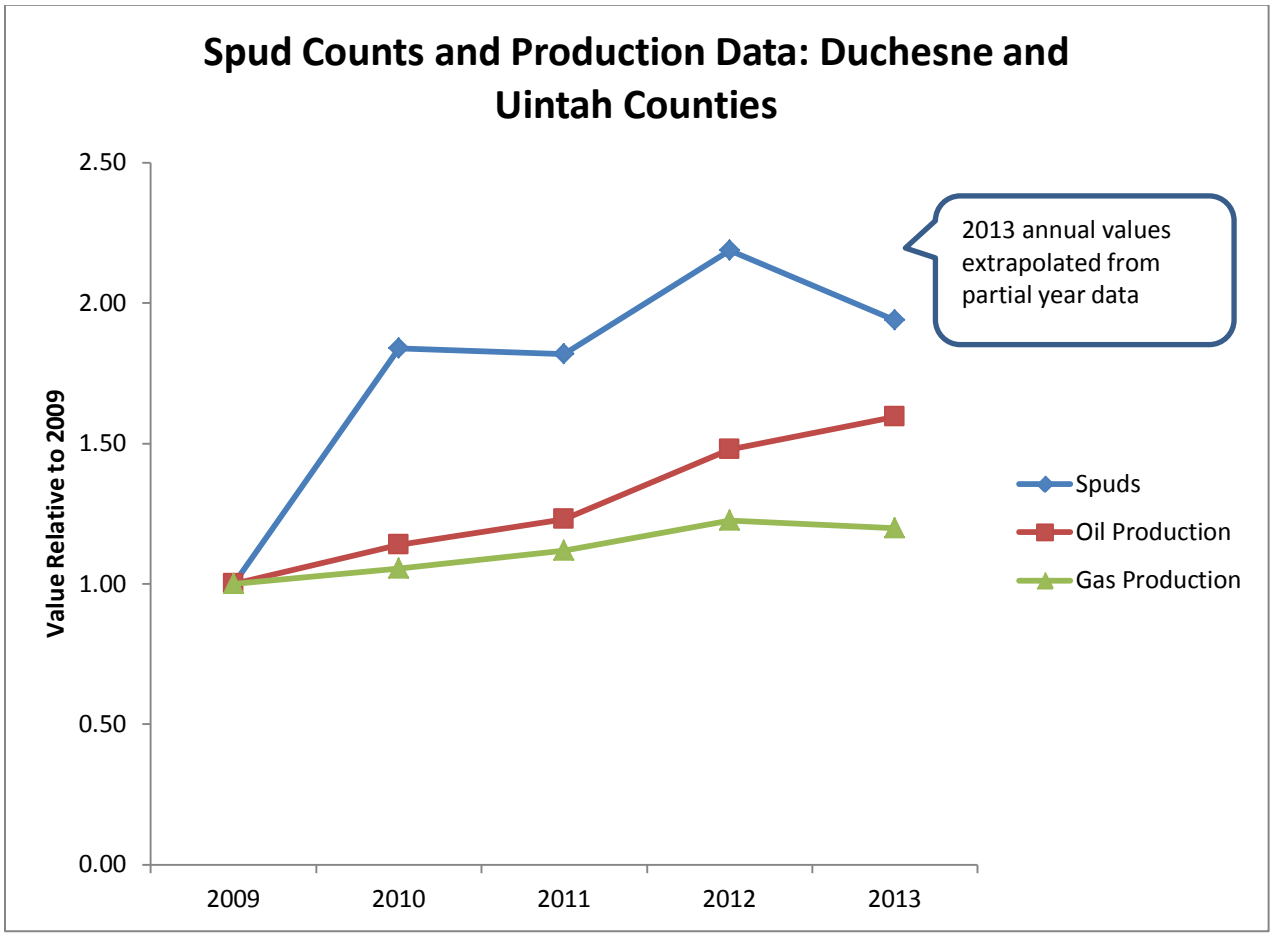


**Figure 2-4. Recent annual drilling and production activity trend in the Uinta Basin relative to 2009 (note 2013 spud counts [indicating number of wells where drilling was started] are extrapolated based on January – October data; 2013 production statistics are extrapolated based on January – June data; all data from the Utah Dept. of Natural Resources http://oilgas.ogm.utah.gov).**

***A.3: What is the climatological frequency of meteorological conditions that are conducive to ozone formation in the Uinta Basin?***

*Background*

Ozone concentrations in excess of the NAAQS were observed in the Uinta Basin during the first three months of 2010, 2011, and 2013 but concentrations were much lower in 2012. These inter-annual fluctuations have been demonstrated to be caused almost entirely by variations in the frequency and severity of meteorological conditions favorable to ozone formation (see responses to questions A.1 and A.2 above). A similar situation exists in the Upper Green River

Basin of southwestern Wyoming as illustrated in Figure 2-5: ozone NAAQS exceedances are observed in some years but concentrations remain well below the NAAQS in other years.

Attainment of the ozone NAAQS is based on a three year average of the annual fourth highest daily maximum 8-hour average concentration. Thus, the frequency of occurrence of meteorological conditions conducive to ozone formation plays a crucial role in determining the attainment status of the Basin. Estimates of the frequency of occurrence of ozone conducive conditions are also useful in planning future field studies.

*Finding A.3.1: Analyses of data from 1950 – 2012 indicates that ozone conducive conditions occur on at least some days during about half of all winter seasons, and ozone levels characteristic of a severe season such as the 2010-2011 season can be expected to occur approximately 20% of the time (an average of one in five seasons) given the level of precursor emissions characteristic of the past three seasons.*

Mansfield and Hall (2012SR, Ch. VII) performed an analysis of meteorological conditions in the Uinta Basin over the 63-year period 1950 – 2012 and estimated the historical frequency of meteorological conditions conducive to formation of elevated ozone levels. Mansfield and Hall developed a quadratic regression model that predicts the daily maximum 1-hour average ozone concentration at Ouray based on key meteorological parameters including but not limited to snow depth, low level temperature lapse rate and surface temperature at 1,400 m asl (representing the lowest point in the basin). The model was fitted to data from three consecutive mid-December to mid-March winter seasons starting with the 2009-2010 season (the first season for which ozone data were available). Model predictions of daily maximum ozone concentrations were then examined for the full 63-year meteorological data set to determine the predicted frequency of conditions associated with high ozone concentrations. Results of this analysis showed that, *assuming emission levels equivalent to the average levels occurring during the 2010, 2011, and 2012 winter seasons*, five out of the last 23 winter seasons (22%) are estimated to have had conditions at least as favorable to the formation of high ozone events as occurred during the high ozone winter of 2010-2011, whereas 7 out of the last 23 winter seasons (30%) are estimated to have had conditions at least as unfavorable to ozone formation as occurred during 2011-2012. In addition, the regression model results show that approximately half of all seasons had meteorological conditions capable of producing at least 10 days with 1-hour ozone exceeding 75 ppb. It must be noted, however, that these results are based on observations of the correlations between ozone and meteorological conditions over just three winter seasons (2010, 2011, and 2012); inclusion of 2013 data may alter the estimated frequencies of conditions conducive or not conducive to ozone episodes.

*Conclusions*

Based on the limited data currently available, meteorological conditions conducive to ozone exceedances of 75 ppb occur in approximately half of all winter seasons, although the high (low) ozone conditions in 2011 (2012) were the result of more extreme events corresponding to approximately the 20$^{th}$ (70$^{th}$) percentile years. These estimates may change when 2013 data

are included in the analysis. It is worth noting that ozone exceedances were recorded in the Basin in three of the last four winter seasons.

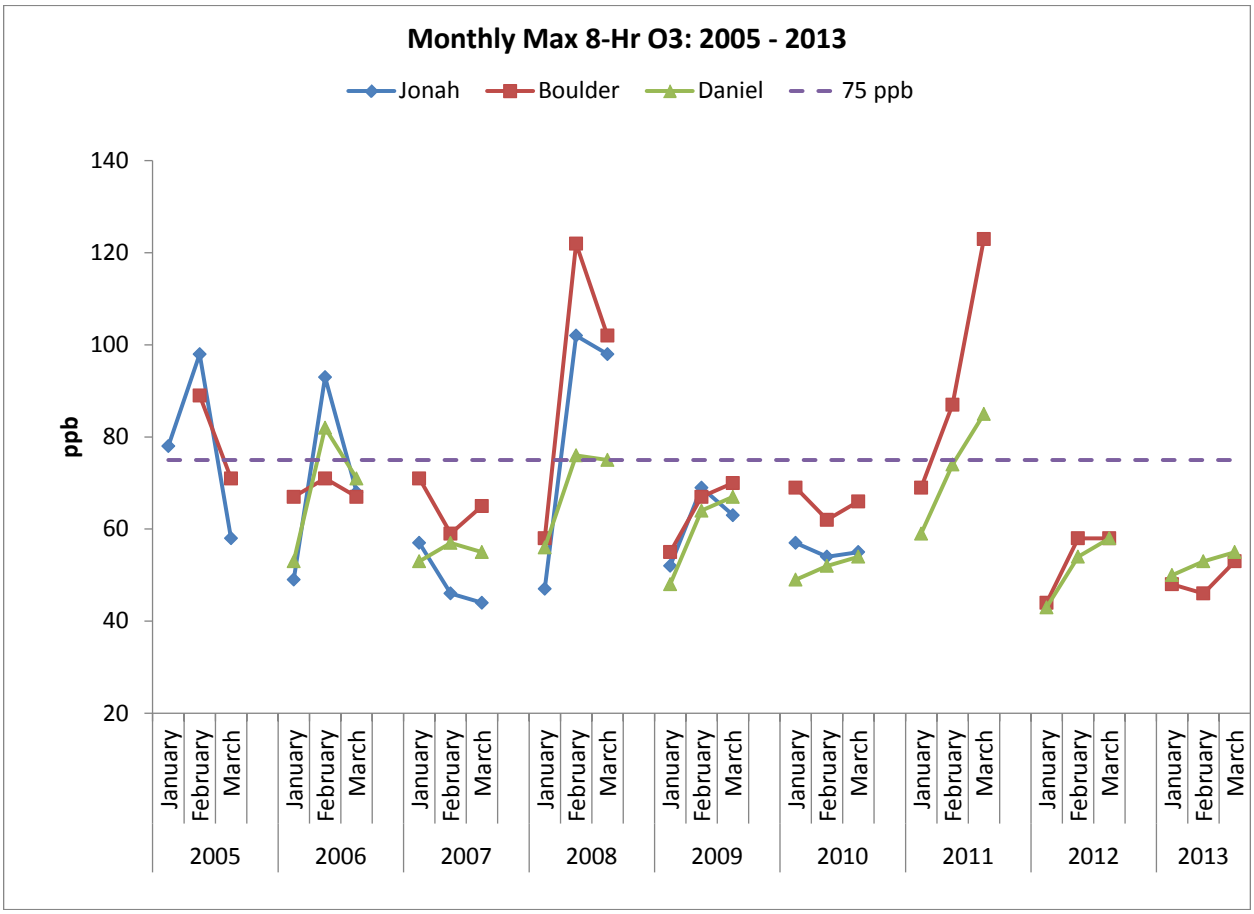


**Figure 2-5. Monthly maximum 8-hour average ozone concentrations during the winter ozone season at monitoring sites in the Upper Green River Basin of southwestern Wyoming.**

### *A.4: What role does transport of ozone or ozone precursors into the Basin play in generating elevated ozone concentrations?*

*Background*

Determining the relative contributions of sources located outside of the Basin to ozone episodes in the Basin is a fundamentally important step in designing an appropriate control strategy. While studies conducted to date have not specifically focused on the question of transport of ozone and precursors into the Uinta Basin, they do provide a considerable amount of information about the likely influence of transport on Basin air quality.

Regional background ozone measured at remote locations in the intermountain West have been reported by Vingarzan (2004) to range from 37 to 47 ppb (range of annual medians for Yellowstone and Rocky Mountain National Parks) and by Brodin et al. (2010) to range from 27 to 50 ppb (10th to 90th percentile range for wintertime near Boulder, Colorado). Ozonesonde

data collected well above the surface inversion during January through March 2008 in the UGRB showed concentrations ranging between 55 and 65 ppb (ENVIRON, 2008). In the absence of local production, ozone within the Uinta Basin is expected to be transported from global and regional sources, and concentrations are expected to fall within the range of these background values.

In evaluating the significance of the role of background ozone in local ozone episodes, it is important to keep in mind that local ozone production does not simply add to the pre-existing background ozone. Instead, local precursor emissions and resulting reaction products interact with background ozone and ozone precursors in complex ways. As a result, the contribution of background pollutants transported into the Basin to in-Basin ozone levels depends on the chemical conditions existing in the Basin and can be best evaluated using a photochemical model that accurately simulates ozone formation under winter conditions. Modeling tools such as Ozone Source Apportionment Technology (OSAT; ENVIRON, 2013) and sensitivity analyses such as the higher-order direct decoupled method (Hakami et al., 2003; Cohan et al., 2005) can then be used to evaluate the contributions of transported species to ozone production in the Basin.

*Finding A.4.1: The occurrence of high surface ozone concentrations within the Basin during UBOS 2013 cannot be attributed to transport of ozone or precursors from outside of the Basin. Strong evidence exists that the large majority of $NO_x$ and VOC in the Basin are emitted by local sources.*

Daytime ozone concentrations at regional locations outside of the Uinta Basin at the time of high surface ozone events inside the basin ranged from 30 to 60 ppb (see Figure 2-6). Ozone concentrations measured inside the Basin above the temperature inversion by balloon borne sensors, the TOPAZ lidar, and aircraft during these periods were also in the 40 to 60 ppb range as described in Sections 4, 5, 6 and 8. These values are consistent with the typical western US winter background ozone levels described above and confirm the isolation of the air mass within the Basin below the inversion from air outside of the Basin and over the Basin above the inversion.

The lack of any nearby precursor sources and the isolation of the surface air mass within the Basin from the surrounding region under the strong, shallow inversions characteristic of episode events strongly suggest that precursor transport into the basin is not an important factor (Martin et al., 2011). Measurements of alkanes (the least reactive and therefore longest lived VOC species) made at the upwind Fruitland monitoring site averaged far lower than at sites within the Basin proper (see Section 3). Aircraft measurements of methane above the temperature inversion during high ozone periods were close to hemispheric background levels as compared to the much higher values observed below the inversion (Section 4) and VOC concentrations in the Basin were observed to be highly correlated with methane (Section 5).

Meteorological data collected during UBOS 2013 showed the presence of light boundary layer winds and recirculation patterns within the Basin (Section 3), further confirming that ozone

formation within the shallow Basin boundary layer is not influenced to any significant extent by transport of material from outside the Basin.

*Conclusions*

Taken together, observations of the horizontal and vertical distributions of ozone, ozone precursors, and winds from the 2013 ozone episodes clearly show that ozone buildup within the Basin boundary layer to levels far above typical intermountain western US background levels is a local phenomenon which is not linked to any outside source.

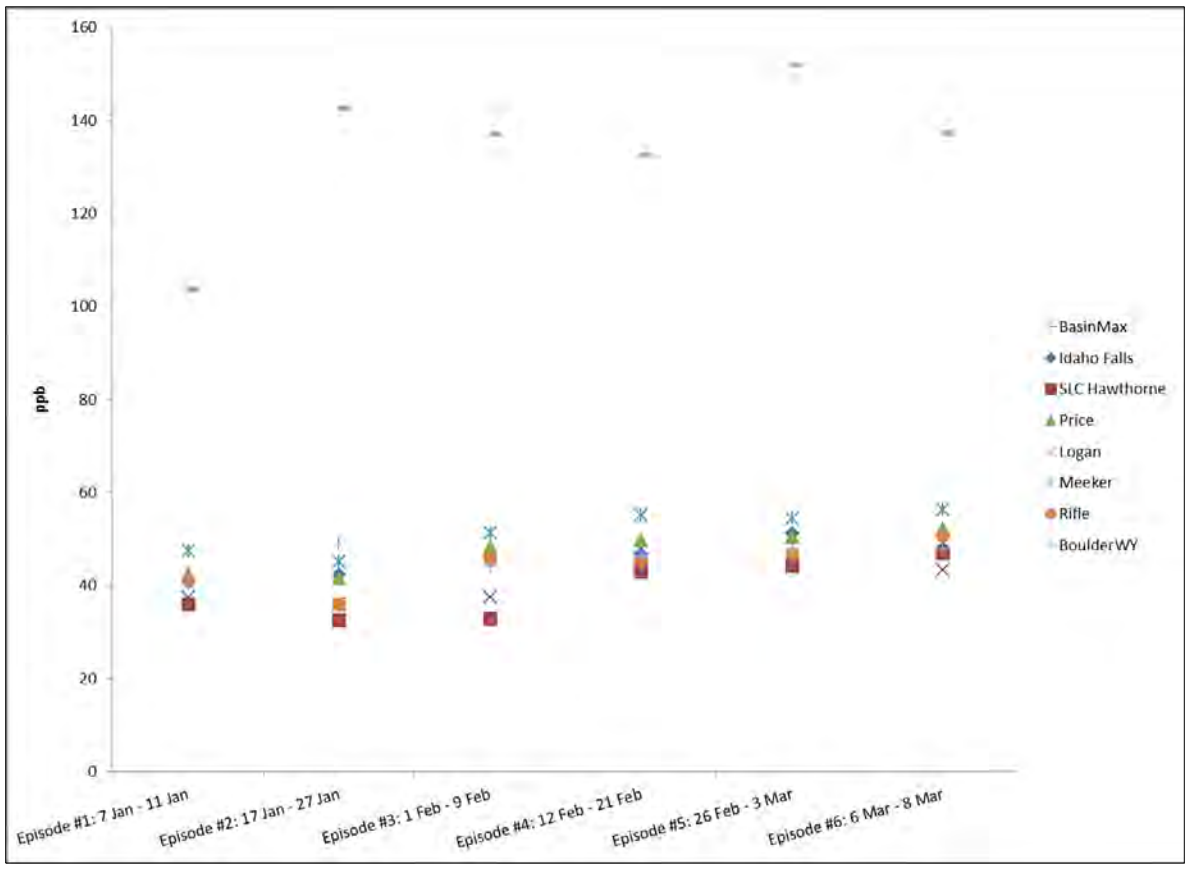


**Figure 2-6. Daily maximum 8-hour average ozone concentrations at locations outside of the Uinta Basin and the maximum concentration over sites within the Basin during each January – March 2013 ozone episode.**

### *A.5: What similarities and differences are there between the Uinta Basin and the Upper Green River Basin in Wyoming?*

*Background*

Winter ozone episodes have been observed in both the Upper Green and Uinta Basins and these basins share many similar features. Comparisons of conditions in the Upper Green River Basin (UGRB) with conditions in the Uinta Basin are therefore relevant to understanding the

factors associated with Uinta Basin ozone episodes. A significant amount of data collection and analysis has been conducted in the UGRB, and results from the UGRB studies can help inform the analysis of data collected in the Uinta Basin and guide future work in both basins.

*Finding A.5.1: Winter ozone episodes in the Uinta Basin and UGRB have many key characteristics in common and data collected in either location are likely to be informative of factors associated with episodes in both basins.*

Both the Uinta Basin and the UGRB are arid basins surrounded by higher terrain and located in sparsely populated portions of the Green River drainage (Figure 2-7). The two basins are separated by a distance of roughly 250 km and share a similar climate, although the UGRB is about 600 m higher in elevation and 2.5° more northerly in latitude than the Uinta Basin. The Uinta Basin is larger, covering approximately 27,700 $km^2$ compared to 18,700 $km^2$ for the UGRB. Both basins experience elevated ozone concentrations during winter cold pool events that can last up to several days at a time. Both basins contain intensive oil and gas exploration and production activity. However, oil production is greater in the Uinta Basin while gas production dominates in the UGRB (see Figure 2-8). The Uinta Basin contains about 8,000 active wells (Utah Department of Natural Resources; http://oilgas.ogm.utah.gov/Statistics/Statistics.cfm), the UGRB about 5,500 (WOGCC, 2012).

Annual emissions estimates from oil and gas activity in Duchesne and Uintah counties for 2011 are 17,838 tons of $NO_x$ and 111,289 tons of VOC (Section 9). By comparison, estimated annual oil and gas emissions in the UGRB ozone nonattainment area for 2011 are 4,558 tons of $NO_x$ and 15,688 tons of VOC (http://deq.state.wy.us/aqd/Actual%20Emissions.asp). It should be noted however that oil and gas emission estimates in general, and VOC emission estimates in particular, are subject to large uncertainties, making emission comparisons between the two basins less meaningful than they would otherwise be.

Populations in both basins are concentrated in small towns. Uintah and Duchesne counties have a combined population of 51,195 (1.8 people per $km^2$), while the population of Sublette County, Wyoming is 10,247 (0.5 people per $km^2$; from 2010 Census).

A review of field measurements, data analyses, and modeling results for the UGRB was prepared by Hall et al. (2012). These analyses clearly confirm the association of winter ozone episodes with snow cover, strong inversions, and light winds. Elevated ozone concentrations have not been observed in the UGRB in the absence of snow cover. Data collected during the 2011 and 2013 winter ozone episodes in the Uinta Basin (Martin et al., 2011 and this report) show that meteorological conditions during those events were very similar to those observed during UGRB ozone events with respect to the presence of snow cover, strong inversions, and light surface winds. Similar to the UGRB, data collected during UBOS 2011-12 showed little local ozone production in the absence of snow cover. During the 2012-13 winter, however, ozone levels were quite high in the Uinta Basin, with 8-hour average concentrations exceeding 75 ppb on many days as described in Section 3. In contrast, snow cover was much sparser and generally windy conditions prevailed in the UGRB, resulting in generally low ozone levels with no exceedances of the 75 ppb 8-hour standard (MSI, 2013).

Despite the similarities noted above, some important differences in the characteristics of ozone episodes exist between the two basins. Of particular importance is the fact that early season (December to mid-February) ozone episodes in the Uinta Basin have a characteristically longer time scale than in the UGRB, often exhibiting a gradual buildup of pollutant levels over a period of several days (Section 3, Figure 3-1). Although multi-day episodes do occur in the UGRB, episode lengths tend to be shorter (Hall et al., 2012). These differences are consistent with the larger size of the Uinta Basin which is hypothesized to result in a more persistent cold air pool. There also appears to be a slight shift in the winter ozone season between the two basins, with episodes more common in January and less common in late March in the Uinta Basin. This seasonal shift is likely associated with the 2.5° more southerly latitude and 600 m lower elevation of the Uinta Basin.

Despite the differences between the two basins noted above, the overall similarities of climate, emission sources, and winter ozone episode characteristics of the two air basins suggest that collection and analysis of field study data in either basin can provide valuable information applicable to both.

*Finding A.5.2: The Uinta Basin has some unique characteristics that will require development of an ozone control strategy designed specifically for the Basin.*

Some details of ozone production in the Uinta Basin are likely to be different from the UGRB. Given the greater amount of oil production in the Uinta Basin, VOC speciation and reactivity and VOC/$NO_x$ ratios are likely to differ between the two basins. As discussed in Section 3, the mix of VOC in oil-producing areas of the Uinta Basin is different than in the gas-producing areas; a higher alkane/aromatic ratio was observed at Wells Draw where oil production dominates as compared to Seven Sisters where gas production dominates. It should be noted that the presence of the 500-MW coal-fired Bonanza power plant within the Uinta Basin does not appear to be a factor in the basin's ozone production because the plume is lofted above the cold pool, which is isolated within the shallow boundary layer (as shown in Section 8). The UGRB does not contain a comparable large point source of $NO_x$ emissions, but this is not likely to be a differentiating factor. $NO_x$ emission sources and distribution are also different for the two basins. Data presented in Section 3 show less $NO_x$ in oil-producing than in gas-producing areas. The Uinta Basin has a higher population (and associated urban and traffic emissions) and significantly more agricultural production than the UGRB (Hall et al., 2012).

ENVIRON (2008) showed that ozone episodes in the UGRB are associated with recirculation of pollutants driven by a diurnal nighttime drainage and daytime upslope flow pattern. Measurements and analysis of surface flow patterns during 2013 Uinta Basin ozone events described in Section 3 also showed a similar diurnal pattern in the river drainages, but overall surface flow patterns were more complex due to the greater complexity in topography of the Uinta Basin and the larger size of the Basin, especially in the east-west dimension, which increases the influence of westerly winds aloft on surface flow patterns as described in Section 10.

*Conclusions*

Sufficient similarities between the Uinta Basin and the UGRB exist to support the application of data analysis results from one basin to gain a better understanding of ozone production dynamics in the other. Surface air flow and the mix of precursor emissions in the Uinta Basin, however, are different from the UGRB, and the design of emission control strategies for the Uinta Basin cannot rely solely on studies from the UGRB (or vice versa).

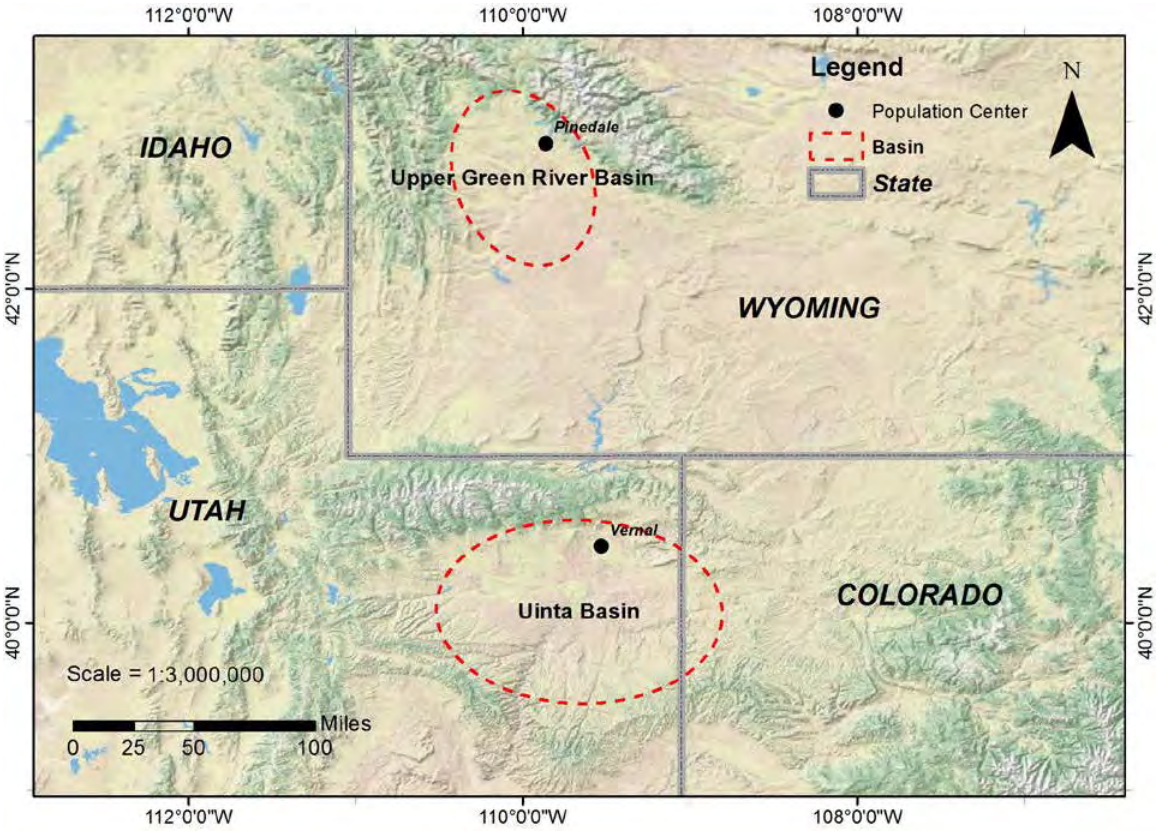


**Figure 2-7. Uinta and Upper Green River basins.**

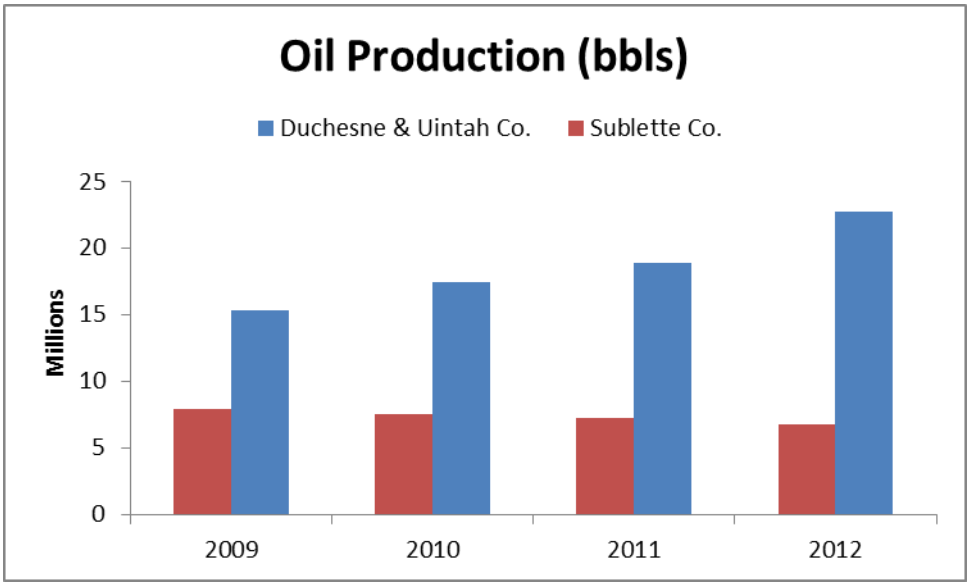


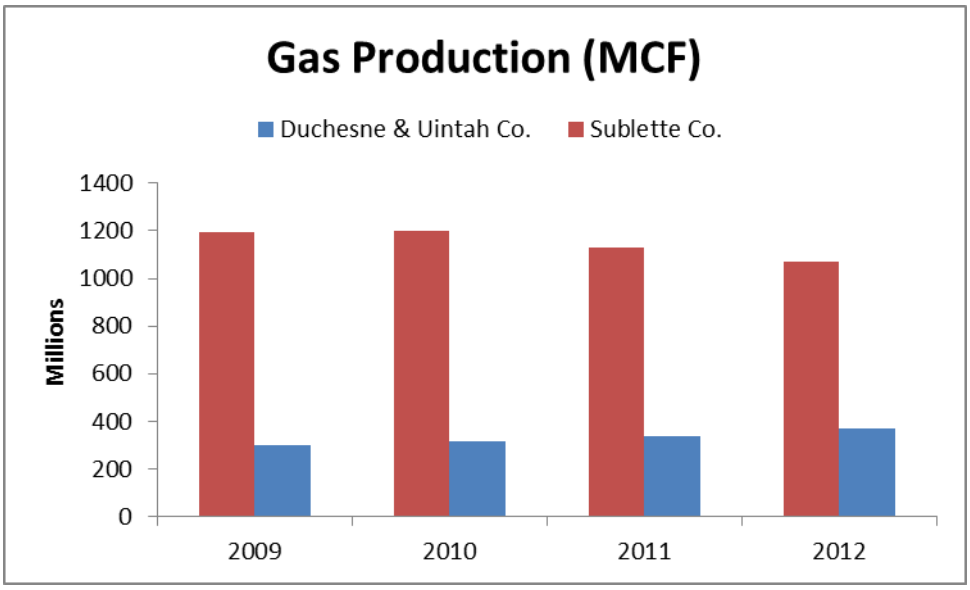


**Figure 2-8. Annual oil and gas production in the Uinta Basin (Duchesne and Uintah counties; Utah DOGM, 2013) and the Upper Green River Basin (Sublette County; WOGCC, 2013).**

***A.6: Is there significant vertical stratification of precursors and, if so, what role does this play in ozone formation?***

*Background*

VOC emissions in oil and gas production operations are expected to be released closer to the surface and to be less thermally buoyant than $NO_x$ emissions. While $NO_x$ emissions occur almost entirely from fuel combustion sources and are released as heated exhaust gasses at heights ranging from near surface (e.g., heaters and boilers, on- and off-road vehicles) to small-

or medium-sized stacks at stationary sources (e.g., compressor stations) to tall stacks (e.g., power plants), a large portion of VOC emissions are released from well sites or other equipment at approximately the same temperature as the surrounding air (Section 9). Some researchers have hypothesized the presence of a vertical stratification of VOC and $NO_x$ under the very stable atmospheric conditions characteristic of ozone episodes. Any resulting vertical gradients in VOC/$NO_x$ ratios would produce vertical variations in ozone production and destruction rates and could impact ozone responses to emission control strategies. For example, ozone formation during the morning hours may proceed more rapidly at locations and elevations with optimal VOC/$NO_x$ ratios, and these rapidly formed ozone plumes could later impact downwind monitoring stations after being mixed to the surface during the late morning and afternoon. Knowledge of any such vertical stratification is needed to fully explain and accurately model the pattern of ozone and precursors observed over surface monitoring networks and the impacts of alternative emission control strategies.

*Finding A.6.1: Vertical gradients in ozone precursors were observed at Horsepool.*

Measurements of $NO_x$ and speciated VOC at four levels between 2 m and 150 m at Horsepool are consistent with near surface sources of VOCs and $NO_x$, although $NO_x$ appears to be somewhat more evenly mixed within the first 50 m as shown in Figures 6-8 and 6-11 in Section 6. $NO_x$ may be more evenly mixed because sources of $NO_x$ emissions are of varying heights and some plume rise from these sources can be expected. However, the $NO_x$ measurement used to obtain these vertical profiles is also known to suffer from a positive bias due to interference from $NO_z$ species formed in the atmosphere from $NO_x$ emissions, and $NO_z$ can be expected to be more well mixed than the primary $NO_x$. High-resolution time series of both VOC and $NO_x$ measurements, as well as for methane, show numerous short-period spikes consistent with impacts at Horsepool from multiple point sources of both pollutants (Section 5). Vertical profiles of VOC/$NO_x$ ratios were not analyzed. However, vertical ozone profiles from the tethersonde measurements made during UBOS 2013 show ozone formation taking place simultaneously at all vertical levels within an approximately 80 m deep layer as shown in Figure 2-9 (see also Section 8, Figures 8-34 – 8-40), indicating that any vertical variations in precursors do not appear to have resulted in any significant vertical stratification of ozone. These findings are consistent with either a rapid mixing (at least on the timescale of ozone formation) within an approximately 80 m deep daytime turbulent boundary layer at Horsepool (based on the observed 1650 m asl mixed layer top and 1569 m asl Horsepool site elevation), even during the cold pool events as shown in Section 8, a constant rate of ozone formation throughout the mixed layer, or both.

*Finding A.6.2: Available data combined with one dimensional modeling employing reasonable assumptions suggests that high daytime HONO concentrations, if real, are most likely confined to a very shallow layer, at most a few tens of meters deep.*

Measurements of HONO during 2013 ozone episode conditions between 1 and 7.25 m agl showed high concentrations correlated with solar radiation intensity as described in Section 5, consistent with a photochemically driven source, although the validity of these measurements is still uncertain. Concentrations at 7.25 m were consistently lower than at 1 m during the day,

whereas the opposite was true at night (see Section 5, Figure 5-35), indicating the presence of a daytime photochemical source of HONO from the snow surface and HONO loss at the surface overnight. Application of a simple 1-dimensional model of turbulent vertical diffusion and HONO loss via photodissociation suggests that, even if they are correct, the high daytime HONO concentrations drop off rapidly with height, approaching very small values within a few tens of meters above the surface. A more detailed examination of vertical ozone profiles is needed to determine if these measurements are valid and if there is a discernible effect of this shallow HONO layer on ozone formation.

*Conclusions*

There is no strong evidence to suggest that the vertical profiles of VOCs and $NO_x$ within the polluted boundary layer differ significantly enough to impact ozone formation. This conclusion is supported by the observation of near uniform morning ozone production throughout the boundary layer seen in the tethersonde data. There is evidence of stratification of $NO_x$ from the Bonanza plume above the inversion layer and associated ozone titration as shown in Sections 4, 5, and 8, but this does not affect the high ozone concentrations observed within the polluted boundary layer.

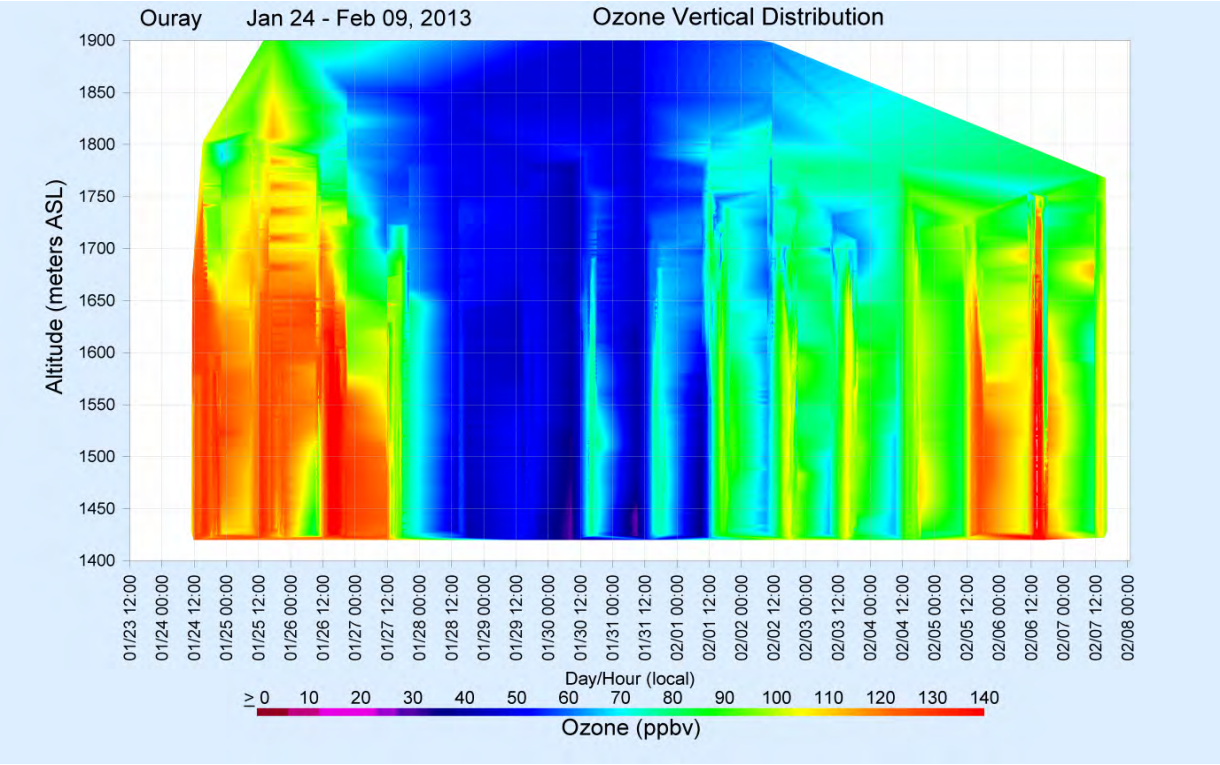


**Figure 2-9. Contour plot of ozone concentrations above the Ouray Wildlife Refuge January 24 - February 7 based on thethersonde data (see Section 8).**

## 2.3 Part B: Atmospheric Chemistry of Ozone Formation

### *B.1: Do VOC speciation and reactivity in the Basin have unique characteristics that contribute to wintertime ozone production?*

*Background*

VOC emissions from oil and gas exploration and production activities result from releases of natural gas (e.g., venting, blowdowns, pneumatic device bleeding), evaporative emissions from gas processing (dehydration and sweetening), and produced liquids handling and storage, as well as oil handling and storage and a variety of combustion sources. These sources have very different VOC speciation profiles from VOC sources typically found in large urban areas. Due to the widely differing reactivities of individual VOC species, variations in VOC composition can have significant impacts on ozone formation and the relative efficacy of VOC and $NO_x$ control strategies. A thorough understanding of VOC speciation in the Uinta Basin and of the reactivities of VOC species under winter ozone episode conditions is therefore an important prerequisite to the design of effective ozone control strategies.

*Finding B.1.1: Observed hydrocarbon species abundances at most locations sampled in the Uinta Basin differ significantly from those found in large urban areas, but are similar to those found in other western U.S. oil and gas production regions.*

Methane concentrations in the Uinta Basin were often eight times above background values in 2013 as compared to as much as five times above background in 2012 (Section 6). Elevated methane has also been observed in the UGRB (ENVIRON, 2008) and the Denver – Julesburg Basin (Petron et al., 2012). Urban area methane levels are significantly lower than in the oil and gas basins. Natural gas NMHC speciation is heavily weighted towards ethane and other light alkanes, resulting in an ambient NMHC mixture in the gas fields that is markedly different from mixtures typically encountered in large urban areas. Data collected during UBOS 2012 and 2013, as well as in the UGRB, show that NMHC emissions throughout the basin are strongly influenced by fugitive releases of natural gas as evidenced by high methane levels and strong correlations of alkanes with methane (see Section 5). Resulting NMHC compositions in the Uinta Basin are thus very different from those in typical urban areas such as Pasadena, CA as shown in Figure 2-10. Concentrations of iso-pentane and n-pentane were much higher at Horsepool than in the Pasadena samples and are more similar to samples collected by NOAA researchers in Weld County, Colorado, in the Wattenberg Gas Field (Figure 2-12). In addition, ratios of iso- to n-pentane at Horsepool were significantly lower than in the Pasadena samples. As pointed out in 2012SR, the Horsepool and Weld County ratios are similar to iso- to n-pentane ratios found in Wattenberg gas composition analyses, whereas the Pasadena ratio is similar to that of light duty vehicle exhaust. Detailed raw gas composition analyses for the Uinta Basin are needed to validate these findings, and comparisons with NMHC speciation in the UGRB are needed.

High methanol concentrations were observed at Horsepool and spikes in methanol levels were correlated with spikes in formaldehyde (see SR2012). Further data collection and analysis is needed in the UGRB to determine if similar conditions exist there.

While the Uinta basin data in Figure 2-10 are from 2012, the 2013 NMHC composition for directly emitted species was very similar to that in 2012, but most species concentrations in 2013 were enhanced by a factor of 1.5 to 3.5 due to the much shallower boundary layer in 2013 as compared to 2012. This was also true for methanol and formaldehyde as shown in Figure 2-11, but other secondary VOC oxidation products such as acetone, acetaldehyde, and methyl ethyl ketone (MEK) levels were 8 to 12 times higher in 2013, consistent with a greater production rate of these oxygenated VOCs as a result of enhanced photochemical activity in 2013.

Analysis of NMHC samples collected during UBOS 2013 at different locations in the Basin (Section 3) showed that aromatics were enriched relative to alkanes at locations in the gas field (Seven Sisters) as compared to the oil field (Wells Draw). Methanol concentrations were also highest in the gas field as measured at Horsepool and Seven Sisters. Based on higher total NMHC concentrations, greater aromatic fraction and methanol, the overall reactivity of NMHCs in the gas field is higher than in the oil field (Section 3, Table 3-4).

*Conclusions*

Data collected over the past two winters in the Uinta Basin show that the characteristics of the VOC mixture in the Basin are very different from those found in urban areas. VOCs in the Basin are dominated by relatively unreactive alkanes associated with natural gas exploration and production sources as is the case in other oil and gas producing basins. NMHC concentrations reach high levels in areas of the Basin with many active wells; concentrations of alkanes at Horsepool during the 2013 study were roughly a factor of two higher in 2013 than in 2012 (see Sec. 5, Figure 5-16). Results from the 2012 study (2012SR) showed that concentrations of alkane, cycloalkane, and aromatic VOCs in the Basin were an average of 6.5 times higher than those in Weld County, Colorado, an area with intensive oil and gas production and that $C_2 – C_8$ alkanes and $C_6 – C_8$ aromatics during the 2012 study averaged 18 times higher than the average mixing ratios for 25 U.S. cities reported by Baker et al. (2008). Thus, concentrations of alkanes and aromatics averaged on the order of 10 times higher during 2013 in the Basin as compared to Weld County and roughly 40 times higher than in other U.S. urban areas. Alkanes at Horsepool during the 2013 study were hundreds of times above global background levels (see Section 6, Table 6-1). In contrast, highly reactive alkenes are nearly absent in the Basin, which is in sharp contrast to typical urban VOC mixtures where gasoline powered motor vehicles and other combustion and evaporative sources of alkenes are more common. Thus, ozone production in the Basin appears to be dominated by the relatively slow reactions involving alkanes (see summary of MIR-weighted concentrations in Section 3, Table 3-4 and OH-reactivity weighted abundances in Section 5, Figure 5-13). High methanol concentrations are also observed in the Uinta Basin and methanol concentration spikes are correlated with formaldehyde spikes indicating a common source. Formaldehyde was found to be a key contributor to radical production as discussed in Finding B.2.1 below, so identifying and quantifying formaldehyde sources is important for development of ozone control strategies.

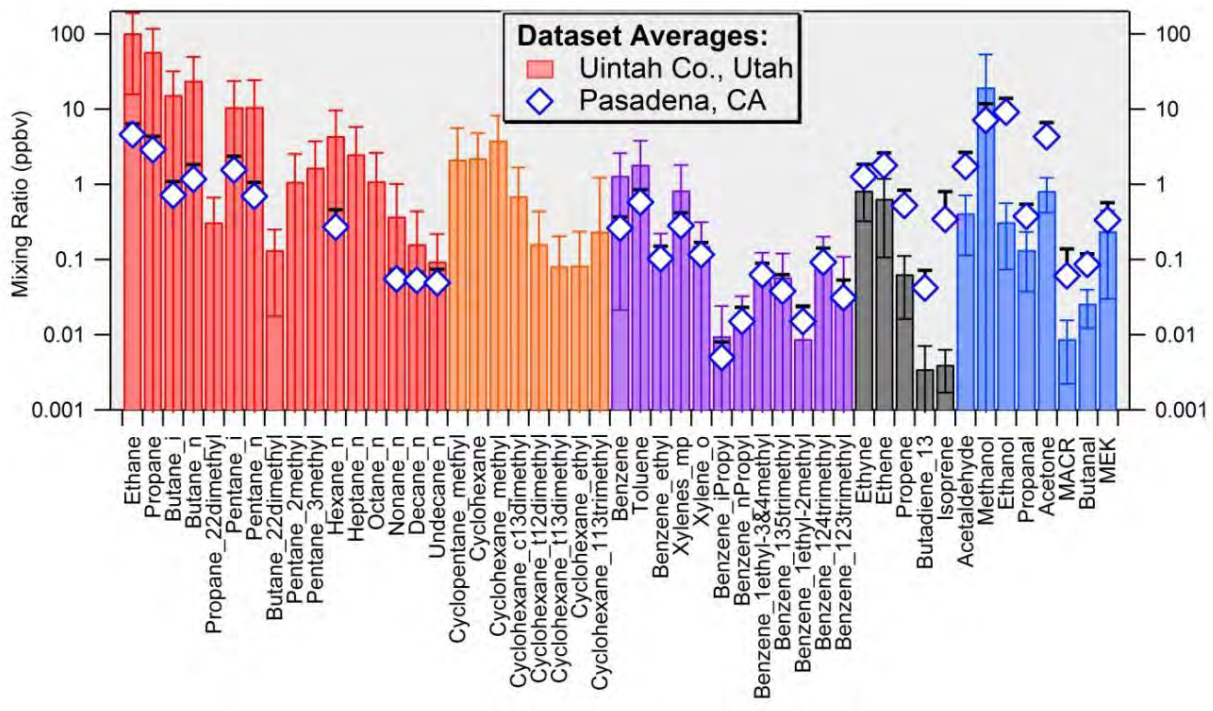


**Figure 2-10. Mean mixing ratios collected during 15 January – 29 February, 2012 at Horsepool and during May – June 2010 at Pasadena, CA (Source: 2012SR).**

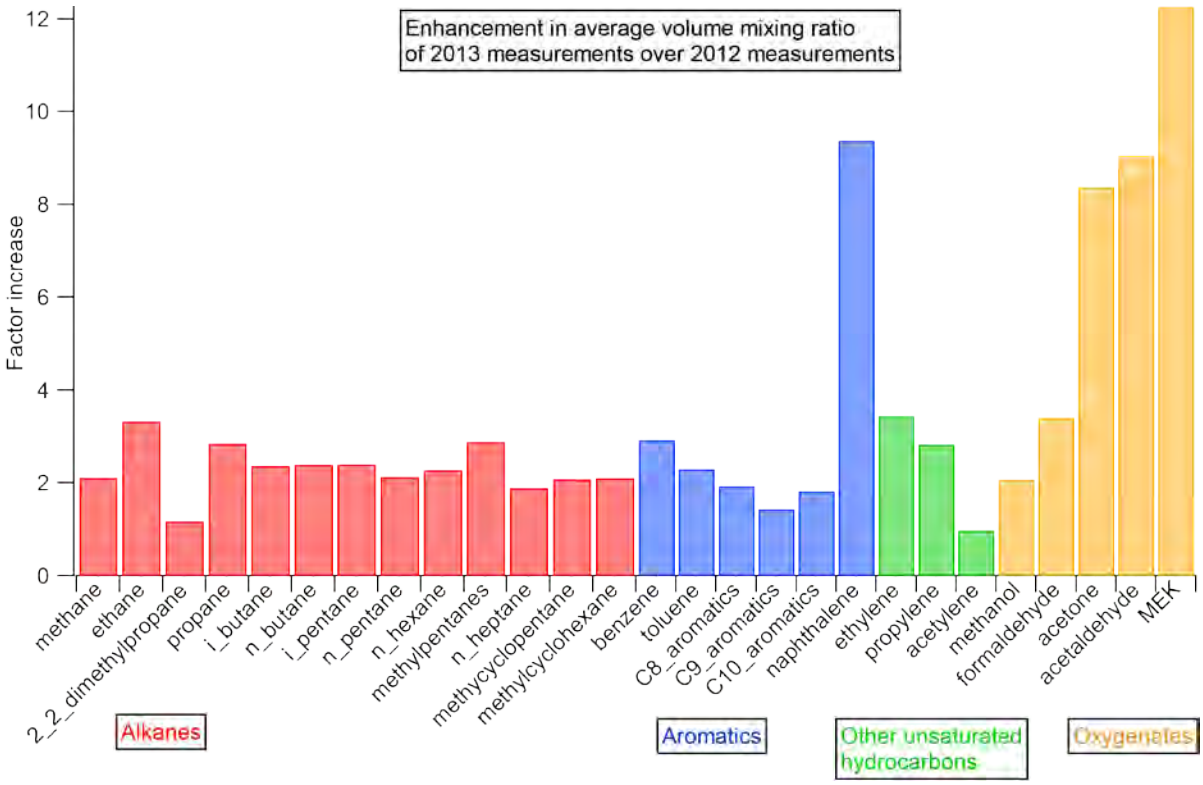


**Figure 2-11. Fractional increase in all measured VOCs at Horsepool from 2012 to 2013 (see Section 5).**

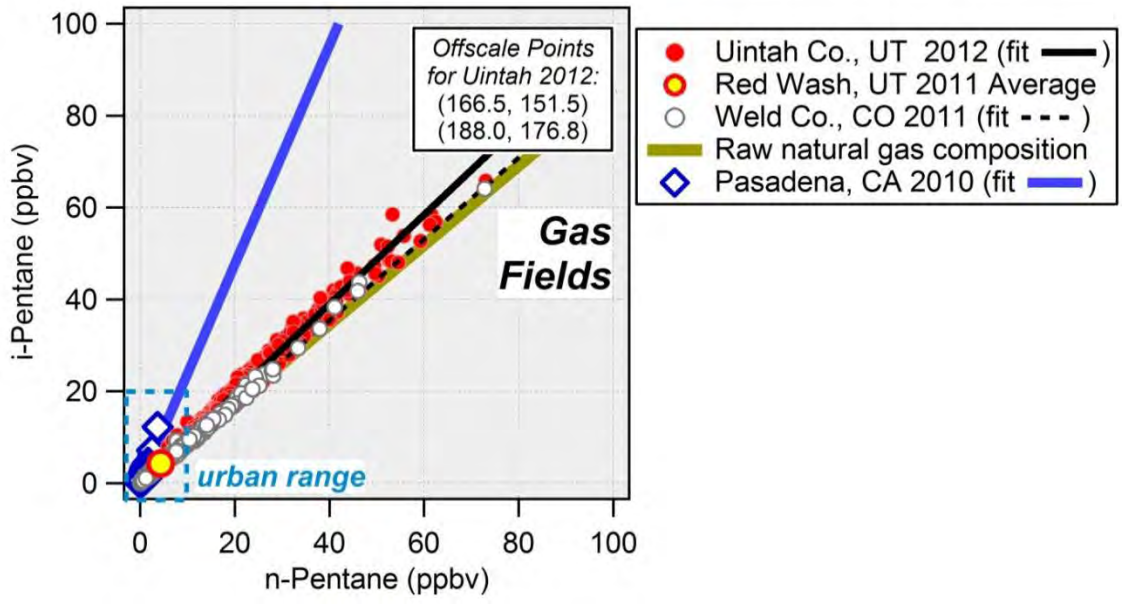


**Figure 2-12. Iso-pentane to n-pentane ratios from data collected during 15 January – 29 February 2012 at Horsepool, during 21 – 25 February 2011 at Red Wash, during 2011 in Weld County, CO, and during May-June 2010 in Pasadena, CA (source: 2012SR).**

### *B.2: Do pathways for ozone production exist that are unique to wintertime ozone events?*

*Background*

Our current understanding of ozone formation processes in polluted environments is based mostly on summertime ozone episodes occurring in large urban areas. Comparatively little is known about winter ozone formation in rural areas where the emissions budget is heavily influenced by oil and gas exploration and production activities. Studies of winter ozone episodes in the UGRB have shown that these winter episodes are associated with snow cover and very stable "cold pool" atmospheric conditions, and that ozone formation under these conditions is largely driven by the strong actinic UV flux resulting from the high albedo of the snow surface and the elevated concentrations of precursor pollutants trapped under the low level temperature inversion (ENVIRON, 2008; Schnell et al., 2009; Stoeckenius and Ma, 2010). Analyses of field study data and photochemical box modeling studies performed to date (Nopmongcol et al., 2010; Martin et al., 2011; Carter and Seinfeld, 2012) suggest that these two factors are key to the production of elevated winter ozone concentrations. In this respect, winter episodes are no different from summer episodes; both require a high UV flux, stable atmospheric conditions, and adequate concentrations of precursors. Recent studies suggest, however, that there may be some significant unique features of winter episode chemistry in the Upper Green River and Uinta basins which set these winter episodes apart from those occurring during the summer months in urban areas.

Winter conditions in the Uinta Basin and UGRB differ from urban summer conditions primarily with respect to temperature, VOC composition, and the presence of snow on the ground. As a result of these key differences, modeling techniques traditionally used to evaluate potential control strategies for reduction of summer urban ozone levels may not work well for analysis of winter ozone.

In general, low winter temperatures decrease chemical reaction rates, alter the branching of some key reactions, and reduce volatility, though the effect of temperature on some reaction rates is not fully understood (2012SR, Section 7; Martin et al., 2011; Carter and Seinfeld, 2012). Low temperatures also limit water vapor mixing ratios; for example, the water vapor mixing ratio at 0°C, 50% humidity, and atmospheric pressure of 850 mbar is 2 g/kg, compared to more than 15 g/kg at 30°C and 50% humidity. A major pathway for the production of OH radicals in summer urban ozone episodes is photolysis of ozone followed by reaction of the freed oxygen atom with water vapor. Less water vapor in the atmosphere will limit OH production from that pathway.

VOC composition in the winter ozone basins is heavily skewed towards alkanes associated with raw natural gas as compared to more common fuel combustion and evaporative profiles found under warmer conditions in urban areas as described under Question B.1 above. Significant amounts of methanol (which may additionally be contaminated with formaldehyde) have also been found in the winter ozone basins, reflecting its use as an antifreeze agent in oil & gas operations. In addition, methane concentrations are well above levels found in urban areas.

Finally, the snow surface has many chemical properties which differ from surfaces typical of urban areas in the summer. Analyses of data from pristine remote environments (Greenland and Antarctica) have identified sources of alkenes and $NO_x$ within snow that appear to evolve via heterogeneous photochemistry (Swanson et al., 2002; Helmig et al., 2007). Heterogeneous reactions on snow surfaces could contribute to winter ozone formation. For example, elevated mid-day HONO concentrations over snow have been reported in the UGRB (ENVIRON, 2010; Rappenglueck, 2010). This finding is consistent with a hypothesized mechanism of formation of HONO from nitrites found in the snow in the presence of sunlight (Grannas et al., 2010). Daytime heterogeneous HONO production has the potential to significantly increase peak ozone concentrations under VOC limited conditions.

*Finding B.2.1: The dominant sources of radicals that drive ozone production during winter episodes in the Uinta Basin are formaldehyde and HONO rather than ozone photolysis, as is typical of summer urban area episodes. The magnitude of the HONO source during the winter episodes is still uncertain.*

Analyses of measurements conducted at the Horsepool site in 2013 and comparisons with similar measurements taken during the 2012 study reveal several key features that are unique to winter ozone chemistry. Foremost among these is the report of high daytime concentrations of a species that is apparently HONO at levels between 1 and 7.25 m above the ground during the 2013 episodes. The average concentration in 2013 was ten times the 2012 average when snow was absent. The average concentration in 2013 was well in excess of the steady state concentration of HONO expected from reaction of NO with OH radical, indicating the presence of a strong source. Diurnal profiles showed peaking during the middle of the day in 2013 in sharp contrast to the night and early morning peaks found in 2012 (see Figure 2-13). Analysis of the 1 – 7.25 m gradient in the apparent HONO in 2013 showed that the species generally decreases with height during the day and increases with height at night. These results are consistent with a photochemical source of HONO in the snow; estimates of the maximum surface HONO flux (3.6 ppbv/hr) developed as described in Section 5 are on the same order of magnitude as an estimate of 2.25 ppbv/hr developed by Rappenglück, based on measurements during winter ozone episodes in the UGRB (Rappenglück et al., 2013).

Calculations of radical production rates from photolysis of ozone, HONO, HCHO, and $ClNO_2$ described in Section 5 show that HONO and HCHO were the dominant radical sources during the 2013 study. This is in sharp contrast to urban summer conditions observed in Pasadena, CA during the CALNEXT 2010 study where radical production was more balanced between photolysis of ozone, HONO, and HCHO (see Figure 2-14). This makes the winter ozone episodes "unconventional" in the sense that radical production (which is the key driving factor in ozone production) is largely due to HONO and HCHO photolysis rather than ozone photolysis, and this unconventional feature of the winter episodes must be accurately represented in models used to evaluate control strategies.

As noted in Section 5, the large contribution of HONO photolysis to OH radical production calculated for the 2013 Uinta Basin episodes is based on HONO concentrations measured at 7.25 m agl. However, calculations based on a 1-dimensional model under reasonable

assumptions described in Section 5 indicate that the high HONO concentrations are most likely confined to a shallow layer above the surface no more than on the order of 10 m deep. Thus, it appears very likely that average HONO within the ~150 m deep mixed layer are much lower due to a rapid decrease of HONO with height and the HONO radical production rate would therefore be lower than shown in Figure 2-14. Nevertheless, the combination of HONO and HCHO photolysis is clearly the main radical source during winter episodes, and this has significant implications for control strategies. Production from $ClNO_2$ was lower in the Uinta Basin in 2013 as compared to 2012, most likely because the snow cover helped suppress the availability of Cl from soil dust.

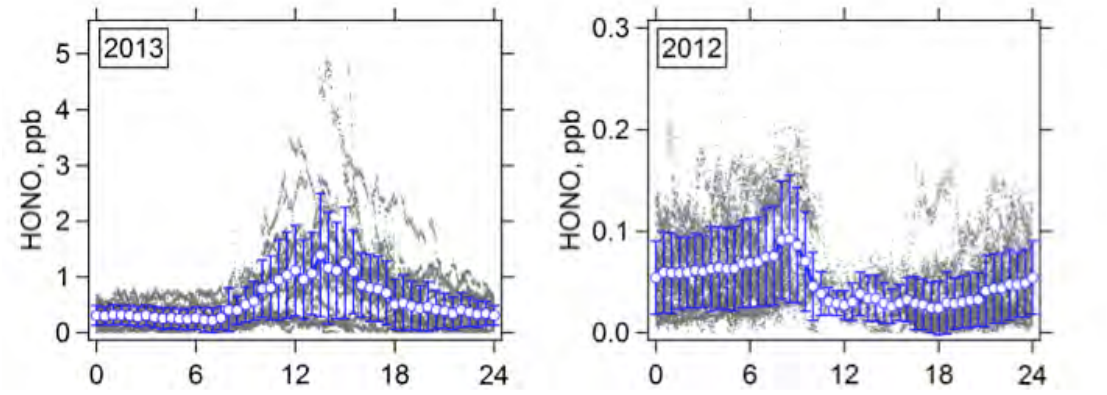


**Figure 2-13. Diurnal variations of a species that is apparently HONO in 2012 and 2013 at Horsepool (Source: Sec. 5).**

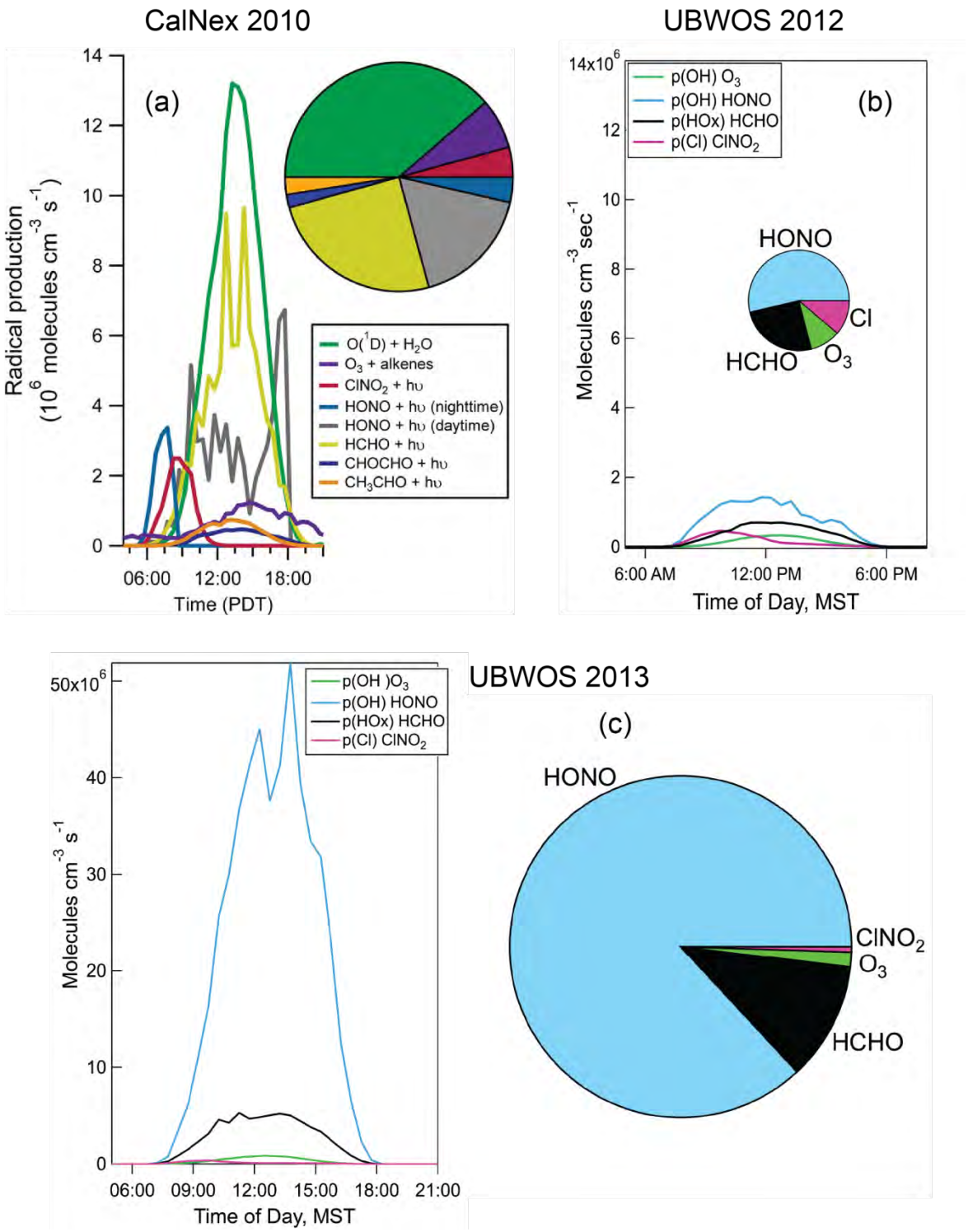


**Figure 2-14. Summaries of the radical sources found during (a) CalNex2010, (b) UBOS 2012, and (c) UBOS 2013. Note that the CalNex and UBOS 2012 results are on the same scale, HONO (HCHO) is shown in light blue (black) in (b) and (c) but in medium blue and gray (yellow) in (a) and the areas of the pie charts are scaled to the total of the radical sources (Source: Sec. 5).**

*Finding B.2.2: Nighttime conversion of $NO_x$ to $HNO_3$ is a major factor in the total reactive nitrogen budget and nitrate deposited on the snow and particle surfaces may possibly be an important source of daytime HONO production.*

An understanding of the reactive nitrogen budget is an important prerequisite for designing an effective ozone control strategy. $NO_x$ emissions from combustion sources take part in the photochemical reactions that form ozone and are processed over the course of the day into other odd nitrogen species including HONO, $HNO_3$, PAN and $RONO_2$. In addition, $N_2O_5$ and $ClNO_2$ are formed at night. These $NO_x$ production species are collectively referred to as $NO_z$.

While $NO_x$ concentrations at Horsepool during 2013 were similar to those observed during 2012, $NO_y$ concentrations were significantly higher, indicating a much higher degree of photochemical processing of $NO_x$ during 2013. The major $NO_z$ (operationally defined as $NO_y$ minus $NO_x$) species observed in 2013 were $HNO_3$ and PANs with some contribution from HONO during the daylight hours. Concentrations of $HNO_3$ were observed to be eight times higher in 2013 as compared to 2012 at Horsepool (see Section 5, Figure 5-33), and nitrate and nitrite concentrations in the top 1 cm of snow increased with time after fresh snow was deposited (see Section 5, Figure 5-39). Daytime HONO production in the snow surface, if real, is possibly linked to $HNO_3$ deposition as described under Finding B.2.1 above. The resulting recycling of $NO_y$ species into $NO_x$ makes $NO_x$ controls less effective for ozone reduction than would otherwise be the case.

*Conclusions*

Results from UBOS 2013 reveal several aspects of ozone formation chemistry unique to winter events. Formaldehyde, and to an unknown extent HONO, were found to be the biggest contributors to the pool of chemical radicals responsible for ozone formation, rather than the traditional radical source, photolysis of $O_3$ itself. However, the quantitative contribution of HONO to the radical pool is uncertain at this time because of uncertainties in the HONO measurement and because the high HONO concentrations observed up to 7.25 m agl, which were used as the basis for the radical production estimates, may not be valid, and, even if they are valid, most likely do not extend throughout the mixed layer. Better estimates of the daytime HONO concentrations, vertical profile, and source term as well as a more complete understanding of the sensitivity of this source to $NO_x$ emissions are a critical requirement for development of useful models of winter ozone formation.

## 2.4 Part C: Sources of Ozone Precursor Emissions

### *C.1: What are the primary sources of ozone precursor emissions in the Basin? What is the spatial distribution of precursor sources?*

*Background*

Ozone precursor emissions in the Uinta Basin are associated with a variety of sources. Oil and gas extraction activities dominate. Associated sources include gas plants, compressors, well site sources (drill rigs, frac pumps, pump jacks, tanks, dehydrators, fugitives, etc.), pipelines, on-road and non-road mobile sources, produced water evaporation ponds, reserve pits, and other

miscellaneous sources (Figure 2-15). Other anthropogenic emissions consist of typical urban (residential, commercial, and light industrial) source emissions associated with the approximately 50,000 Basin residents, agricultural activities, a 500 Megawatt coal-fired electric generation unit (the Bonanza plant), and phosphate and gilsonite mining. Non-anthropogenic emissions in the Basin include biogenic emissions of isoprene and other VOC and natural hydrocarbon seeps.

A complete and accurate emissions inventory is a fundamental component of air quality management, and is vital to the development of an accurate photochemical model simulation for use in ozone control strategy design. Uncertainties in emission totals and the spatial and temporal patterns of emissions are a significant source of potential errors in model predictions. Emission inventories should therefore be evaluated for consistency with available independent data sources. For example, ratios of key species in the inventory should match ratios obtained from ambient measurements and any discrepancies should be investigated before the inventory is used as the basis for making major regulatory decisions.

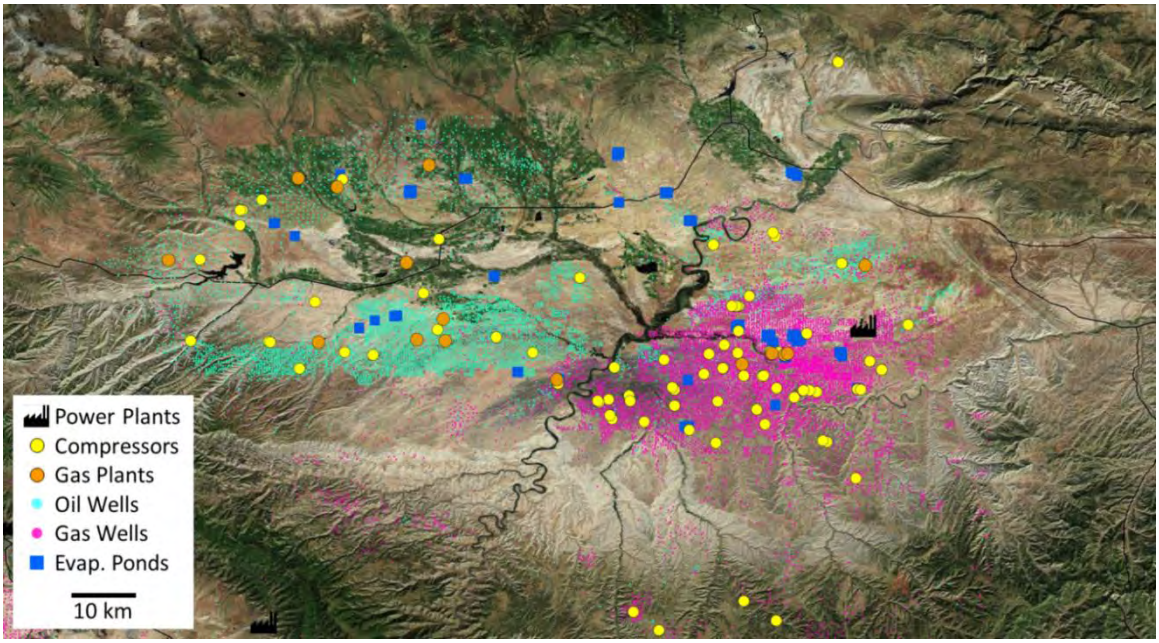


**Figure 2-15. Locations of oil and gas related emissions sources in the Uinta Basin (the location of the Bonanza power plant is also shown).**

*Finding C.1.1: Oil and gas-related sources are responsible for the majority of $NO_x$ and VOC emissions in the Uinta Basin.*

A discussion of emissions data for the Uinta Basin is presented in Section 9. Emissions data for Duchesne and Uintah counties from the 2011 UDAQ submittal to the National Emissions Inventory together with the Western Regional Air Partnership (WRAP) Phase III oil and gas inventory are listed in Table 2-2 and illustrated in Figure 2-16. The oil and gas sector is by far the dominant source of VOC and low level $NO_x$ emissions. Although biogenic VOC emissions are

significant (31% of total VOC on an annual basis), they are reduced to near zero levels during the winter months. $NO_x$ emissions from the Bonanza power plant contribute 22% to total $NO_x$ from all sources but, as pointed out below, emissions from the Bonanza plant are lofted above the low-level inversion during ozone episode conditions and therefore do not contribute significantly to ozone formation.

Observations made during the 2013 study confirm that the Bonanza power plant plume does not appear to contribute any significant amount of $NO_x$ or other contaminants to the polluted boundary layer during ozone episodes. As shown in Figure 2-17, the thermally buoyant Bonanza plume rises upwards from the 183 m (600 ft) stack and penetrates through the temperature inversion layer. As a result, emissions from the Bonanza plant are effectively isolated from the boundary layer in which the high ozone concentrations occur. While it is possible that some of the plume material may eventually be re-entrained into the mixed layer at the Basin margins, the amount of recirculation is likely to be minimal, especially during the strong inversion periods associated with high ozone levels. Other observations of the Bonanza plume include four aircraft vertical profiles in which a plume of enhanced CO, $CO_2$, and $NO_2$ and depressed ozone can be seen between 1800 and 1900 m asl, well above the ~1650 m asl mixed layer top (Sections 4 and 8).

Another indication of the dominance of oil and gas sources in the Basin is the strong correlation ($r^2$ = 0.88) of average VOC concentration measured at surface sites with the number of producing wells within 15 km of the monitoring site as presented in Section 3, although the relationship of $NO_x$ to oil and gas sources is more difficult to discern in these data.

*Conclusions*

Results from the 2012 and 2013 field studies, as well as the available emission inventory data, all support the conclusion that emissions of VOCs and $NO_x$ from oil and gas exploration and production activities are the primary drivers of ozone formation in the Basin. Although the Bonanza power plant is a major source of $NO_x$ in the Basin, this material does not contribute significantly to ozone formation in the Basin during winter episodes.

**Table 2-2. UDAQ 2011 Emissions Inventory (tons/year) based on the Utah NEI submittal and updated WRAP Phase III inventory (Source: Sec. 9, Table 9-2).**

| County | Source | $NO_x$ | $PM_{2.5}$ | $SO_x$ | VOC |
|---|---|---|---|---|---|
| **Duchesne** | Oil & Gas | 7,805 | | 125 | 34,787 |
| | All Other Activity | 3,220 | 382 | 18 | 1,864 |
| | Biogenic - Summer Only - Trees, Crops, Plants | 0 | | 0 | 22,390 |
| | | | | | |
| **Uintah** | Oil & Gas | 10,033 | | 209 | 76,502 |
| | All Other Activity | 1,728 | 978 | 20 | 1,921 |
| | Biogenic - Summer Only - Trees, Crops, Plants | 0 | 0 | 0 | 29,153 |
| | Bonanza Power Plant | 6,590 | 433 | 1,178 | 46 |
| | | | | | |
| **TOTAL** | Oil & Gas | 17,838 | 0 | 334 | 111,289 |
| | All Other Activity | 4,948 | 1,360 | 38 | 3,785 |
| | Biogenic - Summer Only - Trees, Crops, Plants | 0 | 0 | 0 | 51,543 |
| | Bonanza Power Plant | 6,590 | 433 | 1,178 | 46 |

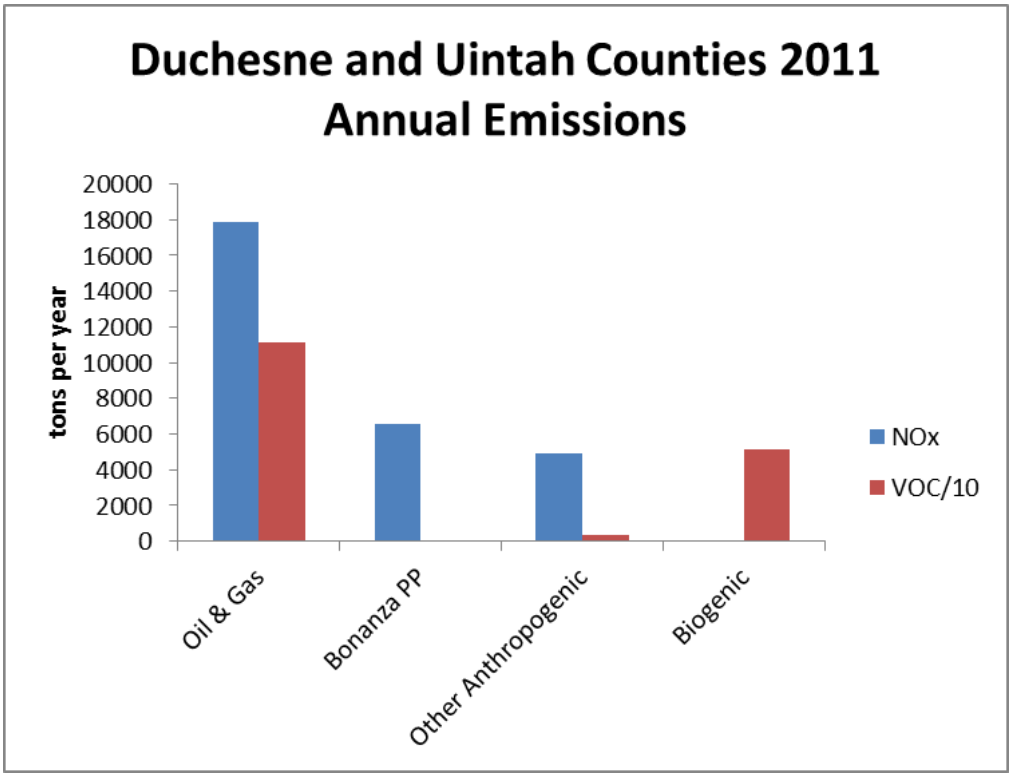


**Figure 2-16. Summary of emissions by source category. (Source: Sec. 9, Table 9-2).**

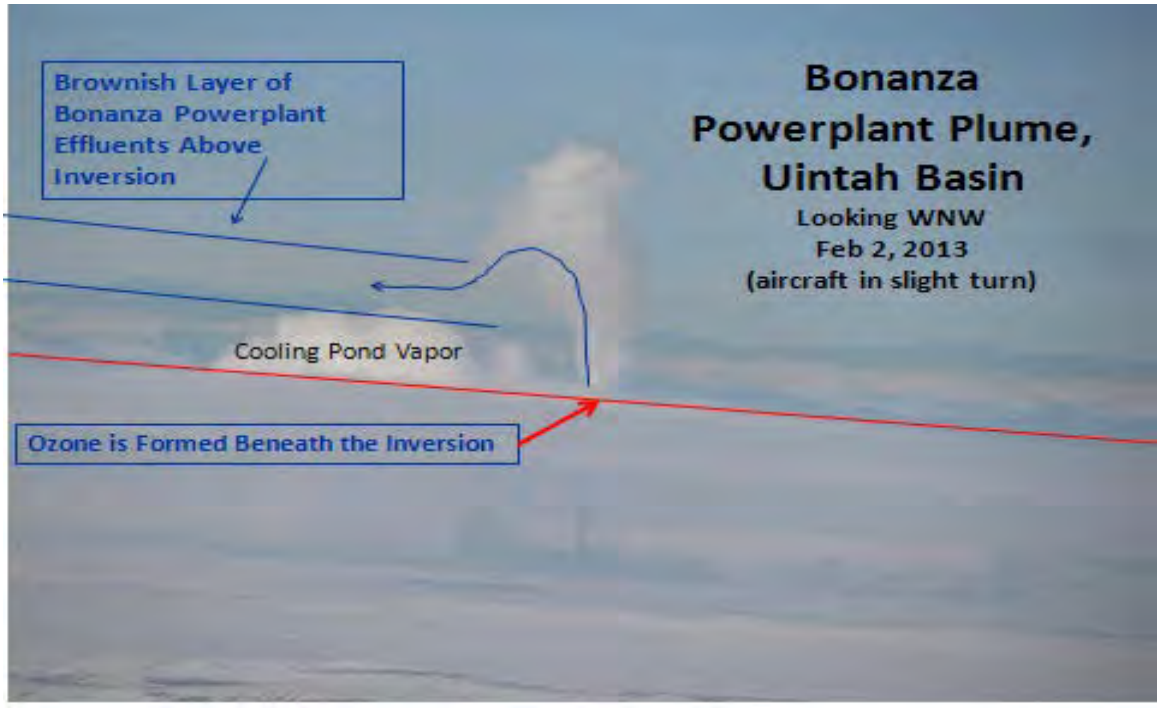


**Figure 2-17. Bonanza power plant with buoyant exhaust plume and water vapor from the cooling ponds during a winter temperature inversion on 2 February 2013. The top of the stack is 1715.8 m and the plume generally rose an additional 2 to 3 stack heights before leveling out in the 1900 to 2200 m range; the inversion base was generally between 1600 and 1750 m (photographed by Colm Sweeney, CIRES/NOAA).**

***C2: Do ambient measurements and emission inventories agree for ozone precursor emissions in the Basin?***

*Background*

Development of reliable estimates of the expected response of ozone to reductions in precursor emissions requires an accurate emission inventory for input to photochemical models. However, activity data and emission factors used to develop inventories are subject to uncertainties which may be significant for some types of sources, such as fugitive emissions of natural gas. Quality assurance of emissions inventories via reconciliation with ambient air quality data is therefore an important component of air quality management.

Various techniques can be used to validate emissions estimates using ambient data. One approach is to measure pollutant fluxes downwind of a source or group of sources and apply inverse modeling to back calculate the corresponding source emission rate. This method has been used to estimate methane emissions from the Denver-Julesburg Basin in Weld Co., CO. (Petron, et al., 2012). Pollutant flux measurements have also been successfully conducted downwind of evaporation ponds using remote sensing techniques (Thoma, 2009). Researchers from the Utah State University recently completed a preliminary assessment of fluxes from

evaporation ponds in the Uinta Basin under winter conditions (see Section 9). Flux measurement methods require collection of a sufficient amount of concentration data to adequately characterize the pollutant flux within the source plume, and such extensive data sets are not always available. This is particularly challenging for complexes of sources which may not have coherent plumes. In addition, these methods are unable to provide information on emissions from individual sources which may be contributing to the overall source complex plume.

Another approach to inventory evaluation involves reconciliation of emissions ratios of key ozone precursor species (e.g., VOC/$NO_x$) with corresponding ratios in the ambient data. This approach can provide useful information on potential inaccuracies in the inventory, so long as emissions of one species (typically NOx) can be assumed to be reasonably well characterized. Care must also be taken to include only data that are not significantly impacted by *in situ* chemical transformations and that data are properly filtered to insure that the comparisons are performed on a consistent "apples to apples" basis (e.g., Stoeckenius et al., 2004).

Direct comparisons of predicted species ratios from photochemical models with observations can also provide a useful check on the inventory so long as the simulation of chemical transformations can be assumed to be reasonably accurate.

*Finding C.2.1: Near source measurements performed by the NOAA mobile laboratory in 2012 are generally consistent with emissions profiles for various source types used in the 2008 WRAP inventory.*

Measurements of VOCs were performed by the NOAA GMD mobile laboratory during UBOS 2012 at locations immediately downwind of different gas wells and oil wells in Uintah and Duchesne counties, gas wells near Rangely, CO, a flow-back pond from a well undergoing fracking, a newly producing gas well, and various other point sources (compressor stations, etc.). As described in Section 5, VOC composition varied significantly by source type. VOC emissions from oil wells were found to be skewed more towards heavier compounds as compared to emissions from gas wells with particular enhancement in aromatics. Results from the mobile lab drive-by of a gas well showed that methane was found to be highest downwind of the separator, toluene, and other aromatics downwind of the condensate tank, and methanol downwind of the methanol and condensate tanks. Overall, results from the mobile lab are in qualitative agreement with VOC composition variations by source type included in the 2008 WRAP emission inventory. However, mobile lab results do not provide a quantitative assessment of emission rates.

*Finding C.2.2: While a wealth of data was collected during UBOS 2012 and 2013, additional analyses of these data are needed to provide results that can be used to infer quantitative information concerning emissions. These analyses will be reported as they are completed.*

Although reconciliation of emission inventories with ambient measurements is difficult and subject to numerous sources of uncertainty, it is likely to provide some useful information

regarding the accuracy of inventory estimates and an indication of where additional scrutiny of the inventory is most needed.

*Conclusions*

Oil and gas exploration and production activities are the dominant sources of ozone precursors in the Uinta Basin, though other significant sources exist. Further work to refine emissions estimates and to verify inventories using ambient measurements is needed along with comparisons of modeled to measured concentrations.

## 2.5 Part D: Mitigation Strategies

### *D.1: What possible mitigation strategies should be considered for adoption in the Uinta Basin?*

*Background*

Determination of an optimal ozone control strategy for the Uinta Basin will require the development of a high quality photochemical modeling database. Data available from the UBOS are insufficient by themselves to determine the level of control that could eventually be required to achieve ozone-reduction objectives. Furthermore, it is not known at this time whether winter ozone problems in the Basin will be more effectively mitigated by $NO_x$ or VOC controls, nor is it known whether control requirements will need to vary across the Basin. $NO_x$ emissions reductions under VOC limited conditions (low VOC/$NO_x$ ratios) can result in increases in ozone (Nopmongcol et al. 2010; Carter and Seinfeld, 2012). VOC emission reductions, on the other hand, do not typically lead to an increase in ozone formation, but marginal reductions in VOCs may be largely ineffective under strongly $NO_x$ limited conditions (very high VOC/$NO_x$ ratios). In general, ozone production can be expected to transition between VOC and $NO_x$ limited conditions at different times and locations. Thus, application of state-of-the-art photochemical grid models is necessary to identify the best combination of VOC and $NO_x$ controls needed to achieve ozone reduction goals. Photochemical simulations using a simple box model (Gery and Crouse, 1990) with data collected at different times and locations in the UGRB showed ozone formation to be VOC limited in some cases and $NO_x$ limited in another (Carter and Seinfeld, 2012). Box model simulations of conditions in the Uinta Basin during the UBOS 2012 study, when snow cover was not present, showed that the limited amount of ozone production which did occur was most likely radical limited and thus sensitive to reductions in VOC rather than $NO_x$ (Edwards et al., 2013). These findings do not necessarily apply under the snow covered, cold air pool conditions associated with ozone episodes, however. Several groups, including the Utah Department of Environmental Quality (UDEQ), U.S. EPA, and Utah State University, have begun meteorological and photochemical modeling studies of the Basin. A preliminary meteorological modeling study of the 26-30 January 2013 inversion episode is described in Section 10.

*Finding D.1.1: Episodic or seasonal emission controls may be a useful ozone reduction strategy for the Uinta Basin.*

Ozone levels in excess of EPA's current ambient standard only occur during winter inversion periods which require very specific conditions (generally fair weather with weak pressure gradients, low sun angles, and snow-covered ground). Ozone on the majority of days during the year is below the EPA standard and exceedances of the standard do not occur every year. Thus, control measures designed to reduce ozone under the specific winter inversion conditions or during the time when such conditions are likely to occur have the potential to be a cost-effective strategy. For example, certain types of activities such as blowdowns for which operators have some scheduling flexibility could be avoided during winter inversion events. Similarly, spuds could be scheduled as much as possible for months outside of the peak winter ozone season (roughly mid-January to mid-March). As noted above, UDEQ has instituted a set of recommended voluntary seasonal emission controls and an air quality forecast system (http://www.airquality.utah.gov/aqp/forecast.php?id=vl) for Uintah and Duchesne counties.

*Finding D.1.2: Reductions in emissions of VOCs, especially highly reactive VOCs, are likely to be beneficial.*

Under most conditions, VOC reductions will result in ozone reductions, although the sensitivity of ozone to VOC reductions will vary. Highly reactive VOCs such as formaldehyde and aromatics are of particular importance (formaldehyde was found to be a major source of the radicals that drive ozone production at Horsepool, as described in Section 5) and these VOCs are preferentially emitted from specific sources. Sources such as dehydration units and produced liquids evaporative losses are rich in aromatics. Primary formaldehyde sources include diesel engine exhaust and potentially the use of formaldehyde contaminated methanol (as evidenced by the high correlation of formaldehyde and methanol concentration spikes observed at Horsepool in 2012 and 2013, see Section 5). Formaldehyde is also formed in the atmosphere from VOC precursors, so reducing emissions of these precursors will result in lower formaldehyde concentrations and less production of radicals. The relative contributions of primary and secondary sources to total formaldehyde are currently uncertain. A simple regression model derived in Section 5 from data collected in 2013 based on the assumption that secondary production scales with the $O_x$ (sum of $O_3$ and $NO_2$ ) mixing ratio suggests that 63% was from secondary production, 30% from primary sources, and 7% background. Additional data are needed to identify the most effective formaldehyde reduction strategies. Analysis of VOC samples collected during UBOS 2013 indicates low concentrations of alkenes and therefore little if any contribution of these highly reactive species to the overall VOC reactivity in the Basin (Sections 3 and 5).

*Finding D.1.3: Emission reductions at the Bonanza power plant are unlikely to have any effect on winter ozone episodes.*

As summarized in Section 2.4, results from the UBOS 2013 study clearly show that the Bonanza power plant plume is injected above the inversion layer during winter ozone episodes and therefore does not contribute significantly to the high ozone levels observed below the

inversion layer. Therefore, reductions in emissions from Bonanza would not result in a significant ozone reduction benefit under episode conditions.

*Finding D.1.4: Additional data collection and analysis is needed to more fully evaluate the likely sensitivity of peak ozone concentrations to reductions in $NO_x$ emissions.*

The effectiveness of $NO_x$ reductions will depend on the degree to which unreactive $NO_z$ is converted to reactive $NO_x$ by heterogeneous chemistry on snow or suspended particle surfaces, e.g., the conversion of $HNO_3$ to HONO in snow. As discussed in Section 2.3 above, measurements from Horsepool indicate that photochemical production of HONO in the snow is occurring, although the validity and strength of this source remains uncertain. The most likely mechanism behind this HONO source involves photolysis of nitrates that have been deposited on the snow, forming nitrites which then undergo a reversible acid-base reaction to form HONO as described in Section 5. Evidence for this includes daytime near surface HONO concentrations that correlate with solar radiation and generally decrease with height (thus indicating an upward flux of HONO) along with high nitrite concentrations in the snow which increased day-to-day during the ozone episode and which correlated with snow nitrate concentrations. While HONO production from snow therefore likely scales with nitrate deposition which would in turn be sensitive to $NO_x$, the form of this relationship may very well not be a simple linear one in which a given percent reduction in $NO_x$ produces an equivalent percent reduction in nitrate deposition and HONO production. Additional study is needed to further evaluate the relationship of HONO to $NO_x$ emissions under winter episode conditions.

*Conclusions*

Additional work is needed to understand the potential sensitivity of ozone to $NO_x$ and VOC emission reductions during winter episodes. Of particular importance is quantification of the strength of the HONO source(s) and further investigation of the heterogeneous chemical reactions involved so as to gain a better understanding of the potential impact of $NO_x$ emission reductions on HONO production. Additional work is also needed to evaluate effective controls targeting formaldehyde. Absent this additional information, VOC reductions – particularly controls focused on large reductions in fugitives and targeted reductions of sources of aromatics and primary formaldehyde – can be expected to result in lower ozone levels.

Recent rulemakings by the U.S. EPA and the UDEQ are expected to result in reductions of VOC emissions in the Basin. Applicable EPA rule revisions issued in April, 2012 include New Source Performance Standards (NSPS) for the oil & gas industry (http://www.epa.gov/airquality/oilandgas/ ) which targets VOC emissions from well completions (requiring so-called “green completions”), liquids storage tanks, and some new or modified well-site equipment and compressor stations and National Emission Standards for Hazardous Air Pollutants (NESHAPS) which limit VOC emissions from new and existing glycol dehydrators. EPA also instituted a permitting program for sources in Indian Country in 2011 (http://www.gpo.gov/fdsys/pkg/FR-2011-07-01/pdf/2011-14981.pdf). UDEQ recently implemented a General Approval Order mechanism which is applicable to upstream oil and gas sources and is expected to result in emissions reductions (particularly VOC emission reductions)

from new sources via implementation of Best Available Control Technology requirements. UDEQ has also compiled a set of recommended Voluntary Seasonal Ozone Controls (http://www.deq.utah.gov/locations/uintahbasin/seasonalcontrols.htm) which are mostly targeted at detection and reduction of fugitive VOC emissions and avoiding carrying out of maintenance procedures, such as blow downs, that result in bursts of VOC emissions during winter inversion conditions.

## 2.6 Part E: Additional Information Needs and Modeling Issues

### *E.1: What special challenges does the basin pose for meteorological modeling?*

*Background*

The Uinta basin is a broad, 27,700 $km^2$ mountain basin containing numerous, relatively low (order of tens to hundreds of meters) topographic features. During the high ozone periods in the 2011 and 2013 Uinta Basin campaigns, the region had relatively light (1 - 4 m/s) low-level (surface to 500 m agl) winds. Light wind conditions in mountainous terrain typically feature thermally driven slope and mountain-valley wind systems associated with differential diurnal surface heating and cooling cycles. These wind systems, often referred to as katabatic wind systems, blow up-valley or upslope during the day and downslope or down-valley at night (nocturnal drainage flows). At a given time of day, in other words, the local winds blow from a preferred direction for several hours each day, so that the winds and their effects (e.g., transport) show up in multiday averages or composites of the data.

Thermal forcing of katabatic wind systems may be weak during the winter months due to low solar angles and short day lengths, making the systems difficult to detect. So important questions are: Is there a discernible diurnal signature to the low-level winds in the Uinta Basin under winter ozone episode conditions and what impact do these local thermally driven slope flows have on the transport of pollutants? Of particular interest is the potential for recirculation of pollutants as a result of the diurnal upslope/downslope wind reversal. This type of recirculation pattern has been documented in the Upper Green River Basin (ENVIRON, 2008).

When larger scale synoptic pressure patterns produce winds blowing across the upstream rim of the Uinta Basin, the resulting dynamic forcing on the top of the pool of cold, stable air contained within the Basin may introduce dynamic forces resulting in perturbations on the weakly forced katabatic surface wind regimes within the Basin. The resulting complex wind patterns are known to be difficult to reproduce with current mesoscale meteorological models.

Winds blowing across the upstream rim of the Basin often appear as wave-like features impinging into the basin (most commonly from the west) and can bring clean air into the basin. Radiosonde vertical profiles of wind and temperature (Section 8) and initial modeling work (Section 10) suggest that winds from the east just above the surface develop in response to this upstream dynamical forcing. Future modeling studies will provide more insight into these terrain-flow interactions as possible transport mechanisms for ozone and its chemical precursors in addition to the thermally-driven flows.

During the 2011 and 2013 measurement campaigns, the concentrations of ozone were found to vary considerably across the Basin, consistent with both spatial variations in precursor sources and terrain elevations. Transport over the complex terrain within the Basin also plays a role in determining the spatial ozone pattern. High concentrations were measured at the lowest-elevation sites in the Green River valley, which could be explained by drainage flows, but high concentrations were also seen at higher-elevation sites to the east of the river-valley sites.

Weak winds require a precise measurement system to detect them. Data from NOAA/ESRL's High-Resolution Doppler Lidar (HRDL) has been shown to satisfy this requirement. Although a scanning system, HRDL is able to produce accurate profiles of the mean wind at vertical resolutions of less than 5 m through the lowest several hundred meters of the atmosphere, extending up to 2 km. The HRDL was located at the Horsepool site during UBOS 2012 and 2013, so it sampled the wind conditions in the eastern portion of the basin. While the instrument was able to capture fine detail at this site, results from meteorological data collected at multiple sites within the Basin presented in Section 3 indicate that wind conditions at Horsepool are likely not representative of other regions within the basin.

The traditional meteorological models that would likely be used to support air quality modeling in the basin were developed with a primary goal of weather forecasting. As such, much of the research focus and evaluation of the models has focused on the ability of the models to replicate the weather phenomena important to weather forecasting (i.e., frontal passage movement, hurricane track, cyclogenesis). Fewer development resources have been spent on the applicability of the models for simulating the important features for weakly forced flows under cold pool conditions such as would be important in the Uinta Basin. In addition, current numerical model boundary-layer schemes struggle to accurately simulate aspects of highly stable atmospheric conditions. It is important that particular attention be given to the model application and evaluation methodology, and that physics parameterizations most appropriate for use in the extremely stable environment be used when applying the models in the basin.

*Finding E.1.1: Very different wind patterns and dynamic processes were identified under strong as compared to weak wind regimes during UBOS 2012 and 2013.*

During UBOS 2012, strong-wind periods were generally dominated by synoptic-scale meteorological systems (winter storms) typical of mid-latitude locations in winter. Under these conditions, the near-surface winds reflect the stronger winds aloft, as illustrated in Figure 2-18.

During weak-wind periods when the synoptic-scale pressure gradients are minimal, the effects of local forcing become evident so long as the forcing is strong enough. Figure 2-19 shows the evolution of wind profiles on a day when such forcing is clear. On this day, the near-surface winds were light, but the nighttime winds had a distinct easterly component, and daytime winds were from the west up to a height of several hundred meters. Although many light-wind days during UBOS 2012 exhibited perturbations superimposed on the local winds by traveling disturbances, the diurnal pattern was observable in HRDL profiles on most light-wind days, and in composites of all days when the winds aloft were light (< 4 m/s). Thus HRDL was able to detect a diurnal pattern in the near-surface winds in the vicinity of Horsepool, with light

easterly flow draining toward the Green River valley at night and light westerly upslope flow during daytime hours. The easterly flow is consistent with the appearance of high concentrations in the lowest areas of the basin, and the daytime westerlies can explain the secondary appearances of high concentrations on higher ground to the east of the river bottom.

*Finding E.1.2: Meteorological data collected at stations around the Basin showed significant variations in winds across the basin and with time of day. Meteorological models must capture the spatiotemporal variability of boundary layer flows above the surface layer that are not observed by the surface meteorological network.*

Figure 2-20 shows average day and night wind vectors at 14 meteorological stations around the Uinta Basin during February 2012. The black arrows indicate monthly mean wind direction from 13:00 to 15:00 local time, and red arrows indicated monthly mean wind direction from 03:00 to 05:00 local time. The size of the arrow is proportional to the mean wind speeds for each time period. These results show that day and night mean wind directions are not consistent across the Basin, even among some sites that are in relatively close proximity. Most of the sites exhibit upslope/downslope flow that leads to near-180 degree shifts in wind direction between night and day. The directions of the day-night flows are not consistent at different sites, and appear to be influenced by the local terrain. Thus, the complex topography of the Basin likely leads to complex surface flows that transport ozone and its precursors around the Basin. This spatial heterogeneity can be magnified during inversion conditions conducive to ozone formation, since temperature inversions are typically accompanied by low speed surface winds and variable wind directions. Afternoon winds during 2013 ozone episodes show significant spatial heterogeneity (see Figures 2-21 and 2-22). Because of the complex topography of the Basin and its influence on surface flow and, by extension, pollutant transport, it will be critical that models of ozone formation include high resolution simulations of topography and meteorology. Data from the extensive network of meteorological stations used in UBOS work will be able to inform and validate such an effort. In addition, data from vertical profiles of wind from radiosondes, tethersondes, and the HRDL lidar (Sections 5 and 8) indicate significant variations in wind speed and direction with height. Thus, modeling efforts to provide spatiotemporal details on above-surface winds will be critical.

*Finding E.1.3: Transport in the basin is influenced both by locally induced flows and interactions with synoptic scale flows. Meteorological models must adequately capture both phenomena to accurately simulate flows within the basin.*

During high ozone periods in the 2013 measurement campaign the basin was observed to have Persistent Cold Air Pools (PCAPs) characterized by relatively light winds and a strong temperature inversion (Section 3.1). However, the basin was periodically cleaned out by larger scale synoptic flows in between the high ozone periods. Figure 2-21 shows wind conditions and the low ozone concentrations on 28 January, just two days after one of the season's highest ozone days in the basin. A storm front arrived on 27 and 28 January and was associated with relatively high winds in many parts of the Basin on 28 January. Winds at high elevation sites during this period were from the south. Wind speeds within the Basin were lower on

subsequent days, allowing another inversion to form and ozone concentrations to rebuild. By the afternoon of 6 February (Figure 2-22), ozone concentrations exceeded 100 ppb at many sites. Wind at high elevations continued to be from the south throughout this period, and wind at lower elevation sites in the Basin was light and variable. On 8 February, however, wind at high elevation sites changed directions and blew from the north (Figure 2-23). Following this synoptic scale change, wind at low elevation sites within the Basin continued to be light and variable, but a partial mix-out of ozone from the Basin nevertheless occurred, and ozone concentrations dropped to less than 100 ppb at all sites.

To properly simulate the evolution of the high ozone events will require that the meteorological model be able to simulate both the synoptic scale forced conditions during low ozone events and mix-out conditions, as well as the more locally generated PCAP events during the high ozone periods. In addition, the ability of the models to simulate partial mix-outs arising from terrain-flow interactions immediately downwind of the surrounding mountain ranges will be critical during long-lived PCAPs.

*Finding E.1.4: Many shallow layers are observed during persistent cold air pools and models must include adequate vertical resolution to capture observed phenomena.*

The boundary-layer depth and structure during UBOS persistent cold air pools were estimated using backscatter and backscatter gradients from the two University of Utah ceilometers deployed in the basin (Section 3.2). On most days, distinct layering of the vertical structure of the boundary-layer backscatter was observed (Figure 2-24). Another feature that is apparent from Figure 2-24 is the diurnal variations in the depth of the surface-based polluted layer. These diurnal variations are associated with similar variations in the temperature structure of the boundary-layer. On the 24$^{th}$ January, the depth of the surface-based polluted layer was observed to be near 300 m during the overnight hours, but increased to nearly 500 m during the afternoon.

The University of Colorado Balloon based ozone monitor (Section 6) also showed significant vertical structure in ozone concentration. The vertical distribution of ozone throughout the duration of the campaign is illustrated in Figure 2-25 as a color contour plot showing the full record of the ECC sonde ozone data for Horsepool. The three high ozone build-up events are evident in the warmer colors on the color scale, which here goes to 175 ppbv. The vertical structure reveals that ozone builds up in both mixing ratio (concentration) and in height during the inversion events. The highest ozone is consistently confined within the lowest 100 – 150 m above ground level and at many times appears to be well-mixed within the shallow boundary layer. With the exception of one day in mid-February, relatively low ozone (i.e., < 75 ppbv) was present above 1900 m asl throughout the measurement period. The clean-out periods (i.e., January 28 – 31 and February 10 – 11) brought this relatively clean background air down to the surface, resulting in ground-level ozone values on the order of 30 – 60 ppbv.

The meteorological models must be configured to properly capture the vertical stratification observed during UBOS 2013. This may require higher vertical resolution than is typically employed for meteorological modeling for air quality applications. It will also require testing

various PBL schemes and other physics parameterizations as well as model initialization to determine which settings are most appropriate for these high-stratification events. It will also be critical to evaluate the photochemical model against the aloft special study data to assure that the model is able to adequately reproduce the observed phenomenon. Some initial modeling analyses are presented in Section 10.

*Conclusions*

During high ozone periods the low-level transport is dominated by fairly shallow (50-400 m deep), weak (1-4 $ms^{-1}$), and highly variable locally driven flow patterns. During mix-out and partial mix-out events the flows are more influenced by stronger (> 10 $ms^{-1}$) winds associated with large-scale weather disturbances. Additionally, during high ozone events vertical profiles of pollutants and winds within the basin were observed to have quite distinct layering structure that could impact pollutant transport. It is critical that the meteorological model be configured to capture these local scale flow features, and future research focused on developing model physics parameterizations appropriate for the extremely stable environment is needed. In addition, accurate specification of land use and snow cover will be a critical component for any meteorological modeling efforts.

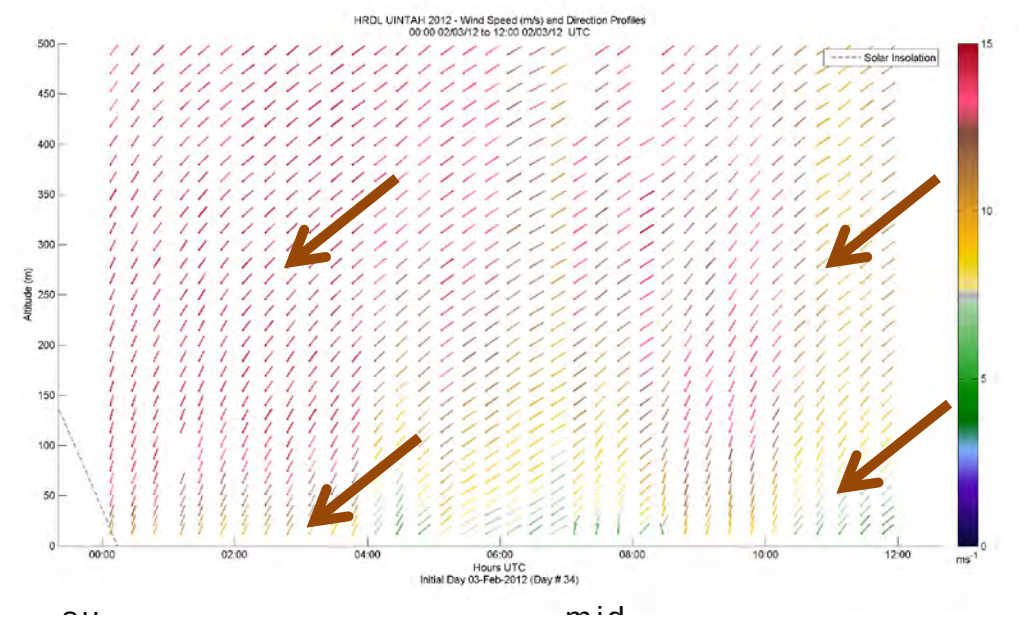


**Figure 2-18. Profiles of 20-min wind speed and direction at Horsepool for 0000-1200 UTC on 3 February 2012, showing strong northeasterly flow at 500 m above ground, extending down to the surface (arrows). Wind barbs indicate direction from which winds were blowing, and color coding of barbs indicates wind speed as shown on color bar. Horizontal axis is time (UTC, which is 7 hr ahead of MST), and vertical axis is height above ground (m).**

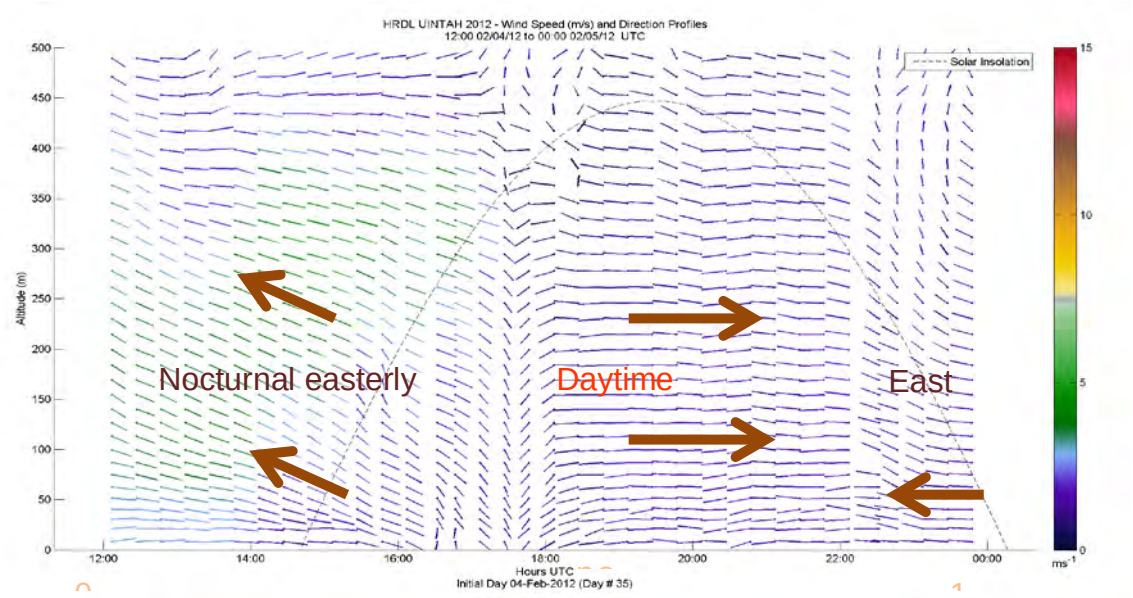


**Figure 2-19. Profiles of 20-min wind speed and direction at Horsepool for 1200 UTC, 4 Feb to 0000 UTC, 5 Feb 2012, showing diurnal cycle of winds below 500 m. Dotted black curve is clear-sky solar flux, indicating time of day. Wind barbs and axes as in Figure 2-18.**

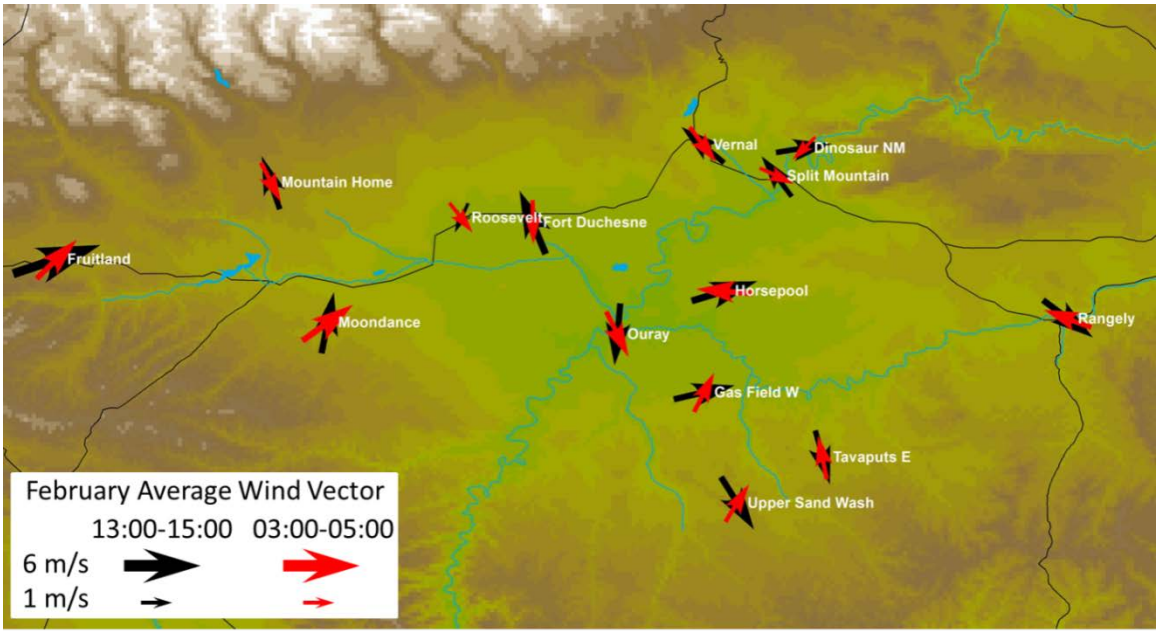


**Figure 2-20. Mean day and night wind vectors at 14 meteorological stations around the Uinta Basin in February 2012. (Source: SR2012).**

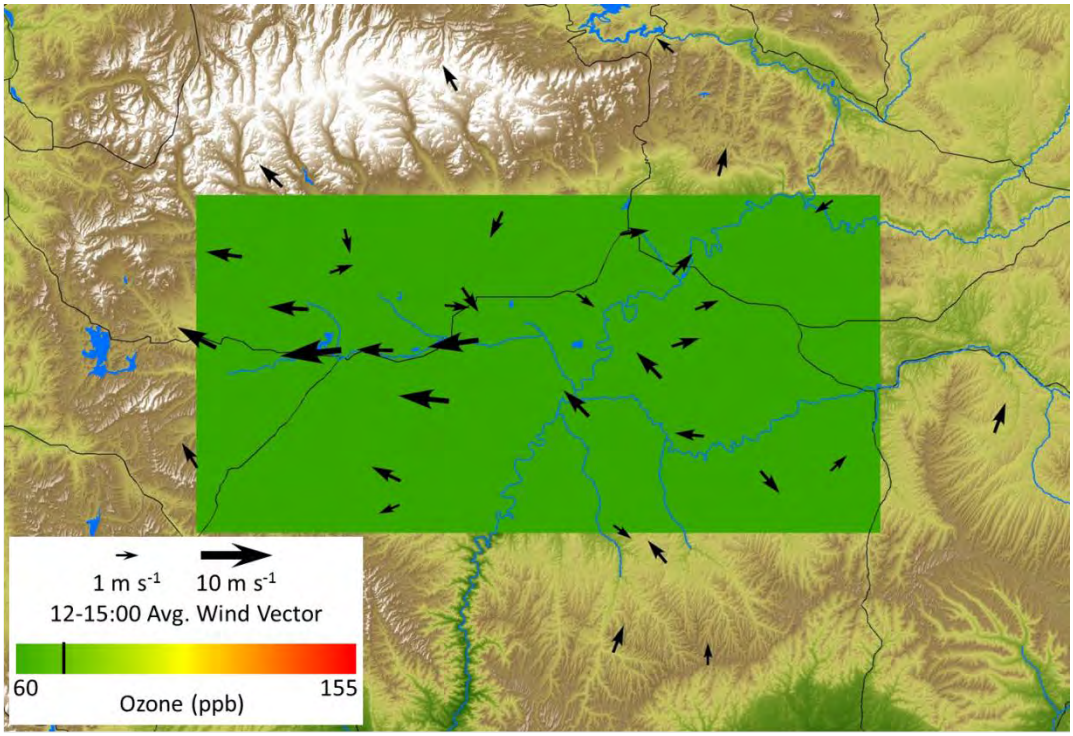


**Figure 2-21. Daily maximum ozone concentrations and afternoon composite wind vectors from surface sites on 28 January 2013 during a stormy period between inversion episodes. Arrows indicate wind direction. The black line on the ozone color scale indicates 75 ppb.**

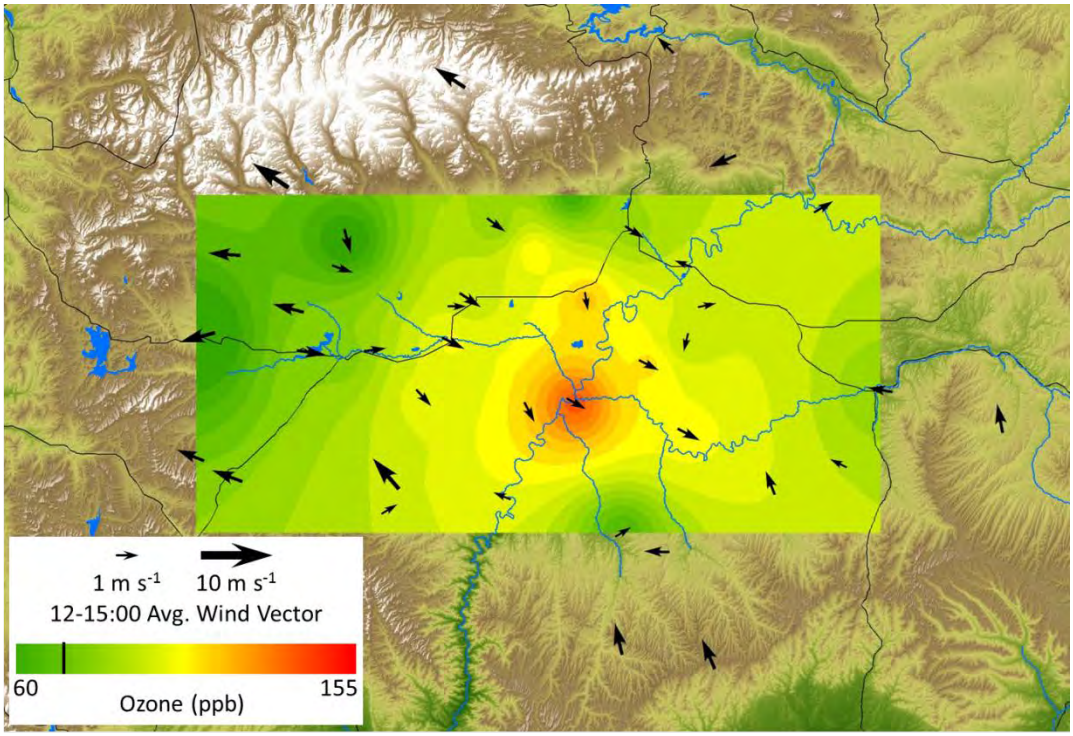


**Figure 2-22. Daily maximum ozone concentrations and afternoon composite wind vectors from surface sites on 6 February 2013 during an inversion episode.**

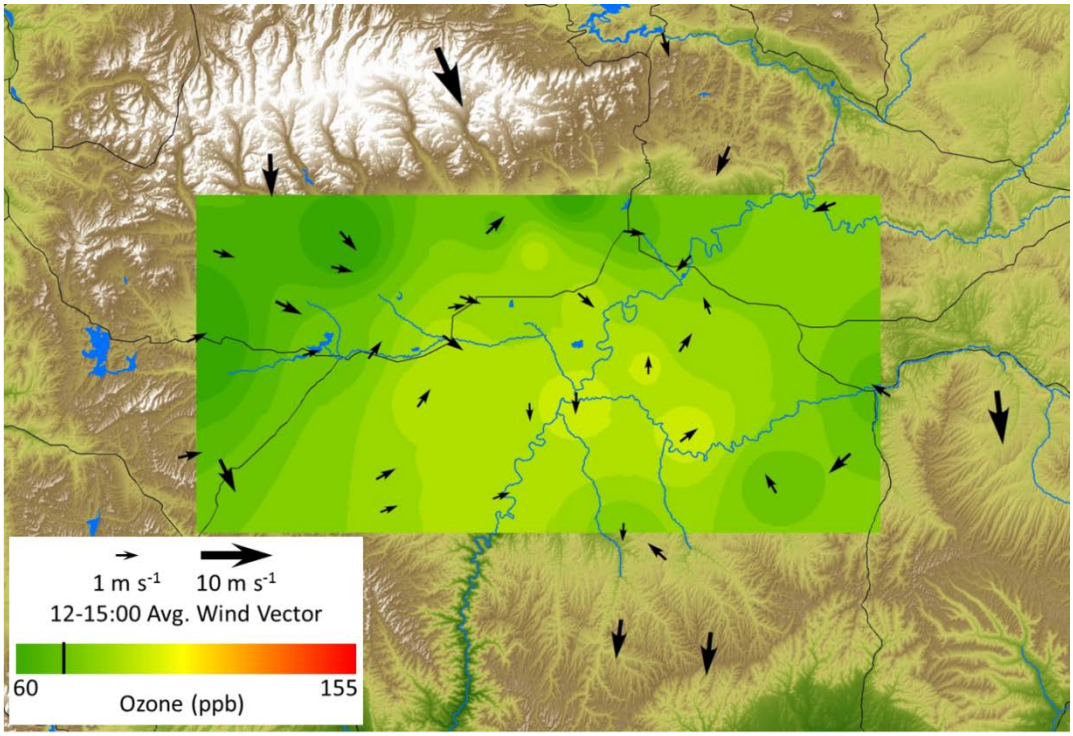


**Figure 2-23. Daily maximum ozone concentrations and afternoon composite wind vectors from surface sites on 8 February 2013.**

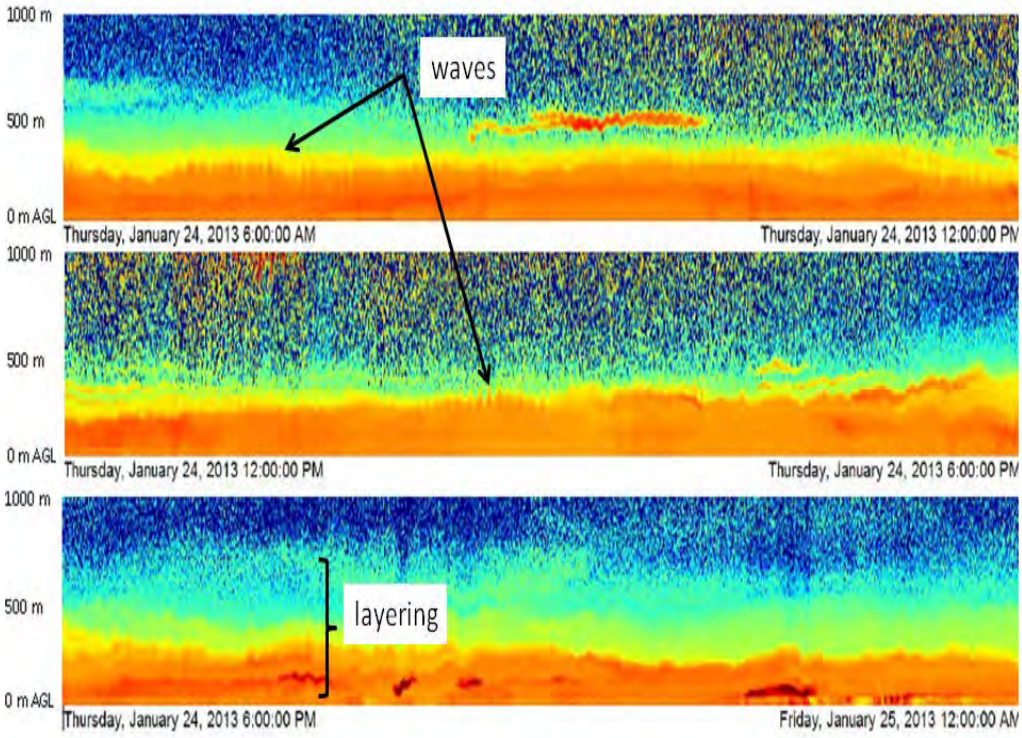


**Figure 2-24. Ceilometer aerosol backscatter on 24 January 2013 at Roosevelt, UT. Higher (lower) backscatter implying higher (lower) aerosol concentration denoted by warm (cool) colors.**

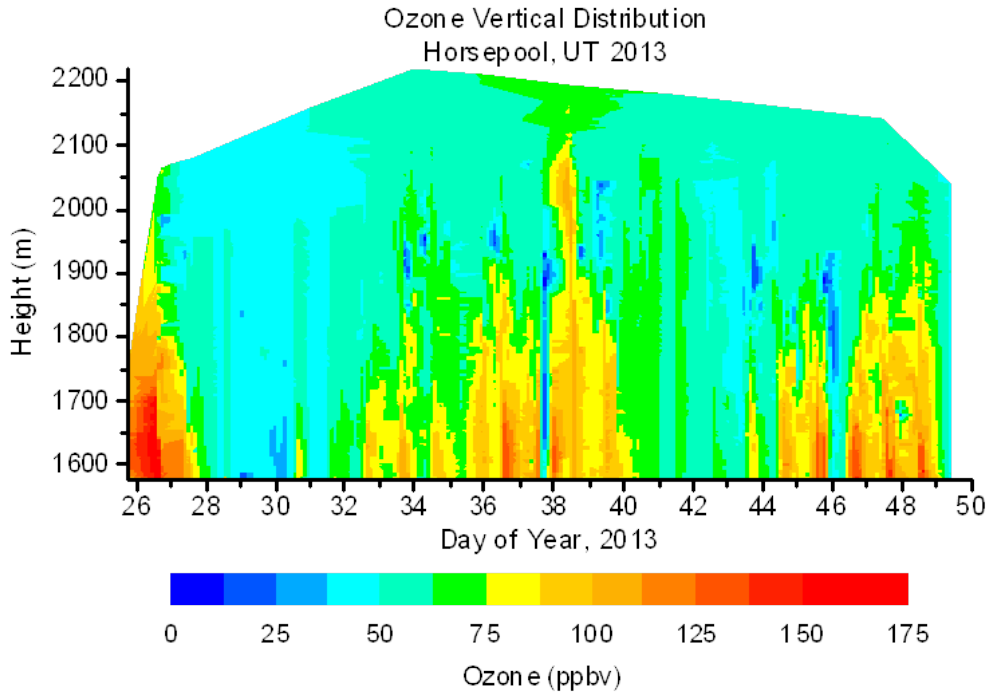


**Figure 2-25. Contour plot showing the complete record of ozone measurements acquired from the ECC tethersondes launched by the CU-INSTAAR group at Horsepool between 26 January and 18 February, 2013.**

***E.2: Can the formulation of existing 1-D box and more complex transport and chemical models represent the observed phenomena in the Basin? If not, what are the most urgent measurement needs for improving the model representation?***

*Background*

Three dimensional photochemical modeling is the most comprehensive tool available for 1) understanding details of the ozone formation process, 2) evaluating ozone sensitivities to changes in precursor emissions, and 3) predicting the effects of emissions control strategies. One-dimensional photochemical box models are useful tools for evaluating chemical mechanisms and performing sensitivity analyses. For model simulations to be useful, however, they must faithfully reproduce key mechanisms of ozone formation and transport operating in the Uinta Basin. Merely demonstrating that a model is able to accurately reproduce the observed temporal and spatial distribution of ozone is not sufficient, as this does not ensure that ozone sensitivities to changes in precursor emissions will also be accurately predicted. Modelers typically refer to this problem as "getting the right answer for the wrong reason." Models must be carefully evaluated against ambient measurements of ozone, precursors, and meteorological parameters.

In contrast to urban summertime ozone episodes for which all existing photochemical models used in regulatory applications were originally developed and evaluated, relatively little is

known about winter ozone episodes in air basins in which emissions are dominated by oil and gas sources. Research is needed, therefore, to fully evaluate the applicability of existing models to winter ozone events and to identify any necessary modifications to model formulation.

*Finding E.2.1: Data from the UBOS and UGRB studies indicate that current model chemical mechanisms may need to be modified to account for 1) potential daytime HONO formation and 2) temperature effects on chemical reaction rates.*

As pointed out in Section 2.3, the radical budget during winter ozone episodes at Horsepool is primarily driven by a combination of production from formaldehyde and potentially HONO rather than ozone photodissociation as is the case in most summer urban episodes, and apparent high concentrations of near-surface HONO appear to be associated with a daytime production via heterogeneous reactions on the snow surface. Current air quality models do not represent the accumulation and transformation of nitrogen species in snow that may be associated with this HONO source. Using additional measurements of HONO that will be carried out in the 2014 UBOS, however, it may be possible to develop simple parameterizations to represent the source of HONO in snow.

Box modeling of ozone formation in the UGRB by Carter and Seinfeld (2012) and Nopmongcol et al. (2010) showed that existing chemical mechanisms (SAPRC-07 and CB05, respectively) generate peak ozone levels on par with observed values. However, sensitivity analyses performed by Carter and Seinfeld identified significant differences in VOC reactivities between the winter conditions in the UGRB and standard summer urban conditions. They also showed that the potential daytime production of HONO from $NO_2$ via heterogeneous reactions on the snow surface could contribute significantly to ozone production under some conditions.

Box modeling based on conditions observed in the Uinta Basin during the UBOS 2012 study (Edwards et al., 2013) showed that ozone production during this period was radical limited and thus highly sensitive to VOC levels, despite the observed high VOC/$NO_x$ ratios. Attempts by Edwards et al. to reproduce higher levels of ozone by approximating conditions expected to have occurred if snow cover had been present and a cold air pool had formed (higher UV albedo and lower mixing height with higher precursor concentrations) increased predicted maximum ozone but did not reproduce the high levels of ozone observed in previous years, suggesting that additional factors are at play during winter episodes. This finding raises uncertainties regarding the sensitivity of ozone to precursor reductions under snow covered, cold air pool conditions.

As indicated by Martin et al. (2011), existing chemical mechanisms that were developed and evaluated against data representative of summer urban conditions may not fully account for the effects of cold winter temperatures on reaction rates and the relative distributions of reaction products. Carter and Seinfeld (2012) also noted that the temperature sensitivities of some reaction mechanisms have not been fully evaluated. While results from these studies suggest that overall reactivity is lower under colder temperatures, quantitative research in this area is needed.

*Finding E.2.2: Results from initial attempts to simulating meteorological conditions in the Uinta Basin using a prognostic mesoscale model show that significant additional evaluation of various combinations of the available model physics options and possibly additional model development will be needed to properly simulate meteorological fields characteristic of winter ozone episode events.*

WRF simulations of the Jan 26-30, 2013 high ozone period have been prepared by researchers at Utah State University (Section 10). Preliminary analysis of simulation results showed that in general the WRF captured the timing and basic structure of the inversion at sites within the basin and captured the inversion breakup on Jan 28 caused by a storm passage. However, the model appeared to have a systematic warm bias during the high ozone period and underestimated the observed near surface temperature gradient between Ouray and Horsepool (Figure 2-26). Near-surface warm bias is a common problem encountered in simulation of cold pool events (Holstag et al., 2013). During the period studied using various combinations of model physics options, WRF was ultimately found to overestimate wind speeds in the near-surface layer with a relatively large bias of up to 4 m/s. Increasing horizontal grid resolution from 1300 m to 800 m did not improve model performance in simulating wind speed and other meteorological quantities in the near-surface layer. While the WRF simulation described in Section 10 shows promise, it is going to be necessary to more fully examine the WRF model performance against the rich observation network and to more fully explore the impact of alternative combinations of available model options on model performance. It is likely that additional model development will be necessary to properly capture the subtle but important meteorological features in the Basin. Meteorological modeling of the Basin is being conducted by other research groups, including the University of Utah, as described in Section 3 (Section 3.2).

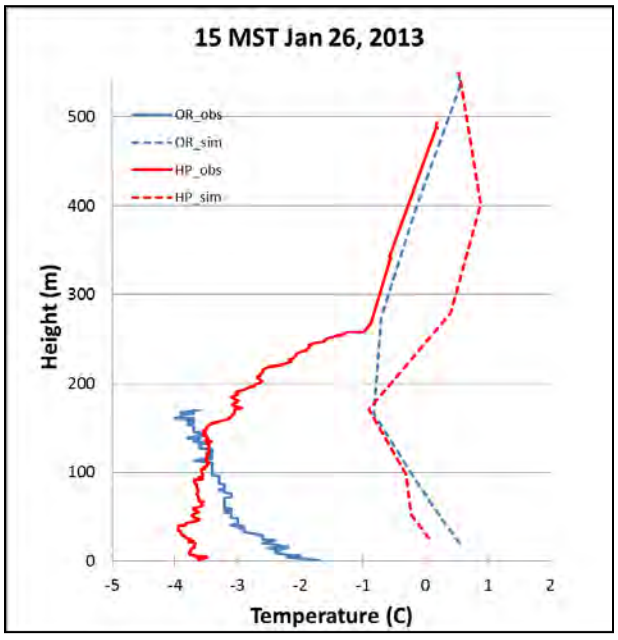


**Figure 2-26. Observed (solid) and simulated (dash) temperature vertical profiles at Ouray (blue) and Horsepool (red) at 15 MST on Jan 26, 2013.**

*Conclusions*

Additional development of both meteorological and photochemical models is needed to adequately simulate wither ozone episodes. While current model chemical mechanisms are able to roughly reproduce observed peak ozone concentrations when used in simple box models with observed initial conditions, there are concerns whether these mechanisms, when used in photochemical grid models, might not be able to accurately simulate the impact of emission reductions on ozone levels. Results from UBOS 2013 and the Upper Green Winter Ozone Study indicate that winter ozone models must incorporate additional chemical reactions involved in mid-day HONO production and properly account for the impact of cold temperatures on reaction rates and branching ratios. Additional work on meteorological models is also needed as current modeling approaches have significant difficulty simulating the cold pool conditions associated with winter ozone episodes.

***E.3: What are the main issues regarding winter ozone formation that should be the focus of future studies?***

*Background*

Results from the UBOS 2012 and 2013 studies, together with results from the Upper Green Winter Ozone Study, have significantly improved our understanding of the key characteristics of winter ozone episodes in western oil and gas basins. Of particular value are the comparisons of measurements made during UBOS 2012 when ozone episodes did not occur with those made during UBOS 2013 when several high ozone episodes were observed. As with any scientific endeavor, however, these studies have also identified several issues which require further investigation.

*Finding E.3.1: Additional measurements are needed to investigate the validity of the reported HONO measurements to determine if the hypothesized large HONO source is in fact important. If it is, additional measurements are needed to validate and accurately characterize the vertical distribution and temporal variations of HONO and reduce uncertainties in vertical flux calculations for HONO and related species (HCHO, $HNO_3$ and $N_2O_5$). Model chemical mechanisms must be updated to incorporate heterogeneous HONO production.*

Results from UBOS 2013 identified a potentially significant daytime, surface HONO source when snow is present as discussed in Section 2.3 and Section 5, but much uncertainty remains about the strength of this source and the resulting vertical extent of elevated daytime HONO concentrations. It must be noted that the HONO concentration measurements were made using a single method (acid CIMS – see Section 5.2.9) and require verification by comparison with other measurement methods such as LP-DOAS (Stutz et al., 2000) and LOPAP (Kleffmann et al., 2002). HONO measurements by instruments utilizing a variety of detections schemes are needed at higher elevations above the surface to better quantify the source strength.

*Finding E.3.2: Additional data are needed to quantify the contributions of different sources of primary formaldehyde.*

Results from UBOS 2013 showed that formaldehyde is a key source of radicals that drive ozone production under winter episode conditions, but the relative contributions of different potential sources of directly emitted formaldehyde such as use of methanol contaminated with trace amounts of formaldehyde or diesel engines, are not well characterized. This makes it difficult to design control strategies that target formaldehyde. Chemical analysis of methanol used during winter oil and gas operations for possible formaldehyde contamination and better inventories of other formaldehyde sources are needed.

*Finding E.3.3: Additional work is needed to build a meteorological model simulation able to accurately capture the key features of cold pool conditions associated with winter ozone episodes.*

Current meteorological models have well known deficiencies when it comes to simulating cold pool conditions (see, for example, Holstag et al., 2013). Initial attempts at simulating Uinta Basin winter cold pool events by several groups including Utah State University, University of Utah, and NOAA are consistent with this experience, exhibiting overestimation of surface temperature, PBL height, and surface wind speeds. Additional evaluation of alternative model options and model development will be needed to achieve more accurate simulations of these challenging conditions.

*Finding E.3.4: Additional emission inventory development work and inventory evaluation studies are needed.*

Simulations of ozone episodes in the Uinta Basin are crucially dependent on accurate spatially and temporally resolved emissions data. Current emission inventory development work as described in Section 9.1 requires further refinement although inventory data have been used in model simulations which have been found to produce elevated ozone concentrations. Additional inventory development work is needed, focusing in particular on refining VOC speciation profiles and evaluating poorly characterized sources such as methanol use (and hypothesized associated formaldehyde) and produced water storage and treatment for which current data are limited (see Section 9.2).

*Conclusions*

While much has been learned about winter ozone episodes from the UBOS and UGWOS studies, additional, targeted data collection and analysis as described in Findings E.1.1 – E.1.6 above is needed to complete our understanding of these unusual events.

## 2.7 References

ENVIRON, 2013. CAMx User's Guide Comprehensive Air Quality Model with Extensions, Version 6.0. ENVIRON International Corp., Novato, CA (http://camx.com/download/default.aspx, last access: November, 2013).

Carter, W.P. and J.H. Seinfeld, 2012. Winter ozone formation and VOC incremental reactivities in the Upper Green River Basin of Wyoming. Atmospheric Env. 50 (2012) 255-266.

Cohan, D. S., A. Hakami, Y. Hu, and A. G. Russell, 2005. Nonlinear Response of Ozone to Emissions: Source Apportionment and Sensitivity Analysis. Environ. Sci. Technol., 39, 6739-6748.

Edwards, P.M., C.J. Young, K. Aikin, J.A. deGouw, W.P. Dube, F. Geiger, J.B. Gilman, D. Helmig, J.S. Holloway, J. Kercher, B. Lerner, R. Martin, R. McLaren, D.D. Parrish, J. Peischl, J.M. Roberts, T.B. Ryerson, J. Thornton, C. Warneke, E.J. Williams, and S.S. Brown, 2013. Ozone photochemistry in an oil and natural gas extraction region during winter: simulations of a snow-free season in the Uintah Basin, Utah. Atoms. Chem. Phys. Discuss., 13, 7503-7552.

ENVIRON, 2008. 2008 Upper Green River Winter Ozone Study. ENVIRON International Corp., T&B Systems Inc., Meteorological Solutions Inc., October (http://deq.state.wy.us/AQD/Upper%20Green%20Winter%20Ozone%20Study.asp).

ENVIRON, 2013. CAMx User's Guide: Comprehensive Air Quality Model with Extensions, Version 6.0. ENVIRON International Corp., May (www.camx.com).

Gery, M.W. and R.R. Crouse, 1990. User's Guide for Executing OZIPR, EPA-9D2196NASA, U.S. EPA, Res. Tri. Park (www.epa.gov/scram001/userg/other/ozipr.pdf).

Grannas et al., 2007. An overview of snow photochemistry: evidence, mechanisms and Impacts, Atmos. Chem. Phys., 7, 4329–4373, 2007.

Hakami, A., M. T. Odman, and A. G. Russell, 2003. High-order, direct sensitivity analysis of multidimensional air quality models. Environ. Sci. Technol., 37, 2442-2452.

Hall, C., M. Mansfield, H. Shorthill, and S. Lyman, 2012. Upper Green River Basin winter ozone: summary of public information about the Wyoming phenomenon, Utah State University Office of Commercialization and Regional Development, CRD/12---275B, 2012.

Holstag, A. A. M., G. Svensson, P. Bass, S. Basu, B. Beare, A.C.M. Beljaars, F.C. Bosveld, J. Cuxart, J. Lindvall, G.J. Steeneveld, M. Tjernstrom, and B.J.H. Van De Wiel, 2013. Stable atmospheric boundary layers and diurnal cycles: challenges for weather and climate models. Bull. Amet. Soc., V94, N11, 1691-1706.

Kleffmann, J., J. Heland, R. Kurtenbach, J. C. Lörzer, and P. Wiesen, 2002. A new instrument (LOPAP) for the detection of nitrous acid (HONO), Environ. Sci. Pollut. Res., 9, 48-54.

Lyman, S. and Shorthill, H., 2013. Final Report: 2012 Uintah Basin Winter Ozone & Air Quality Study. Doc. No. CRD13-320.32, Commercialization and Regional Development, Utah

State University, 1 February (http://rd.usu.edu/files/uploads/ubos_2011-12_final_report.pdf).

Martin, R., K. Moore, M. Mansfield, S. Hill, K. Harper, and H. Shorthill, 2011. Final Report: Uinta Basin Winter Ozone and Air Quality Study, December 2010 – March 2011. EDL/11-039, Energy Dynamics Lab., Utah State University Research Foundation, Bingham Research Center, Vernal, Utah, 14 June.

MSI, 2013. Final Report: 2013 Upper Green River Winter Ozone Study. Meteorological Solutions, Inc. and T&B Systems, August (http://deq.state.wy.us/aqd/Upper%20Green%20Winter%20Ozone%20Study.asp).

Nopmongcol, O., G. Yarwood, and T. Stoeckenius, 2008 Winter Ozone Box Model Study. Novato, CA: ENVIRON International Corp., 2010.

NRC (National Research Council), 1991. Rethinking the Ozone Problem in Regional and Urban Air Pollution. National Academy Press, Washington, DC.

Pétron, G., et al., 2012. Hydrocarbon emissions characterization in the Colorado Front Range: A pilot study, J. Geophys. Res., 117, D04304, doi:10.1029/2011JD016360.

Rappenglück, B., et al., 2013. Strong wintertime ozone events in Wyoming. Atmos. Chem. Phys. Discuss., 13, 17953-18005.

Schnell, R.C., S.J. Oltmans, R.R. Neely, M.S. Endres, J.V. Molenar, and A.B. White, 2009. Rapid photochemical production of ozone at high concentrations in a rural site during winter. Nature Geoscience, 18 January (DOI 10.1038/NGEO415).

Solomon, P., E. Cowling, G. Hidy, and C. Furiness, 2000. Comparison of scientific findings from major ozone field studies in North America and Europe. Atmospheric Env. 34 (2000) 1885-1920.

Stoeckenius, T.E., G. Mansell, C. Tran, S. Coulter-Burke, M. Jimenez, and G. Wilson, 2004. "Top-Down Evaluation of Mobile6 Based Emission Inventories in Four Cities Via Reconciliation Of HC/NOX and CO/NOX Ratios with Ambient Monitoring Data." Presented at 14th CRC On-Road Vehicle Emissions Workshop. San Diego, California, March.

Stoeckenius, T. and L. Ma, 2010. A Conceptual Model of Winter Ozone Episodes in Southwest Wyoming. ENVIRON International Corp., Novato, CA, 29 January (http://deq.state.wy.us/AQD/Ozone%20Conceptual%20Model%20Report_Sublette%20County.asp).

Stutz,J., E.S. Kim, U. Platt, P. Bruno, C. Perrino, and A. Febo, 2000. UV-visible absorption cross section of nitrous acid, J.Geophys.Res., 105,14,585–14,592,2000.

Thoma, E., 2009. Measurement of Emissions from Produced Water Ponds: Upstream Oil and Gas Study #1. EPA/600/R-09/132. National Risk Management Research Lab, U.S. Environmental Protection Agency, October.

Vingarzan, R., 2004. A review of surface ozone background levels and trends, Atmospheric Env., 38(21), 3431.

# 3.0 DISTRIBUTED MEASUREMENTS OF AIR QUALITY AND METEOROLOGY

***Section 3.1. Spatial, Seasonal, and Inter-annual Aspects of Wintertime Ozone***

Seth Lyman, Marc Mansfield, Howard Shorthill, Randy Anderson, Chad Mangum, Jordan Evans, and Tate Shorthill

Office of Commercialization and Regional Development, Utah State University, Vernal, Utah

***Section 3.2. Observations and Numerical Modeling of the Atmospheric Boundary Layer in the Uinta Basin***

John Horel, Erik Crosman, and Erik Neemann

Department of Atmospheric Sciences, University of Utah, Salt Lake City, Utah

***Section 3.3. Use of the CALMET Diagnostic Model to Simulate Winter Inversions***

Michael Christiansen and Trevor O'Neil

Department of Chemistry, Utah State University, Vernal, Utah

## 3.1 Spatial, Seasonal, and Inter-annual Aspects of Wintertime Ozone

### 3.1.1 Introduction

Ozone concentrations have been measured continuously in the Uinta Basin since fall 2009. During winter 2009-10, monitoring stations at Ouray and Red Wash observed ozone concentrations that exceeded the Environmental Protection Agency (EPA) standard. Following the discovery of this new phenomenon, stakeholder concern led to the establishment of several additional air quality monitoring stations to support subsequent studies. Seventeen stations operated around the Uinta Basin during winter 2010-11, and 30 operated during winter 2011-12. Martin et al. (2011) and Lyman and Shorthill (2013) highlight the results of these studies. This section contains an analysis of ozone, precursor, and meteorology data from 20 monitoring sites that operated around the Basin during winter 2012-13, and an analysis of variability across the four years of available ozone data.

### 3.1.2 Methods

#### 3.1.2.1 Ozone Measurements

Ten of the air quality monitoring stations in the Uinta Basin during winter 2012-13 were operated by Utah State University (USU), and ten were operated by other organizations. Table 3-1 contains a list of all monitoring stations, including locations, elevations, and responsible operators. Data and methods used for stations operated by other organizations were obtained from EPA's AQS database (https://ofmext.epa.gov/AQDMRS/aqdmrs.html). We utilized 2B Technology Model 205 or 202 ozone monitors at most of the stations, and we operated an Ecotech Model 9810 ozone analyzer at the Horsepool site. We performed calibration checks at all USU stations at least every other week using NIST-traceable ozone standards. Calibration

checks passed if monitors reported in the range of ±5 ppb when exposed to 0 ppb ozone, and if monitors were within ±7% deviation from expected values when exposed to 90 and 140 ppb ozone. We only included data bracketed by successful calibration checks in the final dataset.

**Table 3-1. Air quality monitoring stations that operated during winter 2012-13.**

| Site Name | Operator | Data Availability | Latitude | Longitude | Elevation (m) | VOC | $NO_x$ |
|---|---|---|---|---|---|---|---|
| Dinosaur NM | NPS | AQS dbase | 40.4371 | -109.3047 | 1463 | N/A | N/A |
| Duchesne | USU | USU | 40.1615 | -110.4011 | 1682 | N/A | N/A |
| Fruitland | UDAQ | AQS dbase | 40.2087 | -110.8403 | 2021 | canister | active NO, $NO_2$ |
| Seven Sisters | USU | USU | 39.9813 | -109.3454 | 1618 | canister | passive $NO_2$ |
| Gusher | USU | USU | 40.2935 | -109.6575 | 1557 | N/A | N/A |
| Horsepool | USU | USU | 40.1437 | -109.4672 | 1569 | active | active NO, $NO_2$, $NO_y$ |
| Lapoint | USU | USU | 40.4040 | -109.8157 | 1674 | N/A | N/A |
| Little Mtn. | USFS | AQS dbase | 40.5368 | -109.7001 | 2624 | N/A | N/A |
| Mountain Home | USU | USU | 40.4319 | -110.3821 | 2234 | N/A | N/A |
| Myton | EPA/STI | AQS dbase | 40.1948 | -110.0622 | 1550 | N/A | active NO, $NO_2$ |
| Ouray | EPA/Golder | AQS dbase | 40.0548 | -109.6880 | 1464 | N/A | active NO, $NO_2$ |
| Rabbit Mtn. | Enefit/Tetra. | AQS dbase | 39.8687 | -109.0973 | 1879 | N/A | active NO, $NO_2$ |
| Rangely | NPS/BLM | AQS dbase | 40.0869 | -108.7616 | 1648 | N/A | active NO, $NO_2$ |
| Red Wash | EPA/Golder | AQS dbase | 40.1972 | -109.3525 | 1689 | N/A | active NO, $NO_2$ |
| Roosevelt | UDAQ/USU | AQS dbase | 40.2942 | -110.0090 | 1587 | active | active NO, $NO_2$, $NO_y$ |
| Sand Wash | USU | USU | 39.8390 | -109.9150 | 1416 | N/A | N/A |
| Seep Ridge | USU | USU | 39.7539 | -109.5460 | 1975 | N/A | N/A |
| Vernal | UDAQ | AQS dbase | 40.4531 | -109.5097 | 1606 | canister | active NO, $NO_2$ |
| Wells Draw | USU | USU | 40.0670 | -110.1510 | 1768 | canister | Passive $NO_2$ |
| Whiterocks | EPA/STI | AQS dbase | 40.4694 | -109.9304 | 1841 | N/A | active NO, $NO_2$ |

#### 3.1.2.2 Ozone Precursor Measurements

We measured NO, true $NO_2$ (via a photolytic converter), and $NO_y$ at Roosevelt and Horsepool with AQD/Teledyne-API and Ecotech systems, respectively, and calibrated the systems weekly with NO standards, monthly with $NO_2$ standards via gas phase titration, and at the beginning and end of the campaign with nitric acid and n-butyl nitrate permeation tubes (for $NO_y$). A number of sites operated by other organizations measured NO and $NO_2$ via a molybdenum converter-based system (measurement contains some $NO_y$), and we obtained these data from EPA's AQS database. We performed supplemental $NO_2$ measurements at some sites from February 1 through February 8 using Radiello $NO_2$ passive samplers (Table 3-1). We deployed Radiello samplers for one week and analyzed them according to Radiello protocols on a Dionex ion chromatograph. Radiello samples were blank corrected and also corrected to concentrations of $NO_2$ measured with automated instruments at co-located sites.

We measured 57 ozone-forming nonmethane hydrocarbons (NMHC) in 30-minute and hourly samples at Horsepool and Roosevelt, respectively, during January and February. NMHC were analyzed by sample concentration on activated carbon traps, followed by desorption into automated gas chromatography-flame ionization detection systems. We calibrated these systems every other week with certified gas standards. We also performed supplemental NMHC measurements at some sites from February 1 through February 8 using evacuated stainless steel canisters. Canisters were filled from 7 to 9 AM on 1, 3, 6, and 8 February. Some of these samples were analyzed with the Roosevelt automated gas chromatograph, but most were analyzed by a commercial laboratory using gas chromatography and flame ionization detection. Canister samples utilized automated sampling timers and critical orifice-based flow controllers. All wetted parts were either stainless steel or stainless steel coated with deactivated fused silica. All canister sampling components were cleaned between each use by repeatedly flushing with hot, humidified nitrogen. EPA PAMS compounds (EPA, 2003) were measured by the automated systems at Horsepool and Roosevelt, and PAMS compounds and methanol were measured with canister systems. Methanol was analyzed via gas chromatography and mass spectrometry by a commercial laboratory.

#### 3.1.2.3 Meteorological Measurements

We operated solar radiation sensors, including incoming and outgoing short wave, long wave, UV-A, and UV-B at Horsepool, and incoming and outgoing shortwave radiation at Roosevelt. We operated a comprehensive, research grade meteorological instrument suite at Horsepool and lower cost meteorological measurements (Davis VantagePro) at some other sites. In addition, we downloaded meteorological data collected by others from the EPA AQS database and from http://mesowest.utah.edu.

#### 3.1.2.4 Spatial Data Analysis

Data from all sites were visualized and interpolated using ArcGIS software. Relationships among measured parameters and a variety of spatial variables were investigated using ArcGIS and SPSS software. The following variables were considered in terms of proximity to study sites (5, 10, 15, 20, 25, or 50 km radius):

- Number of producing wells (oil, gas, both),
- Amount of oil and gas production (February 2013),
- Number of drill rigs,
- Number of compressor stations and gas plants (with estimated $NO_x$ and VOC emissions),
- Number and surface acres of produced water ponds,
- Human population,
- Elevation, and
- Difference between elevation of site and of surrounding terrain.

These parameters were analyzed in correlation and multiple regression analyses to determine the best predictors of observed ozone and precursor concentrations.

### 3.1.3 Results and Discussion

#### 3.1.3.1 Ozone Concentrations and Distribution

Measurements made in the Uinta Basin show that, relative to the three previous winter seasons, the winter of 2012-13 had the highest number of ozone exceedance days, highest maximum concentrations of ozone, and largest affected area of elevated ozone. Five research sites experienced more than 30 days of exceedances of EPA's National Ambient Air Quality Standard (NAAQS) during the 2012-13 season[1]. The only sites in the Basin that had fourth highest daily maximum 8-hour average ozone concentrations below 75 ppb were those more than 2000 m above sea level (Tables 3-1 and 3-2).

In contrast to conditions within the Basin, air quality monitoring stations outside of the Uinta Basin but within other intermountain West basins, including those within Wyoming's Upper Green River Basin, did not experience elevated ozone during the winter of 2012-13 (Table 3-2). Hall et al. (2013) analyzed the relationship between inversion conditions, snow cover and ozone in several intermountain West basins. While pointing out that further investigation is needed, Hall et al. concluded that basins without intensive oil and gas production do not experience high winter ozone levels even when strong inversions and snow cover are present. One potential explanation for this result is that basins without large amounts of oil and gas production may have lower VOC or NOx concentrations or VOC/NOx ratios that are less conducive to ozone formation. However, further study would be needed to confirm this.

The Uinta Basin experienced seven distinct inversion episodes during which ozone at multiple monitoring stations exceeded the NAAQS (Figure 3-1). Of these, a 13-day episode that began 15 January and continued through 27 January was the longest. Episodes in January and early February tended to be longer, whereas episodes in late February and early March were shorter and exhibited more rapid increases in ozone concentrations. The highest ozone concentrations of the study period were observed in early March, while the greatest number of sites exceeded the NAAQS in late January. Adequate snow cover and a series of prolonged inversion conditions (Figure 3-2) allowed for the observed ozone production. As soon as temperatures warmed enough to melt the snow from the Basin, which occurred around 10 March, significant ozone production ceased.

[1] The NAAQS for ozone is 75 ppb, calculated over three calendar years as the average of the fourth highest 8-hr average daily maximum ozone concentration, though any measured concentration above 75 ppb commonly is referred to as "exceedance."

**Table 3-2. Statistics for 8-hour average ozone concentrations at sites around the Uinta Basin and at select sites in Utah and the intermountain West from November 2012 through March 2013.**

| Sites within Uinta Basin | Mean | Median | Max | Min | 4th Highest Daily Max | Days of Exceedance |
|---|---|---|---|---|---|---|
| Dinosaur NM | 45.8 | 41.5 | 126.0 | 2.0 | 113.4 | 26 |
| Duchesne | 34.7 | 34.1 | 112.4 | 2.6 | 87.1 | 12 |
| Fruitland | 39.8 | 41.6 | 64.5 | 5.8 | 60.5 | 0 |
| Gusher | 58.9 | 53.6 | 129.7 | 13.7 | 117.6 | 38 |
| Horsepool | 57.8 | 49.7 | 139.0 | 17.0 | 131.5 | 41 |
| Lapoint | 65.0 | 59.9 | 115.6 | 30.8 | 109.4 | 26 |
| Little Mtn. | 49.4 | 49.7 | 72.3 | 29.3 | 66.9 | 0 |
| Mountain Home | 46.8 | 46.6 | 74.7 | 14.9 | 71.0 | 0 |
| Myton | 52.6 | 48.5 | 109.4 | 15.6 | 97.7 | 17 |
| Ouray | 47.7 | 39.9 | 141.6 | 6.1 | 132.4 | 39 |
| Rabbit Mtn. | 44.6 | 43.0 | 107.3 | 18.1 | 82.5 | 8 |
| Rangely | 38.2 | 35.8 | 106.1 | 6.1 | 91.0 | 11 |
| Red Wash | 50.1 | 42.5 | 124.0 | 11.4 | 114.0 | 36 |
| Roosevelt | 44.9 | 40.1 | 110.8 | 9.8 | 104.0 | 29 |
| Sand Wash | 55.0 | 49.5 | 127.5 | 11.1 | 122.0 | 33 |
| Seep Ridge | 48.7 | 47.3 | 95.1 | 14.9 | 80.8 | 8 |
| Seven Sisters | 47.4 | 41.1 | 152.0 | 4.0 | 137.7 | 31 |
| Vernal | 37.1 | 33.4 | 114.9 | 5.4 | 102.1 | 22 |
| Wells Draw | 49.5 | 45.8 | 131.5 | 15.1 | 108.0 | 26 |
| Whiterocks | 55.9 | 54.8 | 95.7 | 31.8 | 86.8 | 7 |
| **Sites outside Uinta Basin** | **Mean** | **Median** | **Max** | **Min** | **4th Highest Daily Max** | **Days of Exceedance** |
| Boulder (WY) | 31.8 | 32.4 | 49.8 | 5.8 | 47.6 | 0 |
| Idaho Falls | 35.1 | 35.7 | 51.2 | 9.2 | 49.0 | 0 |
| Logan | 17.5 | 16.8 | 44.0 | 2.0 | 43.3 | 0 |
| Meeker | 39.7 | 40.6 | 59.1 | 20.8 | 55.9 | 0 |
| Price | 34.9 | 35.3 | 57.8 | 8.4 | 51.1 | 0 |
| Rifle | 22.0 | 21.5 | 51.6 | 2.0 | 46.6 | 0 |
| Salt Lake City | 15.9 | 14.0 | 47.8 | 2.0 | 46.0 | 0 |

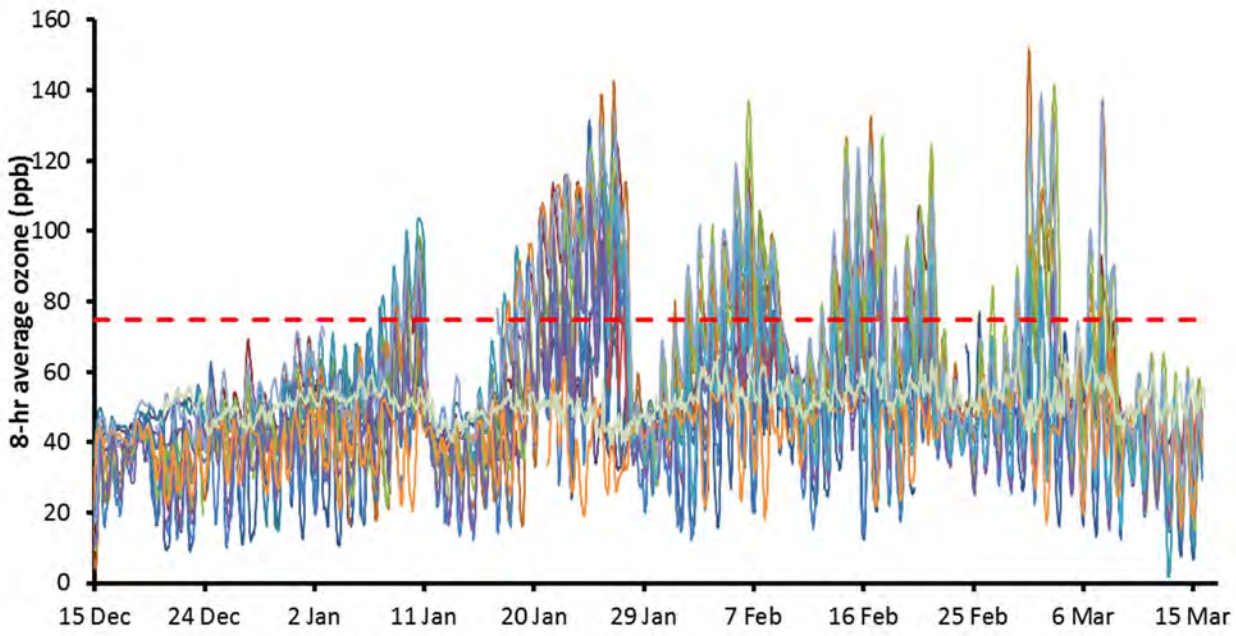


**Figure 3-1. Time series of 8-hour average ozone concentrations at all monitoring sites in the Uinta Basin, winter 2012-13. EPA NAAQS of 75 ppb is shown as a red dashed line.**

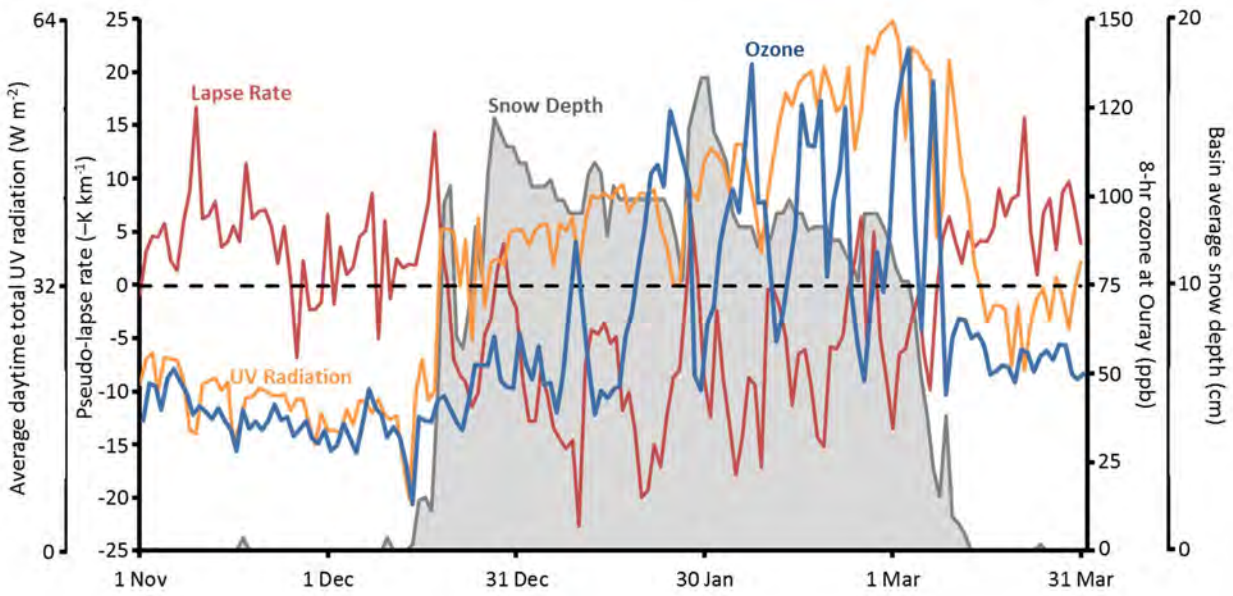


**Figure 3-2. Time series of average snow depth from five stations in the Uinta Basin, pseudo-lapse rate for the Basin, 8-hour average ozone at Ouray, and average total daytime UV-A and UV-B radiation (average during daytime hours of the sum of upwelling and downwelling UV-A and UV-B) at Horsepool, winter 2012-13. The pseudo-lapse rate was derived from the change in temperature with elevation at surface meteorological stations in the Basin. The dashed black line indicates a lapse rate of zero and an ozone concentration of 75 ppb. A more negative lapse rate indicates a stronger inversion.**

Highest ozone concentrations were observed consistently in the area of the Basin that lies south of Vernal containing a high density of natural gas wells (Figures 3-3, 3-4, and 3-5), though ozone distribution exhibited unique characteristics during different inversion episodes. Figure 3-3 shows that for the entire study period, high elevation sites and sites on the margins of the Basin had the lowest ozone concentrations, while lower elevation sites and sites in the area south of Vernal had the highest.

During the 13-day inversion episode that culminated on 26 January, elevated ozone concentrations extended far beyond the Ouray-Horsepool-Seven Sisters area south of Vernal, and eight-hour average ozone for that day exceeded 100 ppb at ten sites, including sites on the edge of the Basin like Rangely and Rabbit Mountain (Figure 3-4). In contrast, during a shorter inversion episode in early March, only four sites exceeded 100 ppb, and many sites on the margins of the Basin, experienced no exceedances of the NAAQS for ozone (Figure 3-5).

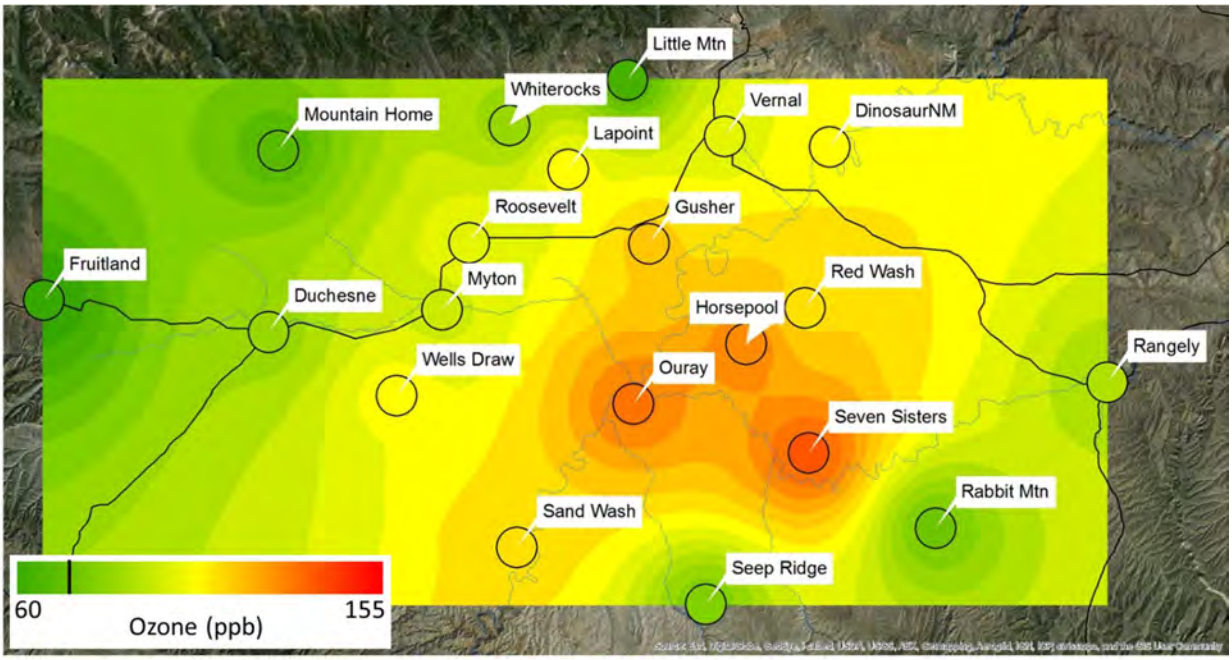


**Figure 3-3. Fourth-highest daily maximum 8-hour average ozone concentrations for all sites in the Uinta Basin, winter 2012-13. The black line on the color scale indicates 75 ppb.**

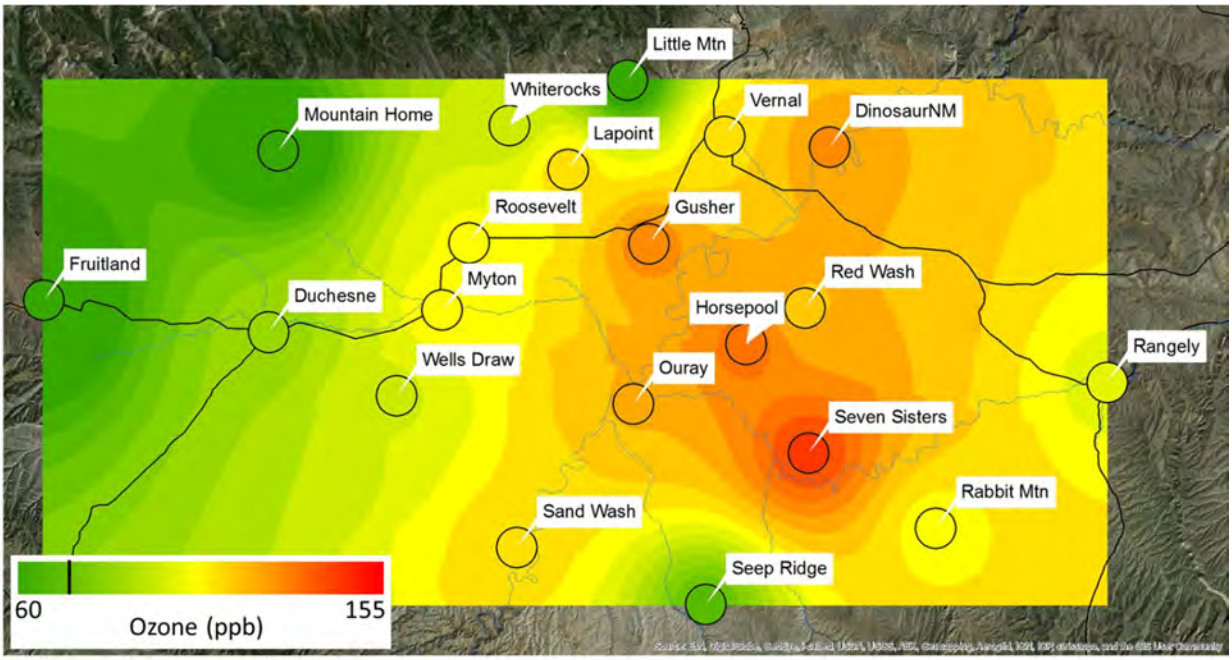


**Figure 3-4. Maximum 8-hour average ozone concentrations for all sites in the Uinta Basin, 26 January.**

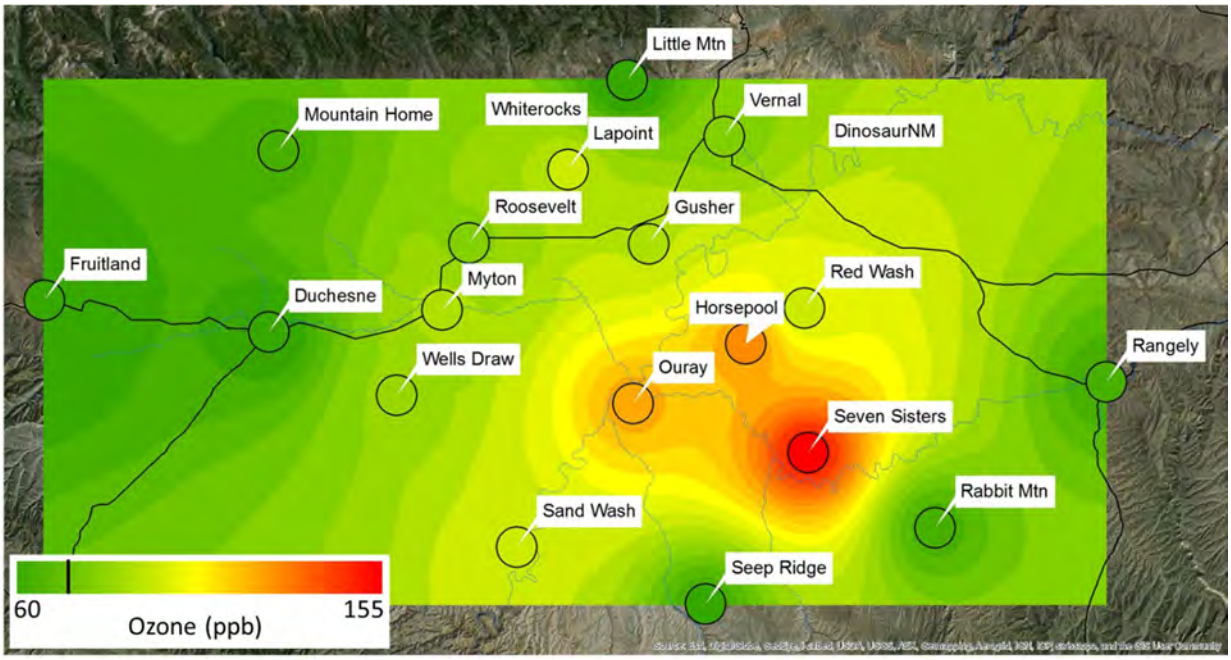


**Figure 3-5. Maximum 8-hour average ozone concentrations for all sites in the Uinta Basin, 1 March.**

Ozone concentrations during inversion episodes were strongly correlated with elevation, were correlated with proximity to oil and gas operations (Figure 3-6), and were less consistently correlated with other spatial metrics (Table 3-3). The correlation of ozone with oil wells was much weaker than the correlation with gas wells. Gas wells tended to be in areas of lower elevation, while oil wells did not ($R^2$ = 0.26, p = 0.02 for relationship between average elevation in a 25 km radius around study sites and the number of producing gas wells in the same radius), which could at least partly explain the better correlation of ozone with gas production. The average day-night difference in ozone concentration at a given site was significantly correlated with elevation and the number of people living nearby (Table 3-3).

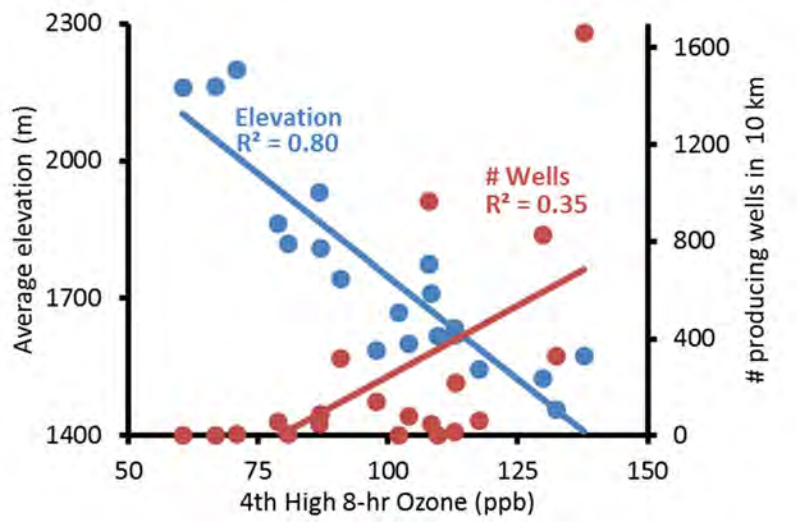


**Figure 3-6. Relationship between fourth highest daily maximum 8-hr average ozone concentration for winter 2012-13 and average elevation within 10 km of a monitoring station (in blue) and number of producing oil and gas wells within 10 km of a monitoring station (in red). Linear regression lines and Pearson $R^2$ values are also shown.**

Correlations of ozone with elevation and oil and gas production metrics were often weaker when maximum ozone on individual high ozone days, rather than ozone statistics for the whole winter season, was used (Table 3-3). For example, proximity to oil and gas production was not a significant predictor of ozone concentrations on 6 February, a day with high ozone, but it was a significant predictor on 26 January and 1 March, the days with the highest ozone values of the entire season. Correlations on 26 January and 1 March were weaker than those for the whole season. It is probable that meteorological conditions (especially air transport) on individual high ozone days obscured the impact of proximity to oil and gas production on ozone concentrations.

Correlations for spatial parameters were calculated within 5, 10, 15, 20, 25, and 50 km radii from sites, and the radii with strongest correlations are shown in Table 3-3. In general, correlations at different radii were similar to those shown, but correlations with oil and gas metrics tended to be strongest at larger radii, while correlations with population and average elevation were stronger at smaller radii.

We also explored whether the difference between the study site elevation and the average elevation of the surrounding terrain was a useful predictor of ozone concentrations. For example, the Sand Wash site was deep in the mouth of Desolation Canyon, and the average terrain in a 10 km radius around the site was 218 m higher than the elevation of the site itself. We hypothesized that sites surrounded by higher terrain would have stronger local inversion characteristics, perhaps leading to increased ozone production. No significant correlations were observed, however, between ozone concentrations and the difference between site

elevation and surrounding terrain elevation, indicating that sites in canyons or river bottoms were not more prone to ozone production than nearby areas.

**Table 3-3. Pearson correlation coefficients (r) for relationships between ozone and spatial parameters. "N.S." Indicates that the correlation was not significant (α = 0.05).**

| | Site Elevation | Average Elevation | # Oil & Gas Wells | # Oil Wells | # Gas Wells | Monthly Oil Prod. | Monthly Gas Prod. | Population |
|---|---|---|---|---|---|---|---|---|
| **Radius from site** | **--** | **10 km** | **50 km** | **50 km** | **50 km** | **50 km** | **50 km** | **5 km** |
| Highest 8-hr ozone | -0.79 | -0.89 | 0.77 | N.S. | 0.66 | N.S. | 0.65 | N.S. |
| 4$^{th}$ highest 8-hr ozone | -0.76 | -0.90 | 0.75 | N.S. | 0.64 | N.S. | 0.63 | N.S. |
| # Exceedance days | -0.75 | -0.90 | 0.74 | N.S. | 0.62 | N.S. | 0.61 | N.S. |
| Day-night difference ozone | -0.61 | -0.54 | N.S. | 0.53 | N.S. | 0.52 | N.S. | 0.56 |
| 26 Jan max. 8-hr ozone | -0.84 | -0.93 | 0.67 | N.S. | 0.59 | N.S. | 0.57 | N.S. |
| 6 Feb max. 8-hr ozone | N.S. | -0.50 | N.S. | N.S. | N.S. | N.S. | N.S. | N.S. |
| 1 Mar max. 8-hr ozone | -0.61 | -0.76 | 0.74 | N.S. | 0.65 | N.S. | 0.65 | N.S. |

Multiple linear regression was employed to better understand the relationship between ozone and spatial parameters (as in Lyman and Gustin, 2009). In multiple regression analysis, a linear regression equation that incorporates more than one independent variable is used to predict the dependent variable, and the predictive value of independent variables can be individually assessed. Many of the independent variables considered in this study are correlated with each other, and the multiple regression method is able to show the value of each variable in predicting ozone concentration without the obscuring effects of this inter-correlation.

All parameters listed in the Methods section were utilized in the linear regression analysis. An iterative process of including and excluding parameters was employed to determine whether each possible independent variable added additional predictive power to the multiple regression model. Ultimately, elevation was found to be the best predictor of ozone concentration. The exact elevation of study sites was less useful, however, than the average elevation of the terrain surrounding the study sites, and average elevation in a 10 km radius of sites was the best predictor (Figure 3-6, Table 3-3).

While average elevation in a 10 km radius was able to explain 80% of the variability in the fourth highest 8-hour average ozone concentration among study sites (i.e., $R^2 = 0.80$), adding the number of producing oil and gas wells within 10 km of study sites with average elevation in a multiple regression model added 10% more predictive power (i.e., $R^2 = 0.90$). In other words, with only information about elevation and proximity to oil and gas activity, ozone concentrations during winter 2012-13 can be predicted at a given location in the Basin with 90% accuracy.

The spatial distribution of compressor stations, gas plants, and produced water impoundments was strongly correlated to that of oil and gas wells, and including these facilities in the analysis did not improve the quality of the regression. Oil production and gas production were worse predictors of ozone concentrations than the number of oil and gas wells. Using the number of gas wells within 10 km, rather than the number of oil and gas wells together, was as useful as the number of oil *and* gas wells at predicting ozone ($R^2$ = 0.90), but using the number of oil wells within 10 km was not ($R^2$= 0.81; proximity to oil wells variable was not significant, with p = 0.45). This finding could indicate that emissions associated with gas production are more important in ozone production than emissions associated with oil production, either because natural gas-related emissions are more reactive, or because they are more abundant on a per-well basis. On the other hand, the insignificance of the oil well variable could be due, at least in part, to the fact that there are fewer oil wells than gas wells in the Basin and they are less densely distributed, so with the limited number of study sites available the relationship between ozone and oil well locations was not statistically detectable. Oil wells clearly do emit NMHC and $NO_x$ that are active in ozone production (see Section 3.1.3.2), and a similar study with more sites in the oil-producing areas of the basin may lead to a better correlation of ozone with proximity to oil wells.

While correlations of ozone with proximity to oil and gas production were strongest when larger radii were used, in the multiple regression analysis the number of wells within 10 km was the strongest predictor of ozone concentrations. While average elevation within 10 km and number of producing wells within 10 km explained 90% of the variability in fourth highest ozone, substituting the number of producing wells within 50 km allowed for explanation of only 81% of variability, and the number of wells was not a significant independent variable (p = 0.42).

Located in Colorado on the eastern edge of the Uinta Basin, the Rangely site, which is a regulatory site used by EPA to assess attainment status with respect to the NAAQS, has three years of ozone data with an average greater than 75 ppb. Some have speculated that high ozone in Rangely is due to transport of ozone and precursors from Utah (Webb, 2011). While the multi-year Uintah Basin Ozone Study (UBOS) certainly has focused on Utah (e.g., maps of oil and gas production included in the 2012 UBOS final report only showed wells in Utah), a dense field of 668 producing oil and gas wells exists within 15 km of the Rangely monitoring station (Figure 3-7). As pointed out in Section 8, Rangely is included within the region of the Basin that is below the average inversion height observed in 2013. We therefore hypothesize that some air exchange between Rangely and the Utah portion of the Uinta Basin occurs, such that ozone experienced in Rangely is due to a combination of local (i.e., within Colorado) and regional (i.e., within Utah) precursor sources.

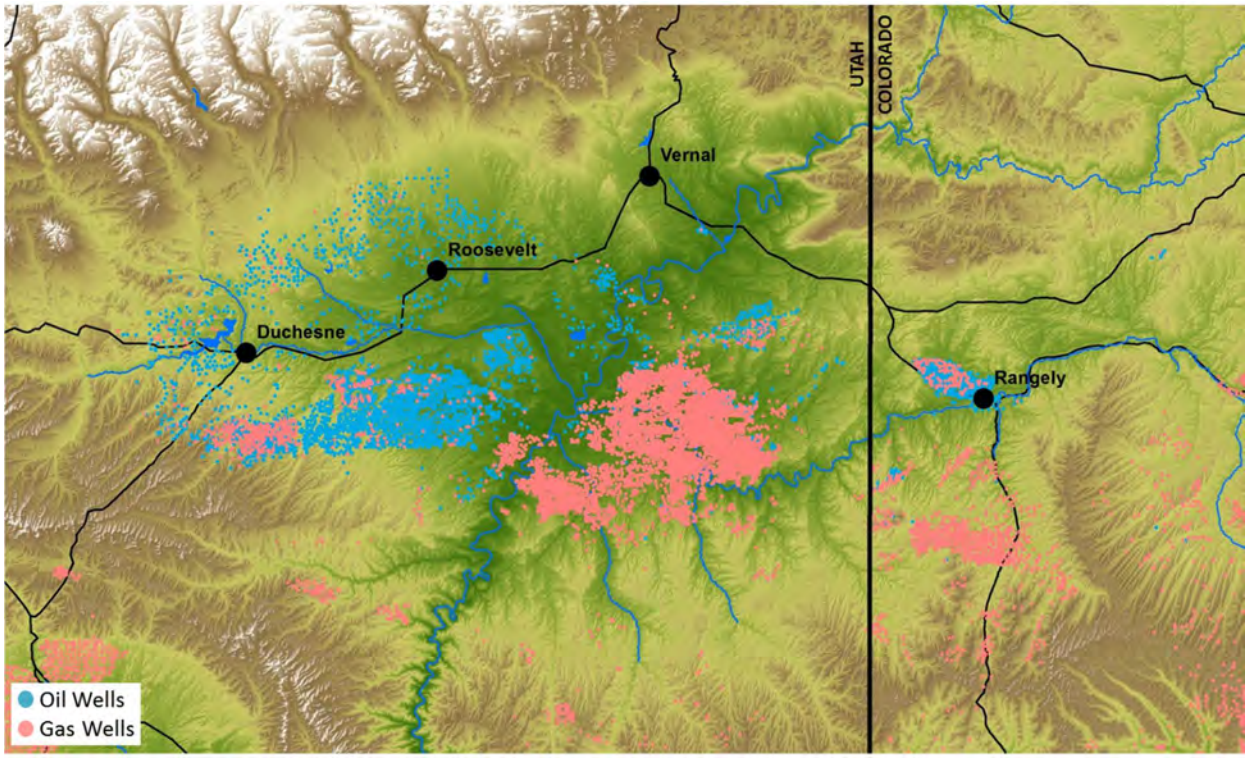


**Figure 3-7. Producing oil and gas wells in and around the Uinta Basin. Wells were considered "producing" if they reported oil or gas production during February 2013.**

### 3.1.3.2 Distribution of Nonmethane Hydrocarbons

Concentrations of NMHC[2] increased during inversion episodes, though the distribution of NMHC remained mostly the same. The highest NMHC concentrations were consistently observed at the Seven Sisters site, which is located in an area of intense natural gas production south of Vernal (Figures 3-8 and 3-9). At the height of an inversion episode on 6 February, the distributions of alkanes and aromatic compounds were similar, with highest concentrations at the Seven Sisters and Horsepool sites, followed by Roosevelt, and then by Vernal and Wells Draw (Figure 3-9). Fruitland, a site remote from oil and gas activity on the western edge of the Uinta Basin, consistently had the lowest NMHC concentrations. This spatial distribution of NMHC was similar to observations during non-inversion conditions during winter 2011-12 (Lyman et al., 2013).

[2] The term "VOC" usually omits methane and ethane since they are less reactive than most other volatile organics, while "NMHC" refers to *all* nonmethane organics, regardless of reactivity.

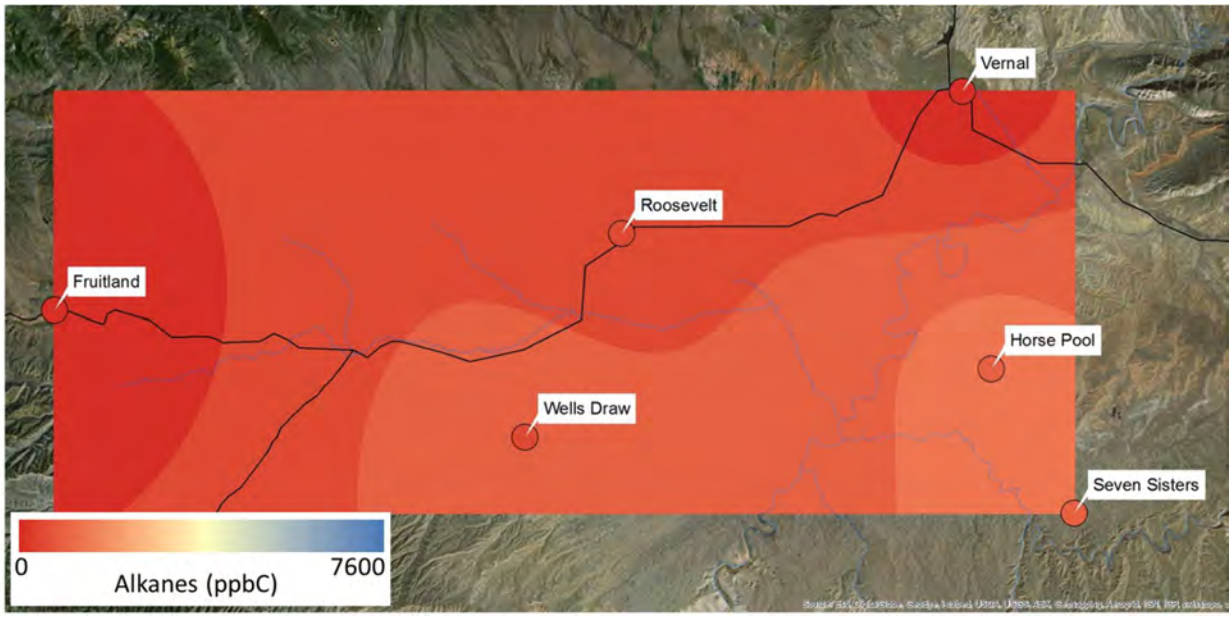


**Figure 3-8. Sum of all alkanes measured on 1 February (the start of an inversion episode) at six sites around the Uinta Basin.**

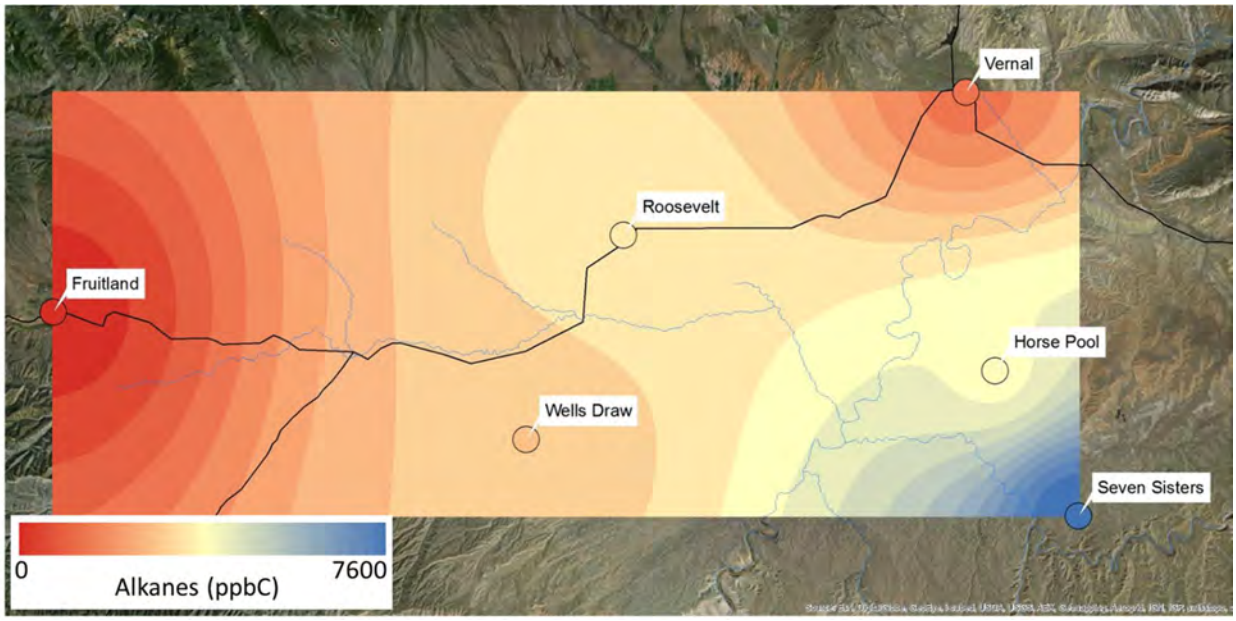


**Figure 3-9. Sum of all alkanes measured on 6 February (day of highest ozone during the inversion episode noted in previous figure) at six sites around the Uinta Basin.**

The ratio of alkanes to aromatics was higher at Wells Draw, a site in an area of intense oil production, than at Seven Sisters, a site in an area of mostly gas production, echoing observations made during non-inversion conditions in winter 2011-12 (Lyman et al., 2013). Alkene concentrations were also highest at Wells Draw (Figure 3-11). The source of higher

alkenes in this oil producing region is uncertain, though fuel combustion is known to be an important source of alkenes (Doskey et al., 1992), and pump jack engines in this area may be a significant alkene source. Methanol distribution was similar to alkane distribution (Figure 3-12).

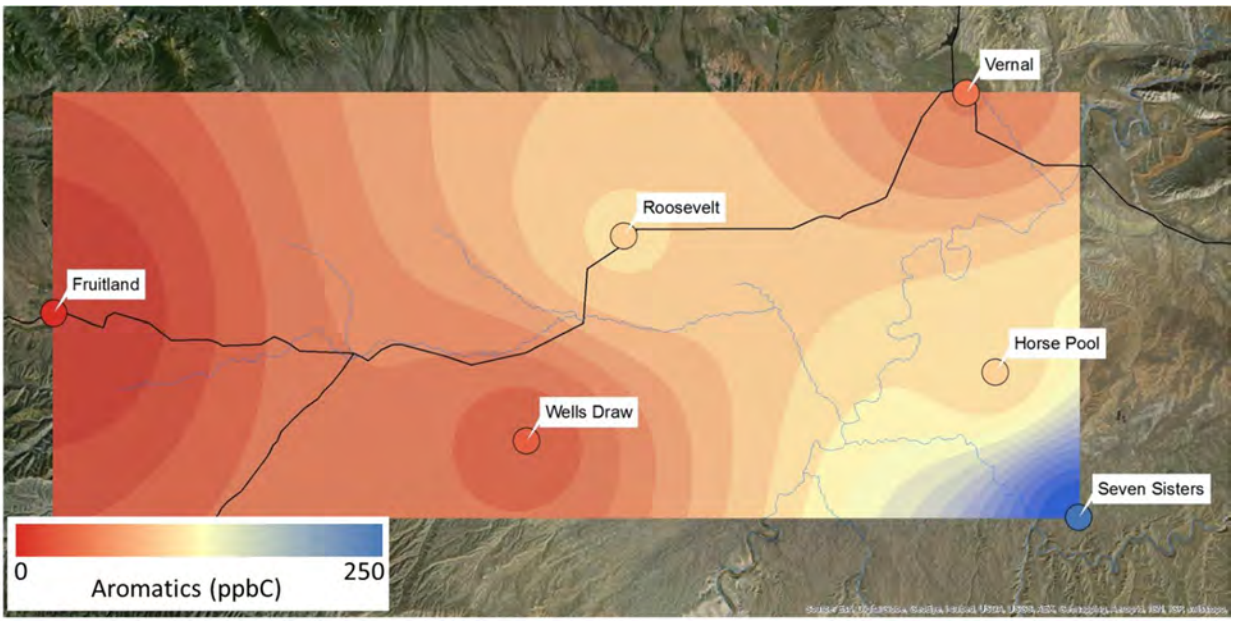


**Figure 3-10. Sum of all aromatics measured on 6 February (day of highest ozone during an inversion episode) at six sites around the Uinta Basin.**

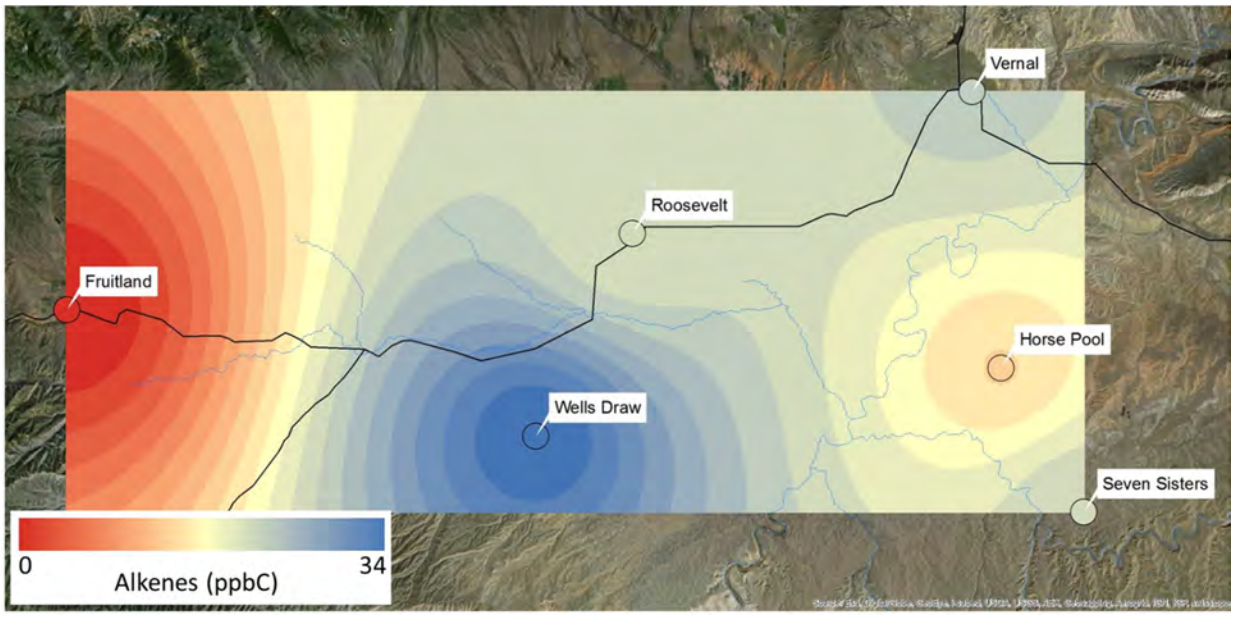


**Figure 3-11. Sum of all alkenes measured on 6 February (day of highest ozone during an inversion episode) at six sites around the Uinta Basin.**

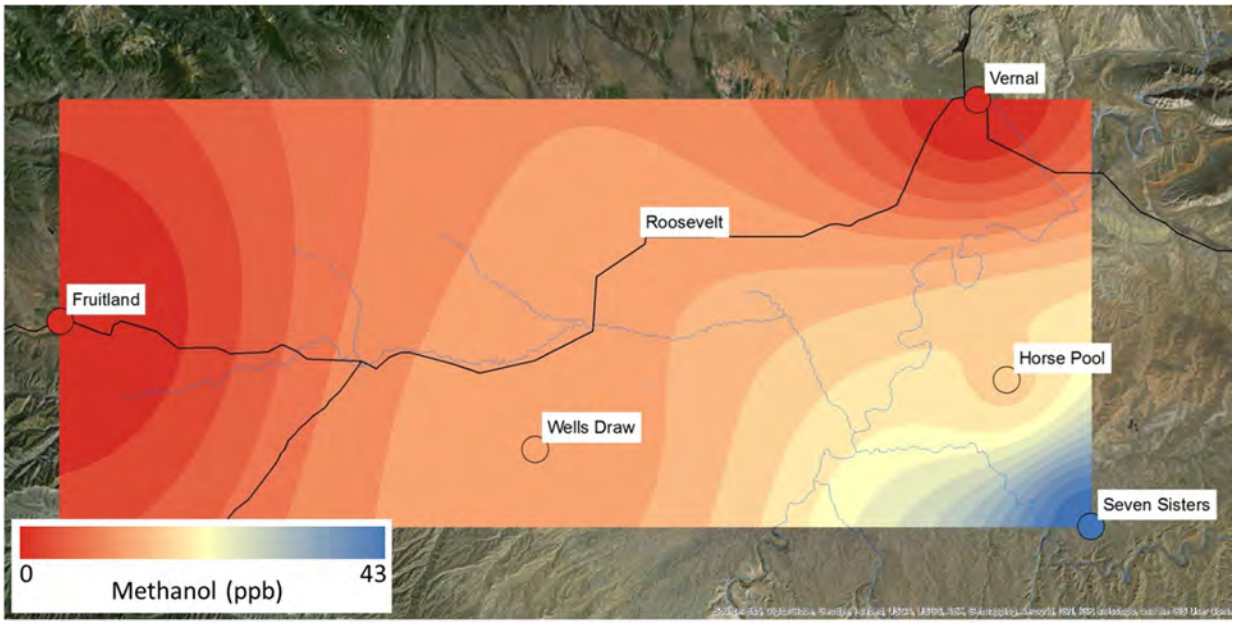


**Figure 3-12. Methanol measured on 6 February (day of highest ozone during an inversion episode) at five sites around the Uinta Basin.**

Different NMHC have different reactivities (i.e., different ability to produce ozone). The ability of VOC to produce ozone can be measured via Maximum Incremental Reactivity (MIR; Carter, 2009). MIR uses box model simulations parameterized to maximize the sensitivity of ozone production to changes in NMHC concentrations. An MIR for a compound is the unit change in ozone production that occurs with a corresponding change in that compound. Since NMHC speciation is different at different sites around the Uinta Basin, MIR can provide a more useful means than NMHC abundance alone to determine the potential of NMHC to form ozone at various study sites. Ideally, MIR scales should be developed using meteorological and other conditions specific to the study area, but this is not yet feasible for the Uinta Basin because of uncertainties in wintertime ozone chemistry. In this work, we use the MIR scale from Carter (2009) as an approximation for MIR in the Uinta Basin during winter inversion conditions.

In Table 3-4, NMHC concentrations and corresponding MIR are shown for 6 February, the highest ozone day during an inversion episode that occurred during the first eight days of February. MIR are shown in units of µg of ozone produced per cubic meter of air. These values were derived by multiplying the concentration of individual compounds (units of µg per $m^3$ of air) by the MIR for that compound (units of µg of ozone produced per µg of the organic compound under consideration) and indicate the maximum amount of ozone that could be produced from that amount of NMHC. Two µg $O_3$ $m^{-3}$ are approximately equivalent to 1 ppb of ozone.

**Table 3-4. NMHC concentrations and MIR for six sites in the Uinta Basin on 6 February.**

| | | Horsepool | Vernal | Wells Draw | Fruitland | Seven Sisters | Roosevelt |
|---|---|---|---|---|---|---|---|
| **Concentrations** | | | | | | | |
| Alkanes | ppbC | 3847.9 | 1428.4 | 2829.7 | 168.5 | 7679.9 | 3548.5 |
| Alkenes | ppbC | 14.4 | 22.7 | 34.6 | <2.0 | 21.8 | 20.2 |
| Aromatics | ppbC | 105.0 | 54.8 | 36.0 | 7.2 | 251.9 | 107.3 |
| Alkanes | ppbv | 2283.9 | 847.4 | 1699.4 | 100.7 | 4519.6 | 2117.1 |
| Alkenes | ppbv | 9.9 | 14.3 | 19.5 | <1.0 | 16.9 | 12.4 |
| Aromatics | ppbv | 55.4 | 28.2 | 18.4 | 3.9 | 134.1 | 56.5 |
| Methanol | ppbv | 23.4 | <5 | 16.2 | <5 | 57.5 | -- |
| Ethane | ppbv | 202.4 | 65.6 | 145.9 | 8.1 | 370.9 | 153.7 |
| **Maximum Incremental Reactivities** | | | | | | | |
| All NMHC | µg $O_3$ $m^{-3}$ | 1917.3 | 827.6 | 1406.6 | 86.7 | 4076.6 | 1839.6 |
| Alkanes | µg $O_3$ $m^{-3}$ | 1649.8 | 633.4 | 1206.0 | 74.9 | 3405.5 | 1505.4 |
| Alkenes | µg $O_3$ $m^{-3}$ | 51.5 | 85.7 | 119.2 | <10 | 105.2 | 104.7 |
| Aromatics | µg $O_3$ $m^{-3}$ | 203.1 | 109.3 | 69.3 | 11.8 | 541.9 | 230.3 |
| Methanol | µg $O_3$ $m^{-3}$ | 15.2 | <4 | 10.5 | <4 | 37.4 | -- |
| Ethane | µg $O_3$ $m^{-3}$ | 202.4 | 65.6 | 145.9 | 8.1 | 370.9 | 153.7 |
| Alkanes | % of total | 86.05 | 76.54 | 85.74 | 86.42 | 83.54 | 81.83 |
| Alkenes | % of total | 2.69 | 10.36 | 8.48 | <10 | 2.58 | 5.69 |
| Aromatics | % of total | 10.59 | 13.21 | 4.93 | 13.58 | 13.29 | 12.52 |
| Methanol | % of total | 0.79 | <0.5 | 0.75 | <0.5 | 0.92 | -- |
| Ethane | % of total | 10.56 | 7.93 | 10.37 | 9.31 | 9.10 | 8.36 |

At every site, including Fruitland, NMHC was comprised mostly of alkanes, and alkanes made up the majority of total MIR. In other words, the majority of ozone at the sites can be expected to have been produced from reactions involving alkanes. The percentage of total MIR attributable to aromatics and alkenes varied somewhat among sites. Aromatics contributed more than 10% of MIR at all sites except Wells Draw, and Vernal, Roosevelt, and Wells Draw were the only sites with more than 3% of MIR due to alkenes. Methanol contributed less than 1% of total MIR in all cases, while ethane, often considered too unreactive to regulate (EPA, 2003), made up 7-11% of total MIR at the study sites.

Because such a large percentage of NMHC in the Uinta Basin is alkanes (95-97% as ppbC at the six sites in this study), these compounds make up the vast majority of total MIR, even though they are low on the MIR scale relative to alkenes and most aromatics. Thus, while emissions controls that focus on aromatics and alkenes because of their high reactivity may produce more benefit at a lower cost, focus on highly reactive VOC alone is not likely to be adequate to control ozone pollution in the Basin.

Though only six distributed NMHC monitoring stations existed during winter 2012-13, statistically significant correlations were observed with a number of spatial and other variables. Figure 3-13 shows that the same predictors of ozone concentrations (area average elevation and proximity to oil and gas activity) were also strong predictors of NMHC. Alkanes, aromatics, and methanol were all strongly correlated with each other, with total NMHC, and with ozone

(Table 3-5, Figure 3-14). Alkenes, on the other hand, exhibited few significant correlations, owing to their dramatically different distribution relative to other NMHC categories (Figure 3-11). Alkenes were correlated with proximity to oil wells, indicating that processes associated with oil production may be larger sources of alkenes than processes associated with natural gas production.

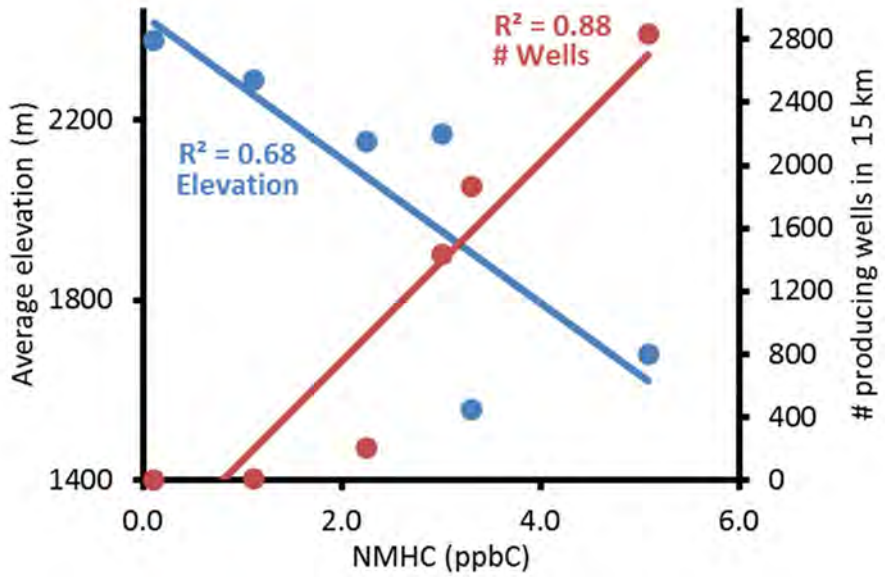


**Figure 3-13. Relationship between 1-8 February average total NMHC concentration and average elevation within 25 km of monitoring stations (in blue) and number of producing oil and gas wells within 15 km of monitoring stations (in red). Linear regression lines and Pearson $R^2$ values are also shown.**

**Table 3-5. Pearson correlations (r) for average NMHC concentrations for 1-8 February at the six sites shown in Table 3-4. "N.S." Indicates the correlation was not significant (α = 0.10).**

| | NMHC (ppbC) | Alkanes (ppbC) | Alkenes (ppbC) | Aromatics (ppbC) | Methanol (ppbv) |
|---|---|---|---|---|---|
| Alkanes (ppbC) | 0.99 | -- | N.S. | 0.80 | 0.96 |
| Alkenes (ppbC) | N.S. | N.S. | -- | N.S. | N.S. |
| Aromatics (ppbC) | 0.82 | 0.80 | N.S. | -- | 0.81 |
| Methanol (ppbv) | 0.95 | 0.96 | N.S. | 0.81 | -- |
| Highest 8-hr ozone | 0.92 | 0.90 | N.S. | 0.81 | 0.81 |
| 4$^{th}$ highest 8-hr ozone | 0.92 | 0.91 | N.S. | 0.87 | 0.86 |
| 26 Jan max. 8-hr ozone | 0.81 | N.S. | N.S. | 0.91 | N.S. |
| 6 Feb max. 8-hr ozone | 0.84 | 0.86 | N.S. | N.S. | N.S. |
| 1 Mar max. 8-hr ozone | 0.93 | 0.91 | N.S. | 0.93 | 0.95 |
| # Wells in 15 km | 0.94 | 0.91 | N.S. | 0.73 | 0.98 |
| # Oil wells in 15 km | N.S. | N.S. | 0.73 | N.S. | N.S. |
| # Gas wells in 15 km | 0.84 | 0.81 | N.S. | 0.85 | 0.96 |
| Population in 15 km | N.S. | N.S. | N.S. | N.S. | N.S. |
| Avg. elevation in 25 km | -0.83 | -0.82 | N.S. | -0.75 | -0.93 |

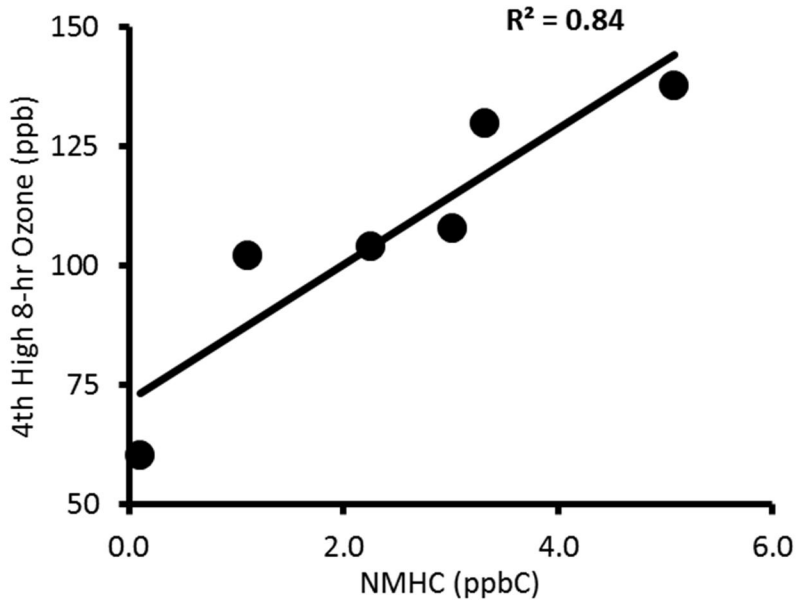


**Figure 3-14. Relationship between 1-8 February average total NMHC concentration and fourth highest 8-hour ozone concentration at study sites. A linear regression line and Pearson $R^2$ value is also shown.**

3.1.3.3 Distribution of Oxides of Nitrogen

Figures 3-15 through 3-17 show the distribution of $NO_x$ during three inversion episodes. $NO_x$ tended to be highest in populated areas and areas with more natural gas production, especially the Seven Sisters site, which is in the area of maximum well density in the Basin and is near several large compressor stations and gas plants.

In general, $NO_x$ concentrations were highest during January inversion episodes and decreased as the winter progressed. The lapse rate in the Uinta Basin was most negative (indicating that inversions were stronger) in January and became less negative as the winter progressed (Figure 3-2). The stronger inversions in early winter likely were more effective at trapping ozone precursors, while stronger solar radiation later in winter likely inhibited inversion formation and allowed for more dilution of emitted precursors.

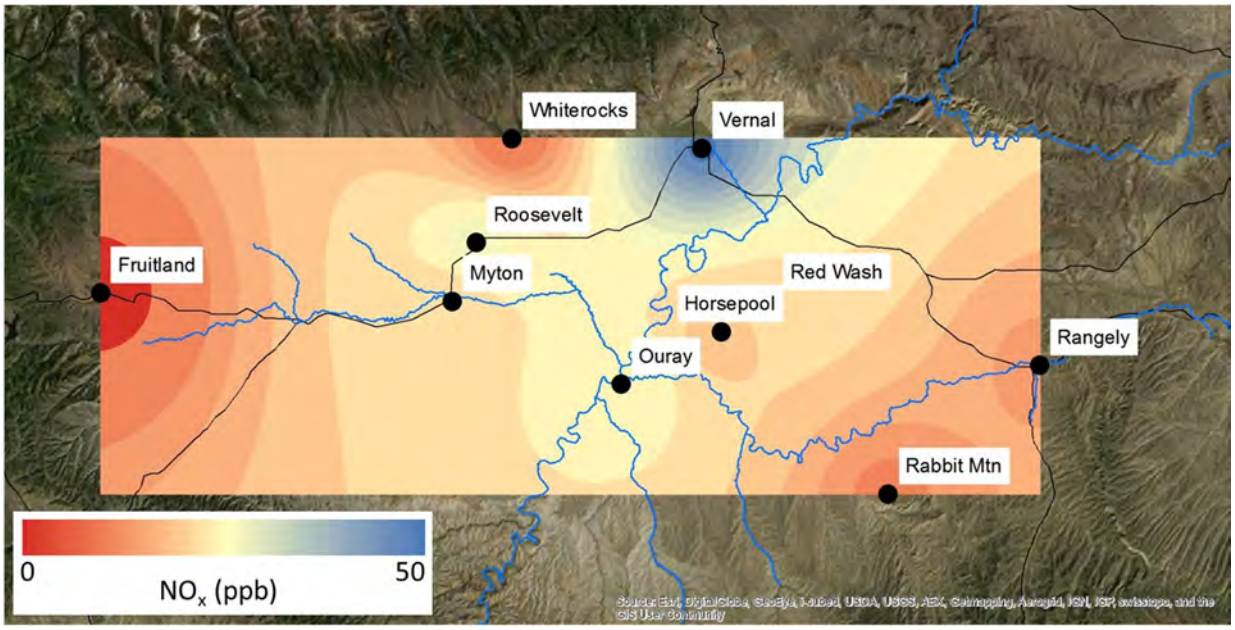


**Figure 3-15. Average $NO_x$ at ten sites during an inversion episode that occurred 20-26 January.**

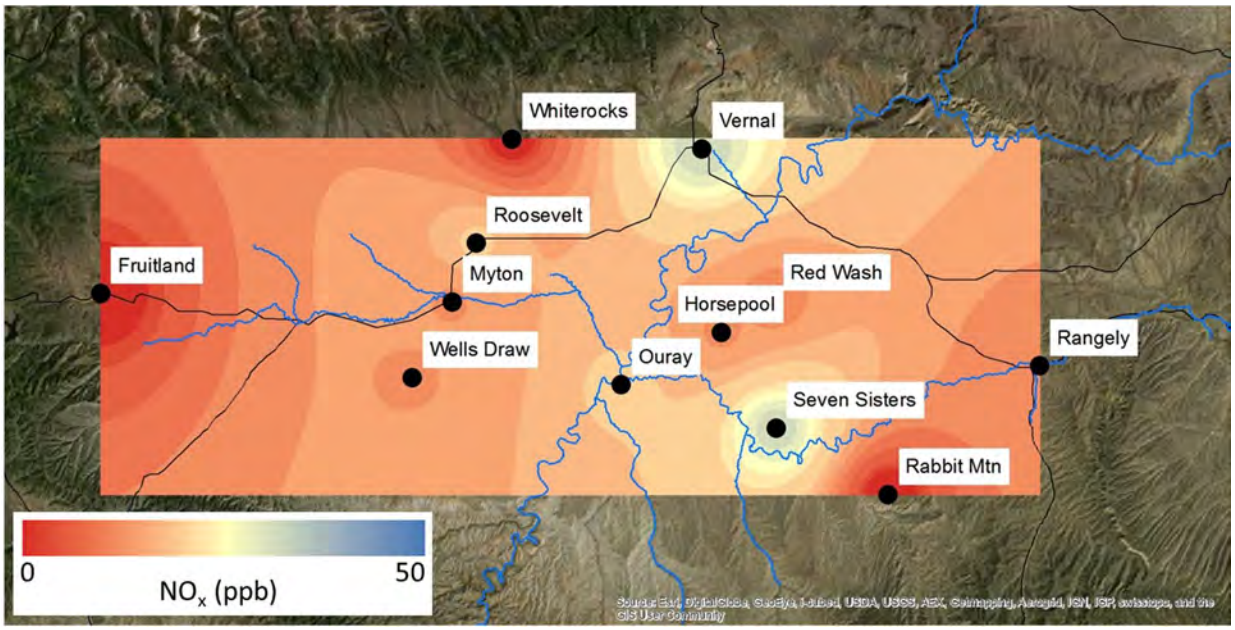


**Figure 3-16. Average $NO_x$ at twelve sites during an inversion episode that occurred 30 January through 5 February. $NO_x$ concentrations shown for Wells Draw and Seven Sisters are derived from passive Radiello samplers.**

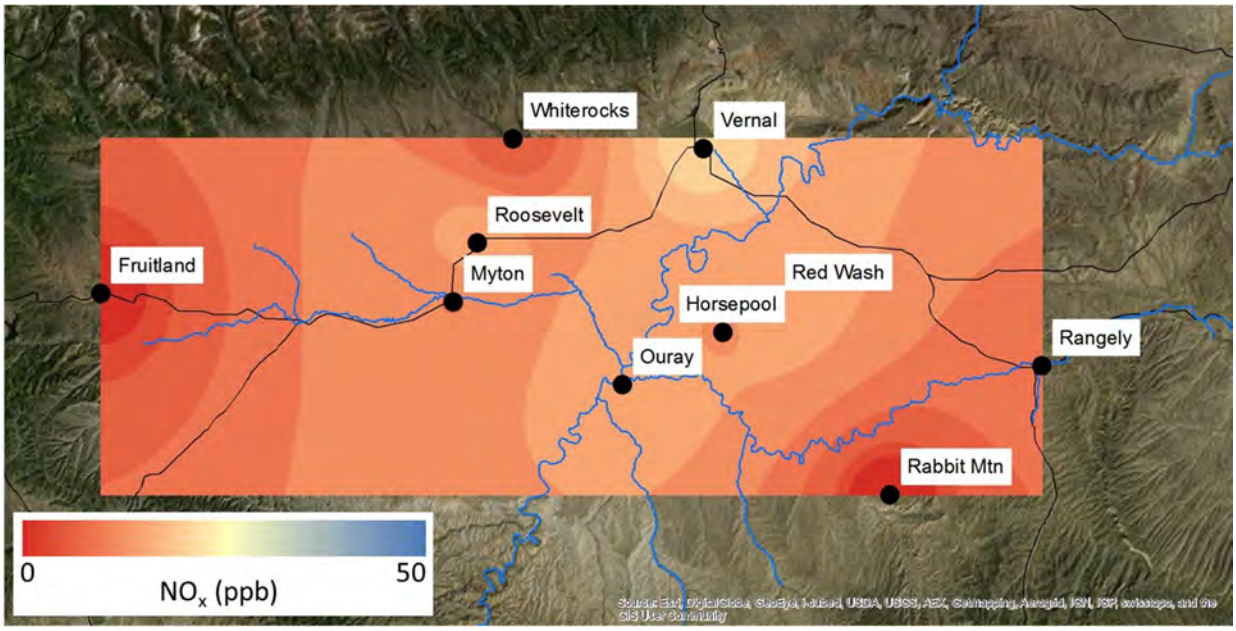


**Figure 3-17. Average $NO_x$ at ten sites during an inversion episode that occurred 1-3 March.**

$NO_x$ concentrations at most sites were collected with instruments that utilize molybdenum oxide converters to transform $NO_2$ to NO. Because these converters also transform some $NO_y$ (i.e., the sum of all reactive nitrogen compounds, including NO and $NO_2$, $HNO_3$, HONO, particulate nitrogen, and other compounds) to NO, the $NO_2$ and $NO_x$ values obtained from these instruments were biased (high). Since the $NO_x$ analyzer at Horsepool utilized a photolytic $NO_2$ converter that does not transform $NO_y$, $NO_2$ concentrations at that site were not biased.

Since different sites may not have the same ratio of $NO_x$ to $NO_y$, correcting $NO_x$ values collected with molybdenum converters to true $NO_x$, or vice versa, is problematic. Fortunately, molybdenum converter $NO_x$ measurements were collected at Horsepool by the University of Colorado (CU research group of D. Helmig; instrument provided by Utah Department of Environmental Quality) from 1 through 18 February, and we were able to conduct a comparison of the two methods. The molybdenum converter-based instrument pulled air from 2 m above ground, while the USU instrument pulled from 4 m above ground, and the two inlets were about 50 m apart. Figures 3-18 and 3-19 show that NO concentrations measured by the two systems were comparable, but $NO_x$ concentrations were very different and were relatively weakly correlated. Figure 3-20 shows that the molybdenum converter-based $NO_x$ measurement was better correlated with $NO_y$ than with true $NO_x$.

$NO_y$ concentrations at Horsepool, and presumably at sites throughout the Uinta Basin, were much higher than true $NO_x$ during inversion episodes, and the $NO_x$ concentrations presented in Figures 3-15 through 3-17 should be interpreted as $NO_x$ + some portion of $NO_y$. For Figures 3-15 through 3-17, $NO_x$ at Horsepool was calculated based on the relationship between measured $NO_y$ and molybdenum converter $NO_x$. In Figure 3-16, $NO_x$ for the Wells Draw and Seven Sisters sites was calculated based on the relationship between true $NO_2$ measurements collected by

Radiello passive samplers and molybdenum converter $NO_x$ measurements at Fruitland, Vernal, and Horsepool.

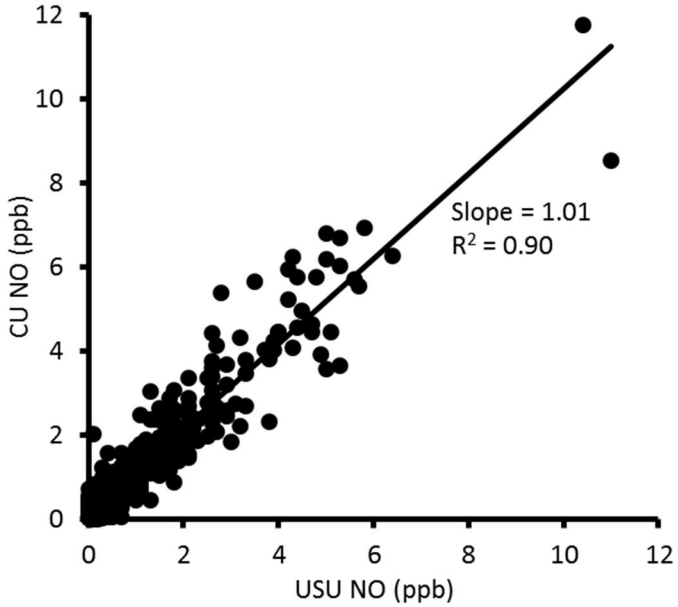


**Figure 3-18. Comparison of NO measured by a photolytic $NO_x$ analyzer (USU) to a molybdenum converter-based $NO_x$ analyzer (CU). The linear regression curve, $R^2$ value, and slope of the relationship are also shown.**

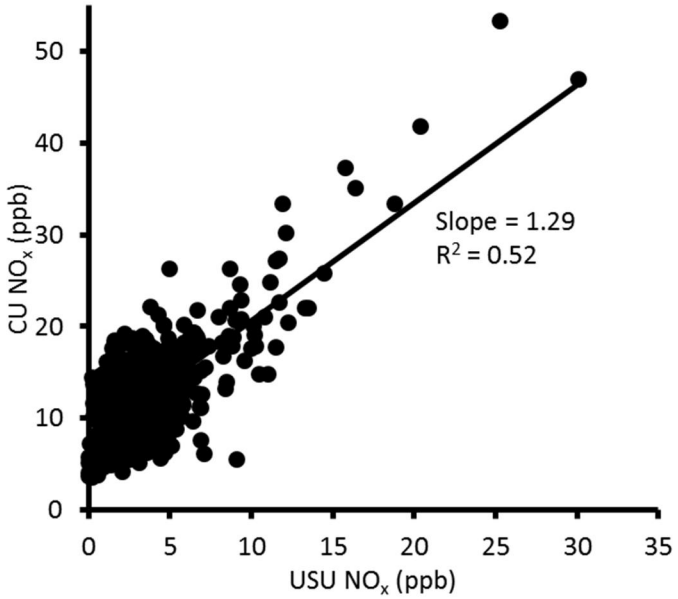


**Figure 3-19. Comparison of $NO_x$ measured by a photolytic $NO_x$ analyzer (USU) with a molybdenum converter-based $NO_x$ analyzer (CU). The linear regression curve, $R^2$ value, and slope of the relationship are also shown.**

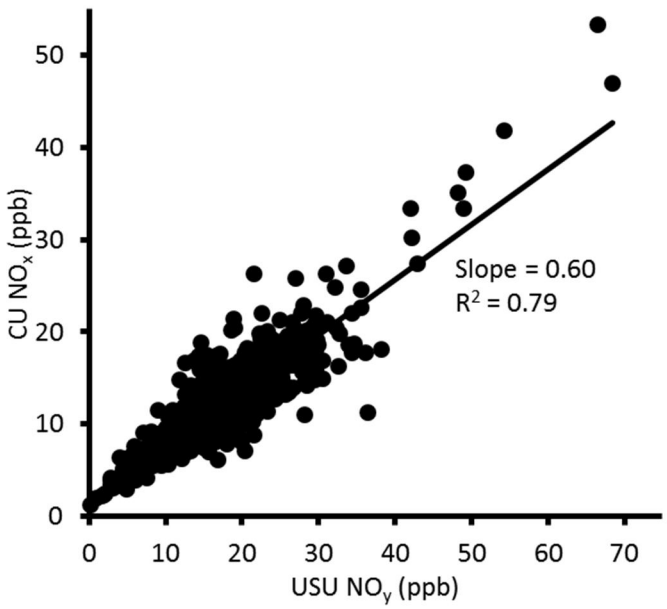


**Figure 3-20. Comparison of $NO_y$ (USU) with $NO_x$ measured by a molybdenum converter-based $NO_x$ analyzer (CU). The linear regression curve, $R^2$ value, and slope of the relationship are also shown.**

$NO_x$ concentrations at Vernal and Roosevelt were among the highest observed at any study site and exhibited the largest diurnal changes, with highest $NO_x$ in the morning hours (Figure 3-21), likely due to diurnal traffic patterns in these cities. Red Wash, located only 250 m from a well-traveled highway, also showed significant diurnal variability, but the peak $NO_x$ at Red Wash was at midday. $NO_x$ also peaked at midday at the Ouray and, to some extent, Horsepool sites, similar to observations made during winter 2011-12 (Lyman et al., 2013). A counter at the Horsepool site during winter 2011-12 observed highest traffic at midday.

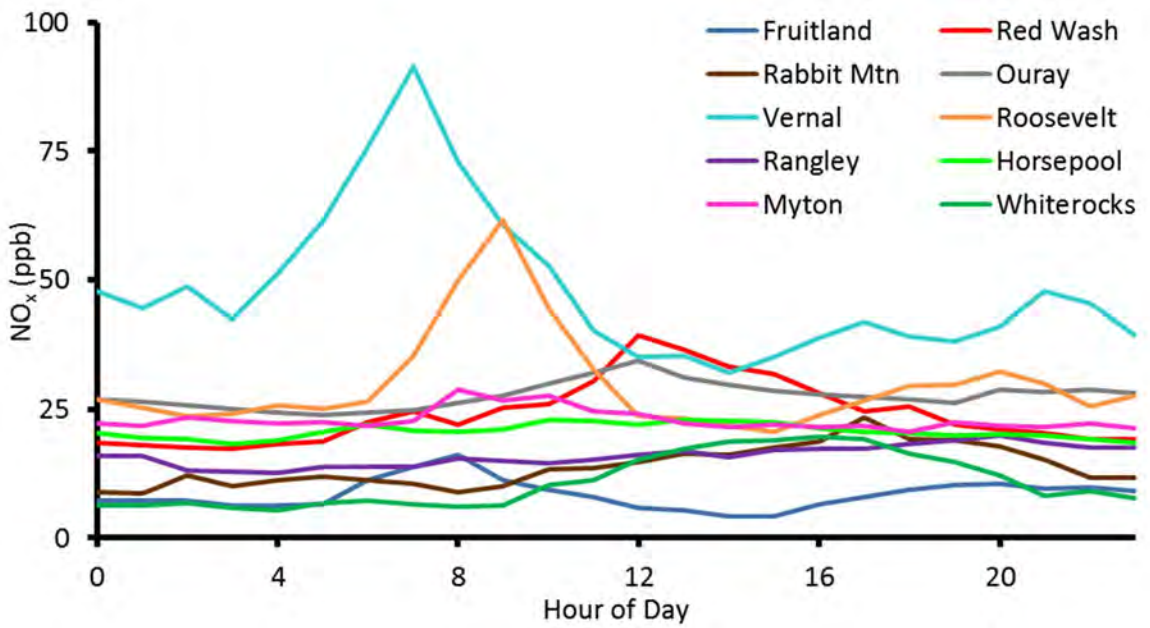


**Figure 3-21. Diurnal change in $NO_x$ concentrations at 10 sites around the Uinta Basin during the 20-26 January inversion episode.**

Table 3-6 and Figure 3-22 show that the spatial distribution of $NO_x$ was, in some instances, correlated with the spatial distribution of ozone. This relationship was not significant for the distribution of $NO_x$ over the entire study period, but was significant for $NO_x$ distribution during some inversion episodes. $NO_x$ distribution was strongly correlated with the difference between day and night ozone concentrations, probably because ozone can be destroyed by NO at night, and sites with high $NO_x$ also tend to be sites with higher nighttime NO. Correlations between $NO_x$ concentrations and proximity of study sites to oil and gas operations were either not significant or weak, but $NO_x$ was correlated with population and elevation.

$NO_x$ concentrations during the 31 January through 5 February period were not significantly correlated with total NMHC measured during the same period ($p = 0.391$), but they were correlated with aromatics ($R^2 = 0.61$, $p = 0.07$). When 1-8 February average NMHC and 31 January through 5 February $NO_x$ were used as independent variables to predict 6 February ozone in a multiple linear regression model, the $NO_x$ variable was not significant ($p = 0.77$). However, the tendency of $NO_x$ to destroy ozone under some conditions may have confounded this relationship, and, as discussed previously, $NO_x$ measurements used here also contain $NO_z$ compounds that are not direct ozone precursors. In addition, ozone production has a non-linear dependence on $NO_x$ concentration, so a linear regression model cannot reliably evaluate the relationship of ozone to $NO_x$.

**Table 3-6. Pearson correlations (r) of average $NO_x$ during different periods with ozone and spatial metrics. "N.S." Indicates that the correlation was not significant (α = 0.10).**

| | Avg. $NO_x$ 20-26 Jan. | Avg. $NO_x$ 1-3 Mar. | Avg. $NO_x$ 31 Jan.-5 Feb. | Avg $NO_x$ 15 Jan.-10 Mar. |
|---|---|---|---|---|
| Highest 8-hr ozone | N.S. | 0.63 | 0.62 | N.S. |
| 4th highest 8-hr ozone | N.S. | 0.73 | 0.65 | N.S. |
| # Exceedance days | N.S. | 0.77 | 0.57 | 0.56 |
| Day-night difference ozone | 0.88 | 0.78 | 0.81 | 0.86 |
| 26 Jan max. 8-hr ozone | N.S. | N.S. | 0.68 | N.S. |
| 6 Feb max. 8-hr ozone | N.S. | 0.67 | 0.50 | N.S. |
| 1 Mar max. 8-hr ozone | N.S. | N.S. | 0.59 | N.S. |
| # wells in 5 km | N.S. | N.S. | 0.51 | N.S. |
| Population in 5 km | 0.83 | 0.64 | 0.57 | 0.82 |
| Avg. elevation in 5 km | -0.65 | -0.79 | -0.64 | -0.64 |

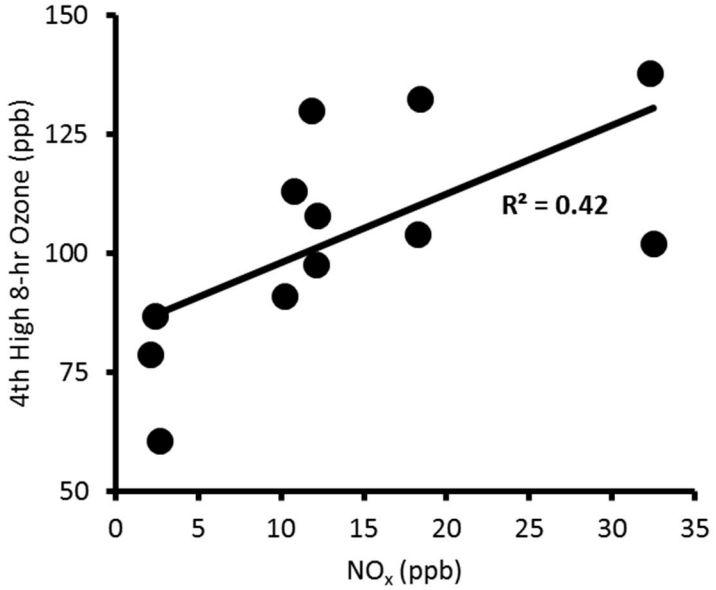


**Figure 3-22. Relationship between 31 January through 5 February molybdenum converter-based $NO_x$ concentration (contains some $NO_y$) and fourth highest 8-hour ozone concentration at 12 study sites. A linear regression line and Pearson $R^2$ value are also shown.**

### 3.1.3.4 Influence of Transport Patterns on Ozone During an Inversion Episode

UBOS study participants and others operated dozens of meteorological stations in and around the Uinta Basin during winter 2012-13. Meteorology, particularly wind speed and direction, was an important determinant of ozone production in the Basin. Figures 3-23, 3-24, and 3-25 show ozone concentrations and wind vectors prior to and during an inversion episode that occurred from 31 January through 8 February.

Figure 3-23 shows wind conditions and the low ozone concentrations of 28 January, just two days after one of the season's highest ozone days in the Basin. A storm front arrived on 27 and 28 January and was associated with relatively high winds in many parts of the Basin on 28 January, as shown. Winds at high elevation sites during this period were from the south. Wind speeds within the Basin were lower on subsequent days, allowing another inversion to form and ozone concentrations to rebuild. By the afternoon of 6 February (Figure 3-24), ozone concentrations exceeded 100 ppb at many sites. Wind at high elevations continued to be from the south throughout this period, and wind at lower elevation sites in the Basin was light and variable (Figure 3-24). On 8 February, however, wind at high elevation sites changed directions and blew from the north (Figure 3-25). Following this synoptic scale change, wind at low elevation sites within the Basin continued to be light and variable, but a partial mix-out of ozone from the Basin nevertheless occurred, and ozone concentrations dropped to less than 100 ppb at all sites.

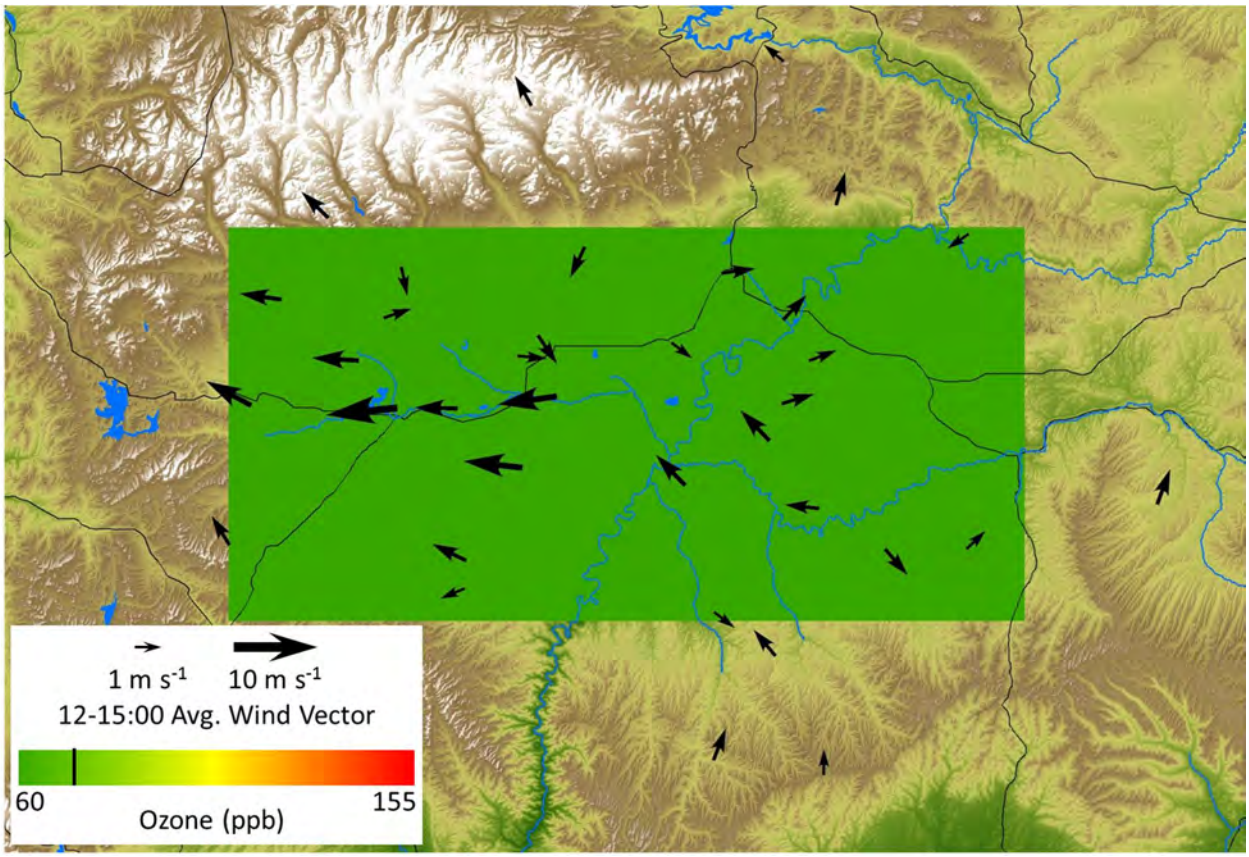


**Figure 3-23. Daily maximum ozone concentrations and wind vectors from surface sites on 28 January during a stormy period between inversion episodes. Arrows indicate wind direction. The black line on the ozone color scale indicates 75 ppb.**

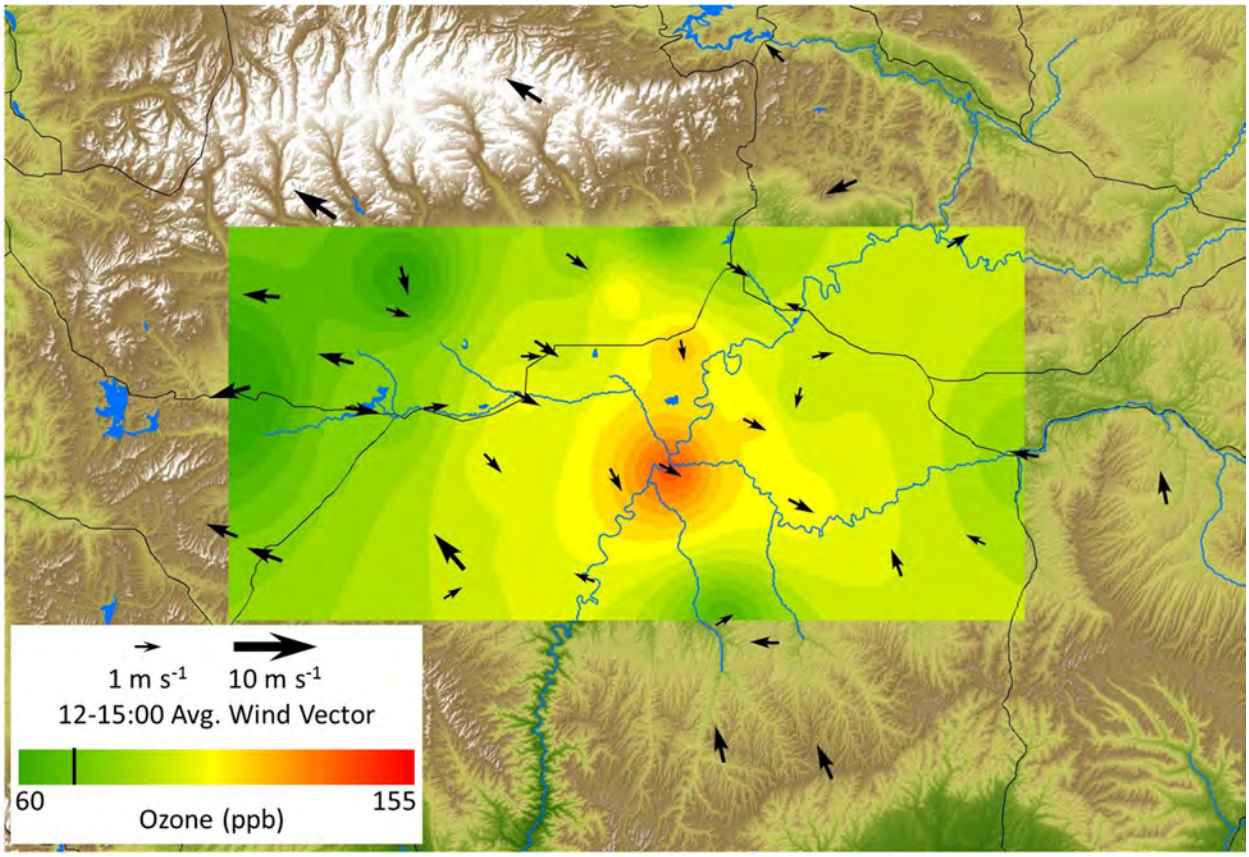


**Figure 3-24. Daily maximum ozone concentrations and wind vectors from surface sites on 6 February during an inversion episode.**

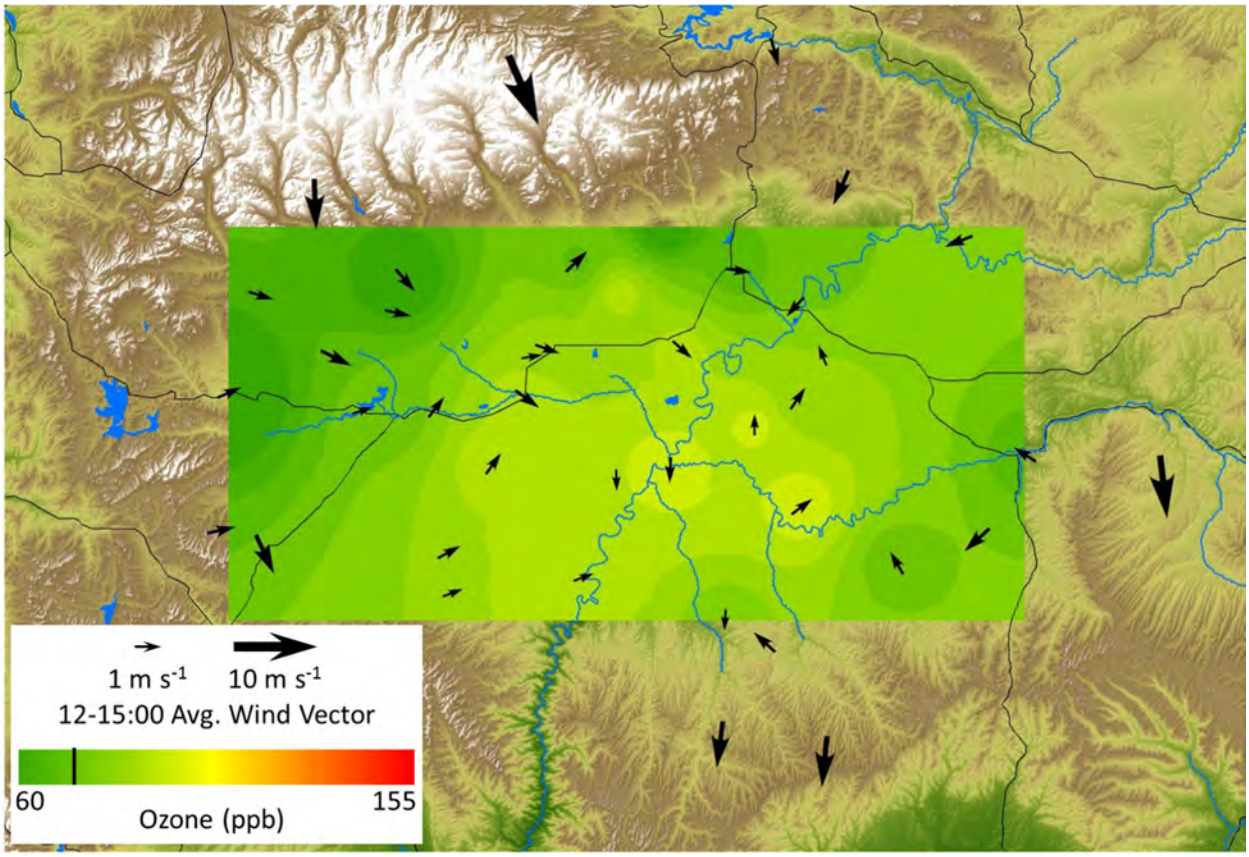


**Figure 3-25. Daily maximum ozone concentrations and wind vectors from surface sites on 8 February.**

### 3.1.3.5 Seasonal Changes in Ozone and Precursor Chemistry

While inversions became weaker (less negative lapse rate) as the winter ozone season proceeded from January through March, maximum ozone concentrations increased and took fewer inversion days to reach maxima (Figure 3-2). Figures 3-26, 3-27, and 3-28 show average ozone and precursor concentrations for each hour of the day during three inversion episodes that occurred in January, February, and March. Concentrations of ozone precursors decreased with each successive episode, but the amount of ozone produced each day (i.e., the difference between morning and afternoon ozone concentrations) increased. Average total NMHC (TNMHC) was 37% lower during 1-3 March than during 20-26 January, and $NO_2$ was 63% lower, but daily ozone production was 64% higher during 1-3 March than during the earlier period. The average daytime total UV radiation (average of the sum of incoming and outgoing UV-A and UV-B for daylight hours) was 51% higher during 1-3 March, and daily maximum temperature was 10.5 °C higher, probably accounting for the observed increase in daily ozone production.

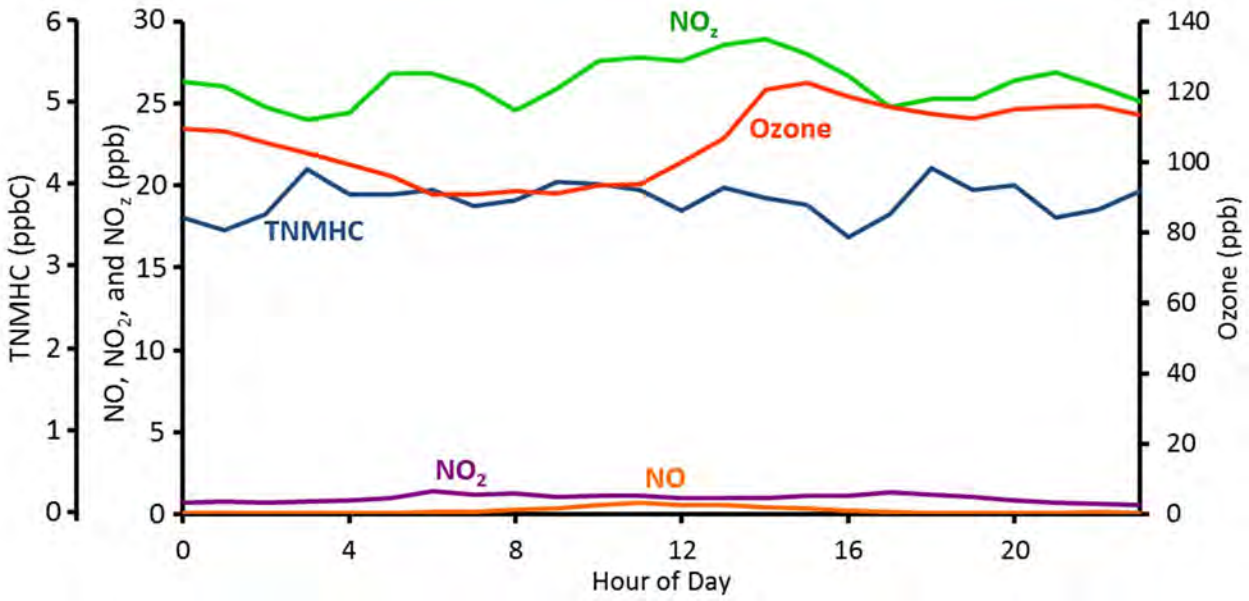


**Figure 3-26. Diurnal average concentrations of ozone and precursors at Horsepool, 20-26 January.**

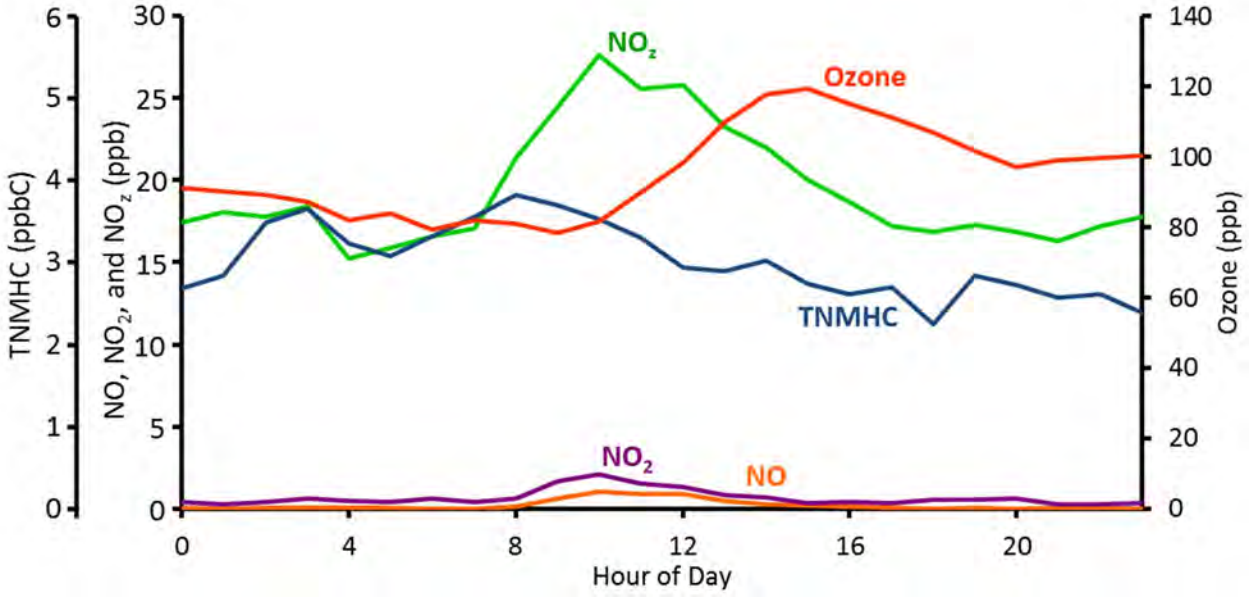


**Figure 3-27. Diurnal average concentrations of ozone and precursors at Horsepool, 4-6 February.**

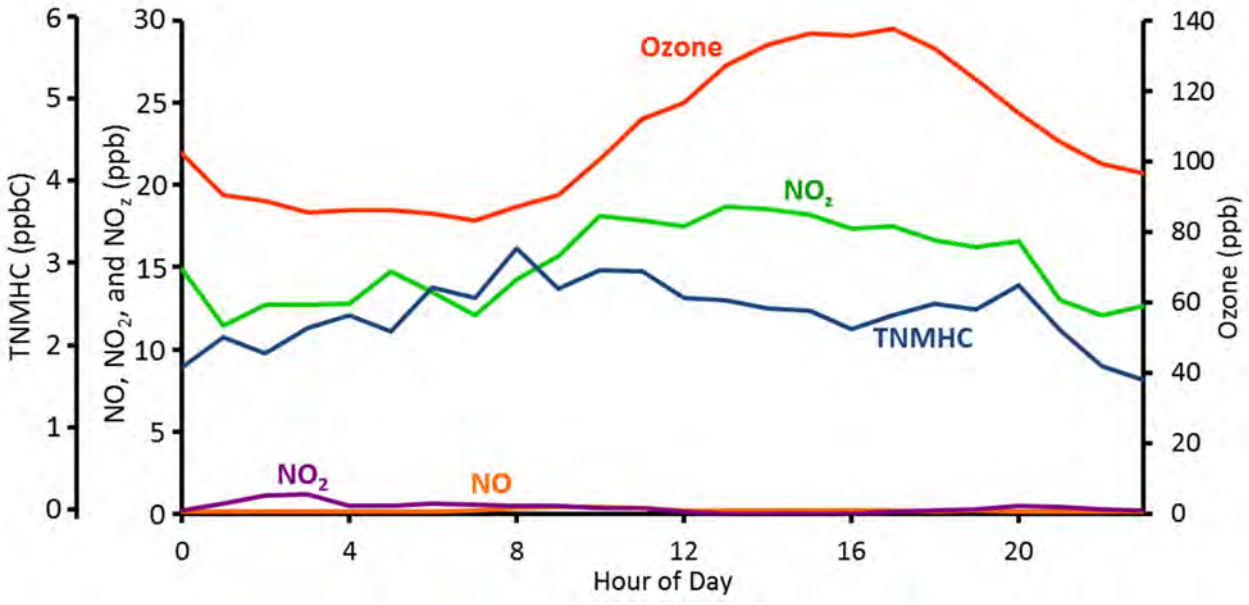


**Figure 3-28. Diurnal average concentrations of ozone and precursors at Horsepool, 1-3 March.**

Ozone production efficiency is the ratio of production of ozone and $NO_2$ (also called "odd oxygen" or $O_x$) to the removal of $NO_x$; more simply, it is the number of ozone molecules produced for each molecule of precursor consumed (Lin et al., 1988; Sillman, 1999). The linear regression slope of the relationship between ozone and $NO_z$ ($NO_z$ is the sum of $NO_x$ reaction products, or $NO_y - NO_x$) and between $O_x$ and $NO_z$ have often been used to approximate ozone production efficiency, since the compounds that comprise $NO_z$ are end products of $NO_x$ photochemistry (e.g., Trainer et al., 1995). A higher ozone to $NO_z$ slope indicates that more ozone is produced per molecule of $NO_x$ consumed. Deposition or other loss of $NO_z$ from the atmosphere is not accounted for in this metric, however, and a higher slope could also mean that $NO_z$ is being removed more efficiently.

Figure 3-29 shows the slope of the relationship between ozone and $NO_z$ at Horsepool on days with maximum ozone greater than 90 ppb, calculated as described by Chou et al. (2009). This figure provides evidence that ozone production efficiency increases from early to late winter in the Uinta Basin, probably because temperature and available solar energy increases. Since some of the increase in the ozone to $NO_z$ slope over time could be due to increased $NO_z$ deposition, the values in Figure 3-29 should be used with caution. The trend of increasing efficiency in ozone production from early to late winter, however, is likely to be robust.

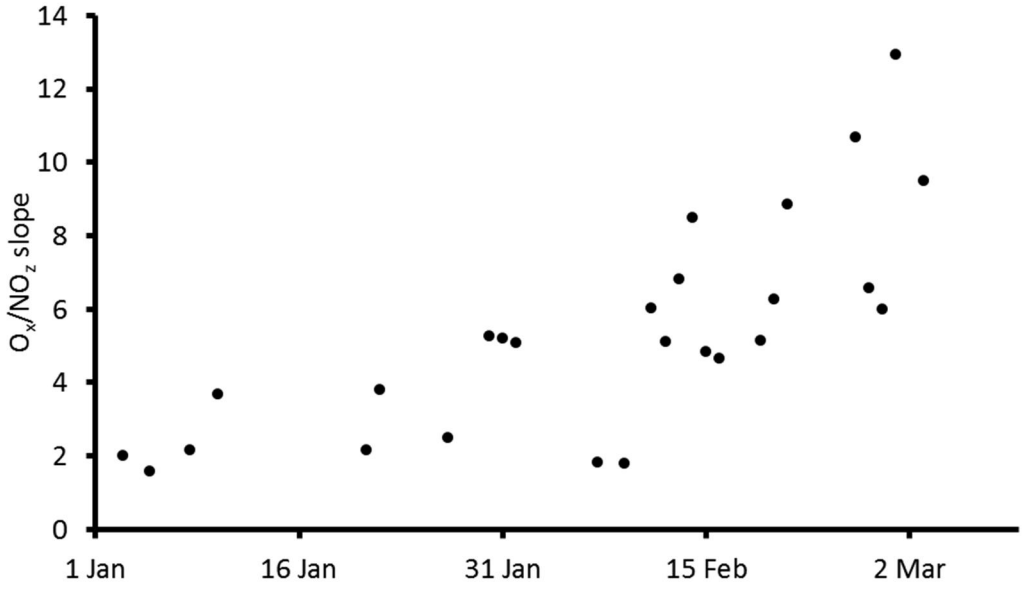


**Figure 3-29. Slope of the linear regression relationship between $O_x$ and $NO_z$ at Horsepool, January-March. Only days with maximum ozone greater than 90 ppb are shown.**

Photochemical indicators are metrics based on ambient measurements that can indicate whether ozone production in a region is more sensitive to VOC controls (VOC sensitive) or $NO_x$ controls ($NO_x$ sensitive) (Sillman, 1999). A number of photochemical indicators have been used, but the ratio of ozone to $NO_y$ has been most commonly used and has been evaluated in a number of studies (Stein et al., 2005). The rationale for use of this indicator ratio, as explained by Sillman (1999), is that the major sinks for radicals in the ozone photochemical process are peroxides and $NO_z$, especially $HNO_3$. Radical production exceeds the rate of $NO_x$ emissions in $NO_x$ sensitive regimes, while the opposite is true in VOC sensitive regimes (see also Kleinman, 1994). In cases with more radicals than $NO_x$ ($NO_x$ sensitive), less $NO_x$ is available to react with radicals to produce $HNO_3$ and other $NO_z$, so more peroxides are produced relative to $HNO_3$. In the opposite case, more $HNO_3$ and other $NO_z$ can be expected. Thus, the ratio of peroxides to $NO_z$ is a relative indicator of $NO_x$ versus VOC sensitivity. Ozone production is proportional to the production of odd hydrogen radicals, and since direct peroxide measurements are rarely available, the ratio of ozone/$NO_y$ or ozone/$NO_z$ is often used.

Unfortunately, cutoff values or ranges that indicate $NO_x$ versus VOC sensitivity in the ozone/$NO_y$ ratio or other indicators can be different for different regions (Stein et al., 2005), and caution must be exercised in using cutoff values from other studies, especially when emissions or chemistry may be unique, as with wintertime ozone in the Uinta Basin. Determination of appropriate cutoff values to distinguish whether $NO_x$ or VOC controls would be more effective is best achieved through utilization of a photochemical model, and indicator ratios can be useful for verifying model-based determinations of $NO_x$ or VOC sensitivity.

Since a verified photochemical model is not yet available for the Uinta Basin, the value of the ratio of ozone/$NO_y$ that would indicate $NO_x$ versus VOC sensitivity cannot be reliably

determined. However, the transition between these two states is gradual, and higher ozone/$NO_y$ ratios always indicate movement *towards* $NO_x$ sensitivity (Sillman, 1999). Figure 3-30 shows that the ozone/$NO_y$ ratio steadily increased from early to late winter in the Uinta Basin. The ozone/$NO_z$ ratio, another common indicator, showed a similar trend (not shown). Together, these indicators provide evidence that more radicals are produced during late-season ozone events in the Uinta Basin (which also would tend to increase ozone production efficiency, as discussed above) and that early-season events are more likely to be VOC sensitive than late-season events.

In previous (urban summertime) studies, the transition region between $NO_x$ and VOC sensitive regimes has been characterized by ozone/$NO_y$ ratios between 5.6 and 15 (Stein et al., 2005). The ozone/$NO_y$ ratio at Horsepool is within this range by mid-February, but it is inappropriate to use urban summertime studies in comparison with wintertime ozone production in the Uinta Basin. It is possible that VOC controls in the Uinta Basin will be more effective at reducing ozone than $NO_x$ controls early in the year, but that $NO_x$ controls will have increasing effectiveness as the winter season proceeds, but further work, including photochemical modeling, will be required to determine this definitively. Seasonal transitions from $NO_x$ sensitivity in warm seasons to VOC sensitivity in cool seasons have been observed by others, and are likely due to decreased UV radiation and water vapor concentration, both factors that limit radical production (e.g., Jacob et al., 1995).

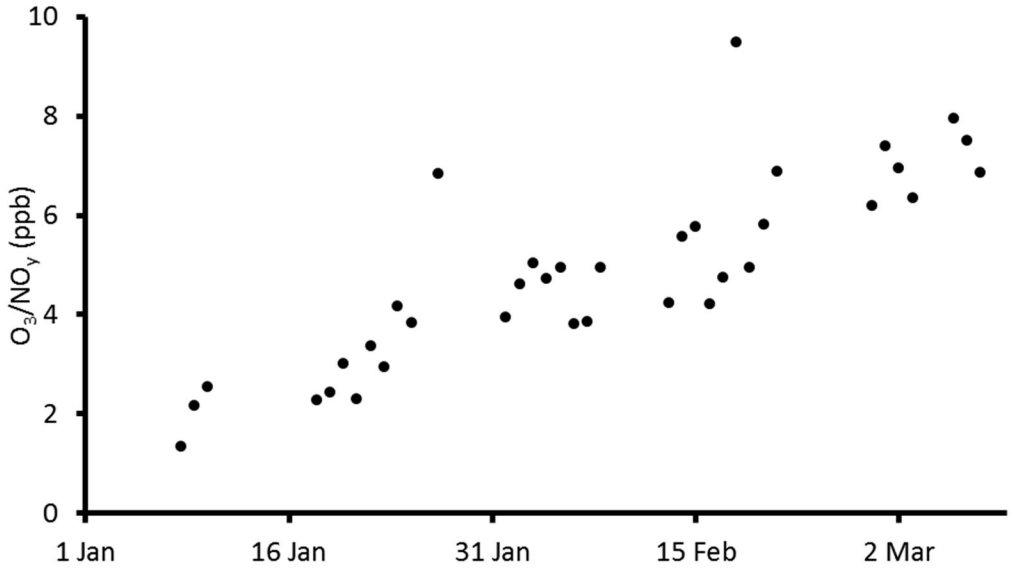


**Figure 3-30. Ratio of ozone to $NO_y$ at Horsepool, January-March. Only days with maximum ozone greater than 90 ppb are shown.**

### 3.1.3.6 Interannual Variability in Wintertime Ozone

Figure 3-31 shows a time series of ozone concentrations at several sites in the Uinta Basin from July 2009 through 15 March, 2013. The Ouray and Red Wash air quality monitoring stations

began operation in July 2009. During winter 2009-10, both sites experienced multiple exceedances of the NAAQS for ozone (75 ppb). Subsequently, regulatory monitors in Roosevelt, Vernal, and Rangely were added. As Figure 3-31 shows, exceedances of the NAAQS have been observed during three of the four years in the Uinta Basin for which continuous ozone monitoring data is available. The Utah Department of Environmental Quality also measured ozone in Vernal during 2006 and 2007, but those data are not publicly available and are not included here. No wintertime exceedances of the NAAQS were measured during that period.

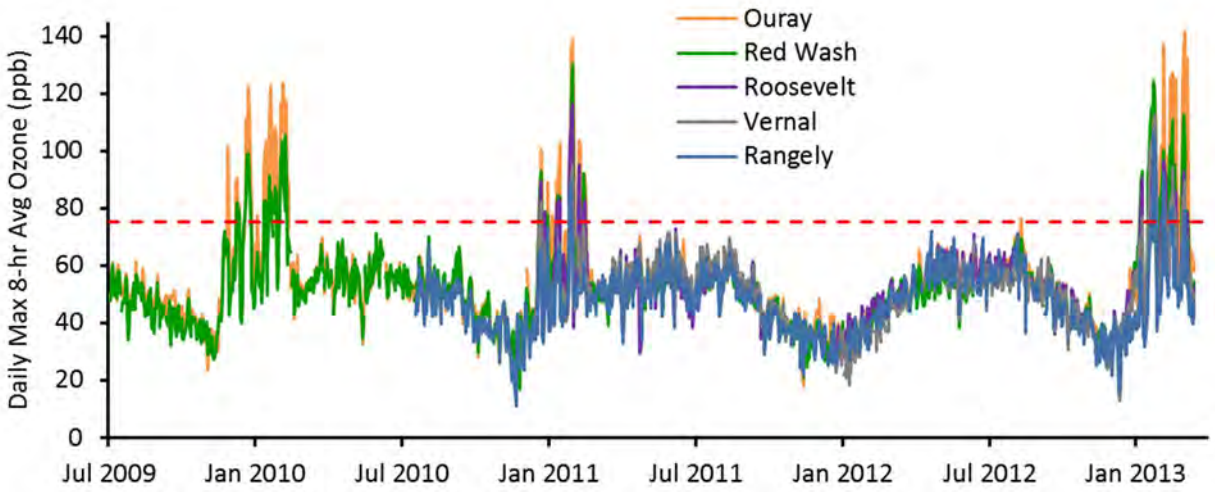


**Figure 3-31. Time series of daily maximum 8-hour average ozone concentration at five sites in the Uinta Basin, July 2009-March 2013. The red dashed line shows 75 ppb, the EPA NAAQS for ozone.**

Table 3-7 summarizes ozone statistics from the five sites shown in Figure 3-31 for each of the years that data are available. Data are organized by calendar year rather than by winter season, since summertime exceedances have also occurred (albeit rarely), and since a nonattainment designation, if made by EPA, will be based on the average of the annual fourth highest daily maximum 8-hour average concentration averaged over three consecutive calendar years (i.e., the "ozone design value"). Based on data collected between 1 January 2011 and 15 March 2013, the average of the three annual fourth highest daily maximum 8-hour average ozone concentrations at Rangely is 78 ppb and thus exceeds the 75 ppb ozone NAAQS. The Ouray and Red Wash sites are not regulatory, but their current ozone design values are 106.5 and 92.9 ppb, respectively. Ozone data has been collected in Vernal and Roosevelt since January 2011, but 2011 data were collected by USU and are not regulatory. These sites, as a result, only have two years of regulatory data. The two-year averages of the fourth highest regulatory value for Vernal and Roosevelt are 83.4 and 85.5, respectively. In order to maintain a design value less than 75 ppb, the fourth highest 8-hour average ozone concentration for 2014 will have to be no higher than 58 ppb for Vernal and 54 ppb for Roosevelt, which is unlikely.

**Table 3-7. Ozone summary statistics for five sites in the Uinta Basin over five calendar years. The Vernal, Roosevelt, and Rangely sites are regulatory; Ouray and Red Wash are not. All values shown were calculated from daily maximum 8-hour average concentrations.**

| | Mean | Median | Max | Min | 4th Highest Daily Max | # of Exceedance Days |
|---|---|---|---|---|---|---|
| **2009** | | | | | | |
| Ouray | 47.2 | 47.9 | 101.5 | 23.4 | 67.4 | 1 |
| Red Wash | 44.8 | 43.7 | 72.3 | 27.3 | 67.6 | 0 |
| Vernal | -- | -- | -- | -- | -- | -- |
| Roosevelt | -- | -- | -- | -- | -- | -- |
| Rangely | -- | -- | -- | -- | -- | -- |
| **2010** | | | | | | |
| Ouray | 56.7 | 54.5 | 123.6 | 20.3 | 117.3 | 40 |
| Red Wash | 54.4 | 53.6 | 105.4 | 17.0 | 98.9 | 30 |
| Vernal | -- | -- | -- | -- | -- | -- |
| Roosevelt | -- | -- | -- | -- | -- | -- |
| Rangely | 42.3 | 42.2 | 67.2 | 11.1 | 58.8 | 0 |
| **2011 (Vernal and Roosevelt sites were operated by USU and were not regulatory)** | | | | | | |
| Ouray | 54.0 | 52.8 | 138.6 | 18.1 | 119.6 | 24 |
| Red Wash | 51.6 | 51.8 | 130.2 | 21.3 | 98.3 | 21 |
| Vernal | 55.5 | 55.6 | 95.1 | 33.1 | 84.9 | 7 |
| Roosevelt | 56.2 | 54.7 | 116.3 | 29.3 | 103.6 | 19 |
| Rangely | 48.6 | 50.0 | 88.6 | 21.9 | 73.4 | 3 |
| **2012** | | | | | | |
| Ouray | 49.3 | 50.5 | 76.5 | 18.8 | 67.6 | 1 |
| Red Wash | 47.5 | 48.8 | 69.5 | 21.5 | 66.4 | 0 |
| Vernal | 45.7 | 46.8 | 68.9 | 14.5 | 64.8 | 0 |
| Roosevelt | 50.3 | 51.6 | 70.9 | 14.6 | 67.0 | 0 |
| Rangely | 46.7 | 47.4 | 71.9 | 15.9 | 69.6 | 0 |
| **2013 (through 15 March)** | | | | | | |
| Ouray | 81.8 | 79.8 | 141.6 | 38.4 | 132.4 | 39 |
| Red Wash | 74.8 | 73.6 | 124.0 | 38.8 | 114.0 | 36 |
| Vernal | 67.2 | 63.4 | 114.9 | 37.5 | 102.1 | 22 |
| Roosevelt | 68.0 | 64.2 | 110.8 | 37.0 | 104.0 | 29 |
| Rangely | 56.4 | 52.4 | 106.1 | 31.7 | 91.0 | 11 |

### 3.1.4 Summary

The spatial distribution of ozone and NMHC concentrations observed during winter 2012-13 largely can be explained by elevation and proximity to oil and gas production. This finding shows that ozone production in the Basin depends on intensity of inversions (elevation dependent) and intensity of emissions. The spatial distribution of ozone was found to be more closely correlated with NMHC than with $NO_x$, perhaps indicating that NMHC sources are more important than $NO_x$ sources for ozone production, but 3D photochemical modeling will be required before a definitive determination can be made of the sensitivity of ozone production to NMHC versus $NO_x$.

Ozone production efficiency increased from early to late winter, allowing ozone to be produced more rapidly during later season ozone events, even while precursor concentrations were lower. During early winter, lower temperatures and reduced sunlight increase the likelihood that the Uinta Basin is VOC sensitive (i.e., VOC controls would be most effective at mitigating ozone pollution). It is possible that the Basin transitions from VOC to $NO_x$ sensitivity as the winter proceeds.

Though ozone concentrations above 75 ppb have occurred during three of the past four winters in the Uinta Basin, only the Rangely monitoring station has the requisite three years of regulatory data to permit a nonattainment area designation. By 2014, the Vernal and Roosevelt stations are likely to meet this benchmark.

### 3.1.5 Acknowledgements

We are grateful to the Uintah Impact Mitigation Special Service District; the Utah Science, Technology, and Research Initiative; the Department of Energy; and Mr. Marc Bingham for financial support of this work. We thank the Bureau of Land Management for providing equipment for remote ozone monitoring and to Detlev Helmig and Chelsea Stevens of the University of Colorado for providing access to molybdenum converter-based $NO_x$ data they collected at the Horsepool site. We are also grateful to the Utah Department of Environmental Quality for providing space for our monitors at Roosevelt.

## 3.2 Observations and Numerical Modeling of the Atmospheric Boundary Layer in the Uinta Basin

### 3.2.1 Introduction

The atmospheric boundary layer occurring during persistent cold air pools (PCAPs) can be highly variable in both space and time and is influenced by a wide range of atmospheric processes (Lareau et al., 2013). The Uinta Basin, being a deep and extensive basin with an ideal bowl-shaped topography, is sheltered during PCAPs from the effects of weak weather disturbances. However, moderate weather systems and the westerly winds associated with these disturbances typically impact the boundary-layer in the western third of the basin and the top portion of the cold pool throughout the remainder of the Uinta Basin as turbulent mixing occurs between the relatively calm, polluted surface-based cold air pool and the clean, windy, disturbed air aloft**.** The extensive horizontal scale and deep nature of the Uinta Basin results in intense, long-lived, and complex PCAPS. Below the inversion top capping the boundary-layer, multi-level stable layers with varying flow direction and intensity were often observed during the 2013 UBWOS.

A series of targeted meteorological measurements were conducted in the Uinta Basin in January and February 2013 with the specific goal to better characterize the boundary-layer (height, temperature, winds, cloud cover, multi-layered structures) in the Basin. The targeted observations consisted of two ceilometers to observe boundary-layer height and aerosol concentration; rawinsondes to observe the profiles of temperature, moisture, and wind from the boundary-layer and continuing high above the surrounding terrain; and a fixed and a mobile

weather station used in concert with the Mesowest network to characterize the surface meteorological conditions. The synthesis and ingestion of all available surface weather station data available from all UBWOS scientists into http://mesowest.utah.edu has also been conducted as a part of this study**.** A crucial contribution from this study to the larger UBWOS scientific data collection efforts is the inclusion of observations in the region from near the surface through the top of the inversion, which can extend in some cases up to 1000 m AGL in depth, and typically several hundred meters higher than tethersonde observations collected by other research teams.

In addition, numerical WRF modeling simulations are being conducted as part of this study to characterize basin-wide wind flow characteristics. Due to the complexity of the terrain around the basin, and the complex interactions between synoptic westerly flow and the underlying boundary-layer, scattered point measurements and profiles of winds in the basin have proven insufficient to characterize the basin winds as a whole. Analysis of wind profile measurements from rawinsondes at Roosevelt and the NOAA wind lidar at the Horsepool site illustrate the localized nature of boundary-layer flows. Consequently, we expect that measurements at either of these sites cannot be applied uniformly to the basin as a whole. Thus, a gridded hourly model forecast of winds in the boundary-layer in the Uinta Basin is being produced using the WRF model in addition to surface wind analyses from the Utah 2-Dimensional Variational Analysis (Tyndall and Horel, 2013) that incorporates Mesowest observations.

The study reported here adds crucial observations to the existing datasets available to characterize the meteorology of the boundary-layer and the region just above the boundary-layer in the Basin. This study shows (1) temporal variations in boundary-layer height, (2) multiple layering within the stable boundary-layer, (3) daytime easterly flows within the boundary-layer between the surface and 500 m aloft on some days, (4) significant impacts of westerly flow intrusions in the Basin, and (5) that low cloud cover is most frequently observed within the lowest portions of the basin.

### 3.2.2 Methods

#### 3.2.2.1 Monitoring Sites and Observations

The location of the University of Utah meteorological monitoring sites as well as the location of all available Mesowest sites within the basin ( http://mesowest.utah.edu ingests data from all available sources for surface meteorological data) are shown in Figure 3-32.

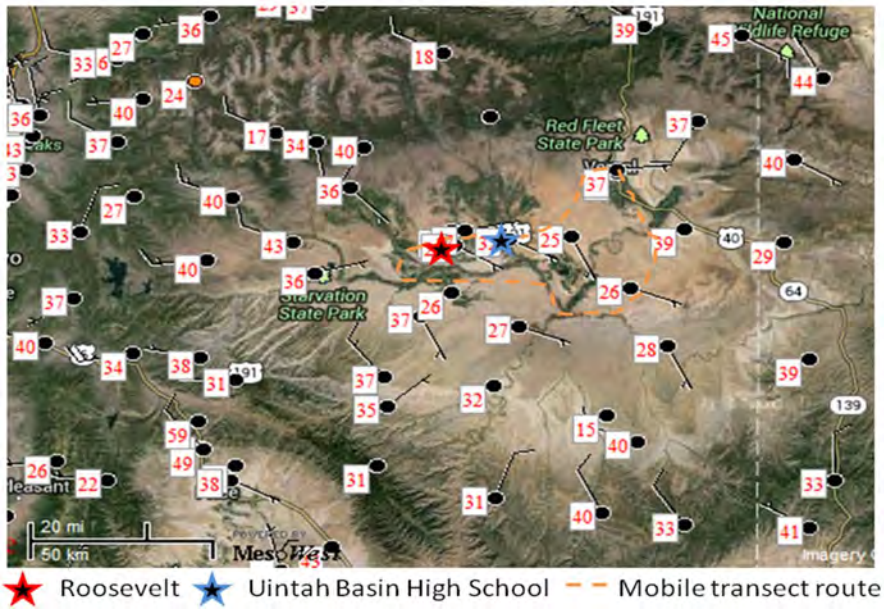


**Figure 3-32. Location of key targeted University of Utah meteorological instrumentation sites and mobile transect route. All Mesowest stations available during the UBWOS are shown by black dots.**

The meteorological monitoring for this study focused on the western part of the region identified as having high ozone levels (Lyman and Shorthill, 2013). This region was chosen to allow for spatial intercomparisons with meteorological observations conducted by other scientists at the Horse Pool and Ouray locations.

A CL-31 Viasala ceilometer was deployed between 17 January and 16 February 2013 at Roosevelt. A Viasala CK-12 Ceilometer was installed at the Uintah Basin High School in January and remained at that location through the entire 2012-13 UBWOS campaign. Graw DFM-06 radiosondes were launched at 1800 UTC from the Roosevelt site on the 26$^{th}$ of January, 16$^{th}$ of February, and every day between 1 February and 8 February, inclusive (except on 5 February when the radiosonde was launched from the Uintah Basin High School as part of an educational outreach activity). Photos of several of the key instruments are shown in Figure 3-33.

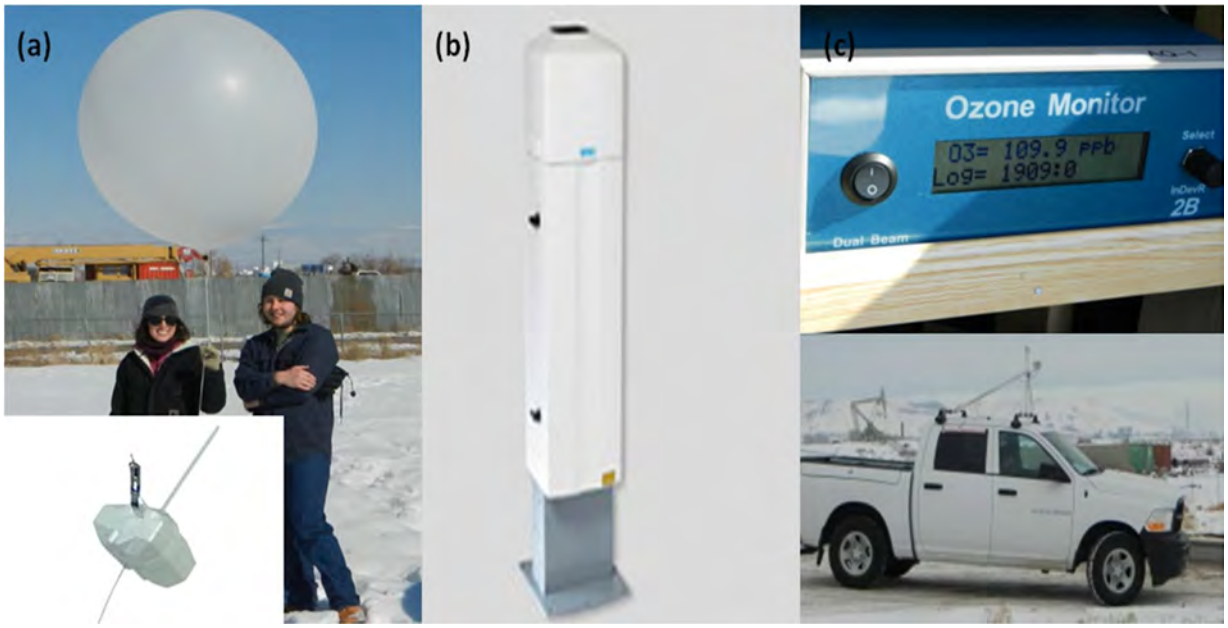


**Figure 3-33. Instruments used during targeted meteorological observations in the Uinta Basin. (A) Graw DFM-06 radiosondes, (b), Viasala CL-31 ceilometer, (c) Meteorological and ozone mobile unit.**

The coordinates (latitude, longitude, elevation) of the sites shown in Figure 3-32 as well as the instruments deployed at each site, the dates data were collected from these instruments, and the available processed data sets for general scientific use by the UBWOS scientists, as well as the temporal frequency of the data collected are listed in Table 3-8.

**Table 3-8. University of Utah targeted meteorological observations location and dates.**

| Site Name | Latitude | Longitude | Elevation (m) | Instrument | Dates data collected (2013) | Available data | ΔT |
|---|---|---|---|---|---|---|---|
| Roosevelt | 40.26560 | -110.04120 | 1561 | Viasala CL-31 ceilometer | 19 January – 16 February | Excel file with hourly aerosol depth and median backscatter | 1 hr |
| | | | | Met station with sonic anemometer and net solar radiation | 26 January – 16 February | Temperature, humidity, U, V, and W wind speed and direction, solar radiation | 5 min |

| Site Name | Latitude | Longitude | Elevation (m) | Instrument | Dates data collected (2013) | Available data | ΔT |
|---|---|---|---|---|---|---|---|
| | | | | GRAW DFM-06 rawinsonde | 26 January; 1-4 January; 6-8 January; 16 February | Temperature, humidity, and wind speed and direction | 1 second |
| Uintah River High School | 40.282140 | -109.86297 | 1544 | Viasala CK-12 ceilometer | 16 January – end of UBWOS | Excel file with aerosol depth | 1 hr |
| | | | | GRAW DFM-06 rawinsonde | 5 January | Temperature, humidity, and wind speed and direction | 1 sec |
| Mobile met and ozone | na | na | na | 2B technologies 205; | 25 January; 1, 2, 4, 6, 7, 16 February | Temperature, humidity, and wind speed and direction, ozone | 1 min |
| Roosevelt | **40.26560** | **-110.04120** | **1561** | Viasala CL-31 ceilometer | 19 January – 16 February | Excel file with hourly aerosol depth and median backscatter | 1 hr |
| | | | | Met station with sonic anemometer and net solar radiation | 26 January – 16 February | Temperature, humidity, U, V, and W wind speed and direction, solar radiation | 5 min |
| | | | | GRAW DFM-06 rawinsonde | 26 January; 1-4 January; 6-8 January; 16 February | Temperature, humidity, and wind speed and direction | 1 second |

The estimates of hourly aerosol depth from Roosevelt and the Uintah River High School has been used in combination with an algorithm searching for vertical gradients in ceilometers backscatter to calculate an estimate of boundary-layer depth each hour during cloud-free periods.

All targeted observations conducted during the UBWOS study by the University of Utah are available at http://home.chpc.utah.edu/~u0198116/ubos/obs.html, while all surface meteorological data from the Mesowest network in the Uinta Basin are archived at http://mesowest.utah.edu.

#### 3.2.2.2 WRF Modeling

Numerical simulations of PCAP evolution in the Uinta Basin are being conducted. Hourly wind estimates for the basin surface and multiple levels aloft are currently being processed for the seven PCAPs that were observed during the UBWOS and will be available at the following website as the simulations are completed:
http://home.chpc.utah.edu/~u0198116/ubos/numerical.html.

Detailed information regarding the model set-up and domain used in the simulations are also available within those web pages.

### 3.2.3 Results and Discussion

#### 3.2.3.1 Timing of Persistent Cold Air Pools During UBWOS

Seven persistent cold air pools were observed in the Uinta Basin between January and March 2013. The approximate starting and ending dates for these PCAPS are:

- PCAP 1: 6-11 January 2013 (~6 days)
- PCAP 2: 15-29 January 2013 (~15 days)
- PCAP 3: 31 January – 10 February 2013 (~11 days)
- PCAP 4: 12 – 17 February 2013 (~6 days)
- PCAP 5: 18-20 February 2013 (~3 days)
- PCAP 6: 26 February – 3 March 2013 (~6 days)
- PCAP 7: 6-9 March 2013 (~4 days)

During each of these PCAPs, variations in the boundary-layer height, intensity and depth of the vertical temperature inversion, and both boundary-layer winds and synoptic winds above the PCAP were observed. Hence, while it is difficult to generalize about Uinta Basin PCAPS, there were some characteristics observed during all PCAPS. First, the boundary-layer wind speeds were light and variable (less than 2 $ms^{-1}$) in the lowest portions of the valley such as Ouray and Horsepool, but were much stronger and variable along the mid-valley foothills into the higher foothills (5-15 $ms^{-1}$). Weak up valley flows during the day and down valley flows at night prevail within the major river valleys. The temperature inversions between the lowest elevations and the upper foothills varied in strength from isothermal conditions (temperature constant with height) to over 10 $^{o}C$. The vertical distribution of the stability gradient varied widely during the UBWOS study, occurring several hundred meters above the surface during days with cloud-topped mixed layers to only a few 10s of meters above the surface on days with strong surface radiation inversions. In the following subsections we discuss in more depth the observational and numerical modeling findings regarding the boundary-layer characteristic in the Uinta Basin during the 2012-2013 UBWOS.

### 3.2.3.2 Boundary-Layer Height and Structure

The boundary-layer depth and structure during UBWOS persistent cold air pools were estimated using backscatter and backscatter gradients from the two University of Utah ceilometers deployed in the basin. On most days, distinct layering of the vertical structure of the boundary-layer backscatter was observed (Figure 3-34).

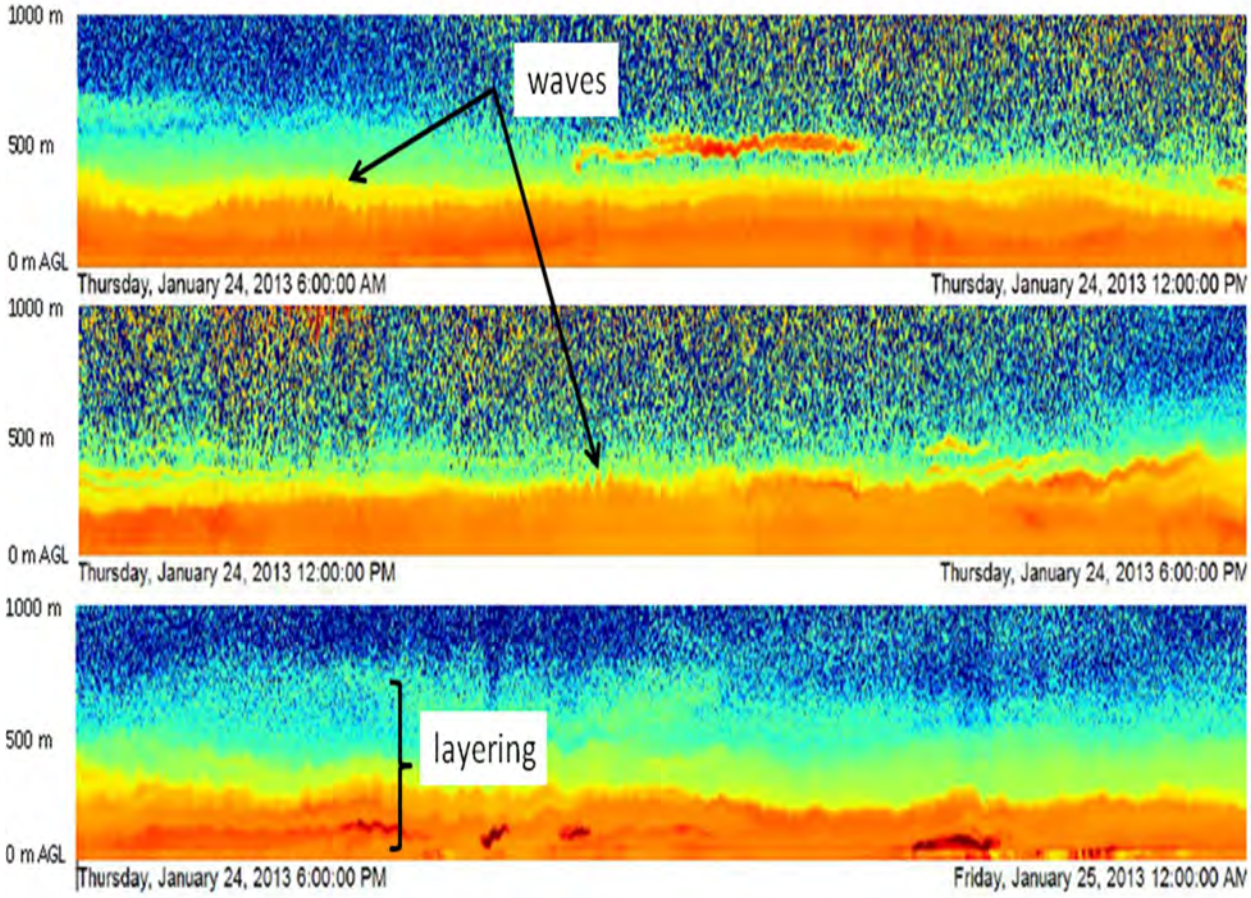


**Figure 3-34. Ceilometer aerosol backscatter on 24 January 2013 at Roosevelt, UT. Higher backscatter denoted by warm colors and lower aerosol concentrations indicated by cool colors.**

These layered structures in the vertical profile of aerosol backscatter were typically associated with layered structures in the vertical temperature and wind fields observed in the once-daily rawinsonde launches from Roosevelt (not shown, rawinsonde data available at U Utah UBWOS website). Along the top of the primary polluted boundary-layer, gravity waves were observed as seen in Figure 3-34. It is the depth of this primary surface layer that is used to estimate aerosol depth using gradient methods. Above the primary polluted layer located in the first 200-400 meters of the boundary-layer, a transition layer was sometimes observed. In this layer, mixing and dispersion from synoptic flows impinging on the top of the temperature inversion resulted in lower aerosol concentrations and the aforementioned gravity waves.

Alternating layers of high and reduced aerosol concentrations embedded within stable boundary layer were observed on numerous occasions. Another feature that is apparent from Figure 3-34 is the diurnal variations in the depth of the surface-based polluted layer. These diurnal variations are associated with similar variations in the temperature structure of the boundary-layer. On the 24th January (Figure 3-34), the depth of the surface-based polluted layer was observed to be near 300 m during the overnight hours, but increased to nearly 500 m during the afternoon. The depth of the aerosol layer observed during the UBWOS varied not only from day to day but also from one persistent cold air pool to another as shown in Figure 3-35.

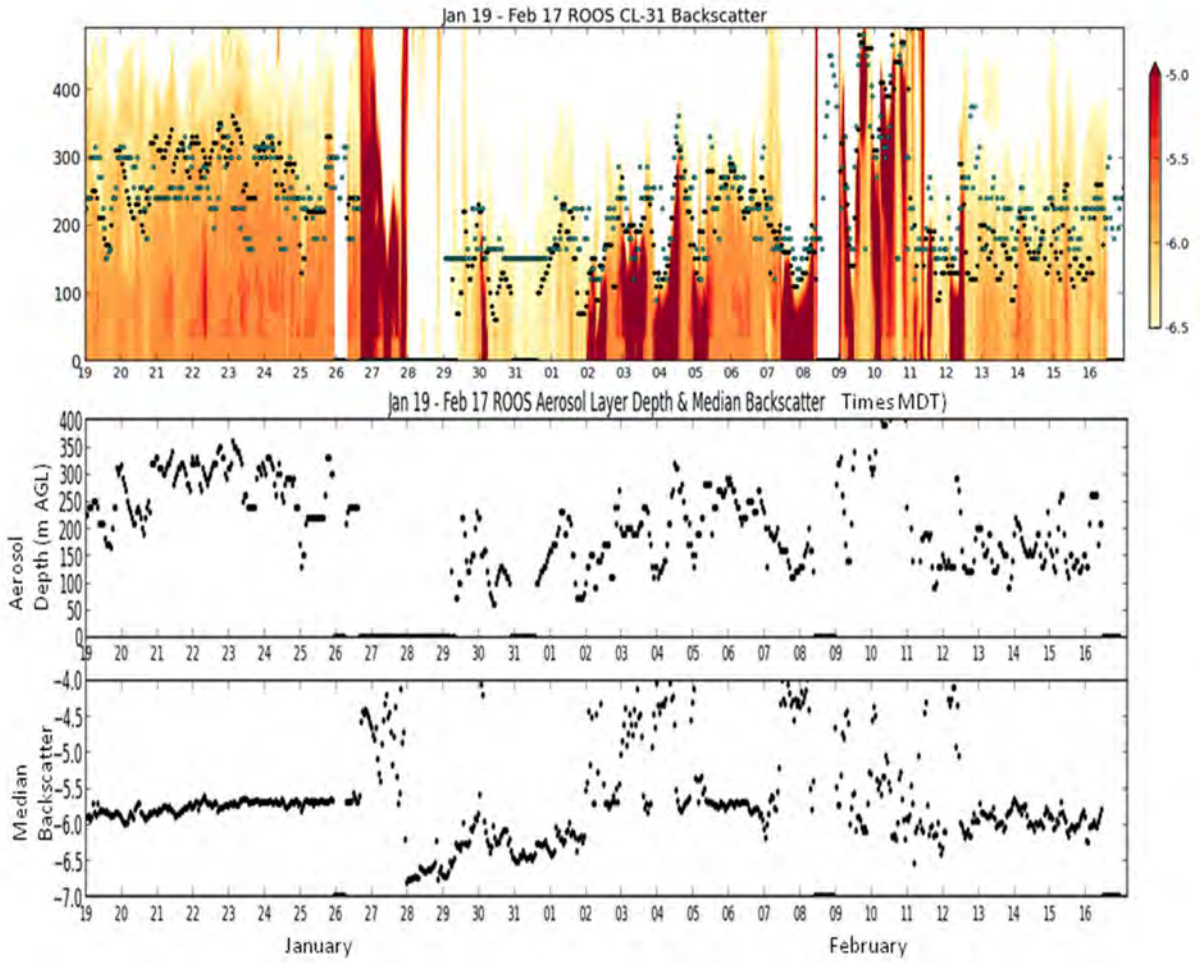


**Figure 3-35. Aerosol backscatter between 19 January 2013 and 17 February 2013 at Roosevelt (top), depth of the dominant aerosol layer (middle) and median backscatter values for region below the calculated aerosol depth (bottom).**

During PCAP 2, which occurred between 15-29 January 2013, the estimated depth of the primary aerosol later was 200-300 m AGL. During the following event (PCAP 3, 31 January – 10 February 2013), the primary aerosol layer showed significantly greater diurnal and temporal variation than during PCAP 2, with the mean aerosol depth approximately 100 m lower than

that observed during the preceding event. Fog, deeper cloud layers, and precipitation (dark red features in Figure 3-35) complicate the analysis of aerosol layer depth during PCAP 3. During PCAP 4 (12 – 17 February 2013), the mean aerosol depth was also approximately 100 m lower than that observed during PCAP 2.

#### 3.2.3.3 Boundary-Layer Winds and Flow Interactions

Describing the boundary-layer winds in the Uinta Basin is challenging as a result of (1) limited wind data above the surface and (2) highly variable (both spatially and temporally) wind patterns evident in Mesowest surface observations, rawinsonde observations at Roosevelt, and lidar observations at Horsepool. Detailed meteorological analysis has resulted in identifying several noteworthy wind features in the Uinta Basin during UBWOS 2013:

Surface and rawinsonde observations indicate an easterly flow both at the surface and extending aloft through the western 2/3$^{rd}$ of the Basin (the extent and intensity of the easterly flow varies from day to day, modulated by the boundary-layer thermal structure and other unknown factors). However, insufficient data exists to quantify the importance of the elevated easterly flow in basin-wide transport at this time. Numerical modeling work is underway to address this issue. Figure 3-36 shows rawinsonde observations on two days during PCAP 3 on 2 and 4 of February 2013 when, within an elevated strong stable layer approximately 350 m deep, 2-4 ms$^{1}$ easterly jets were observed. It is unclear whether the easterly flow is a return flow in response to the westerly flow forcing observed at the top of the inversion, and this question is an issue for future exploration.

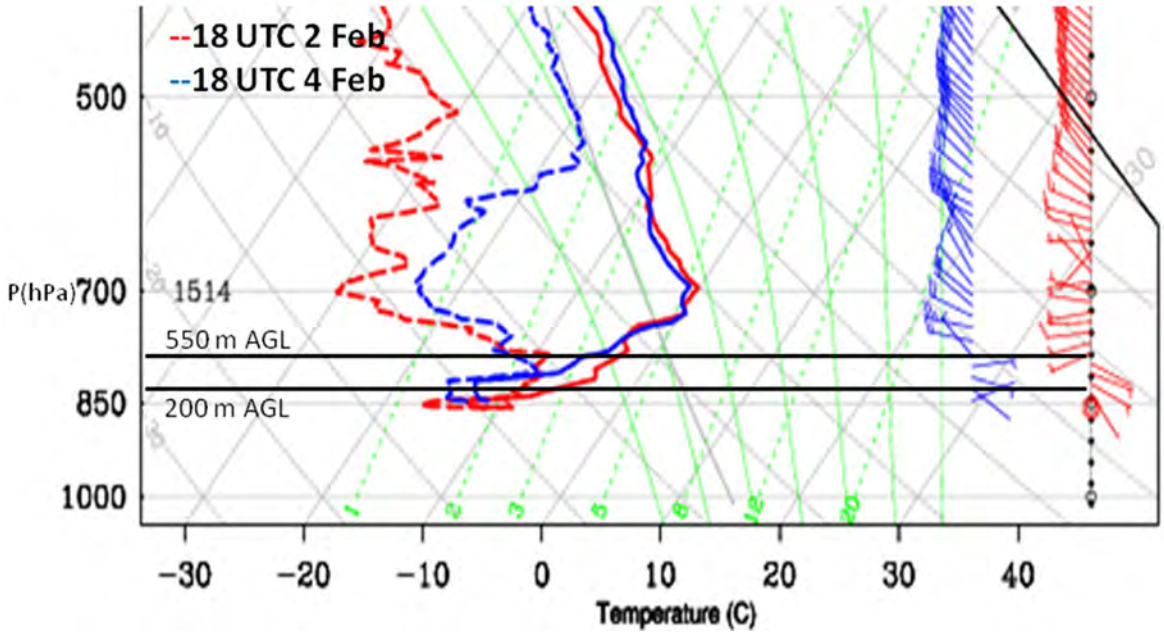


**Figure 3-36. Skew-T plot showing temperature, dew point temperature, and wind speed and direction for 2 and 4 February 2013 at 1800 UTC.**

Highly variable westerly wind intrusions were noted during most of the 7 PCAPs during the UBWOS. These winds resulted in turbulent mixing and dilution of the PCAP both at the top of the boundary layer and on the Western side of the basin. T hese winds resulted in dramatic fluctuations in temperature and pollutant concentrations in the Starvation Reservoir and Duchesne area and in some cases a strengthening of the temperature inversion as downslope flow warmed the air at the top of the PCAP. Modeling work is currently being conducted to address questions related to this issue. Figure 3-37 shows modeled variations in 775 mb winds speeds. Depending on elevation, the 775 mb level is 400-800 m above the ground surface and represents the winds at the top of the inversion during this episode.

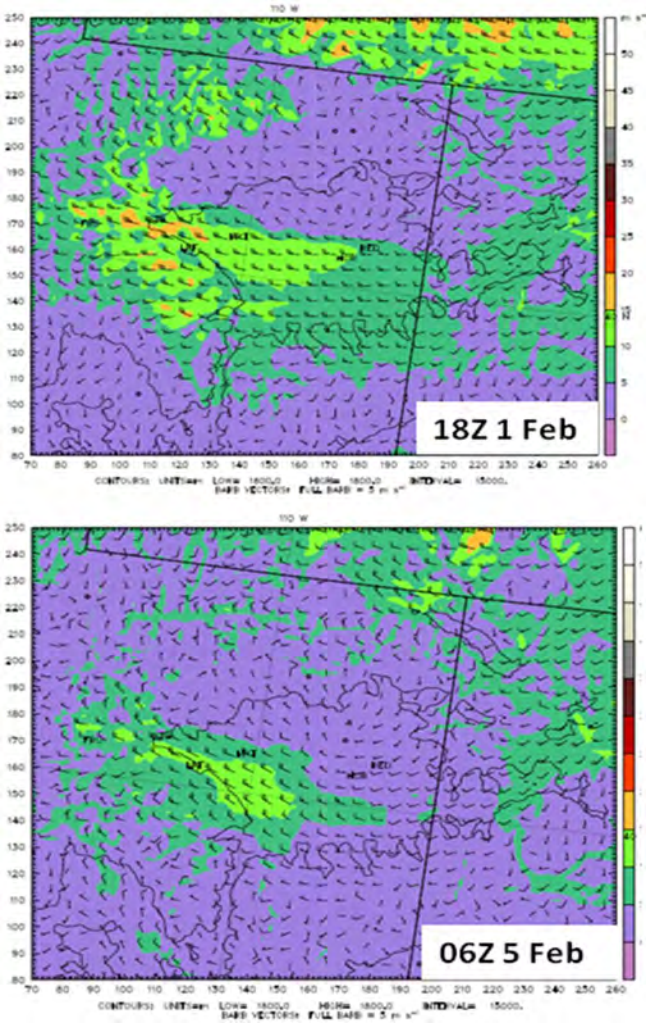


**Figure 3-37. 775 hPa level wind speeds (shaded and barbs) and direction for WRF numerical simulations during the 30 January-10 February 2013 persistent cold air pool in the Uinta Basin.**

It is important to recognize that these periods of strong westerly air bring in fresh, relatively unpolluted air into the Basin, and do not result in transport of ozone from the Wasatch Front into the Basin.

Additional numerical modeling of boundary-layer flows and interactions between synoptic and boundary-layer flows are being conducted at the University of Utah and the results of these modeling studies will be made available at the following website: http://home.chpc.utah.edu/~u0198116/ubos/numerical.html

### 3.2.3.4 Boundary-Layer Clouds

Boundary layer clouds were highly variable during the UBWOS study. The ceilometer data provides a quantitative measure of total cloudy hours during the UBWOS, as the ceilometers retrievals are quickly saturated by high backscatter from clouds. The spatial extent of clouds can be assessed from satellite imagery. Daily MODIS images from Aqua and Terra satellites can be accessed from the University of Utah UBWOS observations website. The extent of low cloud cover during the UBWOS PCAPS can be highly variable, as shown in Figure 3-38.

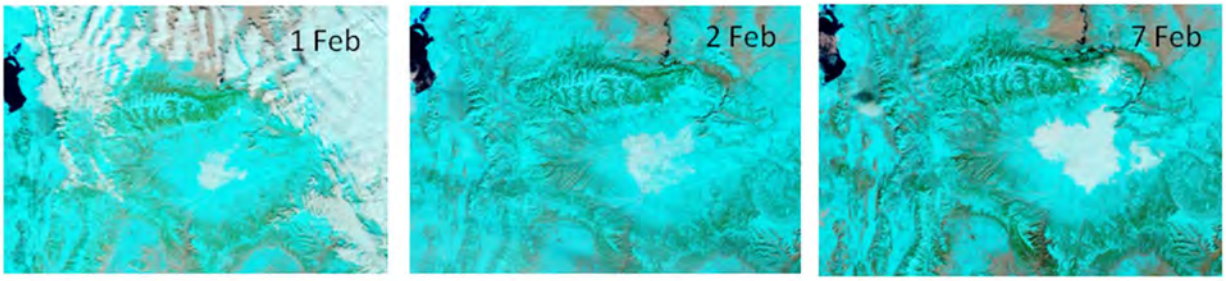


**Figure 3-38. Afternoon MODIS satellite imagery showing snow (blue) and clouds (white) during 1, 2, and 7 February 2013.**

For example, much of the basin was covered in clouds on 7 February, whereas only the region around Ouray was observing clouds during the afternoon satellite passes on 1 February. Estimates of low cloud occurrence and spatial extent in the basin during afternoons between 1 January – 12 March 2013 are listed in Table 3-9.

**Table 3-9. Occurrence of low clouds in MODIS using AQUA satellite imagery data retrieved at mid-afternoon during UBWOS.**

| Date | Low cloud occurrence in Aqua satellite pass (Y, N or NAN (for obstructing high clouds) | Estimated fraction of basin (%) covered by low clouds |
|---|---|---|
| 1 January | Y | <25% |
| 2 January | N | |
| 3 January | N | |
| 4 January | N | |
| 5 January | N | |
| 6 January | N | |
| 7 January | N | |
| 8 January | N | |
| 9 January | N | |
| 10 January | N | |
| 11 January | N | |

| Date | Low cloud occurrence in Aqua satellite pass (Y, N or NAN (for obstructing high clouds) | Estimated fraction of basin (%) covered by low clouds |
|---|---|---|
| 12 January | N | |
| 13 January | N | |
| 14 January | N | |
| 15 January | N | |
| 16 January | N | |
| 17 January | N | |
| 18 January | N | |
| 19 January | N | |
| 20 January | N | |
| 21 January | N | |
| 22 January | N | |
| 23 January | NAN-high clds | |
| 24 January | NAN—high clds | |
| 25 January | NAN—high clds | |
| 26 January | NAN—high clds | |
| 27 January | NAN—high clds | |
| 28 January | NAN—high clds | |
| 29 January | NAN—high clds | |
| 30 January | N | |
| 31 January | N | |
| 1 February | Y | <10% |
| 2 February | Y | <25% |
| 3 February | N | |
| 4 February | Y | <50% |
| 5 February | N | |
| 6 February | NAN-high clds | |
| 7 February | Y | >50% |
| 8 February | NAN-high clds | |
| 9 February | Y | >50% |
| 10 February | Y | >50% |
| 11 February | Y | <50% |
| 12 February | N | |
| 13 February | N | |
| 14 February | N | |
| 15 February | N | |
| 16 February | N | |
| 17 February | N | |
| 18 February | N | |
| 19 February | N | |
| 20 February | NAN-high clds | |
| 21 February | N | |
| 22 February | N | |
| 23 February | NAN-high clds | |
| 24 February | N | |
| 25 February | N | |
| 26 February | N | |
| 27 February | N | |

| Date | Low cloud occurrence in Aqua satellite pass (Y, N or NAN (for obstructing high clouds) | Estimated fraction of basin (%) covered by low clouds |
|---|---|---|
| 28 February | N | |
| 1 March | N | |
| 2 March | N | |
| 3 March | N | |
| 4 March | N | |
| 5 March | N | |
| 6 March | N | |
| 7 March | N | |
| 8 March | NAN-high clds | |
| 9 March | N | |
| 10 March | N | |
| 11 March | N | |
| 12 March | NAN-high clds | |

### 3.2.4 Summary

Intense, long-lived PCAPs are common during winter and generally encompass the entirety of the Uinta Basin. Below the inversion top in the boundary-layer, complex multi-level stable layers with varying flow direction and intensity were often observed during the 2013 UBWOS.

Meteorological data from laser ceilometers, rawinsondes, and surface and satellite platforms during the UBWOS provide an enhanced view of the spatiotemporal evolution of the boundary-layer. The key data sets currently available for download at the University of Utah UBWOS study webpage are:

- Ceilometer estimates of Uinta Basin aerosol depth and relative intensity.
- Rawinsonde profiles of boundary-layer winds, temperature and moisture, as well as observations of the synoptic winds impinging on the PCAP from aloft.
- Transects of co-located meteorological data (temperature, humidity, winds) and ozone data in a circular loop from Roosevelt to Vernal, Horsepool, Ouray, Myton, and back to Roosevelt.
- Integration within MesoWest data archive of surface weather station data from all available networks (e.g., NWS, Utah State University, University of Utah, AIRNOW, Utah Dept Air Quality, SNOTEL).
- Numerical model simulations of basin-wind boundary-layer and synoptic winds.

In addition to providing this crucial information for retrospective model validation studies and volume budget calculations within the basin, this study showed that:

- Multi-layer structures often exist in both rawinsonde temperature and ceilometers backscatter profiles, indicating a complex multi-layer pattern of pollutant transport existing within the Basin.

- The depth of the boundary layer as measured by the laser ceilometer during UBWOS persistent cold air pools ranged from 70-400 m.
- Westerly intrusions of synoptic winds into the western portions of the Basin are relatively common occurrences and may affect transport patterns of pollutants in the boundary-layer (including driving return easterly flows). Numerical modeling experiments are currently being conducted to test this hypothesis.
- Easterly flows in the boundary-layer during the daytime were a commonly observed flow regime in the western 2//3$^{rd}$ of the basin. Numerical modeling will be conducted to determine if these flows are thermally-driven or dynamically-driven and whether they occur only during the afternoon or during nighttime as well.

## 3.3 Use of the CALMET Diagnostic Model to Simulate Winter Inversions

### 3.3.1 Introduction

The major precursors to ozone formation—$NO_x$ and VOC—are emitted by a variety of sources. To determine the contributions to ozone production of these different sources in the Uinta Basin, meteorological models that accurately reproduce transport conditions during winter inversions are needed. A realistic meteorological model of the region will enable us to observe how pollutant transport from sources within and outside of the Basin affects ozone and precursor concentrations in the Basin.

Forecasting models such as the Weather Research and Forecasting (WRF) model, however, have difficulty accurately simulating winter inversion conditions. The CALMET diagnostic model, on the other hand, builds meteorological simulations from actual measurements of meteorological conditions, potentially allowing it to capture key features of winter inversions that are not accurately simulated by the physics parameterizations within WRF. Thus, in this work we sought to determine the value of CALMET as a diagnostic tool for meteorological conditions in the Basin. If successful, CALMET model output can be used to better understand transport patterns and inversion characteristics during ozone episodes.

### 3.3.2 Methods

We incorporated data from all available meteorological stations, both at the surface and aloft, from an intensive UBOS study period (28 January to 8 February) for input to the most current version (6.42) of CALMET, an EPA-approved modeling program. This program was recently employed in a similar study of ozone precursor transport in the Upper Green River Basin of southwestern Wyoming (Rairigh, 2010).

We utilized a horizontal grid resolution of 1.5 km$^2$, and a 300 × 300 km modeling domain that extends 9 to 75 km beyond each edge of the Uinta Basin. Meteorological data were extracted from stations located either inside or up to 80 km beyond this area in all directions. Table 3-10 lists the 68 stations used. A 3D rendering of the modeling domain is shown in Figure 3-39. Upper air data were extracted from sites at Salt Lake City, UT; Grand Junction, CO; Denver, CO; and Riverton, WY. Vertical layers used for the model are shown in Table 3-11, and range from 10 to 3,500 meters above ground level.

**Table 3-10. Stations from which data were used in the CALMET model.**

| Station | Station Name | Station | Station Name |
|---|---|---|---|
| 1 | OURAY | 35 | ROOSEVELT |
| 2 | MEEKER AIRPORT | 36 | CHEPITA |
| 3 | VERNAL AIRPORT | 37 | FRUITLAND |
| 4 | HEBER AIRPORT | 38 | PRICE |
| 5 | BRYSON CANYON | 39 | PORTABLE RWIS |
| 6 | BADGER WASH | 40 | DRY RIDGE |
| 7 | CART CREEK | 41 | ROOSEVELT |
| 8 | HANNA NEAR DUCHESNE NW 24 | 42 | LITTLE RED FOX |
| 9 | BLACK TAIL | 43 | MOUNTAIN HOME |
| 10 | NUTTERS RANCH | 44 | MOON LAKE NEAR ALTONA |
| 11 | KINGS PONIT | 45 | INDIAN CANYON SUMMIT |
| 12 | HORSE RIDGE | 46 | US-40 @STARVATION |
| 13 | UPPER SAND WASH | 47 | YELLWOSTONE DRAINAGE |
| 14 | YAMPA PLATEAU | 48 | WEST FORK BLACK SMITH |
| 15 | DIAMOND RIM | 49 | VERNAL |
| 16 | FIVE MILE | 50 | SPLIT MOUNTAIN |
| 17 | BEAR RIVER | 51 | UPPER P.R. CANYON |
| 18 | DRAGON ROAD | 52 | CURRANT CREEK PEAK |
| 19 | GREEN RIVER | 53 | †RANGELEY COLORADO |
| 20 | LADORE | 54 | NORWAY |
| 21 | HUNTER CREEK | 55 | DEER VALLEY |
| 22 | RATTLESNAKE BENCH | 56 | WILD HORSE |
| 23 | DINOSAUR NM SUCCESS | 57 | RIFLE |
| 24 | CRAIG MOFATT AIRPORT | 58 | WINTER RIDGE |
| 25 | BRUIN POINT | 59 | MYTON |
| 26 | HELPER @ US 6 | 60 | RAYS VALLEY |
| 27 | CALICO | 61 | *SAND WASH |
| 28 | SOLDIER SUMMIT | 62 | *PARIETTE DRAW |
| 29 | PRICE AIRPORT | 63 | *SEVEN SISTERS |
| 30 | FLATTOP MOUNTAIN | 64 | *SEEP RIDGE |
| 31 | PINTO | 65 | *WELLS DRAW |
| 32 | HEBER US-40 | 66 | *MOUNTAIN HOME |
| 33 | SALT LAKE CITY | 67 | *GUSHER |
| 34 | PRICE | 68 | *HORSEPOOL |

*USU Sites †Site omitted because reported data were incomplete

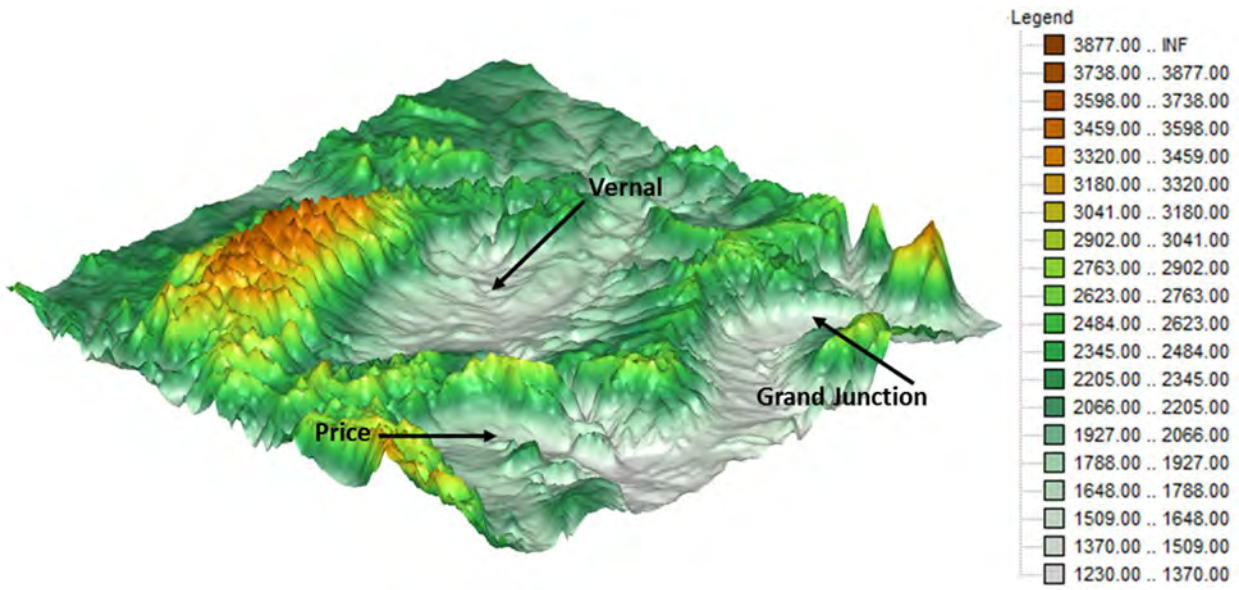


**Figure 3-39. 3D elevation map of the CALMET modeling domain. Approximate locations of Vernal, Price, and Grand Junction are shown.**

**Table 3-11. Vertical layers utilized in the CALMET model.**

| Layer # | Layer top (m above ground level) |
|---|---|
| 1 | 10 |
| 2 | 20 |
| 3 | 60 |
| 4 | 100 |
| 5 | 150 |
| 6 | 200 |
| 7 | 350 |
| 8 | 500 |
| 9 | 750 |
| 10 | 1000 |
| 11 | 2000 |
| 12 | 3000 |
| 13 | 3500 |

### 3.3.3 Results and Discussion

#### 3.3.3.1 CALPUFF Model Animations

CALMET can be coupled with the 3D-modeling software CALPUFF, which generates animated plume dispersion models. In concert with this work, we created a video of a twelve-hour plume dispersion model that uses five hypothetical source points. These are publicly available online and illustrate the value of the CALMET modeling system (https://www.youtube.com/watch?v=5lTZeAfBSR4&feature=c4-overview&list=UUpUkAZfpeUBMmA_zAAERyZw).

### 3.3.3.2 Wind Speed and Direction

Ground-level (10 m) wind field vectors are shown below in Figures 3-40 through 3-43. Each of these figures was taken from 6 February 2013, the day of highest ozone concentration during an inversion period. On this day, the CALMET-predicted wind speeds within the Uinta Basin remained low (less than 3 m/s). At 3:00 local time (Figure 3-40), wind within the Basin flowed primarily from the south. By 9:00 (Figure 3-41), wind in the Basin was low and variable, but tended to blow mostly from east to west. This pattern held, for the most part, at 15:00 (Figure 3-42), but by 21:00 (Figure 3-43), winds were from the south on the east side of the Basin, and from the west on the west side of the Basin.

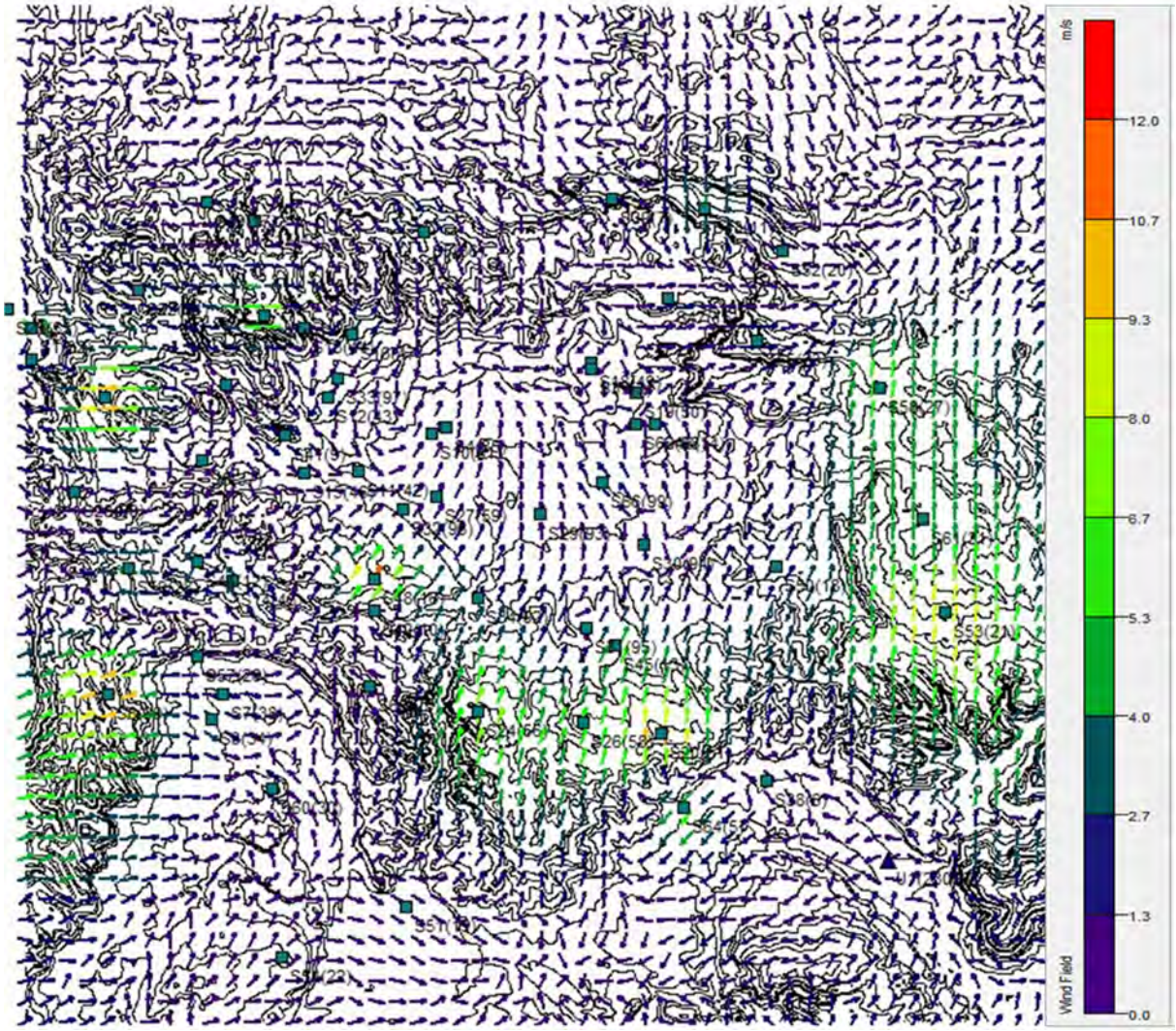


**Figure 3-40. Ground-level (10 m) wind vectors at 3:00, 6 February.**

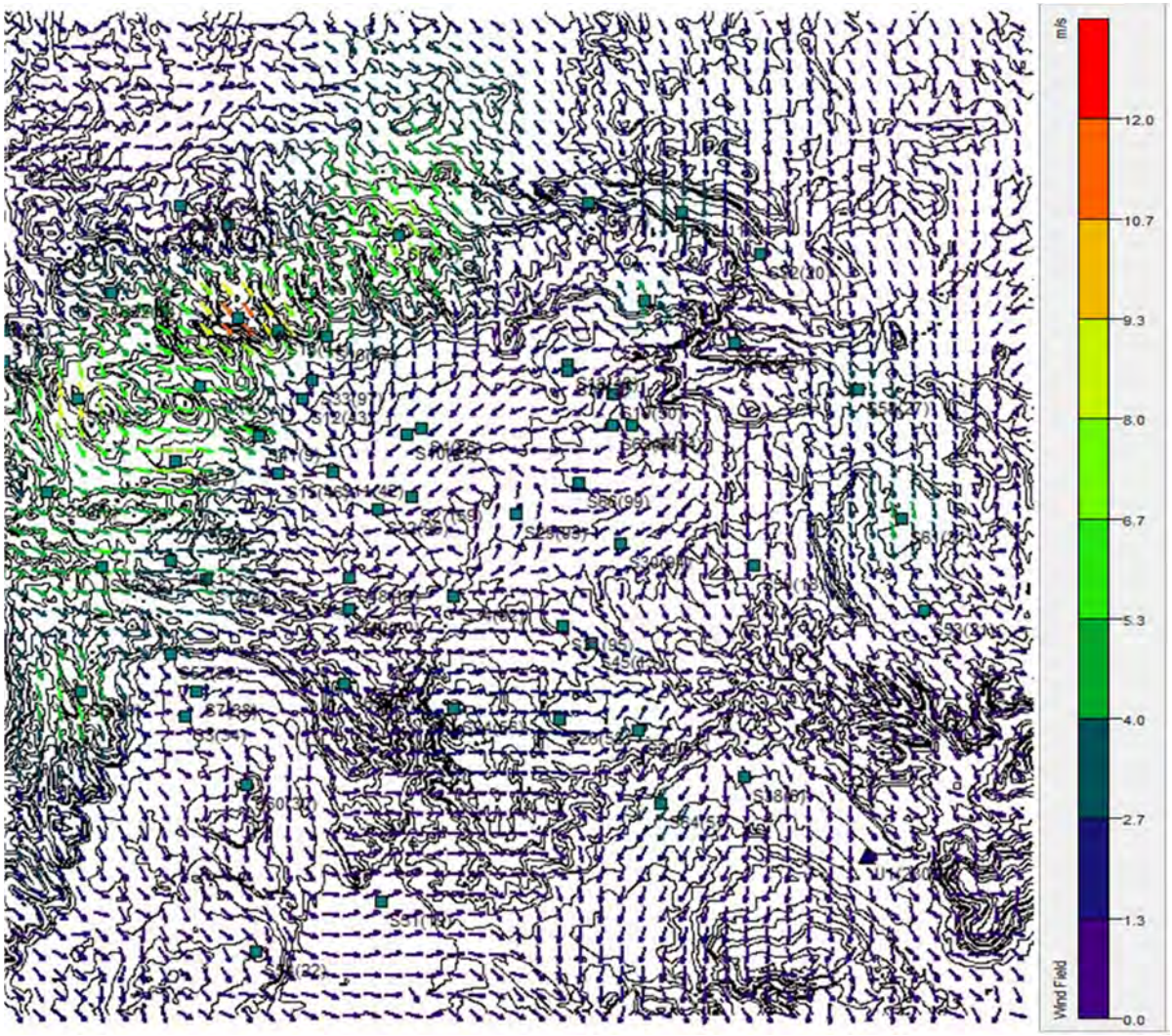


**Figure 3-41. Ground-level (10 m) wind vectors at 9:00, 6 February.**

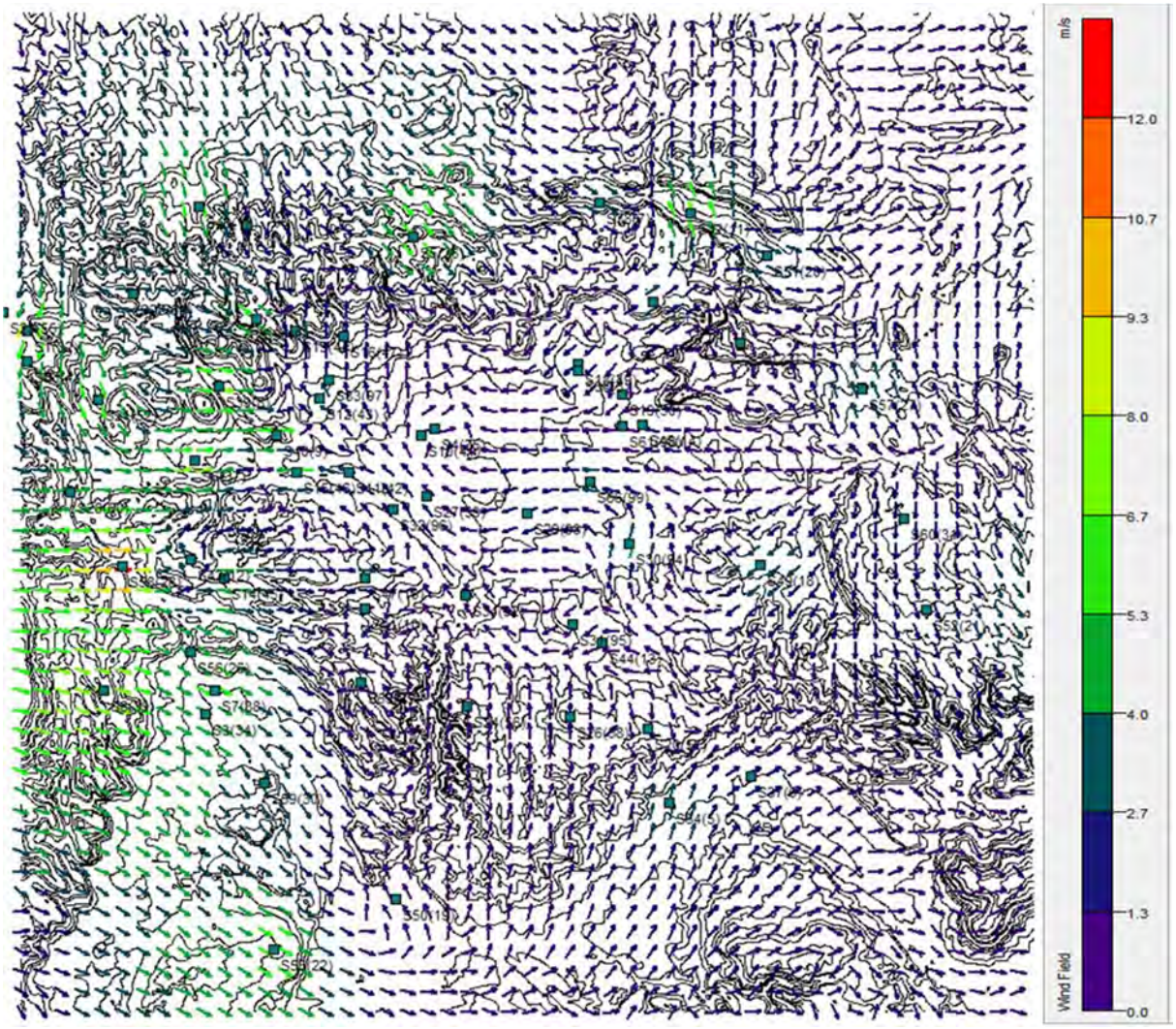


**Figure 3-42. Ground-level (10 m) wind vectors at 15:00, 6 February.**

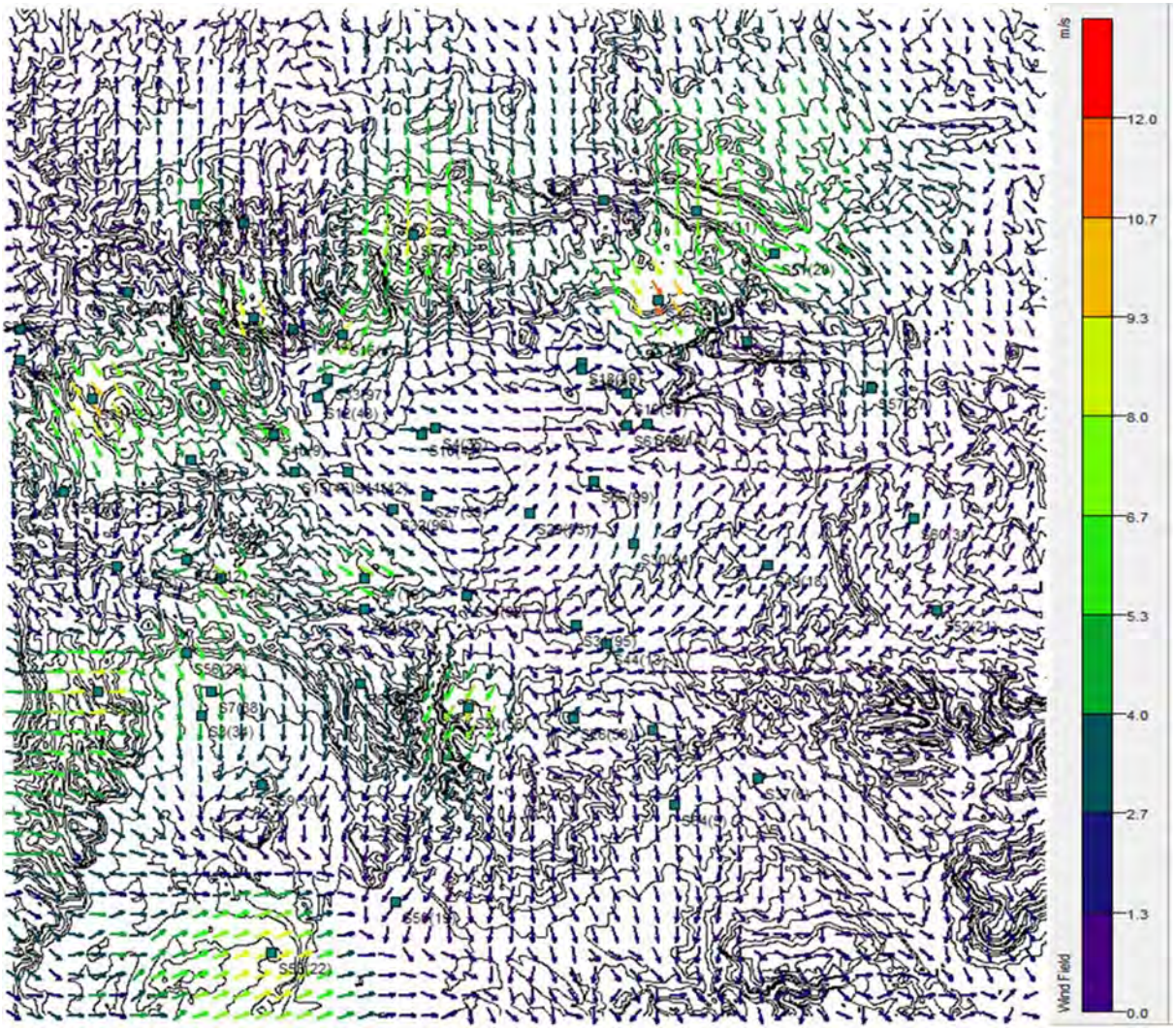


**Figure 3-43. Ground-level (10 m) wind vectors at 21:00, 6 February.**

We extracted ground-level (10 m) wind directions and speeds, as well as temperature, from the model at the locations of select surface meteorological stations and compared them with measured data. Table 3-12 shows results from two stations, Dragon Road and Sand Wash. Modeled and measured wind speed, wind direction, and temperature were well correlated at Dragon Road, but modeled and measured wind speed and direction were poorly correlated at Sand Wash. The Sand Wash site is located within Desolation Canyon, and at the 1.5 km horizontal resolution used, CALMET was not able to fully resolve terrain or wind patterns within the canyon. Also, measured wind speed was low, often zero, in Sand Wash, while modeled wind speed was never zero, further confounding the comparison.

**Table 3-12. Slope, $R^2$ value, and percent deviation for the relationship between measured and modeled wind speed, wind direction, and temperature at the Dragon Road and Sand Wash sites. Percent deviation rows show values ± 95% confidence intervals.**

| | Dragon Road | Sand Wash |
|---|---|---|
| **Wind Speed** | | |
| Slope | 1.01 | -0.03 |
| $R^2$ | 1.00 | 0.01 |
| Percent Deviation | 0.8 ± 0.3% | 20 ± 84% |
| **Wind Direction** | | |
| Slope | 0.68 | 0.19 |
| $R^2$ | 0.59 | 0.02 |
| Percent Deviation | 7.8 ± 10.2% | 9.4 ± 16.8% |
| **Temperature** | | |
| Slope | 0.93 | 1.04 |
| $R^2$ | 0.85 | 0.92 |
| Percent Deviation | 0.0 ± 0.1% | 0.3 ± 0.1% |

#### 3.3.3.3 Temperature

A surface-level temperature contour map for observations made at 10:00 local time on 7 February 2013 is shown in Figure 3-44. This figure shows an inversion, with areas of lowest elevation having temperatures less than 0 °C, and areas of highest elevation having temperatures up to about 10 °C. Site S49 shown in the upper left corner has a temperature of more than 20 °C, which is extremely unlikely for early February. We expect the temperature at this site is inaccurate, and it will be removed from future analyses.

To determine whether changes in temperature with height were being accurately simulated by the model, we extracted temperature from the different vertical layers of CALMET and compared them to temperature measured with a moored balloon on 6 February at Pariette Draw. Figure 3-45 shows the average measured and modeled vertical temperature profile for the period from 12:00 to 15:00. CALMET does simulate the presence of a temperature inversion, but the inversion occurs higher in the model than in reality, and the model predicts a decrease in temperature with height under the inversion that does not exist in the measurements, leading to a divergence of about 6 °C between measurements and the model at 275 m above ground.

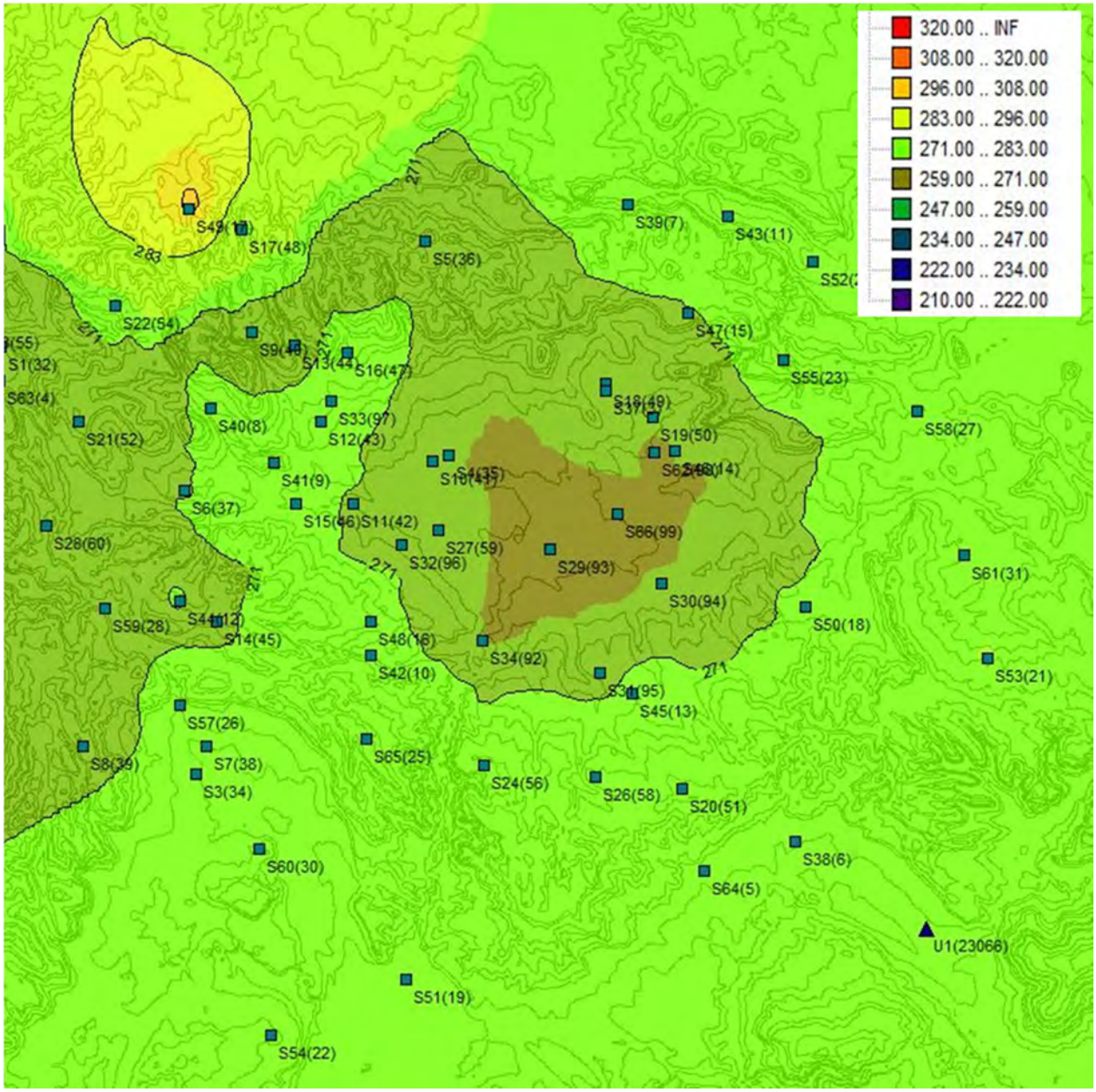


**Figure 3-44. Surface temperature contour map for 10:00, 7 February.**

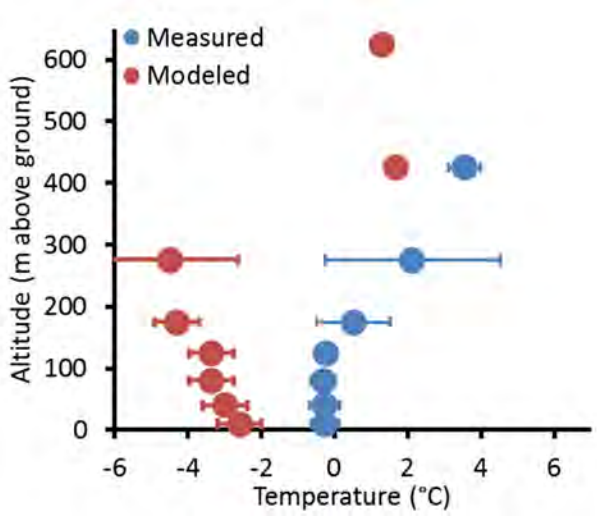


**Figure 3-45. Measured and modeled vertical temperature profile for 12:00 to 15:00, 6 February at Pariette Draw.**

### 3.3.4 Acknowledgements

We gratefully acknowledge funding for this project from the Uintah Impact Mitigation Special Service District.

## 3.4 References

Carter, W.P.L., 2009. *Development of the SAPRC-07 Chemical Mechanism and Updated Ozone Reactivity Scales*, College of Engineering, University of California, Riverside, California.

Chou, C.C., C.Y. Tsai, C.J. Shiu, S.C. Liu, and T. Zhu, 2009. Measurement of $NO_y$ during campaign of air quality research in Beijing 2006 (CAREBeijing-2006): Implications for the ozone production efficiency of $NO_x$, *J. Geophys. Res., 114*, D00G01, doi: 10.1029/2008JD010446.

Doskey, P.V., J.A. Porter, and P.A. Scheff, 1992. Source fingerprints for volatile non-methane hydrocarbons, *J. Air Waste Manage. Assoc., 42*, 1437-1445.

EPA, 2003. *Interim Guidance on Control of Volatile Organic Compounds in Ozone State Implementation Plans, OAR-2003-0032*, Environmental Protection Agency, Research Triangle Park, North Carolina.

Hall, C., R. Anderson, M. Mansfield, S. Lyman, and H. Shorthill, 2013. *A Survey of Basins and Valleys in the Western U.S.A. for the Capacity to Produce Winter Ozone*, Office of Commercialization and Regional Development, Utah State University, Logan, Utah. Available at http://rd.usu.edu/files/uploads/2013_final_report_basins.pdf.

Jacob, D.J., L.W. Horowitz, J.W. Munger, B.G. Heikes, R.R. Dickerson, R.S. Artz, W.C. Keene, 1995. Seasonal transition from $NO_x$- to hydrocarbon-limited conditions for ozone production over the eastern United States in September, *J. Geophys. Res., 100*, 9315-9324.

Kleinman, L.I., 1994. Low and high-$NO_x$ tropospheric photochemistry, *J. Geophys. Res., 99*, 16831-16838.

Lin, X, M. Trainer, and S.C. Liu, 1988. On the nonlinearity of tropospheric ozone, *J. Geophys. Res., 93*, 15879-15888.

Lyman, S. and H. Shorthill (Eds.), 2013. *Final Report: 2012 Uintah Basin Winter Ozone and Air Quality Study*, *CRD13-320.32*, Office of Commercialization and Regional Development, Utah State University, Logan, Utah.

Lyman, S.N, and M.S. Gustin, 2009. Determinants of atmospheric mercury concentrations in Reno, Nevada, U.S.A., *Sci. Tot. Environ., 408*, 431-438.

Martin, R.S., K. Moore, M. Mansfield, S. Hill, K. Harper, and H. Shorthill, 2011. *Final Report: Uinta Basin Winter Ozone and Air Quality Study, EDL/11-039*, Energy Dynamics Laboratory, Utah State University Research Foundation, Logan, Utah.

MSI, 2013. *Final Report: 2013 Upper Green Winter Ozone Study,* Meteorological Solutions, Inc. and T&B Systems, August. (Available at http://deq.state.wy.us/aqd/Upper%20Green%20Winter%20Ozone%20Study.asp).

Rairigh, K., 2010. *Draft Upper Green River Winter Ozone Study: CALMET Database Development – Phase II,* Wyoming Department of Environmental Quality, Cheyenne, Wyoming.

Sillman, S., 1999. The relation between ozone, $NO_x$, and hydrocarbons in urban and polluted rural environments, *Atmos. Environ., 33*, 1821-1845.

Stein, A.F., E. Mantilla, M.M. Millan, 2005. Using measured and modeled indicators to assess ozone-$NO_x$-VOC sensitivity in a western Mediterranean coastal environment, *Atmos. Environ., 39*, 7167-7180.

Trainer, M., B.A. Ridley, M.P. Buhr, G. Kok, J. Walega, G. Hubler, and D.D. Parrish, 1995. Regional ozone and urban plumes in the southeastern United States: Birmingham, a case study, *J. Geophys. Res., 100*, 18823-18834.

Tyndall, D., and J. Horel, 2013. Impacts of mesonet observations on meteorological surface analyses, *Wea. Forecasting, 28,* 254-269.

Webb, D., 2011. 'Big-city' ozone goes rural, *The Daily Sentinel: Grand Junction, Colorado*, March 24.

# 4.0 ANALYSIS OF AIRCRAFT OBSERVATIONS

***Anna Karion, Sam Oltmans, Gabrielle Pétron, Colm Sweeney, and Russ Schnell***

***NOAA/GMD and CU/CIRES***

## 4.1 Introduction and Methodology

During the UBOS 2013 campaign, a single-engine Cessna 210 aircraft (owned and operated by Kalscott Engineering, www.kalscott.com) was deployed in the Uinta Basin by NOAA Global Monitoring Division's (GMD) aircraft program. Instruments drew air through dedicated inlets installed under the aircraft's starboard wing (Figure 4-1). On-board instrumentation included high-frequency analyzers for carbon monoxide (CO), carbon dioxide ($CO_2$), methane ($CH_4$), and water vapor ($H_2O$) (Picarro G2401m), nitrous oxide ($NO_2$) (Los Gatos Research), and ozone ($O_3$) (2B Systems). NOAA's custom flask packages were used to collect discrete air samples over the Uinta Basin and sent back to NOAA for analysis of 50+ trace gases, including CO, $CO_2$, $CH_4$, and light hydrocarbons such as $C_3H_8$ (propane), n-$C_4H_{10}$ (butane), i- and n-$C_5H_{12}$ (pentane), $C_2H_2$ (acetylene), $C_6H_6$ (benzene). The same air samples were then analyzed for additional hydrocarbons, including heavier compounds, at the Institute of Arctic and Alpine Research (INSTAAR) at the University of Colorado. GPS location and time information, temperature, relative humidity, and ambient pressure measurements were also collected onboard and synchronized with the ambient mole fraction measurements. Measurements of trace gases both from the in-situ continuous analyzers (except for $O_3$ and $NO_2$) and the flask packages are all reported on the NOAA/WMO calibration scales as dry air mole fractions (moles per mole of dry air), using methods outlined in Karion et al. (2013) and online at http://www.esrl.noaa.gov/gmd/ccgg/aircraft/packages.html. The 2B UV photometric $O_3$ analyzer was calibrated against a NOAA/GMD maintained standard that is regularly compared with a U.S. NIST standard and compared with the NOAA/GMD standard before and after the campaign. Measurements of $NO_2$ have an internal instrument "zero cycle" calibration but are not otherwise calibrated.


(a) (b)

**Figure 4-1. Photographs of the Cessna 210 aircraft that sampled over the Uinta Basin in February 2013. (a) Three inlets and two temperature and humidity probes were installed under the starboard wing. (b) View of the snow covered Uinta Basin from the aircraft.**

Seven flights were conducted over an 8-day period from January 31 to February 7, 2013. During this time snow-covered ground, low surface temperatures, low wind speeds and minimal cloud cover all provided excellent conditions for a temperature inversion that trapped surface emissions within the topographic boundaries of the Uinta Basin. Pollutants emitted at the surface within the basin were essentially trapped in a shallow boundary layer up to approximately 1650±50 meters above sea level (masl) (100-200 meters above ground level (magl), depending on the elevation). Research flights surveyed the region, generally flying either at low altitude within the mixed surface layer and the inversion layer or dipping in and out of the inversion layer. Flights were conducted during a multi-day episode of ozone pollution at the surface to characterize some of its spatial and temporal features.

During the 8-day period over which the aircraft flights were conducted, surface ozone built up from approximately background levels of 60 ppb to over 130 ppb. The distribution of $O_3$ during the flight of February 2, 2013 is shown in Figure 4-2 along with a depiction of the terrain in the basin. The first flight on January 31 occurred after the basin had been flushed out by the passage of a frontal system three days earlier. The final flight on February 7 took place just prior to the passage of another weather disturbance that again led to the flushing of ozone and related gases measured by the aircraft, bringing concentrations back to near background levels. The buildup and dispersal of ozone and related constituents across the basin are captured in the seven flights over the 8-day period.

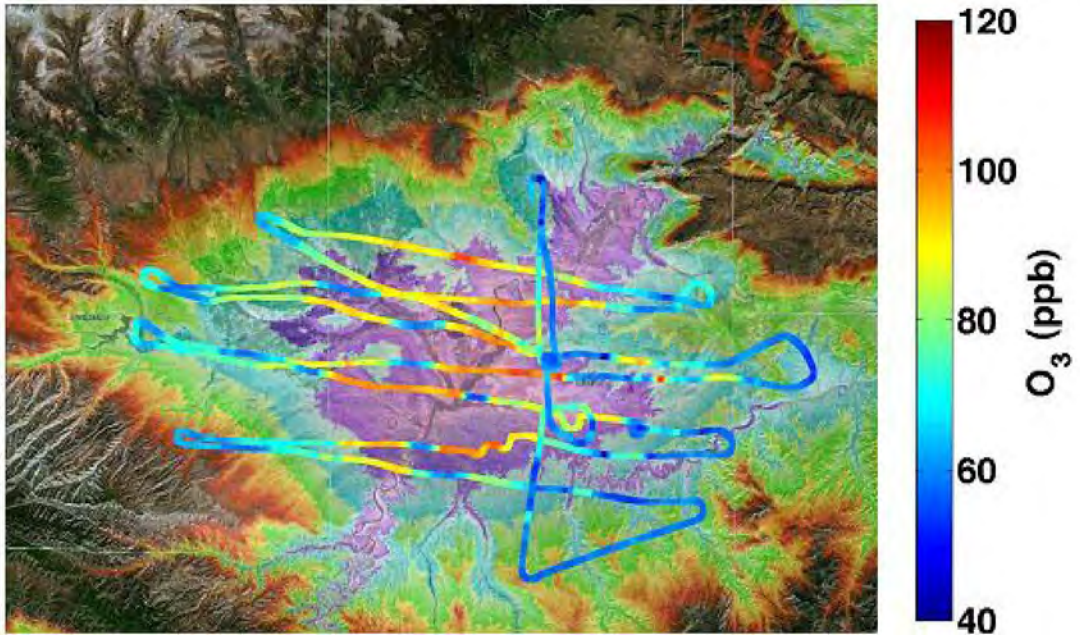


**Figure 4-2. Flight tracks over the Uinta Basin on February 2, 2013 colored by $O_3$ mole fraction in parts per billion (ppb). Data from all altitudes is shown overlain on topography of the Uinta Basin. The 1600 m elevation is at the boundary between the purple and turquoise color band.**

Section 4.2 details the spatial distribution of $CH_4$, CO, $CO_2$, and $NO_2$ through the basin and their interrelationships, Section 4.3 presents the characteristics of ozone measured through the basin and relationships with the other measured constituents and Section 4.4 presents the vertical distribution of ozone and the other constituents. Data from the airborne flask sampling, including measurements of volatile organic compounds (VOCs), are presented in Section 4.5.

## 4.2 Spatial Distribution of $CH_4$, CO, $CO_2$, and $NO_2$

The spatial distributions of $CH_4$, CO, $CO_2$, and $NO_2$ within the shallow boundary layer were investigated during the campaign. Figure 4-3 shows the distribution of $CH_4$ (a,c) and CO (b,d) measured over the Uinta Basin on February 2, 2013. Panels (c) and (d) only show data collected below 1650 masl (i.e. within the shallow mixed boundary layer) on that day. The measurements in the mixed surface layer indicate that $CH_4$ and CO are not as evenly distributed in the basin as $O_3$ (see Section 4.3). We infer that low and variable winds during the inversion conditions inhibited vigorous horizontal mixing, so that the emissions of these species did not advect far from their original source. Horizontal wind measurements by high-resolution Doppler lidar (HRDL) at Horsepool support this conclusion: during the period from February 1 to February 7 surface winds were low (averaging between 1-1.5 m/s in the boundary layer) and changing direction, so that horizontal transport of emissions within the basin was minimal.

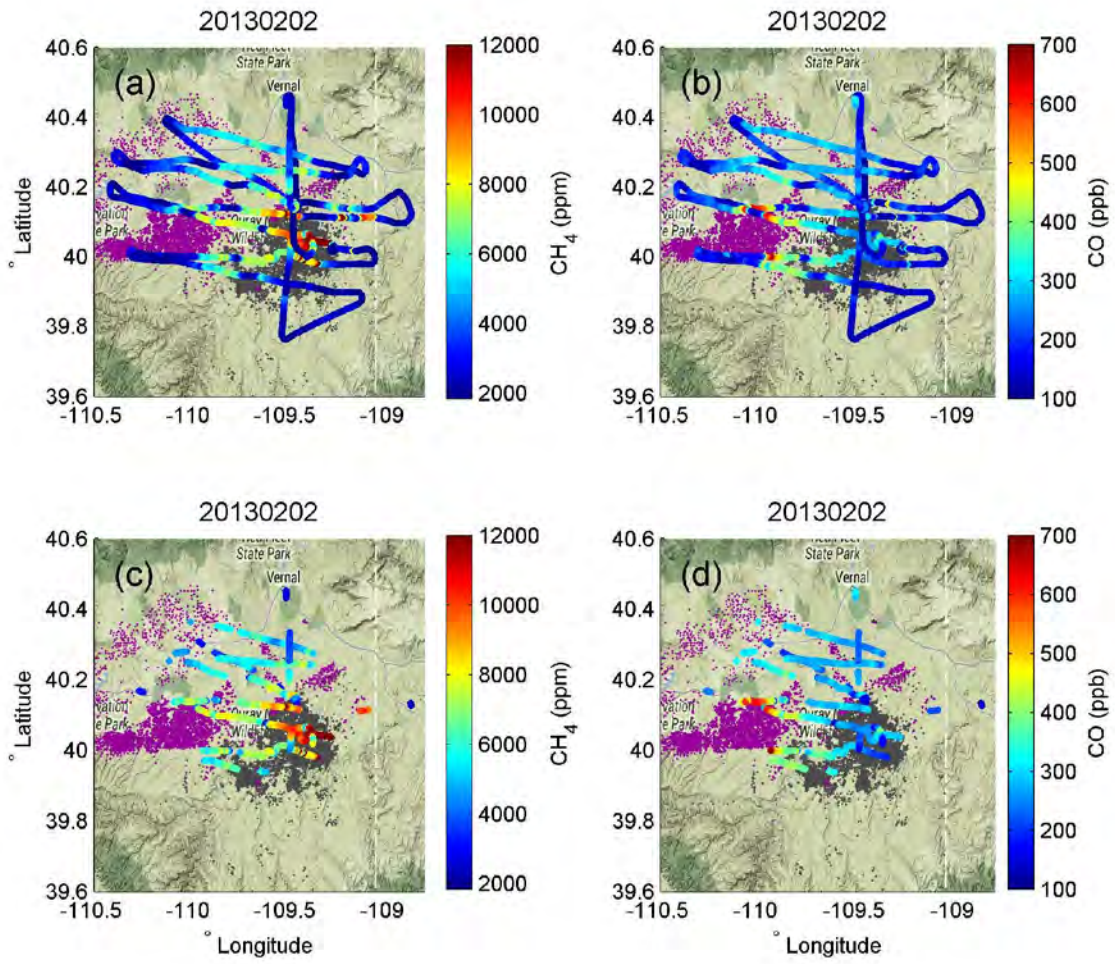


**Figure 4-3. Map of the flight track on February 2, 2013 over the Uinta Basin colored by (a,c) $CH_4$ and (b,d) CO. Figures (a) and (b) show the full track, while (c) and (d) show the flight track portions below 1650 masl only. Locations of oil and gas wells are shown as purple and gray dots, respectively.**

To analyze the extent of trace gas enhancements and their differences across the various regions of the basin, the flight tracks were separated into four quadrants: South-East (SE), South-West (SW), North-West (NW) and North-East (NE). Trace gas observations from each quadrant were colored differently and correlations between the different species for altitudes below 1650 masl were investigated (Figure 4-4).

An analysis of the measurements collected on February 2, 2013 shows elevated CO in the SW quadrant relative to all the other species and relative to the other quadrants. In the SE, $CH_4$ is enhanced more per unit CO than in the SW, while in the SW, more CO is generated per unit $CH_4$ (Figure 4-4c). In the SW, more CO is generated per unit $CO_2$ as well, indicating a potential source with inefficient combustion emissions in that area. The enhancement ratio of CO to $CO_2$ in the SW (green in Figure 4-4(b)) is significantly greater than those reported in the literature

for either direct tailpipe vehicular emissions (9-18 ppb CO per ppm $CO_2$ ([Bishop and Stedman, 2008]) or urban areas (10-14 ppb CO/ppm $CO_2$, [Miller et al., 2012; Peischl et al., 2013; Turnbull et al., 2011; Wunch et al., 2009], black lines in Figure 4-4(b)). The measurements shown in Figure 4-4 do not include data points taken within the power plant plume; that plume was present above the 1650 masl layer as will be discussed in Section 4.4.3. However, we note here for later reference that the power plant plume shows correlations of 6-10 ppb CO per ppm $CO_2$ (not shown), consistent with the solid and dashed black lines in Figure 4-4(b). The relatively larger enhancements of CO in the SW quadrant and enhancements of $CH_4$ in the SE are present in all flights; Figure 4-5 shows the CO to $CH_4$ and CO to $CO_2$ correlations for all seven flights in 2013.

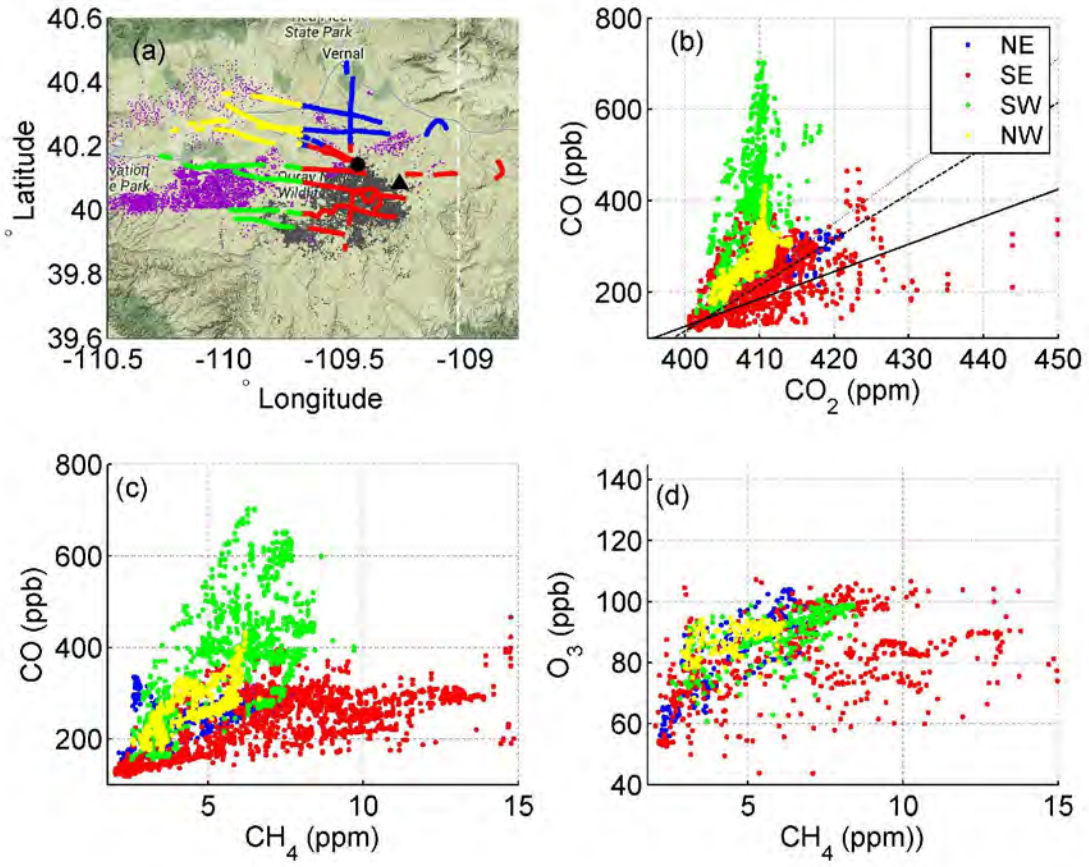


**Figure 4-4. Spatial analysis of trace gas dry air mole fraction correlations during the February 2, 2013 flight. (a) Map of the flight track below the inversion (1650 masl) colored by quadrant (red: SE, blue: NE, yellow: NW, green: SW). The location of Horsepool is noted with a black circle; the Bonanza power plant is a black triangle; gas wells are in gray; oil wells are in purple. (b) Correlation plot of CO with $CO_2$ in the four quadrants. Black dotted line shows a molar ratio of 12 ppb CO per ppm of $CO_2$, dashed line is 10 ppb per ppm, and solid line is 6 ppb/ppm. (c) Correlation plot of CO with $CH_4$, indicating more CO emission per unit $CH_4$ in the SW quadrant, and more $CH_4$ per unit CO in the SE. (d) Correlations of $CH_4$ with $O_3$ show less spatial separation, supporting the observation that $O_3$ is observed more uniformly through the region.**

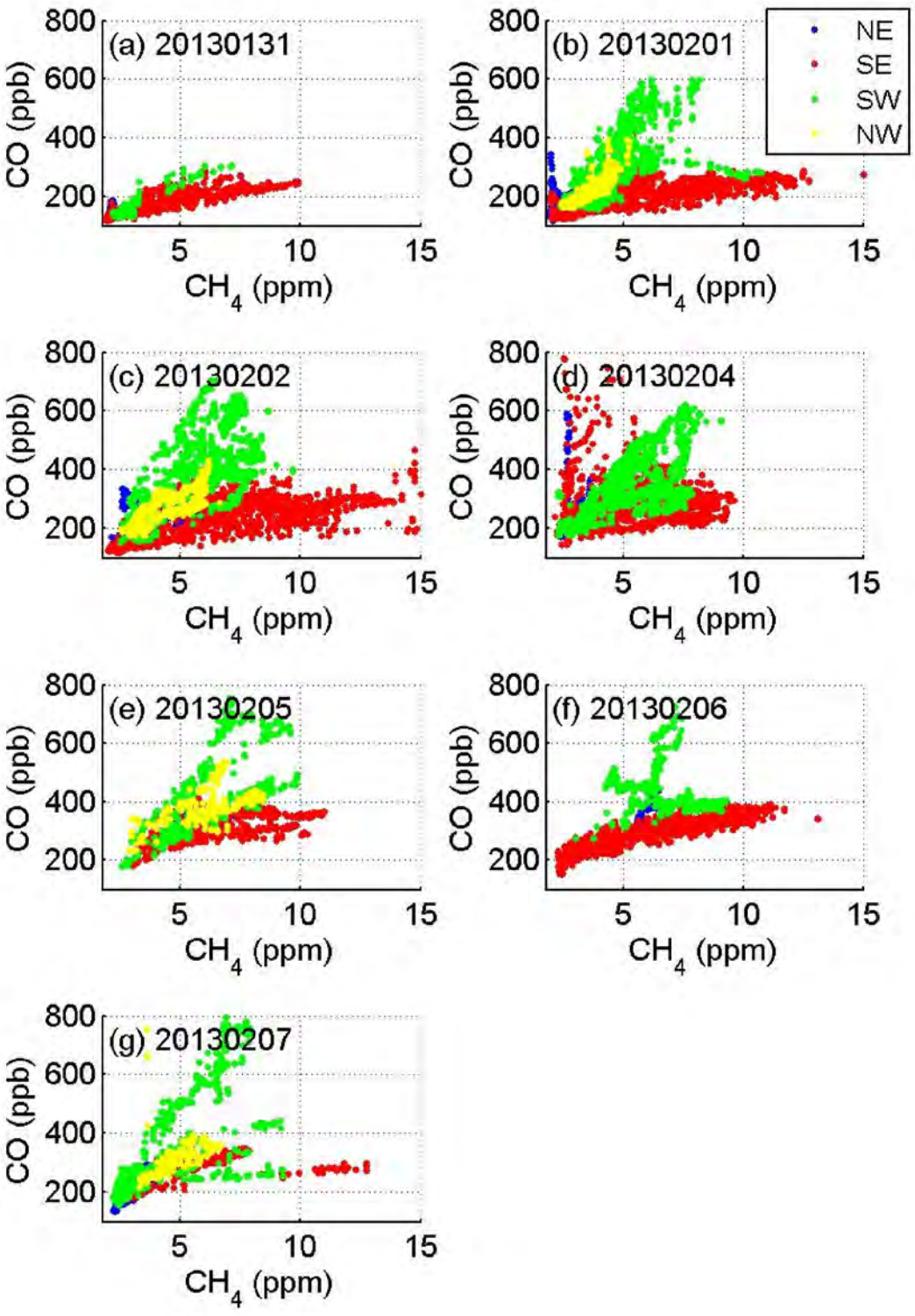


**Figure 4-5. Correlations of CO with $CH_4$ over the different quadrants of the basin for the seven flights, with the flight date indicated in each panel (YYYYMMDD).**

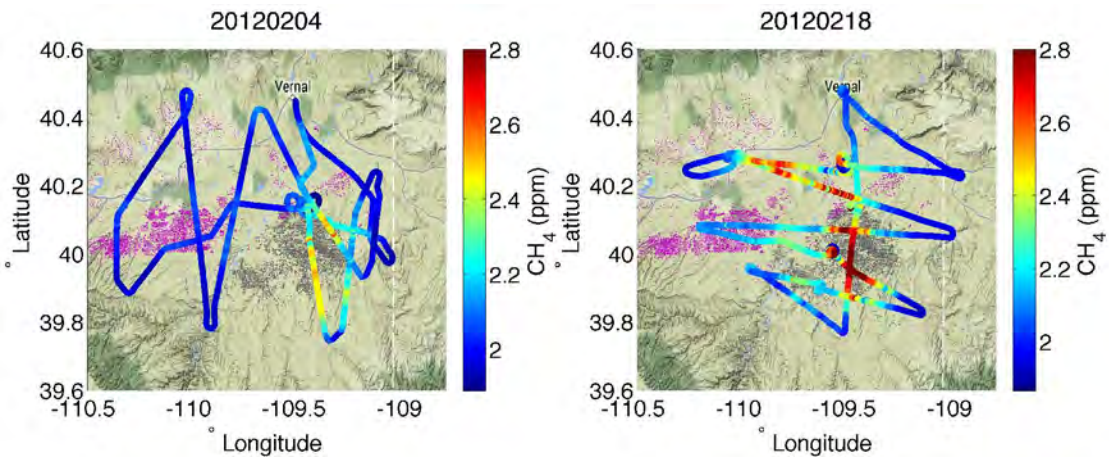


**Figure 4-6. Flight tracks from (a) February 4 and (b) February 18, 2012 showing elevated $CH_4$ over the gas wells (gray dots) during low-wind conditions, in the same region that $CH_4$ was enhanced in the 2013 flights, with lower enhancements in the western portion of the basin over the oil wells (purple dots).**

Based on ground measurements from the NOAA mobile laboratory in 2012 that showed high CO to $CO_2$ and CO to $CH_4$ emissions ratios from pump-jack engines in the oil field, we suspect that emissions from inefficient combustion of the pump-jack engines in the SW portion of the basin may be the cause of the large CO mole fractions observed there. An oil rig fire in the NW quadrant of the region (40.36 N, -110.01 W) that started on January 22, 2013 was likely still an emissions source until it was out fully on February 6, and may have also influenced the aircraft measurements. However, the NW quadrant does not show CO as elevated as the CO measured in the SW, so we do not believe that the fire was the primary source of the CO enhancements observed farther south.

On most days, $CH_4$ mole fractions are lower in the NW and SW quadrants than in the SE, showing that the gas field in the southern part of Uintah County has higher $CH_4$ mole fractions than the oil field. This was also observed in flights conducted the previous year, in February 2012 (Figure 4-6), indicating that a significant portion of $CH_4$ emissions in this quadrant is likely persistent. Possible $CH_4$ emission sources in the SE quadrant include a dense array of compressor stations and two processing plants (the Chipeta Plant Complex and Stagecoach/QEP); there is also a large density of natural gas-production wells in the area as well, so the exact mix of sources and their relative contribution are still unknown.

Although $NO_x$ are mainly emitted from combustion sources (just as CO is), the most elevated $NO_2$ is not observed in the same region as the elevated CO (Figure 4-7 shows correlations of $NO_2$ to CO for the different quadrants). In the flight data, $NO_2$ mole fractions are highest in the same SE region as the elevated $CH_4$, although it is not well correlated with $CH_4$ (Figure 4-8). Based on the flight data, it appears that the formation of $NO_2$ is occurring preferentially near the processing plants and compressor stations in the SE quadrant. Additional analysis of the chemistry and horizontal transport is needed to confirm this conclusion.

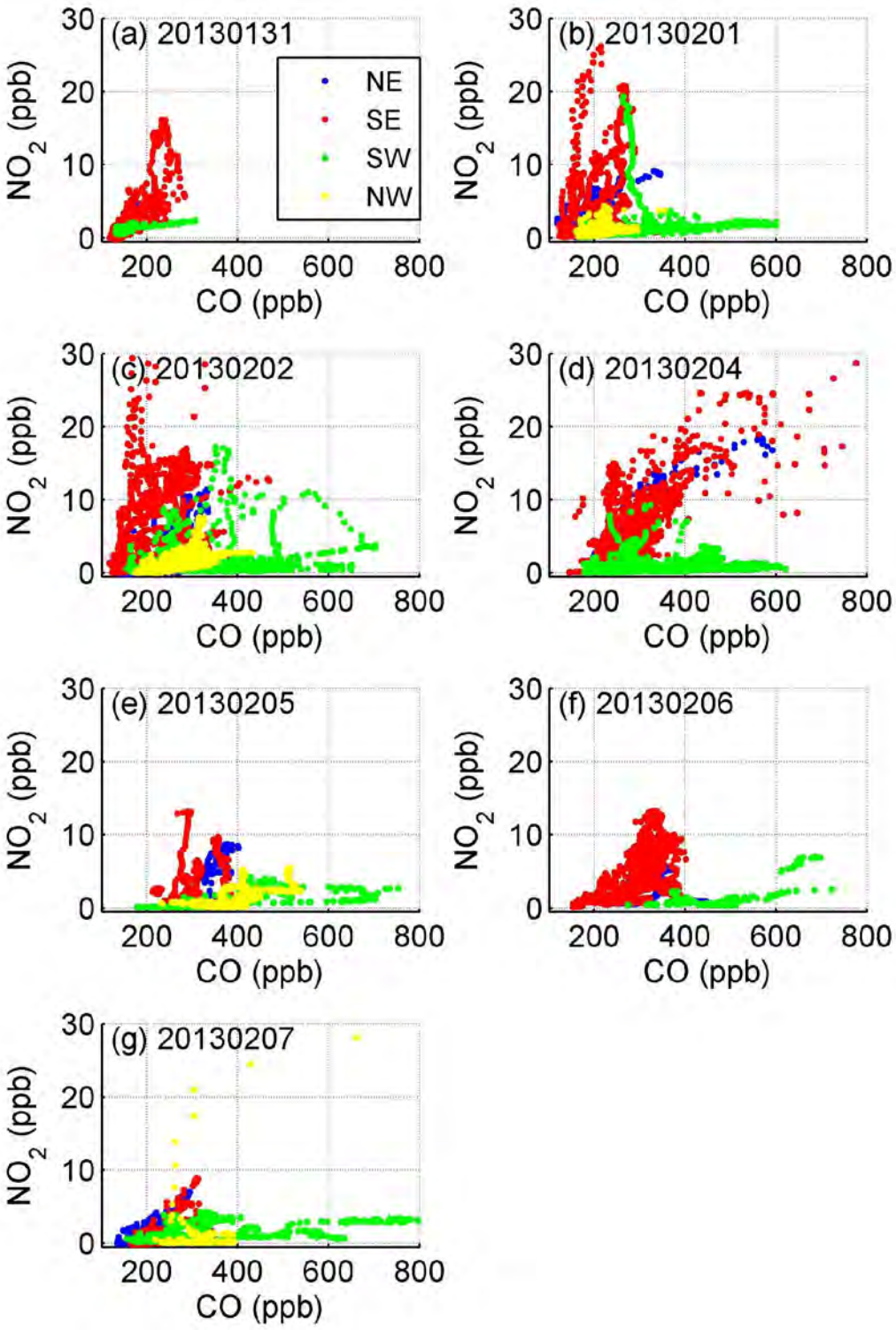


**Figure 4-7. Relationship between $NO_2$ and CO measurements from the aircraft for different quadrants in the basin (date of flight indicated in each panel, YYYYMMDD). $NO_2$ is more enhanced in the SE, while CO is enhanced in the SW.**

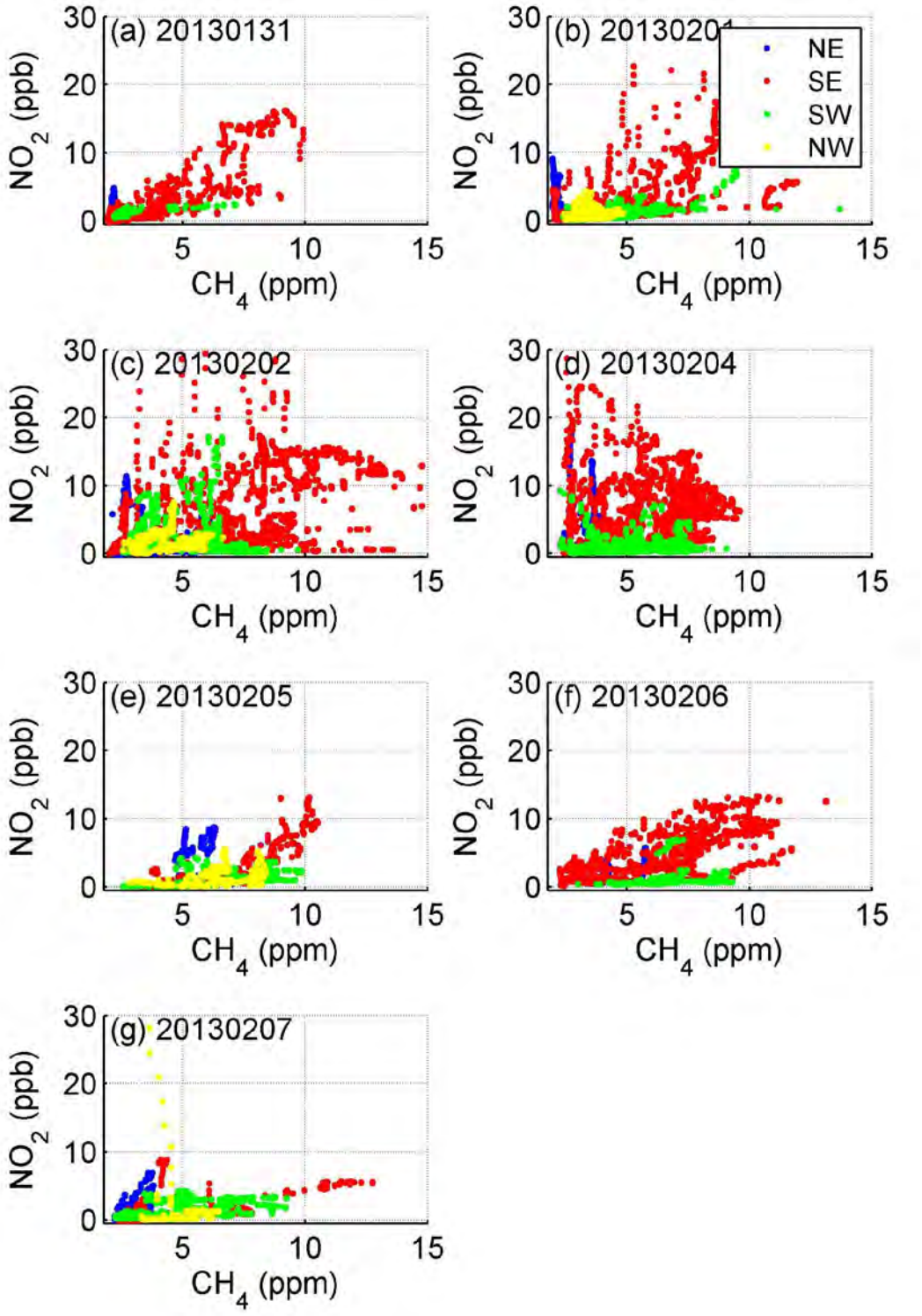


**Figure 4-8. Relationship between $NO_2$ and $CH_4$ measurements from the aircraft for different quadrants in the basin (date of flight indicated in each panel, YYYYMMDD). $NO_2$ and $CH_4$ are both enhanced in the SE quadrant (red points), but not always well-correlated.**

## 4.3 Spatial Distribution of Ozone and Relationship to Other Constituents

As a secondary pollutant the distribution of ozone both spatially (horizontal and vertical) and temporally reflects photochemical production and loss involving precursor emissions, dispersal of these emissions within the basin and redistribution of ozone due to air motions within the basin. Both the VOC and NOx sources are not uniformly distributed over the Basin but are generally strongest in the SE sector (in Uintah County) where the major gas field is located. This is seen in the elevated levels of methane (Figures 4-3(c) and 4-5) and the accompanying non-methane hydrocarbons that strongly correlate with methane (Figures 4-22 and 4-23 in Section 4.5). Although the $NO_2$ measurements on the aircraft are not a direct measurement of the emitted NO, the high $NO_2$ amounts over the SE sector (Figures 4-7 and 4-8) indicate that there is a significant local NO source through the strong interrelationship between NO and $NO_2$ ($NO + O_3 \rightarrow NO_2 + O_2$ and $NO_2 + h\nu \rightarrow NO + O$).

### 4.3.1 Distribution of Ozone over the Uinta Basin

The distribution of ozone across the basin for flights between January 31 and February 6 below 1650 masl is shown in Figure 4-9 (flights on February 7 did not cover a significant portion of the basin). Several key features should be noted. There is a continuing buildup in the highest ozone concentrations through the progression of the flights. On January 31, $O_3$ mixing ratios over most of the basin are less than about 70 ppb with values near 80 ppb in the SE sector. By February 1 ozone is already >80 ppb over much of the basin and the high values are not confined to the SE. This pattern continues as ozone builds throughout the course of the week, reaching values in excess of 130 ppb. The flights on February 1 and 2 have the most extensive coverage of the basin below 1650 masl and very clearly show that high ozone is ubiquitous throughout the basin. The aircraft flight times in the afternoons are representative of the ozone resulting from the daytime photochemical production.

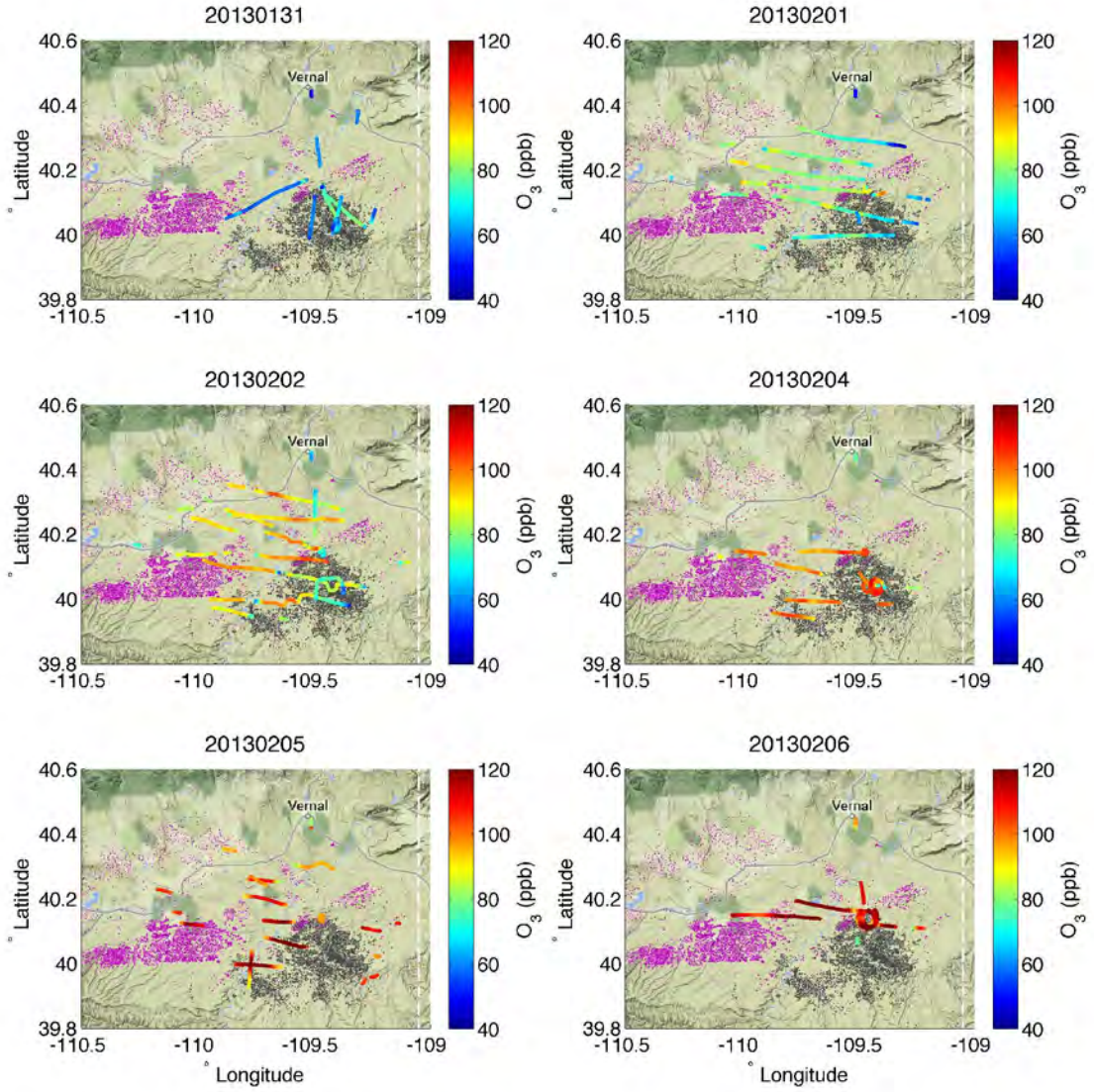


**Figure 4-9. Map of flight tracks below 1650 masl on January 31, February 1, 2, 4, 5 and 6, 2013 over the Uinta Basin colored by $O_3$ mixing ratio in ppb. The flight date (YYYMMDD) is indicated in the title of each panel. Oil wells are indicated by purple points, gas wells by dark gray points.**

### 4.3.2 Relationship of Ozone to Other Constituents Measured on the Aircraft

Though $CH_4$ values (and accompanying non-methane hydrocarbons including ozone precursor VOCs) are highest near the gas fields in the SE sector (Figure 4-3(c)), high $CH_4$ values and high coinciding NMHC mole fractions in discrete air samples are seen across the basin indicating a high potential for ozone production.

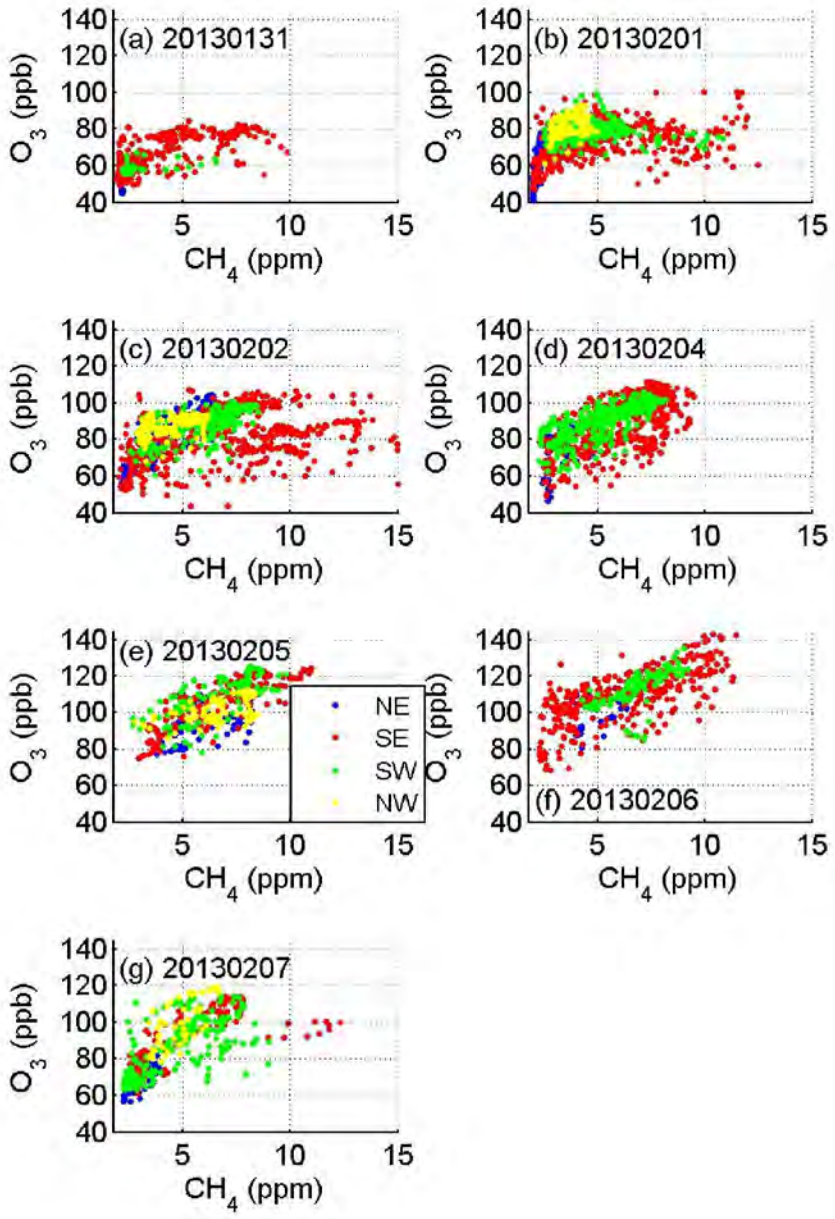


**Figure 4-10. Relationship between $O_3$ and $CH_4$ measurements from the aircraft for different quadrants in the basin (date of flight indicated in each panel, YYYYMMDD). $CH_4$ is highest in the SE quadrant (red points), but is not well-correlated with $O_3$ for $CH_4$ above ~8 ppm.**

In general ozone amounts increase with increasing methane although for the very highest methane values (>8 ppm), seen primarily in the SE sector where the primary gas field is located, this is not the case, especially when peak ozone values are <100 ppb (Figure 4-10). The relationship between ozone and methane appears similar throughout the basin with the exception of the very high methane in the SE.

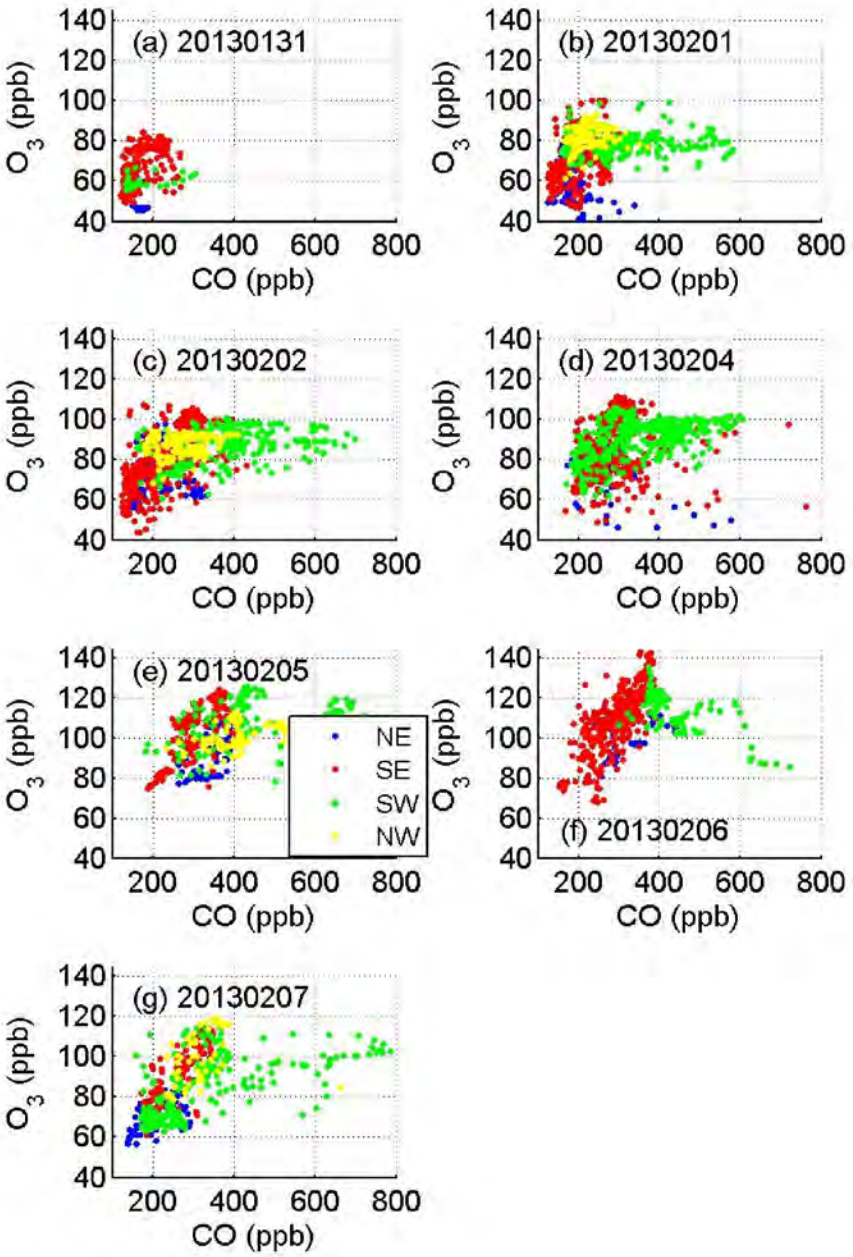


**Figure 4-11. Relationship between $O_3$ and CO measurements from the aircraft for different quadrants in the basin (date of flight indicated in each panel, YYYYMMDD). CO is highest in the SW quadrant (green points), but is not well-correlated with $O_3$ for CO above 400 ppb.**

In the $NO_x$-VOC dominated ozone production chemistry in the Uinta Basin, CO has a lesser role as an ozone precursor but may be indicative of a combustion source that also emits NO. Figure 4-11 shows a general increase in ozone with increasing CO. The most anomalous feature is the very large CO values in the SW sector that do not correlate with ozone. These much higher CO values in the SW are apparent in the relationship with all the trace gases measured on the aircraft including $CH_4$, $CO_2$, and $NO_2$ (see Figures 4-6).

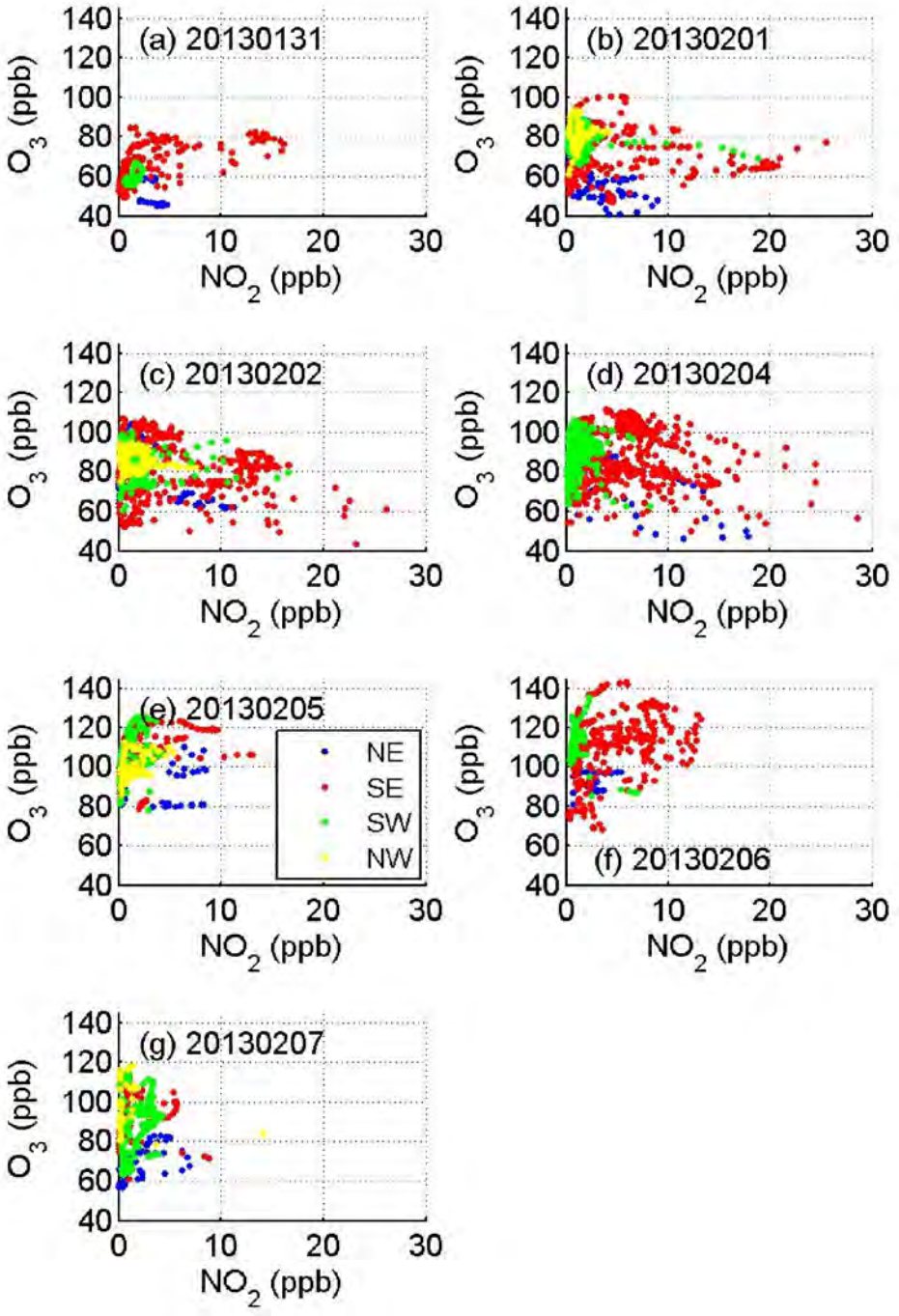


**Figure 4-12. Relationship between $O_3$ and $NO_2$ measurements from the aircraft for different quadrants in the basin (date of flight indicated in each panel, YYYYMMDD). $NO_2$ is consistently highest in the SE quadrant (red points), but is not well-correlated with ozone.**

As noted earlier, $NO_2$ is photochemically interrelated with $O_3$ and NO but is not expected to maintain a conservative relationship with $O_3$. As can be see seen in Figure 4-12, $O_3$ and $NO_2$ are not well correlated. While occasional values of $NO_2$ >5 ppb are seen in all of the sectors, this level is regularly seen in the SE sector (red points) suggesting this is an area of NO emissions.

With this sector also a strong source of $CH_4$ (although $CH_4$ is not always well-correlated with $NO_2$ as noted earlier – see Figure 4-8) and with the strong source of accompanying non-methane hydrocarbons, this sector dominated by the gas field operations appears to be the focal point for the precursor emissions responsible for ozone production in the Uinta Basin.

## 4.4 Vertical Distribution of Ozone and Other Constituents

During each of the seven aircraft flights in 2013, the aircraft conducted two or more vertical profiles, in which measurements were collected either in a spiral ascent or descent, or during an ascent/descent that also transited horizontally. Data collected during these profiles are valuable in assessing the extent of vertical mixing within the inversion layer, quantifying the gradient in mole fractions of species above and within the layer, and observing features that exist entirely above the inversion layer. They also illustrate the ozone buildup over several days within the lowest portion of the profiles.

### 4.4.1 Mixing within the Inversion Layer

Aircraft vertical profiles (Figures 4-13 - 4-19) generally show that the various trace gases are strongly enhanced and sometimes well-mixed below the height of the inversion. This altitude varied slightly depending on location within the basin, day, and time of day, but was generally at 1650±50 masl. Figure 4-13 shows a vertical profile conducted on January 31 over the ground site at Horsepool, in the north of the natural gas field (see Figure 4-14(b)). Figure 4-14 shows the timing (a) and location (b) of the profiles on February 1 that have been selected and shown in Figure 4-15. Figures 4-16 - 4-17 and 4-18 - 4-19 are the same as Figures 4-14 - 4-15, but for the flights of February 2 and 5, 2013.

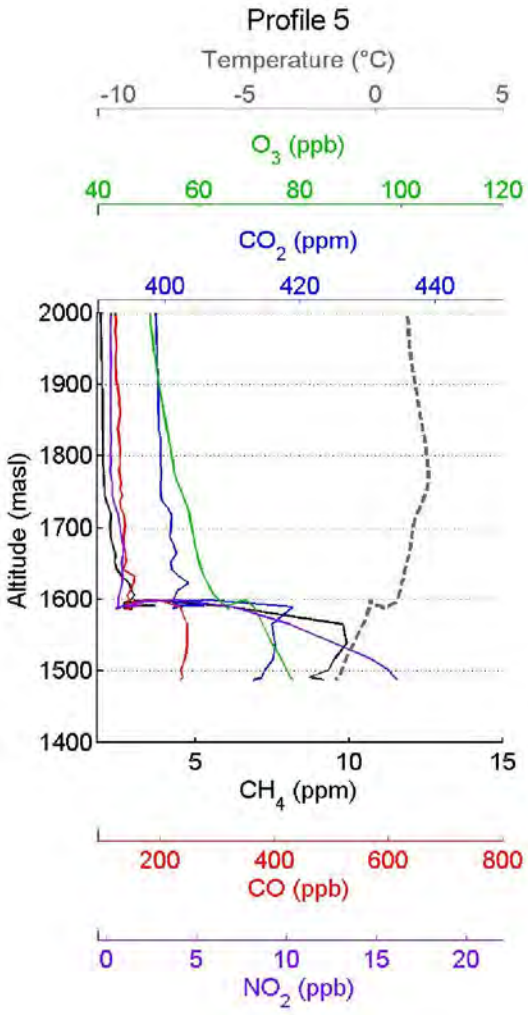


**Figure 4-13. Profiles of constituents measured on the aircraft on January 31 in the vicinity of the natural gas field and gas processing plants. Note the enhancements of all species beneath the temperature inversion observed at 1600 masl.**

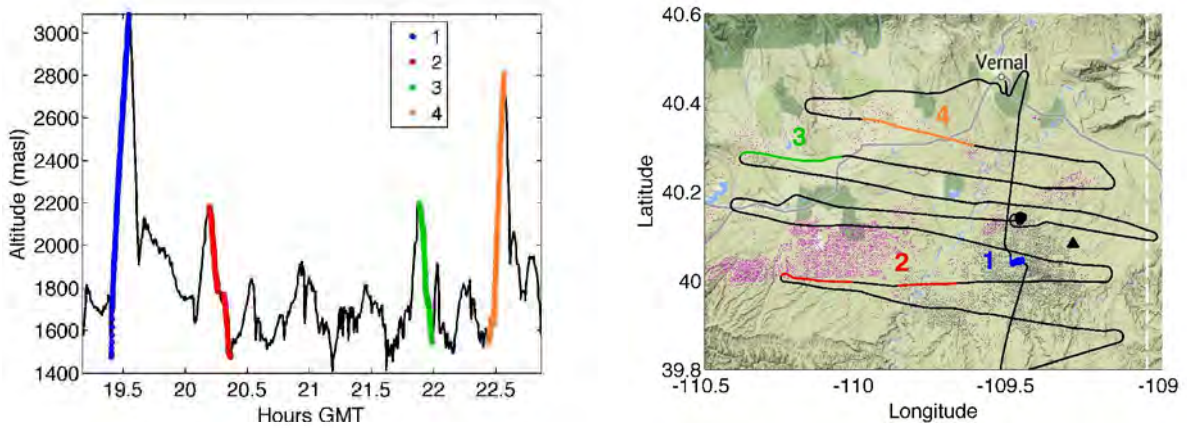


**Figure 4-14. (a) Time series of flight on February 1, 2013, with the profiles highlighted. (b) Corresponding locations of the profiles in the Uinta Basin, shown along with the oil (purple) and gas (gray) well locations. The Bonanza Power Plant is located at the black triangle and Horsepool at the black dot.**

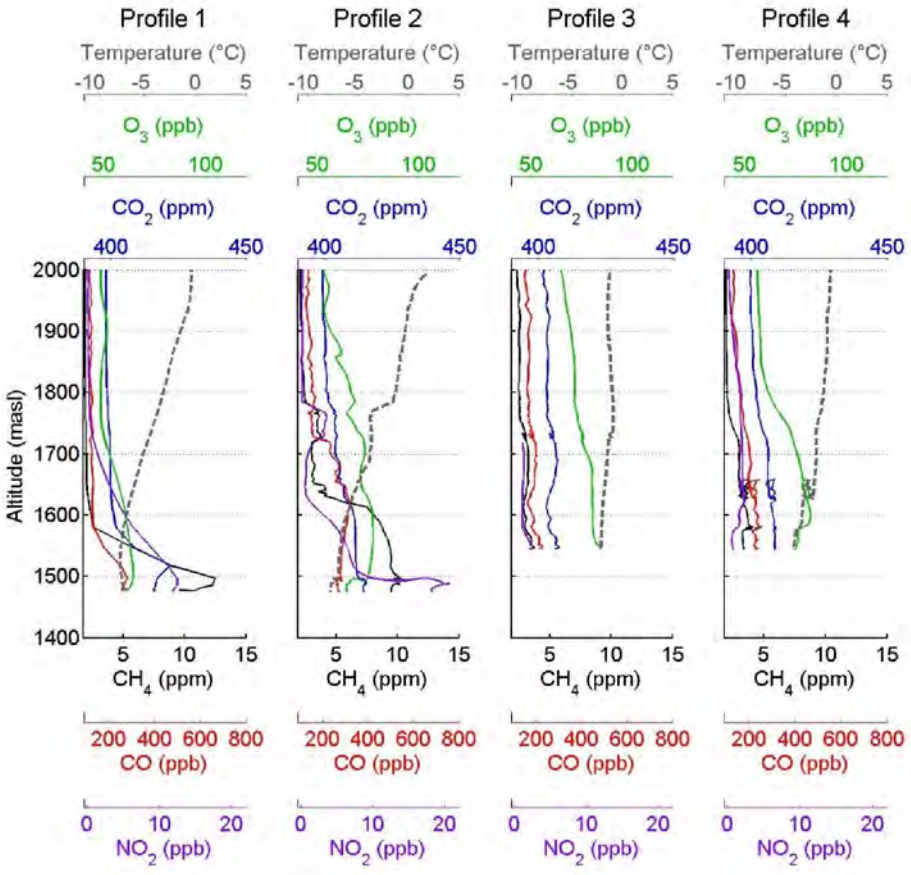


**Figure 4-15. Four vertical profiles of $CH_4$ (black), CO (red), $CO_2$ (blue), $O_3$ (green), $NO_2$ (purple), and temperature (gray dashed) on February 1, 2013. Profile times and locations are indicated in Figure 4-14.**

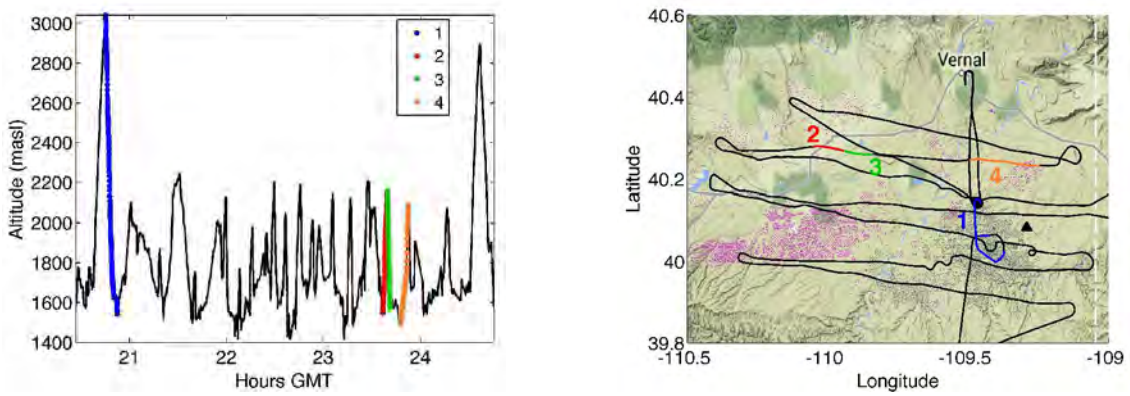


**Figure 4-16. (a) Time series of flight on February 2 2013, with the vertical profiles highlighted. (b) Corresponding locations of the profiles in the Uinta Basin, shown along with the oil (purple) and gas (gray) well locations. The Bonanza Power Plant is located at the black triangle close to the blue numeral 1. Profile 4 is located over the ground site in Horsepool.**

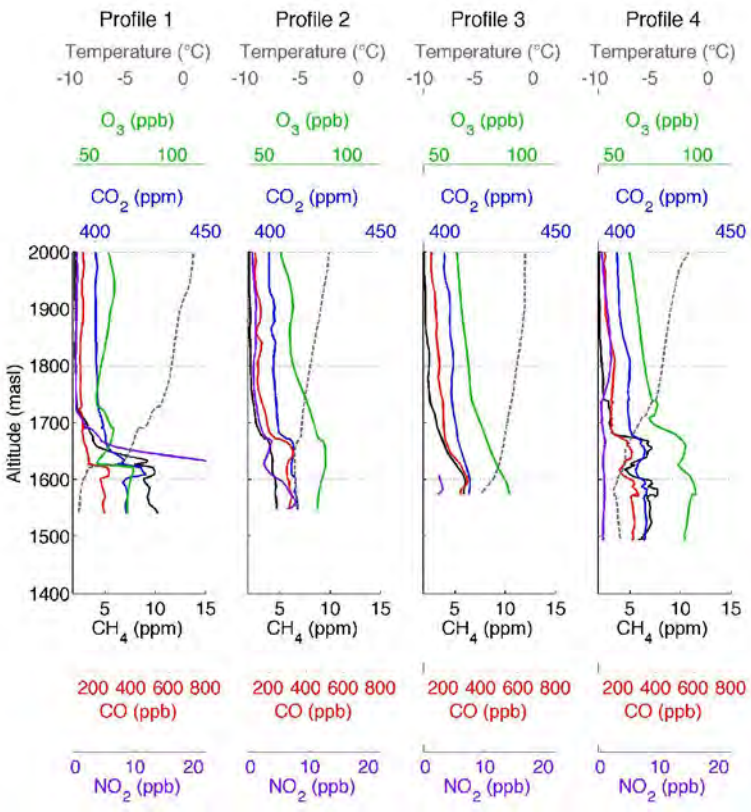


**Figure 4-17. Four vertical profiles of $CH_4$ (black), CO (red), $CO_2$ (blue), $O_3$ (green), $NO_2$ (purple), and temperature (gray dashed) on February 2, 2013. Profile times and locations are indicated in Figure 4-16.**

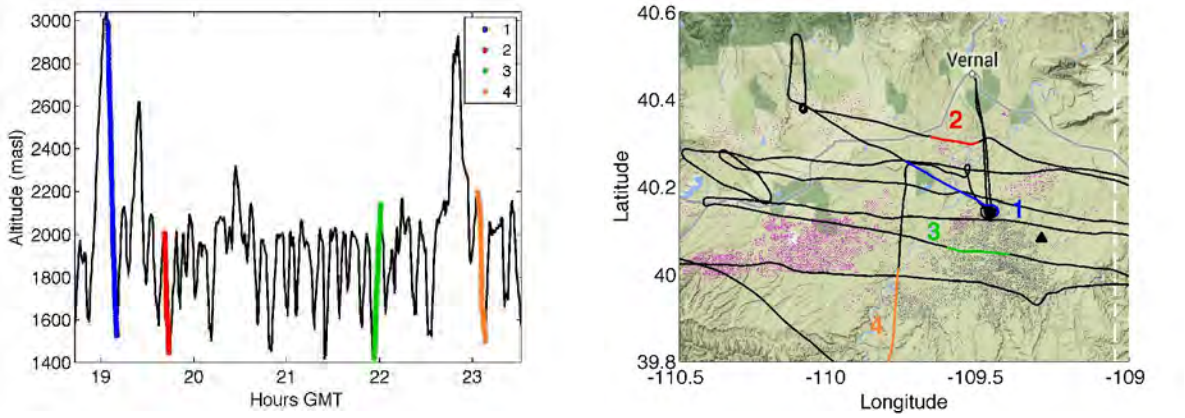


**Figure 4-18. (a) Time series of flight on February 5 2013, with the profiles highlighted. (b) Corresponding locations of the profiles, shown along with the oil (purple) and gas (gray) well locations. The Bonanza Power Plant is located at the black triangle. Profile 1 was conducted near the Horsepool site.**

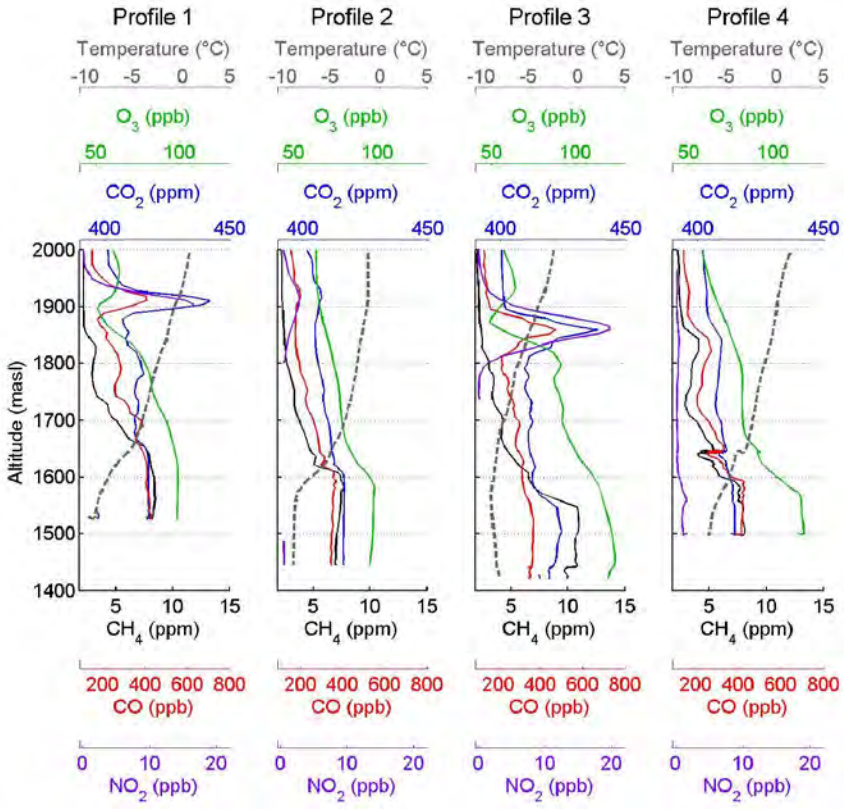


**Figure 4-19. Four vertical profiles of $CH_4$ (black), CO (red), $CO_2$ (blue), $O_3$ (green), $NO_2$ (purple), and temperature (gray dashed) from the flight on February 5, 2013. Profile times and locations are indicated in Figure 4-18.**

Most vertical profiles after January 31 (Figures 4-15, 4-17, and 4-19) illustrate the sharp gradient observed in most of the trace gases, generally at altitudes of 1600-1700 masl; the location of the trace gas mole fraction gradients generally corresponds to the altitude of the strongest gradient in temperature. Below this gradient, $O_3$, $CH_4$ and other constituents are almost always clearly enhanced above their free-tropospheric values.

### 4.4.2 Ozone Vertical Structure

Details on the vertical structure of ozone and particularly the way in which the buildup of ozone takes place with height is best captured with the three tethered ozonesonde sites (Ouray, Fantasy Canyon, and Horsepool) and the ozone lidar at the Horsepool location. These results are discussed in other sections of this report. The vertical profiles obtained on the aircraft flights provide vertical detail on the relationship of ozone with the other measured constituents. The profiles also show how ozone and the other gases are distributed in the vertical across the basin and particularly the differences near the gas field with large precursor sources.

The structure of the profiles has significant variations both in the vertical and spatially in the Basin. Profiles on February 1 (Figures 4- 14 - 4-15), February 2 (Figures 4-16 - 4-17), and February 5 (Figures 14-8 - 4-19) capture many of the important features seen in the aircraft profiles. The limited sampling below 1650 masl on January 31 (see Figure 4-9) shows only a small buildup of ozone and other constituents in the layer below 1650 masl in the SW sector or to the north and south of the gas field (not shown). In the heart of the gas field (Figure 4-13) there was a well-mixed layer below ~1600 masl with enhanced ozone (~80 ppb), and CO (~300 ppb), and very high $CH_4$ (~10 ppm) and $NO_2$ (~15 ppb near the surface). This is an indication that emissions from the gas field were building after the flushing of the basin that took place three days earlier (based on measurements from surface and ozonesonde observations) and significant ozone production was occurring, but was not generally widespread over the basin.

On February 1 flights covered a large portion of the basin and vertical profiles were conducted both in the gas field and well away from the field (Figures 4-14 - 4-15). Profile 1 in Figure 4-15 was carried out in the heart of the gas field (Figure 4-14). The top of the lowest inversion is only at about 1550 masl. Very high levels of $CH_4$ and $NO_2$ are confined beneath this shallow inversion. Ozone is only modestly elevated in mixing ratio (approximately 10-40 ppb above the free tropospheric values). Above the inversion the concentrations of all of the measured gases gradually decline toward background levels by ~1700 masl. In profile 2 (Figure 4-15) just to the SW of the main gas field (Figure 4-14), $CH_4$ and $NO_2$ are very high and ozone is somewhat higher than in profile 1. The enhanced concentrations are mixed up to ~1800 masl consistent with the lack of strong low altitude temperature inversion. Profiles 3 and 4, measured well away from the gas field, have higher $O_3$ and much lower concentrations of the other measured gases. This picture is consistent with significant photochemical $O_3$ production occurring as the $O_3$ precursors are dispersed across the basin.

On February 2 a profile in the gas field (profile 1 – Figures 4-16 - 4-17) shows a strong, shallow inversion with a top at ~1625 masl with strongly enhanced gas concentrations. Just above this

inversion is a very shallow layer with even higher levels of $CH_4$ and extremely high $NO_2$ with a significant dip in $O_3$ indicating titration by NO and conversion to $NO_2$. This is in contrast to profile 2 just to the west of the gas field (Figure 4-17) where a similar inversion structure has enhanced ozone but $NO_2$ levels are lower. Ozone below the inversion is also higher than in the gas field reaching ~100 ppb. Profile 3 to the NW of the gas field has a well-mixed layer below the inversion with $O_3$ of ~100 ppb again indicative of continuing $O_3$ production as precursors move out of the gas field.

Profiles on February 4 (not shown) have generally well-mixed conditions through a somewhat deeper boundary layer that extends up to 1800 masl in several profiles. For all six profiles on this day $O_3$ mixing ratios in the boundary layer are over 100 ppb. On February 5 the profiles all have well defined temperature inversion with a top at or just above 1600 masl (Figure 4-19). The trace constituents are well-mixed in the layer. Ozone is above 100 ppb, but somewhat different from the other days as $O_3$ is highest near the natural gas field exceeding 120 ppb (profiles 3 and 4). All the profiles show a gradual decrease of the trace gas measured concentrations including $O_3$ up to ~1850 masl. This layer above the lower sharp inversion layer is a characteristic in most of the profiles obtained by the aircraft and represents mixing out of the lowest surface layer into a gradient layer above.

### 4.4.3 Evidence of Bonanza Power Plant Plume in Vertical Profiles

Profile 4 on February 2 (Figure 4-17) and Profiles 1 and 3 on February 5 (Figure 4-19), as well as on February 4 (not shown), show clear evidence of a plume from the coal-fired Bonanza Power Plant, with enhancements in $CO_2$, CO, and $NO_2$ but with low $CH_4$ and a corresponding depletion in $O_3$. The power plant plumes were encountered in relatively close proximity to the power plant (~10-16 km). The low $CH_4$ along with lower $O_3$ are a clear indication that this plume did not originate from surface sources within the boundary layer. The depression of the $O_3$ mixing ratio below the tropospheric background measured outside the plume is a clear indication of $O_3$ titration by the power plant emitted NO. A buoyant plume of emissions from the power plant, whose stack height is at 182 m above ground level, or 1715 masl, is lofted above the 1600-1700 masl inversion layer, and remains above the inversion in a layer that varies in height between 1800 and 1950 masl. This is also shown in photographs taken from the aircraft during the campaign, which clearly show the buoyant plume from the plant above the hazy inversion layer below (Figure 4-20). We conclude that it is unlikely that the power plant emissions contributed significantly to the pollution observed at the surface during this strong temperature inversion event.

**Figure 4-20. Photograph taken from the aircraft of the Bonanza Power Plant and its plume rising above the inversion layer on February 2, 2013.**

## 4.5 Flask Samples from Aircraft

Discrete whole air samples were collected in glass flasks aboard the aircraft throughout the seven flights of 2013. Flask samples were also collected in the previous year, in February 2012. Here we present measurements of the whole air collected in flasks in both years, which were analyzed by NOAA's Global Monitoring Division (GMD) in Boulder, CO. In both years, flask samples were also measured at the University of Colorado's Institute of Arctic and Alpine Research (INSTAAR) for additional non-methane hydrocarbons (NMHC), and here we present a subset of that data from 2013. The locations of flask samples over the Uinta Basin in both years are shown in Figure 4-21, along with point sources of possible emissions and oil and gas wells. The 2013 flasks were preferentially sampled near Horsepool, while in 2012 more uniform sampling was achieved.

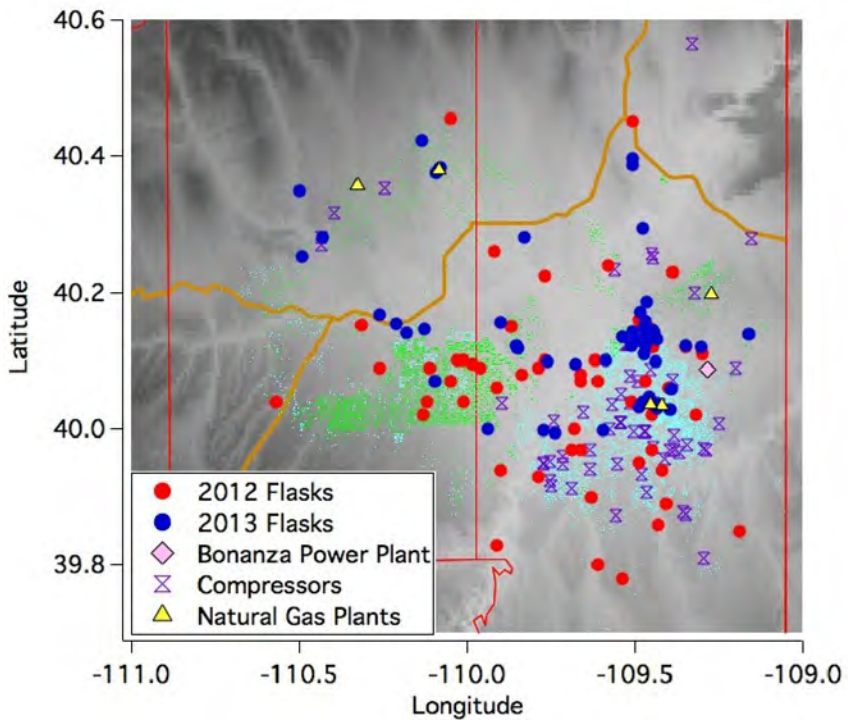


**Figure 4-21. Location of flask samples collected in 2012 (red) and 2013 (blue) over the Uinta Basin. Gas wells are indicated in light blue and oil wells in green.**

### 4.5.1 Comparison of Flask Sample Measurements in 2013 and 2012

Figure 4-22 (panels 1-5) shows the measurements of light hydrocarbons that are components of raw natural gas as they correlate with $CH_4$ in air samples collected in flasks aboard the aircraft in 2012 (gray) and 2013 (blue, red, yellow or green according to the location of the sample collection). Mole fractions of propane ($C_3H_8$), n-butane (n-$C_4H_{10}$), n-pentane (n-$C_5H_{12}$), isopentane (i-$C_5H_{12}$), and benzene ($C_6H_6$) show high correlation with $CH_4$ in both years. Figure 4-22 (bottom right panel) also shows the relationship between CO and $CH_4$ measured in flask samples in each year; these gases are less well correlated, as discussed in the previous section for the continuous data. As seen in the continuous data (Figure 4-5), CO is more enhanced per unit $CH_4$ in the SW quadrant of the basin (green). Figure 4-23 shows 2013 measurements of several additional hydrocarbons in the same flasks (from University of Colorado's INSTAAR), all showing correlation with $CH_4$ and significant enhancements. Some hydrocarbons show higher enhancements per unit $CH_4$ in the NW and SW quadrants (green and yellow), over the oil field, than in the NE and NW (red and blue), over the gas field. All species were present in significantly higher concentrations in 2013 compared with 2012, most likely because of the shallow layer in which emissions were trapped in 2013 and the lack of winds flushing the basin. In 2012, boundary layer heights were between 500 and 1000 m above ground level during the campaign, while in 2013 the emissions were trapped in a boundary layer of only 100-300 meters.

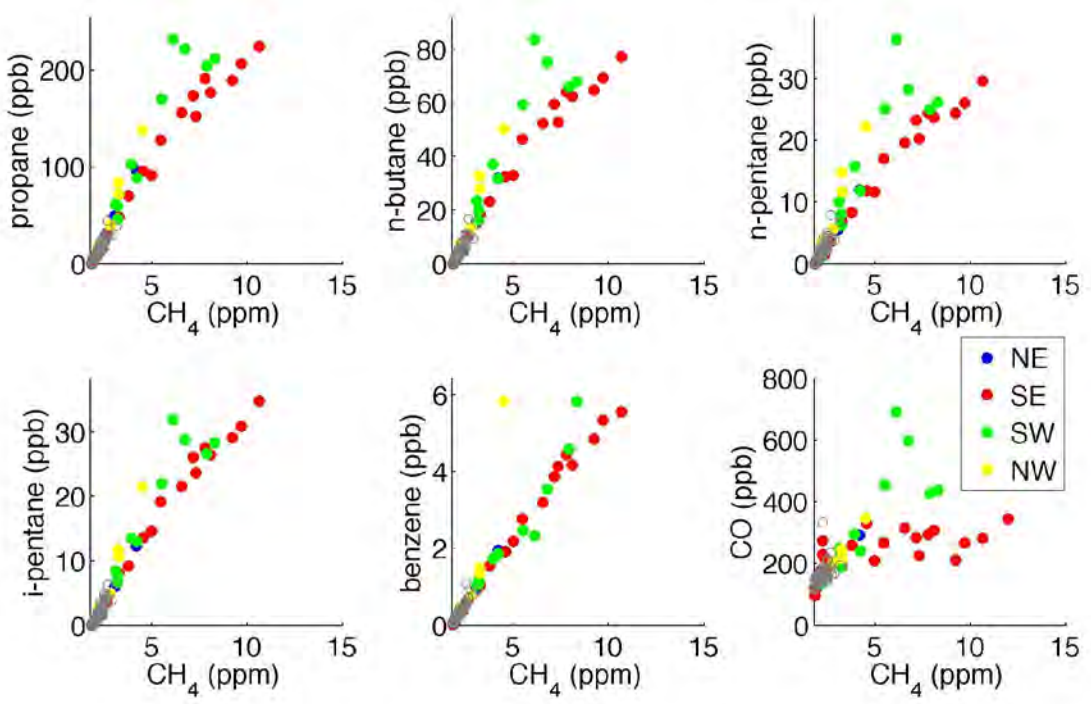


**Figure 4-22. Measurements of light hydrocarbons (first five panels) and CO (bottom right) plotted against $CH_4$ mole fraction from air samples collected in flasks over the Uinta Basin in 2013 (blue, red, green or yellow based on quadrant) and 2012 (gray). All data from NOAA/GMD.**

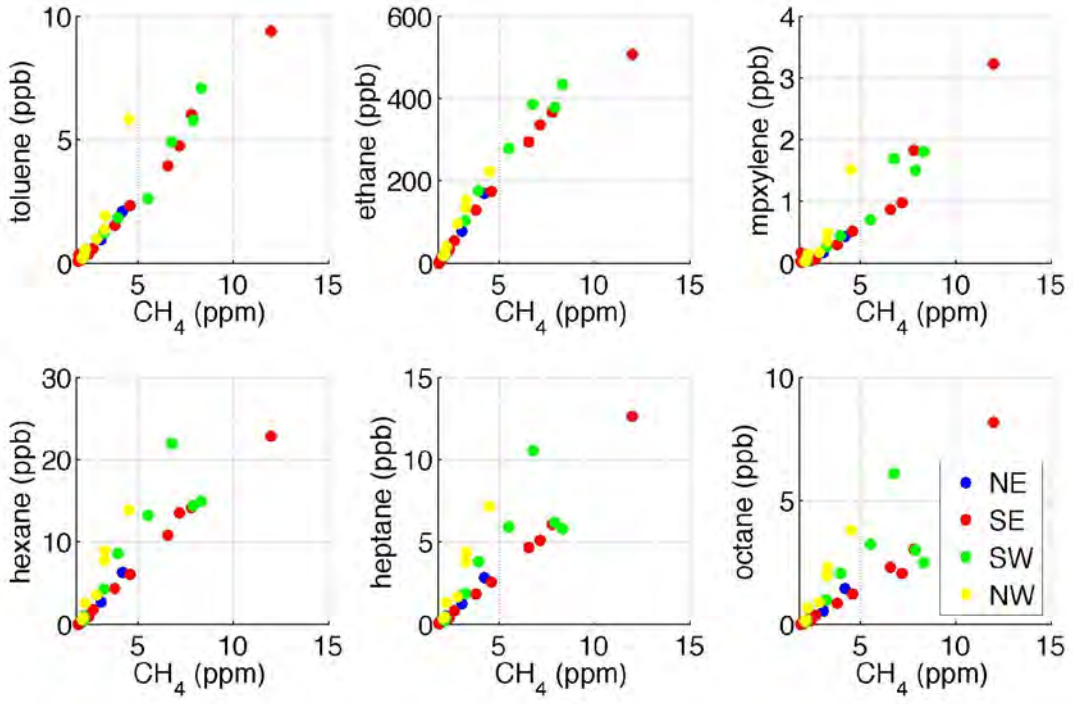


**Figure 4-23. Measurements of heavier hydrocarbons in flasks collected aboard the aircraft, January 31 - February 7, 2013, colored by quadrant ($CH_4$ from NOAA/GMD and NMHC from CU INSTAAR).**

## 4.6 Conclusions

Continuous measurements of $O_3$, $CH_4$, CO, $CO_2$, and $NO_2$ along with periodic flask measurements during seven aircraft flights between January 31 and February 7, 2013 present an unprecedented picture of both the horizontal and vertical distribution of key atmospheric constituents across the Uinta Basin. With optimal conditions for enhanced $O_3$ production during the winter of 2013, the relationship between precursor emission sources and $O_3$ production across the basin was established. Highest concentrations of $CH_4$ and related non-methane hydrocarbons and $NO_2$ were observed over the natural gas field in the SE portion of the basin. Longer-lived gases such as $CH_4$, CO, and $CO_2$ were more uniformly dispersed across most of the basin and were significantly elevated above background levels. These results suggest that the natural gas field is the likely primary source of $O_3$ precursor emissions. High $O_3$ mixing ratios were often seen well away from the gas field itself, strongly indicating ongoing photochemical production as precursors are dispersed across the basin. The strongest enhancements were seen in a relatively shallow surface layer with a strong temperature inversion with a top near 1650±50 masl. There was a gradient layer above this inversion with elevated constituent mixing ratios that gradually declined to near tropospheric background values between 1800 – 1900 masl. Even in the SW sector (over the oil production field), where very high CO values were found on all flights, $O_3$ was not higher than in other locations. $O_3$ was

positively correlated with CO over the Basin (Figure 4-11) as might be expected when the CO source is associated with combustion where NO, a primary $O_3$ precursor, is also emitted. In the SW sector, however, high $NO_2$ was not generally measured with the very high CO found in this sector and there was no indication of additional $O_3$ formation.

The highest values of CO measured during the flights were in the SW sector over the region of oil production in Duchesne County. No other constituents measured in this sector showed values elevated above those seen in other parts of the basin. In particular, there was no indication of additional $O_3$ production seen in conjunction with these very high CO values. Neither high $CO_2$ nor $NO_2$ values accompanied these high CO amounts. Correlation plots between CO and other constituents often showed a much different relationship in the SW quadrant, over the oil field, than seen in the other portions of the basin. No immediate source was identified for the strong CO emissions, but the signature of a high CO to $CO_2$ enhancement ratio indicates a source with inefficient combustion, possibly from the pump jack engines operating in the oil field.

A number of profiles in relatively close proximity (~16 km) to the Bonanza power plant encountered a layer of enhanced CO, $CO_2$ and $NO_2$ but with no enhancement in $CH_4$ and slightly depleted $O_3$ at an altitude of 1800 – 1900 masl. This composition of trace gas levels was a clear indication of transit through the Bonanza power plant plume. Visual identification of the plume, the altitude of the plume based on the stack height and plume rise, and its composition were clear indicators that the plume had risen through the strong inversion layer. There was also no sign of mixing of the plume from above the inversion back downward to the surface where it could contribute to $O_3$ production within the geographical boundaries of the study .

## 4.7 References


Bishop, G. A., and D. H. Stedman, 2008. A decade of on-road emissions measurements, *Environmental Science & Technology*, *42*(5), 1651-1656.

Karion, A., C. Sweeney, S. Wolter, T. Newberger, H. Chen, A. Andrews, J. Kofler, D. Neff, and P. Tans, 2013. Long-term greenhouse gas measurements from aircraft, *Atmos. Meas. Tech.*, *6*(3), 511-526.

Miller, J. B., et al., 2012. Linking emissions of fossil fuel $CO_2$ and other anthropogenic trace gases using atmospheric ($CO_2$)-C-14, *J. Geophys. Res.-Atmos.*, *117*.

Peischl, J., et al., 2013. Quantifying sources of methane using light alkanes in the Los Angeles basin, California, *Journal of Geophysical Research: Atmospheres*, n/a-n/a.

Turnbull, J. C., et al., 2011. Assessment of fossil fuel carbon dioxide and other anthropogenic trace gas emissions from airborne measurements over Sacramento, California in spring 2009, *Atmos. Chem. Phys.*, *11*(2), 705-721.

Wunch, D., P. O. Wennberg, G. C. Toon, G. Keppel-Aleks, and Y. G. Yavin, 2009. Emissions of greenhouse gases from a North American megacity, *Geophys. Res. Lett.*, *36*, 5.

# 5.0 INTENSIVE CHEMICAL MEASUREMENTS AT HORSE POOL

James M. Roberts[1], Patrick R. Veres[1,2], Bin Yuan[1,2,] Carsten Warneke[1,2], Felix Geiger[3], Peter M. Edwards[1,2,] Robert Wild[1,2], William Dube[1,2], Gabrielle Petron[4], Jonathan Kofler[4], Andreas Zahn[3], Steven S. Brown[1], Martin Graus[1,2], Jessica Gilman[1,2], Brian Lerner[1,2], Jeff Peischl[1,2], Joost A. de Gouw[1,2], Rui Li[1,2], Timothy Bates[5], Patricia Quinn[5], Abigail Koss[1,2], Shao-Meng Li[6], David D. Parrish[1,2], Christoph J. Senff[1], Andrew O. Langford[1], Robert Banta[1], Randall Martin[7], Robert Zamora[8], Shane Murphy[9], Jeff Soltis[9], Robert Field[9]

1. Chemical Sciences Division, NOAA Earth System Research Laboratory, Boulder, CO.,
2. Cooperative Institute for Research in the Environmental Sciences, NOAA and University of Colorado, Boulder, CO.
3. Karlsruhe Institute of Technology, IMK-ASF, Karlsruhe, Germany
4. Global Monitoring Division, NOAA Earth System Research Laboratory, Boulder, CO.,
5. NOAA Pacific Marine Environmental Laboratory, Seattle, WA.
6. Environment Canada, Toronto, Canada
7. Department of Civil and Environmental Engineering, Utah State University, Logan, UT.
8. Physical Sciences Division, NOAA Earth System Research Laboratory, Boulder, CO.,
9. Department of Atmospheric Sciences, University of Wyoming, Laramie, WY.

## 5.1 Introduction and Background

The UBOS 2012 intensive campaign at the Horse Pool site took place under anomalous conditions of no snow cover, higher than normal temperatures, and no 'cold pool' events. As such, the 2012 data are most useful for source characterization, and as indicators of slow photochemistry typical of wintertime North America. The 2012 study represented a significant effort, including several groups that provided complementary measurements. The 2013 study plan was formulated so that the intensive measurements would only be deployed if and when high $O_3$ conditions were established. Because of this contingency, and owing to substantial field commitments later in the year by a number of groups including NOAA/CSD, the 2013 effort was smaller and more focused. The 2013 study concentrated on photochemical radical sources, associated photochemical marker species, and snow chemistry. By mid-January 2013, it was clear that conditions would be conducive to high ozone events, and the decision was made to deploy the Horse Pool intensive measurements. The results of those measurements are described in this section. As will be shown, much can be learned by contrasting the 2012 and 2013 results, as they indicate both the differences in magnitude of $O_3$ and radical sources, large differences in the associated photochemical product species, and the presence of a snow layer that contained high levels of deposited material.

## 5.2 Site Configuration and Experimental Approach

The UBOS 2013 campaign was conducted between Jan 23 and Feb 21 at the same location as the 2012 Horse Pool Intensive study. Figure 5-1 shows a photograph of the site as it was configured in 2013. The Lidar and PMEL aerosol vans were deployed essentially as they were in

2012, and the main differences were in how the gas phase measurements were configured. Most of the inlets for gas phase measurements were fixed to a moveable carriage, on the sampling tower shown in Figure 5-1, which was switched from 1m to 7.25 m above ground level (agl) every 20 minutes, for approximately 8 days during the project. Several of the instruments that had unique inlet requirements, such as the $NO_3$, $N_2O_5$ and NOy CaRD instruments used inlets that were fixed at approximately 4 m agl. The ground south and west of the tower was cordoned off to provide as natural a snow surface as possible, however servicing of the inlets did disturb the area immediately around the base of the tower somewhat. The south and west sectors were kept clear as those were the most common daytime prevailing wind sectors during the 2012 study.

The measurements deployed during the 2013 Horse Pool intensive study are listed in Tables 5-1 and 5-2. Where noted, some of the measurement methods were identical to those fielded in 2012 [*J.M. Roberts et al.*, 2013] and will not be discussed in detail here. New measurements or aspects of measurements that differed from the 2012 Study will be detailed below.

### 5.2.1 $NO/NO_2/NOy/O_3/NO_3/N_2O_5$ by Cavity Ring-Down Spectroscopy

The measurement techniques for nitrogen oxides were very similar to those used in the 2012 UBOS study, and only significant differences will be noted below. The nighttime nitrogen oxides, $NO_3$ and $N_2O_5$, were measured using a custom-built cavity ring-down spectrometer (CaRDS), the working principles of which are described in detail in the 2012 report. Only the inlet configuration was a noteworthy difference, and is discussed here. The inlet for this instrument consisted of a 1/4" O.D. teflon tube that was extended about 1 meter above the roof of the trailer, 4 m agl total. Since aerosol accumulating inside this tube can decrease inlet transmission for $NO_3$ and $N_2O_5$ [*Fuchs*, 2008], the inlet was replaced with a clean tube on a daily basis. To measure the extent of these losses, inlet transmission comparisons were made between day-old and new tubing using a synthetic crystalline $N_2O_5$ sample stored on dry ice. A constant flow of clean air over the sample produced a constant gas-phase output of $N_2O_5$. The comparison between measurement through old and new tubing showed an average 8% decrease in $N_2O_5$ transmission efficiency over one day of use.

A separate CaRDS instrument was used to measure $NO_2$, NO, $NO_y$, and $O_3$, also based on the same principles of the instrument described in 2012. It measures the concentration of $NO_2$ in four 50 cm optical cavities and after quantitative conversion of either NO (by reaction with excess $O_3$) or $O_3$ (by reaction with excess NO) in two of them. This instrument sampled from a fast-flow inlet attached to the moving carriage on the tower. The main difference between the 2012 and 2013 versions is the addition of a fourth channel that measures total $NO_y$. A quartz oven heated to 650° C serves as the inlet, with roughly 3 mm of quartz extending out of the heated metal enclosure. This ensures that the front end of the inlet stays above 100° C, minimizing losses of $HNO_3$ to the inlet walls. The oven temperature was chosen such that the $NO_y$ compounds are thermally dissociated to NO and $NO_2$ without the need for catalytic conversion [Wild et al., 2013 in preparation, [*Day et al.*, 2002]. The addition of excess $O_3$, as in the channel that measures total $NO_x$, ensures that any NO is converted to $NO_2$.

One inadvertent effect of the NOy conversion oven was the creation of semi-volatile organic compounds from VOCs in ambient air. This material coated the high-reflectivity mirrors enough to cause severe degradation of the ring-down time constant. To counteract this, we installed a hydrocarbon "kicker," a tube which is permeable to hydrocarbons but impermeable to $NO_x$ [Thermo Electron Corporation], in between the oven and the optical cavity. A sheath counter-flow transported the hydrocarbons out an exhaust line.

The $NO_2$ channels were calibrated as in 2012, resulting in ±3% accuracy for $NO_2$ and $O_3$, and ±5% for $NO_x$. We conservatively claim an accuracy for $NO_y$ of ±10%, due to difficulty in calibrating conversion efficiencies of our heated inlet, as well as a small but non-negligible interference from $NH_3$. The accuracies for the $NO_3$ and $N_2O_5$ measurements are 15%, in part due to the uncertainty in determining inlet losses.

### 5.2.2 $O_3$ and Winds by Lidar

NOAA/ESRL/CSD deployed two of its lidar remote sensing instruments to the 2012 and 2013 Uintah Basin Ozone Studies (UBOS): the High Resolution Doppler Lidar (HRDL) and the Tunable Optical Profiler for Aerosol and oZone (TOPAZ) lidar. Both instruments were situated at the Horse Pool site.

#### 5.2.2.1 HRDL Doppler Wind Lidar

HRDL provided profiles of horizontal wind speed and direction, horizontal wind speed variance, vertical wind speed and its variance and skewness, and un-calibrated aerosol backscatter at a time resolution of 20 minutes. Profiles of horizontal wind speed and its variance, wind direction, and un-calibrated aerosol backscatter retrieved with HRDL in scanning mode are measured to within 5 meters of the surface and with 5-meter vertical resolution. The maximum range of the HRDL measurements depends on atmospheric aerosol loading, and the presence of clouds, fog, and precipitation. Technical specifications of HRDL are given in Table 5-3, including 30-m range resolution, a minimum range of 190 m, a maximum range of 3-4 km, rms velocity precision of less than 20 cm $s^{-1}$, and azimuth-elevation scanning capability covering more than a hemisphere, because of HRDL's ability to scan to negative elevation angles. Full 360° scans in azimuth at fixed elevation provide data over a cone in the atmosphere, whereas scanning in elevation provides data over a vertical cross section or vertical slice of atmosphere. The scan data are analyzed and averaged over vertical intervals Δz and time intervals Δt to generate mean vertical profiles of the horizontal wind from near the surface to 1½ -2 km above ground, where the analyzed Δz near the surface is <5 m and the instrument precision of the *mean* wind speeds becomes <5 cm $s^{-1}$. For this project a scan sequence of 20 min allowed a variety of scans (conical, vertical slice, vertical staring) to be performed, so wind-profile data are available at 20-min intervals, as shown in Figure 5-2. The profiles in Figure 5-2 were composited from a sequence of 4 conical scans at 1°, 3°, 15° and 30° elevation angles. Preliminary HRDL data were posted in near real time (about 10 minutes after they were recorded) on a web site, where they were available for other study participant to use in the interpretation of their data and to plan the UBOS flight operations. Details about the HRDL instrument are given in Table 5-3 and descriptions of the retrievals of the various data products can be found in Grund et al. (2001) and Tucker et al. (2009).

#### 5.2.2.2 TOPAZ Ozone Lidar

The TOPAZ lidar measured vertical profiles of ozone and aerosol backscatter from near the surface up to a few kilometers AGL. TOPAZ is based on a state-of-the-art, solid state, tunable laser that emits laser pulses in the ultraviolet spectrum at three wavelengths between 285 and 300 nm [*Alvarez II et al.*, 2011]. Prior to the UBOS 2012 study, TOPAZ was converted from a downward-looking airborne system into a zenith-pointing instrument that was installed into a truck with a roof-mounted two-axis scanner (Fig 3.3). The scanner permits pointing of the laser beam at several shallow elevation angles at a fixed but changeable azimuth angle. Zenith operation is achieved by moving the scanner mirror out of the laser beam path. During the UBOS studies, repeated scans at 2, 6 (2013 only), 10, and 90 degrees elevation angle were performed approximately every 5 minutes. The dwell time at each angle was 75 seconds. The ozone and aerosol backscatter profiles from the various elevation angles were spliced together to create composite vertical profiles extending from 15 m up to about 3 km AGL. The effective vertical resolution of the composite ozone profiles increases with altitude from 3 to 90 m. The ozone and aerosol profiles were reported at time resolutions of 5-15 minutes. Similar to HRDL the maximum range of the TOPAZ measurements is affected by clouds, fog, and precipitation. The airborne version of TOPAZ has been used in several air quality field campaigns since 2006 and has been extensively tested and compared with collocated in situ ozone sensors [*Langford et al.*, 2011; *Senff et al.*, 2010]. Details about the new, truck-mounted version of the TOPAZ lidar can be found in Alvarez et al. (2012).

### 5.2.3 $CH_4$, $CO_2$, $H_2S$ by Integrated Cavity Output Spectroscopy

These species were measured using two different commercial systems (Picarro Instruments): a combination $CH_4/H_2S$ instrument fielded in conjunction with the University of Wyoming; and a combination $CH_4/CO_2$ instrument fielded in conjunction with NOAA/GMD. The two instruments had approximately 7 days of overlap during which they compared favorably (to with-in their stated uncertainties). While the time resolution of these instruments was nominally 2 seconds, the measurements were averaged and archived as one minute averages. Higher time resolution data are available on request. The inlet for the $CH_4/H_2S$ instrument was connected to the fast flow inlet used by the VOC instruments. The inlet for the $CH_4/CO_2$ instrument was connected to the same high flow inlet that the $NO/NO_2/O_3$ instrument used and so was raised and lowered as part of the tower experiment. The over-all uncertainties were (1% + 4 ppbv), (1% + 2ppbv) for the $CH_4$ channels that were part of the $H_2S$ and $CO_2$ instruments, respectively, (0.4% + 3ppbv) for the $H_2S$ channel, and (1% + 0.2 ppmv) for the $CO_2$ channel of each instrument.

### 5.2.4 $SO_2$ by UV Fluorescence

Sulfur dioxide was measured with a modified Model TEII 43s commercial instrument that operates on the principle of pulsed UV fluorescence. Modifications centered around shortening the response time by increasing the sample flow rate. The overall uncertainties in the measurement were ±(15% + 0.15ppbv).

### 5.2.5 Acyl Peroxynitrates/Nitryl Chloride

Measurements of acyl peroxy nitrates ($RC(O)OONO_2$) and nitryl chloride ($ClNO_2$) were acquired with the same chemical ionization mass spectrometric technique use during the 2012 study. The GC/ECD system used in 2012 was not fielded during the 2013 campaign. The inlet used for this measurement was the same configuration as 2012 and placed on the moveable carriage on the sampling tower. Calibrations of PAN (acetyl peroxynitrate = $CH_3C(O)OONO_2$) and $ClNO_2$ and inlet tests were performed in the manner as 2012, and the results of these inlet tests were used to correct the ambient data. Additional calibration efforts were done for PPN (propionyl peroxynitrate = $CH_3CH_2C(O)OONO_2$), APAN (acrylyl peroxynitrate = $CH_2CHC(O)OONO_2$), MPAN (methacrylyl peroxynitrate = $CH_2C(CH_3)C(O)OONO_2$) and CPAN (crotonyl peroxynitrate = $CH_3CHCHC(O)OONO_2$) so those species were also reported (the sum of MPAN and CPAN were reported as MPAN because they appear at the same mass). The overall uncertainties of these measurements were ±(20% + 25pptv) for $ClNO_2$, ±(15%+ 5pptv) for PAN, ±(20% + 5 pptv) for PPN, ±(20% + 5 pptv) for APAN, and ±(20% + 5 pptv) for CPAN + MPAN.

### 5.2.6 VOCs by PTRMS

Two proton-transfer-reaction time-of-flight mass spectrometers were deployed at the Horse Pool site during UBOS 2013, the same quadrupole-based PTR-MS deployed during the 2012 intensive, and a new instrument based on a time-of-flight mass spectrometer (PTR-TOF-MS), owned by the University of Wyoming and jointly operated with the Chemical Sciences Division (CSD) of NOAA. The PTR-TOF-MS instrument was deployed in parallel with a PTR-MS instrument operated by CSD of NOAA in order to enhance the amount of high resolution volatile organic compound (VOC) data collected as well as to validate this relatively new VOC measurement technique. Throughout the duration of the measurements, the PTR-MS and PTR-TOF-MS instruments both sampled from the same inlet manifold and were operated under similar conditions. The methods for the CSD PTR-MS were essentially the same as in 2012 and so will not be discussed in detail here, instead the following description will focus on the new instrument.

The principal of the PTR-TOF-MS is identical to that of PTR-MS with the exception of the mass spectrometric technique utilized and is described in detail elsewhere [Graus et al. 2010, and references therein]. Briefly, $H_3O^+$ is produced in a hollow cathode ion source and allowed to react with VOC that have a higher proton affinity (PA) than $H_2O$ in a reaction chamber. The resulting $VOC{\bullet}H^+$ ions are detected together with the primary ions using a mass spectrometer, either a quadrupole in the PTR-MS or a time-of-flight in the PTR-TOF-MS. Compounds that are detected at high sensitivity with these techniques are oxygenates, aromatics, nitriles and alkenes. Alkanes are typically undetectable using the PTR chemistry, as the driving chemistry is relatively insensitive to this class of compounds. The time-of-flight mass spectrometer acquires full mass spectra on a sub 10-Hz timescale with a high degree of mass resolution. This allows for monitoring of all detectable species, both known and unknown, on a higher time resolution and sensitivity than the standard PTR-MS with quadrupole mass spectrometric detection. Mass detection with PTR-TOF-MS is accurate to 40 parts-per-million by mass (0.004 amu for a mass of 100 amu) whereas the standard quadrupole mass spectrometer used in PTR-MS can only obtain unit mass resolution. As such, the PTR-TOF-MS has the ability to distinguish between isobaric

compounds (e.g. compounds with the same nominal mass but different molecular formulas). One example of this is the successful separation of isoprene ($C_5H_8$, mass = 68.1170) and furan ($C_4H_4O$, mass = 68.0740) with PTR-TOF-MS where this would be impossible using the standard PTR-MS instrument.

During the UBOS intensive period, continuous PTR-TOF-MS mass spectra were obtained ranging from m/z (i.e., amu) 10 – 500 and averaged such that the time resolution of the measurements was set to 10 seconds. Post-acquisition data analysis was performed according to procedures described elsewhere [*Müller et al.*, 2013]. VOC data are reported in parts-per-billion by volume (ppbv) when calibration data is available; otherwise normalized counts per second (ncps) are reported. In all, over 60 masses and corresponding molecular formulas are reported using the PTR-TOF-MS data collected during the UBOS 2013 intensive period.

### 5.2.7 $C_2$-$C_{10}$ HCs by GC-FID

A total of 17 volatile organic compounds (VOCs) were measured in-situ by a research-quality, single channel, gas chromatograph-flame ionization detector. The inlet for the GC-FID consisted of a 15m unheated Teflon line (0.25inch o.d. standard wall), which was positioned on a tower at the same location as other VOC instrument inlets. The inlets were attached to a movable platform that sampled between 1 and 7.25m above ground level. Ambient air was pulled continuously at a rate of approximately 5L min-1, resulting in an inlet residence time of less than 15 seconds. From this high-flow sample stream, a smaller sample flow was diverted through water and carbon dioxide traps and into a cryogenic trap for five minutes. For each sample, this smaller flow was adjusted between 10 and 70 sccm to adapt to wide variations in ambient hydrocarbon concentrations. After the five minute sample acquisition period, the analysis sequence was begun by flash heating the cryogenic trap from -160 to 110°C, injecting the sample onto a 50m Al2O3/KCl PLOT column. The column was then ramped from 75 to 200°C over 12 minutes in order to separate C2 to C6 hydrocarbons. The eluent was analyzed by flame ionization detection, which sensitively detects hydrocarbons. The sample collection (5min) and analysis sequence (25 min) repeated automatically every 30 min beginning on the hour and half-hour. The accuracy and precision were dependent on compound and sample flow rate, but were generally <20% and <5%. The GC-FID was extensively calibrated during- and post-campaign using nine individual calibration mixtures ranging from 0 to 1000ppbv. Cross-calibrations were conducted with the INSTAAR GC-MS used during the 2013 Horse Pool measurements, and the NOAA GC-MS used during the 2012 Horse Pool measurements, to ensure valid measurement comparisons.

### 5.2.8 Carbonyls Measured by DNPH Cartridges

For comparison with datasets collected by other investigators and to get a measure of potential Basin-wide distributions, personnel from Utah State University also measured concentrations of ambient, low molecular carbonyl compounds by collection onto commercially-purchased dintrophenylhydrazine (DNPH)-coated cartridges (Supelco, LpDNPH S10L) at Roosevelt and Vernal. The collected samples were transported to USU's Utah Water Research Laboratory (UWRL) and analyzed using high performance liquid chromatography (HPLC) following the general protocols outlined in EPA Compendium Method TO-11A [*EPA*, 1999]. TO-11A

commercially-purchased standards, and associated dilutions, were used for HPLC peak identification and quantification. Field blanks were taken once per day, and laboratory blanks and spiked samples were also analyzed.

These samples were collected from Feb. 13-25, 2013, a period in which a strong inversion and ozone buildup was observed (~130 ppb $O_3$), followed by a partial Basin washout during the evening of Sunday, Feb. 18$^{th}$, followed by a moderate $O_3$ buildup (~115 ppb $O_3$) until the end of the overall study period. The samples at Roosevelt were collected three times per day over two hour periods (8:00-10:00, 11:00-13:00, and 14:00-16:00) using a Tisch Environmental Model 423, 3-Channel Carbonyl Sampler. The samples at Vernal were collected nominally twice per day (8:00-10:00 and 11:00-13:00) using an assembled system consisting of ¼" Teflon tubes, a mass flow controller (Cole-Parmer EW-32907-69), a vacuum pump, and a digital timer. After each 2-hr sampling period at Vernal the DNPH cartridges were manually changed. On occasion, as the opportunity presented itself, additional 2-hr samples were also obtained from the Vernal location. The Tisch system and the mass flow controller used at Vernal were calibrated prior to field deployment and sampled at a nominal flow rate of 1.0 Lpm. To guard against unwanted ozone interferences, KI scrubbers preceded each of the DNPH cartridges and were replaced approximately half way through the sampling period. Additionally, a 47 mm Teflon filter and Teflon filter housing were used at the ambient inlets to the system to protect against particle collection onto the DNPH cartridges.

### 5.2.9 Acids by NI-PT-CIMS

The NI-PT-CIMS fielded in 2013 is the same as the instrument fielded in 2012, with only minor changes. The instrument was connected to the same high flow inlet that supplied the PTR-MSs and GC/FID, which consisted of a 3/8"O.D. PFA tube, thermostated at 35C, and operated at a total flow rate of 20 SLPM. A smaller flow (800 SCCM) was sampled off of that into the Acid CIMS. Zeroing was accomplished by periodically switching a carbonate denuder/catalyst system inline that removed all acids, including HCl. Calibrations were performed routinely for formic acid and before and after the project for the other acids. The exception to that was a series mid-project calibration and inlet tests for HONO that confirmed the HONO response characteristics of the instrument. A series of inlet test were performed with $NO_2$ and $H_2O$ to determine the presence and magnitude of any inlet production of HONO from those species. The results of those tests were consistent with previous tests [*J. M. Roberts et al.*, 2010; *VandenBoer et al.*, 2013] and confirmed that $NO_2$ could produce at most a 5% interference in HONO measurements. It should be noted that in contrast to many urban areas, ambient $NO_2$ levels were quite modest on average (4.3 ±4ppbv) and the HONO/$NO_2$ values measured in this study were quite high (0.21 ±0.3). Tests of another potential interfering agent, peroxynitric acid ($HO_2NO_2$), were performed in the laboratory after the experiment and qualitatively indicated that $HO_2NO_2$could produce a positive interference in the detection of HONO by this method. The precise magnitude of this interference was not yet been determined.

### 5.2.10 Aerosol Particle and Snow Measurements

#### 5.2.10.1 Aerosol Measurements – NOAA/PMEL

The sampling methods and protocols for the aerosol measurements made in 2013 were essentially the same as for the 2012 intensive, and many of the details of those measurements have been described previously [*Bates et al.*, 2008]. The only significant differences was that the average temperature and RH in the sample line measured downstream of the impactors was 24.3 ± 1.9°C and 10.3 ± 3.9%, respectively in 2012 and 23.7 ± 2.6°C and 8.8 ± 3.4% in 2013.

#### 5.2.10.2 Snow Sampling

Snow samples were collected 2 or 3 times per day during the project. Snow samples were collected in 1 L glass mason jars that had been pre-rinsed in deionized water. The snow samples (0-3cm depth) were collected from undisturbed snow at a number of sites, all within 1.3 km of the Horse Pool site. During each snow sample collection, 2 to 6 jars of snow were collected. Each sampling set included at least two samples from the top 3 cm of the snow surface. The snow was kept frozen until melting and filtering, generally 1 to 18 hours after collection. The snow was melted in a microwave oven over a period of a few minutes and the melt water was immediately filtered through a 25 mm diameter 0.4 um pore size nucleopore filter. The filtrate volume was measured and an aliquot of filtrate was collected for analysis for major ions by ion chromatography (IC). Aliquots of the filtrate were also collected in glass sample jars for TOC analysis and UV-Vis analysis. The filters were dried and stored in a freezer.

#### 5.2.10.3 Snow Analysis

*TOC/TON* – Filtered snow samples were acidified with hydrochloric acid (HCl) to a pH less than 2, stored in pre-cleaned glass vials and refrigerated until analysis. Samples were analyzed for total organic carbon (TOC) and total nitrogen (TN) with a Shimadzu TOC-VCSH instrument with a TNM-1 nitrogen unit. A solution of hydrogen potassium phthalate as a carbon standard and potassium nitrate ($KNO_3$) as a nitrogen standard, acidified to a pH of 2, was used to generate five point calibration curves for both TOC and TN with an $R^2$ greater than 0.99. The instrumental method has an uncertainty of ±0.06 ppm for TOC and ±0.02 ppm for TN. The precision for these measurements was less than 2% for both measurements. A 3 ml aliquot of each sample was loaded into the instrument and sparged with zero air to remove any $CO_2$. Finally, 150µl was injected into the heated platinum combustion tube. The best three of five injections were averaged to obtain the final TOC and TN concentrations.

*Anions and Cations* – Filtered snow samples were injected directly into the ion chromatographs used for ambient aerosol sample analysis (section 3 above). The IC analysis was generally done within 48 hours of snow sample collection.

*Light absorbing carbon* – The transmittance spectrum of each filter was measured in an integrating-sandwich spectrophotometer that incorporates an integrating sphere as one side of the sandwich (ISSW;[*Grenfell et al.*, 2011]). The integrating-sandwich configuration is designed to minimize the effect of scattering by the aerosols on the filter, so that the measured signal is a function only of the losses due to light absorption. A set of standard filters containing known (weighed) amounts of BC in the form of Monarch-71 soot was used to calibrate the system for

conversion from measured signal to black carbon loading (µgC/cm$^2$ on the filter). The calibration standards were pre-filtered to produce a size distribution generally representative of atmospheric BC (0.4 µm mass mean diameter).

### 5.2.11 Ammonia Measurements

Ammonia measurements were made in the Uinta Basin, by the Randall Martin group at Utah State University, at several sites during the 2013 intensive. These measurements are presented in this section since they are most effectively interpreted and are most applicable in the context of detailed aerosol composition measurements as were made at the Horse Pool site.

Previous measurements identified ammonium nitrate ($NH_4NO_3$) and ammonium sulfate ($[NH_4]_2SO_4$) as significant contributors to the particulate mass, specifically $PM_{2.5}$, as measured at several locations throughout the Uinta Basin [*Martin et al.*, 2011; *UBWOS*, 2013]. As such, it became of interest to assess the availability of ambient gas-phase ammonia ($NH_3$) within the Basin for potential reaction with nitrate and sulfate species resulting on secondary particle formation.

Ogawa passive samplers (Ogawa USA, Inc., Pompano Beach, Florida) were used to determine time-averaged concentrations of ambient $NH_3$ at four locations: Horse Pool, Ouray National Wildlife Refuge, Roosevelt, Vernal, and Redwash. It should be noted that Horse Pool site was the location of the multi-group intensive photochemistry study for both 2012 and 2013.

The Ogawa samplers consist of a solid Teflon cylinder with two open, but sample-isolated ends, each containing a reactive glass fiber substrate impregnated with citric acid. The substrate is mounted between two stainless steel screens situated behind a diffusion-barrier end-cap containing 25 holes (open area of 0.785 cm$^2$). Absorption substrates can be placed in both ends for the purpose of replication, which was utilized during this study. The passive samples are more completely described in Roadman et al. (2003) and Reese (2009).

Prior to deployment, the samplers were prepared by placing a commercially-purchased, coated substrate in each end of the sampler. Once loaded, the samplers were stored in individual air-tight plastic bags inside individual, air-tight, screw-top brown vials until deployment at the sampling locations. During the sampling period, the samplers were attached to associated support clips and then covered by a cap to protect the sampler from rain, dust, and wind. Figure 5-4 shows the passive sampler in place without and with the protective cap (the latter at the Redwash site). Following the sampling periods, the total deployment time was noted and the samplers were returned to the plastic bags and vials and were stored under dark, refrigerated conditions until transfer to the Utah Water Research Laboratory (UWRL) for quantification.

At the UWRL, the samples were recovered by placing the substrates in individual 30 ml sample vials and adding 8 ml of DDW (double-de-ionized water) to each vial. The vials were then placed on a sonicator for 10 minutes. Following sonication, 10 µg of 0.5 M hydrochloric acid (HCl) was added to each sample to make certain the ionic ammonium form was maintained in the aqueous solution to prevent any re-volatilization and loss of the collected $NH_3$ from

solution. Four milliliters of sample solution was then filtered into IC vials for analysis using non-sterile syringes and 0.2 µm nylon filters.

Final quantification was performed via ion chromatography. The IC instrument (Dionex Corporation) was equipped with an AS 40 Automated Sampler, CE20 Conductivity Detector, GP 40 Gradient Pump, Membrane Suppressor, LC Chromatography Oven, IonPac® CS12A cation column, CG12A cation guard column, and a 500 µL sample loop. The IC method used for analysis of $NH_4^+$ had a 13-minute run time method and 0.03 M sulfuric acid ($H_2SO_4$) solution as eluent. IC standards were prepared with 0.0745 g of powdered $NH_4Cl$ and DDW to 250 ml, creating a 100 ppm solution. This stock 100 ppm solution was then used to create standards in steps of 0.1, 0.2, 0.4, 0.6, 0.8, and 1 ppm $NH_4^+$ concentration, which were then analyzed on the IC instrument to create the standard curve. DDW blanks and continuous calibration verification (CCV) standards were also analyzed systematically throughout sample analysis to help ensure quality control. Conversion of liquid $NH_4^+$ concentrations to ambient gas-phase $NH_3$ concentrations are fully described in Roadmen et al. (2003).

### 5.2.12 Mobile Lab Measurements from 2012

The UBOS 2012 study included a ground site at Horse Pool, Utah and the NOAA GMD mobile laboratory. The Horse Pool ground site was fully equipped with a large suite of gas phase and aerosol measurements and only the instruments used in this study are described here. VOC measurements were made using PTR-MS instruments: the NOAA PTR-MS, which is described in detail by de Gouw and Warneke (2007) and the Karlsruhe Institute of Technology (KIT) ULW-PTR-MS (ultra-light weight PTR-MS). PTR-MS is an on-line mass spectrometric technique for measuring VOCs in the atmosphere. In PTR-MS, $H_3O^+$ ions are used to ionize the compounds of interest in a reaction chamber and the primary and product ions are detected by a quadrupole mass spectrometer [*de Gouw and Warneke*, 2007]. The NOAA PTR-MS was deployed at the Horse Pool ground site for the duration of the study in January-February 2012, while the KIT PTR-MS was used at the ground site for the first three weeks for detailed comparisons and onboard the mobile laboratory for the next three weeks. The two PTR-MS instruments had similar reaction chambers and mass spectrometers, but the KIT ULW-PTR-MS was optimized for instrument size and weight and was 130 lbs compared to the standard PTR-MS, which is about 250 lbs. At the time of the study, the KIT ULW-PTRMS had a somewhat lower sensitivity of around 100-200 cps/ppbv compared to about 500-1000 cps/ppbv of the NOAA PTR-MS. After the study, the sensitivity of the KIT PTR-MS has improved by about a factor of 3. Calibrations were performed at the Horse Pool ground site every other day using a calibration standard that included 10 different VOCs including oxygenates, aromatics and other compounds, and the MOCCS [*Veres et al.*, 2010] system for formaldehyde. The measurements at the ground site are averaged to 1-minute data and the individual compounds on the mobile laboratory were measured for 0.5 seconds every 19 seconds.

At the ground site the two instruments used the same inlet, the same calibration set-up and were located in the same trailer. The two instruments agreed for all reported VOCs within 10%, which gives a good confidence for the comparison of the ground site data with the mobile laboratory data.

VOCs were also measured at Horse Pool using an on-line gas chromatograph-mass spectrometer (GC-MS). The GC-MS sampled air for 5 minutes every 30 minutes and measured among others speciated $C_2$-$C_{12}$ alkanes, $C_5$-$C_8$ cycloalkanes, $C_6$-$C_9$ aromatics and methanol. The instrument is described in more detail elsewhere [*Gilman et al.*, 2010; *Gilman et al.*, 2013].

Methane was measured at Horse Pool using a 2-channel Picarro for $CO_2$ and methane and on the NOAA GMD mobile laboratory using a 4-channel Picarro for $CO_2$, CO, methane and water [*Petron et al.*, 2012].

### 5.2.13 Meteorological Measurements

NOAA/ESRL/Physical Sciences Division deployed an instrumented 20 m tower, ventilated broadband solar and IR Eppley radiometers, heated tipping bucket rain gage, snow depth sensor, and a bistatic acoustic sounder (3.4 m resolution, 6.0 m minimum range) at Horse Pool for both the 2012 and 2013 campaigns. The tower instrumentation included surface pressure, air temperature and relative humidity (2, 10, and 20 m), fast response sonic anemometer/ thermometer (6,16 m), wind speed and direction (10, 20 m). Soil moisture, soil heat flux and soil temperature at 5, 10, and 20 cm depths were observed during the 2013 field season.

Data from the standard meteorological instrumentation and radiometers were archived at 1.0 min intervals. The fast response anemometer/thermometers were sampled at 10.0 Hz. The raw 10.0 Hz samples were archived. Net radiative fluxes, turbulent heat fluxes and turbulent momentum fluxes were estimated using the radiometric and sonic anemometer/thermometer data sets. Jpeg images of the backscattered power measured by the sodar were generated at 30 minute intervals.

## 5.3 Results and Discussion

The results of the 2013 Horse Pool intensive measurements stand in stark contrast to those from the 2012 campaign. The 2013 intensive period was characterized by snow coverage and associated persistent cold pool periods lasting a week or more, during which $O_3$ built up to levels over 150 ppbv. The precursors of $O_3$, VOCs and NOx, showed contrasting behavior relative to 2012; primary VOCs and methanol were factors of 2-4 higher and secondary VOCs were often factors of 10 higher. NOx levels (NO + $NO_2$) were about the same, however NOx product compounds (e.g. PAN, $HNO_3$) were often 10 times higher in 2013. The solar actinic fluxes were about 50% higher in 2013 owing to the surface albedo being 85 to 95% in 2013 compared to the 2012 average of 35%. Radical sources driving $O_3$ production were dominated by unconventional sources: HONO and HCHO, with $ClNO_2$ and $O_3$ being only minor contributors. Formaldehyde appears to have both primary and secondary sources, and there is some question as to whether HCHO contaminated methanol usage in the Basin is an important source of primary HCHO. Measured HONO levels were quite high in 2013 relative to 2012 and had diurnal profiles that peaked around solar noon, implying a photochemical source. Vertical gradients in HONO implied that there was often a ground/snow source of HONO in the daytime and deposition at night.

The spatial and temporal variability of the ozone and associated cold pool conditions were measured by Lidar instruments during both the 2012 and 2013 campaigns. The results provide quantitative demonstration of the meteorological factors that produce a stable surface layer under cold pool conditions, and provide some guidance concerning the slow rate of transport within and at the margins of the Basin. Ozone vertical profiling was able to provide solid evidence that the NOx from the coal-fired Bonanza Power Plant power plant is lofted above the cold pool inversion and has an insignificant immediate contribution to NOx photochemistry in the Basin. Theoretically, eventual re-entrainment of some of the NOx from the power plant into the stable surface layer could occur but this is unlikely to be a significant factor under most circumstances associated with ozone episodes, at least over the first few days after emission.

Aerosol particle and snow measurements were made during the entire 2013 intensive. In general nitrate and organic carbon were the most abundant aerosol species by mass during the high ozone periods. Nitrate and nitrite built up in the top layers of the snow during the cold pool periods when ozone was building up. The large 'clean-out' event that occurred in the middle of the intensive period, that also involved some snow fall, brought in a cleaner top layer of snow, but was accompanied by deposition of soil-derived material, based on characteristic cations that are associated with soil. The snow also contained substantial black carbon that was deposited during cold pool conditions, hence was of local origin.

The following sections will provide the details of, and some conclusions about, the observations made at the Horse Pool site during the intensive period. Analyses are an on-going process and we expect to build on and refine these results in future publications.

### 5.3.1 Ozone and Odd-Nitrogen Species

Figure 5-5 shows the time series of the $O_3$ measurements during UBOS 2013 acquired with the CaRDS system. A Thermo Electron Corp, Model 42 $O_3$ UV-photometer was also run for much of the UBOS 2013 campaign, and agreed with the CaRDS instrument to within 2%. The CaRDS data will be used in the following discussions as it has better time resolution and precision. Both the diurnal variation and the larger-scale ozone events are clearly visible. 2013 was a high-ozone year, with 20 out of 28 days above the 75 ppbv National Ambient Air Quality Standards (NAAQS) for ozone, shown by the dotted line. Figure 5-6 compares the diurnal averages of $O_3$ during the campaigns in 2012 and 2013. The shaded background regions show approximate times of daylight. Not only are the $O_3$ levels significantly higher in 2013, but the daytime ozone production rates (measured from about 10am to 3pm) increased roughly threefold, going from approximately 2.4 ppbv/hr in 2012 to 7.1 ppbv/hr in 2013.

The comparison of $O_3$ distributions measured in 2012 versus 2013, shown in Figure 5-7, reveal some interesting contrasts. The 2012 $O_3$ measured at Horse Pool was most often below what would be considered a regional background for this season (45 ppbv or so), due to titration by $NO_x$ species and deposition of $O_3$ and $NO_y$ species (i.e., $N_2O_5$). The 2013 $O_3$ distribution observed in 2013 was quite different, with half of the measurements above the 75 ppbv NAAQS, and minimum values of 25-30ppbv, indicated a much reduced role for titration and deposition.

The distributions of odd-nitrogen species also showed marked differences between 2012 and 2013. The distributions of total $NO_y$, $NO_x$, and the ratio $NO_x/NO_y$ are shown in Figures 5-8a-c, for the two years. Total $NO_y$ (Figure 5-8a) was much higher in 2013, consistent with the buildup of $NO_x$ and $NO_x$ product species under stable cool pool conditions. Interestingly, the $NO_x$ levels observed in both years (Figure 5-8b) had quite similar distributions, with only slightly higher values, and an absence of very low mixing ratios in 2013 compared with 2012. As a result the ratio $NO_x/NO_y$ was much higher in 2013, reflecting the much larger degree of photochemical processing that accompanies $O_3$ production. Diurnal plots of $NO_x$, $NO_y$ and $NO_x/NO_y$ (Figures 5-9&5-10) make this point quite clearly; the 2012 data show very little variation in $NO_x/NO_y$ throughout the day; in 2013, there is a consistent decrease in $NO_x/NO_y$ throughout the photochemical day as $NO_x$ is converted to products in the same chemistry that made $O_3$. This processing results in high concentrations of product species: $HNO_3$, PAN, $RONO_2$, aerosol and snow nitrate, and a faster formation rate of the nighttime species $NO_3$ and $N_2O_5$.

The photochemical products of $NO_x$ are operationally defined as $NO_y$-$NO_x$ and collectively termed $NO_z$. The average diurnal composition of $NO_z$ in each year is shown in Figures 5-11&5-12 for 2012 and 2013 respectively. In general the major NOz species in 2012 were PANs and alkyl nitrates in the daytime, and $N_2O_5$ and $ClNO_2$ at night. The major $NO_z$ species in 2013 were $HNO_3$ and PANs, with some contribution from HONO in the daytime. Note that alkyl nitrates were not measured in 2013. Details of these NOz species will be covered in subsequent sections of this chapter.

### 5.3.2 VOCs by GC-FID and PTRMS

The section provides an overview of VOC composition measured at Horse Pool during the 2013 experiment, with some comparisons to the 2012 data set. Figure 5-13 shows VOC composition by molar abundance (volume) (A) and mass (B), and OH reactivity (C). Alkanes and unsaturated hydrocarbons were measured by GC-FID; aromatics and oxygenates were measured by PTR-MS. "OH reactivity" refers to the rate constant for reaction of the species with the OH radical, scaled by the species' molar concentration [*Atkinson and Arey*, 2003; *Atkinson and Aschmann*, 1984]. The chart of OH reactivity is not an exact measurement of how much each compound contributes to ozone production; rather, it provides a conceptual illustration of the major VOCs that contribute to chemical activity. In terms of both mass and molar mixing ratio, methane was the dominant species measured at the Horse Pool site, followed by other lightweight alkanes (ethane, propane, iso- and n-butane, and iso-and n-pentane). Due to the slow reaction rate with OH radical, methane accounts for a much smaller fraction of OH reactivity. OH reactivity was more evenly distributed amongst the longer chain alkanes, with contributions from aromatic HCs, and two of the more abundant oxygenates, methanol and acetaldehyde.

The position of the VOC instrument inlets on a movable platform allowed us to determine chemical gradients between 1 and 7.25 m. An experiment to measure chemical gradients was conducted from 7 February to 11 February by moving the inlet sampling height from 1 to 7.25m every 20 minutes. Figure 5-14 shows the results of this experiment for propane. There is no statistically significant gradient, suggesting that primary emissions are well mixed up to 7.25m, and that there is not a significant surface source or sink of propane. In general, we would not

expect a gradient for species that are not soluble in water and do not have a strong snow source.

Next, we will make a general comparison of VOC measurements at Horse Pool in 2012 and 2013. For a comparison of 2012 Horse Pool data to measurements at Red Wash, Utah, in 2011; Weld County, Colorado, in 2011; and Los Angeles, California, in 2010, refer to the 2012 Uintah Basin Winter Ozone and Air Quality Study Final Report [*Lyman and Shorthill*, 2013]. Mixing ratios of hydrocarbons in 2013 at Horse Pool were significantly higher than corresponding 2012 measurements. Figure 5-15 shows a comparison between 2012 and 2013 of the absolute mixing ratios of compounds with the highest concentrations. Figure 5-16 shows the fractional increase from 2012 to 2013 of all measured VOCs. Alkanes, aromatics, other lightweight unsaturated hydrocarbons, methanol, and formaldehyde increased by a similar amount (by a factor of 1.5 to 3.5), while other oxygenates – acetone, acetaldehyde, and MEK (methyl ethyl ketone, or 2-butanone) – increased by a much larger amount, by a factor of 8 to 12. Acetone, acetaldehyde, and MEK are photochemical products, rather than primary emissions. The much larger enhancement of these oxygenates reflects higher photochemical activity in 2013.

Compound ratios can help identify particular emission sources. Figure 5-17 shows ratios of iso- to n-butane, iso- to n-pentane, and benzene and i-butane to propane, for 2012 and 2013. Ratios did not change significantly from 2012 to 2013. Ratios of other alkanes to propane show similar agreement between 2012 and 2013. This indicates that neither the emission source for these compounds nor the chemical composition of emissions changed significantly between the 2012 and 2013 measurement periods. A time series of total OH reactivity is given in Figure 5-18. The lowest points of VOC OH reactivity (28 Jan. and 09 Feb.) correspond to “clean-out” periods and are roughly comparable to average total OH reactivity for the 2012 measurement period, about 10 $s^{-1}$. The highest VOC OH reactivity periods experienced in 2013 were roughly an order of magnitude higher, around 100 $s^{-1}$.

### 5.3.3 Formaldehyde

Formaldehyde is a VOC of particular interest to the Uinta Basin because it can have a variety of sources, and is potentially an important radical source. Comparisons of formaldehyde to the 2012 measurement period, and an investigation of its sources, are discussed below. In 2012, formaldehyde was found to be strongly correlated with methanol, especially in plumes of primary emissions. Figure 5-19 shows the relationship between formaldehyde and methanol for both 2012 and 2013. Compared to 2012, formaldehyde in 2013 was significantly enriched relative to methanol. This additional formaldehyde was likely photochemically produced.

Several VOC instruments deployed in 2012 and 2013, including the NOAA PTR-MS and the University of Wyoming PTR-ToF and Picarro cavity-ring-down spectrometer, were able to capture short-term peaks in a variety of compounds. These short-term peaks, which lasted over a time scale of a few seconds to 20-30 minutes, were a result of the instruments intercepting plumes of high-concentration primary emissions. Analysis of these plumes is a useful tool for distinguishing different categories of primary emissions. A 60-minute running median was subtracted from the full data set for formaldehyde, methanol, benzene, toluene, and methane,

to isolate plumes of primary emissions for closer analysis. The remaining data contains only peaks of fewer than 60 minutes duration, which excludes variation due to photochemical aging, temperature, etc. Correlations between peaks of various compounds measured by the University of Wyoming PTR-ToF mass spectrometer (formaldehyde, methanol, benzene, and toluene) and Picarro spectrometer (methane) are shown in Figure 5-20. Toluene, benzene, and methane are correlated, and methanol and formaldehyde are correlated, indicating that these compounds are emitted by two distinct processes or sets of processes. A plausible emission source of formaldehyde is industrial methanol, which is stored on wellpads and used by some operators as an antifreeze; however, we do not currently have data to definitively link primary methanol measured at Horse Pool to a specific emission source. Source attribution of formaldehyde was done using a simple linear combination model in which the primary emissions are assumed to be represented by methanol and the secondary production is assumed to be represented by $O_x$ (= $O_3$ + $NO_2$), and there was assumed to be a background of HCHO. The results of this multivariate fit suggest that of the measured HCHO, 63% was secondary, 30% primary, and 7% was background.

### 5.3.4 Comparison of PTR-TOF-MS data and PTR-MS results

A comparison of the PTR-TOF-MS [*Graus et al.*, 2010; *Müller et al.*, 2013] data and PTR-MS data is shown in Figure 5-21 as a time series for various VOCs observed in the Basin (acetone, acetaldehyde, methyl ethyl ketone, and methanol). The corresponding linear regression plots for the comparisons in Figure 5-21 are shown in Figure 5-22. The agreement between the PTR-TOF-MS and PTR-MS was well within the uncertainty of the instruments with a high degree of correlation. In this particular case, the significantly reduced duty cycle of the PTR-TOF-MS technique yields improved detection limits in comparison to the PTR-MS measurements, and can be observed in the lower signal to noise ratio of the PTR-MS measurements. In addition to the species shown in Figure 5-21, Benzene was measured using PTR-TOF-MS, PTR-MS, and GC-FID, which was also present at the UBOS 2013 Horse Pool site operated by NOAA CSD. A comparison of the three benzene measurements is shown in Figure 5-23. It can be seen that compared to the PTR-TOF-MS, the GC-FID measurement is consistently 17% lower, although this difference is still within the reported uncertainties of the two techniques.

### 5.3.5 Carbonyls measured by DNPH Cartridges

During the USU carbonyl sampling exercise, a total of 21 and 14 samples were collected from the Roosevelt and Vernal locations, respectively. As shown in the box-whisker plots of Figure 5-24, 14 different carbonyl species, formaldehyde through 2,5-dimethylbenzaldehyde, were identified at the Roosevelt location and eight species, at typically lower concentrations were identified at the Vernal location. As can be seen, the only species at both locations consistently above 1 ppb(v) were the lowest molecular weight compounds: formaldehyde, acetaldehyde, and acetone.

Figure 5-25 shows the mean values of these species, along with comparisons of NOAA-CSD collected data from the Horse Pool location for the same corresponding time periods. The Roosevelt location showed the statistically highest, at the 95% confidence level, average concentrations of formaldehyde (8.33±0.76 ppb) and acetaldehyde (6.60±0.62 ppb) compared

to Horse Pool (5.12±0.63 ppb and 3.72±0.71, respectively) and Vernal (1.62±0.73 ppb and 1.34±0.32, respectively). While the average acetone concentration at Horse Pool was dominant (6.64±1.34 ppb), it was not statistically different from that observed at the Roosevelt location (4.96±0.69 ppb). As with the other carbonyls, the concentration of acetone observed at Vernal (1.47±0.42 ppb) was significantly lower than that observed at the other two given locations. For further comparison, carbonyl samples collected in 2012, at the Horse Pool location using the DNPH protocol described herein found much lower average formaldehyde, acetaldehyde, and acetone concentrations of 1.73±0.45 ppb, 0.63±0.28 ppb, and 0.68±0.37 ppb, respectively. The 2012 study was during a period of almost no snow cover, few, if any, identifiable inversion periods, and no elevated (exceedances) $O_3$ episodes [*UBWOS*, 2013] .

Formaldehyde, in particular, is well known to be both directly emitted (e.g. motor vehicles, building materials) and photochemically formed via the oxidation of various hydrocarbons, including methanol. Methanol is known to be used as a pipeline additive during freezing conditions and was observed in ambient air at high abundance during both the 2012 and 2013 field campaigns by the NOAA investigators (see above). Typical urban, rural/suburban, and remote concentrations of formaldehyde are estimated to be 1-60 ppb, 0.1-10 ppb, and 0.3-2.0 ppb, respectively [*Finlayson-Pitts and Pitts*, 2000]. This seemingly would indicate the 2013 wintertime low molecular weight carbonyl concentrations, at least at Roosevelt and Horse Pool, are similar to those in more heavily populated areas (urban or suburban/rural) as opposed to remote areas, as might be, at least demographically, suggested for the Uinta Basin.

Some additional insight may be gained into potential HCHO and related emissions or formation mechanisms by examining the typical diurnal behavior observed at the various locations during the sample period (see Figure 5-26). As can be seen, all of the carbonyl compounds displayed an apparent diurnal pattern, generally peaking during the early afternoon sample period. This would be indicative of at least some photochemical formation for some of the carbonyl species. It is also of interest to note that, the concentrations observed at the Vernal location almost always showed the lowest concentrations and the least amount of diurnal variations. Further, it can be seen that the NOAA data from Horse Pool generally showed the greatest degree of "clean out" following the small snow storm on the evening of Feb. 18, 2013, as well as the most rapid rate of build up after the storm passed. This would be supportive of the Horse Pool site being more directly located in the active source emission and photochemical center of the Basin, as opposed to areas more affected by transported air masses (Roosevelt) or more strongly impacted by localized emissions (Vernal).

### 5.3.6 PANs and Nitryl Chloride

Results of the iodide ion CIMS measurements of PANs were quite different in 2013 compared to 2012 while nitryl chloride results were broadly similar to those during UBOS 2012. These results are reflective of several aspects of the chemistry that produces these species. PANs are produced by the same NOx-VOC chemistry that produces $O_3$ and so were much more abundant in 2013. Nitryl chloride results from a combination of nighttime NOx chemistry and soluble chloride, the availability of which was the same or less in 2013 relative to 2012. The details of PANs and $ClNO_2$ observations are described below.

A summary of the PAN levels observed during UBOS 2013 is shown in Figure 5-27 in comparison with levels observed last year, and in several urban photochemical studies including the Pasadena, CA site during CalNex 2010; the LaPorte, TX ground-level site during the TexAQS 2000 study; and at the ground-level site during the Nashville, TN 1999 Study. The UBOS 2013 results were easily the highest of the data sets shown. There are likely three reasons for this: 1) active VOC-NOx photochemistry, 2) thermal stability of PAN at low temperatures, and 3) reduced deposition on snow surfaces relative to typical summertime surfaces.

There are number of PAN-type compounds that are typically observed in the atmosphere [*J.M. Roberts*, 2007], and their relative abundances are reflective of the VOCs that contribute to the VOC-NOx photochemistry in a given air basin [*Williams et al.*, 1997]. Acetyl peroxynitrate ($CH_3C(O)OONO_2$) is the most abundant PAN compound in the polluted troposphere under most circumstances. Propionyl peroxynitrate (PPN) is usually the second most abundant PAN-like compound, with relative abundances in the range of 10 to 15%. The correlation of PPN with PAN during UBOS 2013, shown in Figure 5-28, was very tight ($R^2 = 0.99$) with a high ratio (22%) compared to typical urban areas. This feature of the PANs chemistry is due to the unusual abundance of alkanes in this UBOS environment relative to other PAN-producing species such as alkenes [*Altshuller*, 1993].

The intimate relationship between PAN and $O_3$ formation is one of the well-known features of photochemical ozone pollution [*J Roberts et al.*, 1995]. The correlation of $O_3$ and PAN observed during UBOS 2013 is shown in Figure 5-29 along with correlations from UBOS 2012, the Pasadena site during CalNex 2010, and the LaPorte ground site during TexAQS 2000. Several aspects of these relationships bear commenting on. As noted in the UBOS 2012 report the $O_3$ PAN relationship was dominated by NOx titration and depositional losses; the TexAQS 2000 data show much higher $O_3$/PAN ratios because of the presence of highly reactive VOCs that don't make PAN but do make O3 (e.g. ethylene, 1,3-butadiene) and faster thermal losses of PAN; UBOS 2013 data points have the highest PAN values due to the efficiency of alkanes in making PAN and slower thermal loss of PAN; data from CalNex 2010 are in between UBOS 2013 and TexAQS because the Pasadena urban VOC mixture is not as enriched in highly reactive VOCs as in the Houston Ship Channel and CalNex conditions were intermediate in temperature. All of the data sets that have the higher concentrations showed curvature, which was evidence of less efficient $O_3$ production at highest NOx conditions.

Nitryl Chloride values measured during the UBOS 2013 campaign are summarized in Figure 5-30 along with data from 3 other studies. The values from UBOS 2013 were only slightly lower than those observed in UBOS 2012. These lower values imply that either chloride was less available for reaction or $N_2O_5$ hydrolysis to $HNO_3$ was faster in 2013 due to more aqueous surface area on aerosols and the ground. Another factor could be that the loss of $ClNO_2$ to the snow surface was faster than the loss of $ClNO_2$ to the bare ground that was present in 2012 [*McLaren et al.*, 2012].

Field observations of nitryl chloride are relatively new, however laboratory studies of $ClNO_2$ have been fairly extensive, some going back several decades. The uptake rate of $ClNO_2$ scales as

$Hk^{1/2}$, where H is the Henry's coefficient and k the first order reaction rate. The aqueous solubility of $ClNO_2$ is quite low (H = 0.05 M/atm), however there is potential for significant reactions on snow surfaces, especially highly contaminated surfaces as the snow surfaces in the Uinta Basin appear to be. Vertical gradients in $ClNO_2$ provide one piece of evidence for deposition of $ClNO_2$ to snow surfaces, and are shown in Figure 5-31 for the period. Unfortunately, the $N_2O_5$ inlet was not co-located with the $ClNO_2$ inlet, as the $N_2O_5$ instrument required a shorter inlet that required frequent maintenance. It is possible that significant gradients in $N_2O_5$ led to large gradients in $ClNO_2$ formation rates, making it impossible to derive any quantitative statements about $ClNO_2$ uptake on snow. It should be noted that there were no significant gradients in $ClNO_2$ after sunrise, so potential uptake in snow does not affect the calculation of the radical source from $ClNO_2$.

### 5.3.7 Acids by NI-PT-CIMS

During the UBOS 2013, an acid-CIMS was deployed at Horse Pool site to measure various acids, including hydrochloric acid (HCl), nitric acid (HNO3), nitrous acid (HONO), formic acid and pyruvic+butyric acid. Several other organic acids were also observed by the acid-CIMS, but their concentrations are not reported here due to either low values or no calibration available during the campaign. The important findings from the measurement of various acids are shown individually in the following sections.

#### 5.3.7.1 HCl:

The average concentration of HCl during UBOS 2013 was 0.13±0.19 ppb. Comparison of the 2013 value with 2012 is not available, since concentration of HCl in 2012 was not reported as a result of high background issue. The measured HCl concentration in UBOS 2013 is significantly lower than the concentration at Pasadena site (urban site) during CalNex 2010 (0.82±1.0 ppb). HCl measurements at Horse Pool in 2013 show low concentrations at night and a peak at noontime (Figure 5-32). The peak of HCl at noontime is probably due to the displacement reaction of $HNO_3$, which also shows a noon peak (also seen in Figure 5-32), with $Cl^-$ in aerosol and snow pack to form HCl. However, the enhancement ratio of HCl to $HNO_3$ varied from day to day, suggesting the displacement of HCl from $Cl^-$ may also depend on availability of $Cl^-$ and aerosol or snow pack acidity.

#### 5.3.7.2 $HNO_3$:

$HNO_3$ can be formed from reaction of $NO_2$ with OH at daytime, reaction of $N_2O_5$ with aqueous surfaces (e.g. particles) and reaction of $NO_3$ with VOCs at night time. In any case, $HNO_3$ is regarded as a sink of NOx. $HNO_3$ is also an indicator of chain-terminating reaction during the daytime. The average concentration of $HNO_3$ in 2013 at Horse Pool was 4.5±3.2 ppb, which is 8 times larger than the value (0.54±0.41ppb) in 2012 (Figure 5-33). The diurnal variations of $HNO_3$ in 2013 show highest concentration around noon and lowest concentration in the evening (Figure 5-32). It is interesting that $HNO_3$ concentration increased steadily from 12 am to 6 am. Considering that $HNO_3$ deposits to the ground and aerosol surfaces continuously, the increase of $HNO_3$ before dawn suggests that $HNO_3$ production from reaction of $N_2O_5$ with particles occurred at a rate sufficient to overcome the loss by deposition (which is significant).

5.3.7.3 HONO:

HONO is a key species in the atmosphere because its photolysis is an important source of OH radical. However, the HONO sources are not well understood, as reflected by the unexplained daytime HONO concentrations observed in many studies (see *VandenBoer et al.,* [2013] and references therein). The possible sources include heterogeneous reaction of $NO_2$ with $H_2O$ on particles or surfaces, photolysis of nitrate on particle surfaces or snow pack, and reduction of $NO_2$ via an organic chromophore under sunlight [*Li et al.*, 2008; *Su et al.*, 2011; *Zhou et al.*, 2011 and references therein]. The average of HONO mixing ratio in 2013 at Horse Pool was 0.55±0.58 ppb, significantly larger than the mixing ratio in 2012 (0.05±0.04 ppb) (Figure 5-33). The diurnal variation of HONO in 2013 showed higher concentrations during the daytime and lower at night, in contrast to 2012 during which the highest concentrations were at night and early morning, as shown in Figure 5-34. The HONO concentration in 2013 is far above what can be explained by reaction of NO with OH radical. Both the diurnal profile of HONO concentration and production rate from the unknown source follow very well with the intensities of solar radiation, suggesting that the unknown HONO source is related to sunlight. This high daytime HONO source presents a bit of a conundrum in that photochemical modeling of wintertime $O_3$ both in the UGRB [*Carte and Seinfeld*, 2012], and for UBOS 2013 [*Edwards et al*., 2014, manuscript in preparation] do not require such a HONO source to reproduce the observed $O_3$ and in fact substantially over-predict $O_3$ when the high daytime HONO levels are included.

The moveable inlet attached to the sampling tower allowed for measurement of HONO gradients between 1 and 7.25m. Minor gradients in the range 0-15% were observed for the 2.5 day period when the highest HONO values were present, as shown in Figure 5-35. The average differences between HONO measured when the inlet was down compared to up is also shown in Figure 5-35 and shows that HONO is deposited to the snow at night and emitted from the snow during the during the day. Classic turbulent diffusion theory relates the timescale of transport of a species (t) to a height above the ground ($\sigma$), with an eddy diffusivity $K_z$;

$$t = \sigma^2/2K_z \qquad \text{(Eq 1)}$$

The expected gradient at a height difference of 6.25m can then be calculated as a function of $K_z$ for a chemical species that has a first order loss rate in the atmosphere, which in the case of HONO is simply its photolysis rate, $J_{HONO}$;

$$\%\text{Gradient} = \{1-\exp(-J_{HONO}*\sigma^2/2K_z)\}*100 \qquad \text{(Eq 2)}$$

The result of this calculation for an average daytime maximum $J_{HONO}$ of $0.0016s^{-1}$ is shown in Figure 5-36. The plot shows that the range of observed gradients (0-15%) corresponds to a range of $K_z$ of 1000 to 10000 $cm^2$/sec, which is reasonable for a stable winter daytime boundary layer [*Liu et al.*, 1984]. The range of $K_z$s can then be used to calculate the concentration profiles with height that would be expected at the photolysis rate corresponding to mid-day (0.0016 $sec^{-1}$), as shown in Figure 5-37.

There are several interesting features that are illustrated by Figure 5-37. HONO concentrations fall off fairly rapidly with height for the entire range of $K_z$s used in the analysis. While a tower height of 7.25 m results in observable gradients, tower heights on the order of 15 to 20 m would be ideal. Conversely, it would be very difficult to obtain interpretable HONO gradient measurements at 1.8 m, as was the case in the Wyoming study simply because the differences expected will be within the variability of the ambient signals. The statements on daytime HONO sources in Rappenglück et al. (2013) are based on comparison of all data at 1.8m with all data at 10cm, not comparisons of high and low inlet measurements made consecutively, and are unconvincing for that reason. The above turbulent diffusion analysis indicates that further refinement in the conclusions about the presence or absence of daytime HONO gradients in the Wyoming study are unlikely to be forthcoming. The gradients in Figure 5-37 show that rather than being present in the entire 150m deep PBL, HONO fills only 9 to 21% of the 'box' depending on the value of $K_z$. This feature of the HONO source, when incorporated into the photochemical models, could at least partially resolve the HONO conundrum described above.

The fluxes of HONO emitted from the snow surface can be estimated from the estimated range of $K_z$s and the measured gradients. In the simplest formulation, where $K_z$ is assumed to be constant with altitude, then the flux is simply;

$$F = -n_a K_z(dC/dz) = -n_a K_z(\Delta C/\Delta z) \qquad \text{(Eq 3)}$$

where $n_a$ is a conversion factor, and dC/dz is the HONO gradient. The maximum flux estimated during the gradient measurements was 67 µgN/m$^2$-hr, (18.6 ngN/m$^2$-sec), corresponding to a ΔC of 200 pptv, over 6.25m, and $K_z$ = 10,000 cm$^2$/sec. This value is about 2.5 times higher than laboratory measurements of snow photolysis from the Sierra Nevada mountains [*Beine et al.*, 2008], and several hundred times higher than daytime fluxes measured at Summit Greenland [*Honrath et al.*, 2002]. The UBOS 2013 snow value is about 10 times higher than the highest HONO fluxes reported for boreal forest soils [*Maljanen et al.*, 2013], however soils that have been fertilized or otherwise had substantial nitrogen deposition can be almost 100 times higher than the UBOS 2013 value according to Su et al., (2011).

A volume-concentration based analysis of HONO sources and sinks represents another means of comparison of the UBOS 2013 results with expected chemistry and with data reported by other studies, including Rappenglück (2013). The daytime formation of HONO from HO and NO, and the photolysis of HONO back to HO and NO and reaction of HONO itself with OH are often referred to the HONO "steady state":

$$OH + NO + M \Rightarrow HONO + M \qquad (k_4)$$

$$HONO + h\nu \Rightarrow HO + NO \qquad (J_{HONO})$$

$$HONO + OH \Rightarrow NO + H_2O \qquad (k_5)$$

and the HONO concentration that can be calculated by assuming these reactions are in steady state (i.e., d[HONO]/dt = 0) is referred to as [HONO]ss;

$$[HONO]ss = k_4[OH][NO]/(J_{HONO} + k_5[OH]) \quad \text{(Eq 6)}$$

where [OH] is either measured or modeled, and the other quantities are measured. [HONO]ss is usually quite low for a given air basin. For example during the UBOS 2012 study [HONO]ss was approximately 40% of the measured mid-day HONO, which was 25 pptv [*Edwards et al.*, 2013]. HONO above steady state values is assumed to be supplied by an unknown source, and because the main daytime loss is photolysis, the magnitude of this source can be estimated;

$$HONO_{source} = J_{HONO}\{[HONO]meas - [HONO]ss\} \quad \text{(Eq 7)}$$

The average [HONO]ss during UBOS 2013 was 0.06 ppbv based on a modeled [OH] of $1x10^6$ molec/$cm^3$ from recent chemical modeling work [*P. Edwards*, unpublished results]. The HONO volume source implied by our measured mid-day averaged conditions is 3.6ppbv/hr. This is quite a bit higher than most daytime HONO source estimates, but is on the same order as the results of Rappenglück et al, (2013) who estimated 2.25 ppbv/hr based on data from the 2011 Wyoming Study.

There is a need to understand the origin of the HONO source from snow, in order to understand whether NOx controls would be effective in reducing it. Nitrite concentrations in the snow were quite high during the campaign (0.1-0.5 µM), and increased gradually during the period from 28 Jan.-8 Feb., when ozone and other secondary species also accumulated. Nitrite in snow correlated moderately with nitrate in snow (R=0.70) see Figure 5-38, suggesting nitrite in snow might come from the photolysis of nitrate in snow. Nitrite in the snow can undergo the following reversible acid-bases reaction and HONO in the aqueous phase can partition into the atmosphere:

$$NO_2^-{}_{(aq)} + H_3O^+ \; <=> \; HNO_{2(aq)} + H_2O \quad \text{Eq(8)}$$

$$HNO_{2(aq)} <=> HNO_{2(g)} \quad \text{Eq(9)}$$

$$HONO^* = [NO_2^-]/H(1+K_a/[H^+]) \quad \text{Eq(10)}$$

The equilibrium gas phase HONO concentration ($HONO^*$) depends on snow nitrite concentrations, pH values in snow (Figure 5-39), and the Henry's Law constant, *H*. The circles in the graph show the measurement results of snow near Horse Pool site. This analysis assumes the presence of a liquid layer on the snow, which is reasonable for snow above about -25°C, and uses the balance of measured cations and anions to estimate $[H^+]$. There were two snow events during the 2013 campaign: 28 Jan. and 9 Feb. It can be seen that pH value decreased and nitrite concentration in snow increased, as the snow aged after snow precipitation. The calculated HONO* ranged from below 0.01 ppb to about 0.5 ppb, somewhat lower than measured HONO ambient concentrations. However this is based on ions measured in the top 1 cm of snow, it is quite plausible that the liquid layer on the surface of the snow is more concentrated hence of lower pH. While the ultimate mechanism remains somewhat uncertain, the HONO source from snow likely scales with nitrate deposition to the snow and would be sensitive to reduction in NOx. Whether this relationship has a linear or threshold dependence on $NO_3^-$ deposition is unknown at this time.

#### 5.3.7.4 Formic acid:

Direct emission of formic acid is thought to be low [*Paulot et al.*, 2011], but formic acid is also formed secondarily by oxidation of other volatile organic compounds (VOCs). Formic acid can partition into particle phase and contribute secondary organic aerosol (SOA) formation. Several studies showed that modeled formic acid using a state-of-art chemical mechanism is substantially lower than the measured concentrations in various environments [*Paulot et al.*, 2011; *Sommariva et al.*, 2011; *Stavrakou et al.*, 2012], indicating that improvements in chemical mechanisms are needed. The measured formic acid concentration in 2013 at Horse Pool was 2.34±1.27 ppb, significantly higher than the measured concentration in 2012 (0.58±0.28 ppb) (Figure 5-33). Diurnal variation of formic acid show both morning and afternoon peaks (Figure 5-40). The morning peak may be related to the several fog events during the campaign, whereas the afternoon peak is likely due to secondary formation.

#### 5.3.7.5 Pyruvic+butyric acid:

Pyruvic acid and butyric acid were measured at the same masses in acid-CIMS. The sensitivity of butyric acid is much lower than pyruvic acid in acid-CIMS, thus the concentrations reported here are expected to be mainly from pyruvic acid. The average concentration of pyruvic+butyric acid in 2013 campaign was 47±34 ppt, also much higher than the values in 2012 (7±3 ppt) (Figure 5-33). The diurnal variations of pyruvic+butyric acid show substantially higher concentration in the afternoon (Figure 5-40), suggesting secondary formation is the important source for these two acids. The correlation between formic acid and pyruvic+butyric acid is moderately strong (R=0.68), indicating they share common sources.

### 5.3.8 Radical Source Calculations

The ultimate goal of the UBOS 2013 effort at Horse Pool was to determine the processes that lead to $O_3$ formation, especially the photochemical radical sources that are initiating VOC reactions. The main sources observed in this study, are summarized by the following equations, where $h\nu$ denotes a photon, $\lambda$ is the wavelength and $\phi$ is the quantum efficiency (IUPAC data)[*Ammann et al.*, 2013];

OH Radicals

from $O_3$

$O_3 + h\nu \Rightarrow O(^1D)$ ($\lambda$ <305nm, $\phi$ = 0.90)

$O(^1D) + H_2O \Rightarrow 2OH$

$O(^1D) + M \Rightarrow O(^3P)$

$O(^3P) + O_2 \Rightarrow O_3$

from HONO

$HONO + h\nu \Rightarrow OH + NO$ ($\lambda$ <395, $\phi$ = 1.0)

from HCHO

$HCHO + h\nu \Rightarrow H + HCO$ ($\lambda < 375$, $\phi = 0.04 - 0.78$ )

$H + O_2 \Rightarrow HO_2$

$HCO + O_2 \Rightarrow HO_2 + CO$

(note: $HO_2 + NO \Rightarrow HO + NO_2$ completes OH formation)

Cl Atoms

from $ClNO_2$

$ClNO_2 + h\nu \Rightarrow Cl + NO_2$

The measurements of the chemical precursors that form radicals are described above. Spectral irradiance, the other ingredient that is required to calculate production rates, were estimated from the average irradiances from 2012 and the measured increase in albedo from 2012 (35%) to 2013 (90%) associated with the presence of snow in 2013. The average $O_3 \Rightarrow O(^1D)$ photolysis rate ($J_{O3}$) for 2013 is compared to those measured in 2012 and at the Pasadena site during summer 2010 in Figure 5-41. Average photolysis rates, $J_{HONO}$, $J_{HCHO}$ and $J_{ClNO2}$ were calculated for 2013 in the same manner, in order to estimate the average radical production rate for each of the above processes.

The average production rate for each process is shown in Figure 5-41 along with the estimates from UBOS 2012 and CalNex 2010. The CalNex 2010 plot was taken from Young et al. (2012), who noted that while ozone photolysis was the largest radical source, HONO and HCHO were also apparent, indeed they roughly totaled the source from ozone. In contrast, the UBOS 2013 radical sources were much larger than either of the other studies, and were dominated by HONO and HCHO. It should be noted that the HONO radical source in 2013 is for the values measured at 7.25m above the ground, and for the reasons shown in the previous section on HONO measurements, this is an overestimate in that this source likely decreases rapidly with height, and does not exist throughout the entire boundary layer. This aspect, coupled with the uncertainties in HONO measurements, amplifies the need to better quantify HONO and its vertical distribution.

There are significant differences in the reactivities of some VOCs towards Cl atoms relative to OH radicals. For example, small alkanes are up to 200 times more reactive towards Cl atoms, and methanol is a factor of 60 more reactive towards Cl atoms. This changes the simple picture shown in Figure 5-41, making $ClNO_2$ more important, particularly in this environment in which small alkanes and methanol are especially abundant. For this reason, photochemical models need to include the appropriate Cl atom chemistry.

### 5.3.9 Lidar Measurements

#### 5.3.9.1 Meteorological Processes in the Atmospheric Boundary Layer Using Doppler Lidar

Concentrations of pollutants (including ozone $O_3$, methane $CH_4$, ethane $C_2H_6$, etc.) are determined by emission rates and chemical transformations over a time period, by the 3-D volume occupied by those pollutants, by how well they are mixed within the volume, and by the time constants for mixing out of that volume. The volume is determined by the vertical depth and horizontal extent of distribution of the pollutants. In general, stable, light-wind, cold-surface wintertime conditions are characterized by inhibited mixing, and consequently trapping of surface-emitted species in shallow, ground-based layers, inhomogeneous or "lumpy" concentrations in the horizontal, and layered structure in the vertical.

Instrumentation was deployed to the Uinta Basin during January and February 2013 to study meteorological processes controlling the extent and transport of pollutant species in the horizontal and vertical, and their vertical distribution. Tethered balloons and ozonesondes (to measure profiles of $O_3$ and of atmospheric thermodynamic variables), instrumented light aircraft and mobile vans, and an $O_3$-profiling differential-absorption lidar (DIAL) system are described elsewhere in this report. A Doppler lidar system, NOAA's High Resolution Doppler Lidar (HRDL), described by Grund et al. (2001), was deployed to the Horse Pool site to measure flow properties at high resolution and precision in the lowest 2 km of the atmosphere; this site was in the eastern sector of the Basin. Such high resolution and precision was needed to sample the weak and often shallow flow layers affecting the horizontal and vertical distribution of atmospheric contaminants.

Within the Uinta Basin, mobile van and light aircraft measurements found source activity to be highly variable in the horizontal, as described elsewhere in this report. For example, gas-drilling operations predominantly in the eastern sector of the Basin resulted in higher concentrations of $CH_4$ and other substances, predominant oil extraction in the western sector produced a different mix of airborne chemicals, and significant $NO_X$ emissions were localized in the south-central portion of the Basin near the Chapita site and other places (Figure 4-21). Such spatial source variability means that horizontal transport may play a role in the generation of secondary pollutants by mingling emissions from different source regions. So an important question is whether the weak flows in the Basin could perform this kind of transport in the strongly stable, light-wind wintertime conditions encountered during the high-$O_3$ episodes.

Flow in complex terrain is generally closely related to the topography. Figure 5-42 is a topographic map of the Basin with contours chosen to emphasize basin characteristics—the 1564-m contour between purple and blue represents the elevation of the Horse Pool site, and all elevations above 2164 m appear black, thus clearly outlining the Basin. It is of interest that, although the main drainage of the Uinta Basin is the northeast-southwest-flowing Green River, the Basin orientation is elongated west-east, the Green River marking the mid-basin low point.

Time-height cross sections of HRDL-measured wind profiles for a 24-hr diurnal period are shown in Figure 5-43 for 15 Feb 2013, a day on which 8-hour average ozone concentrations at Horse Pool reached 123 ppb. During nighttime hours the near-surface winds blew from an

easterly direction, but during the day they reversed to westerly. Wind speeds were very weak at 1-2 m $s^{-1}$. The diurnal cycle was clear on this day; on other days this tendency was also observed, although passing synoptic scale disturbances often interrupted the pattern, because the diurnal flows were so weak.

Diurnal cycles of winds in complex terrain are generally driven by the daily heating and cooling cycle at the surface. Over snow-covered surfaces at night, strong cooling occurs which drives shallow downslope drainage flows. On the scale of the Basin, this drainage flow would be from easterly directions at Horse Pool. Daytime westerly flows could be a result of daytime surface heating but this is less certain given the cold temperatures, strong stability, and snow surface. Westerly flow in this part of the Basin would be consistent with a thermally forced, up-basin wind due to surface heating. Instrumented tower data at Horse Pool provides evidence for surface heating in the form of temperature traces at 2, 9, and 18 m above ground, which show the lower-level temperatures much colder at night than higher up, but which crossed over during the morning hours to become 1-2 degrees warmer at the lower levels (Figure 5-44). Positive near-surface heat fluxes, indicative of surface heating, were also evident during the day.

When the surface is warm relative to the adjacent atmosphere, an unstable boundary layer or 'mixed layer,' sometimes referred to as a convective boundary layer (CBL), can form. A signature of a CBL is that the potential temperature profile $\theta(z)$ is approximately constant or slightly decreasing with height, and the profiles of other constituents, such as water vapor, $O_3$, $CH_4$, etc., may also become constant or nearly constant with height. Figure 5-45 shows $\theta$ and $O_3$ profiles from a tethered-balloon system at Horse Pool for 1409 MST (2109 UTC) on 14 Feb. The nearly constant profiles and warm surface indicate a mixed-layer structure. For boundary layers in general, a mixed-layer structure can be produced by wind shear in addition to surface heating, but here the wind speeds, and therefore the shear, are too weak to contribute significantly to the mixing through the CBL. Existence of CBL structure under these conditions is thus another indicator of surface-based heating of the atmosphere.

As discussed in Section 3, high-$O_3$ events coincided with the development of a strong pool of cold air in the Basin. During winter, cold air accumulates in the bottom of the Basin at night but is not mixed out during the day due to relatively weak surface heating consistent with low sun angles, highly reflective snow cover, and short days. The resulting pool of cold air builds in depth and strength, persisting through many days until the process is interrupted by a change in the synoptic pattern (e.g., [*Whiteman et al.*, 1999]) . The cold-air inversion layer, comprising this cold pool, suppresses mixing, so at night, the cold surface generates drainage flows that carry surface-released pollutants to lower regions of the Basin with little vertical mixing. During the day, the warm-surface-based CBL mixes near-surface pollutants upward through the shallow mixed layer, and the daytime flow carries the polluted layer up slope. At Horse Pool, the nocturnal flows were seen to be from an easterly direction, and the daytime up-basin flows, from a westerly direction. Also at the Horse Pool site, Figure 5-45 shows that the CBL only grew to a depth of ~70 m during the day.

Tethered-balloon soundings were taken simultaneously at two other sites in the Uinta Basin, at Ouray low in the Green River Valley (elevation 1430 m) and at Fantasy Canyon (elevation 1470 m) to the south-southeast of Horse Pool at an elevation intermediate between the other two sites (Figure 8-6). Figure 5-46 shows afternoon profiles of θ and $O_3$ at all three sites. A mixed-layer structure was evident at all sites, but the CBL was deepest at the lowest site (Ouray), and shallowest at the highest of the three sites (Horse Pool). Significantly, when plotted against height above sea level (ASL) as the vertical coordinate, the height of the CBL was very similar at about 1650 m ASL at all sites. The top of the inversion layer, marking the top of the cold pool, was also similar at ~1900 m, a value seen on other mid to late episode days. In other words, the cold pool was essentially a lake of cold air filling the Basin and having a relatively flat, level top, as is often evident when fog or stratus clouds occupy the cold pool. In addition, the afternoon mixed layer also tended to have a level top, even though the Basin topography rises and falls beneath it.

Interesting questions are, how do the cold-pool and mixed-layer structure evolve as an episode builds, and is the inversion at the top of the cold pool impenetrable or leaky? Figure 5-47a shows the afternoon vertical structure at the three sites at the beginning of an episode on 1 February, and Figure 5-47b shows mid-episode afternoon profiles four days later on 5 February. The θ profiles on 1 Feb show that the surface-based inversion at the top of the cold pool reached just over 1750 m ASL. As the episode proceeded, the cold pool depth grew to nearly 1950 m by 5 Feb. The afternoon CBL or mixed-layer height, however, remained the same at just under 1650 m ASL as seen in both the θ and $O_3$ profiles. Inversion strengths above the mixed layer of 4°/100 m (1800-1900 m on 5 Feb) to 6°/100 m (1650-1750 m on 1 Feb) represent very strong inversions, which should strongly inhibit vertical displacement and mixing into the inversion layer.

The depth of the shallow mixed layer changed little through the episode, but the layer cooled by 2°C and the $O_3$ produced from concentrated pollutants, which were emitted into and then trapped within this layer, increased by ~40 ppb over the 5-day period (Figure 5-47-left panels). Above the cold-pool inversion on 1 Feb, $O_3$ concentrations were ~50 ppb, which coincided with background values measured during the previous basin clean-out period (29 January) and at rural sites in Utah, such as Canyonlands NP. These low concentrations are seen above 1750 m MSL, corresponding to the cold-pool top. Just below the top of the cold pool, $O_3$ concentrations were significantly above background, indicating that “leakage” of pollutants upward into the strong inversion layer has occurred, most likely as a result of complex flow interactions within the Basin cold pool, as opposed to direct diffusion up through the inversion. This upward displacement of pollutants continued through the episode, as $O_3$ concentrations on 5 Feb exceeded 90 ppb below 1850 m and were well above background up to the top of the cold pool at 1900 m MSL. Such upward escape of pollutants into the inversion layer would have to be accounted for in performing basin-wide pollutant budgets.

Concentrations of many pollutants besides $O_3$ were found to be very high, even when compared with highly polluted urban areas, most notably ethane (Section 6.0). The vertical trapping of pollutants within the Basin by the cold-air inversion layer is a major factor, but the

light-and-variable nature of the winds also contributed. Light winds allow for large doses of emissions into an atmospheric volume as it passes over a source, and the variable winds allow the volume to pass over many sources, sometimes back and forth over a source region. The displacement of a small volume or "parcel" of air can be traced by calculating and plotting layer-averaged trajectories from the 20-min wind profiles (e.g., Figs. 5-2 and 5-43). For flows exhibiting a diurnal cycle, Allwine and Whiteman (1994) have argued that the net trajectory displacement over a 24-hr period is a measure of a "ventilation" effect of these flows. Measured trajectories have been used in prior studies to determine overnight transport of $O_3$ plumes [*Banta et al.*, 1998] and the effects of sea-breeze wind reversals on pollutant transport [*Banta et al.*, 2004; *Banta et al.*, 2011]. Here we use 24-hr forward trajectories to investigate transport and ventilation effects in the Basin.

Examples of 24-hr trajectories calculated from 20-min HRDL winds are given in Figure 5-48 for 30-31 Jan and 14 Feb., starting at about sunset (1700 MST or 0000 UTC). It is important to note that these are single-station trajectories, and the locations of the endpoints in time assumes that the winds over the relevant portions of the Basin are uniform, which is unlikely, especially as the trajectory height is closer to the ground and the location moves farther from the Horse Pool measurement site. The trajectories should be viewed as an indicator of the potential for transport and redistribution.

On 30 January (Figure 5-48a) the easterly drift of the low-level trajectories (black, red) early in the evening (closest to the measurement site) reflect the continuation of the daytime westerly-component flow. This flow reversed to the easterly drainage direction after 2100 MST (0400 UTC; see Figure 5-2). Over the next 9 hr the trajectory traveled more than 70 km to the west, until predawn and daytime flow became more variable and light. Another day showing large trajectory displacements was 31 January (Figure 5-48b). On both days $O_3$ concentrations were less than 80 ppb. In contrast, 14 February was one of the highest pollution days, ozone concentrations exceeding 140 ppb at the Ouray UDEQ monitoring site. Figure 5-48c shows that the 24-hr trajectory displacements below 200 m AGL were ~30 km or less indicating low ventilation factor. The weak, variable winds caused the trajectories to wander about within ~20 km of their origin, accumulating emissions from many sources—and presumably many *types* of source—in this area. The fact that the trajectories maintained direction for a few to several hours—in drainage or upslope flows, for example—means that transport of a few tens of km could occur, even though the winds were light. These distances would be sufficient to expose a traveling volume of air to several types of source within the Basin. In the western part of the Basin, where many sources are above the top of the high-pollution layer coinciding with the daytime mixed-layer (1650 m ±50 m), persistent downslope drainage flows are a potential mechanism for bringing emissions down into the lower levels of the Basin.

Another way to use wind data to trace air movement is backward trajectories, which are constructed by starting at a desired time and height, and using the observed winds to trace air-parcel locations backwards in time. Backward trajectories are useful for inferring potential sources for events occurring at a site. For example, on several occasions, anomalously low ozone concentrations were noted at 300-350 m above the Horse Pool site as described in

Section 8 and also shown in the TOPAZ lidar results below. Figure 5-49 shows backward trajectories for 300 m above Horse Pool passing over the Bonanza Power Plant power plant for one such occurrence. The trajectories passing over the power plant indicates that the $O_3$ "hole" was likely caused by titration of $O_3$ by NO emissions from the plant, as described in the section on TOPAZ results below. In particular, 14 Feb was a day exhibiting high ground-level $O_3$ concentrations at sites within the Basin, but the Bonanza Power Plant effluent plume was *above* the cold-pool inversion and thus completely isolated from the near-surface pollutant layer, at the short time scales involved in the transport of the plume across the Basin. This further illustrates that the Bonanza Power Plant power plant plume did not contribute to the high ground-level $O_3$ during the highest wintertime $O_3$ events.

#### *5.3.9.2* TOPAZ Lidar

The primary objective of deploying the TOPAZ lidar at the UBOS studies was to characterize the vertical structure of ozone from near the surface to a few kilometers AGL at high temporal and spatial resolutions. In the lowest few hundred meters, the TOPAZ ozone profiles complemented the collocated ozone tether sonde measurements at Horse Pool by providing temporal continuity between tether sonde launches. The lidar ozone profile measurements above 500 m AGL provided information about the ozone structure beyond the maximum altitude reachable with the tether sondes. This was critical for detecting ozone layers aloft, which may be associated with long-range transport of ozone in the lower free troposphere or downward mixing of stratospheric ozone. Under the right conditions, these ozone layers aloft can be mixed down to the surface and can impact surface ozone concentrations. One hypothesis that had been put forth prior to the UBOS studies was that the high surface ozone concentrations often observed during the winter months in the Uinta Basin were at least partly caused by long-range or stratosphere-to-troposphere transport of ozone. The ozone lidar observations were crucial for confirming or disproving this hypothesis. During the two UBOS studies, numerous comparisons were performed between the lidar measurements and observations from the tethered ozone sondes, the surface in situ ozone sensors, and the free-flying ozone sondes (2012). Generally, the lidar measurements compared well with the other ozone measurements, and the observed discrepancies were within the stated instrument accuracies of the lidar and the in situ sensors.

##### *UBOS 2012*

The TOPAZ ozone lidar was operated on 14 days between 3 and 29 February 2012 and recorded 62 hours of ozone and aerosol backscatter profile data. In the absence of any high ozone events, the sampling strategy consisted of operating TOPAZ for several hours at a time and covering different segments of the diurnal cycle on different days. TOPAZ ozone data are posted at http://www.esrl.noaa.gov/csd/groups/csd3/measurements/ubwos/topaz/. Figure 5-50 shows a 5-minute average ozone profile observed in the early afternoon on 7 February 2012. This ozone profile was typical for the vertical ozone structure observed during UBOS 2012, which was characterized by unusually warm and snow-free conditions, and fairly deep, well-mixed boundary layers. Figure 5-50 also illustrates how the lidar ozone observations from three elevation angles were spliced together to create a composite vertical profile extending from 15 m to about 3 km AGL.

Figure 5-51 shows all ozone lidar measurements from the 2012 study displayed as normalized probability distribution functions (PDFs) for three altitude ranges: 15 – 200 m AGL, 200 – 1000 m AGL, and 1000 – 3000 m AGL. The mean ozone values for these altitude ranges were approximately 46 ppbv, 48 ppbv, and 52 ppbv, respectively. Figure 5-51 shows that no ozone values above about 75 ppbv were measured with the lidar at any altitude below 3000 m AGL. In particular, no exceedances of the 8-hour National Ambient Air Quality Standard were observed. This lack of high ozone episodes was likely due to the fact that the boundary layer was generally rather deep and well-mixed, which prevented a buildup of high concentrations of ozone and its precursors. The almost complete absence of any snow cover during the UBOS 2012 study prevented the formation of a shallow cold-air pool and the development of strong temperature inversions. As a result, the boundary layer was much deeper and much better ventilated than during typical wintertime conditions in the Uinta Basin. Figure 5-51 also reveals that on average ozone concentrations were increasing slightly with altitude during UBOS 2012. The mean ozone value of about 52 ppbv in the upper altitude bin is typical for background ozone conditions in the lower free troposphere for the western US. The slightly lower ozone values in the two altitude ranges below 1000 m are probably due to titration and surface deposition of ozone. The slight vertical gradient of ozone and the similarity of the ozone PDFs for the three altitude ranges are consistent with the generally well-mixed conditions observed during UBOS 2012.

A few times during the 2012 study, very low ozone values due to titration were observed with the in situ sensors at the Horse Pool site. TOPAZ showed that these low ozone values extended to several hundred meters AGL throughout the well-mixed BL. A trajectory analysis using HRDL lidar wind observations indicated that in these cases the Bonanza Power Plant power plant plume was advected to the Horse Pool site, thus linking the observed ozone titration to the NOx-rich power plant plume.

*UBOS 2013*

TOPAZ was operated on 22 days between 22 January and 18 February 2013 and recorded approximately 230 hours of ozone and aerosol backscatter profile data. Data were collected during most of the diurnal cycle. The ozone and aerosol profiles typically extended up to 2.5 km AGL, except when low clouds were present, which restricted the maximum range of the lidar to the base of the clouds. The lidar was not operated during periods of precipitation and fog. TOPAZ ozone data are posted at http://www.esrl.noaa.gov/csd/groups/csd3/measurements/ubwos13/topaz/. Figure 5-52 gives an overview of all ozone profiles measured during UBOS 2013. Ozone profiles are only shown up to 1000 m AGL to depict the details of the ozone structure in the lowest few hundred meters. Strong lidar signal attenuation due to the high ozone and aerosol concentrations observed in 2013 resulted in small gaps in the spliced ozone (and aerosol backscatter) profiles, shown as white horizontal bars in Figure 5-52. TOPAZ captured the evolution of several high ozone episodes, including their multi-day buildup followed by a partial or complete cleanout of the Uinta Basin due to passing synoptic scale storms. Two complete episodes during the first half of February, the last couple of days of the late January episode, and the first day of ozone buildup starting on 18 February were captured. No data were taken during the 27 January and 8-11 February storms, which were accompanied by precipitation and low clouds. However,

TOPAZ documented the cleanout by a dry cold front on 17 February followed by a quick rebound in ozone (albeit in a very shallow layer) on the next day (see bottom panel of Figure 5-52). From 1 – 7 February, thick fog occurred at the Horse Pool site at night and in the morning, which limited the times when the lidar could be operated.

In contrast to 2012, winter weather conditions during 2013 in the Uinta Basin were more typical, with snow-covered ground and a persistent, shallow cold-pool layer. The strong inversion capping the cold-pool layer coupled with very light boundary layer (BL) winds caused a buildup of pollutants at the Horse Pool site, which after several days led to very high afternoon ozone concentrations of 120 to 150 ppbv. The high ozone episodes came to an end when high winds and strong mixing associated with the storm systems on 27 January, 8 February and 17 February diluted and flushed out the high ozone concentrations. Figure 5-53 shows the time-height cross section of ozone mixing ratio measured with TOPAZ on 17 February when a dry cold front passed over the Horse Pool site around 18:30 MST. This figure also shows the horizontal wind speed and direction profiles observed with the HRDL lidar, which are depicted as wind barbs, color-coded according to wind speed. Strong westerly winds were present above 400 m AGL in the afternoon, which dropped down to the surface in the wake of the passing cold front. As a result, the pollutants in the BL were flushed out and near-surface ozone concentrations dropped from about 130 ppbv to around 50 ppbv in less than one hour. The in situ surface ozone observations from the TECO and NOx cavity ring down instruments at Horse Pool also show this precipitous decrease in ozone.

Figure 5-54 shows 15-minute average ozone profiles for each day TOPAZ was operational. The profiles were observed when BL ozone peaked in the afternoon and are grouped by ozone episode. Despite the snow cover and cold temperatures, the TOPAZ observations show well-mixed ozone profiles up to about 100 m AGL. After several days of pollutant buildup, BL ozone values reached 120-150 ppbv. Above the mixed layer, ozone values gradually decreased to tropospheric background values of around 50 ppbv throughout the several-hundred-meter-deep cold-pool layer and then stayed constant above that up to about 3 km AGL. During the ozone episodes, the lidar observations show no indication of either vertical or horizontal transport of high ozone levels to the surface. This disproves the hypothesis that transport of ozone from outside the Uinta Basin contributes in a significant way to the wintertime high ozone episodes and instead supports the notion that ozone is locally produced in the Uinta Basin.

Just as in 2012, TOPAZ occasionally observed ozone titration as the NOx-rich plume from the nearby Bonanza Power Plant power plant was advected over the Horse Pool site. As an example, Figure 5-55 shows a two-hour time-height cross section from near the surface to 600 m AGL measured with TOPAZ in the evening of 14 February with the coincident ozone tether sonde measurements overlaid. Both lidar and ozone sonde show ozone values below 30 ppbv between 300 and 400 m AGL during a 30-minute period. Contrary to 2012, low ozone values were confined to the upper part of the cold-pool layer above the BL. This suggests that power plant NOx was very likely not part of the precursor mix that led to the high surface ozone values observed in 2013.

### 5.3.10 Ammonia Measurements

The ammonia sampling took place essentially the last week of the inter-group cooperative study, with integrated samples collected February 18-21, 2013. Samples were collected at the Utah Division of Air Quality sites in Vernal (40.45313°N, 109.50971°W) and Roosevelt (40.29419°N, 110.00897°W), the EPA/Golder Associates site located at Redwash (40.19716°N, 109.35250°W), at the entrance to the Ouray National Wildlife Refuge (40.12827°N, 109.66359°W), and at the main site of the cooperative intensive study, Horse Pool (40.14327°N, 109.46801°W). The samplers were all approximately 1.5 – 3.5 m above ground level and covered with the protective rain/wind cap (refer to Figure 5-4).

As can be seen in Figure 5-56, the observed ambient $NH_3$ concentrations were quite low, ranging from 0.12 ppb at Horse Pool and Redwash to 1.03 ppb at Vernal, the Uinta Basin's main population center. The Basin-wide average $NH_3$ concentration was 0.46 ppb. The uncertainty bars in Figure 5-56 represent the range about the median of the duplicate samples at each location; ranges varied from ±0.01 ppb (1.8%) at Roosevelt to ±0.30 ppb (29.6%) at Vernal. Overlaying a contour map of the observed $NH_3$ concentrations onto a relevant Google Earth image (Figure 5-57) shows that the maximum $NH_3$ concentrations are observed in the population center of Vernal. The next highest values were observed at the Ouray location, the lowest elevation site, and in Roosevelt the next most significant population center in the Basin. Observed $NH_3$ concentrations were lowest at the two locations within the oil and gas production areas, Redwash and Horse Pool.

For comparison, Seinfeld and Pandis (1998) and others suggest that typical atmospheric ammonia concentrations are in the range of 0.1 to 10 ppb. Although during inversion episodes it is not expected that that long-range transport would contribute to significant pollutant levels within the Uinta Basin, it can still be informative to examine regional $NH_3$ levels. The National Atmospheric Deposition Program (NADP) which has been monitoring nationwide precipitation chemistry, including ammonium ($NH_4^+$), at more than 250 sites since 1978 [*NADP*, 2013a]; unfortunately there is not a monitoring location within the Uinta Basin. However, as can be seen from Figure 5-58, regional $NH_4^+$ deposition surrounding the target area is expected to be on the low end of the range of observations. In 2007, NADP initiated the Ammonia Monitoring Network (AMoN) which uses passive samplers to determine 2-week integrated ambient NH3 concentrations at about 50 sites around the United States [*NADP*, 2013b]. Once again no sites are located within the Basin, but several sites are within the region and may give insight into regionally expected ambient $NH_3$ values. Table 5-4 shows AMoN $NH_3$ concentrations at various nearby locations for February 12-16, 2013, the time period encompassing the study described herein.

As with the $NH_3$ concentrations observed within the Uinta Basin, Table 5-4 shows the higher, yet still quite low, $NH_3$ levels associated with the more urban areas. However, the Logan, UT location appears to be an anomaly. The area is a relatively small isolated valley, with a population of approximately 115,000 people and a very strong agricultural base, and with a documented history of high ambient ammonia concentrations [*Moore*, 2007; *Zhu*, 2006].

Sources of atmospheric $NH_3$ are well-known and include mobile sources ($NH_3$ is created under reducing conditions in catalytic converters), so-called "slip" from selective catalytic reduction (SCR) systems for $NO_x$ control at power plants, public works such as landfills and wastewater treatment facilities, and agricultural processes. Of these, the agricultural processes are estimated to account for over 80% of the total U.S. ammonia emissions [*EPA*, 2010]. A 2011 emissions inventory for Uintah and Duchesne Counties estimated the annual $NH_3$ emissions of 684.6 and 715.7 tons/yr, respectively [*P. Barickman*, personal communication, 2013]. Similar to the national statistics, it can be seen in Figure 5-59 that agricultural practices are responsible for the largest fraction of $NH_3$ emissions. In Uintah County, livestock production accounts for 64.4% of the total annual emissions, while cropped-related practices account for another 10.6% of the $NH_3$ emissions. For Duchesne County, the two agricultural segments account for 71.9 and 11.5%, respectively.

### 5.3.11 Aerosol Particle and Snow Measurements

The $PM_{2.5}$ dry mass during UBOS 2012 (January 16- February 27, 2012) varied from 1 to 27 μg $m^{-3}$ with an average during the study of 7.5 ± 6.8 μg $m^{-3}$ (Figure 5-60). The $PM_{2.5}$ gravimetric dry mass was well correlated with the sum of the chemically analyzed mass (slope = 0.97, $r^2$=0.89), indicating that the chemically measured species accounted for all of the aerosol mass. The average $PM_{2.5}$ dry mass during UBOS 2013 (January 30- February 21, 2013) was 11.7 ± 4.6 μg $m^{-3}$. The $PM_{2.5}$ gravimetric dry mass was again well correlated with the sum of the chemically analyzed mass (slope = 1.03, $r^2$=0.94). With the lack of snow in 2012, soil was the dominant aerosol component (44%). However, excluding the larger diameter soil particles, the mass fractions of particulate organic matter (POM), $(NH_4)_2SO_4$, and $NH_4NO_3$ were very similar in 2012 and 2013 (Figure 5-61). Excluding soil, the average $PM_{2.5}$ concentration in 2013 was 3 times higher than that measured in 2012 (11.3 ± 4.4 μg $m^{-3}$ vs 3.5 ± 2.1 μg $m^{-3}$). The higher aerosol concentrations are most apparent during the two periods of stagnation centered at February 6 and 15 (Figure 5-60). The mean diameter of the ambient humidity number size distribution was larger in 2013 than in 2012 (Figure 5-62). The larger diameter led to increased aerosol light scattering and a mean $PM_{2.5}$ aerosol surface area that was 4.5 times higher in 2013 than in 2012 (270 $\mu m^2$ $cm^{-3}$ vs. 60 $\mu m^2$ $cm^{-3}$). The larger surface area increases the potential for heterogeneous reactions.

Snow chemistry and optical properties were measured during the 2013 study. Nitrate and nitrite concentrations in the surface snow increased with time between snowfalls (Figure 5-63), increasing the acidity of the surface snow and providing a nitrogen source for the potential formation of atmospheric HONO. The increases with time of nitrate and nitrite in the snow were much greater than the other chemical components relative to the component ratios in the atmospheric aerosol suggesting a gas phase source of nitrogen to the snow. Deposition of soil dust during a period of atmospheric turbulent mixing, mid-experiment, increased aerosol light absorption in the snow.

### 5.3.12 Meteorological Measurements

During the 2012 campaign the lack of snow cover allowed most of the incoming solar radiation to be absorbed by the ground. The resulting surface sensible heat flux driven by this surface heating helped establish well mixed boundary layers that at times exceeded 1.0 km and were documented by the sodar and the NOAA/ESRL/CSD HRDL . Typical peak afternoon surface sensible heat fluxes were on the order of 200 W $m^{-2}$ (Figure 5-64). Snow cover was observed on 19 and 29 February 2012. During those time periods the observed upwelling solar irradiance exceeded 300 W $m^{-2}$ (Figure 5-65). The average surface broadband (.28 – 2.8 μm) albedo measured at Horse Pool during the 2012 intensive observing period was experiment was 0.3.

The first snowfall of the 2012-2013 winter occurred on 18 December 2012. By 10 January 2013 over 10 cm of snow covered the ground at Horse Pool and the ground was frozen to a depth of 20 cm. This snow cover led to strong radiative heat losses from the surface and the formation of strong surface based temperature inversions. Typical daytime surface heat fluxes observed during the 2013 intensive operations period were on the order of 40 W $m^{-2}$ or nearly a factor of five lower than the same period in 2012 (Figure 5-66). The turbulent latent heat fluxes were negligible during the 2013 intensive operations period. The average broadband solar albedo measured at Horse Pool during the 2013 campaign was 0.82 (Fig 5-67). In contrast during the 2012 field season the average albedo was 0.3. The peak down-welling broadband solar irradiance measured at solar noon during the 2013 intensive observation period averaged 650 W $m^{-2}$ (Figure 5-68). Albedos measured over snow covered ground have little spectral dependence in the UV and visible. While the PSD pyranometers do not measure either upwelling or downwelling solar irradiance at wavelengths less than .28 μm, the lack of spectra dependence suggests that albedos at wavelengths associated with photochemistry were at least .80.

### 5.3.13 Further Analysis of the 2012 Mobile Lab VOC Measurements.

The emissions of volatile organic compounds (VOCs) associated with oil and natural gas production in the Uinta Basin, Utah were measured at the Horse Pool ground site with two PTR-MS instruments, and from the NOAA GMD mobile laboratory with the smaller portable PTR-MS instrument. The NOAA GMD mobile laboratory measured immediately downwind of individual sources: (1) gas well production company A, (2) gas well production company B, (3) oil wells, (4) gas wells in Rangely, CO, (5) a flow back pond of a recently hydraulically fractured well, (6) a newly producing gas well and (7) other point sources including compressor stations, injection wells, tank batteries, evaporation ponds and water treatment plants. This allowed investigation of the emissions from point sources in the Uinta Basin that were responsible for the large mixing ratios of VOCs observed at the Horse Pool ground site.

The track of the mobile laboratory is shown in Figures 5-69b-e color-coded by methane, methanol, toluene, and $NO_2$, respectively as it moved in close proximity and downwind (indicated by the wind barbs) of a gas well. The corresponding time series are shown in Figure 5-69a. Over 10 ppm of methane, 40 ppbv of toluene and 500 ppbv of methanol were detected close to this particular gas well. These three compounds illustrate the high mixing ratios close to the well and also that different parts of the gas well are responsible for different emissions.

Methane is high downwind of the separator, toluene and other aromatics downwind of the condensate tanks, methanol downwind of the methanol tank and the condensate tanks, and $NO_2$ downwind of the compressor.

During UBOS 2012 38 different gas wells, 12 oil wells, a newly producing well, a flow back pond from a fracking site, and 17 other point sources such as evaporation ponds, storage tanks and compressor stations were investigated in a similar way as described for the gas well in Figure 5-69. The maximum observed mixing ratios close to the sources for some selected VOCs are shown in Figure 5-70. The mixing ratios of the measured VOCs were averaged during the time the mobile laboratory spent in close proximity, generally within 300 feet, of the wells or the other emission sources and the results are shown in Figure 5-71, summarized for all source categories. Highly elevated mixing ratios of the measured VOCs were found at almost all source locations, but very large differences even between similar point sources existed. The largest relative differences were observed between individual gas wells.

Quantitative comparison of the mobile lab data with the WRAP inventory and with the Horse Pool VOC data is not possible at his time since the mobile lab data did not generate emission rates. However, some qualitative conclusions can be drawn. VOCs emitted by oil wells consisted of heavier compounds compared to gas wells, due to the heavier composition of the liquid extracted by oil wells compared to gas wells. The gas well pad emissions resembled most closely raw gas, but were heavier in composition (i.e, had a higher proportion of larger HCs). Oil well emissions were still heavier, and the main differences compared to gas wells were the aromatic compounds. Collectively, the measurements from oil and gas wells and at Horse Pool were a mixture of raw gas (from the pneumatic devices and pumps and other venting sources) and tank flashing and dehydrator emission, similar to what the WRAP inventory shows. The measurements were broadly consistent with the WRAP inventory: (1) the inventory correctly identifies dehydrators, tank flashing and the pneumatic devices as the major VOC emission sources from the gas and oil wells, (2) oil and condensate tanks emit heavier compounds such as toluene and (3) wellhead, dehydrator and pneumatic devices emit lighter compounds such as methane and light alkanes.

## 5.4 References

Allwine, K. J., and C. D. Whiteman (1994), Single-station integral measures of atmospheric stagnation, recirculation and ventilation. , *Atmos. Eviron.*, *28*, 713-721.

Altshuller, A. P. (1993), PANs in the atmosphere, *J. Air & Waste Manag. Assoc.*, *43*, 1221-1230, doi:10.1080/1073161X.1993.10467199.

Alvarez II, R. J., et al. (2011), Development and application of a compact, tunable, solid-state airborne ozone lidar system for boundary layer profiling, *J. Atmos. Oceanic Technol.*, doi:10.1175/JTECH-D-10- 05044.1.

Alvarez, R. J., C. J. Senff, A. M. Weickmann, S. P. Sandberg, A. O. Langford, R. D. Marchbanks, W. A. Brewer, and R. M. Hardesty (2012), Reconfiguration of the NOAA TOPAZ Lidar for Ground-based Measurement of Ozone and Aerosol Backscatter, paper presented at The 26th International Laser Radar Conference, Porto Heli, Greece, 25-29 June, 2012.

Ammann, M., R. Atkinson, R. A. Cox, J. N. Crowley, R. Hynes, M. E. Jenkin, W. Mellouki, M. J. Rossi, J. Troe, and T. Wallington (2103), Evaluated Kinetic Data*Rep.*, IUPAC Subcommittee for Gas Kinetic Data Evaluation.

Atkinson, R., and J. Arey (2003), Atmospheric degradation of volatile organic compounds, *Chemical Reviews*, *103*(12), 4605-4638, doi:10.1021/cr0206420

Atkinson, R., and S. M. Aschmann (1984), Rate constants for the reactions of $O_3$ and OH radicals with a series of alkynes, *Int. J. Chem. Kinet.*, *16*, 259-268, doi:10.1002/kin.550160308.

Banta, R. M., L. S. Darby, J. D. Fast, J. O. Pinto, C. D. Whiteman, W. J. Shaw, and B. D. Orr (2004), Nocturnal low-level jet in a mountain basin complex. Part I: Evolution and implications to other flow features, *J. Appl. Meteor.*, *43*, 1348-1365.

Banta, R. M., et al. (2011), Dependence of daily peak O3 concentrations near Houston, Texas on environmental factors: Wind speed, temperature, and boundary-layer depth, *Atmos. Environ.*, *45*, 162-173.

Banta, R. M., et al. (1998), Daytime buildup and nighttime transport of urban ozone in the boundary layer during a stagnation episode, *J. Geophys. Res.*, *103*, 22,1598-1522,1544.

Bates, T. S., et al. (2008), Boundary layer aerosol chemistry during TexAQS/GoMACCS 2006: Insights into aerosol sources and transformation processes, *J. Geophys. Res.*, *113*, D00F01, doi:10.1029/2008JD010023.

Beine, H., A. J. Colussi, A. Amoroso, G. Esposito, M. Montagnoli, and M. R. Hoffmann (2008), HONO emissions from snow surfaces, *Environ. Res. Lett.*, *3*, 1-6, doi:10.1088/1748-9326/3/4/045005.

Day, D. A., P. J. Wooldridge, M. B. Dillon, J. A. Thornton, and R. C. Cohen (2002), A thermal dissociation laser-induced fluorescence instrument for in situ detection of $NO_2$, peroxy nitrates, alkyl nitrates, and $HNO_3$, *Journal of Geophysical Research-Atmospheres*, *107*(D5-6), 4046, doi: 4010.1029/2001JD000779.

de Gouw, J. A., and C. Warneke (2007), Measurements of volatile organic compounds in the earths atmosphere using proton-transfer-reaction mass spectrometry, *Mass Spectrometry Reviews*, *26*(2), 223-257.

Edwards, P. M., et al. (2013), Ozone photochemistry in an oil and natural gas extraction region during winter: Simulations of a snow-free season in the Uintah Basin, Utah, *Atmos. Chem. Phys.*, *13*, 8955-8971.

EPA, U. (1999), Compendium of Methods for the Determination of Toxic Organic Compounds in Ambient Air, 2nd Edition, Compendium Method TO-11A, Determination of Formaldehyde in Ambient Air Using Adsorbent Cartridge Followed by High Performance Liquid Chromatography (HPLC) - [Active Sampling Methodology].*Rep. EPA/625/R-96/010b*.

EPA, U. (2010), Our Nation's Air: Status and Trends through 2008*Rep.*, pp6. pp.

Finlayson-Pitts, B. J., and J. N. J. Pitts (2000), *Chemistry of the Upper and Lower Atmosphere*, Academic Press, San Diego.

Gilman, J. B., et al. (2010), Ozone variability and halogen oxidation within the Arctic and sub-Arctic springtime boundary layer, *Atmos. Chem. Phys.*, *10*(21), 10223-10236, doi:10.5194/acp-10-10223-2010.

Gilman, J. B., B. M. Lerner, W. C. Kuster, and J. A. de Gouw (2013), Source Signature of Volatile Organic Compounds from Oil and Natural Gas Operations in Northeastern Colorado, *Environ. Sci. Technol.*, *47*(3), 1297-1305, doi:10.1021/es304119a.

Graus, M., M. Muller, and A. Hansel (2010), High resolution PTR-TOF: Quantification and formula confirmation of VOC in real time, *J. Am Soc. Mass. Spectrom.*, *21*, 1037-1044.

Grenfell, T. C., S. J. Doherty, A. D. Clarke, and S. G. Warren (2011), Light absorption from particulate impurities in snow and ice determined by spectrophotometric analysis of filters, *Appl. Opt.*, *50*, 2037-2048.

Grund, C. J., R. M. Banta, J. L. George, J. N. Howell, M. J. Post, R. A. Richter, and A. M. Weickmann (2001), High-resolution Doppler lidar for boundary layer and cloud research, *J. Atmos. Ocean. Technol.*, *18*, 376-393.

Honrath, R. E., Y. Lu, M. C. Peterson, J. E. Dibb, M. A. Arsenault, N. J. Cullen, and K. Steffen (2002), Vertical fluxes of $NO_x$, HONO, and $HNO_3$ above the snowpack at Summit, Greenland, *Atmos. Environ.*, *36*, 2629-2640.

Langford, A. O., C. J. Senff, R. J. Alvarez II, R. M. Banta, R. M. Hardesty, D. D. Parrish, and T. B. Ryerson (2011), Comparison between the TOPAZ airborne ozone lidar and in situ measurements during TexAQS 2006, *J. Atmos. Ocean. Technol.*, *28*, doi:10.1175/JTECH-D-10-05043.1.

Li, S., J. Matthews, and A. Sinha (2008), Atmospheric Hydroxyl Radical Production from Electronically Excited $NO_2$ and $H_2O$, *Science*, *319*(5870), 1657-1660, doi:10.1126/science.1151443.

Liu, S. C., J. R. McAfee, and R. J. Cicerone (1984), Radon 222 and tropospheric vertical transport, *Journal of Geophysical Research: Atmospheres*, *89*(D5), 7291-7297, doi:10.1029/JD089iD05p07291.

Lyman, S., and H. Shorthill (2013), Final Report 2012 Uintah Basin Winter Ozone & Air Quality Study Rep., Utah State University, Vernal, UT.

Maljanen, M., P. Yli-Pirila, J. Hytonen, J. Joutensaari, and P. J. Martikainen (2013), Acidic northern soils as sources of atmospheric nitrous acid (HONO), *Soil Biol. & Biochem.*, *in press*, doi:10.1016/j.soilbio.2013.08.013.

Martin, R., K. Moore, M. M., S. Hill, K. Harper, and H. Shorthill (2011), Final Report: Uinta Basin Winter Ozone and Air Quality Study: December 2010 – March 2011*Rep.*, Energy Dynamics Laboratory, Bingham Research Center, Utah State University Research Foundation (USURF), , Vernal, UT.

McLaren, R., et al. (2012), Vertical profiles of $ClNO_2$ at a remote terrestrial site: evidence of dry deposition of $N_2O_5$ as a source of $ClNO_2$?, in *Fall Meeting of the American Geophysical Union*, edited, San Francisco.

Moore, K. D. (2007), Derivation of agricultural gas-phase ammonia emissions and application to the Cache Valley, Utah State University, Logan, UT.

Müller, M., T. Mikoviny, W. Jud, B. D. D'Anna, and A. Wisthaler (2013), A New Software Tool for the Analysis of High Resolution PTR-TOF Mass Spectra, *Chemomet. Intell. Lab Sys.*, doi:10.1016/j.chemolab.2013.06.011.

Paulot, F., et al. (2011), Importance of secondary sources in the atmospheric budgets of formic and acetic acids, *Atmos. Chem. Phys.*, *11*(5), 1989-2013, doi:10.5194/acp-11-1989-2011.

Petron, G., et al. (2012), Hydrocarbon emissions characterization in the Colorado Front Range: A pilot study, *J. Geophys. Res.*, *117*, D04304, doi:10.1029/2011JD016360.

NADP (2013a), National Trends Network (NTN), , edited.

NADP (2013b), National Trends Network (AMoN), edited, doi:http://nadp.sws.uiuc.edu/AMoN/.

Rappenglück, B., et al. (2013), Strong wintertime ozone events in the Upper Green River Basin, Wyoming, *Atmos. Chem. Phys. Discuss.*, *13*, 17953-18005, doi:10.5194/acpd-13-17953-2013.

Reese, E. (2009), Comparison of Agricultural Area Source Ammonia Gas Concentration and Measurement Fluxes, MS Thesis, Utah State University, Logan, UT.

Roadman, M. J., J. R. Scudlark, J. J. Meisinger, and W. J. Ullman (2003), Validation of Ogawa passive samplers for the determination of gaseous ammonia concentrations in agricultural settings., *Atmos. Environ.*, *37*, 2317-2325.

Roberts, J.M., et al. (1995), Relationships between PAN and ozone at sites in eastern North America, *Journal of Geophysical Research*, *100*(D11), 22821-22830.

Roberts, J. M. (2007), Peroxyacetic Nitric Anhydride (PAN) and Related Compounds, in *Volatile Organic Compounds in the Atmosphere*, edited by R. Koppmann, pp. 221-268, Blackwell, London.

Roberts, J. M., et al. (2010), Measurement of HONO, HNCO, and other inorganic acids by negative-ion proton-transfer chemical-ionization mass spectrometry (NI-PT-CIMS): Application to biomass burning emissions., *Atmos. Meas. Tech.*, *3*, 981-990, doi:10.5194/amt-3-981-2010.

Roberts, J. M., et al. (2013), Chapter 3. Intensive Measurements at the Horse Pool Site, in *Final report: 2012 Uintah Basin Winter Ozone & Air Quality Study*, edited by S. Lyman and H. Shorthill, pp. 97-174, Utah State University.

Seinfeld, J. H., and S. N. Pandis (1998), *Atmospheric Chemistry and Physics: From Air Pollution to Climate Change*, John Wiley & Sons, Inc., New York.

Senff, C. J., R. J. Alvarez II, R. M. Hardesty, R. M. Banta, and A. O. Langford (2010), Airborne lidar measurements of ozone flux downwind of Houston and Dallas, *J. Geophys. Res.*, *115*, D20307, doi:10.1029/2009JD013689.

Sommariva, R., J. A. de Gouw, M. Trainer, E. Atlas, P. D. Goldan, W. C. Kuster, C. Warneke, and F. C. Fehsenfeld (2011), Emissions and photochemistry of oxygenated VOCs in urban plumes in the Northeastern United States, *Atmos. Chem. Phys.*, *11*(14), 7081-7096, doi:10.5194/acp-11-7081-2011.

Stavrakou, T., et al. (2012), Satellite evidence for a large source of formic acid from boreal and tropical forests, *Nature Geosci*, *5*(1), 26-30, doi:http://www.nature.com/ngeo/journal/v5/n1/abs/ngeo1354.html - supplementary-information.

Su, H., Y. Cheng, R. Oswald, T. Behrendt, I. Trebs, F. X. Meixner, M. O. Andreae, P. Cheng, Y. Zhang, and U. Pöschl (2011), Soil Nitrite as a Source of Atmospheric HONO and OH Radicals, *Science*, doi:10.1126/science.1207687.

Tucker, S. C., W. A. Brewer, R. M. Banta, C. J. Senff, and S. P. Sandberg (2009), Doppler lidar estimation of mixing height using turbulence, shear, and aerosol profiles, *J. Atmos. Ocean. Technol.*, *26*, 673-688.

UBWOS (2013), Final Report: 2012 Uintah Basin Winter Ozone & Air Quality Report, *Rep.*, 65-68, 153-154, 163-165 pp.

VandenBoer, T. C., et al. (2013), Understanding the role of the ground surface in HONO vertical structure: High resolution vertical profiles during NACHTT 2011, *J. Geophys. Res.*, *118*, doi:10.1002/jgrd.50721, 2013.

Veres, P., J. B. Gilman, J. M. Roberts, W. C. Kuster, C. Warneke, I. R. Burling, and J. de Gouw (2010), Development and validation of a portable gas phase standard generation and calibration system for volatile organic compounds, *Atmospheric Measurement Techniques*, *3*(3), 683-691, doi:10.5194/amt-3-683-2010.

Whiteman, C. D., X. Bian, and S. Zhong (1999), Wintertime evolution of the temperature inversion in the Colorado Plateau Basin., *J. Appl. Meteor.*, *38*, 1103-1117.

Williams, J., et al. (1997), Regional ozone from biogenic hydrocarbons deduced from airborne measurements of PAN, PPN, and MPAN, *Geophysical Research Letters*, *24*(9), 1099-1102.

Young, C. J., et al. (2012), Vertically resolved measurements of nighttime radical reservoirs in L

Los Angeles and their contribution to the urban radical budget, *Environ. Sci. Technol.*, *46*, 10965-10973, doi:10.1021/es302206a.

Zhou, X., et al. (2011), Nitric acid photolysis on forest canopy surface as a source for tropospheric nitrous acid, *Nature Geosci*, *4*(7), 440-443.

Zhu, D. (2006), Analysis of wintertime gas- and particle-phase ammonia in association with $PM_{2.5}$ formation in the Cache Valley,, MS thesis, Utah State University, Logan, UT.

# TABLES

**Table 5-1. Chemical measurements made during the 2013 Horse Pool Intensive Study**

| Measurement | Method | P.I. | Time Resol. | Det. Limit, ppbv |
|---|---|---|---|---|
| **Gas-Phase Measurements** | | | | |
| $O_3$, NO, $NO_2$, $NO_3$, $N_2O_5$, | Cavity Ring-Down Spectroscopy | Brown | 1 sec | 0.01 – 0.1 |
| $O_3$ | Lidar | Senff/Lang-ford | 15 min | N/A |
| Acyl Peroxynitrates Nitryl Chloride ($ClNO_2$) | Iodide ion Chemical Ionization Mass Spectrometry | Roberts/ Veres | 1-5 sec | 0.005 |
| $CO_2$, $CH_4$, $H_2S$ | Integrated Cavity Output Spectroscopy | Soltis/ Roberts/ de Gouw | 1 sec | 10 – 1000 |
| $SO_2$ | UV fluorescence | Roberts/ Williams | 1 min | 0.1 ppbv |
| Formaldehyde, Oxygenates, Aromatics, Acetonitrile | Proton-Transfer Reaction Mass Spectrometry Quadrupole MS Time-of-Flight MS | Warneke/ de Gouw Murphy/ Veres | 10sec - 1 min 0.1sec-10sec | 0.01 |
| $C_2$-$C_{10}$ VOCs | On site GC/FID, | Koss/ de Gouw | 30 min | 0.005 - 0.01 |
| Acids: $HNO_3$, HCl, HONO, HNCO, carboxylic acids, | Negative Ion Proton Transfer Mass Spectrometry | Yuan/ Warneke/ de Gouw/ Roberts | 1- 10 sec | 0.01 |
| **Aerosol/Condensed Phase Measurements** | | | | |
| Size-Resolved Aerosol Surface Area | Scanning mobility particle sizer, aerodynamic particle sizer | Bates/ Quinn | 5 min | |
| Organic carbon/ Elemental carbon | Impactor/denuder sampling, thermal/optical analyzer | " | 1 min | |
| Cations/anions | Impactor sampling/ion chromatography | " | | |
| Cations/anions | Particle-into-liquid-sampler/ion chromatography | " | | |
| Gravimetric mass Trace Elements | Impactor/microbalance/x-ray emission spectrometry | " | | |
| Condensation Nuclei | Condensation nuclei counter | " | 1 min | |
| Light scattering and absorption | Nephelometer, absorption photometer | " | | |
| Aerosol Backscatter | Lidar | Senff/ Langford | | |
| | | | | |
| SnowComposition: | | Bates/ Quinn | | |
| Anions/Cations | Grab Sampling, Ion chromatography | " | N/A | |

| Measurement | Method | P.I. | Time Resol. | Det. Limit, ppbv |
|---|---|---|---|---|
| Organic Carbon/ Total Nitrogen | Combustion/catalytic oxidation | " | N/A | |
| Light Absorbing Aerosols | Integrated-sandwich spectrophotometer | " | N/A | |

**Table 5-2. Meteorological measurements made during the 2013 Horse Pool Intensive Study.**

| Measurement | Location | P.I. | Time Resol. |
|---|---|---|---|
| High resolution 3-D Winds | Range 2-5km | Banta | 15-20 min |
| Air Temperature | 2, 9, 18 meters | King/ Zamora | 1 min |
| Soil Temperature | 5, 10, 20 cm | " | |
| Pressure | | " | |
| Snow Depth | | " | |
| Wind Speed/Direction | Sonic Anemometers, 9 and 18 meters | " | 1 sec |
| Precipitation | | " | 1 min |
| PBL depth | SODAR | " | 1 min |
| Net Radiation/Albedo | | " | 1 min |
| Photolysis Rates | Filter Radiometry, Down-welling | Hübler | 1 min |

**Table 5-3. High Resolution Doppler Lidar technical specifications.**

| | |
|---|---|
| Wavelength | 2.0218 µm |
| Pulse energy | 1.5 mJ |
| Pulse rate | 200 Hz |
| Pulse width | 200 ns |
| Scan | Upper hemisphere |
| Range resolution | 30 m |
| Time resolution | 0.02 s |
| Velocity precision | 5 cm $s^{-1}$ |
| Minimum range | 0.2 km |
| Maximum range | 2- 9 km (typically 3 km) |
| Laser | Tm:Lu, YAG diode-pumped, injection-seeded laser |

**Table 5-4. AMoN ambient ammonia concentrations from areas near the Uinta Basin (NADP, 2013b).**

| Site Name | NADP ID | Air miles from Vernal, UT | $NH_3$ (ppb) |
|---|---|---|---|
| Logan, UT | UT01 | 150 | 38.2 |
| Salt Lake City, UT | UT97 | 132 | 3.6 |
| Grand Teton National Park, WY | WY94 | 238 | 0.6 |
| Brooklyn Lake, WY | WY95 | 182 | 0.4 |
| Craters of the Moon National Monument, ID | ID03 | 294 | 1.0 |
| Ft. Collins, CO | CO13 | 230 | 3.0 |
| Rocky Mtn National Park (Long's Pk), CO | CO88 | 210 | 0.4 |

## FIGURES


**5-1. A picture of the UBOS 2013 Horse Pool Intensive site facing North. The individual components are (A) sample tower with automated inlet, (B) NOAA/CSD nitrogen species trailer, (C) NOAA/CSD VOC trailer, (D) NOAA/PMEL aerosol and snow lab, (E) NOAA/CSD HRDLS trailer, (F) NOAA/CSD TOPAZ trailer. Photo credit, Scott Sandberg.**

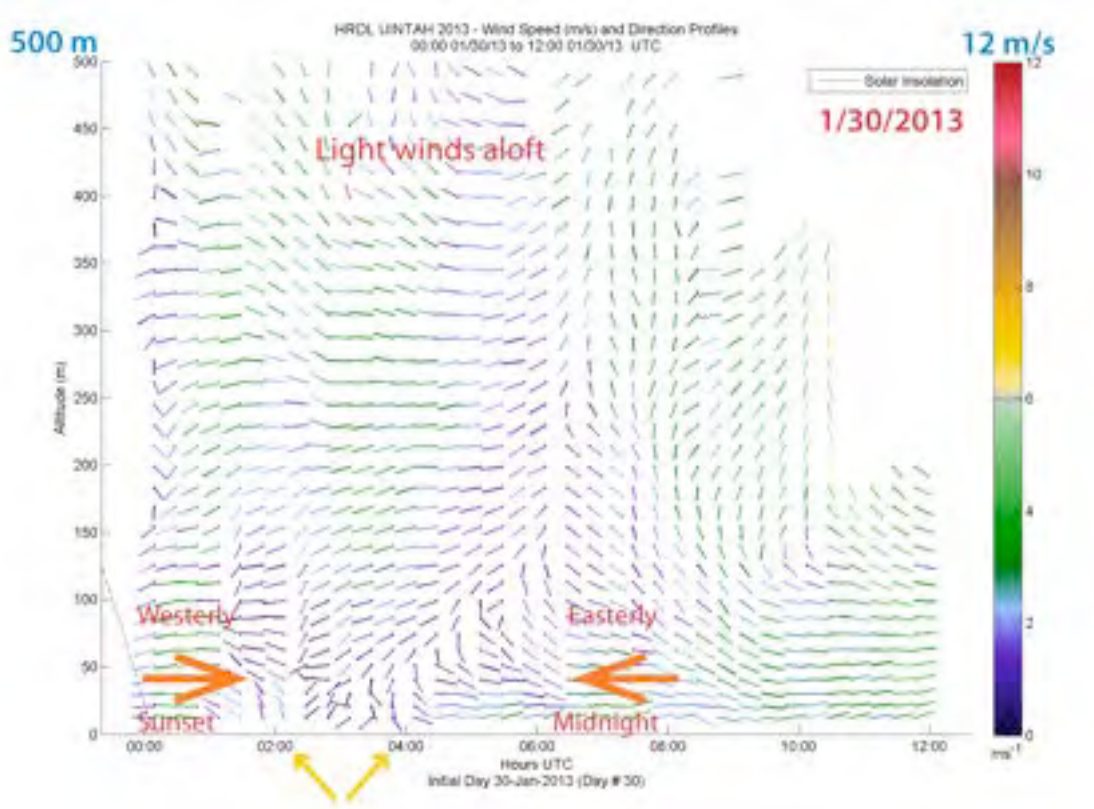


**5-2. Time-height cross section of wind speed and direction on 30 January for 0000-1200 UTC (29/1700-30/0500 MST), using 20-min vertical profiles from HRDL conical scans. Wind barbs point toward direction from which winds were blowing, and color of barbs indicates wind speeds (m $s^{-1}$) as shown in color bar at right. Dashed line (left side of figure) indicates relative solar insolation, declining in late afternoon.**

**5-3. Truck-mounted TOPAZ ozone lidar with roof-top, two-axis scanner.**

**5-4. Deployed Ogawa passive sampler without and with rain/wind cap.**

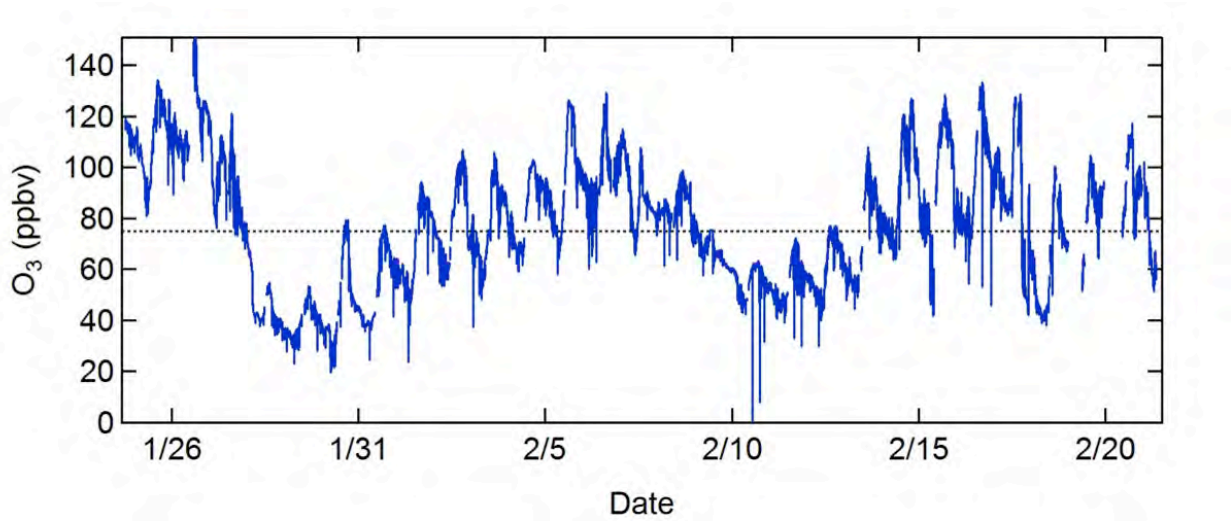


**5-5. Times series of $O_3$ measured at the Horse Pool site by the CaRDS instrument during the UBOS 2013 campaign.**

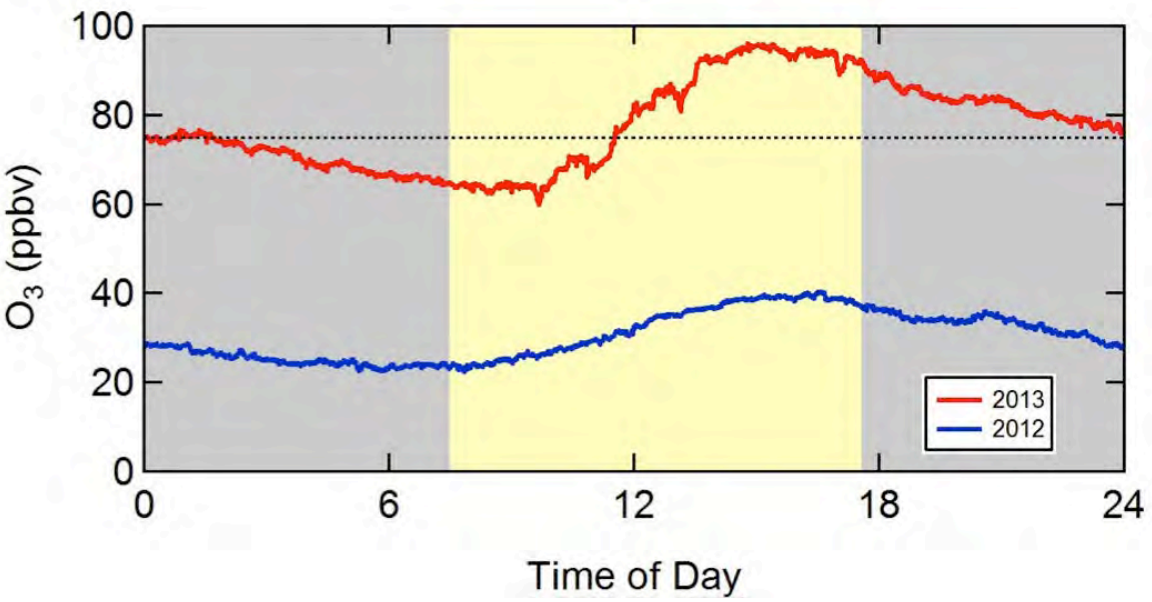


**5-6. Diurnal averages of $O_3$ during the campaigns in 2012 (blue) and 2013 (red). The average daylight period is shown in yellow.**

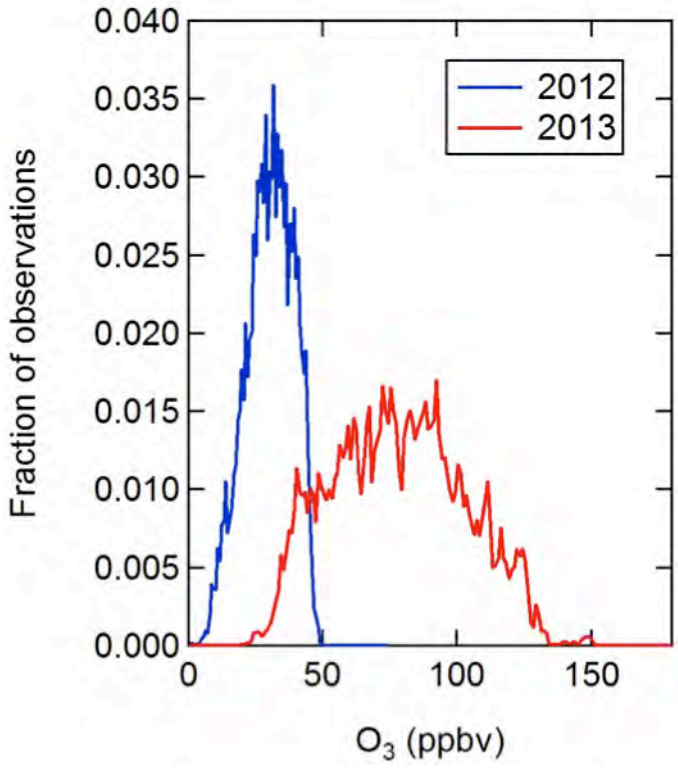


**5-7. Comparison of $O_3$ distributions measured in 2012 (blue) versus 2013 (red).**

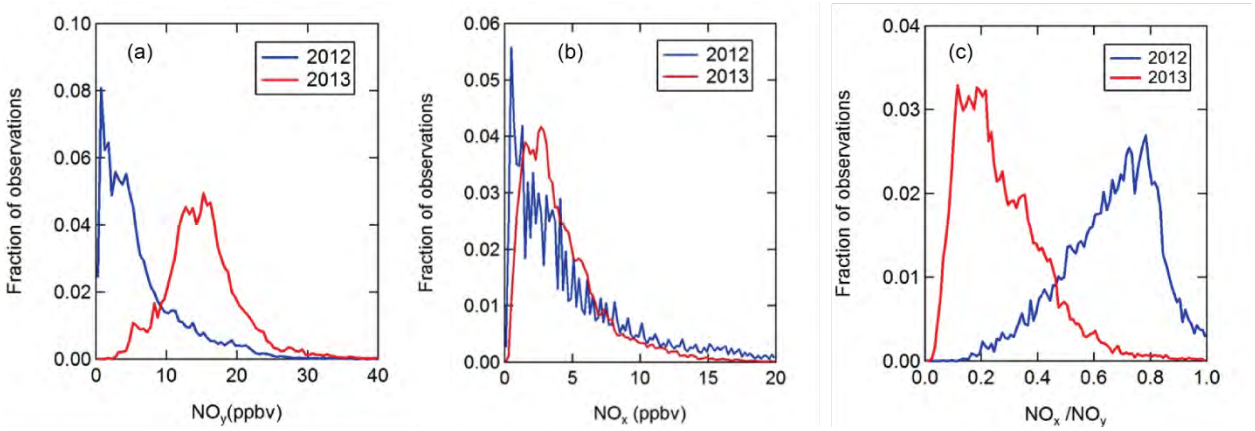


**5-8a-c. The distributions of (a) total $NO_y$, (b) $NO_x$, and (c) the ratio $NO_x/NO_y$. The UBOS 2012 data are in blue and the UBOS 2013 data are in red.**

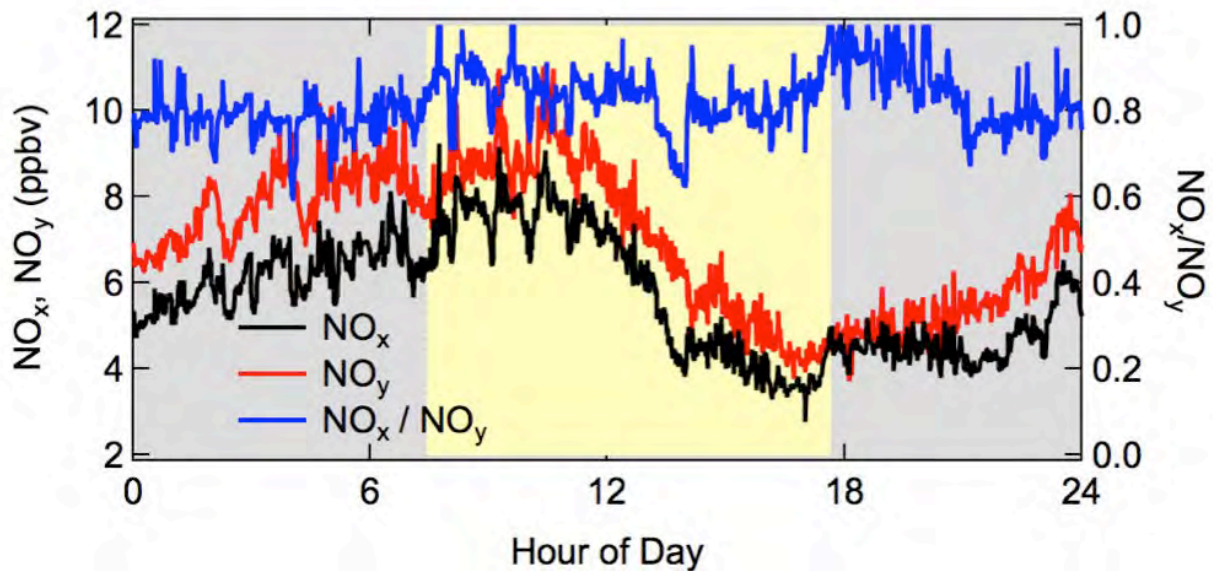


**5-9. Diurnal plot of $NO_x$, $NO_y$ and $NO_x/NO_y$ measured during the 2012 campaign.**

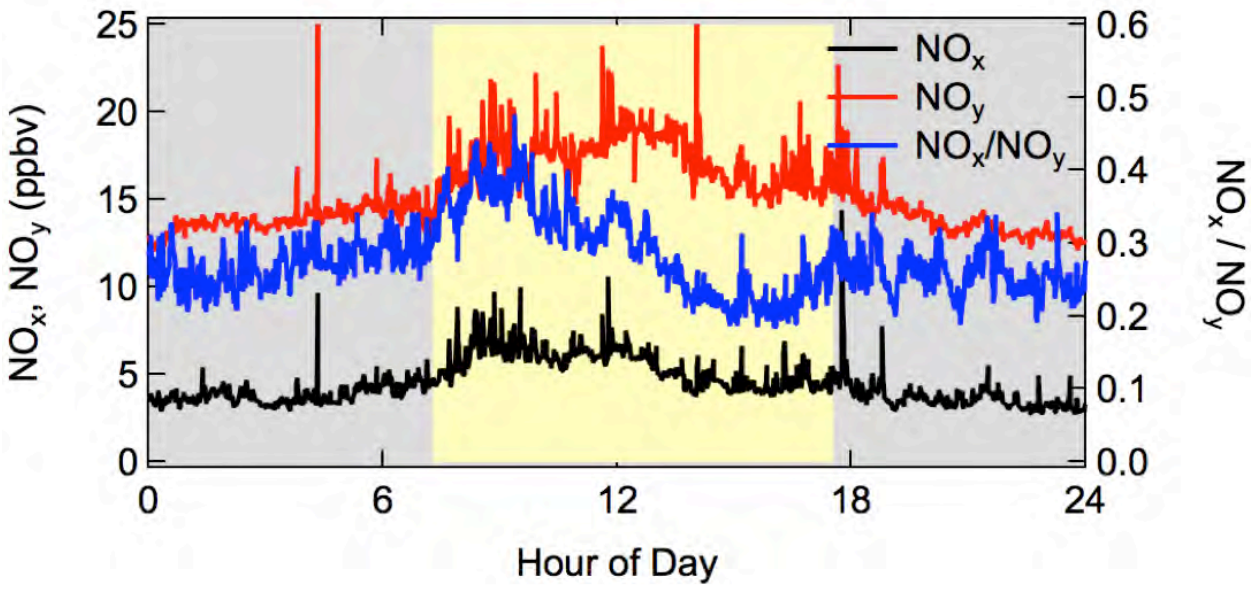


**5-10. Diurnal plot of $NO_x$, $NO_y$ and $NO_x/NO_y$ measured during the 2013 campaign.**

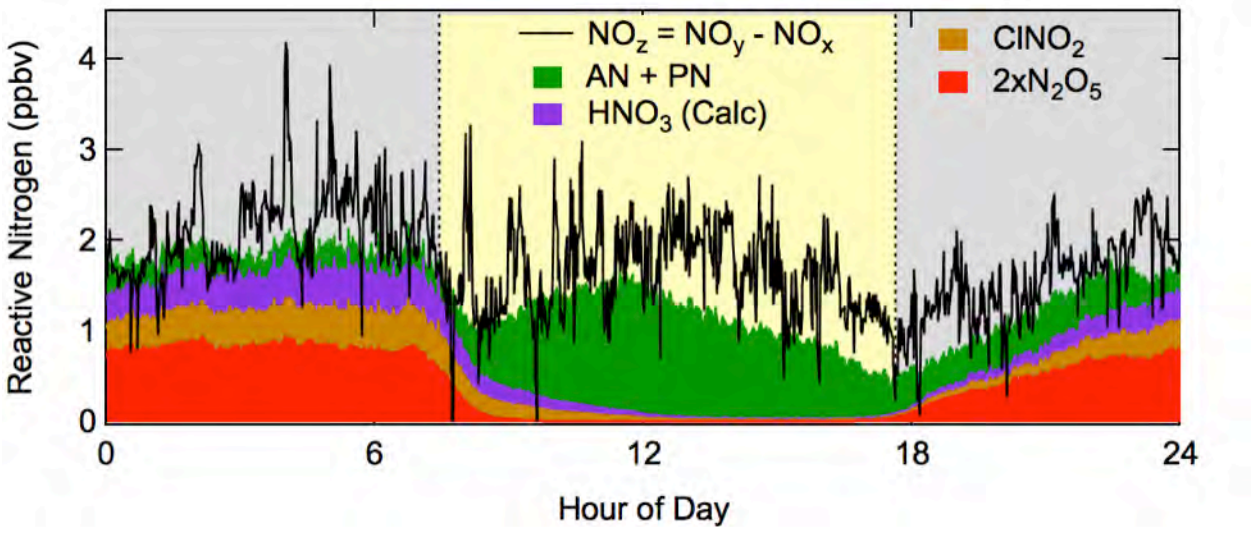


**5-11. The average diurnal composition of $NO_z$ measured during the UBOS 2012 campaign. NOx is in black, NOy is in red and the ratio NOx/NOy is in blue.**

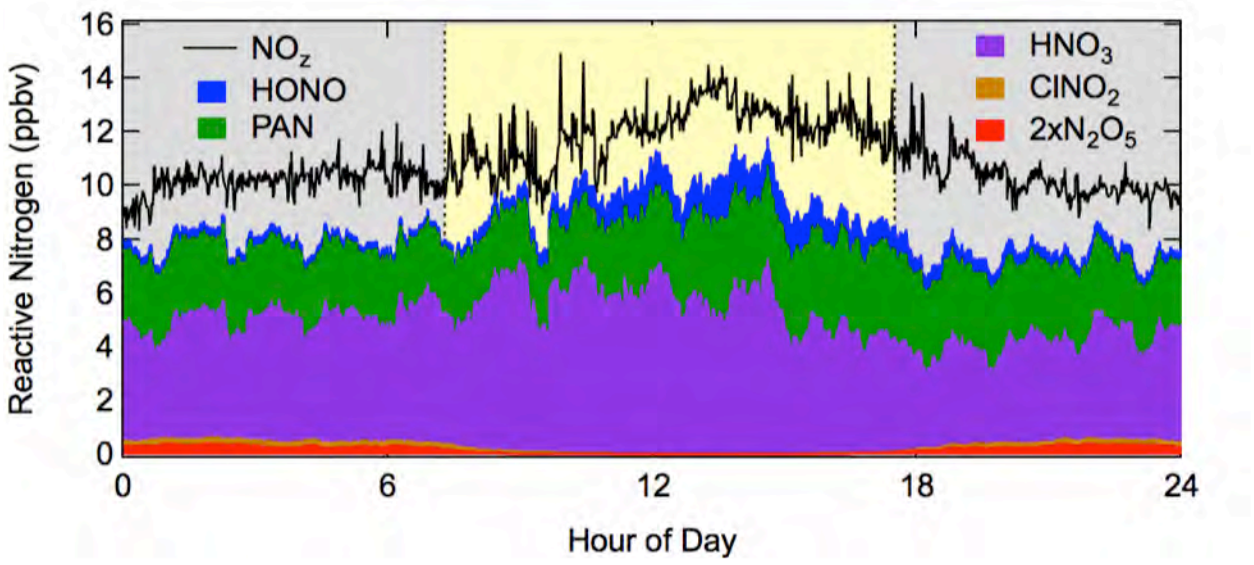


**5-12. The average diurnal composition of $NO_z$ measured during the UBOS 2013 campaign. NOx is in black, NOy is in red and the ratio NOx/NOy is in blue.**

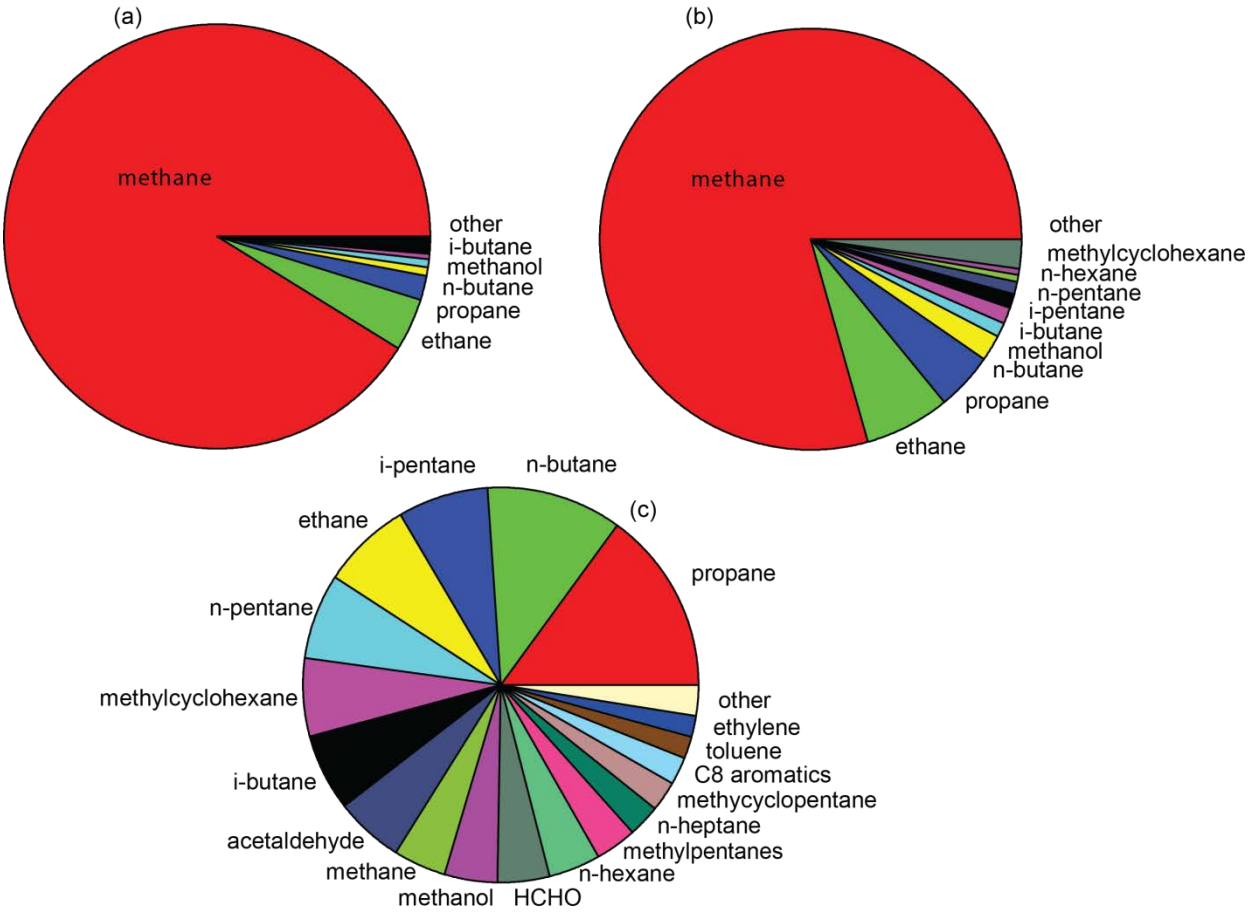


**5-13. VOC composition by molar abundance (volume) (A) and mass (B), and OH reactivity (C) measured during UBOS 2013.**

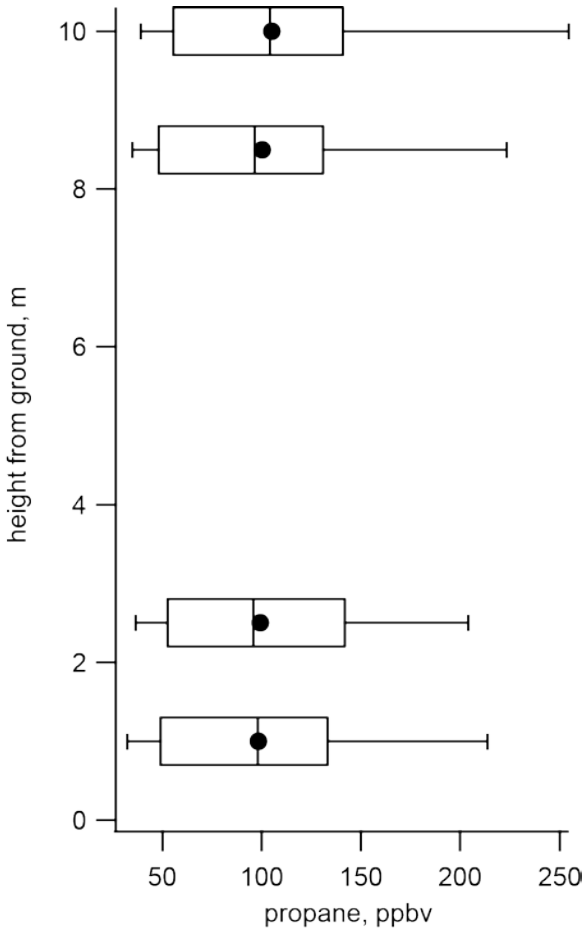


**5-14. Propane measured as a function of inlet height during the periods of height profiling.**

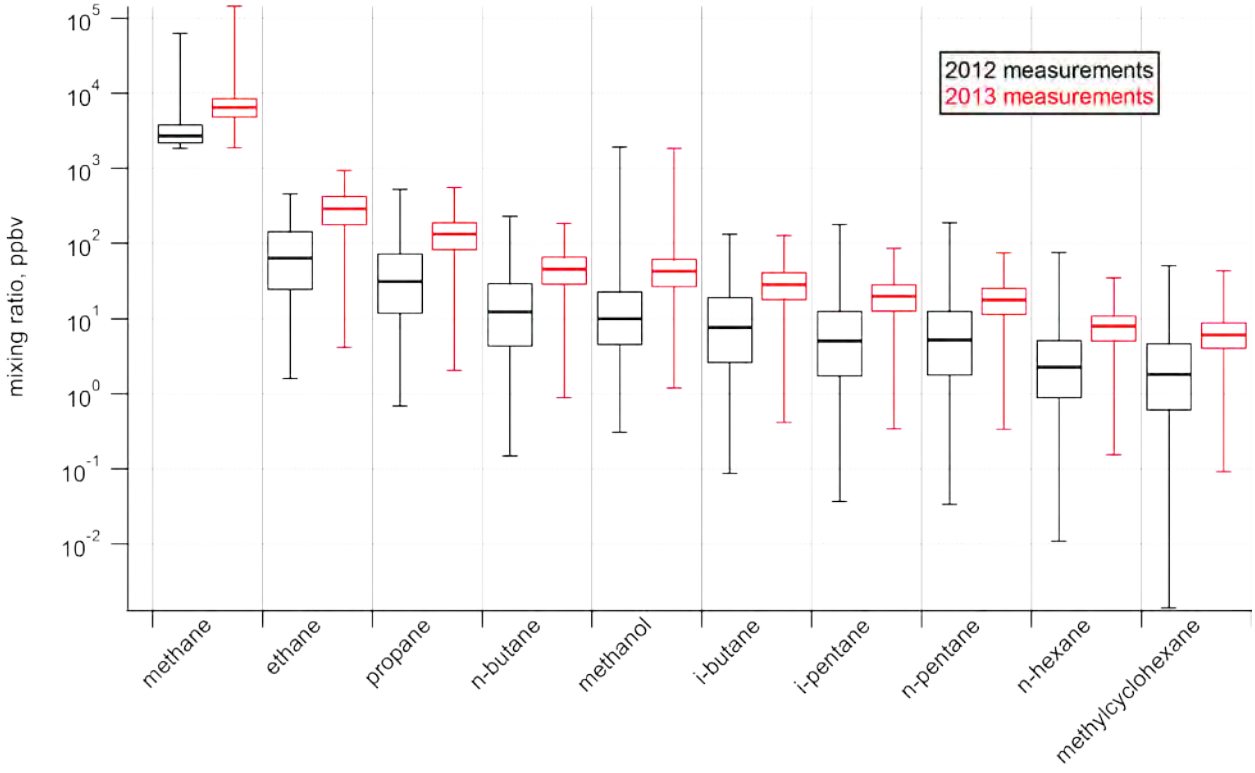


**5.15. Comparison between UBOS 2012 (black) and UBOS 2013 (red) of the absolute mixing ratios of compounds with the highest concentrations.**

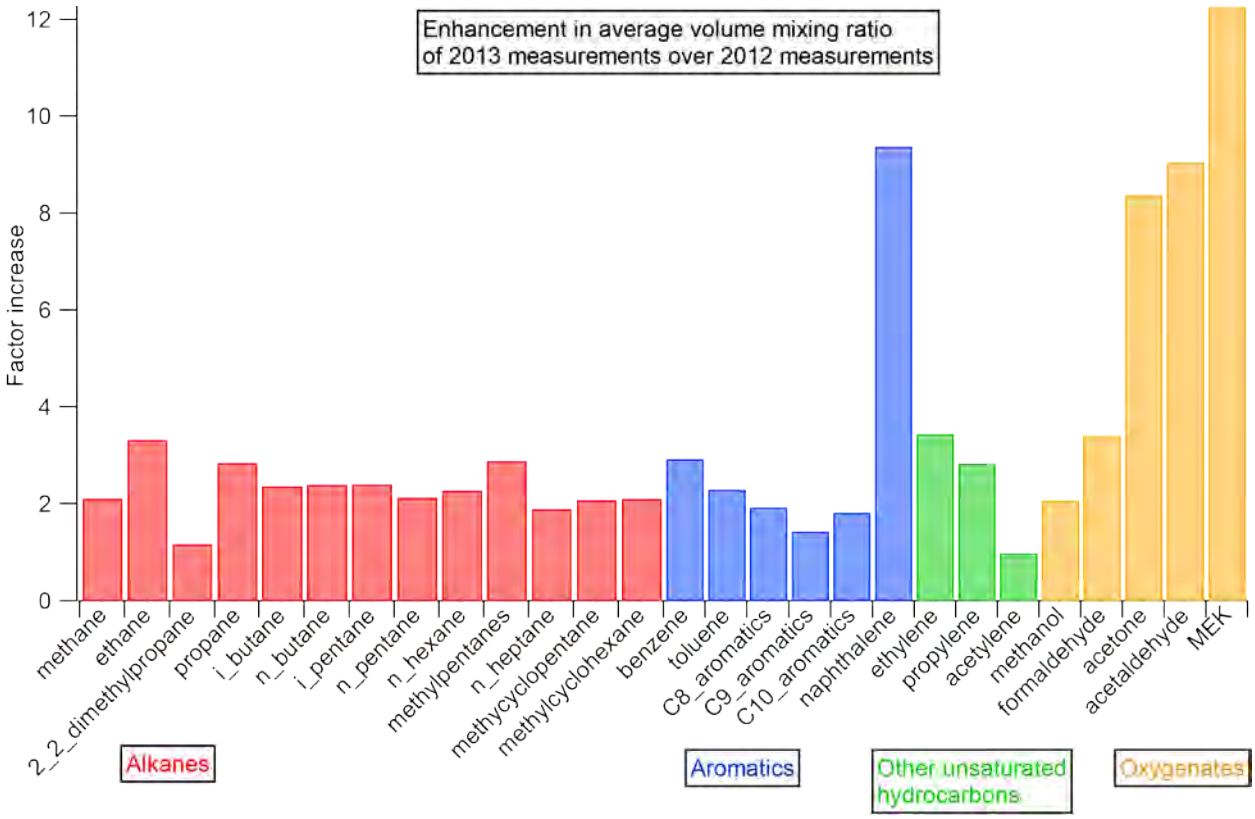


**5-16. The fractional increase from 2012 to 2013 of all measured VOCs.**

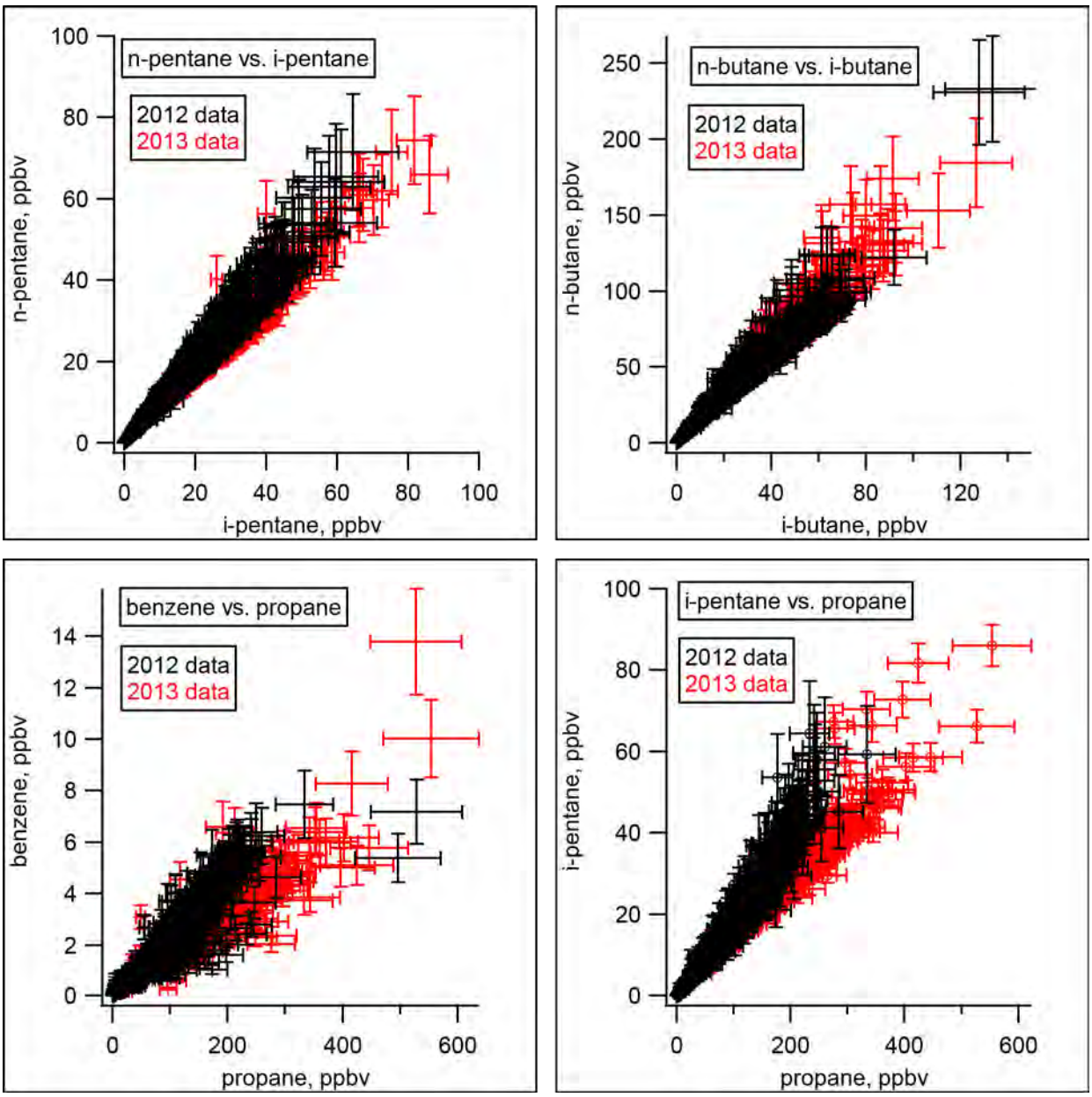


**5-17. Ratios of iso-to n-butane, iso- to n-pentane, and benzene and i-butane to propane, for 2012 and 2013. The black symbols are for 2012 and the red symbols are for 2013, and the error bars are 1s of the measured data.**

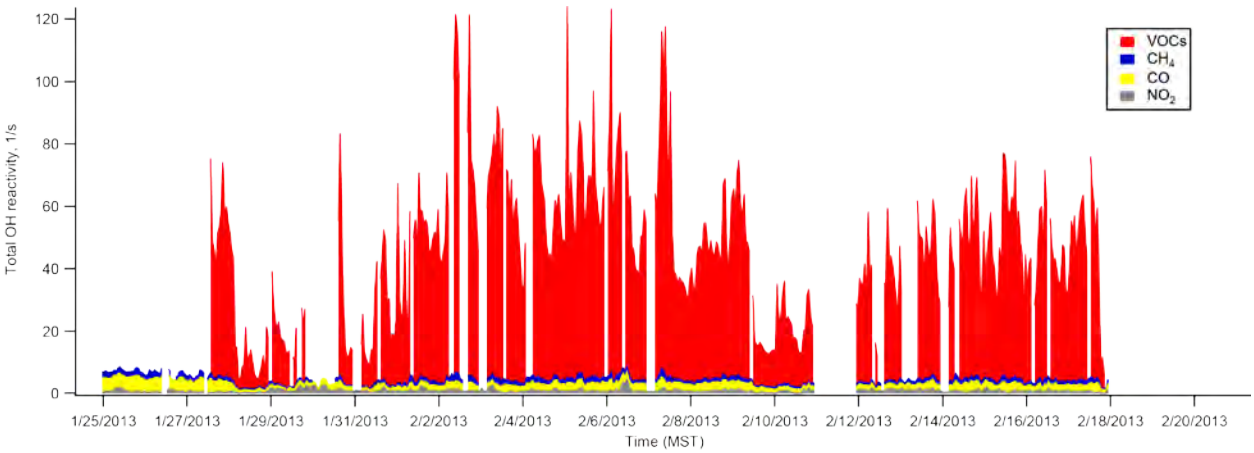


**5-18. Time series of total OH reactivity of VOCs (red), methane (blue), carbon monoxide (yellow) and $NO_2$ (grey).**

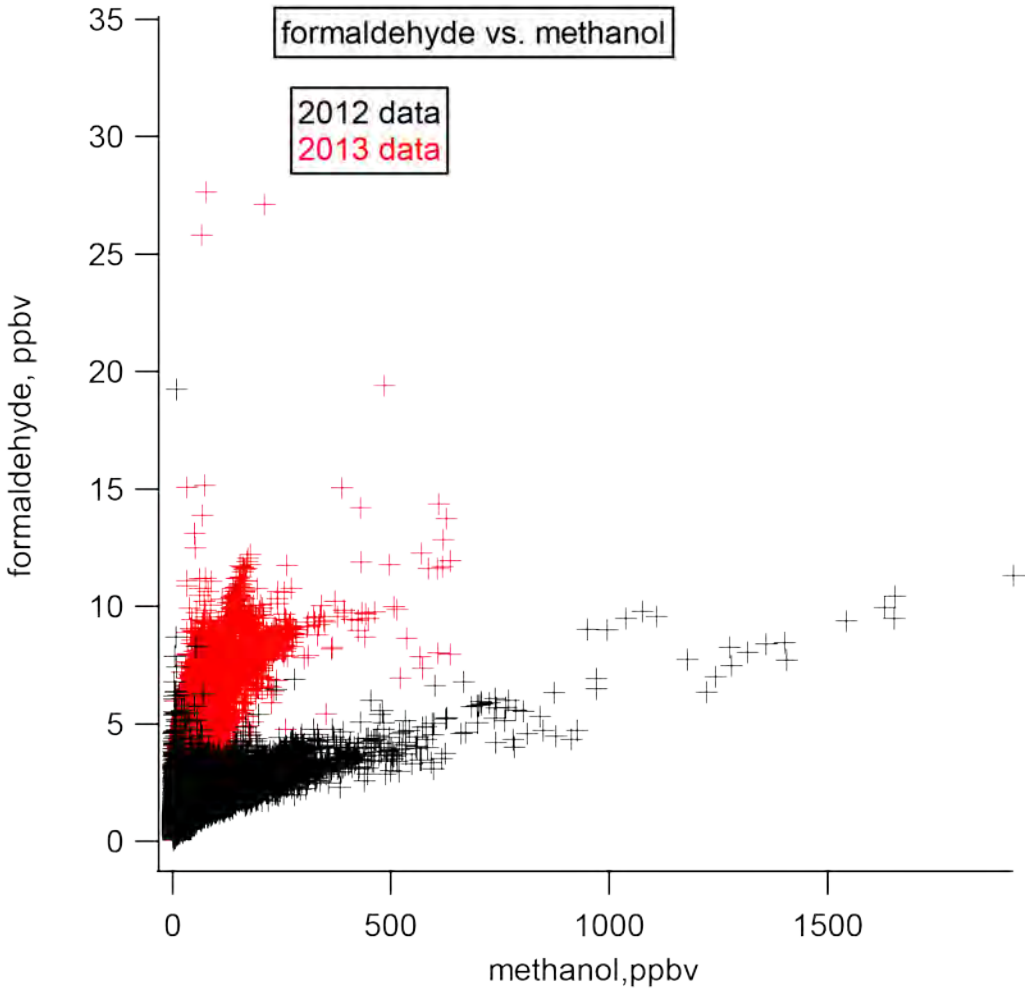


**5-19. The relationship between formaldehyde and methanol for both 2012 (black) and 2013 (red).**

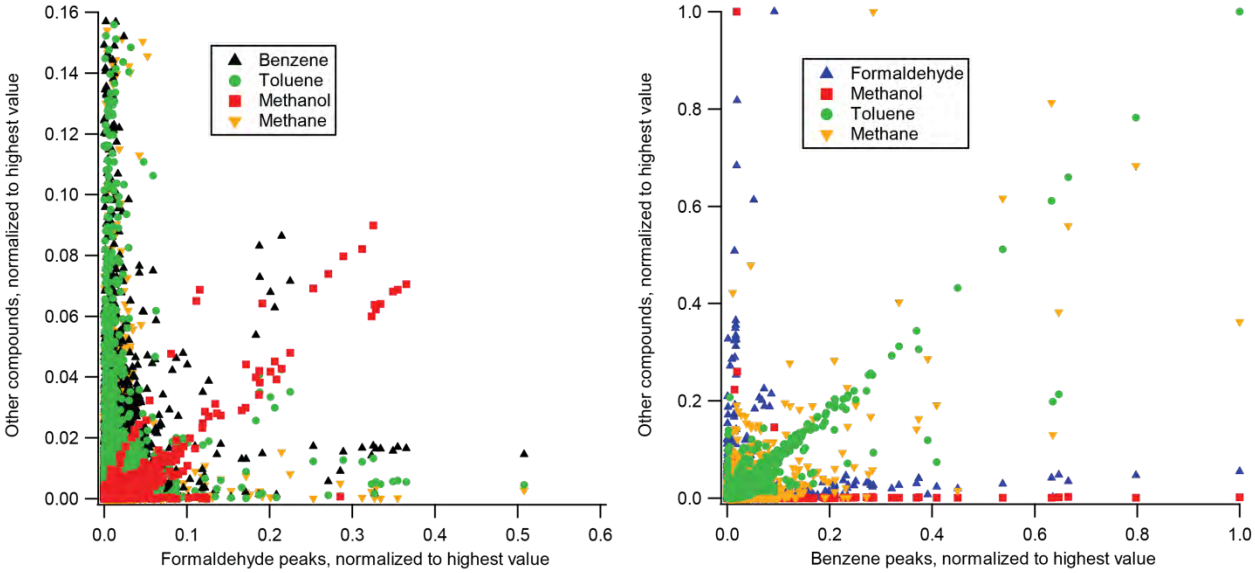


**5-20. Correlations of marker compounds to (a) Formaldehyde, and (b) Benzene.**

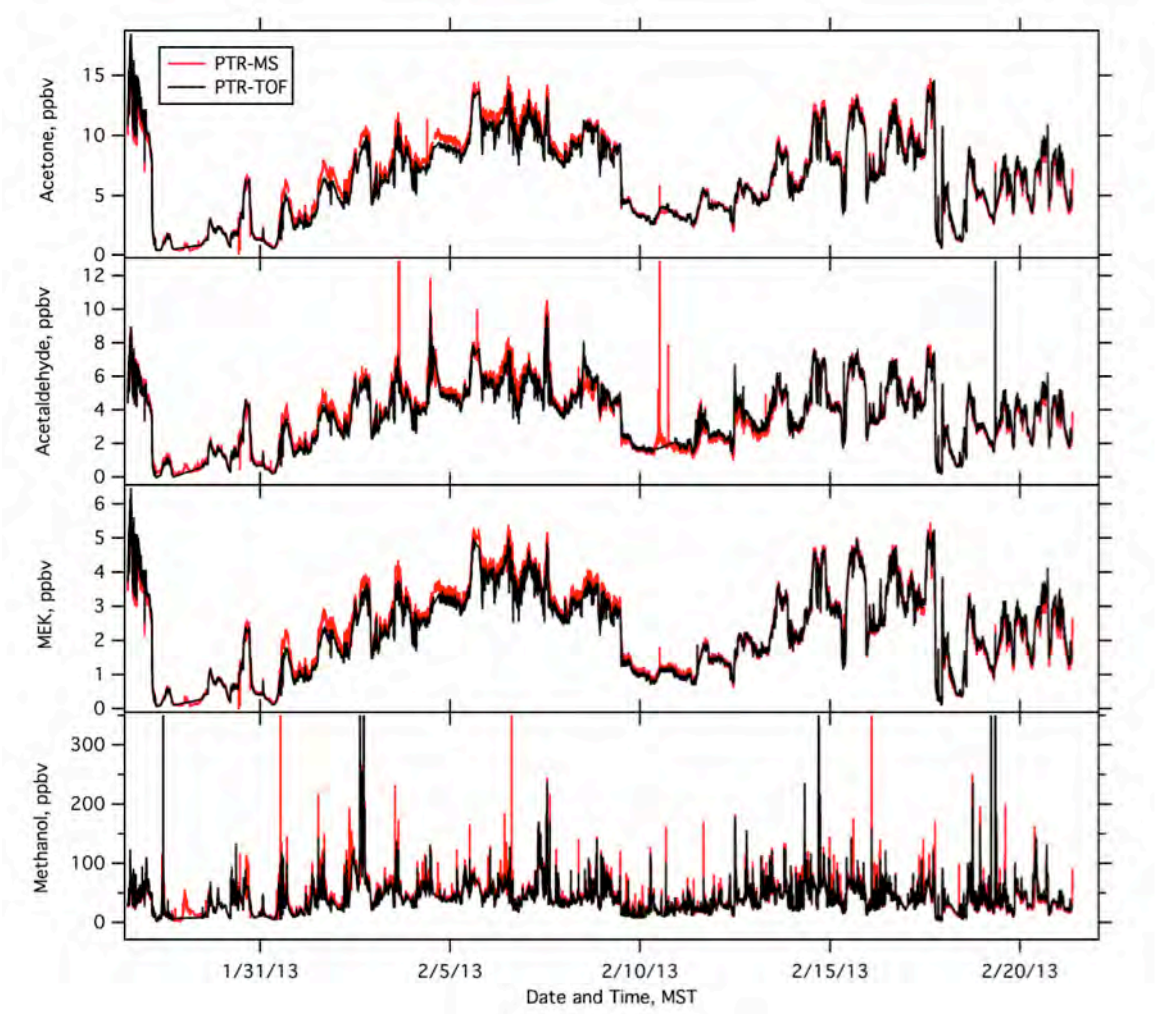


**5-21. Time series of PTR-TOF-MS (black) and PTR-MS (red) VOC measurements made during the UBOS 2013 intensive period. The top three measurements (acetone, acetaldehyde, and methyl ethyl ketone (MEK)) are photochemically produced secondary pollutants formed throughout an ozone event. Methanol (bottom panel) is more indicative of a local emitted primary pollutant.**

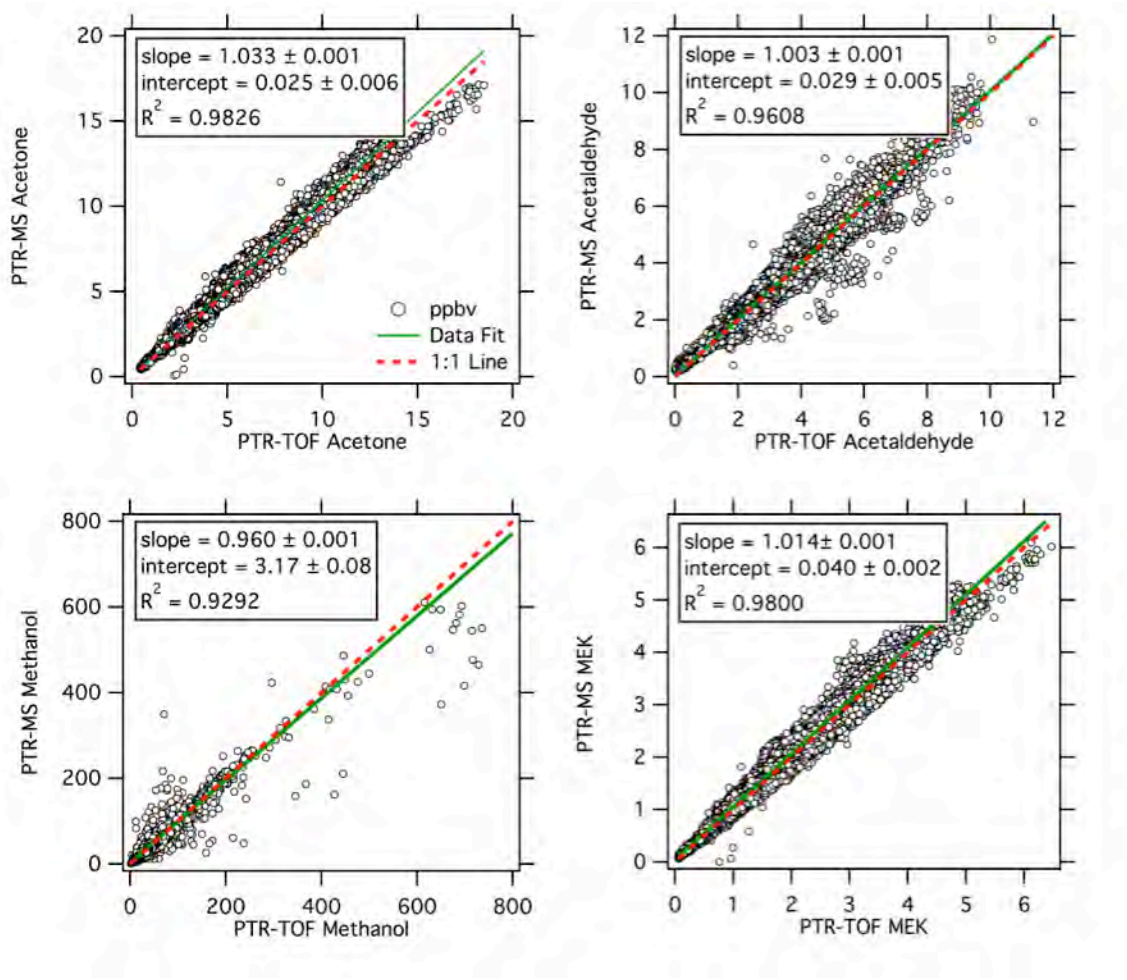


**5-22. Linear regression plots of the PTR-MS and PTR-TOF VOC data collected during the UBOS 2013 intensive period and shown in Figure 1. These measurement techniques show agreement to within 5% for all of the VOC species quantified by both instruments.**

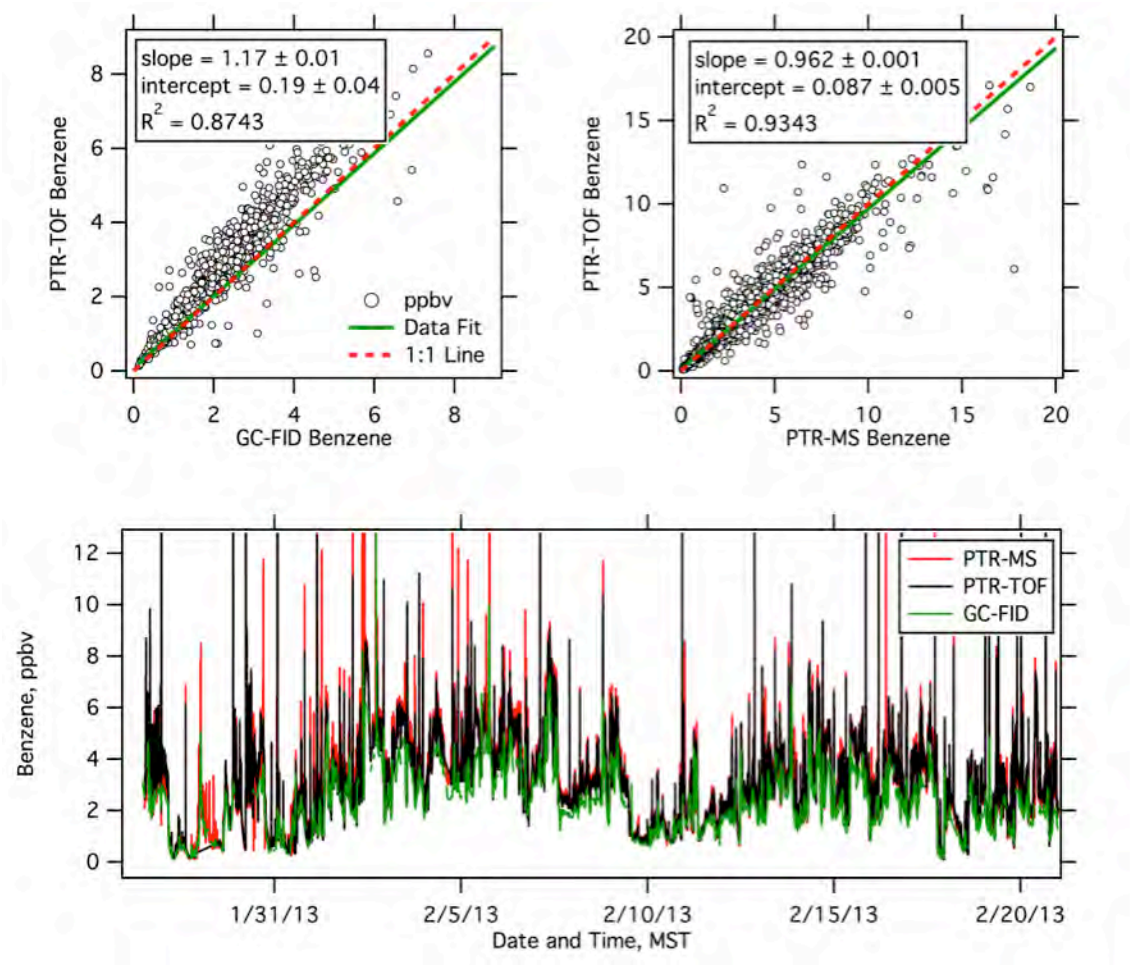


**5-23. A comparison of PTR-TOF-MS, PTR-MS, and GC-FID measurement of benzene during the UBOS 2013 intensive period. The top two panels show linear regression fits of the PTR-TOF to GC-FID (left) and the PTR-TOF to PTR-MS (right) for the data shown in the time series provided in the bottom panel.**

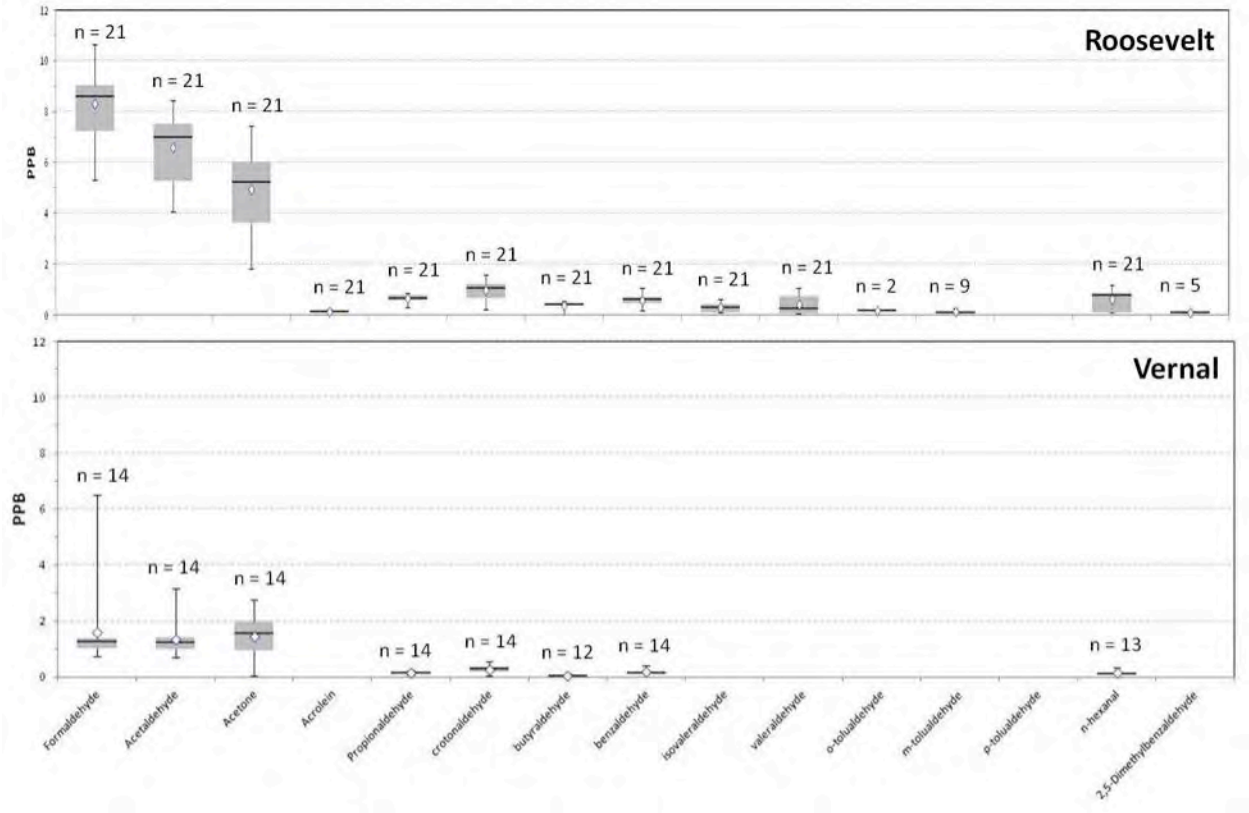


**5-24. Box-whisker plots carbonyl compounds as measured at Roosevelt and Vernal (Feb. 13-25, 2013). The "n" indicates the number of times a particular compound was identified (21 total samples from Roosevelt, 14 total from Vernal).**

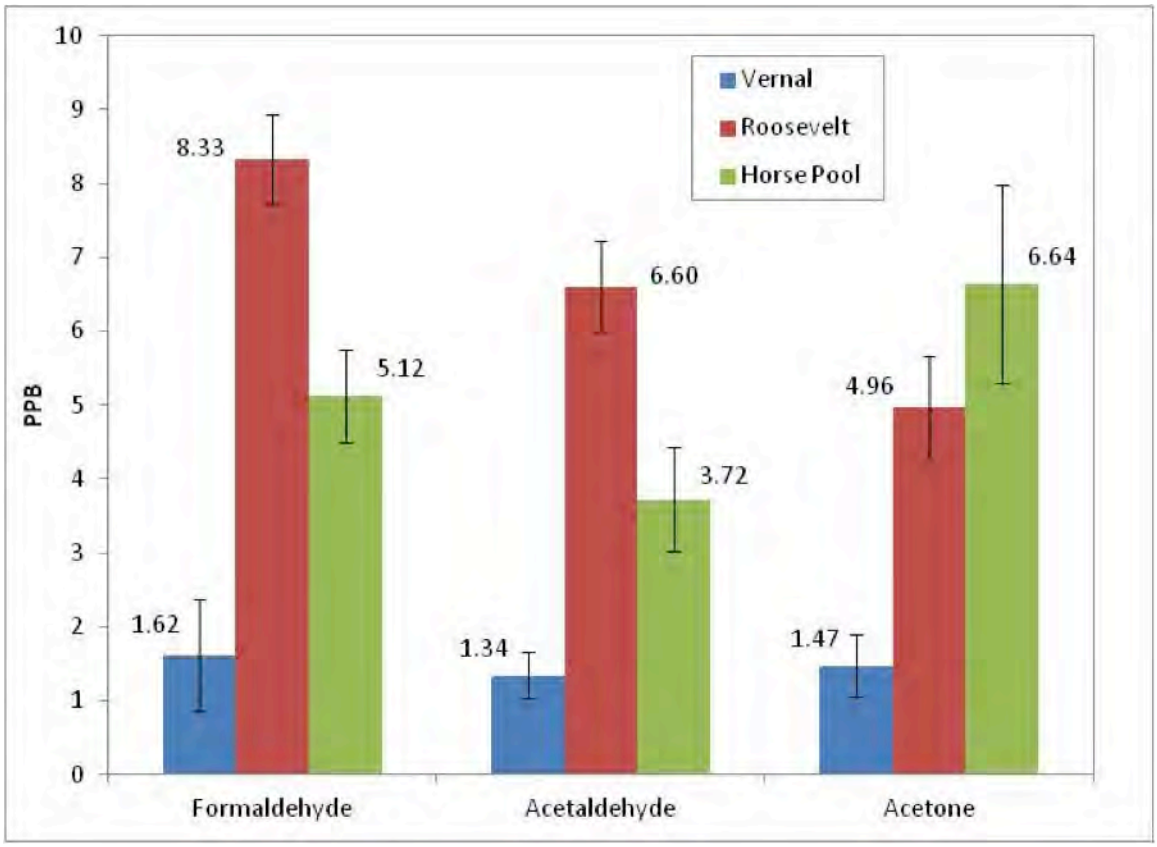


**5-25. Comparison of average ambient formaldehyde, acetaldehyde, and acetone from Roosevelt, Vernal, Horse Pool-NOAA (Feb. 13-25, 2013). The error bars represent the 95% confidence intervals.**

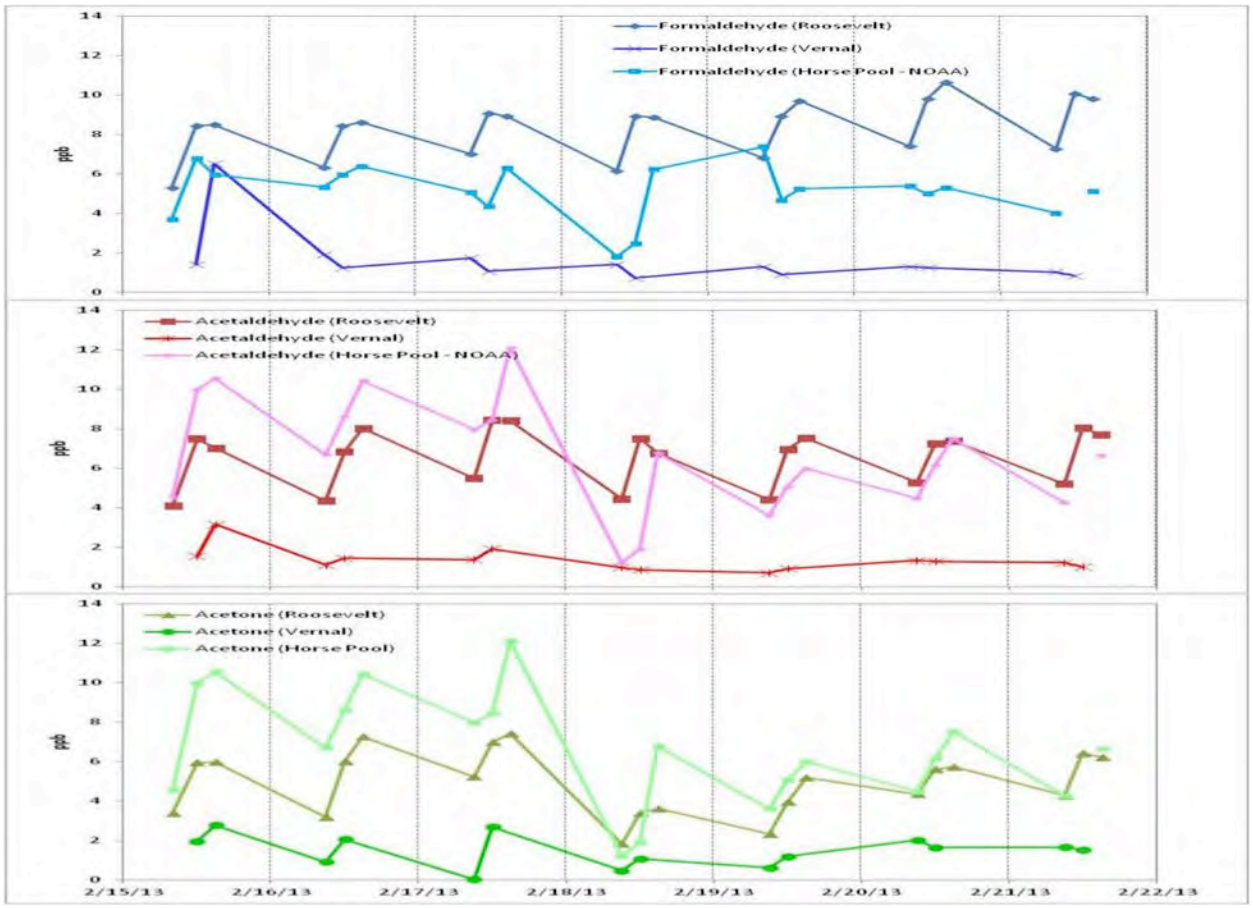


**5-26. Diurnal, time series plots for formaldehyde, acetaldehyde, and acetone as measured at Roosevelt, Vernal and Horse Pool-NOAA (Feb. 13-25, 2013).**

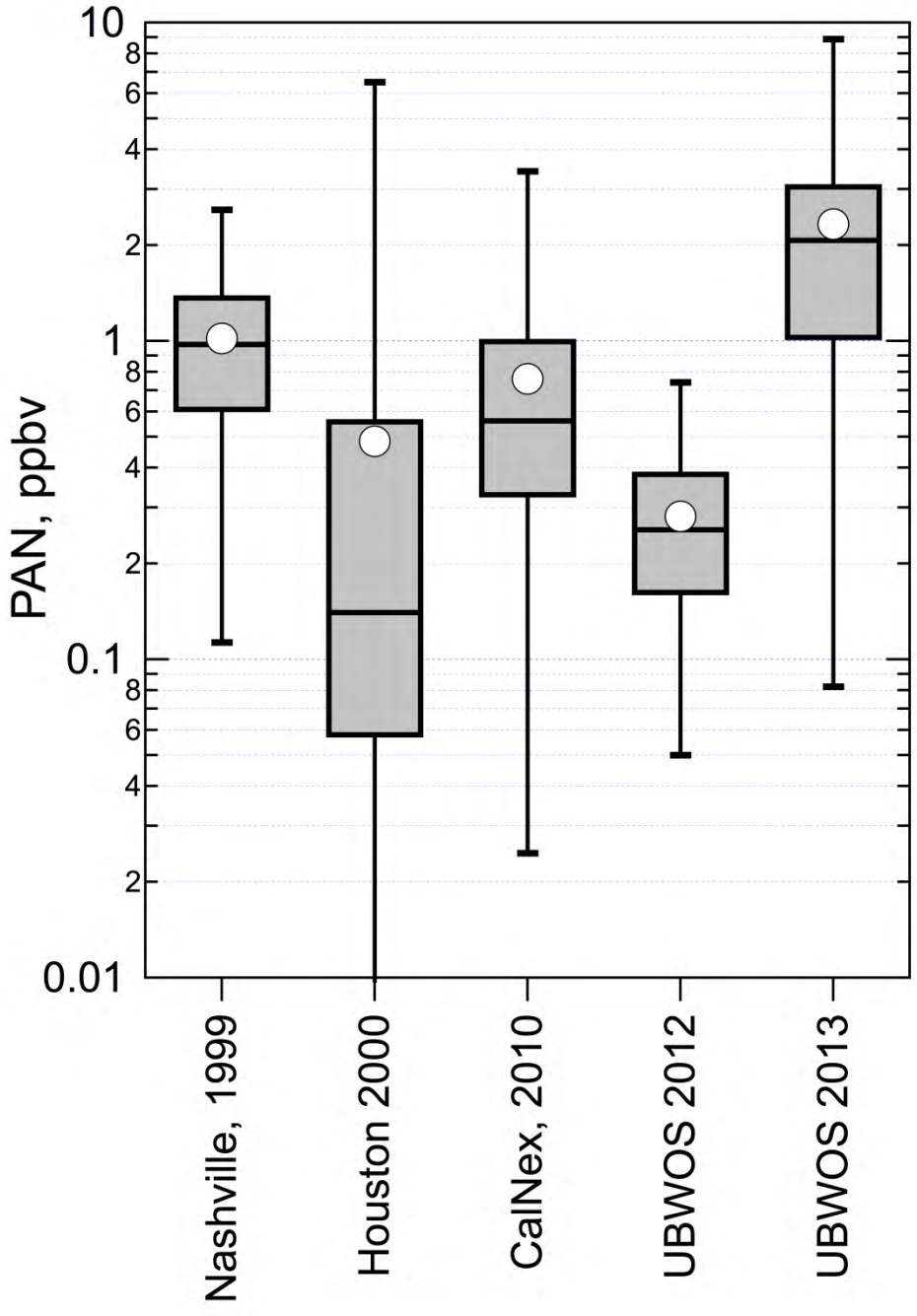


**5-27. Distributions of PAN measurements for the two UBOS studies along with 3 other ground-based studies.**

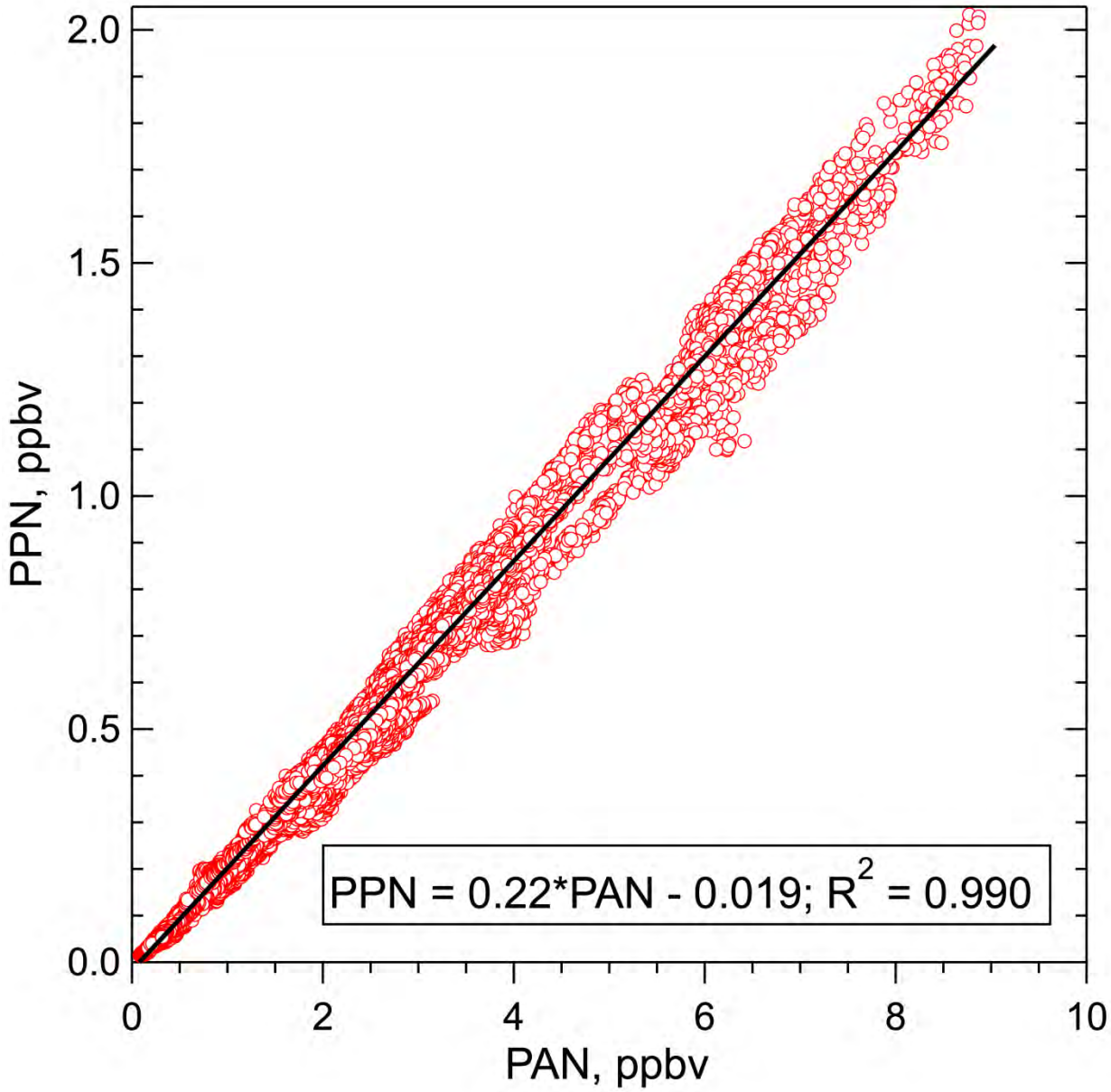


**5-28. The correlation of PPN with PAN observed during the UBOS 2013 intensive.**

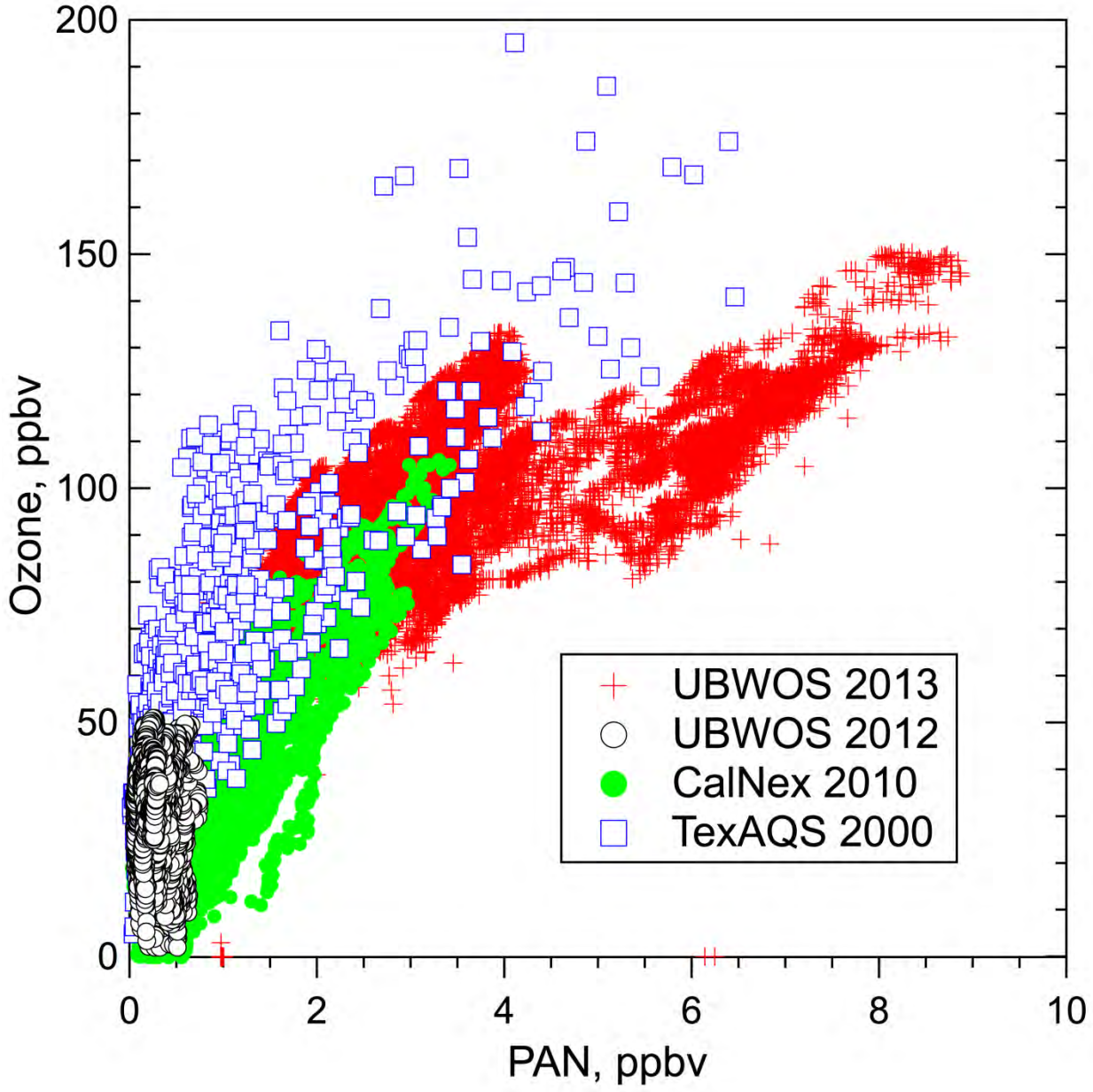


**5-29. The correlation of $O_3$ with PAN for UBOS 2012 (open black circles), UBOS 2013 (red crosses), TexAQS 2000 (open blue squares ) and CalNex 2010 (solid green circles).**

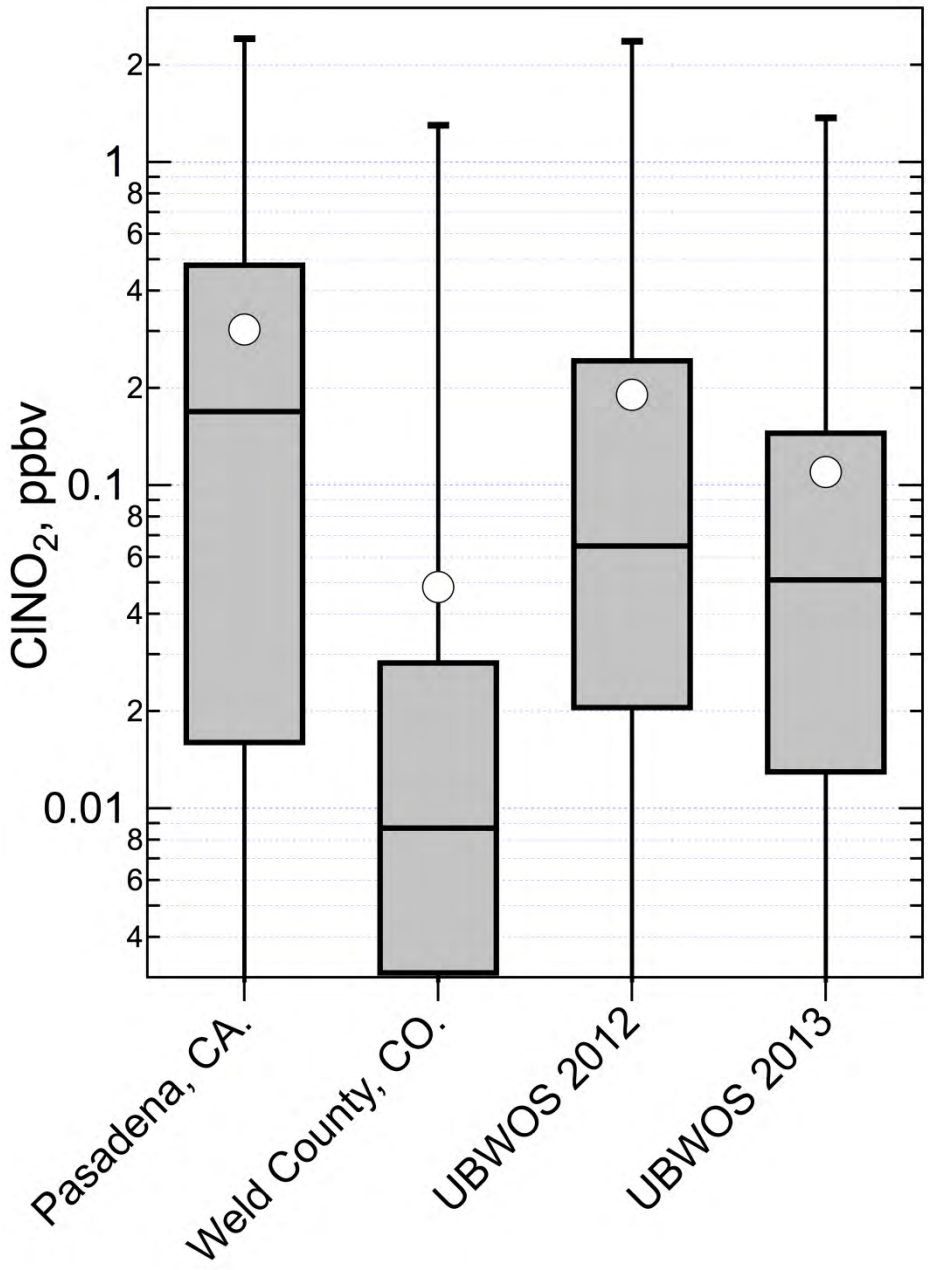


**5-30. Distributions of $ClNO_2$ measurements for the two UBOS studies along with 2 other ground-based studies.**

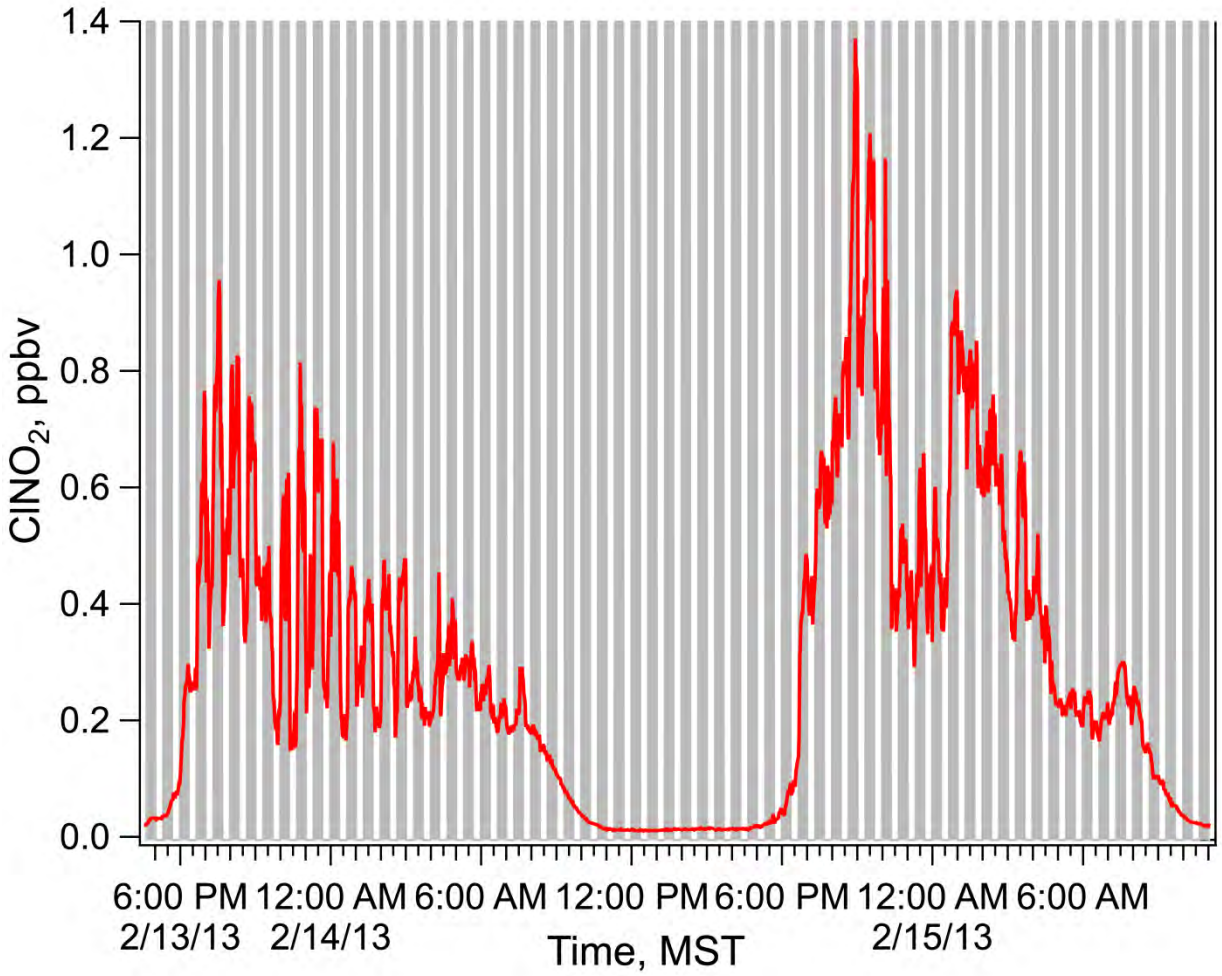


**5-31. Gradients in $ClNO_2$ mixing ratio during the inlet profiling experiment. The grey bands denote when the inlet was at the upper height (7.25 m).**

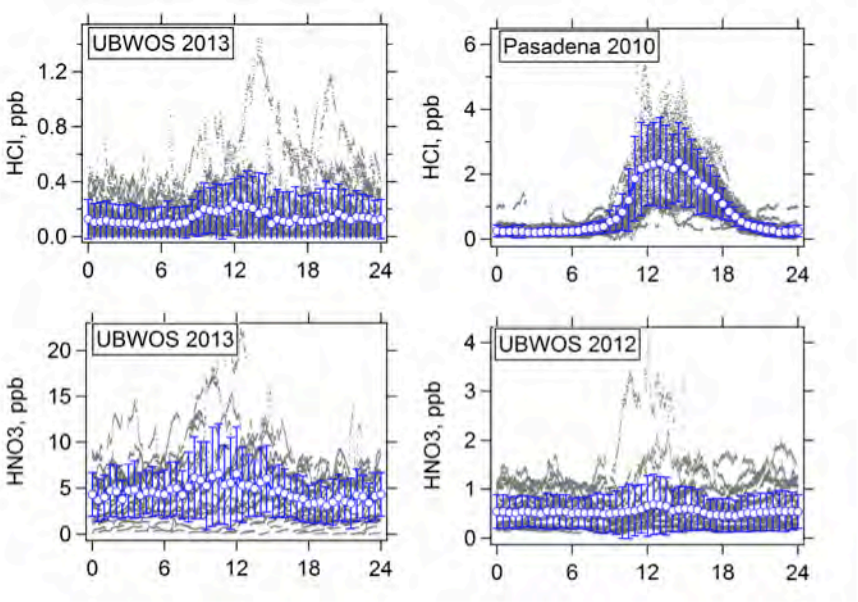


**5-32. Diurnal variations of HCl and $HNO_3$ in 2012 and 2013 at Horse Pool.**

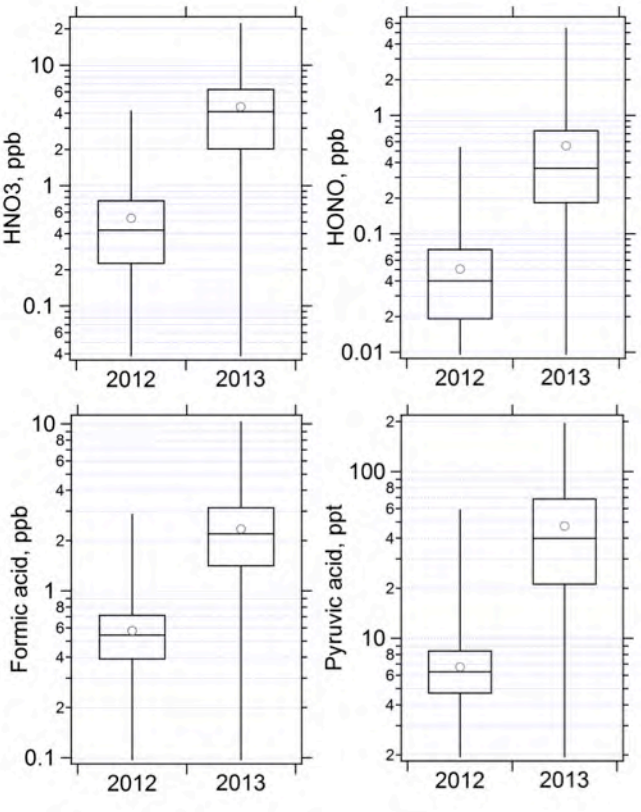


**5-33. Comparison of the measured concentration of $HNO_3$, HONO, formic acid and Pyruvic+butyric acid between 2012 and 2013 at Horse Pool.**

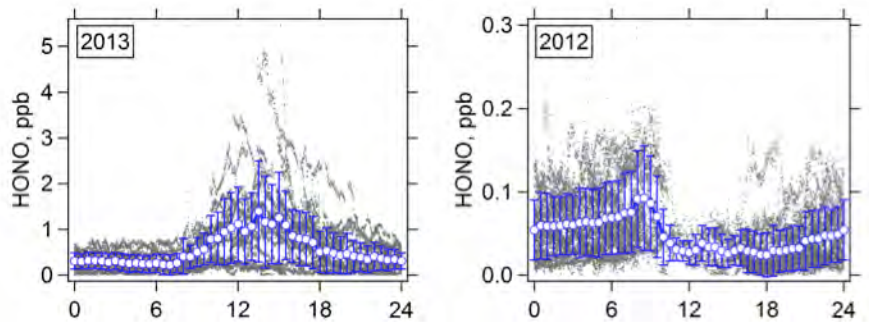


**5-34. Diurnal variations of HONO in 2012 and 2013 at Horse Pool.**

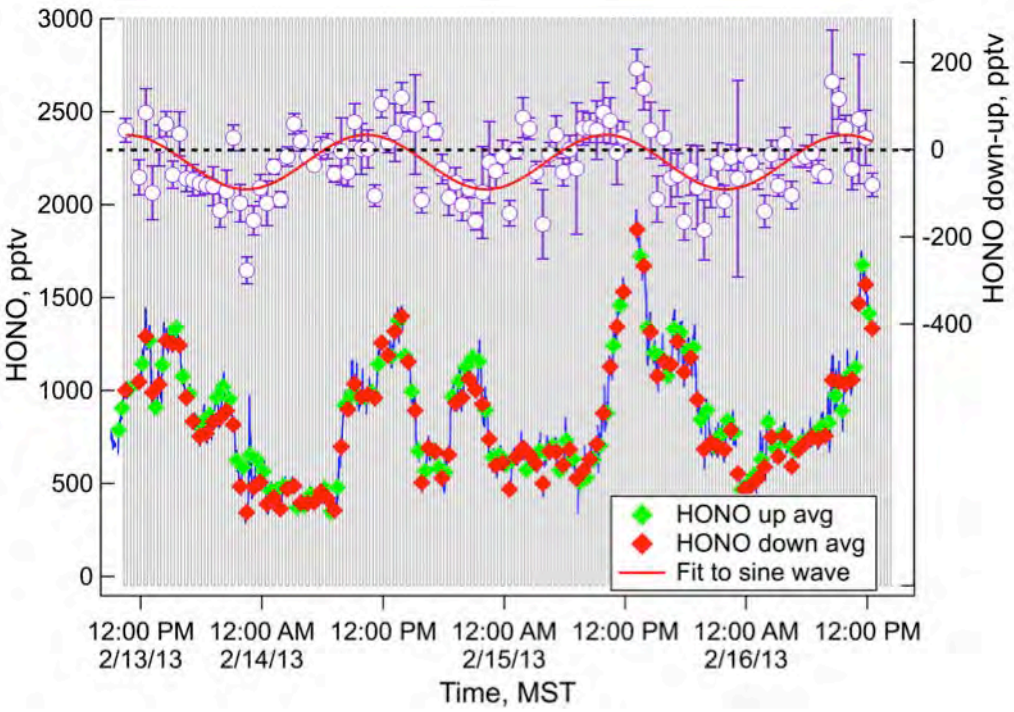


**5-35. Measured HONO during the period when the inlet height was switching between 1m and 7.25 m (grey line). The blue line is the 1 minute average HONO, and the green and red points are the 20 minute averaged HONO measured while the inlet was up, or down, respectively. The difference between the HONO measured with the inlet down and the HONO measured with the inlet up interpolated between measurements is shown in the open purple circles with one standard deviation of the down measurement average shown as error bars.**

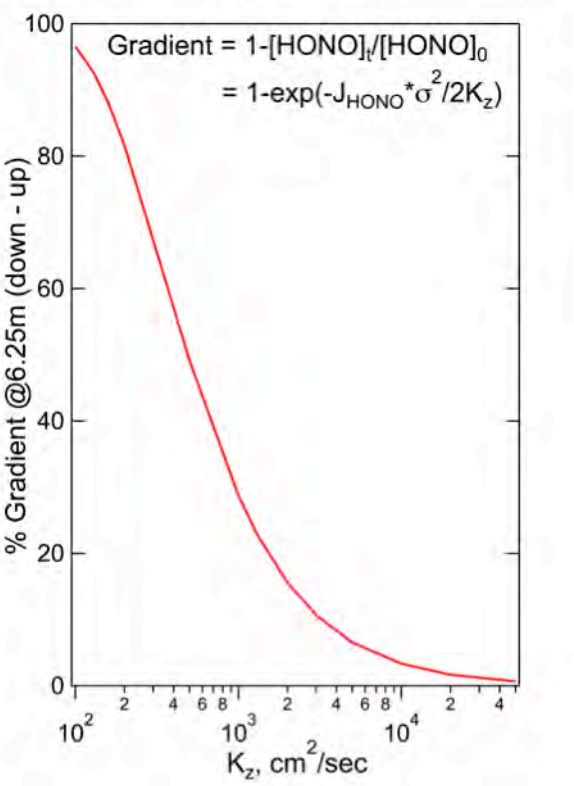


**5-36. The percent gradient for a ΔH of 6.25m, calculated as a function of eddy diffusivity, $K_z$, based on an average photolysis rate of 0.0016 $sec^{-1}$.**

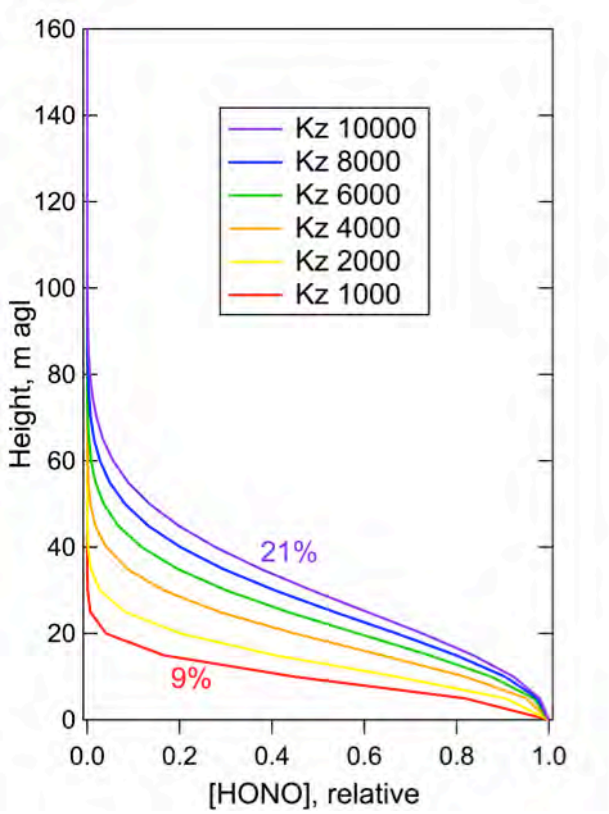


**5-37. Concentration profiles predicted for the range of $K_z$ that corresponded to gradients of ~0 to 15% as shown in Figure 5-36.**

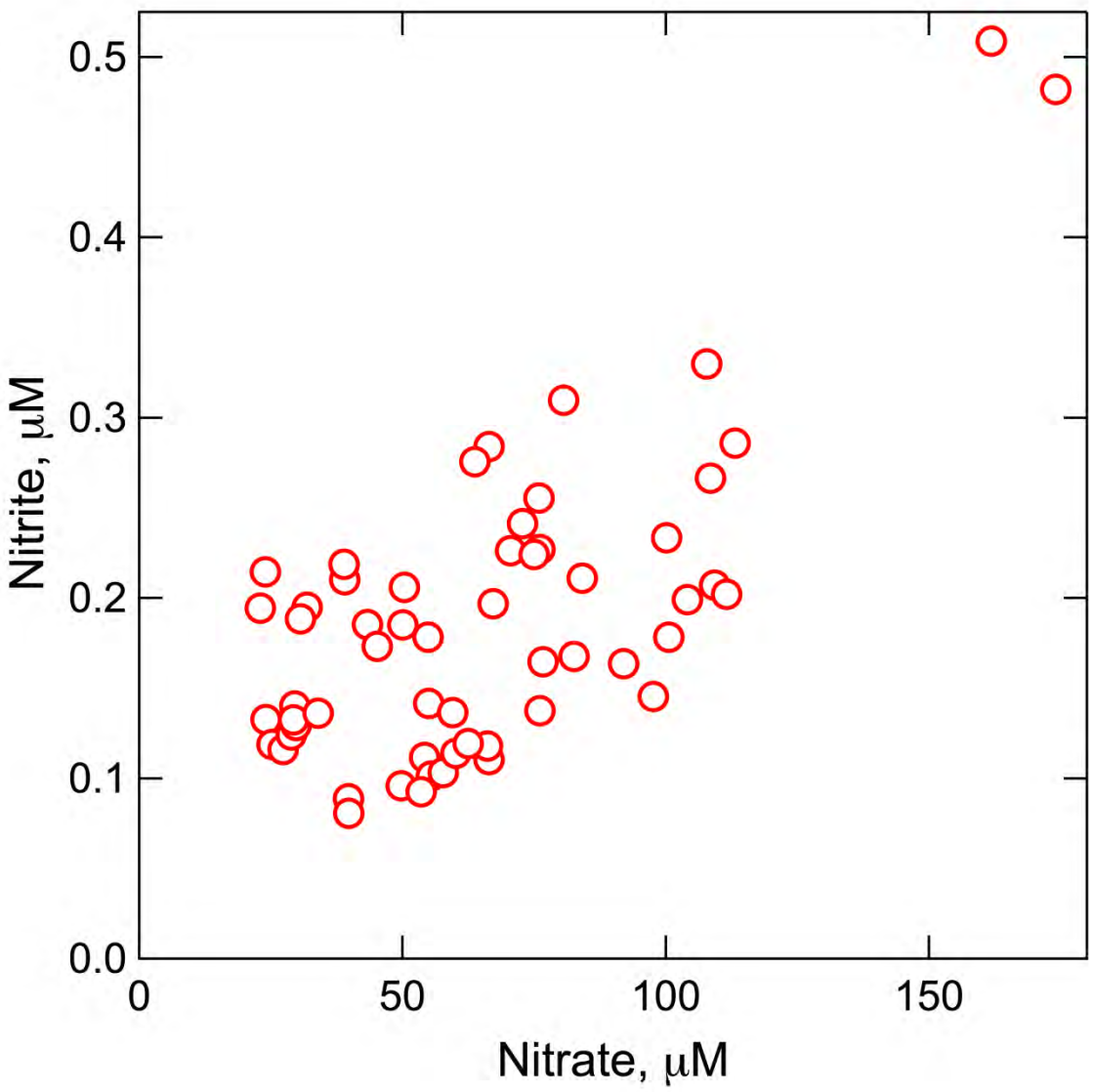


**5-38. The concentration of nitrite in the top layer of snow, versus the concentration of nitrate.**

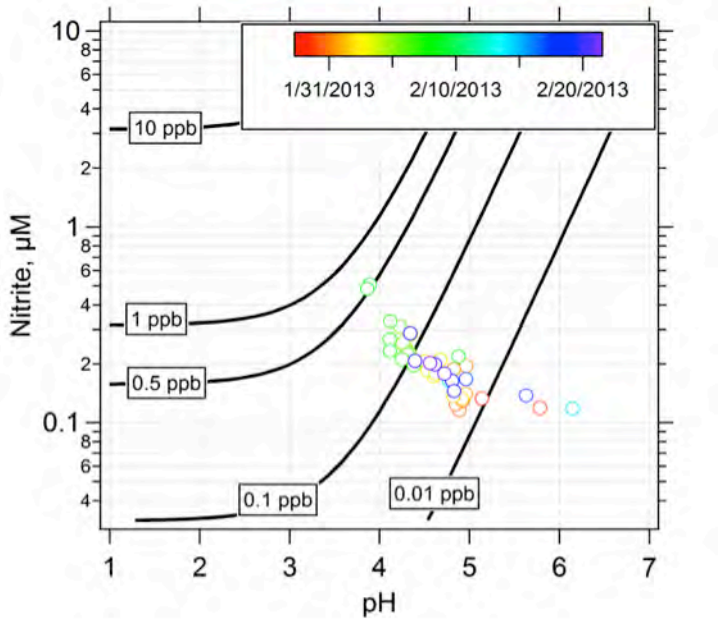


**5-39. The dependency of equilibrium gas phase HONO (HONO*) with pH value and nitrite concentration in the snow. The contour lines are calculated at 268 K (assuming the presence of a liquid layer), which is a regular value for ambient temperature at noon time at Horse Pool site. The circles in the graph represent the measured snow results near Horse Pool site. The circles are color-coded with measurement time.**

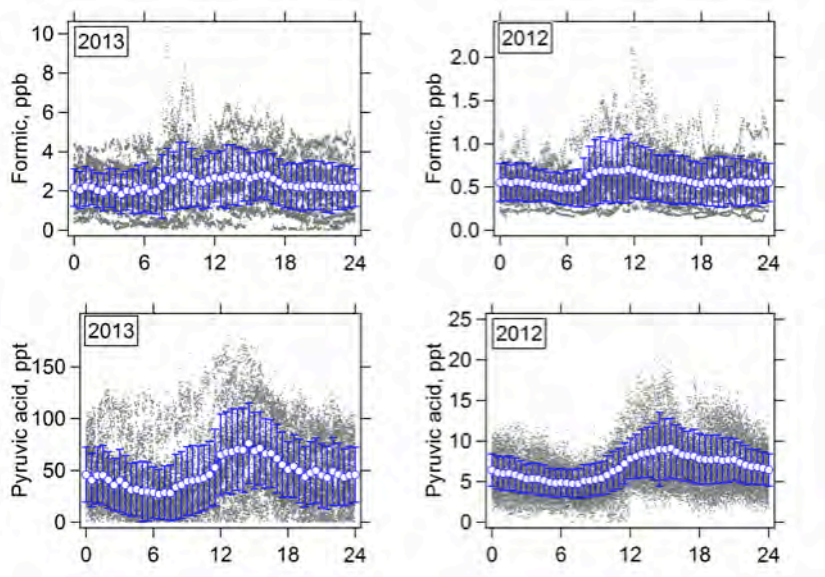


**5-40. Diurnal variations of formic acid and pyruvic+butyric acid in 2012 and 2013 at Horse Pool.**

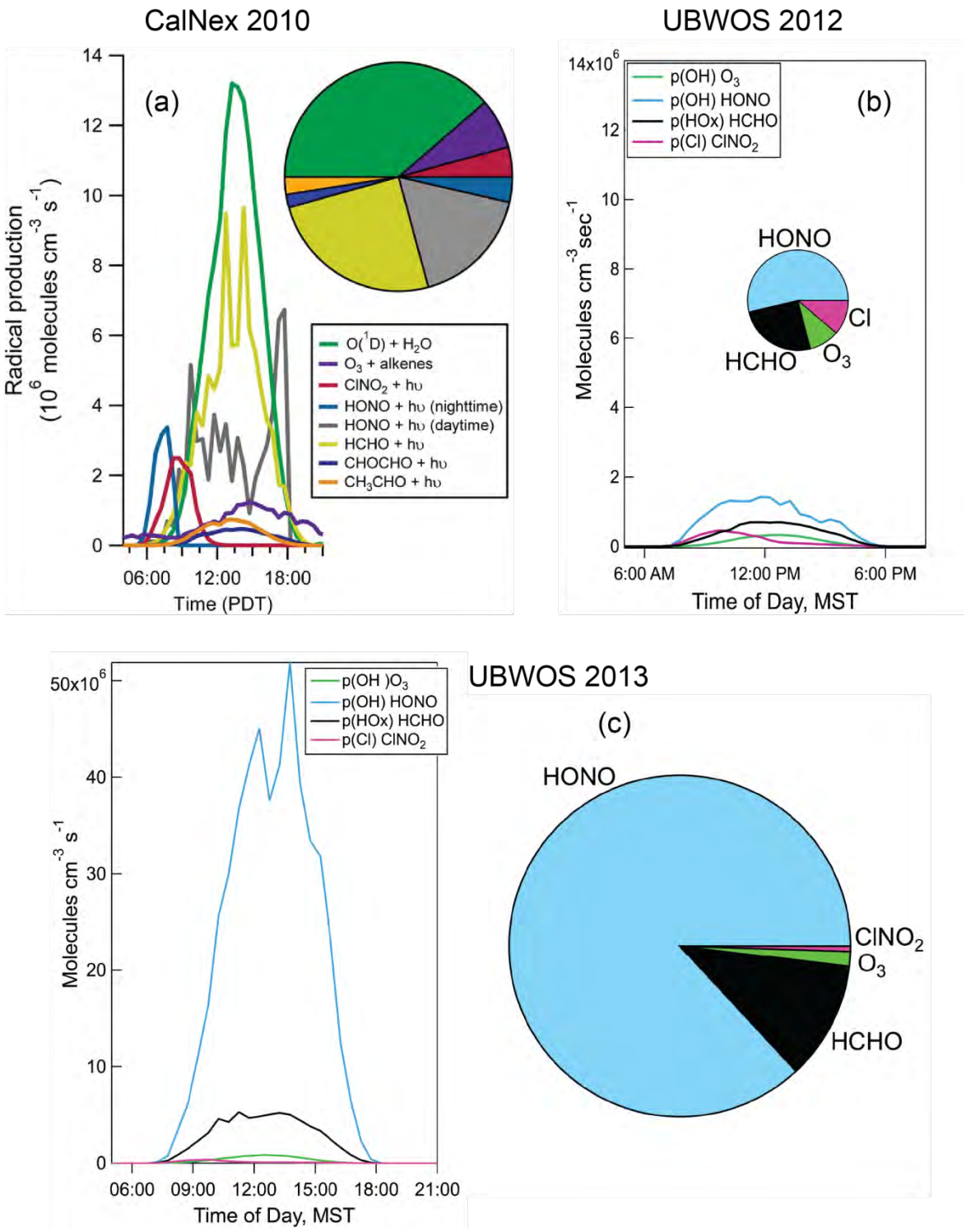


**5-41. Summaries of the radical sources found during (a) CalNex2010, (b) UBOS 2012, and (c) UBOS 2013. Note that the CalNex and UBOS 2012 results are on the same scale, and the areas of the pie charts are scaled to the total of the radical sources.**

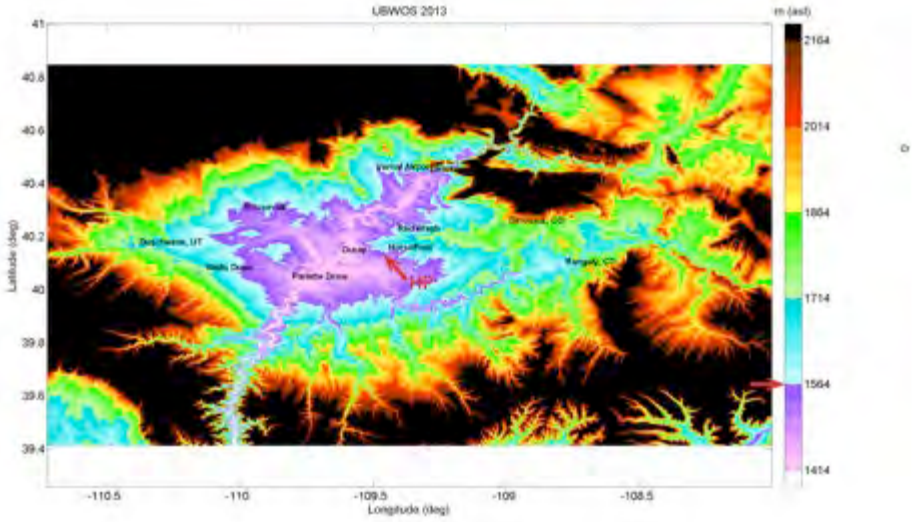


**5-42. Terrain contour map of Uinta Basin region with color scale adjusted to emphasize the nature of the Basin topography. Color scale is adjusted so that elevation of the Horse Pool site (HP: red arrow on map) falls between purple and blue colors (red arrow on color bar).**

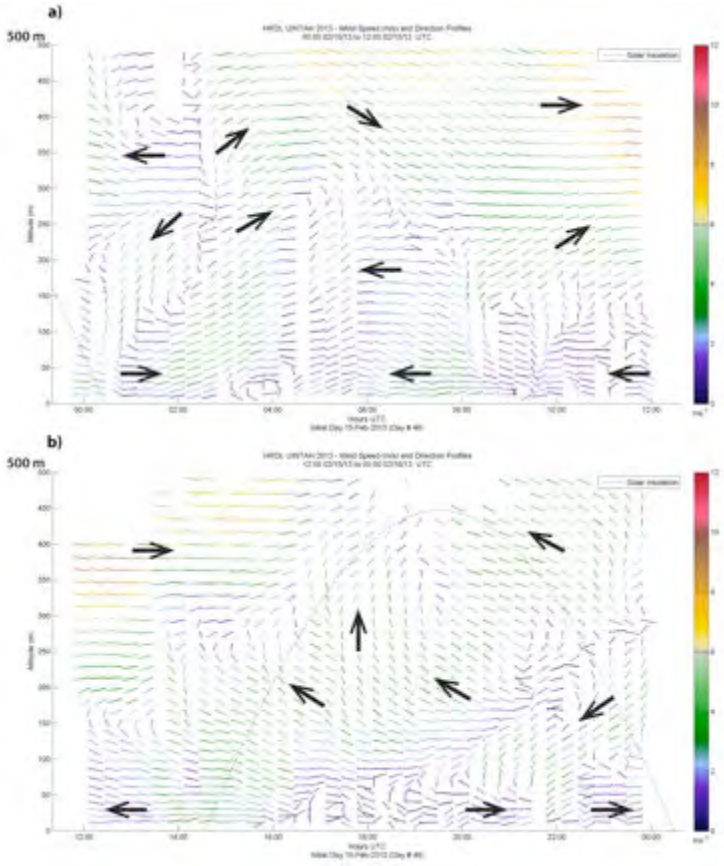


**5-43. Time-height cross sections as in Figure 5-2, showing a 24-hr period on 15 Feb 2013. Dark arrows indicate predominant wind direction.**

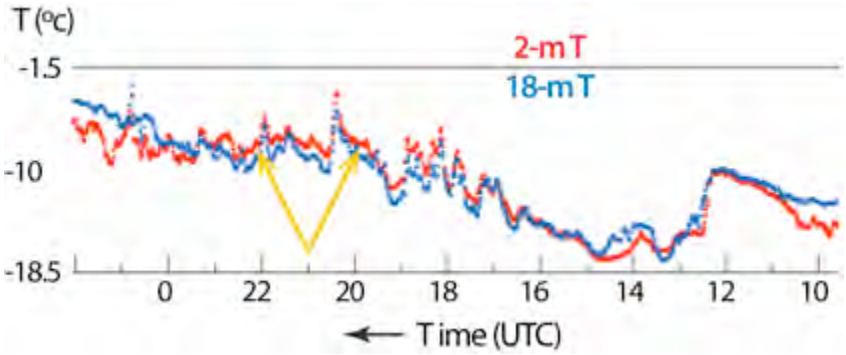


**5-44. Temperature traces at the Horse Pool site at 2 and 18 m above ground on 30 January, showing temperatures 1-2° warmer at the lower level during the day (gold arrows).**

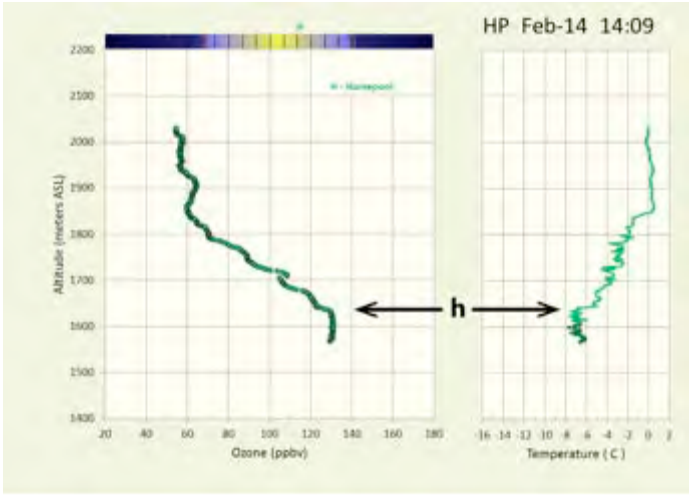


**5-45. Tethered-balloon profiles of $O_3$ (left) and potential temperature θ (right) at the Horse Pool site at 1409 MST (2109 UTC) on 14 February.**

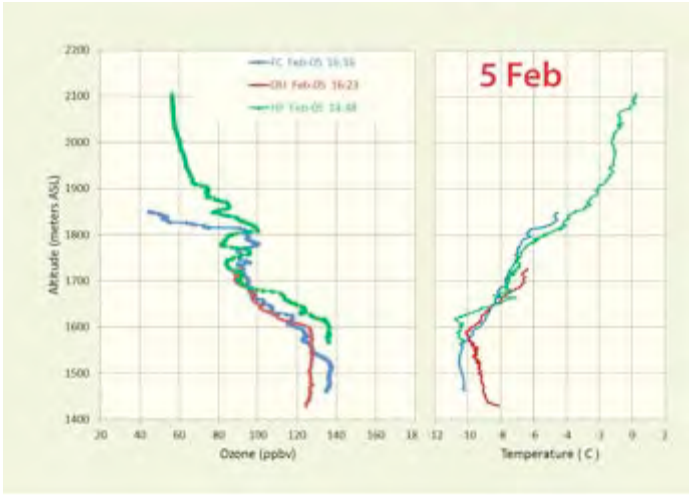


**5-46. Tethered-balloon profiles of $O_3$ (left) and potential temperature θ (right), as in Figure 5-45, at the Horse Pool site (HP: green curves), the Fantasy Canyon site (FC: blue curves), and at the Ouray site (OU: red curves) at approximately 1620 MST (2320 UTC) on 5 February.**

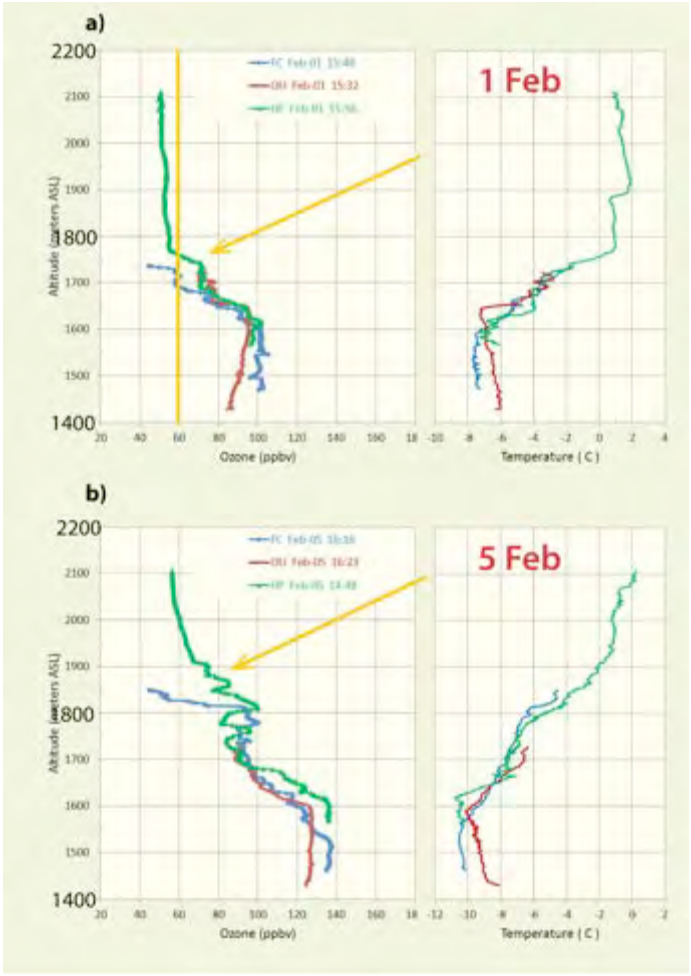


**5-47. Tethered-balloon profiles of $O_3$ (left) and potential temperature θ (right), as in Figure 5-45, at the Horse Pool site (HP: green curves), the Fantasy Canyon site (FC: blue curves), and at the Ouray site (OU: red curves) at approximately 1545 MST on 1 February (top panels) and1620 MST on 5 February (bottom curves). Vertical exchange processes move $O_3$ higher into inversion layer as episode proceeds (gold arrows), but much variation is seen within days and from day to day.**

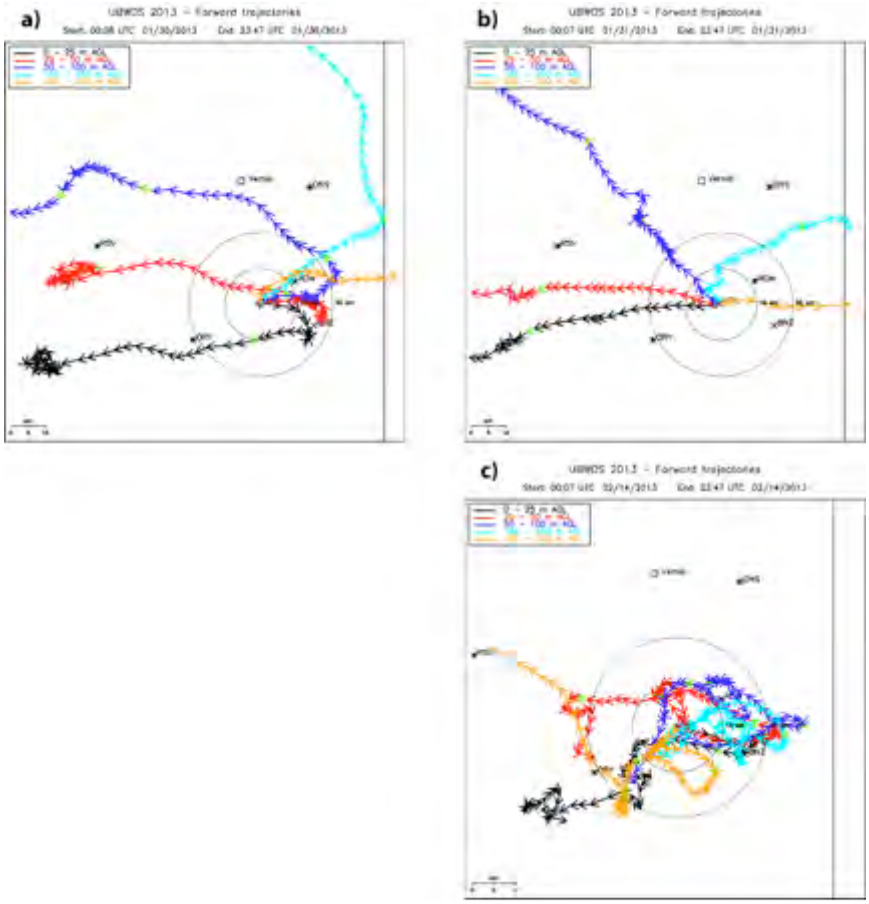


**5-48. 24-hr, single-station trajectories starting at the Horse Pool site at ~0000UTC (1700 MST) for 5 atmospheric levels between 0 and 300 m AGL for 30 January (top left), 31 January (top right), and 14 February (bottom).**

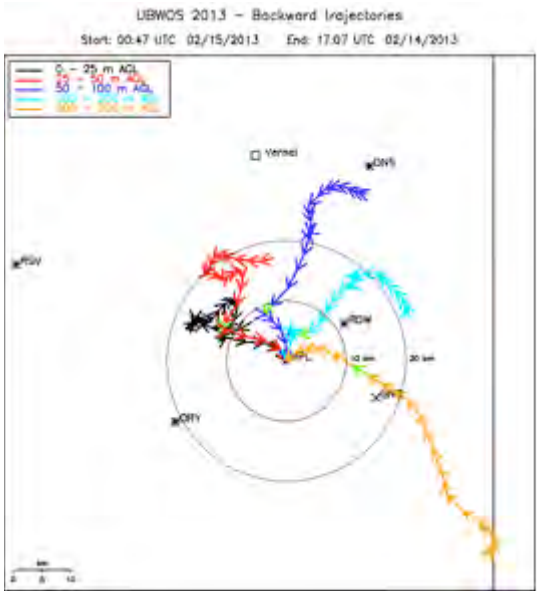


**5-49. Backward trajectories starting at the Horse Pool site at 0047 UTC on 15 February (1747 MST, 14 February), when a marked $O_3$ deficit was observed over the site. The highest trajectory (gold) passed directly over the Bonanza Power Plant power plant (BNZ), whereas the lower profiles did not.**

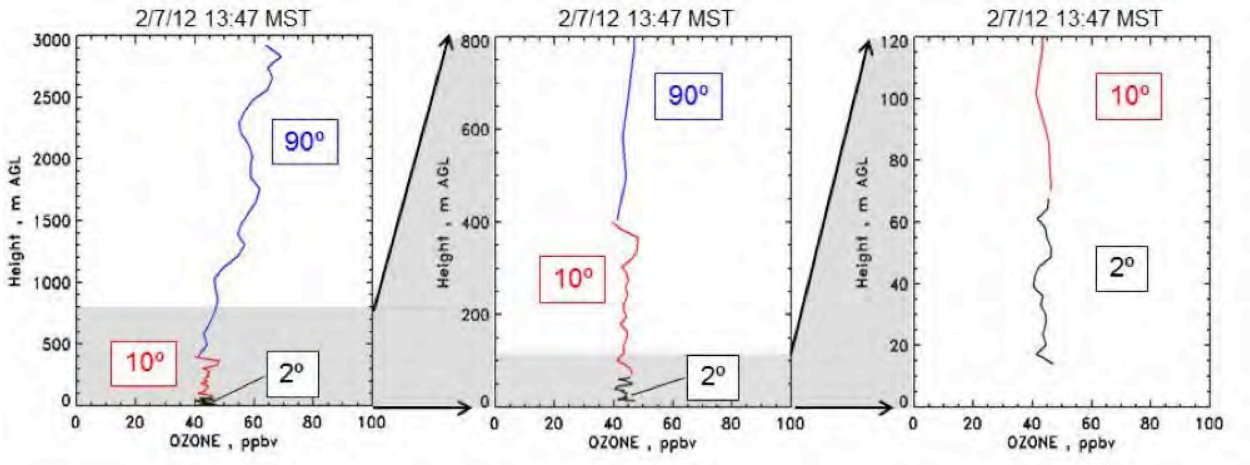


**5-50. Lidar ozone profiles observed at elevations angles of 2°, 10°, and 90°, projected vertically and blended together. The entire profile is shown on the lefthand plot and the middle and righthand plots show successive expansions of the profile. The data were taken on 7 February 2012 during the first UBOS study.**

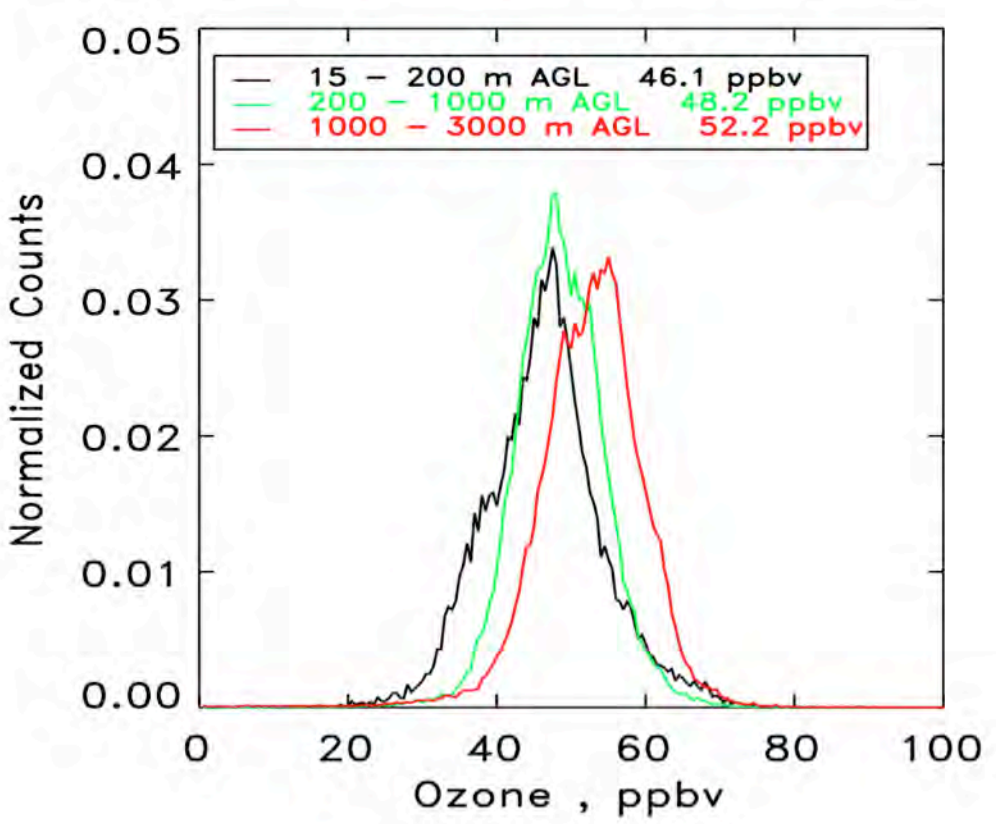


**5-51. Normalized PDFs of all UBOS 2012 ozone lidar measurements for three altitude ranges. Mean ozone values for the different altitude bins are indicated in the legend.**

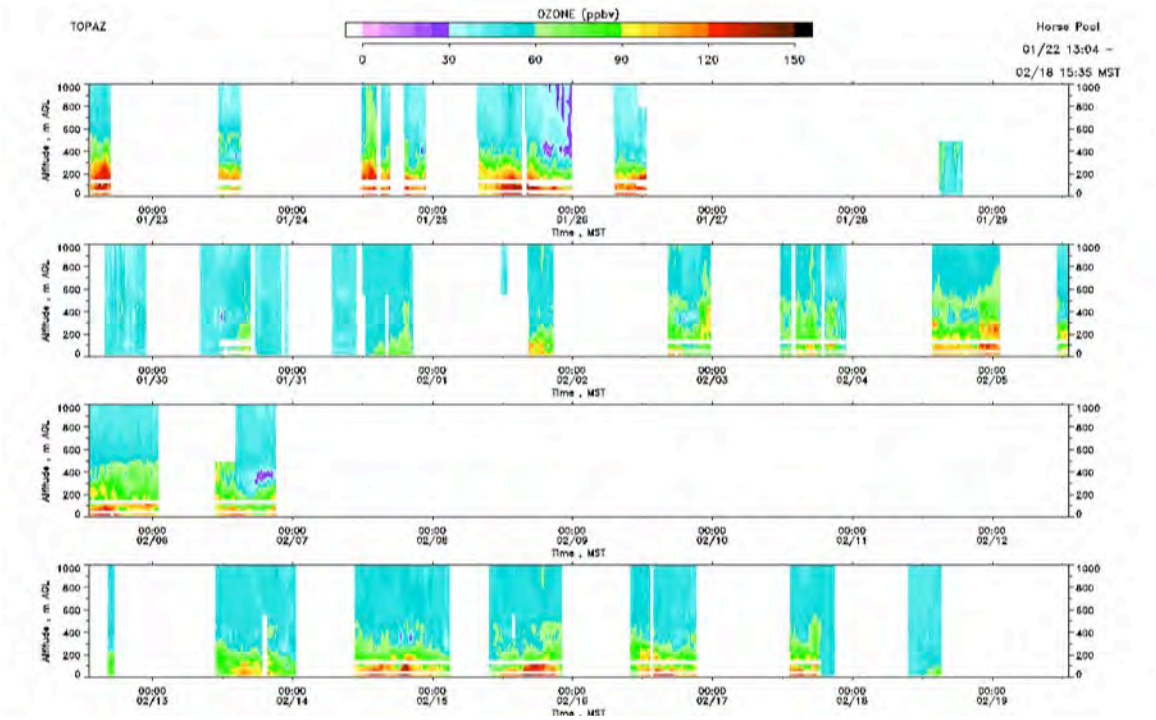


**5.52. Overview of the TOPAZ ozone profile measurement from the UBOS 2013 study. Ozone profiles are only shown up to 1000 m AGL to better depict the ozone structure in the lowest few hundred meters.**

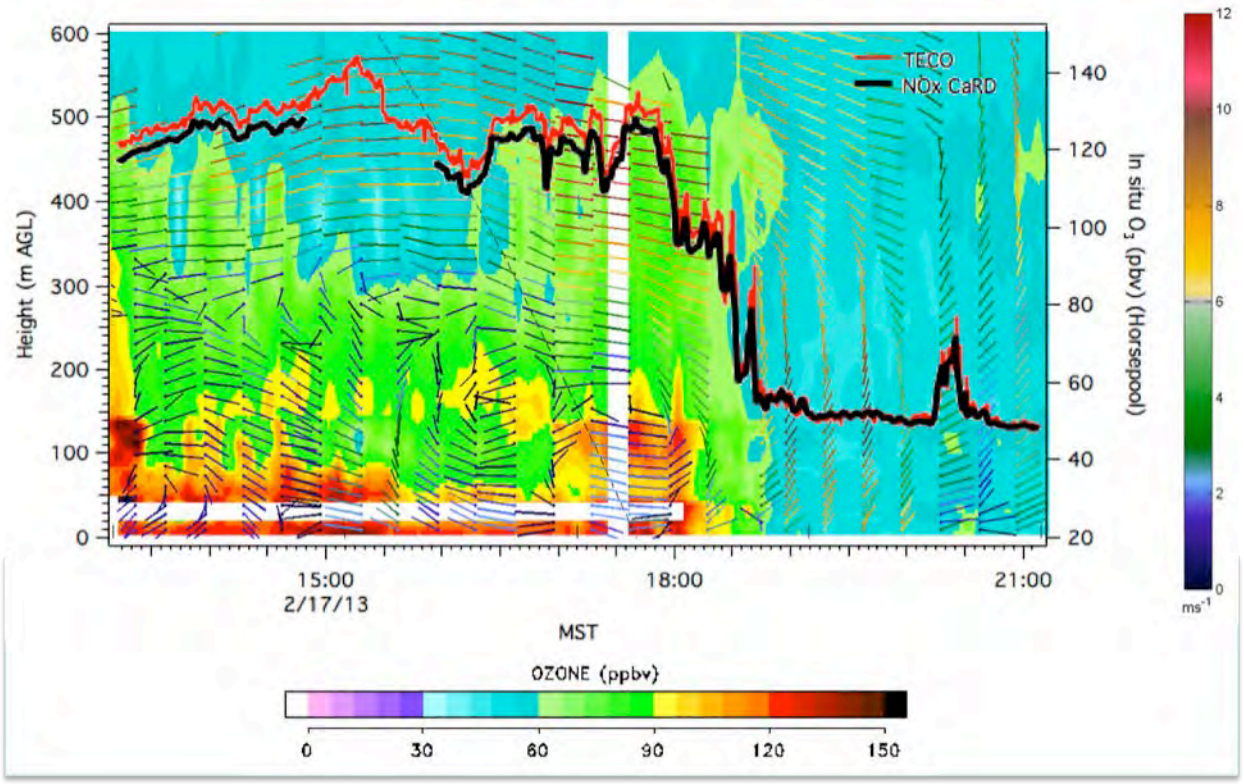


**5-53. TOPAZ ozone time-height cross section up to 600 m AGL on 17 February 2013. HRDL lidar horizontal wind measurements (shown as colored wind barbs) and ozone observations from two in situ sensors (thick black and red lines) are overlaid. The dashed line indicates solar irradiance (arbitrary scale).**

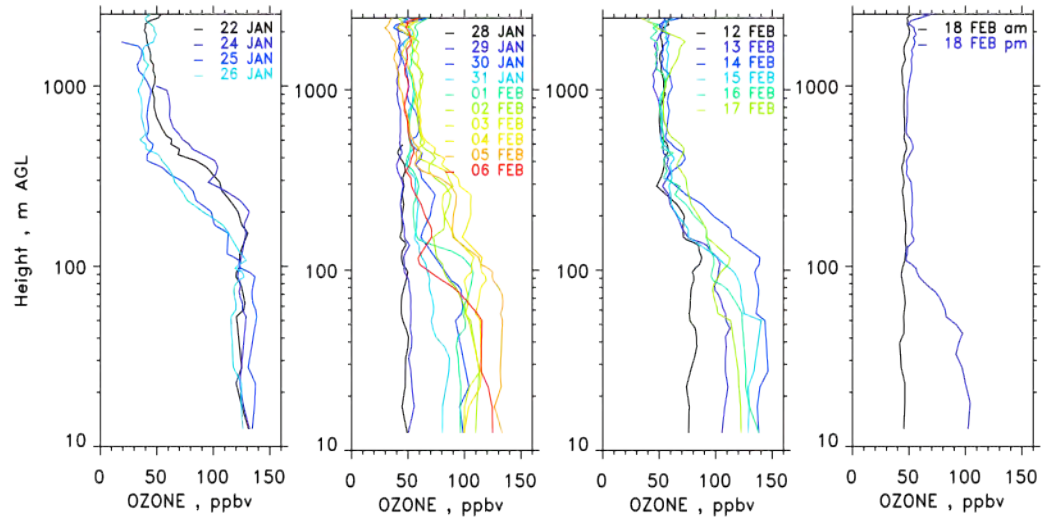


**5-54. 15-min ozone profiles grouped by ozone episode for every day of TOPAZ observations. The profiles were measured when BL ozone peaked in the afternoons.**

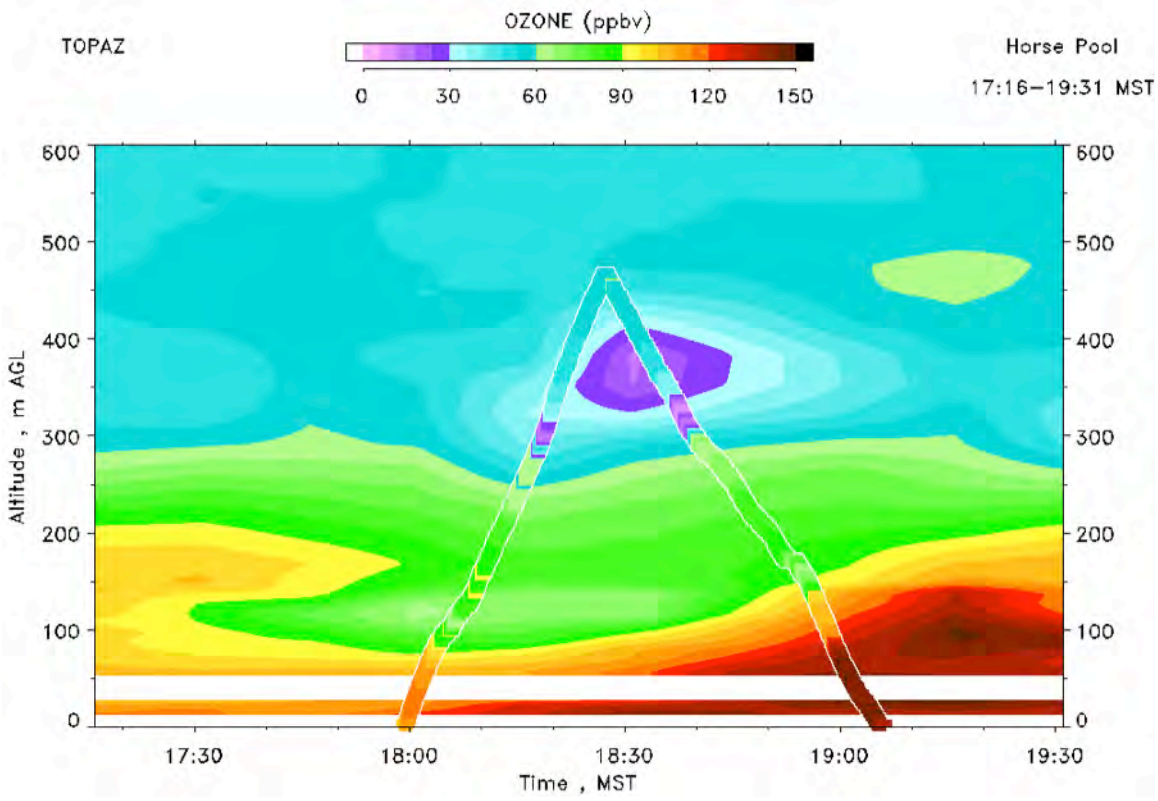


**5-55. TOPAZ time-height cross section of ozone from near the surface to 600 m AGL for 17:16 – 19:31 MST on 14 February 2013. The colored line shaped like an inverted "V" represents the ozone measurements from the collocated tether sonde.**

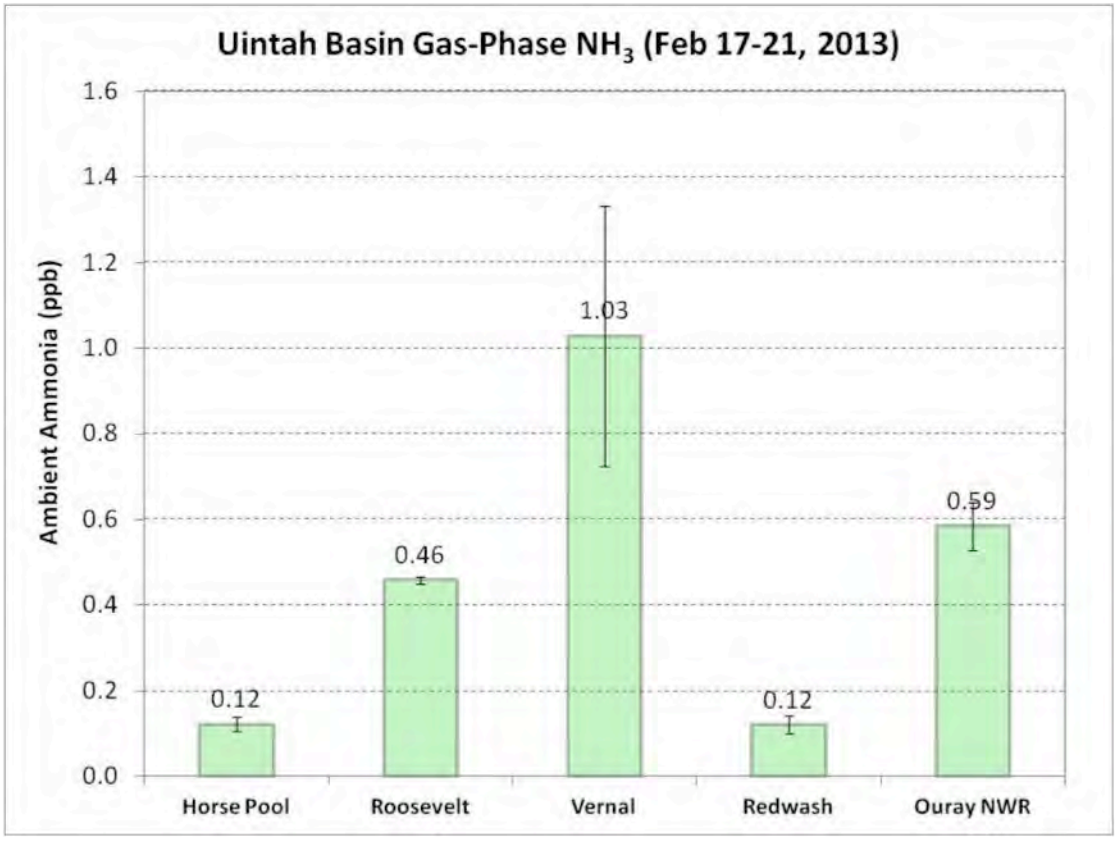


**5-56. Ambient ammonia concentrations at various sites within the Uinta Basin. The error bars represent the range of duplicate measurements at each site.**

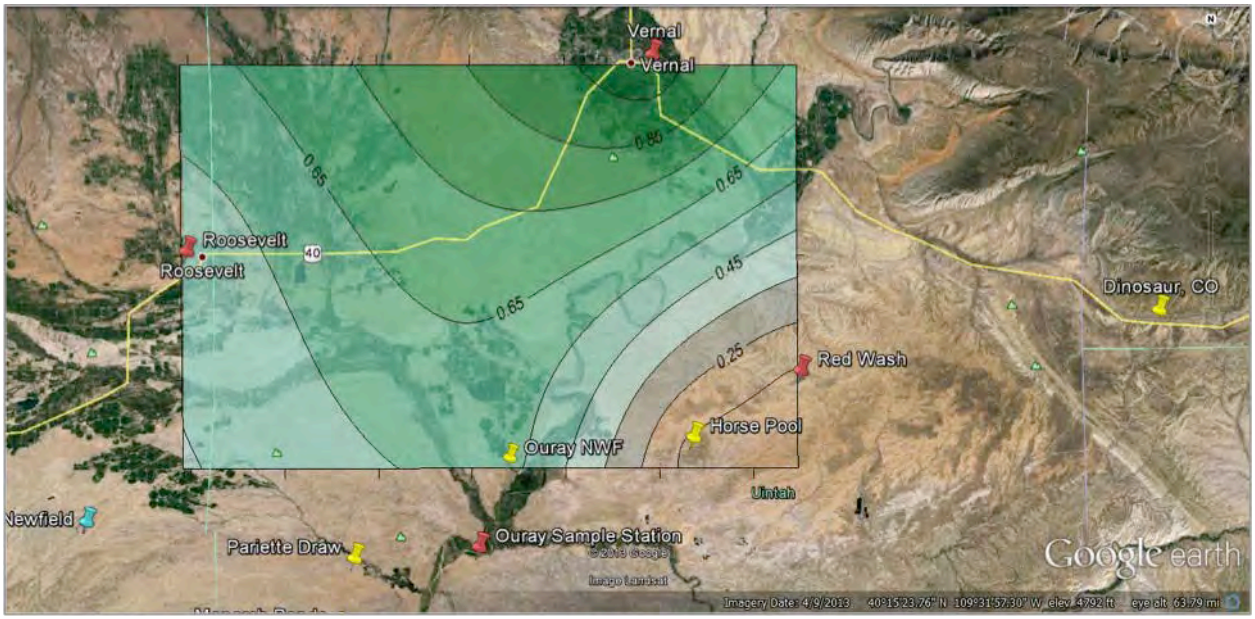


**5-57. Contour plot of ambient ammonia concentrations within the Uinta Basin overlaid onto a Google Earth map.**

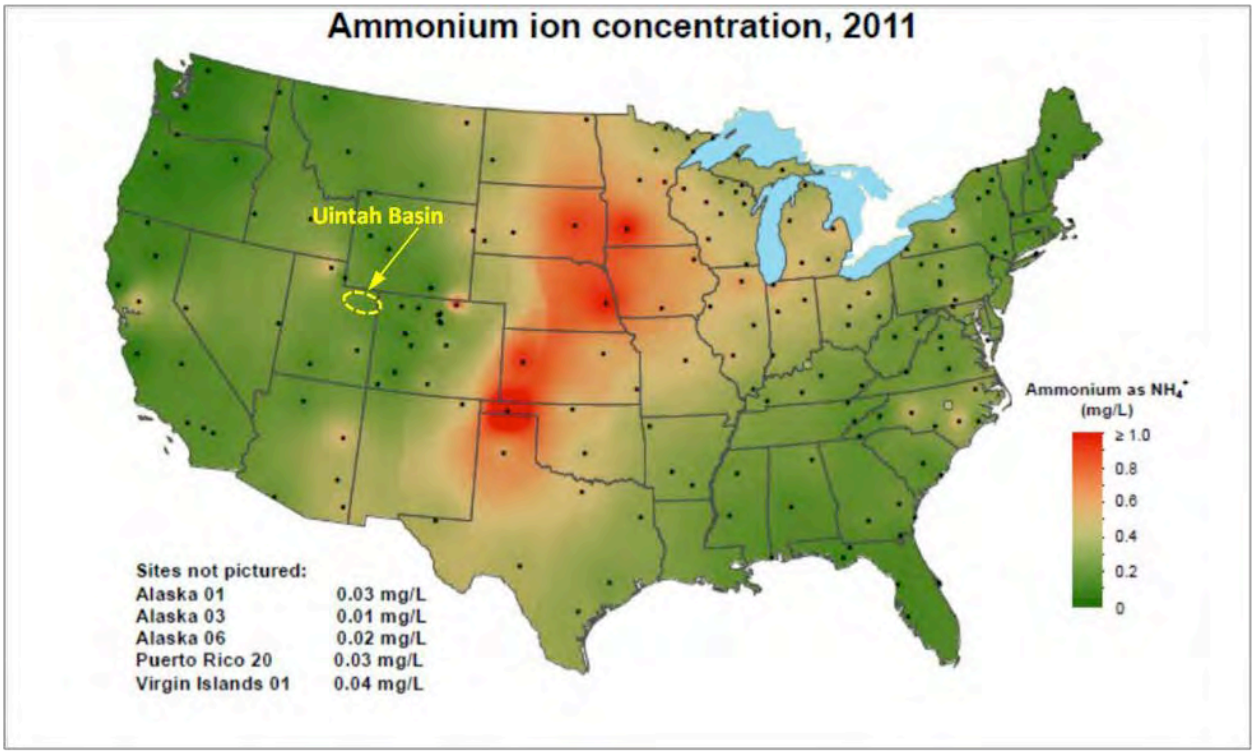


**5-58. National ammonium ion ($NH_4$+) concentrations for 2011 as observed by the National Trends Network (NADP, 2013a).**

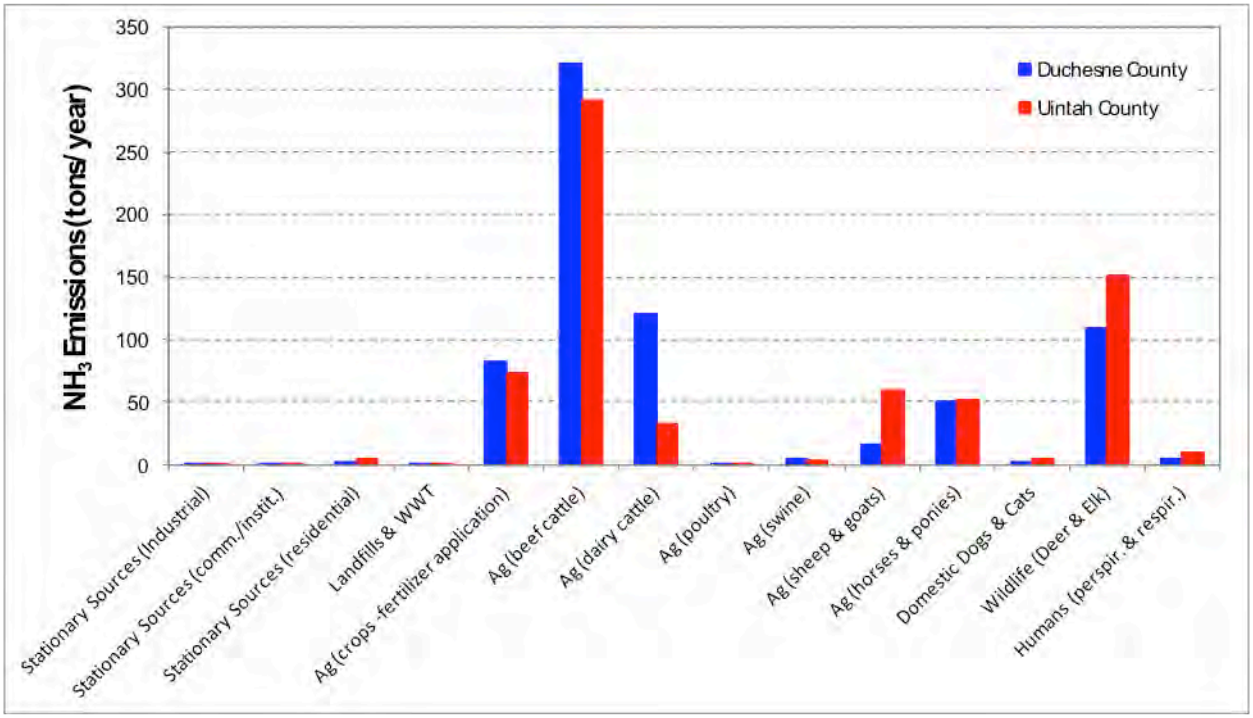


**5-59. Estimated annual $NH_3$ emissions for the two counties making up Utah's Uinta Basin (UDAQ, 2013.)**

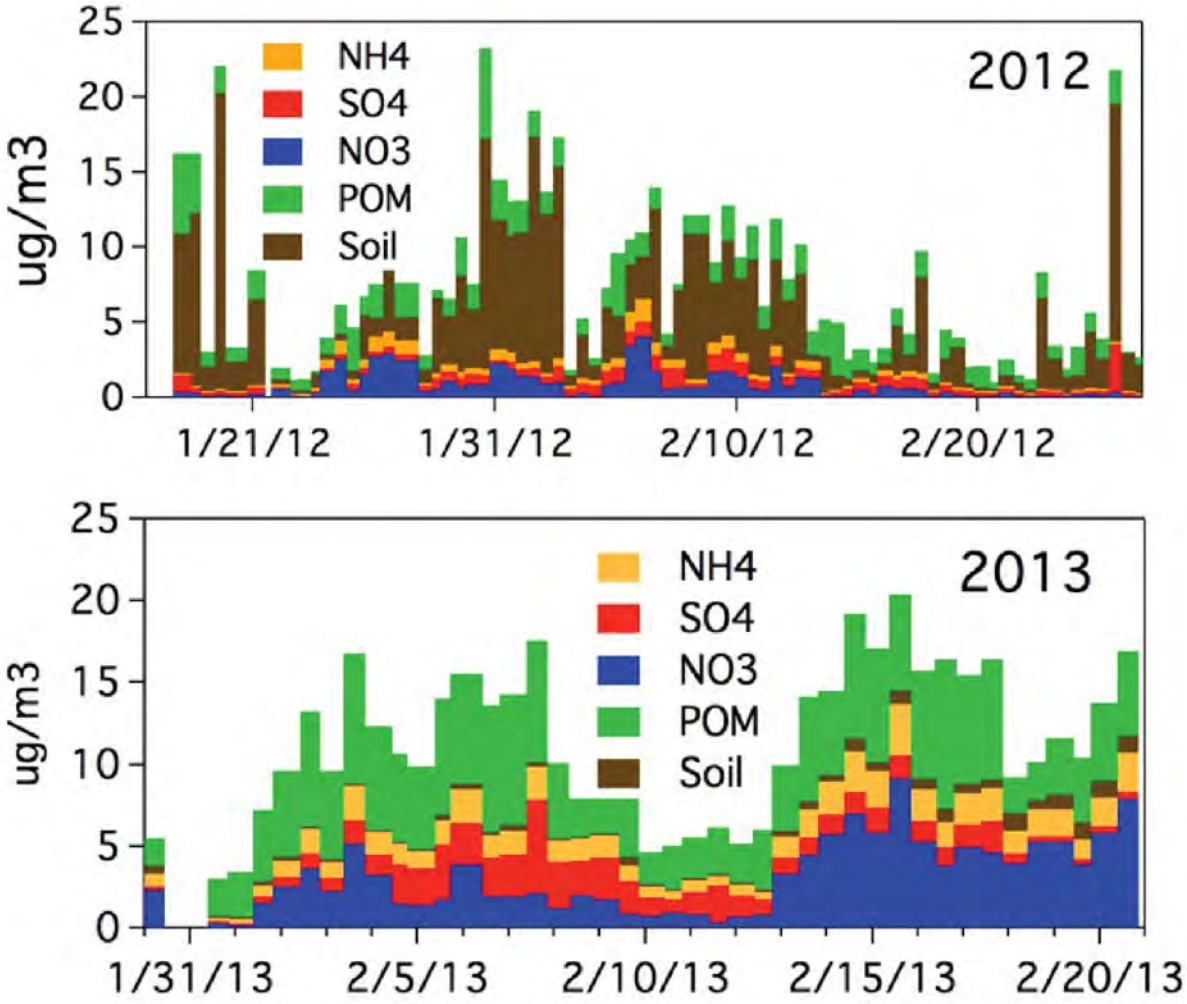


**5-60. A comparison of the PM $_{2.5}$ aerosol mass concentrations between 2012 and 2013.**

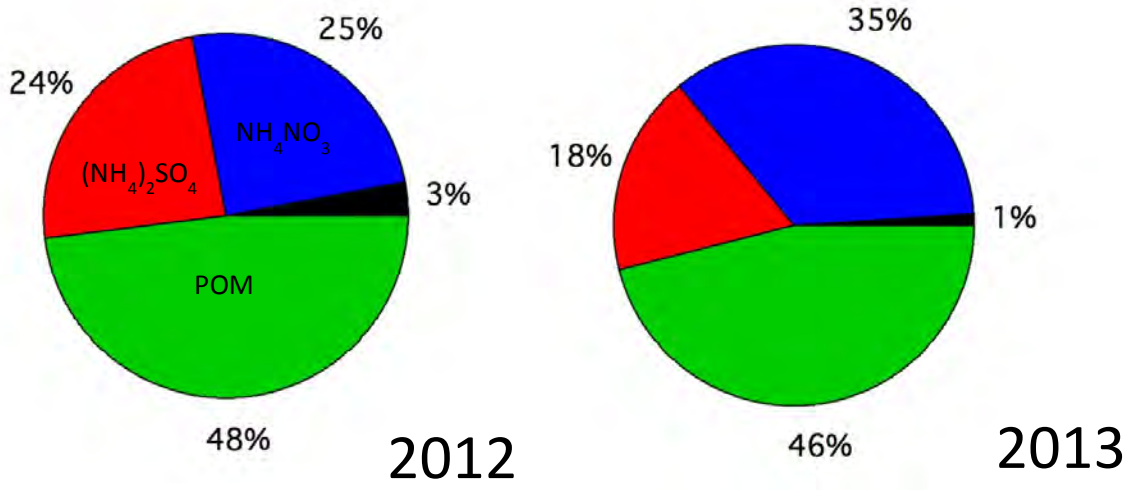


**5-61. Mass fractions of the primary sub micrometer aerosol components in 2012 and 2013 (POM-green; $(NH_4)_2SO_4$ -red; and $NH_4NO_3$ -blue).**

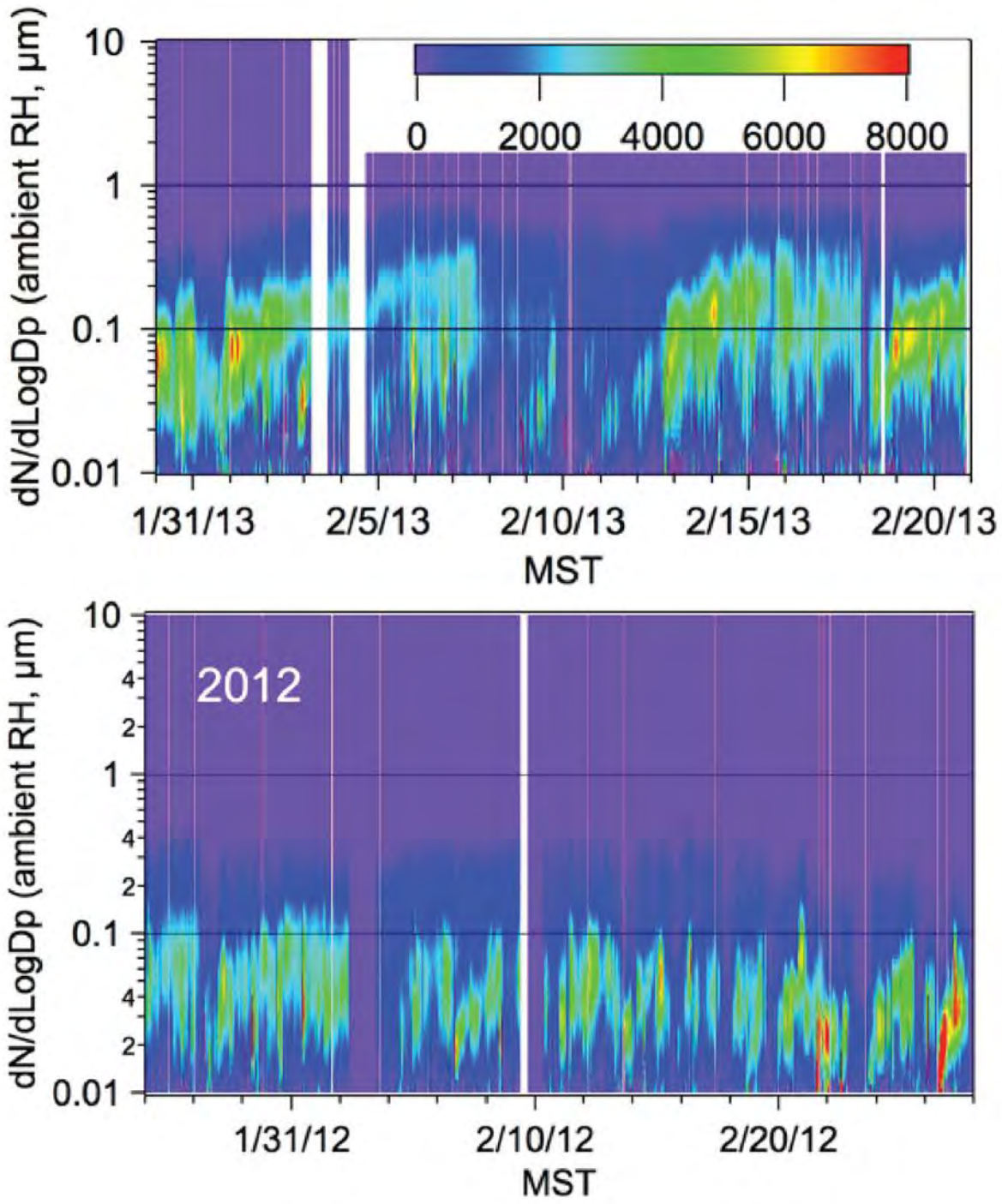


**5-62. Aerosol number size distributions at ambient relative humidity in 2012 (bottom) and 2013 (top) showing the larger mean diameter in 2013.**

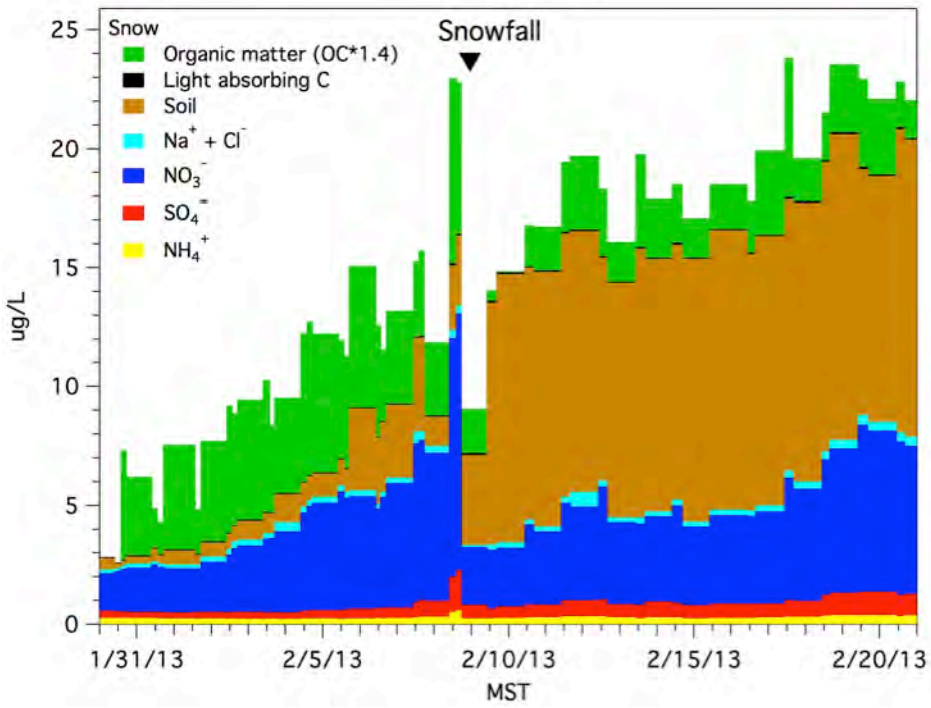


**5-63. Inorganic and organic components in surface (0-3cm) snow measured within 1.3 km of Horse Pool in 2013. Nitrate and nitrite (not shown) concentrations increased in the surface snow with time. The snow fall on February 8 covered the surface snow and reduced the measurable inorganic ion concentrations.**

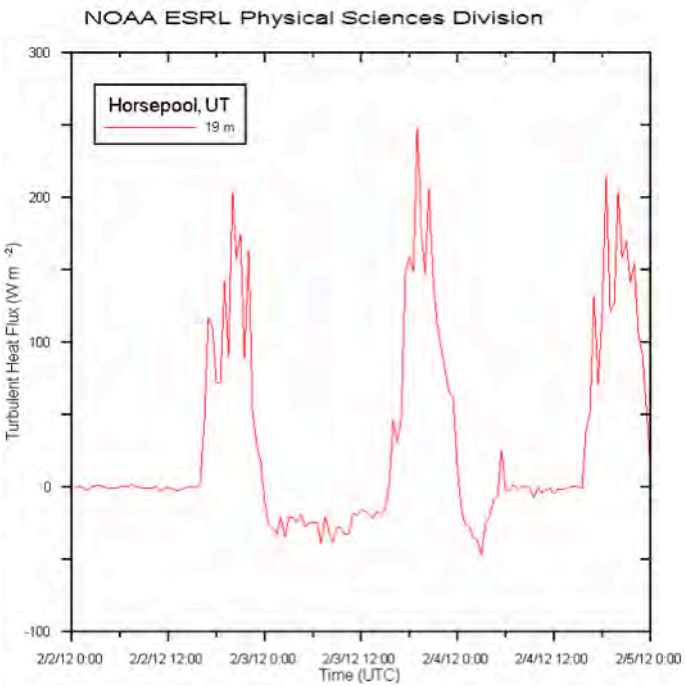


**5-64. Typical surface sensible heat fluxes at the Horse Pool meteorological site during UBOS 2013.**

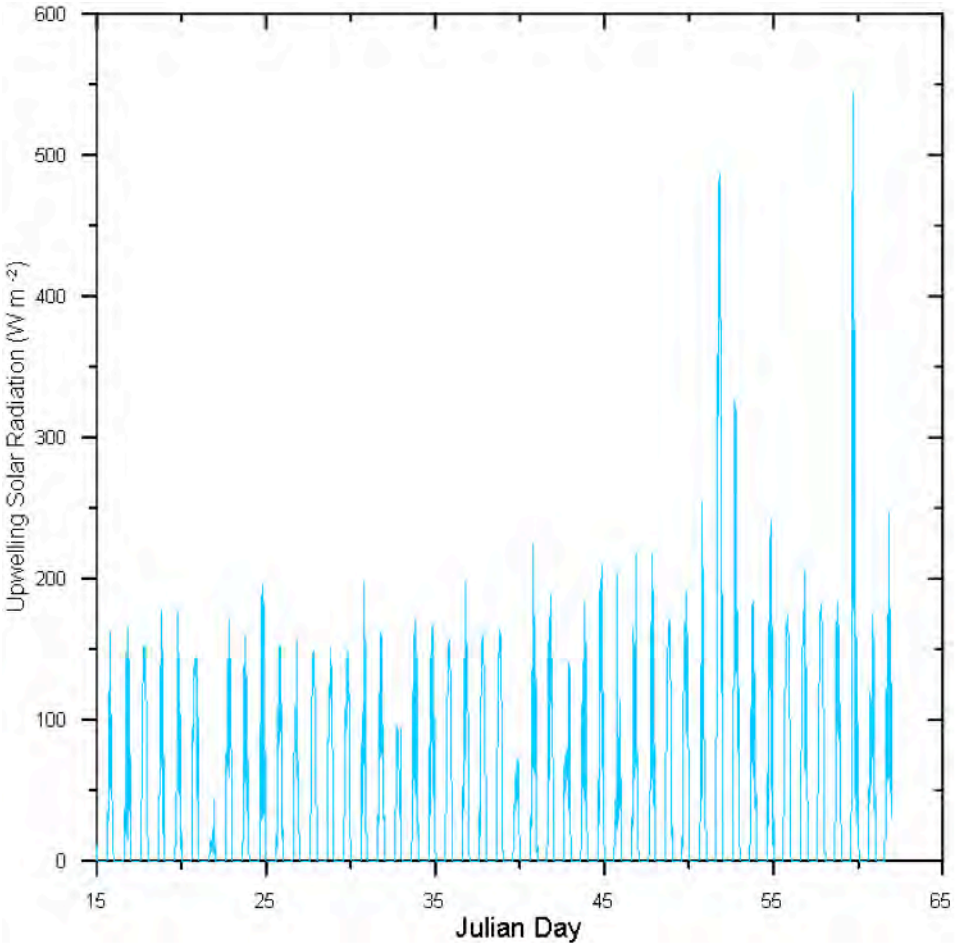


**5-65. Upwelling solar radiation measured at Horse Pool during UBOS 2013.**

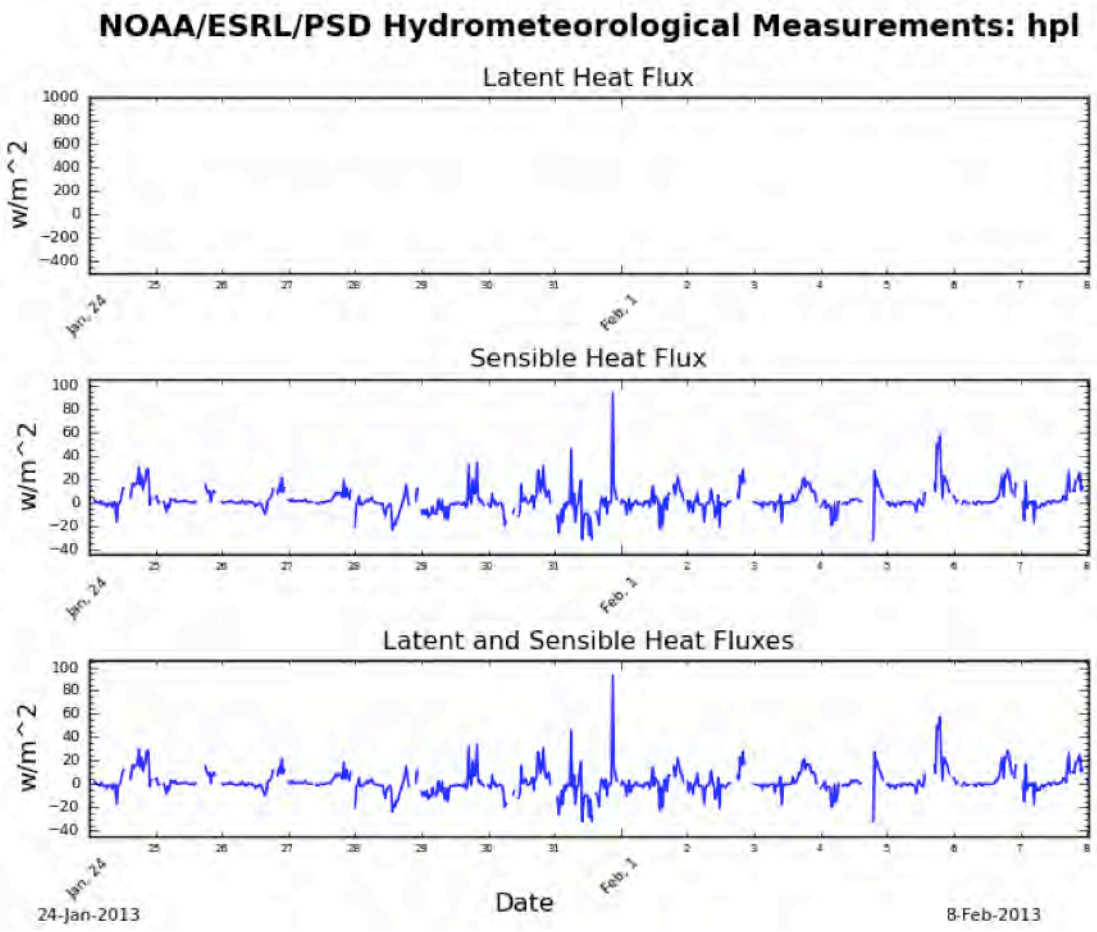


**5-66. Heat fluxes measured at Horse Pool during UBOS 2013.**

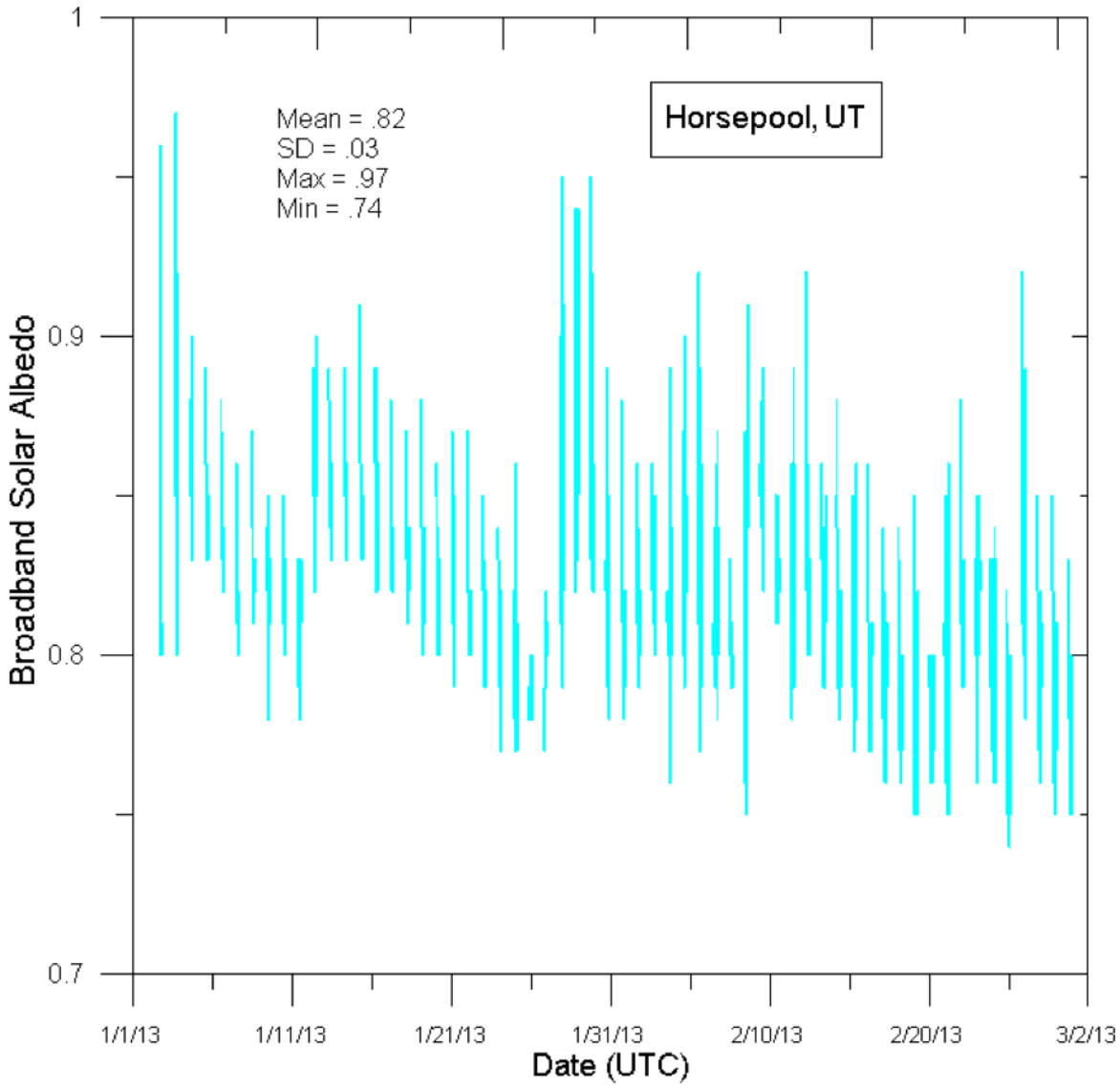


**5-67. Broadband solar albedo at Horse Pool during UBOS 2013.**

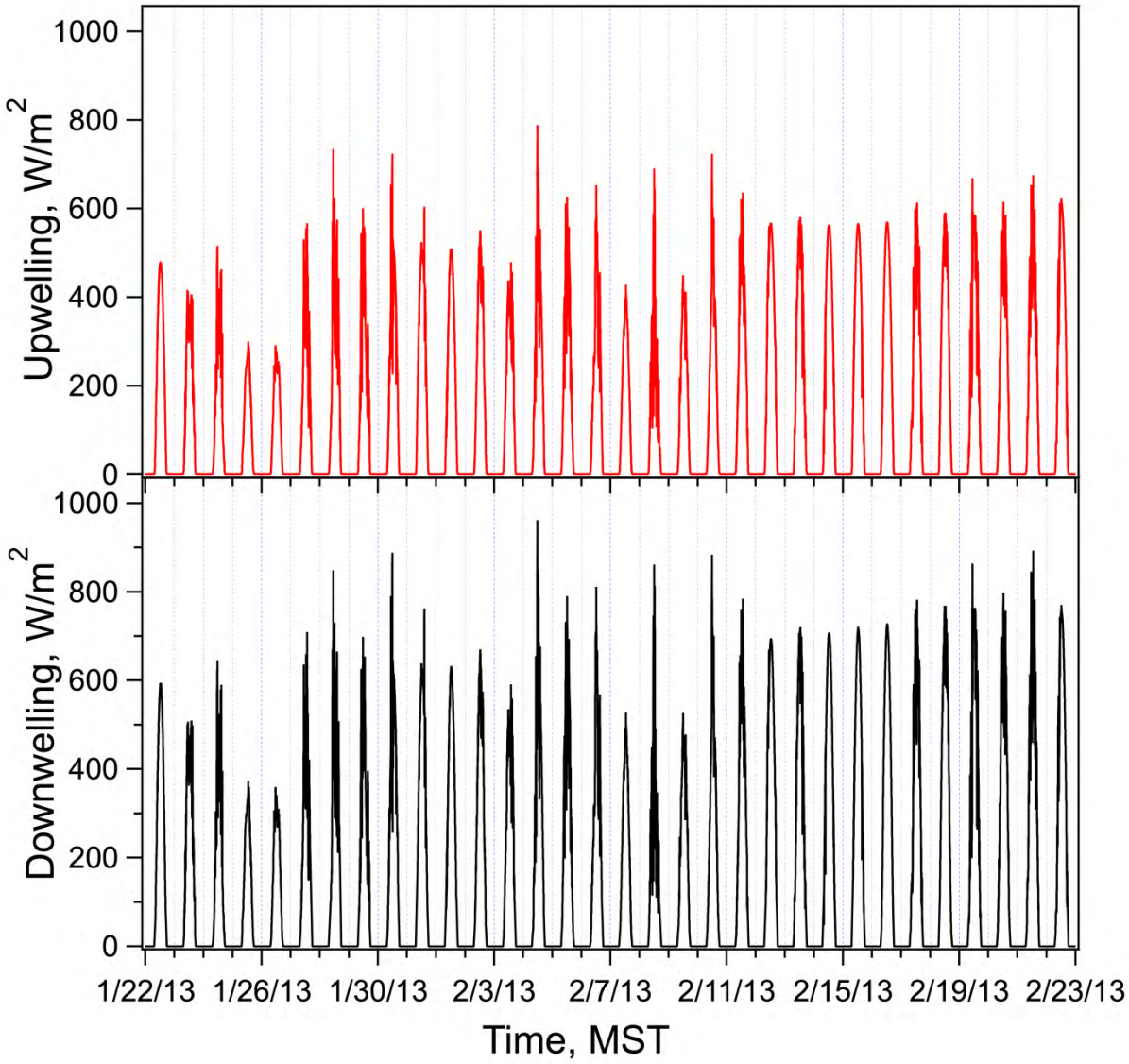


**5-68. The downwelling (black) and upwelling (red) solar irradiances measured at Horse Pool during the UBOS 2013 experiment.**

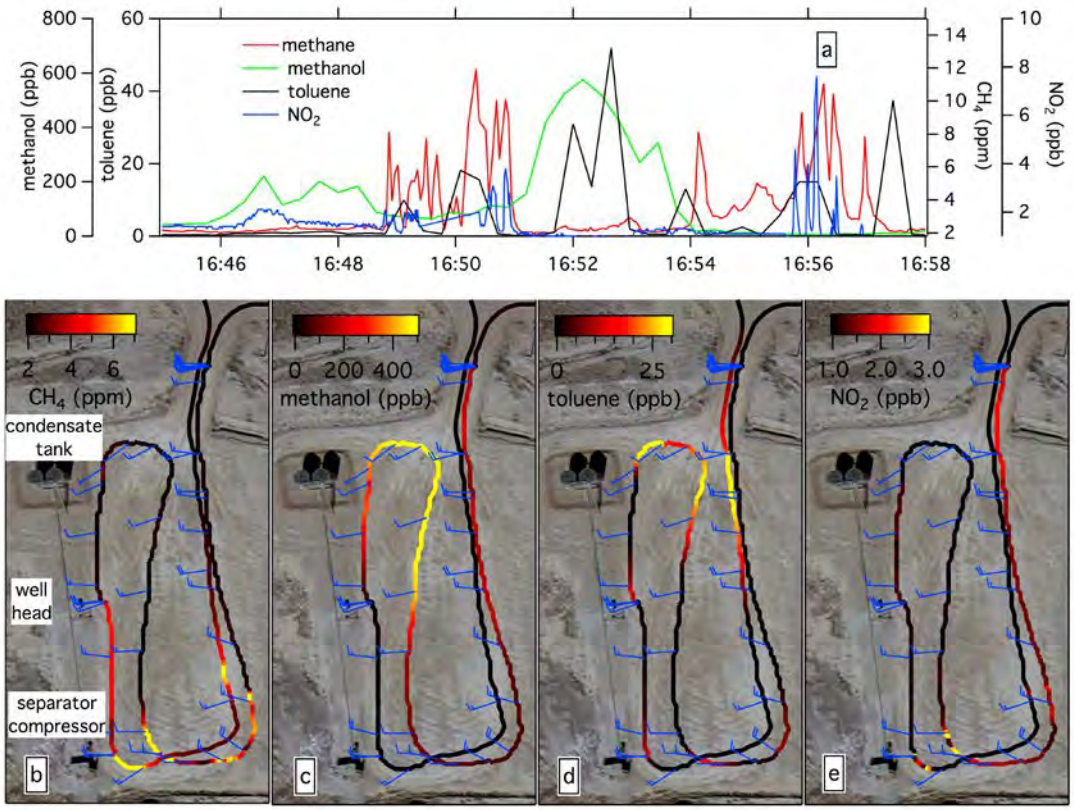


**5-69. An example track close to a gas well, color coded by methane (b), methanol (c), toluene (d) and (e) $NO_2$. The wind barbs indicate prevailing wind direction. The time series during this period is shown in (a).**

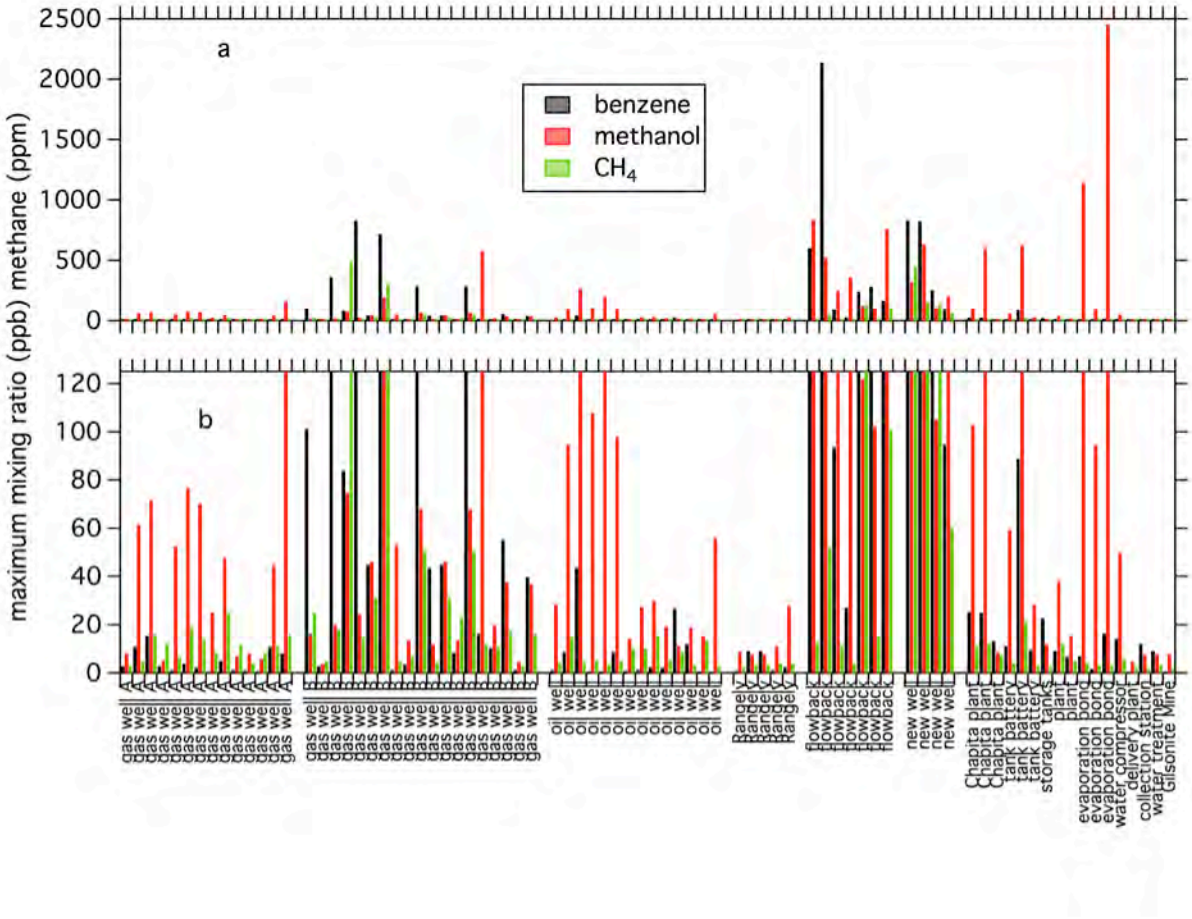


**5-70. The maximum mixing ratios of benzene, methanol and methane observed close to the sources in the Uinta Basin and in Rangely, Colorado in both (a) full scale and (b) small scale.**

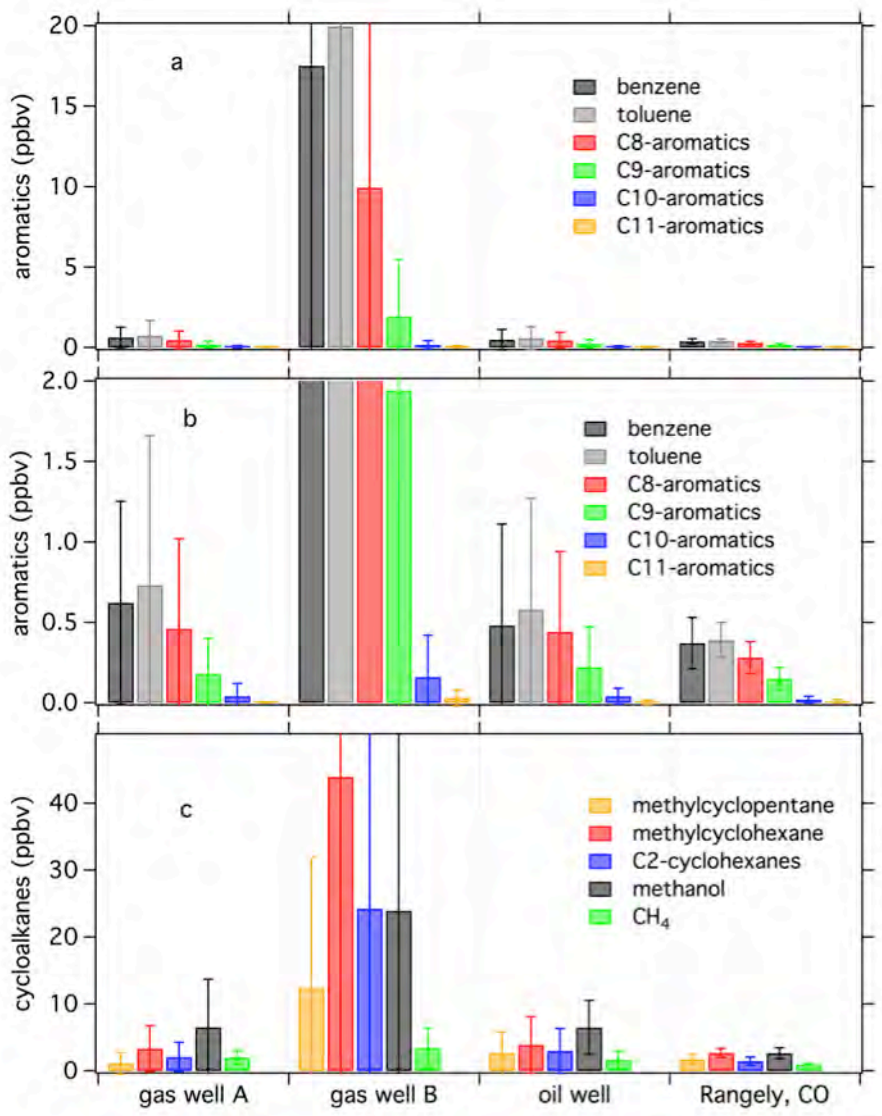


**5-71. Average mixing ratios of the VOCs; aromatics, cycloalkanes, methanol and methane) measured near emission sources in the Uinta Basin, averaged for each category of point sources. The error bars are the standard deviation. All concentrations were normalized to an average wind speed of 2 m/s.**

# 6.0 BALLOON-BORNE VERTICAL PROFILES OF OZONE, METHANE, NON-METHANE HYDROCARBONS, NITROGEN OXIDES AND METEOROLOGICAL PARAMETERS

***Detlev Helmig, Chelsea Stephens, Jeong-Hoo Park, Jacques Hueber, Patrick Boylan, Jason Evans***

***Institute of Arctic and Alpine Research, University of Colorado Boulder***

## 6.1 Objective

The primary objective of this project was to investigate the vertical distribution of relevant trace gases, including ozone, methane, non-methane hydrocarbons, and nitrogen oxides, and meteorological parameters to understand the vertical structure of ozone precursors and ozone production with linkages to boundary-layer conditions during and between inversion events. This project utilized measurements from a surface tower, the CU-INSTAAR tethered balloon platform for measurements of vertical profiles of trace gases, and a NOAA-GMD tethersonde platform for measurement of ozone and meteorological parameters.

## 6.2 Experimental Methods and Instrumentation

### 6.2.1 Study Site and Duration

The study by CU-INSTAAR was conducted at the Horsepool site (~1569 m a.s.l) in the Uinta Basin from January 25 through February 19, 2013. Between two to four CU researchers were on-site at all times throughout this period to allow for 24/7 operation, including midnight tethersonde launches.

### 6.2.2 Experimental Set-Up

Vertical profiles were conducted using a 2 m flux tower, a tethered SkyDoc balloon, and tethered electrochemical cell (ECC) ozone and radio sondes. A trailer housing the instruments was located approximately 10 m from the tower and balloon launch sites. A schematic of the experimental set-up is shown in Figure 6-1.

Vertical profiles of trace gases were conducted at five sampling heights. Sampling lines were placed approximately 30 cm into the snowpack, at 2 m on the flux tower, and at three heights on the SkyDoc balloon tether line, nominally at 50 m, 100 m, and 150 m (balloon heights fluctuated with time). The SkyDoc flew at a maximum height of 500 ft (~170 m) and was raised and lowered using a hydraulic winch. Data coverage with the SkyDoc was nearly continuous, with only brief periods when the balloon was taken down due to inclement weather (e.g., high winds, icing conditions) or for inter-comparisons and instrument calibrations.

Sampling lines were made of PFA Teflon. Balloon sampling lines were approximately 650 ft in length and colored black to prevent in-line photochemistry. These sampling lines have been previously shown to have excellent performance for sampling both ozone and hydrocarbons with very little line loss (< 5 % for ozone and 3 % for hydrocarbons). Sampling lines were

plumbed into a sampling manifold to which the analytical instruments were connected. Four of the sampling lines were continuously measured for ozone using dedicated ozone monitors. All other species were sampled through a switching valve that switched between the five inlets (including the snow inlet) every six minutes, such that a full vertical profile was conducted every 30 minutes.

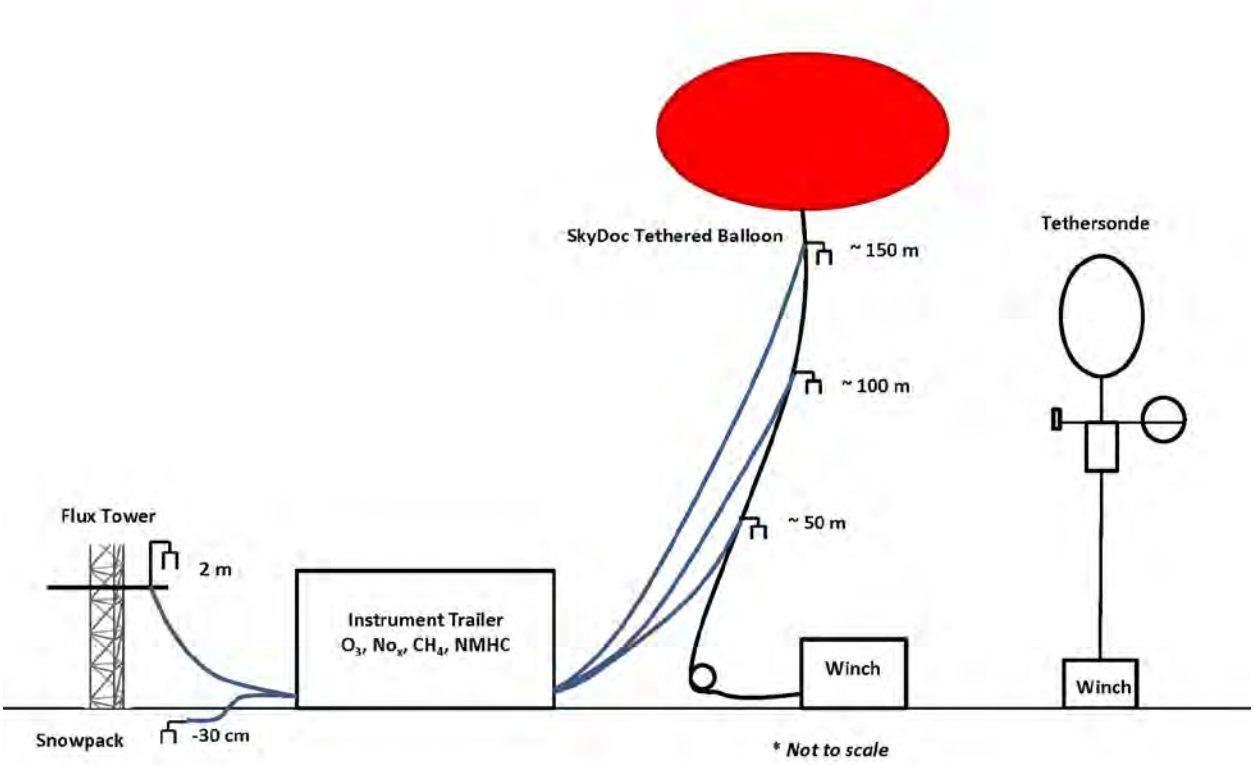


**Figure 6-1. Schematic of the CU-INSTAAR experimental setup during UBOS 2013.**

Vertical profiles of ozone and meteorological parameters to a height of approximately 500 m above ground level were conducted using ECC and radio tethersondes provided by NOAA-GMD. In addition, a battery-powered Kestrel sonde measured temperature, humidity, wind speed and wind direction. Meteorological parameters (temperature, pressure, wind speed, wind direction) were also measured on the 2 m flux tower. Sondes were raised and lowered using a small electric winch. Five to six sonde launches were conducted per day, including an early morning launch (approximately 6:00) and a midnight launch. Figure 6-2 shows the record of sonde launches illustrating the excellent data coverage achieved.

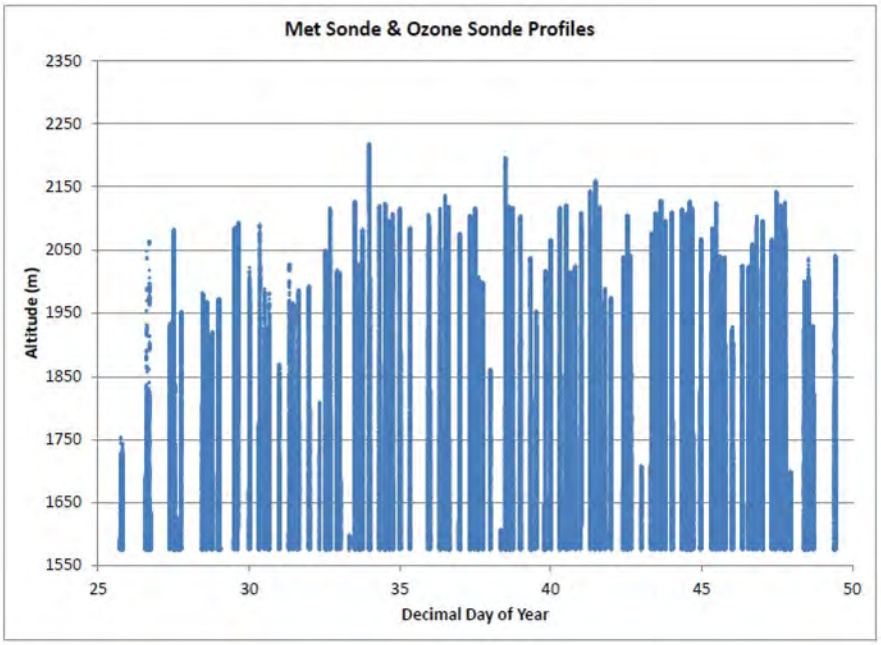


**Figure 6-2. Record of ECC sonde launches and balloon height.**

### 6.2.3 Instrumentation and Procedures

Ozone was measured continuously from the 2 m tower and the three balloon lines using four dedicated commercial UV-absorbance ozone monitors (Thermo, API, and Monitor Labs). An additional Thermo 49i ozone monitor was placed on the switching manifold, measuring ozone at each of the five heights (including in snow) for six minutes each. All ozone monitors were calibrated using a NOAA-GMD referenced laboratory standard prior to deployment. The monitors were routinely zeroed on site using an ozone scrubber, and inter-comparisons were conducted when all of the sampling inlets were placed side-by-side on the 2 m tower.

Methane was measured using a Baseline Series 8900 gas chromatograph with flame-ionization detection loaned to CU-INSTAAR by the State of Utah Department of Environmental Quality. The instrument continuously monitored methane with a time resolution of three minutes using a packed column for separation. Automated calibrations were performed twice a day using a gas standard provided with the instrument. The methane GC was connected to the switching valve on the sampling manifold for vertical profiles.

Nitrogen oxides (NO and $NO_x$ + $NO_y$) were measured using a commercial Teledyne $NO_x$ monitor with a molybdenum oxide converter also loaned to CU-INSTAAR by State of Utah Department of Environmental Quality. The instrument continuously monitored NO and $NO_x$ (with the reported $NO_x$ also including a fraction of $NO_y$ due to the limited $NO_x$ selectivity of the converter) at one-minute time resolution and was connected to the switching valve on the sampling manifold for vertical profiles.

Non-methane hydrocarbons (NMHC) were measured using a field-portable gas chromatograph with flame ionization detection. The GC is a fully automated instrument optimized for analysis of C2-C10 NMHC, covering saturated and unsaturated NMHC and aromatic compounds to the xylenes. The instrument operates by preconcentrating NMHC from 0.5 L of sampled air on a Peltier-cooled micro-absorbent trap. The trap is then flash-heated and NMHC are separated on an $Al_2O_3$ KCl PLOT column by temperature-programmed chromatography followed by flame-ionization detection. This instrument had two identical sampling channels such that one channel continuously sampled from the 2 m tower inlet, and the second channel was placed on the switching valve to conduct vertical profile measurements. The measurement time resolution of the NMHC GC was 36 minutes. Automated calibrations were performed daily from a certified VOC standard gas cylinder. Additional calibration standards and instrument zeroes were performed just prior and to the end of the campaign.

In addition to the in-situ GC measurements, volatile organic compounds (VOC) were also analyzed from whole air samples collected using a Portable Flask Package (PFP) and Portable Compressor Package (PCP). The PFP contains twelve 0.75 L glass flasks that are opened and filled sequentially to 40 psi via computer control. A total of 90 whole air sampled were collected during the campaign distributed among the five inlets. The PFPs were analyzed for VOC at the CU-INSTAAR laboratory in Boulder by GC-FID/mass spectrometry detection. The laboratory GC operates on the same principles as the field GC described above. Instrument blanks and VOC standards are analyzed before and after each set of 12 flask samples. Our laboratory is the core of the Global VOC Monitoring Network program and our standard scale has been cross-referenced on multiple occasions against other participating international laboratories. Our laboratory was audited by the World Calibration Center for VOC twice and found to meet all quality criteria set by the WMO GAW program for VOC.

Meteorological instrumentation was installed on the 2 m tower. This consisted of a wind vane and cup anemometer for wind speed and direction, an RTD temperature probe with aspirated shield, and upward and downward looking radiation sensors.

The tethersonde instrumentation was loaned to CU-INSTAAR by NOAA-GMD. Briefly, these sondes consisted of an ECC ozone sonde that has been used extensively for quantifying ozone, and a radiosonde that measures altitude, temperature, pressure, and water vapor.

## 6.3 Results

### 6.3.1 Ozone

The 2013 campaign experienced several periods of high ozone build-up periods during sustained inversion events. In contrast to the 2012 study, during which there was no snow and ozone remained in the range of 10 – 60 ppbv, in 2013 there was persistent snow-cover throughout the campaign and ozone reached as high as 150 ppbv (Fig. 6-3).

There were three distinct ozone build-up events during the time that the CU-INSTAAR instruments were at Horsepool. Upon arrival at the site, we captured the tail-end of the first event (Event 1) that lasted until January 26 and then was cleaned out by the passage of a low-pressure system. Event 2 began January 31 with ozone increasing until February 7. This was again cleaned out by the passage of a low-pressure system. Event 3 began February 13 and lasted until February 18 when there was a partial cleaning out of the basin. In 2012, although there were no high ozone build-up events, ozone did show a very dynamic behavior with a diurnal profile that peaked in the afternoon and a daytime/nighttime amplitude of 30 – 40 ppbv. The 2013 ozone record shows this same diurnal behavior superimposed on the build-up events with an amplitude of 20 – 50 ppbv.

The vertical distribution of ozone throughout the duration of the campaign is illustrated in Figure 6-4 as a color contour plot showing the full record of the ECC sonde ozone data for Horsepool. The three high ozone build-up events are evident in the warmer colors on the color scale, which here goes to 175 ppbv. The vertical structure reveals that ozone builds up in both mole fraction and in height during the inversion events. The highest ozone is consistently confined within the lowest 100 – 150 m above ground level and at many times appears to be well-mixed within the shallow boundary layer. With the exception of one day, throughout the campaign relatively low ozone (i.e., < 75 ppbv) is present above 1900 m a.s.l. The cleaning out periods (i.e., January 28 – 31 and February 10 – 11) brought relatively clean background air down the surface, resulting in ground-level ozone values on the order of 30 – 60 ppbv.

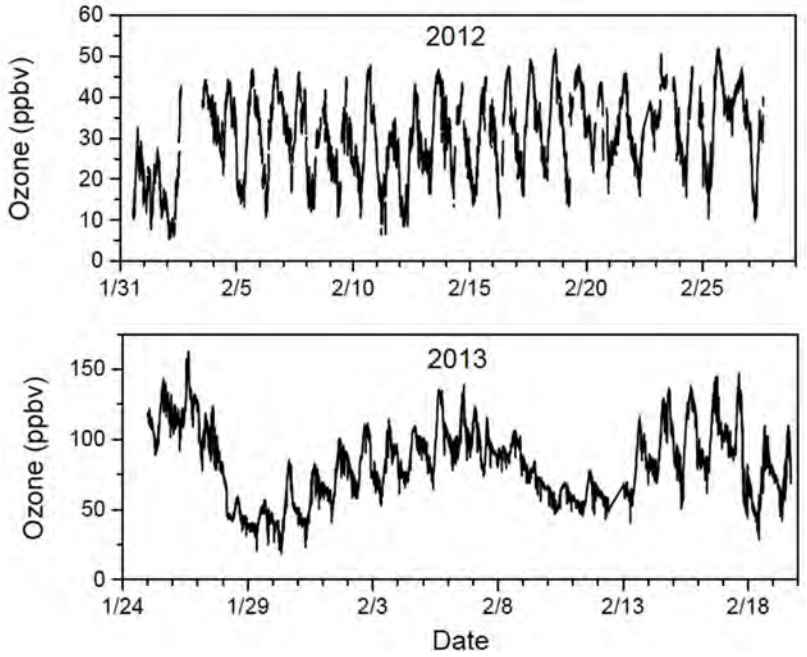


**Figure 6-3. Comparison of ozone measured at 2 m height from the 2012 and 2013 UBOS campaigns (note different y-axis scales).**

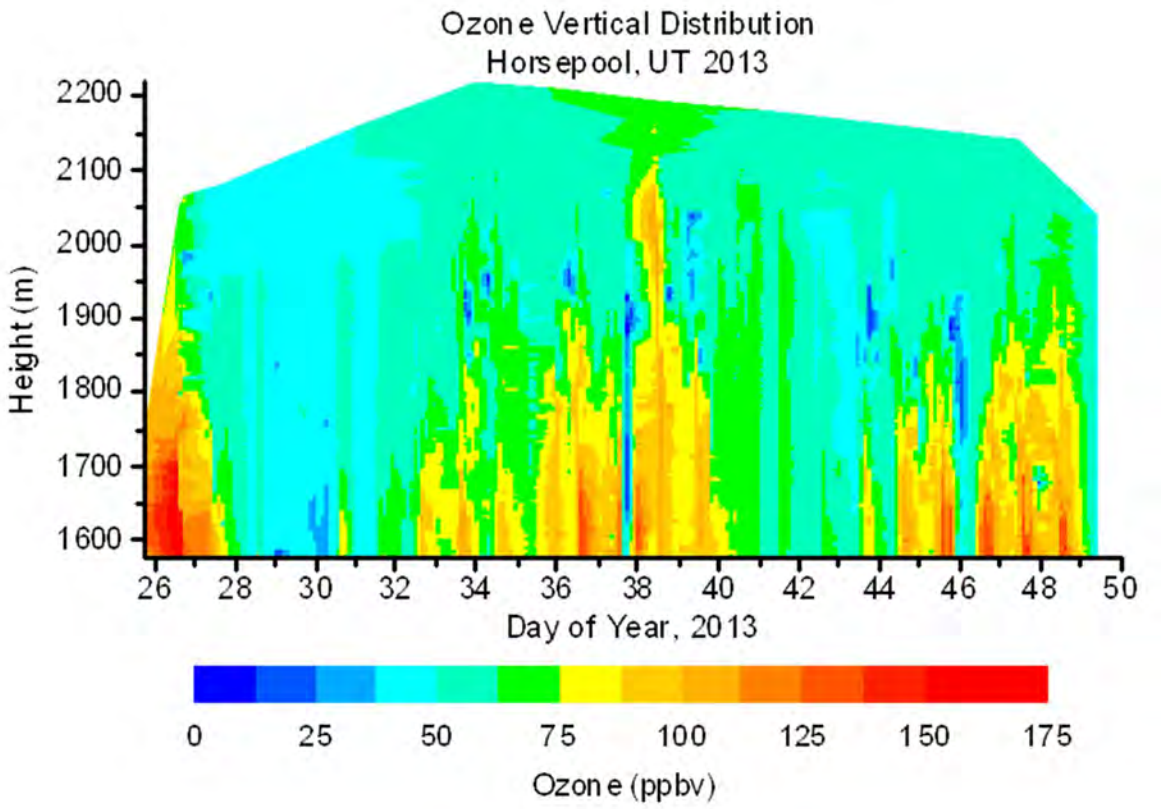


**Figure 6-4. Contour plot showing the complete record of ozone measurements acquired from the ECC tethersondes launched by the CU-INSTAAR group at Horsepool.**

A closer examination of individual ozone vertical profiles reveals the shallow, near-surface enhancement of photochemical ozone production. Figure 6-5 shows ECC sonde profiles for four days of the campaign, contrasting a relatively low ozone period (January 30 and 31) with an ozone build-up period (February 12 and 13). Here it can be seen that for both periods the ozone profiles are relatively consistent with height during the midnight and/or early morning profiles, but that during the day there is photochemical ozone production that is almost entirely confined to the lowest 100 – 150 m above ground level. Even on days prior to the beginning of an ozone build-up event (i.e., January 30) there is significant daytime ozone production near the surface. Notably, the ozone profiles throughout the day tend to converge to a common value in the highest ~ 200 m, or roughly above 1850 m a.s.l., indicating the presence of background air and that the sonde had reached beyond the top of the inversion layer.

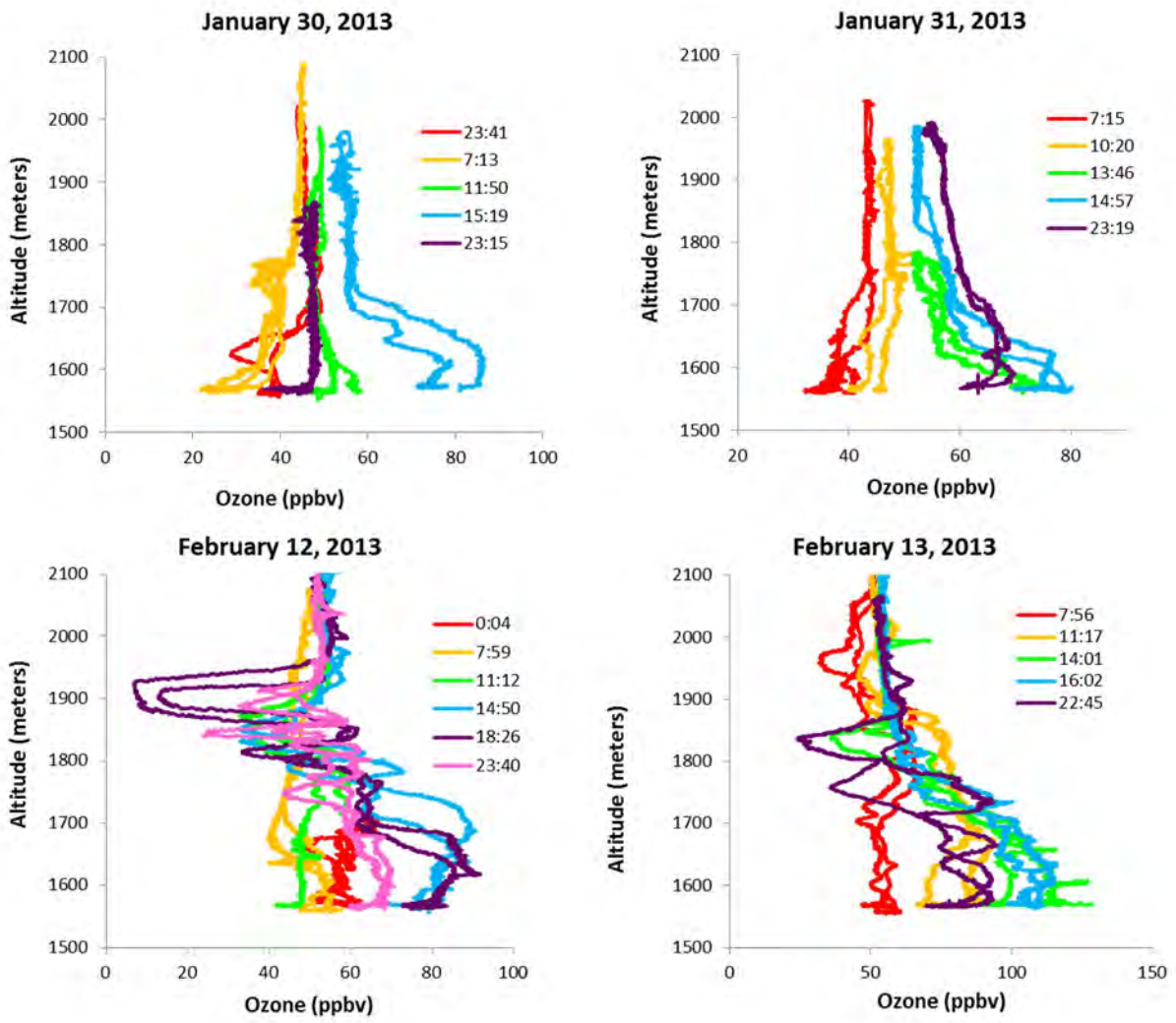


**Figure 6-5. Ozone vertical profiles from the ECC tethersonde for four days of the campaign, illustrating an unstable, relatively low ozone period (January 30 and 31) and a high ozone period during an inversion event (February 12 and 13) (please note the different x-axis scales of the graphs).**

### 6.3.2 Methane

As with ozone, methane values were significantly enhanced during the 2013 campaign as compared to 2012, although both years had methane values that were highly elevated over the regional background (~1.9 ppmv). Whereas in 2012 methane had the highest excursions up to ~10 ppmv, in 2013 methane was often above 15 ppmv at the surface. Figure 6-6 compares the methane time series from 2 m for the 2012 and 2013 campaigns (purple trace) overlaid on ozone (black trace). Most noticeable in comparison of these two data series is the clear build-up in methane mole fraction observed in 2013 coincident with the ozone build-up periods. Indeed, the ozone:methane correlation plots in Figure 6-7 reveal the positive correlation between these two species in 2013, a feature that was absent in 2012. The sharp and short-

lived excursions of methane up to and above 20 µmol/mol indicate an influence from nearby point-sources of methane in the region.

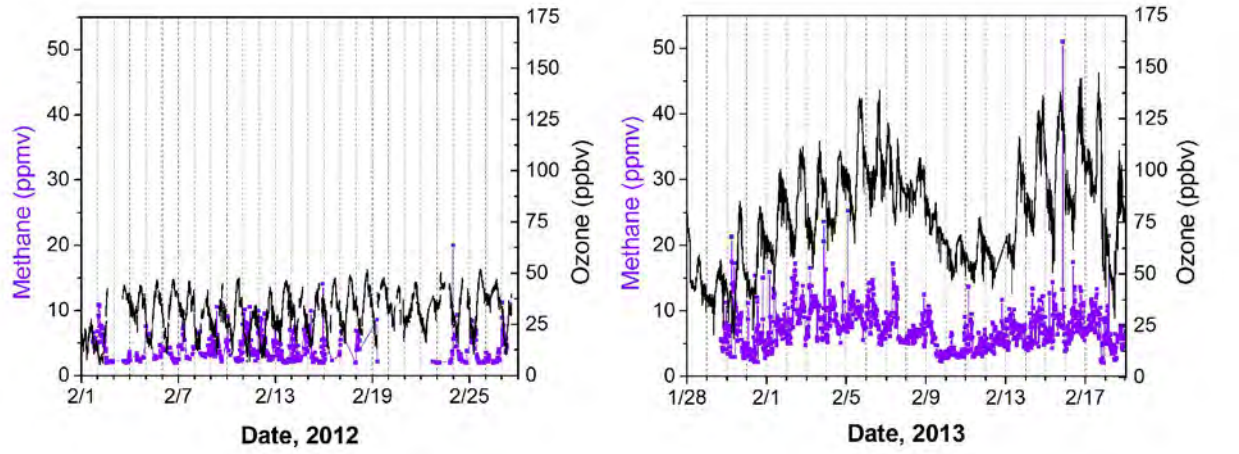


**Figure 6-6. Time series of methane (purple) and ozone (black) comparing the 2012 and 2013 campaigns.**

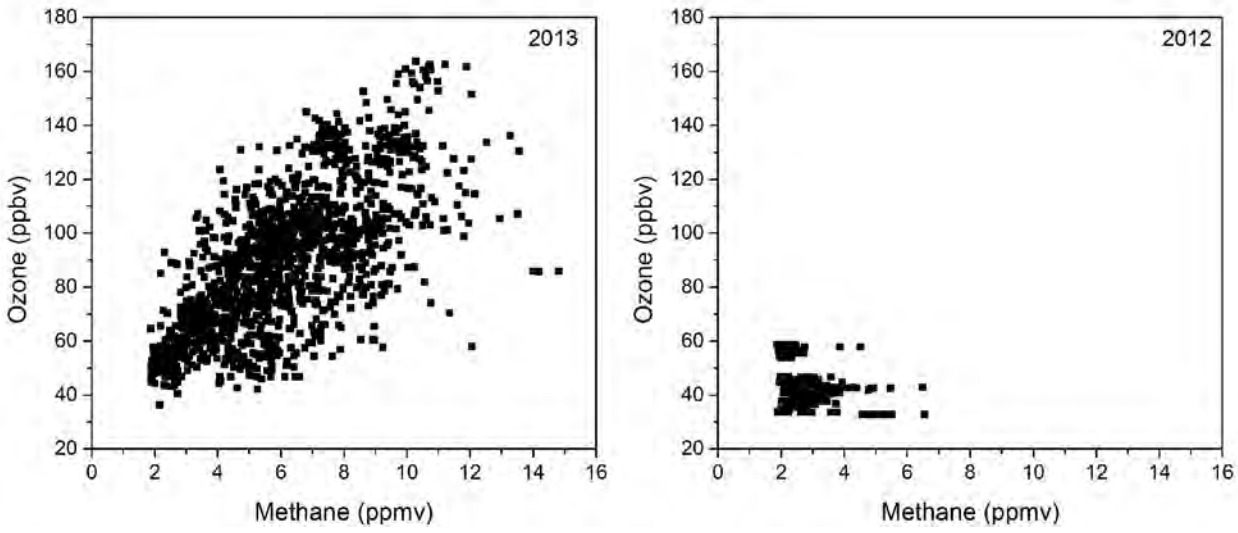


**Figure 6-7. Correlations of ozone and methane for 2013 (left) and 2012 (right).**

The average diurnal behavior of methane also showed marked differences between 2012 and 2013 (Figure 6-8A), which is of interest for this relatively long-lived compound. In 2012, methane showed a diurnal pattern with highest values in the early morning hours, consistent with overnight buildup in a relatively stable nocturnal surface layer, followed by a mid-afternoon minimum with little variability, consistent with relatively deep vertical mixing induced by upward surface heat flux from the bare ground. In 2013, on the other hand,

methane peaked at 08:00 MST and had a less distinct minimum during the afternoon hours, consistent with a much more stable afternoon surface layer over the snow covered ground.

The vertical distribution of methane as measured from the SkyDoc tethered balloon is shown in Figure 6-8B. These data reveal that the highest average mole fraction of methane was present nearest the surface and that the surface level methane showed the highest variability.

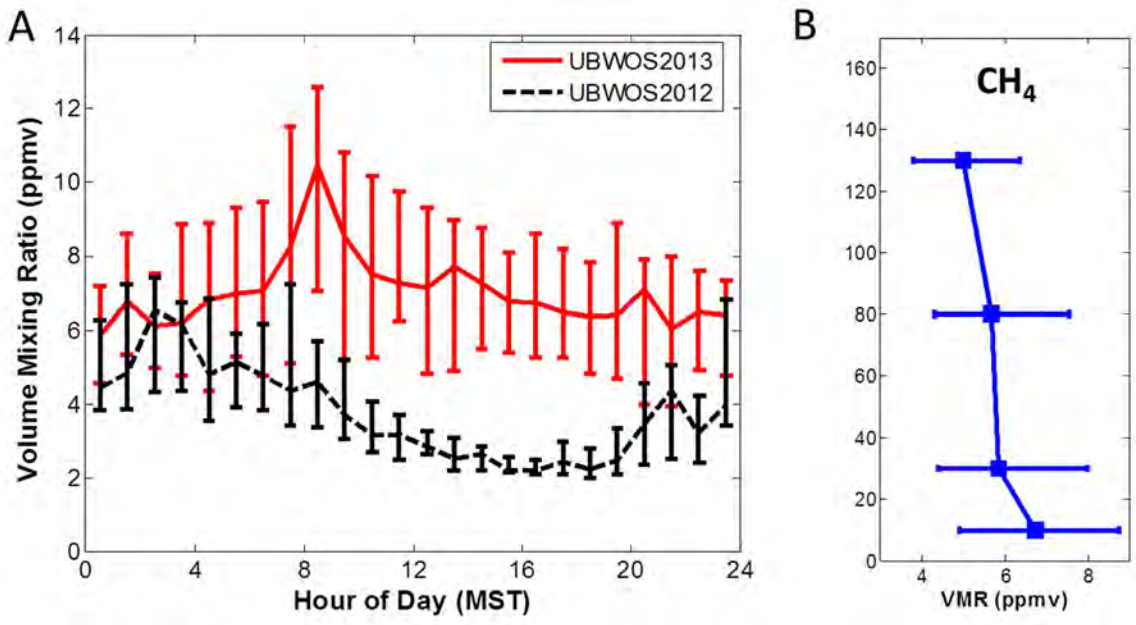


**Figure 6-8. Panel A: Diurnal average for methane comparing the 2012 (black) and 2013 (red) campaigns. Panel B: Average (plus or minus one standard deviation) methane vertical distribution for the 2013 campaign.**

### 6.3.3 Nitrogen Oxides

$NO_x$ levels showed a high variability, with most values ranging between 5-20 ppbv, and occasional spikes exceeding 50 ppbv (Fig. 6-9). Overall $NO_x$ was about 2-3 times higher in 2013 compared to 2012. The comparison of the composite diurnal cycles (Fig. 6-10) illustrates that the enhancement was particularly pronounced during mid-day to afternoon hours. This $NO_x$ comparison points to a similar conclusion as for methane and NMHC (below) that primary emissions accumulated to higher levels in 2013 due to reduced ventilation of the surface layer. The high variability in $NO_x$ may also point towards a relatively inhomogeneous distribution of $NO_x$ sources. NO remained below 0.1 ppbv at night, but rose sharply during morning hours to reach average levels of ~ 2 ppbv around noon time (Fig. 6-9). NO was ~ 50% higher in 2013 compared to 2012. The tethered balloon vertical profile measurements (Fig. 6-11) showed highest $NO_x$ mole fractions at the surface and decreasing levels with height, indicating that most of the $NO_x$ results from nearby sources.

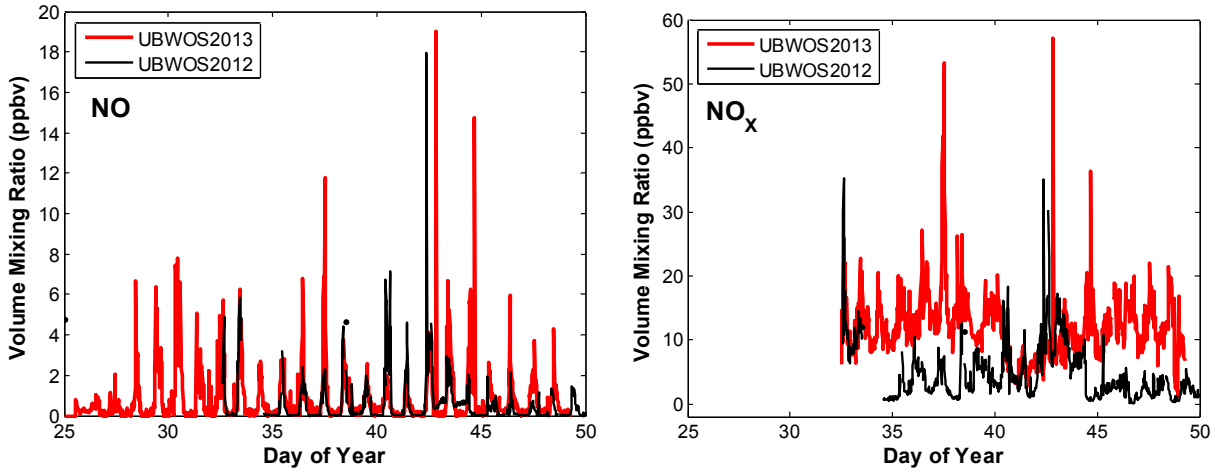


**Figure 6-9. Time series of NO and $NO_x$ from the 2 m tower comparing the 2012 (black) and 2013 (red) campaigns.**

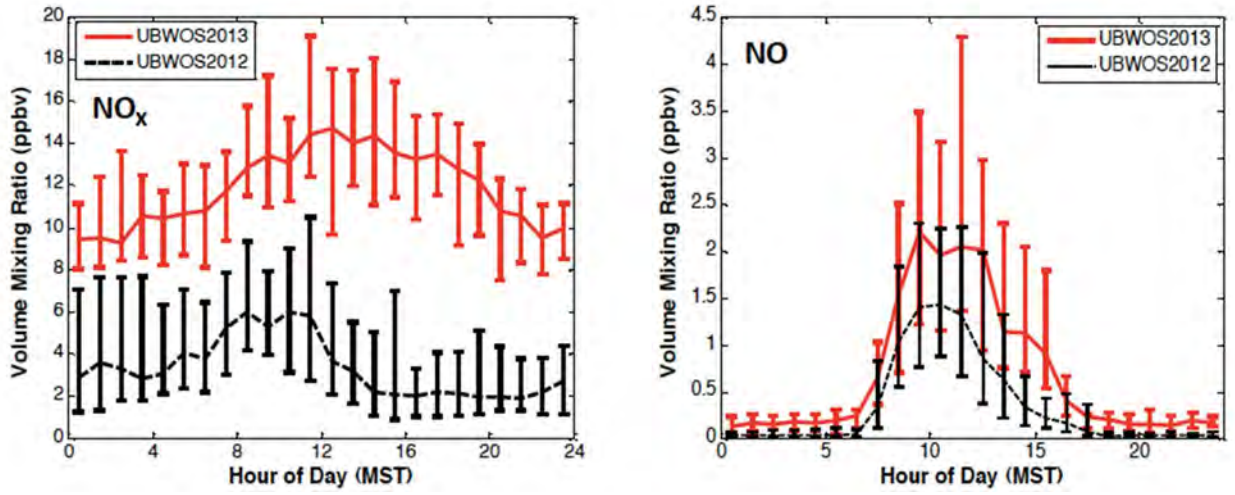


**Figure 6-10. Diurnal averages of $NO_x$ and NO from the 2 m tower comparing the 2012 (black) and 2013 (red) campaigns.**

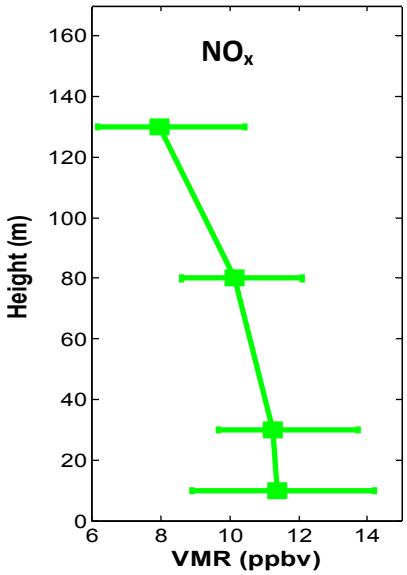


**Figure 6-11. Mean vertical distribution plus standard deviation of $NO_x$ during the 2013 campaign.**

### 6.3.4 Non-Methane Hydrocarbons

Non-methane hydrocarbons serve as precursors to photochemical ozone formation. Data from 2012 and 2013 both show that the light alkanes (i.e., C2 – C5) dominate the NMHC composition in the Uinta Basin. The mass fraction of an individual NMHC compound generally decreased with increasing molecule size. As discussed with other species, the mole fraction of NMHC was significantly enhanced in 2013 in comparison to 2012. Figure 6-12 demonstrates this by showing ethane (red) and propane (blue) overlaid on ozone (black). As with methane, these alkanes show a similar temporal behavior as ozone, building up during the inversion periods and then cleaning out to lower levels (e.g., <100 ppbv for ethane) when a low-pressure system would bring in air from the west.

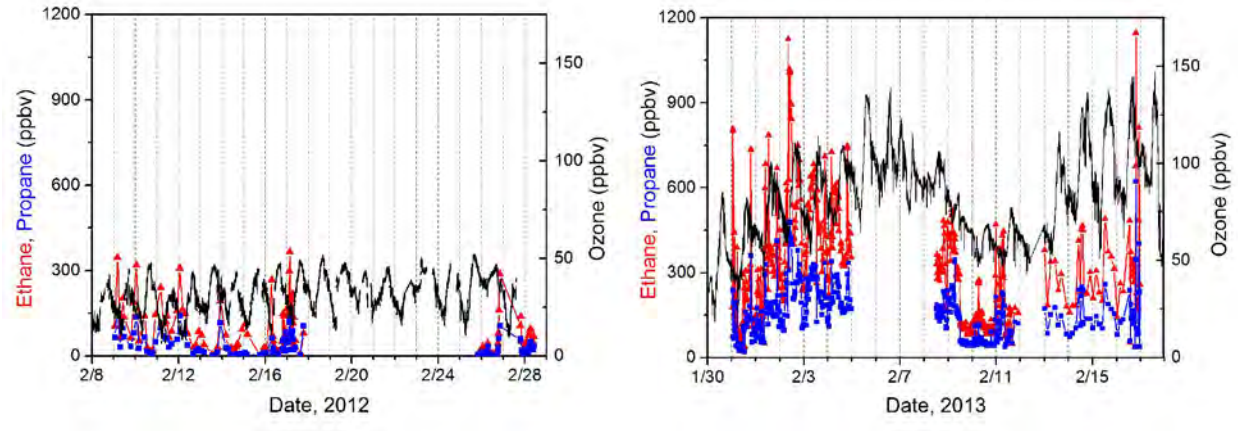


**Figure 6-12. Ethane (red) and propane (blue) time series from the 2 m tower overlaid with ozone (black) comparing the 2012 and 2013 campaigns.**

The NMHC mole fractions observed in the Uinta Basin in both 2012 and 2013 greatly exceeded the regional background values for 40°N as determined by the NOAA-INSTAAR Global Flask Network. The average ethane value for 2013, 320 ppbv, exceeded background by a factor of 160. However, the maximum ethane observed in 2013, which was greater than 1100 ppbv, corresponded to an enhancement of 550-fold over the regional background. The longer alkanes, propane through pentane, had an even greater enhancement over background values than did ethane (Table 6-1).

**Table 6-1. Average values for C2-C5 alkanes observed in 2012 and 2013 in comparison to regional background for 40°N in February as determined by the NOAA-INSTAAR Global Flask Network.**

| Compound | Uinta 2012 Average (ppbv) | Uinta 2013 Average (ppbv | Global Background 40°N, February (ppbv) | Enhancement Factor: Uinta 2013 vs. Background |
|---|---|---|---|---|
| Ethane | 73 | 320 | 2.0 | 160 |
| Propane | 32 | 160 | 0.64 | 250 |
| *i*-Butane | 6.7 | 33 | 0.09 | 367 |
| *n*-Butane | 12 | 51 | 0.17 | 300 |
| *i*-Pentane | 5.4 | 22 | 0.06 | 367 |
| *n*-Pentane | 5.0 | 20 | 0.04 | 500 |

As with the alkanes, the simple aromatic compounds (e.g., benzene, toluene) exhibited strong enhancements in the Uinta Basin, and experienced build-up concurrent with the ozone events. Figure 6- 13 illustrates this with benzene (orange) and toluene (purple) overlaid with ozone (black). Both benzene and toluene were consistently greater than 1 ppbv and at times reached over 10 ppbv. The tight correlation between benzene and ethane indicates a common source for both of these compounds.

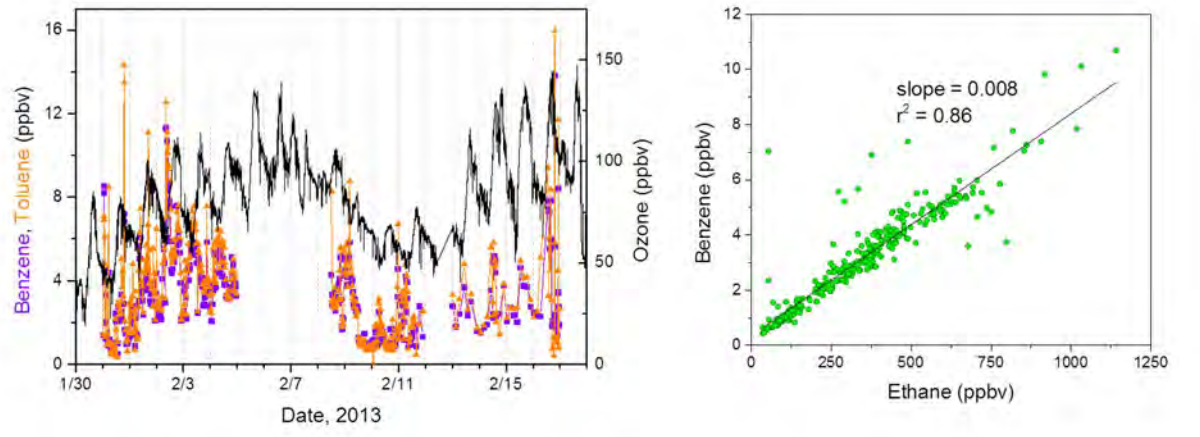


**Figure 6-13. Left: Time series of benzene (orange) and toluene (purple) overlaid with ozone (black) for the 2013 campaign. Right: Linear correlation of benzene and ethane for 2013.**

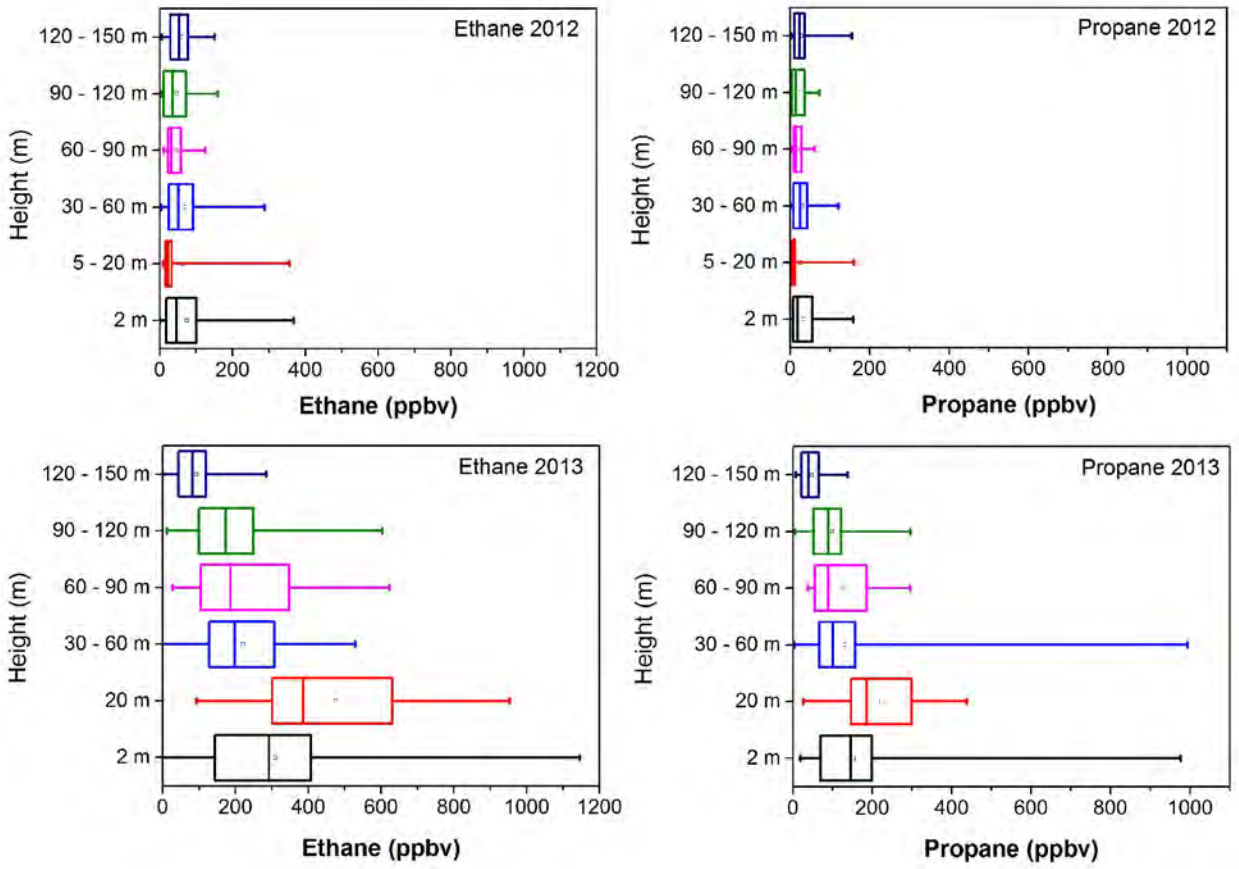


**Figure 6-14. Statistics of the vertical distributions of ethane and propane comparing the 2012 (top) and 2013 (bottom) campaigns. Here, the square marker represents the mean value, the edges of the box represent the 25$^{th}$ and 75$^{th}$ percentiles, the line in the box represents the median value, and the "whiskers" represent the minimum and maximum values.**

Significant differences were observed in the vertical distribution of the NMHC between the 2012 and 2013 campaigns. Figure 6-14 shows the statistics of the vertical distribution of ethane and propane as box and whisker plots. These plots show the dramatic difference in mole fraction at the lowest heights, with the greatest values observed near the surface in 2013. The NMHC appear to be primarily enhanced in the lowest 100 m during the inversion conditions in 2013, consistent with the vertical ozone profiles observed. In 2012, stronger vertical mixing resulted in relatively consistent mole fractions throughout the column. Mole fractions of both compounds were, however, similar in 2012 and 2013 at the highest measurement levels.

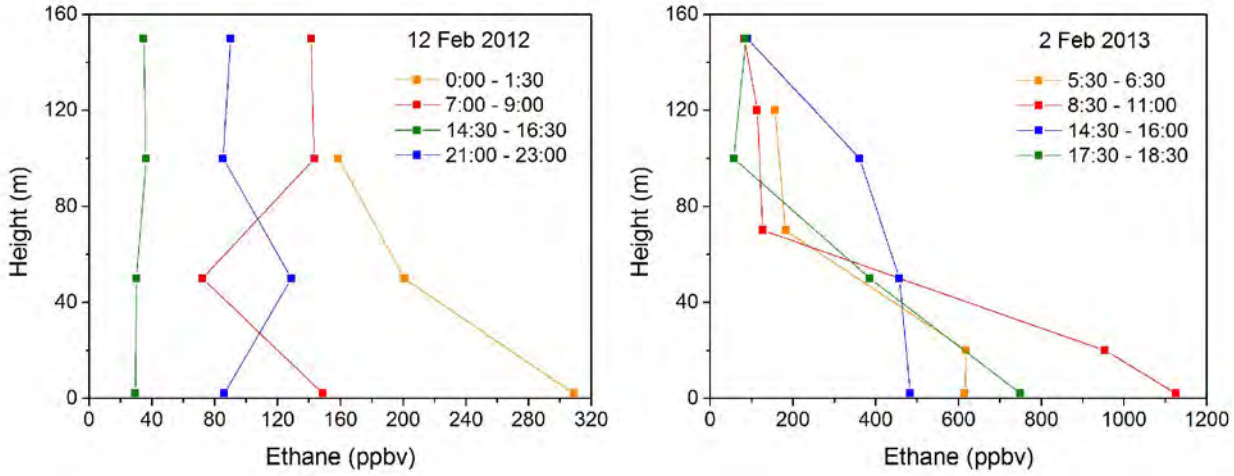


**Figure 6-15. Examples of two days of ethane vertical profiles contrasting a day with relatively strong vertical mixing (February 12) with a day with a shallow boundary layer and minimal vertical mixing (February 2).**

Individual vertical profiles of the NMHC (here shown for ethane in Figure 6-15) reveal the surficial nature of the strongest NMHC enhancements. Unlike for ozone, where mole fractions would build up during the day and reach an afternoon maximum due to photochemical production, ethane as a primary emission exhibited a more "plume-like" behavior with pockets of high NMHC passing over the measurement site in a more sporadic fashion.

### 6.3.5 Snowpack Air Ozone and NMHC Measurements

Ozone and NMHC were measured throughout the 2013 campaign through an inlet placed ~30 cm into the snowpack to sample snowpack air. The ozone record is shown in Figure 6-16A. Ozone within the snowpack air followed a nearly identical temporal pattern as ambient (2 m) ozone, but at significantly lower values. Snowpack ozone was attenuated by 50 – 80%, indicating that the snowpack is not a direct source of the high ozone in the Basin. This furthermore suggests chemical destruction and/or physical adsorption of ozone occurring in the snowpack. This destruction of ozone in the snowpack air is consistent with observations from Arctic and a Rocky Mountain high elevation site (Albert et al., 2002; Helmig et al., 2007; Peterson and Honrath, 2001; Bocquet and Helmig, 2007).

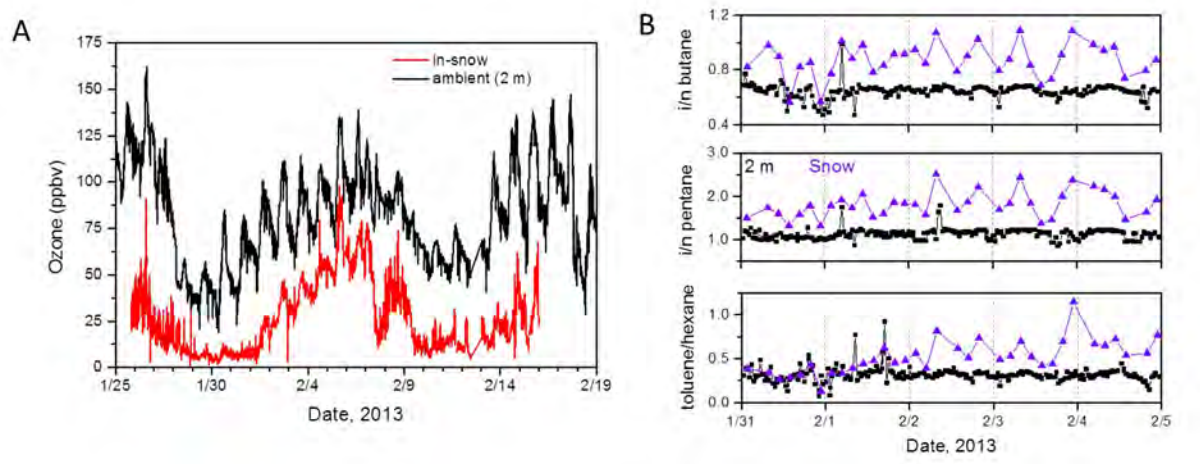


**Figure 6-16. Panel A: Time series of ozone measured from the 2 m tower (black) and from the snowpack inlet (red). Panel B: Time series of select NMHC ratios from the 2 m tower (black) and from the snowpack inlet (purple).**

Figure 6-16B shows time-series of select ratios of NMHC pairs determined from ambient measurements at the 2 m tower and from the snowpack air measurements with the snowpack inlet. Shown are the iso-butane:n-butane ratio, the iso-pentane:n-pentane ratio, and the toluene:hexane ratio. In each case, the ratios are enhanced in the snowpack relative to the ambient air. This enhancement indicates a preferential destruction of n-butane, n-pentane, and hexane relative to iso-butane, iso-pentane, and toluene, respectively. These ratios are indicators of active radical chemistry (Ariya et al., 1998; Jobson et al., 1994; Pszenny et al., 2007; Rudolph et al., 1997), and are suggestive of potential chlorine chemistry in the snowpack.

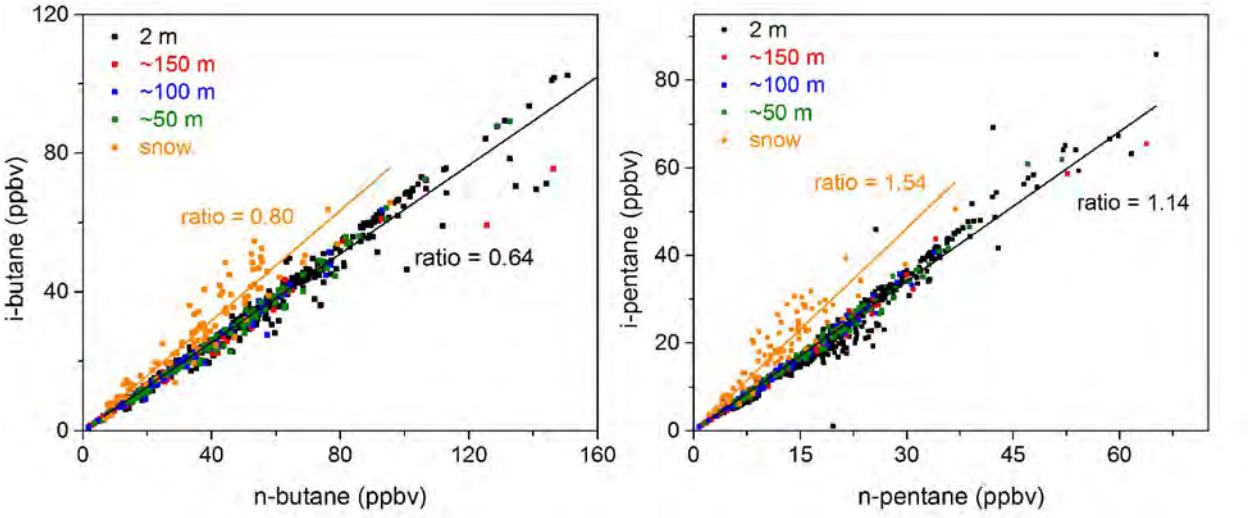


**Figure 6-17. Correlation plots for iso-butane:n-butane and iso-pentane:n-pentane broken up by inlet height.**

The iso-butane/n-butane and iso-pentane/n-pentane ratios have been used extensively in atmospheric research as a proxy for chlorine radical reactions, notably in Arctic environments, since direct measurements of halogen atoms have not been possible (Ariya et al., 1998; Boudries and Bottenheim, 2000; Jobson et al., 1994; Rudolph et al., 1997; Rudolph et al., 1999). This technique is based upon the differences in kinetic rate constants for Cl and OH radicals with these species. The OH radical reacts with both isomers of butane with approximately the same rate constant, and the same is true for the isomers of pentane. However, Cl atoms react preferentially (by a factor of ~1.5) with the n isomer of these compounds. Thus, an enhancement in these isomer ratios is suggestive, but not proof, of active chlorine radical chemistry. Figure 6-17 plots these two ratios, dividing the measurements by inlet height. Here it can be seen that all of the ambient data, regardless of height, clusters tightly around the 0.64 line for the butanes and the 1.14 line for the pentanes. The only data that do not lie on this line are the snowpack data, shown in orange. In both cases, the snowpack ratios are enhanced relative to the ambient air. Figure 6-18 illustrates this in another fashion, but plotting the iso-pentane:n-pentane ratio versus n-pentane and the iso-butane:n-butane ratio versus n-butane. When expressed in this manner, data that fall along a horizontal line would be indicative of OH-dominated oxidation chemistry, whereas data that fall along a vertical line would be indicative of Cl-dominated oxidation chemistry (Jobson et al., 1994). Here it can be seen that, again, the snowpack data deviate significantly from all ambient data, suggesting active radical chemistry occurring in the snowpack air. It should also be noted that ethane, the least reactive of these NMHC, exhibits a nearly identical values between snowpack and 2 m measurements, indicating that the differences in NMHC observed here are not merely a result of slower transport (via diffusion) through the snowpack.

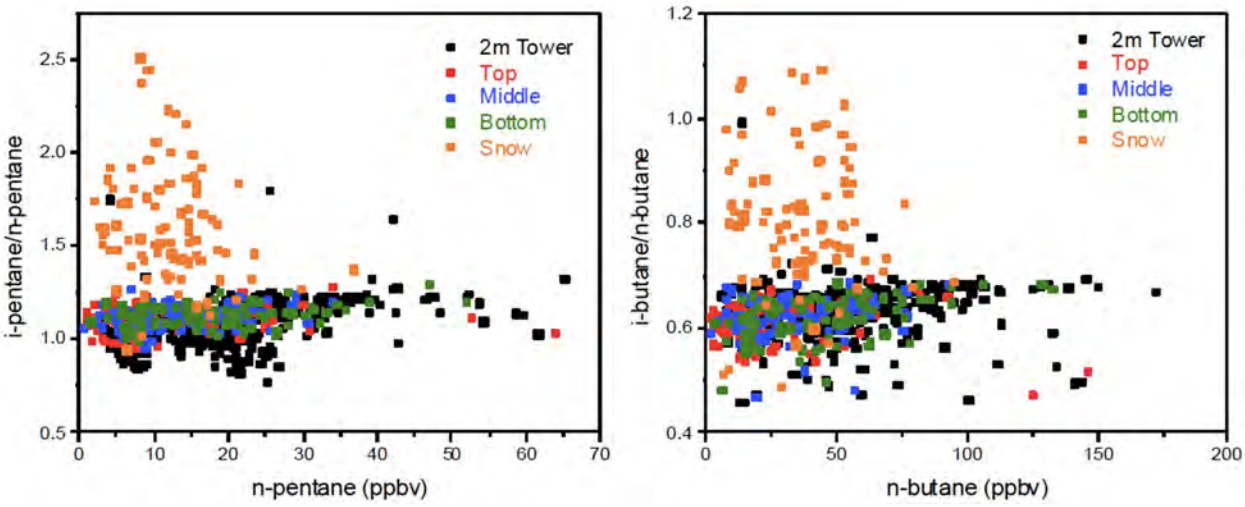


**Figure 6-18. Plots of the iso-pentane:n-pentane ratio versus n-pentane and the iso-butane:n-butane ratio versus n-butane for all NMHC data divided by inlet height.**

### 6.3.6 Meteorological Parameters

The vertical distribution of potential temperature as measured from the balloon soundings is shown in Figure 6-19. This graph illustrates the persistence of the temperature inversion with coldest temperatures and strongest inversions coinciding with the periods of strongest ozone production. The pressure record in Figure 6-20 nicely illustrates how the periods with lower ozone precursor concentrations and lower ozone buildup occurred during times when low pressure systems had moved into the region.

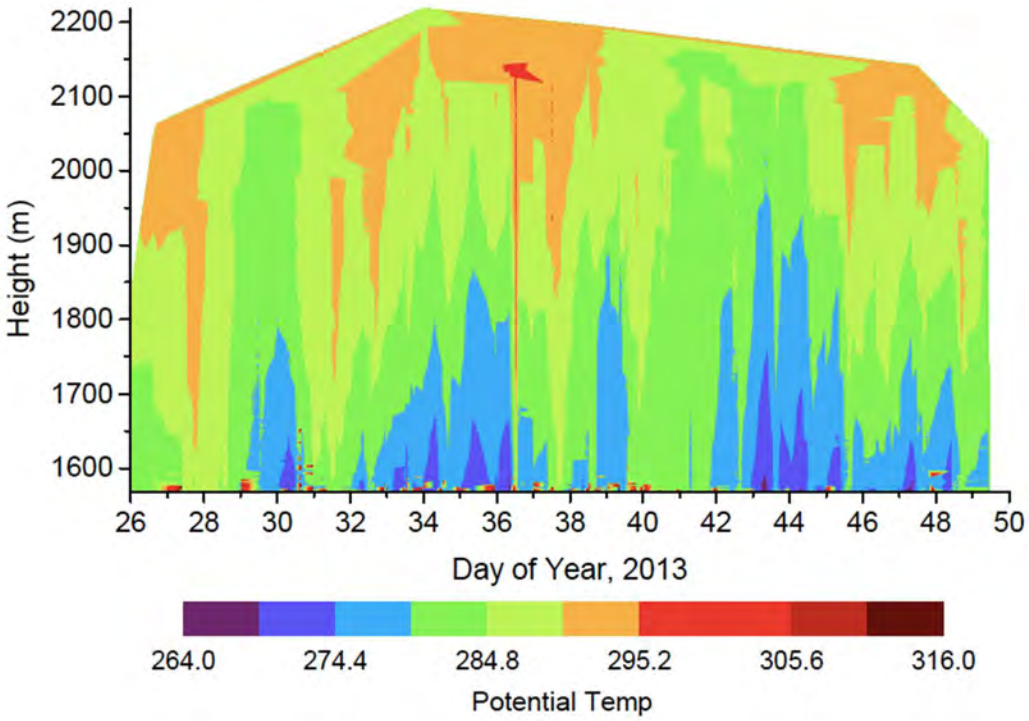


**Figure 6-19. Potential temperature vertical distribution from the tethersonde data.**

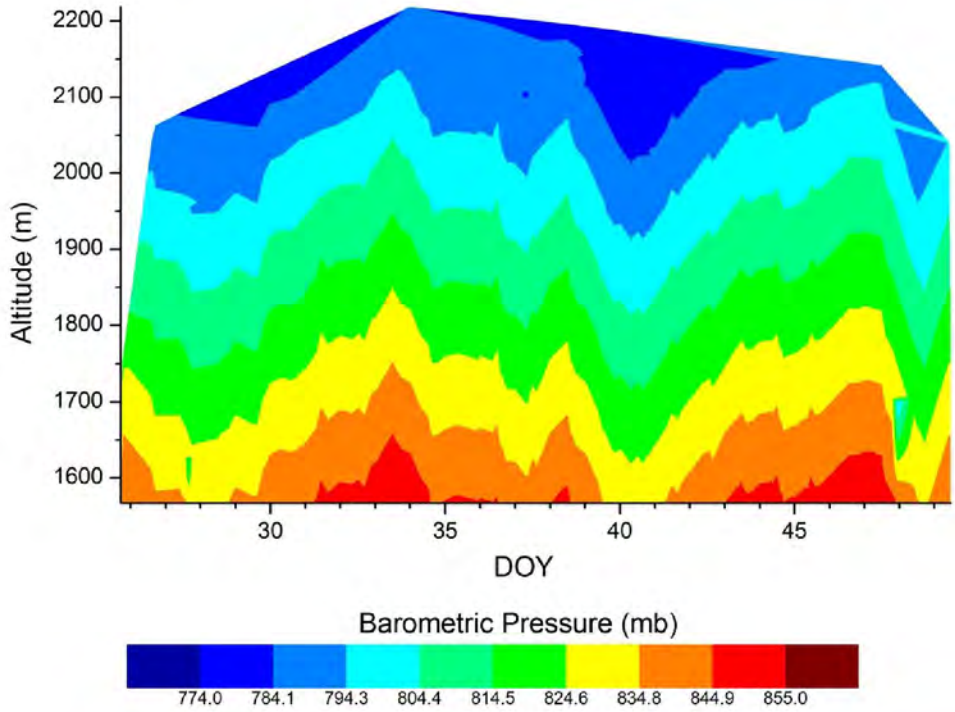


**Figure 6-20. Pressure record from the tethersonde vertical balloon profiles.**

## 6.4 References

Albert, M. R., A. M. Grannas, J. Bottenheim, P. B. Shepson, and F. E. Perron (2002), Processes and properties of snow, Äìair transfer in the high Arctic with application to interstitial ozone at Alert, Canada, *Atmospheric Environment*, *36*(15), 2779-2787.

Ariya, P., B. Jobson, R. Sander, H. Niki, G. Harris, J. Hopper, and K. Anlauf (1998), Measurements of C2-C7 hydrocarbons during the Polar Sunrise Experiment 1994: Further evidence for halogen chemistry in the troposphere, *Journal of Geophysical Research*, *103*(D11), 13169.

Bocquet F., D. Helmig, and S.J. Otlans (2007), Ozone in interstitial air of the mid-latitude snowpack at Niwot Ridge, Colorado. Arctic, *Antarctic and Alpine Research* 39, 375-387.

Boudries, H., and J. Bottenheim (2000), Cl and Br atom concentrations during a surface boundary layer ozone depletion event in the Canadian high Arctic, *Geophysical Research Letters*, *27*(4), 517-520.

Helmig, D., F. Bocquet, L. Cohen, and S. J. Oltmans (2007), Ozone uptake to the polar snowpack at Summit, Greenland, *Atmospheric Environment*, *41*(24), 5061-5076.

Jobson, B., H. Niki, Y. Yokouchi, J. Bottenheim, F. Hopper, and R. Leaitch (1994), Measurements of C2-C6 hydrocarbons during the Polar Sunrise 1992 Experiment: Evidence for Cl atom and Br atom chemistry, *J. Geophys. Res*, *99*(D12), 25355 - 25368.

Peterson, M., and R. Honrath (2001), Observations of rapid photochemical destruction of ozone in snowpack interstitial air, *Geophysical Research Letters*, *28*(3), 511-514.

Pszenny, A. A., E. V. Fischer, R. S. Russo, B. C. Sive, and R. K. Varner (2007), Estimates of Cl atom concentrations and hydrocarbon kinetic reactivity in surface air at Appledore Island, Maine (USA), during International Consortium for Atmospheric Research on Transport and Transformation/Chemistry of Halogens at the Isles of Shoals, *Journal of Geophysical Research: Atmospheres*, *112*(D10).

Rudolph, J., B. Ramacher, C. Plass-Dülmer, K. Ä. Müller, and R. Koppmann (1997), The indirect determination of chlorine atom concentration in the troposphere from changes in the patterns of non-methane hydrocarbons, *Tellus B*, *49*(5), 592-601.

Rudolph, J., B. Fu, A. Thompson, K. Anlauf, and J. Bottenheim (1999), Halogen atom concentrations in the Arctic troposphere derived from hydrocarbon measurements: Impact on the budget of formaldehyde, *Geophysical Research Letters*, *26*(19), 2941-2944

# 7.0 OZONE DEPOSITION VELOCITY DURING SNOW-COVERED AND NON-SNOW-COVERED PERIODS BY EDDY COVARIANCE

***Detlev Helmig, Chelsea Stephens, Jeong-Hoo Park, Jacques Hueber, Patrick Boylan, Jason Evans***

***Institute of Arctic and Alpine Research, University of Colorado Boulder***

## 7.1 Objective

The goal of this project was to directly measure the ozone surface flux in the Uinta Basin by eddy covariance to determine the rate of ozone deposition to the snow to allow for more accurate parameterization in models. The eddy covariance method utilizes fast (10 Hz) measurements of turbulence and ozone and calculates the correlation between the fast fluctuations of vertical wind velocity and ozone mole fraction to determine the magnitude and direction of the surface flux.

## 7.2 Experimental Methods and Instrumentation

### 7.2.1 Study Site and Duration

Flux measurements were conducted by CU-INSTAAR researchers at the Horsepool site (~1569 m a.s.l.) in the Uinta Basin from January 25 through April 2, 2013. This time period allowed for flux measurements to be made during both the snow-covered study intensive measurement period and following the snow melt and subsequent exposure of the dirt surface, as shown by the albedo plot in Figure 7-1. During the intensive period (January 25 – February 19), between two to four CU researchers were on-site at all times. Following the intensive period, the flux instrumentation continued running and was monitored remotely from the INSTAAR lab in Boulder, CO. Two trips were made back to the site for instrument maintenance and the instrumentation was dismantled on April 2.

### 7.2.2 Experimental Set-Up and Instrumentation

Flux measurements were conducted using a 2 m flux tower. To this tower was mounted a Campbell Scientific CSAT-3 three-dimensional sonic anemometer and the inlet to the fast response ozone instrument (FROI). The FROI and computer systems were housed in a temperature-controlled trailer located approximately 10 m from the flux tower.

The FROI is a custom-built instrument that is capable of 10 Hz measurements of ozone mole fraction. It utilizes NO reagent gas to react with ozone to generate a chemiluminescence signal that is detected with a photomultiplier (PMT) detector. The instrument and operation is described in full detail in Bariteau et al. (2010).

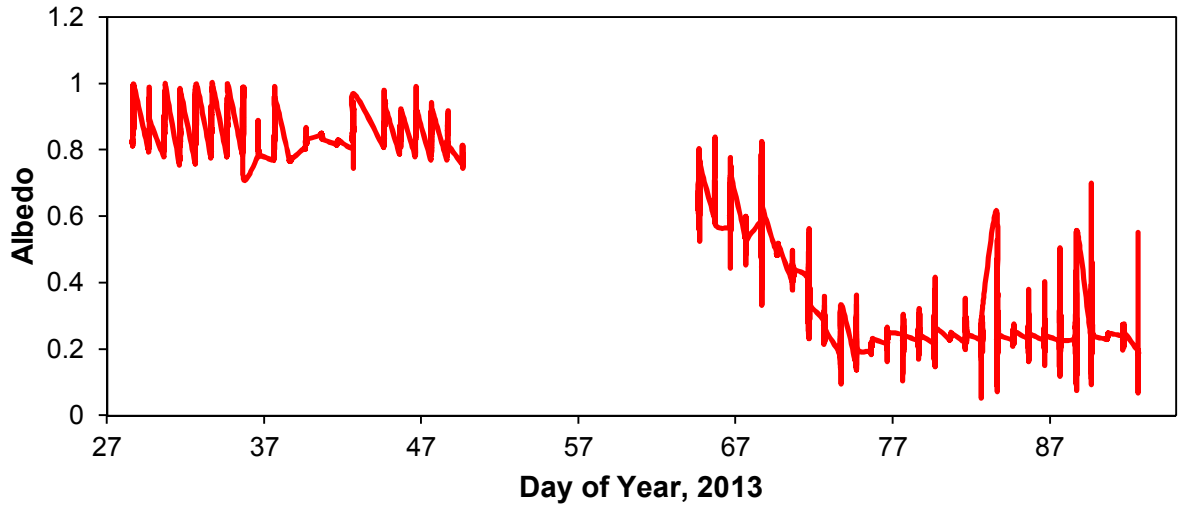


**Figure 7-1. Albedo measured as an indicator of surface snow cover at the Horsepool site during the study period.**

## 7.3 Results and Discussion

Over 1600 hours of ozone flux data were collected during this campaign. Data were filtered for periods of instrument maintenance and calibration, obstructed wind direction, very low winds speeds (< 0.5 m/s), unstable wind direction during the averaging period, and non-stationarity. Ozone data were time-corrected for the sampling lag time resulting from transport time though the sampling line and detrended over the averaging period to remove the influence of strong daytime photochemical ozone formation in this environment.

### 7.3.1 Snow-Covered Period

The land surface in the Uinta Basin consists of dry, sandy soil and low-lying sage brush. During the campaign intensive period, snow cover persisted that was less than half a meter deep. The snow sufficiently covered the soil, but the leaf-less and dry sage brush still protruded well above the snowpack. A histogram of ozone deposition velocity for a portion of the snow-covered period is shown in Figure 7-2. The median daytime deposition velocity is 0.003 cm $s^{-1}$ with a 2-$\sigma$ window ranging from -0.071 – 0.079 cm $s^{-1}$. This result is in the lower end of the range of previous determinations for snow-covered sites (Helmig et al., 2007). In general, ozone fluxes in and out of snow vary widely, with reported exchange velocity results from previous studies over seasonally snow-covered sites in the range of -3.3 to 1.7 cm $s^{-1}$, however, most data are within the range of 0.0 to 0.2 cm $s^{-1}$ (Helmig et al., 2007). In the Arctic, another environment where stably-stratified boundary layer conditions predominate, values were lower, on the order of <0.01 - 0.07 cm $s^{-1}$ depending on the time of year (Helmig et al.,2009). In comparison, midsummer values for lush vegetation surfaces have a much greater ozone deposition velocity of 0.2 – 1.0 cm $s^{-1}$ (Wesely and Hicks, 2000).

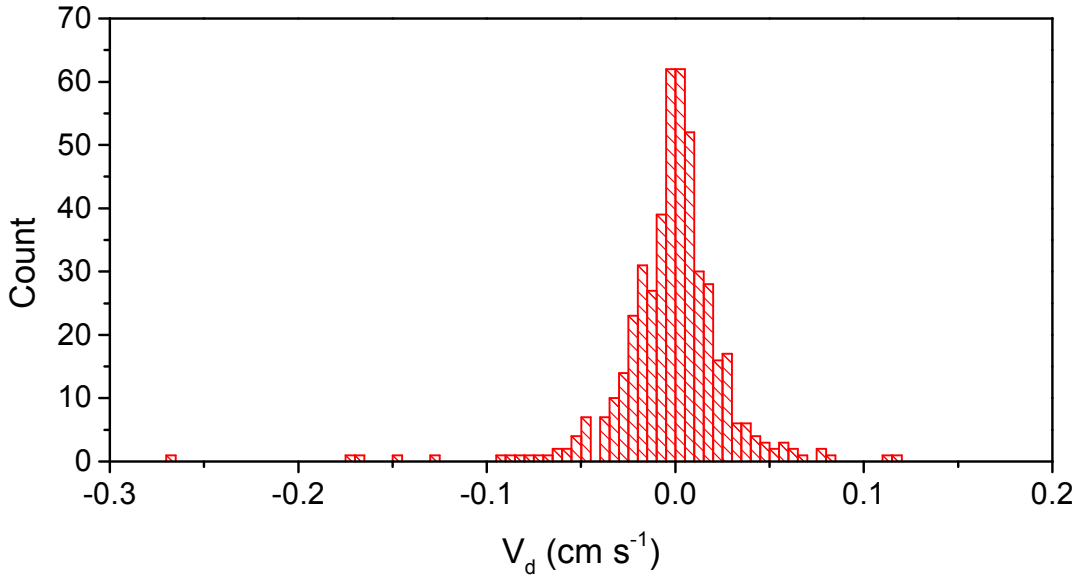


**Figure 7-2. Histogram of ozone deposition velocity calculations for the snow-covered period (early February) inclusive of both nighttime and daytime data. Mean and median ozone deposition velocity were -0.002 and 0.0 cm $s^{-1}$, respectively, with the 2-σ window extending from -0.063 – 0.059 cm $s^{-1}$.**

### 7.3.2 Snow Free Period

The flux experiment continued ~ 2 weeks after the completion of snow melt to capture ozone fluxes during exposure of the bare soil. The sage brush during this period was still dry and leafless, thus the only difference between the two periods studied was the presence of the snow cover on the ground. Here, we use data for the period of March 26 through April 2, which is one week after the measured albedo indicates the snow has melted, to ensure a period of dry (rather than wet or muddy) soil. Figure 7-3 shows a histogram of the deposition velocities from this period. Here, determined ozone deposition velocity values have a wider distribution. The maximum daytime deposition velocity ($V_d$) is 0.14 cm $s^{-1}$, with a median daytime value of 0.02 cm $s^{-1}$. The overall median value, including nighttime data is 0.002 cm $s^{-1}$. The period of wetted soil, between March 17 and March 25, yielded a lower median deposition velocity of 0.001 cm $s^{-1}$.

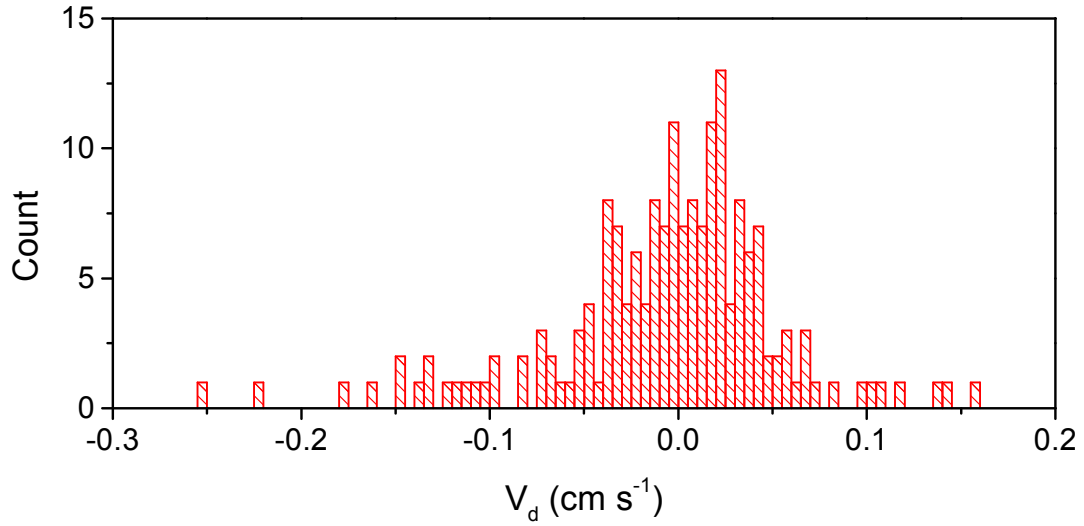


**Figure 7-3. Histogram of ozone deposition velocity calculations for the non-snow-covered period (late March) inclusive of nighttime and daytime data. Mean and median ozone deposition velocities were -0.006 and 0.002 cm $s^{-1}$, respectively, with the 2-$\sigma$ window extending from -0.066 – 0.054 cm $s^{-1}$.**

Reported ozone deposition velocity measurements to soil surfaces in the literature vary widely, and are roughly dependent upon soil type, composition, and moisture content. It has been generally considered that wetted soil is more resistant to ozone uptake than dry soils due to the low water solubility of ozone (Erisman and Van Pul, 1994), but recent studies have found that the controlling factors are much more complex (Stella et al., 2011). Deposition velocities over wet bare soil in Illinois were determined via the gradient method to be 0.04 to 0.2 cm $s^{-1}$ (Wesely et al., 1980). In comparison, eddy covariance determinations of ozone deposition velocity over the Sahara Desert were found to have a maximum daytime $V_d$ of 0.15 cm $s^{-1}$ and a mean of 0.065 cm $s^{-1}$ (Gusten et al., 1996). These authors recommended a daytime $V_d$ of 0.1 cm $s^{-1}$ and a nighttime $V_d$ of 0.04 cm $s^{-1}$ for modeling of desert ecosystems. Our results for the Horsepool site are at the lower end of these previously reported bare soil ozone deposition velocities. These results illustrate that this environment with its dry, sandy soil conditions shows similar ozone uptake behavior as desert-like environments.

## 7.4 References

Bariteau, L., D. Helmig, C. W. Fairall, J. E. Hare, J. Hueber, and E. K. Lang (2010), Determination of oceanic ozone deposition by ship-borne eddy covariance flux measurements, *Atmospheric Measurement Techniques, 3*, 441 – 455.

Erisman, J. W. and A. Van Pul (1994), Parameterization of surface resistance for the quantification of atmospheric deposition of acidifying pollutants and ozone*, Atmospheric Environment, 28* (16), 2595 – 2607.

Gusten, H., G. Heinrich, E. Monnich, D. Sprung, J. Weppner, A. B. Ramadan, M. R. M. Ezz El-Din, D. M. Ahmed, and G. K. Y. Hassan (1996), On-line measurements of ozone surface fluxes: Part II. Surface level fluxes onto the Sahara desert, *Atmospheric Environment, 30* (6), 911 – 918.

Helmig, D., L. Cohen, F. Bocquet, S. Oltmans, A. Grachev, and W. Neff (2009), Spring and summertime diurnal surface ozone fluxes over the polar snow at Summit, Greenland, *Geophys. Res. Lett., 36*, L08809.

Helmig, D., L. Ganzeveld, T. Butler, and S. J. Oltmans (2007), The role of ozone atmosphere-snow gas exchange on polar, boundary-layer tropospheric ozone – a review and sensitivity analysis, *Atmospheric Chemistry and Physics, 7*, 15 – 30.

Stella, P., B. Loubet, E. Lamaud, P. Laville, and P. Cellier (2011), Ozone deposition onto bare soil: A new parameterization, *Agricultural and Forest Meteorology, 151* (6), 669 – 681.

Wesely M. L., D. R. Cook, and R. M. Williams (1980), Field measurement of small ozone fluxes to snow, wet bare soil., and lake water, *Boundary Layer Meteorology, 20* (4), 459 – 471.

Wesely, M. L. and B. B. Hicks (2000), A review of the current status of knowledge on dry deposition, *Atmospheric Environment, 34* (12-14), 2261 – 2282.

# 8.0 TETHERED OZONESONDE AND SURFACE OZONE MEASUREMENTS IN THE UINTA BASIN, WINTER 2013

**Russ Schnell[1], Bryan Johnson[1,] Patrick Cullis[2], Chance Sterling[4], Emrys Hall[2], Rob Albee[3], Allen Jordan[2], Jim Wendell[1], Samuel Oltmans[2], Gabrielle Petron[2] and Colm Sweeney[2]**

1. NOAA Earth System Research Laboratory, 325 Broadway, Boulder, CO
2. CIRES - University of Colorado, Boulder, CO 80305
3. Science and Technology Corporation, http://www.stcnet.com.
4. University of Colorado, Boulder, CO

## 8.1 Introduction

The four main goals of the NOAA ozone group involvement in the Uintah 2013 study were to:

1. Document the vertical and temporal distribution of the wintertime ozone production process in high resolution.
2. Collect data on the spatial distribution of ozone in the basin.
3. Determine whether the Bonanza power plant emissions are contributing precursors for ground level ozone production during temperature inversion (elevated ozone) events.
4. Determine where the ozone precursors originate.

Ozone and temperature profiles from the surface to 250-500 meters above ground level were measured January 24 - February 17, 2013 by tethered ozonesondes operated at Ouray Wildlife Refuge and Fantasy Canyon by the NOAA/ESRL Global Monitoring Division (GMD), and at Horsepool by the Institute for Arctic and Alpine Research (INSTAAR) from the University of Colorado with ozonesondes supplied by NOAA (Map, Figure 8-6). During this period, 735 vertical profiles of ozone, temperature and water vapor were conducted. Ozonesondes were also used to measure surface ozone from a vehicle on drives within the basin. Two free-flying ozonesondes were released during high surface ozone events to provide profiles from the surface to 30,000 meters, putting the surface measurements into perspective and to check for stratospheric intrusions of elevated ozone into the Uinta Basin. In a separate component of the Uinta 2013 study, NOAA flew an instrumented aircraft in the basin. These results are reported separately.

The 2013 study was the second consecutive winter that tethered ozonesondes were used within the Uinta Basin as part of campaigns investigating wintertime high ozone events. The winter conditions in the previous year (2012) were much different than in 2013 with warmer temperatures, the lack of snow cover and the absence of strong temperature inversions in 2012. Ozone measured in 2012 was within normal background ranges from 40-60 ppbv measured at all sites in the basin. The crucial difference in the meteorology influencing ozone formation in 2013 was the presence of persistent snow in the basin (Figure 8-1) and strong emission trapping temperature inversions.

All times are in local Mountain Standard Time (MST, mst) and all altitudes and elevations in meters (m) above sea level (asl).


**Figure 8-1. The presence of snow throughout the Uinta Basin in 2013 was a controlling factor in the production of ozone in 2013 as discussed in various sections of this report.**

### 8.1.1 Ozonesonde Measurements in the Uinta Basin

Ozonesondes have been used at NOAA for more than 25 years for monitoring stratospheric and tropospheric ozone at long term sites and in numerous intensive campaigns. The ozonesondes are typically released on free-flying balloons that reach 30-35,000 m altitude in less than 2 hours. However, for the Uinta Basin campaign, the relatively fast rising balloon (~ 300 meters per minute rise rate) on a typical ozonesonde flight would travel too quickly through the shallow layer of interest near the surface. Therefore, a new custom built tether system, shown in Figures 8-2 and 8-3, was designed to carry an ozonesonde from ground level to a height of 350 meters and back down in 60 minutes or less. Based on the 2011 ozone study within the Uinta Basin (Martin et al., 2011), this height would extend above the top of localized wintertime temperature inversions. Making two profiles per hour at three sites tracked the vertical development of the basin-wide wintertime photochemical ozone production and provided high resolution data for the study of the fine detail of the ozone formation and distribution. Vertical profiles for both ozone and temperature will be very useful to evaluate mesoscale model results.

**Figure 8-2. An automated, portable NOAA tethered ozonesonde system at the Fantasy Canyon site. The tethered ozonesonde system was set up and in operation within an hour of arriving on site. The complete system is battery operated and can be left alone to conduct profiles to a pre-set altitudes, then return to the surface before repeating the cycle. The system will run for ~4 hours before sonde batteries require changing. *Photo: Patrick Cullis, NOAA/CIRES, February 2013.***

**Figure 8-3. A portable NOAA automated ozonesonde tether installation in operation in the late evening at the Ouray Wildlife Refuge site. This system was operated remotely from within the staff house that also served as an ozonesonde preparation and calibration center.** ***Photo: Patrick Cullis, NOAA/CIRES, February 2013.***

In 2013, in addition to the tethered ozonesondes, continuous UV Photometric surface ozone analyzers (TEI) (Figure 8-4) were operated full time at the Ouray National Wildlife Refuge and the Blue Feather pipe yard. The TEI at Ouray provided a comparison for the ozonesonde measurements. In Figure 8-5 is a plot of the Ouray tethersonde and TEI monitor data showing excellent agreement. The comparisons were conducted at the start and end of each tether profile by holding the ozonesonde for ~2 min next to the TEI inlet that was 1 meter above the snow surface. The TEI measurements were ~3 % lower than the ozonesonde measurements, but this is considered excellent agreement for ozone being measured with very different techniques. The ozonesonde measurements operate based on a quantitative chemical reaction, and air flow through the sample chamber is calibrated for each ozonesonde prior to its initial launch.


**Figure 8-4. TEI UV photometric surface ozone analyzer operated full time at the Ouray Wildlife Refuge during the 2012 and 2013 campaigns. An additional unit was operated at the Blue Feather pipe yard in 2013.**

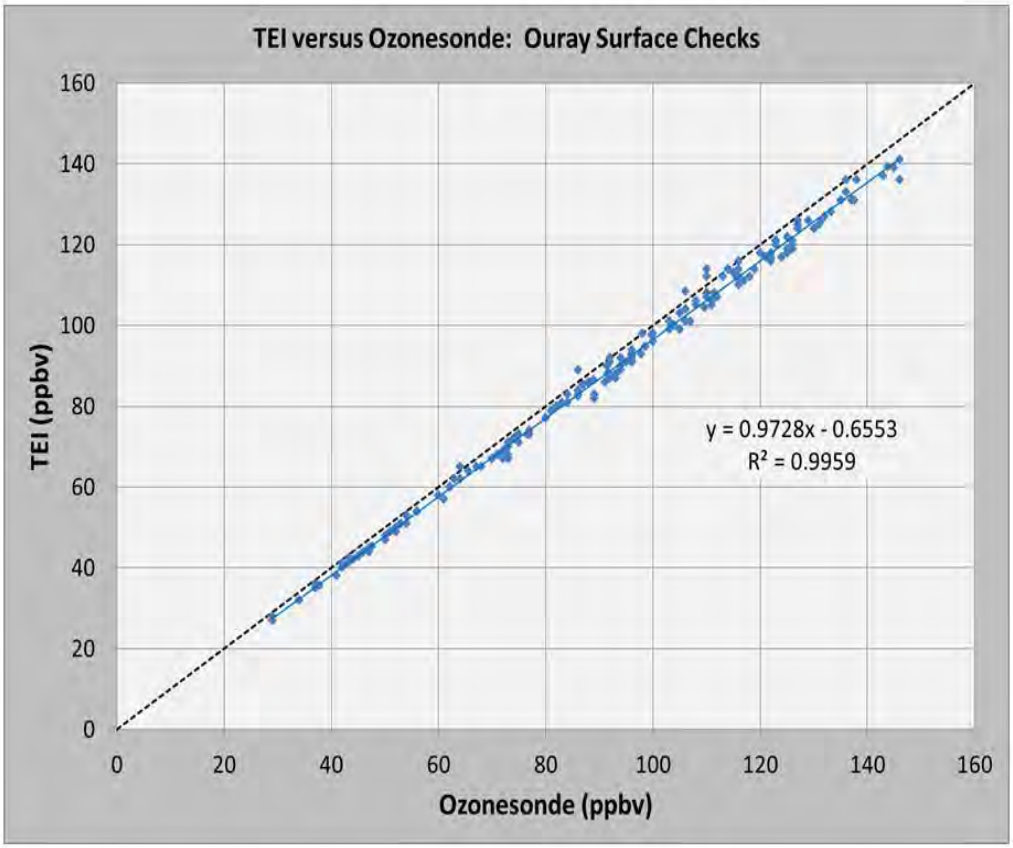


**Figure 8-5. TEI versus ozonesonde measurements prior to each tethered ozonesonde profile ascent at the Ouray Wildlife Refuge site in 2013. The TEI reads about 3% lower than the ozonesondes. This is not considered a significant difference considering the range of ozone concentrations measured.**

### 8.1.2 Ozonesonde Instruments

Ozonesondes are well-suited for vertical ambient and mobile measurements since they are stable under a wide range of temperatures and pressures. The measurement principle is based on the iodometric method, the fast reaction of ozone and iodide ($I^-$) in an aqueous 1% potassium iodide solution. The ozonesonde sensor described by Komhyr et al. (1969, 1995) uses a platinum electrode electrochemical cell. The sensor's output current is linearly proportional to the rate at which ozone is bubbled into the KI solution. Precision is better than ± (3–5)% with an accuracy of about ± (5–10)% up to 30 km altitude based on environmental chamber simulation tests reported by Smit et al. (2007), and from a field ozonesonde intercomparison campaign [Deshler et al., 2008]. Table 8-1 shows the specifications for the instruments used during the Uinta campaigns in 2012 and 2013.

The sensor is interfaced with an Imet radiosonde which measures and transmits ambient pressure, temperature, relative humidity and GPS altitude and location along with the ozone data.

The Uinta ozonesondes were conditioned and prepared according to NOAA standard operating procedures then compared to a NIST-standardized Thermo Environmental UV ozone monitor 49C operating continuously at the Ouray operations site. Final data was QA/QC'd using NOAA viewing and editing software.

**Table 8-1. ECC (electrochemical concentration cell) Ozonesonde.**

**A. Ozonesonde Specifications**

The ozonesonde sensor described by Komhyr et al. [1969, 1995] uses a platinum electrode electrochemical cell. The sensor's output current is linearly proportional to the rate at which ozone is bubbled into the KI solution. Ozone mixing ratio can then be computed from

Equation (1) $PO_3 = 4.30 \bullet (I - I_{BG}) \bullet Tp \bullet PF / P$

Where:
$PO_3$ = Ozone mixing ratio (parts per billion by volume)
I = Cell output current (~ 0-5.0 microamperes)
$I_{BG}$ = Cell background current (typically 0-0.03 microamperes)
Tp = Temperature of sonde pump (K)
PF = Flow rate in seconds per 100 ml of air flow
Measured by a standard soap bubble flow meter with small correction (+2.5% to +3.5%) applied to account for evaporation of the soap bubble solution.
P = Ambient Air Pressure (hectopascals or millibars)

Accuracy Troposphere: ± 2 ppbv (parts per billion by volume) ± 3-5% of reading
Accuracy Stratosphere: ± (5–10%) up to 30 km altitude.
Precision: ± 3-5%

Data frequency: 1 hz

Calibration: No calibration is applied to the ozonesonde data. Ozonesondes are screened before use in the field by checking against the laboratory NIST-standardized Thermo Environmental UV ozone calibrator model 49C at zero, 40 ppbv and 100 ppbv. The ozonesonde must read within 2% of the calibrator before use in the field.

| | Free flying release ozonesonde: | Tethered ozonesonde: |
|---|---|---|
| Altitude Range: | surface to 98,000 feet | surface to 1,000 feet |
| Balloon Rise Rate: | 800 feet/ minute | 35 feet/minute |
| Vertical Resolution: | 160 feet | 7 feet |

**B. InterMet Radiosonde Specifications**

Temperature accuracy/precision: ± 0.2 C / 0.2 C

Humidity accuracy/precision: ± <3% / 2%

Pressure accuracy/precision: ±0.5hPa (millibars) / 0.5 hPa

GPS Altitude: +/- 5 meters (16 feet)

**C. Thermo Scientific 49i Ozone Monitor Specifications**

Principle: Dual path UV Absorption

Accuracy Troposphere: ± 1 ppbv (parts per billion by volume)

Precision: ± 3%

Range: 1-250 ppbv Calibration: NIST Traceable Data frequency: 1 minute averages

**Table 8-2. Uinta Basin primary tethered ozonesonde site locations, number of profiles measured and maximum ozone mixing ratios measured during Jan and Feb, 2012 and 2013.**

| **2012** | | | | | | |
|---|---|---|---|---|---|---|
| Location | Longitude ($^{o}$W) | Latitude ($^{o}$N) | Elevation (meters) | # of tether profiles/dates | $[O_3]$max (ppbv) | |
| Ouray | 109.6446 | 40.1347 | 1430 | 42 Feb 6-27 | 54 | |
| Horsepool | 109.4674 | 40.1431 | 1569 | 62 Feb 7-26 | 59 | |
| Jensen | 109.3519 | 40.3687 | 1454 | 33 Feb 6-28 | 47 | |
| Roosevelt | 110.0082 | 40.2943 | 1587 | 8 Feb 16 | 51 | |
| **2013** | | | | | | |
| Locations | Longitude ($^{o}$W) | Latitude ($^{o}$N) | Elevation (meters) | # of tether profiles/dates | $[O_3]$max (ppbv) | |
| Ouray | 109.6446 | 40.1347 | 1430 | 387 Jan 24 - Feb 7 | 167 | |
| Horsepool | 109.4674 | 40.1431 | 1569 | 216 Jan 24 - Feb 17 | 162 | |
| Fantasy Canyon | 109.3941 | 40.0582 | 1470 | 132 Jan 31 - Feb 7 | 152 | |

### 8.1.3 Tethered Ozonesonde (Tethersonde) Measurements

The ozonesonde tether system was developed by the NOAA Global Monitoring Division for the Uinta Basin field projects. The system is based upon a motorized deep sea fishing rod and reel with 50 pound line. The design includes communication software and data loggers to continuously monitor the radiosonde pressure allowing control of the ascent and descent rates. Temperature and dew point are radioed to the surface in real time as is GPS altitude and Latitude/Longitude coordinates of the instrument package. The system can operate unmanned during ascent and descent and can maintain a level altitude controlled from a laptop computer.

The tethered balloon sites are presented in Figure 8-6 with gas and oil wells shown in blue and red respectively. The sites are also listed in Table 8-2 along with the maximum ozone levels (mixing ratios – parts per billion (ppb) by volume) observed in 2012 and 2013 during the two wintertime campaigns. The absence of high concentrations of surface ozone in 2012 (Figure 8-7) is clearly observed in the ozone vertical profiles when compared to 2013 shown in Figure 8-8.

The NOAA ozone group has collected and processed a huge amount of data in this project. For instance, we have plotted ~1750 graphs and have over a million lines of discrete data files. For this report, we show the minimum number of graphs and analyses to present a cohesive story without overwhelming the reader. All of the 2013 data and graphs may be accessed at: ftp://ftp.cmdl.noaa.gov/ozwv/ozone/Uintah_2013_Tether_OzoneSondes/ .

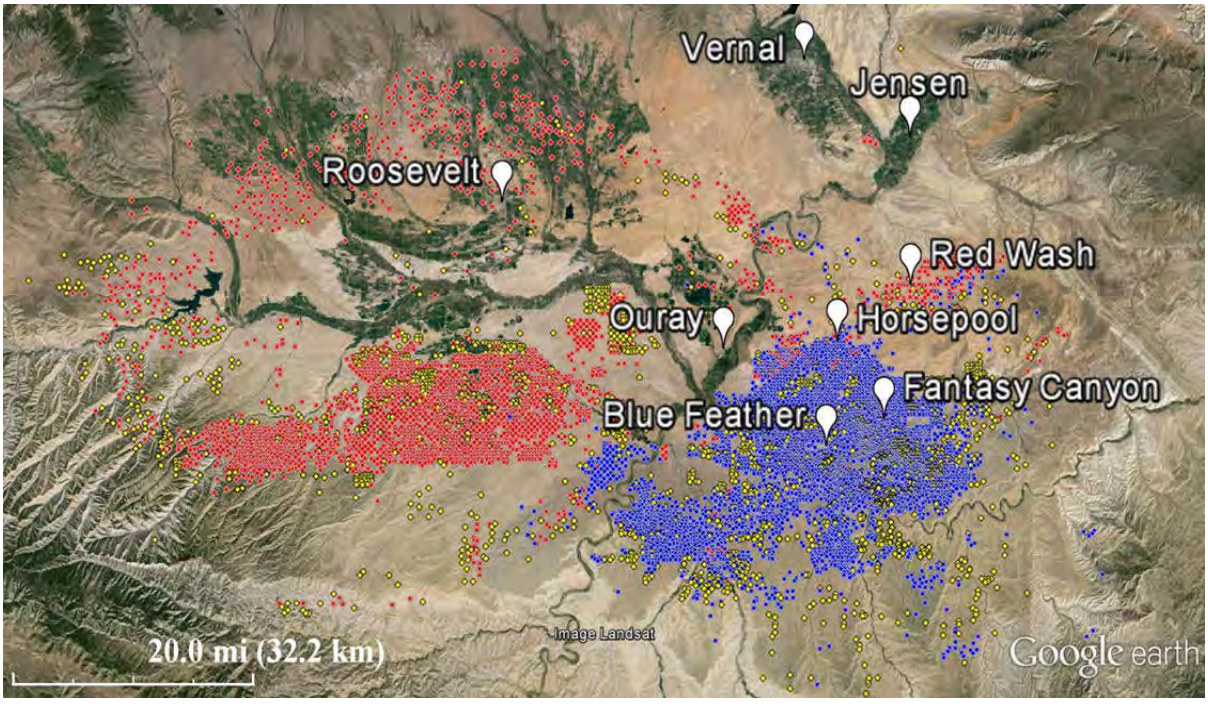


**Figure 8-6. Map of the Uinta Basin with locations of the oil (red) and gas wells (blue) and the tethersonde sites in 2012 (Ouray, Horsepool, Roosevelt and Jensen) and 2013 (Ouray, Horsepool and Fantasy Canyon). Surface ozone monitors were operated at Blue Feather and Ouray in 2013. There is an EPA ozone monitor at Red Wash that the mobile ozone van passed regularly.**

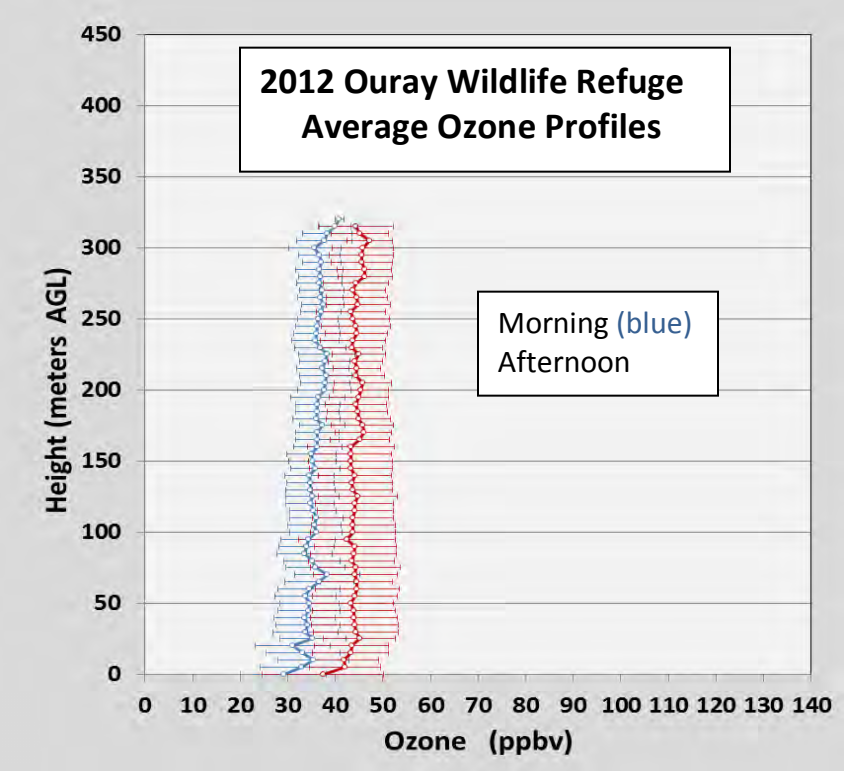


**Figure 8-7. Summary plot of the 2012 average ozone mixing ratios and standard deviations measured at all sites during morning (between sunrise and local noon, in blue) and afternoon (noon to sunset, red). Note the absence of any large ozone production in events in 2012 compared to the range of the ozone measured in 2013 presented in Figure 8-8. The data in Figures 8-7 and 8-8 are plotted on the same scales binned at 5 m elevations.**

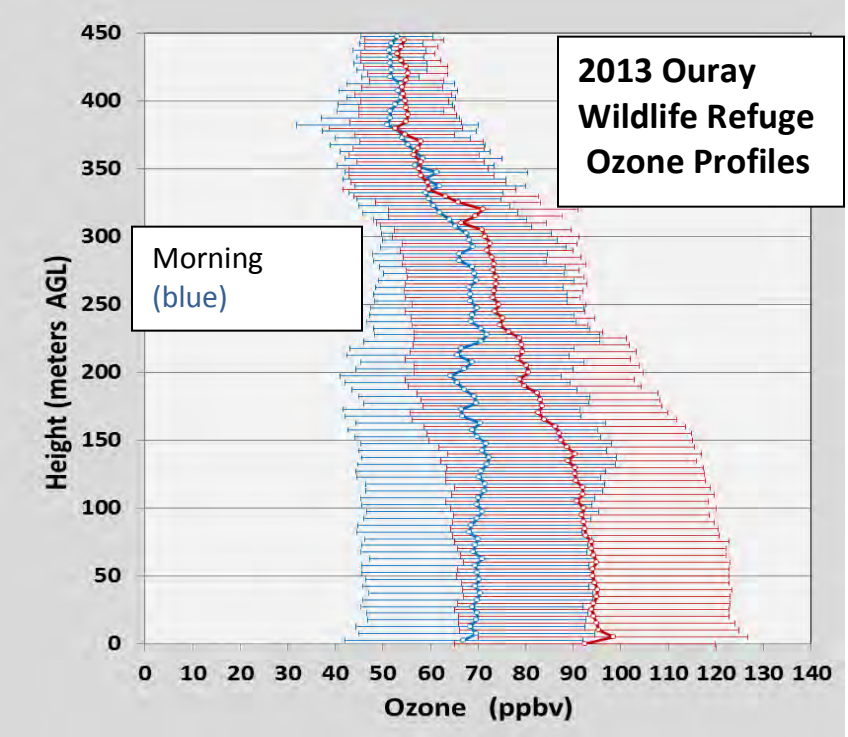


**Figure 8-8. Summary plot of the 2013 average ozone mixing ratio and standard deviations measured at all sites during morning (between sunrise and local noon, in blue) and afternoon (noon to sunset, red). Note the large range of ozone concentrations in 2013 and the large photochemical production of ozone in the afternoons. The data in Figures 8-7 and 8-8 are plotted on the same scales.**

## 8.2 Uinta Basin 2013 Surface Ozone Concentrations

### 8.2.1 Surface and Tethersonde Measurements at Three Sites

Surface ozone concentrations measured between January 15 and February 15, 2013 at Ouray Wildlife Refuge (NOAA), Red Wash (EPA) and Horsepool (NOAA) are presented in Figure 8-9. In this figure three successive wintertime high ozone production events may be observed. The diurnal ozone production cycle and the ozone build-up over time are in clear evidence. The rapid drops in ozone at the end of each cycle are caused by "cleanout" events that occur when fresh air or storms from outside the basin flush out the ozone and ozone precursors that are trapped below shallow, basin wide temperature inversions.

The successive colored arrows point to times that ozonesonde profiles are presented in Figures 8-10 - 8-15. In these figures we show that ozone and temperature profiles were remarkably similar at the three well-distributed sites that are at different elevations. This shows that the inversion layer is relatively constant in altitude across the basin and independent of the height of the surface topography. This constant altitude inversion layer is also observed in the aircraft and surface mobile measurements.

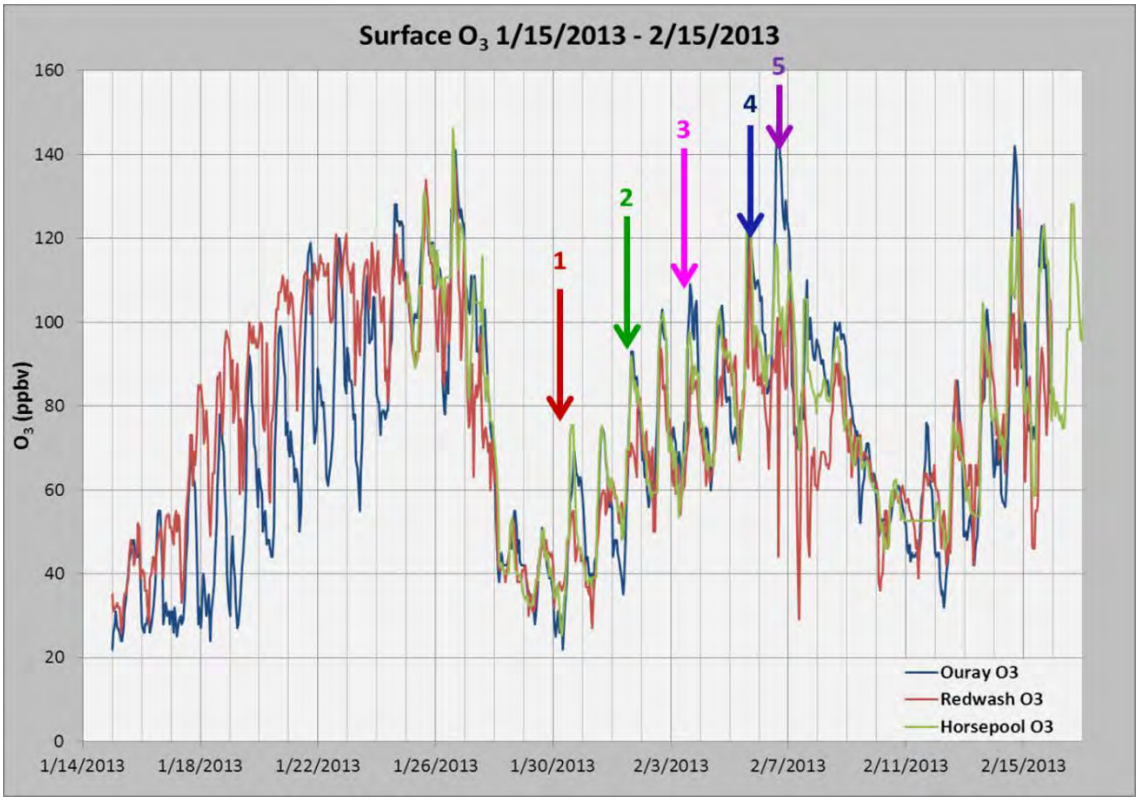


**Figure 8-9. Surface hourly average ozone concentrations measured at three dispersed sites in the Uinta Basin showing the diurnal production of ozone, the build-up of total ozone during an event and the rapid cleanout of the basin that occurs when air from outside the basin enters and mixes down to the surface.**

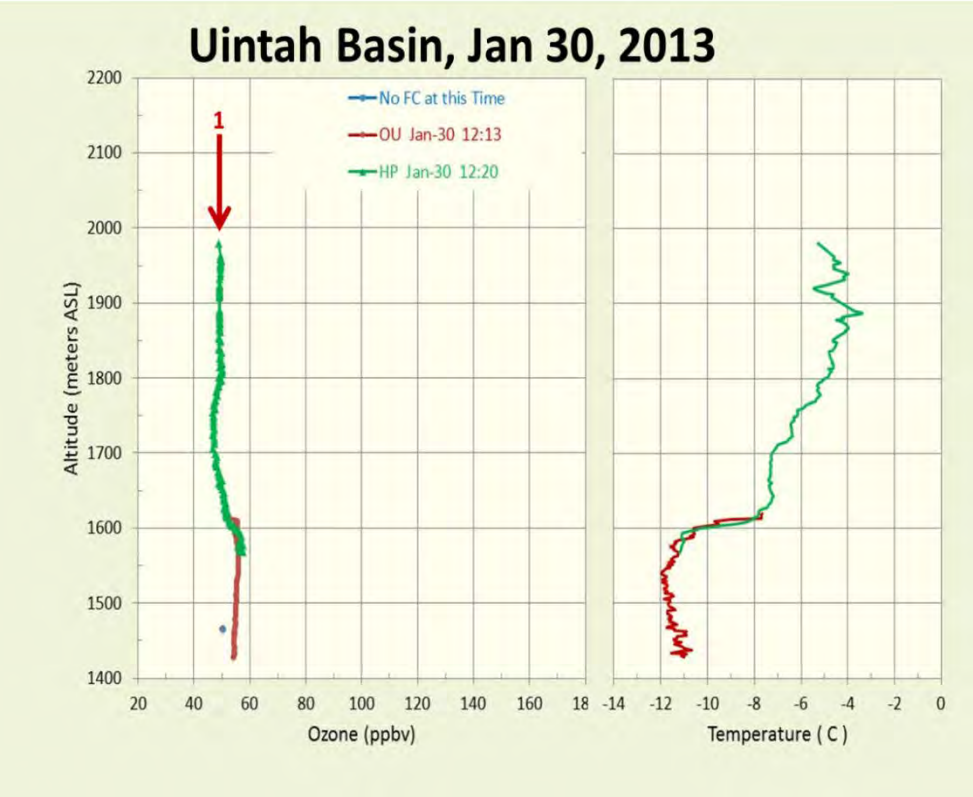


**Figure 8-10. Ozone and temperature profiles from Ouray (OU) and Horsepool (HP) showing that ozone and temperature profiles were similar at these two site separated by 15.1 km in distance and 139 m in elevation. Note the cold surface temperatures and sharp temperature inversion at 1600 m, but no ozone difference across the inversion.**

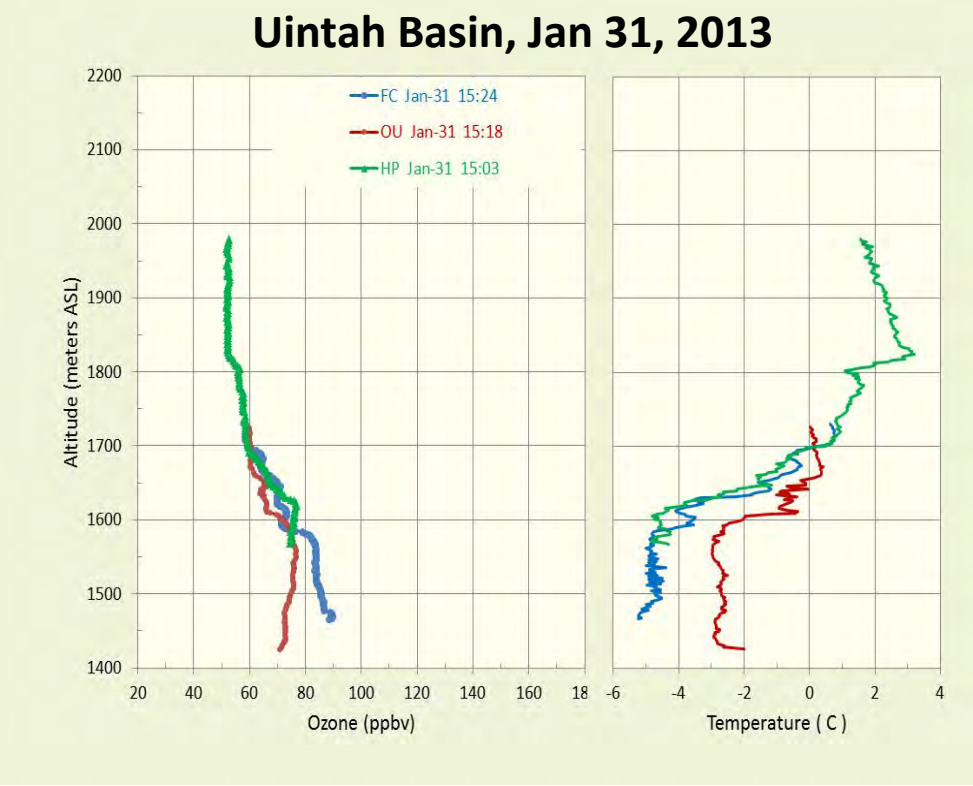


**Figure 8-11. Ozone and temperature profiles from Ouray (OU), Fantasy Canyon (FC) and Horsepool (HP) showing that ozone began increasing on January 31.**

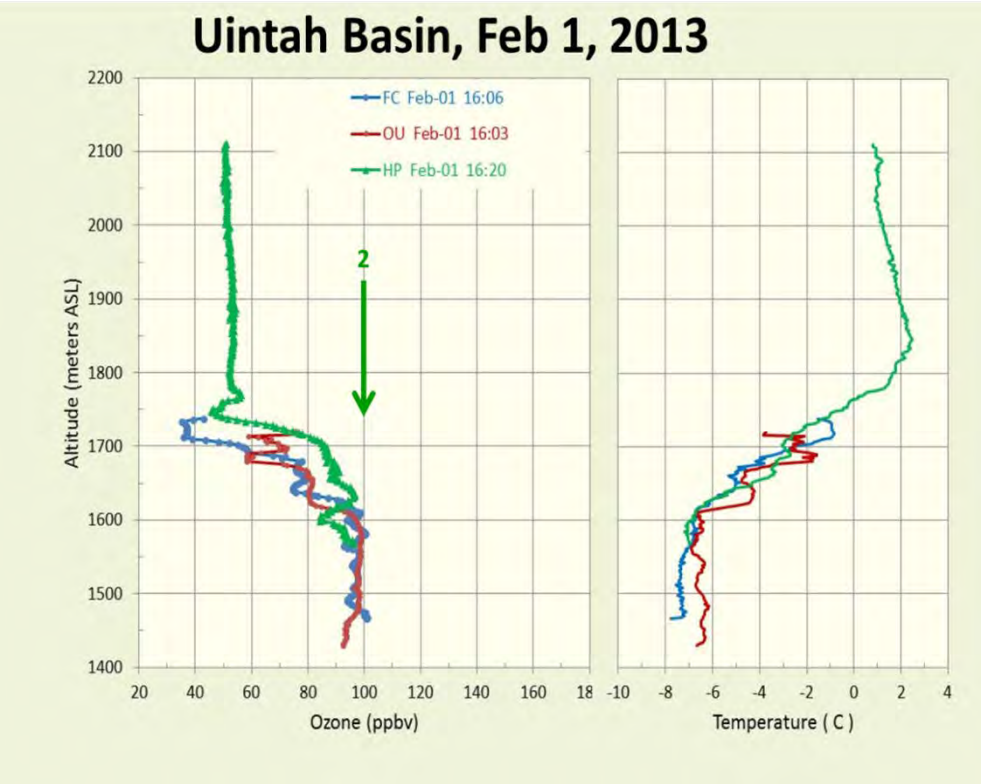


**Figure 8-12. Ozone and temperature profiles from Ouray (OU), Fantasy Canyon (FC) and Horsepool (HP). Fantasy Canyon and Ouray are separated by 23 km in distance and 43 m in elevation with Ouray being lower. Note the build-up of ozone between the surface and 1700 m beneath the top of the temperature inversion layer.**

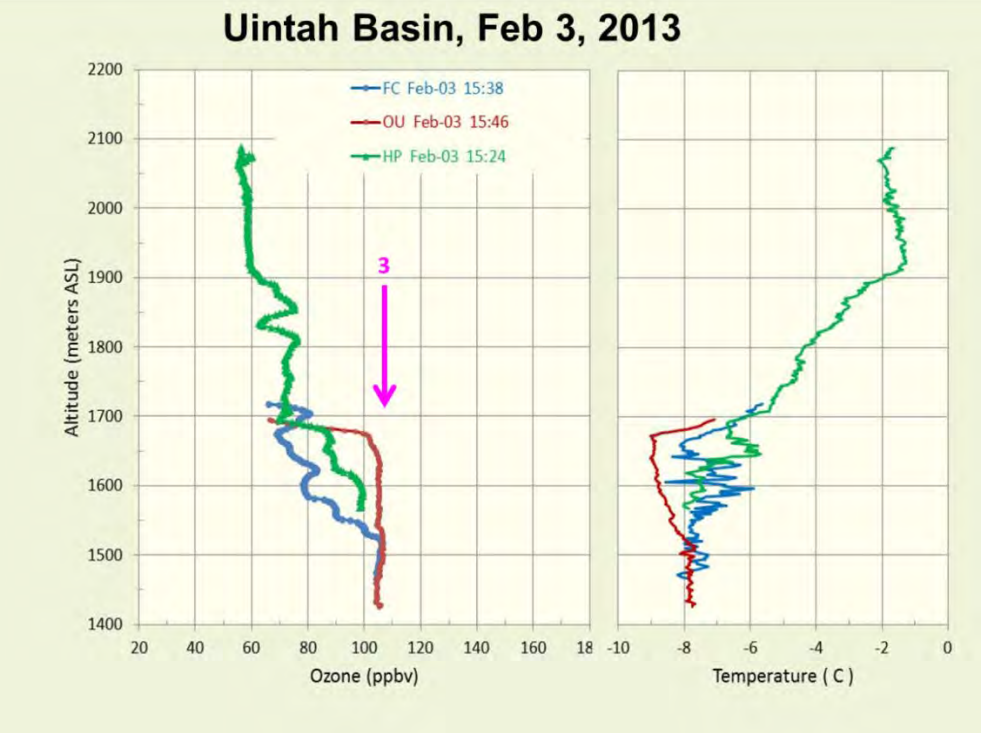


**Figure 8-13. Ozone and temperature profiles from Ouray (OU), Fantasy Canyon (FC) and Horsepool (HP) Feb 3, 2013. The accumulation of ozone was somewhat different now at the three sites with Ouray exhibiting higher concentrations than Fantasy Canyon or Horsepool.**

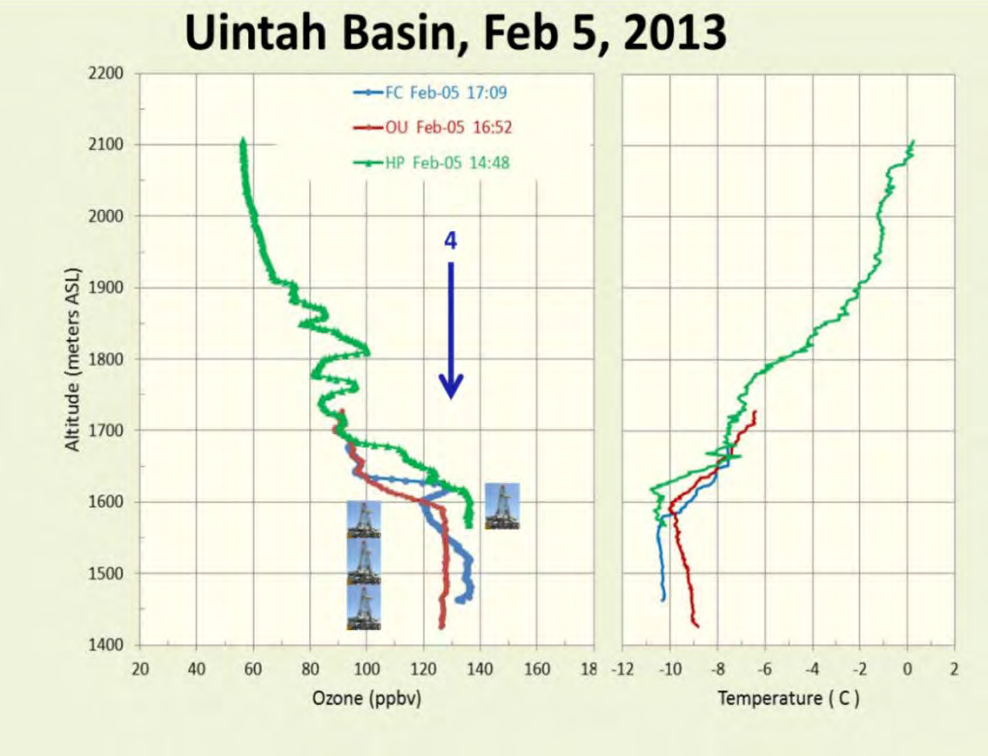


**Figure 8-14. Ozone and temperature profiles from Ouray (OU), Fantasy Canyon (FC) and Horsepool (HP) showing the depth of the ozone layer relative to the height of a 150 foot tall drill rig. This emphasizes how shallow the ozone layer is, especially at Horsepool, which is at a higher elevation than the Ouray or Fantasy Canyon sites.**

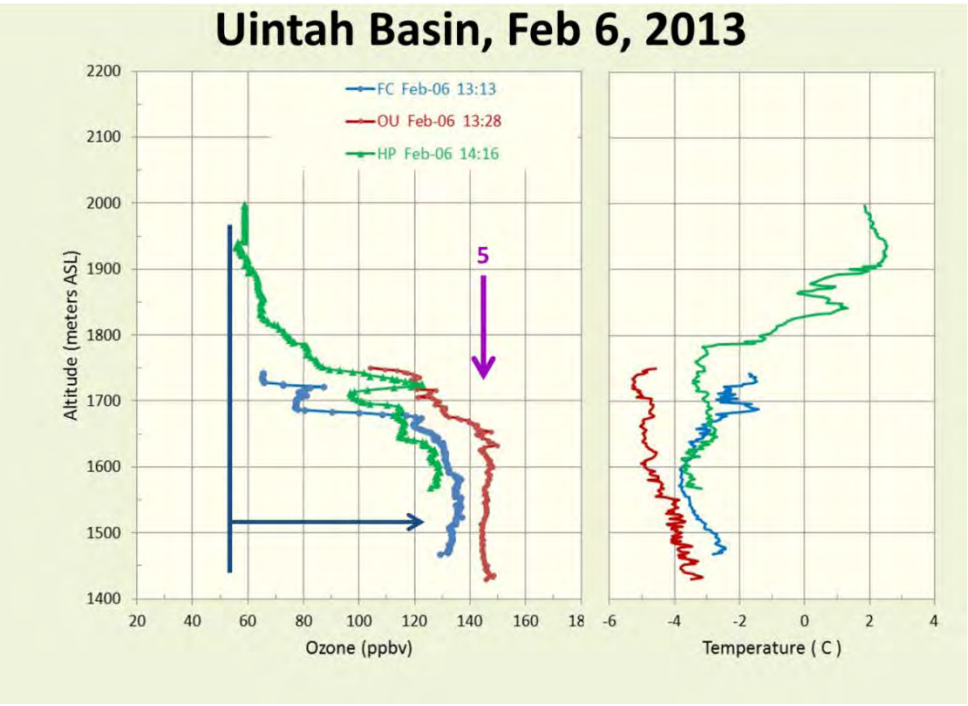


**Figure 8-15. Ozone and temperature profiles from Ouray (OU), Fantasy Canyon (FC) and Horsepool (HP) near the peak in an ozone event. Note how the ozone production is confined to a shallow surface layer and is greater at Ouray which is at a lower elevation in the basin.**

### 8.2.2 Diurnal Ozone Regression and Production during an Ozone Event

As is observed in Figure 8-9, photochemical ozone production is diurnal in nature, reaching a peak in the afternoon then falling off at night. During a major ozone event, between flushings of the basin air, ozone accumulates in a fairly steady rate of ~ 10 ppb/day on a day-to-day basis. In Figures 8-16 through Figures 8-28 are presented tethersonde profiles of ozone measured from the Ouray Wildlife Refuge January 27 – February 6, 2013. The presentation begins with the retreat of ozone concentrations on January 27 (Figure 8-16) from the flushing of the basin with air from the west. The cleanout continued through January 28 (Figure 8-17). On January 29 (Figure 8-18) there was no ozone production in the clean air at the Ouray site. The profiles presented are a small selection of those available in the archive.

On January 30 (Figure 8-19), ozone concentrations in the inversion surface layer at Ouray were less than 30 ppb near the surface with ozone production progressing steadily throughout the day, reaching 78 ppb by 18:03. A similar pattern was observed on January 31 (Figure 8-20). On February 1 (Figure 8-21), ozone production was substantially enhanced over the prior day, reaching just below 100 ppb in the 16:03 and 16:38 profiles. Ozone concentrations did not decrease to background levels overnight and on the morning of February 2 (Figure 8-22) and ozone increased to 105 ppb at Ouray in the 17:16 profile. A similar pattern was observed on February 3 (Figure 8-23) and February 4 (Figure 8-24), but the peak in ozone occurred later in the day at 18:39 on February 4. On February 5 (Figure 8-25), ozone was 80+ ppb by 10:01 and increased to 127 ppb by 16:23 and held there through the last profile at 18:41.

Ozone concentrations remained elevated throughout the night and were at 100+ ppb in the 10:10 profile on the morning of February 6 (Figure 8-26) rising to 165 ppb in the 13:50 profile. After the 13:50 profile, cleaner air began to move into the Uinta Basin at upper levels and by 17:31 ozone concentrations above 1550 m altitude had dropped 85-90 ppb into a 72-78 ppb range. This refreshing of the air from above and then partial recovery of the ozone is illustrated in Figure 8-27 for the same day where the ozone peak at 13:50 is seen to drop up to 16:43 and then partially recover as ozone rich air is sloshed back over Ouray, as illustrated in the 18:15 profile. The cleanout of the basin was not complete on February 6 and by the afternoon of February 7 (Figure 8-28) ozone production added an additional 20 ppb between 11:08 and 13:53. The last profile was taken at 15:11 showing a well-mixed 100 ppb from the surface to 1760 m.

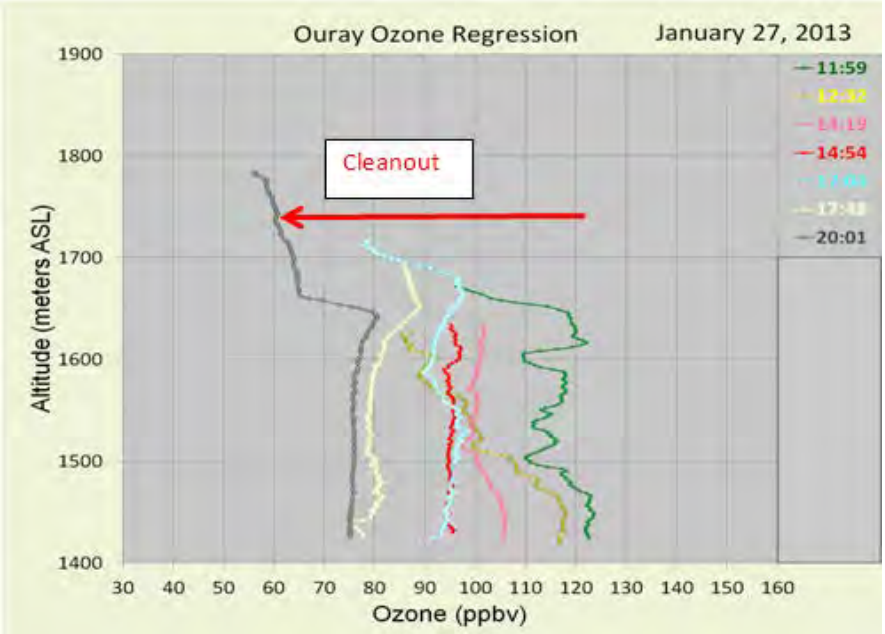


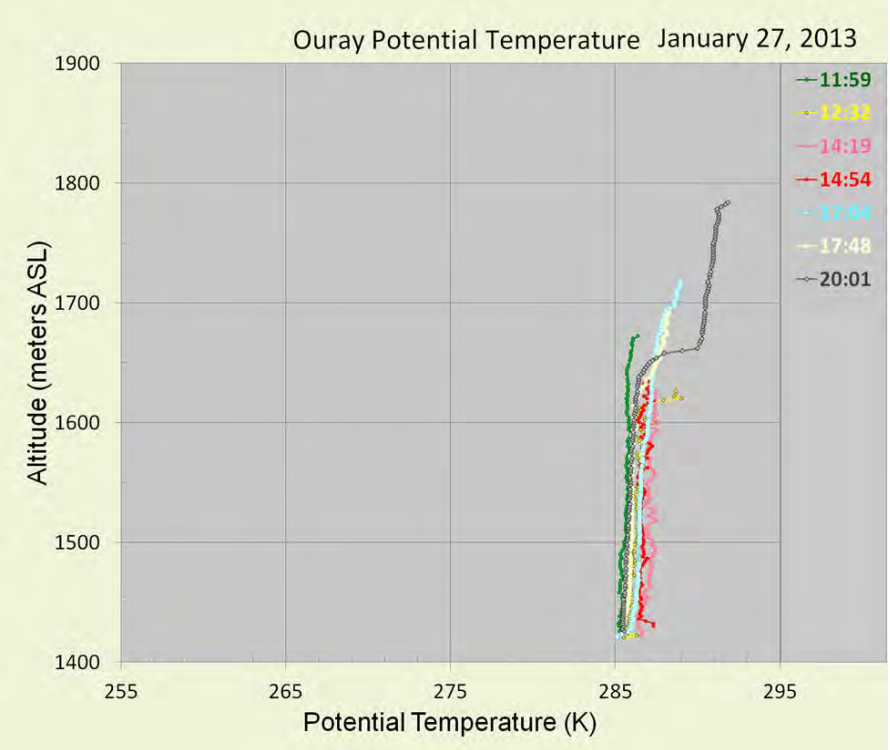


**Figure 8-16. Ozone profiles from the Ouray Wildlife Refuge site (OU) showing that ozone in the 120 ppb range in the noon (11:59) profile decreased during the day to 75 ppb as cleaner air from the west flushed out the stagnant methane and ozone laden air of the previous stagnation event. (Lower) The corresponding potential temperature profiles were constant over this same period with the profile at 2001 showing that mixing of the lower level air was becoming capped in the evening at ~1650 m.**

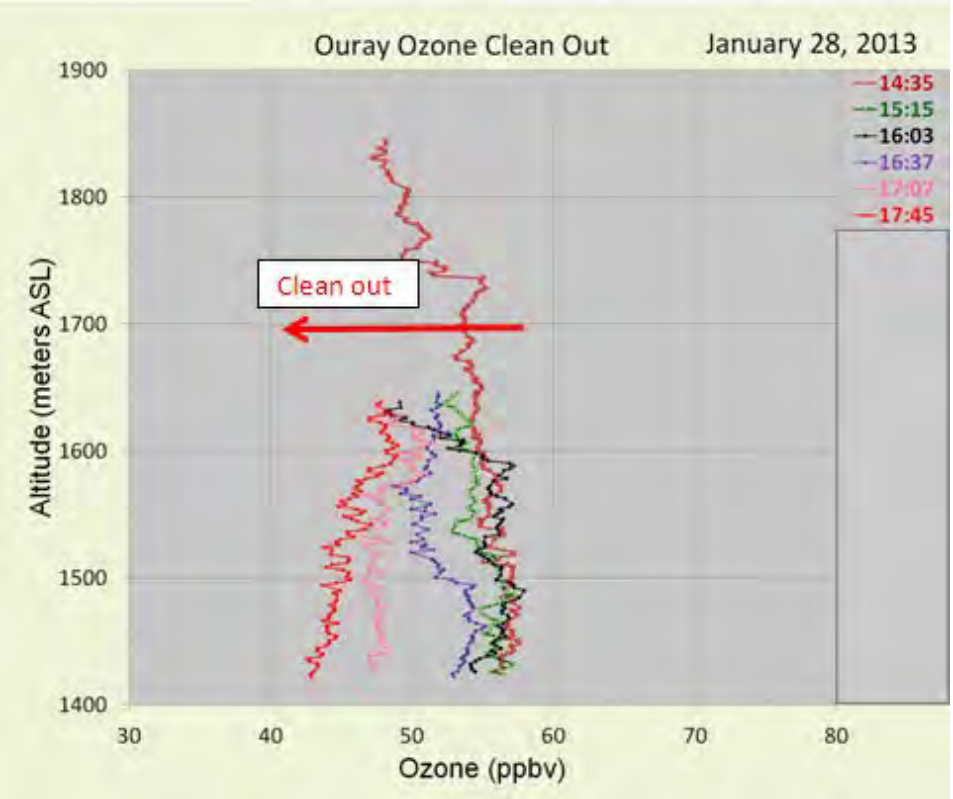


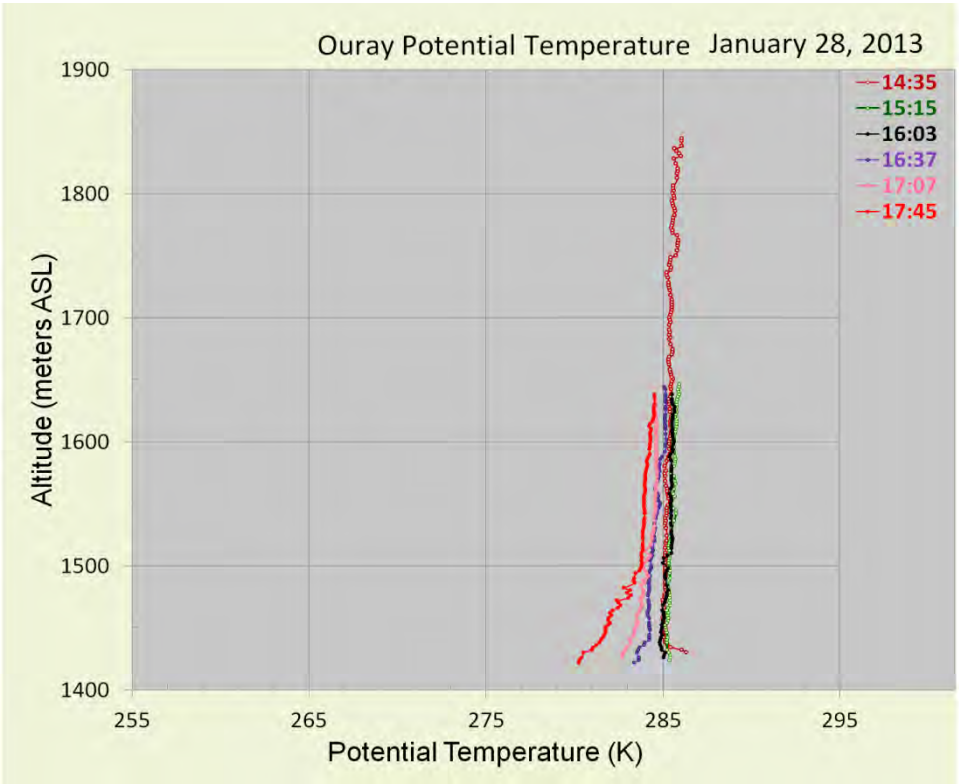


**Figure 8-17. (Upper) Ozone profiles from the Ouray Wildlife Refuge site (OU) showing that as the flushing (cleanout) of the basin progressed, ozone decreased throughout January 28. (Lower) Corresponding potential temperature profiles showed that well-mixed air was entering the basin and that a weak temperature inversion was beginning to develop near the surface in the evening (17:45 profile).**

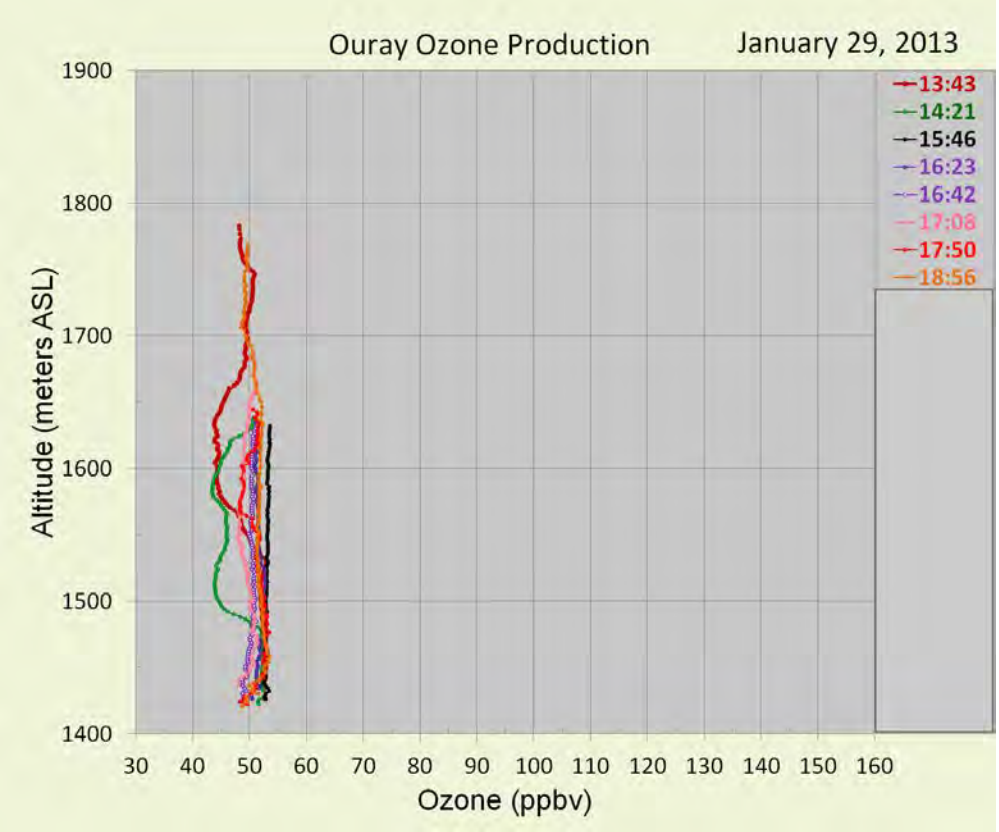


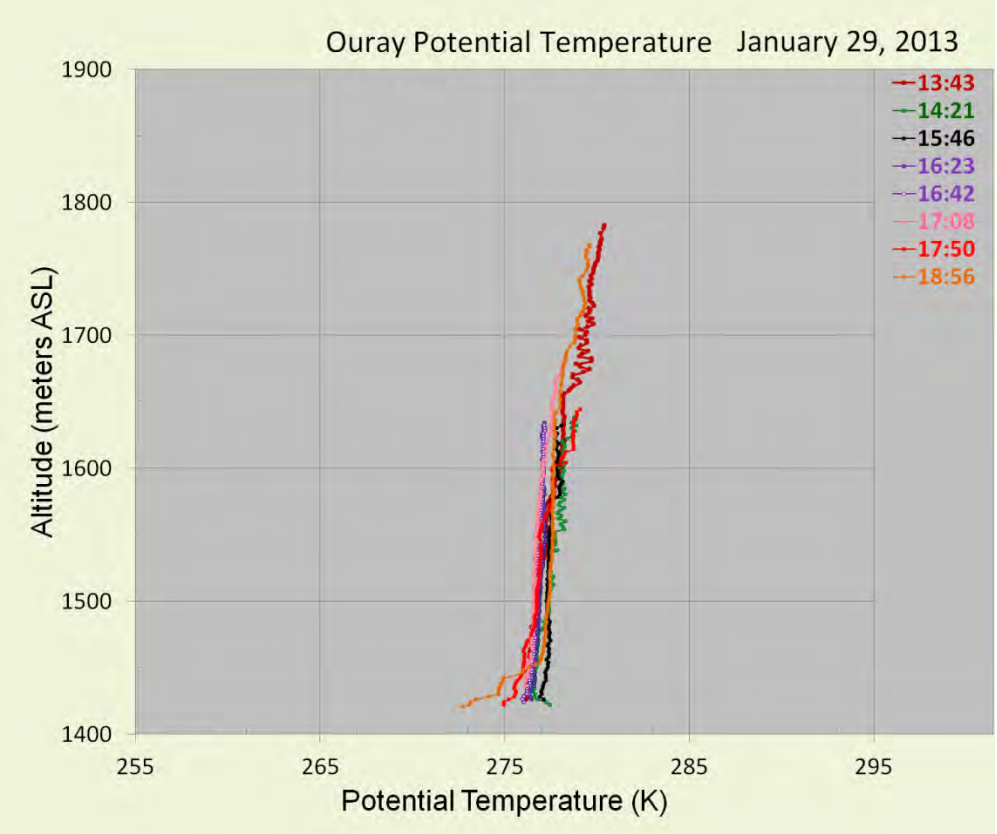


**Figure 8-18. (Upper) By January 29 the basin was flushed out and there was no photochemical ozone production as all the profiles were at background levels throughout the day. (Lower) Potential temperatures show that the air mass was becoming slightly more stable with a shallow temperature inversion developing near the surface in the evening.**

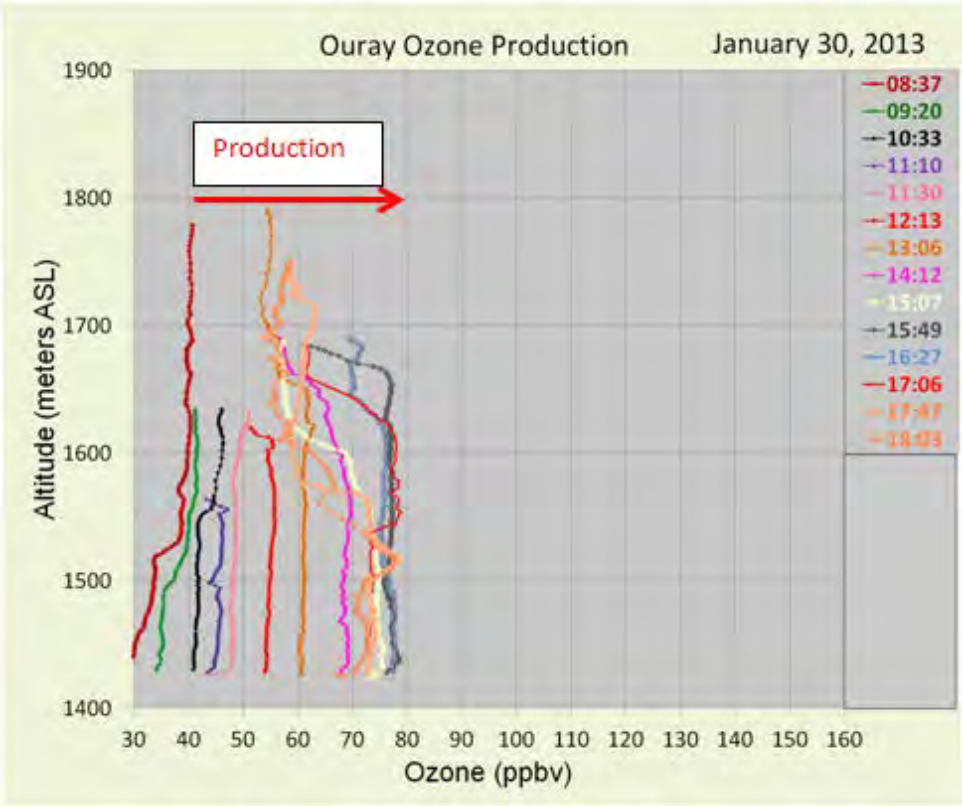


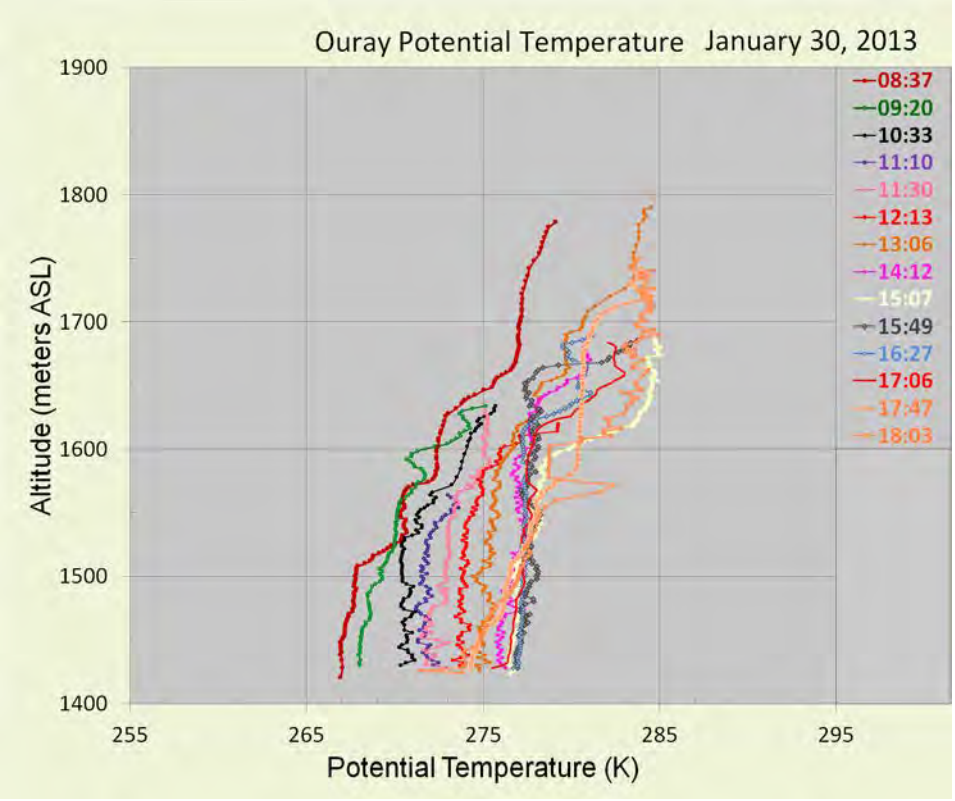


**Figure 8-19. (Upper) By January 30 ozone precursor emissions were collecting in the basin and photochemical ozone production rose from a low of 30 ppb at sunrise to 78 ppb by 15:49. (Lower) Potential temperatures show that the atmosphere was becoming appreciably more stable with a strong inversion base developing at 1600 m.**

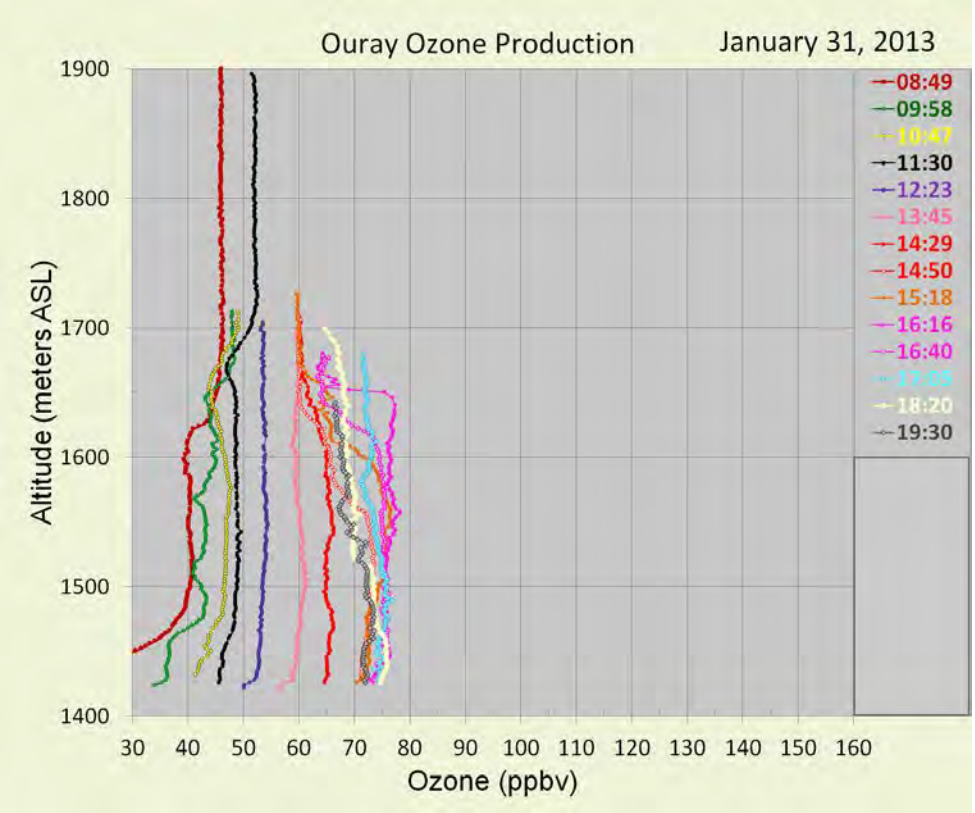


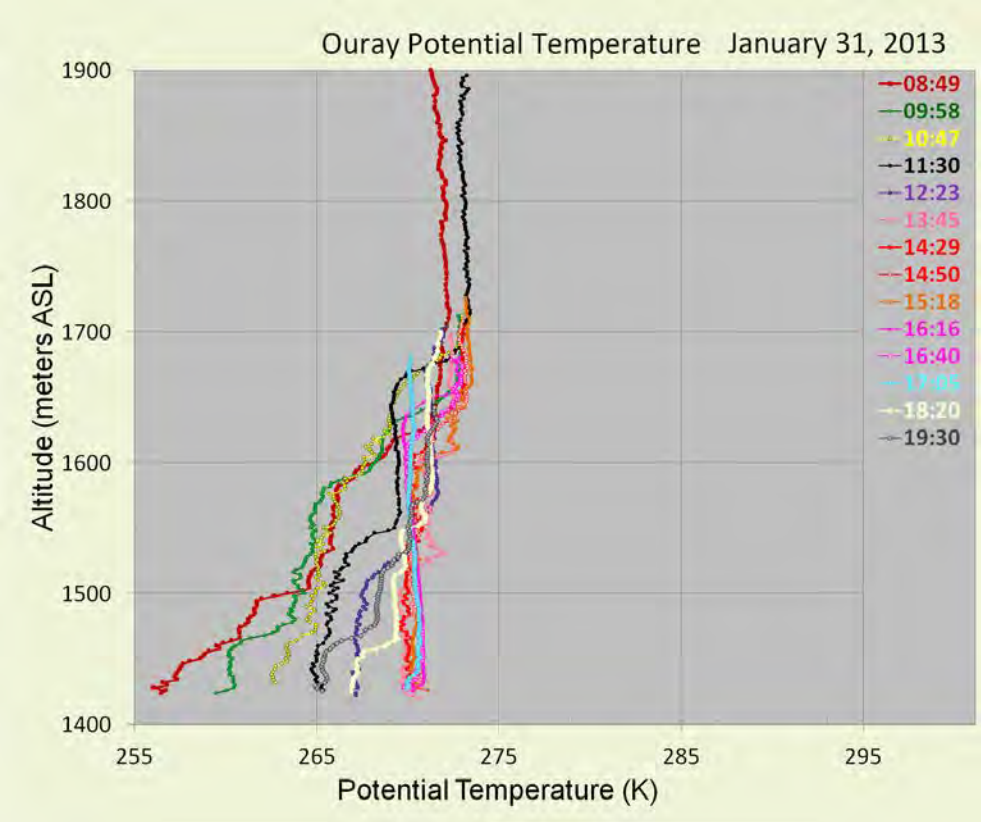


**Figure 8-20. (Upper) Ozone production on January 31 was similar to January 30 with no large carryover of ozone from the previous day. (Lower) Potential temperatures decreased and the air remained stable beneath 1650 m.**

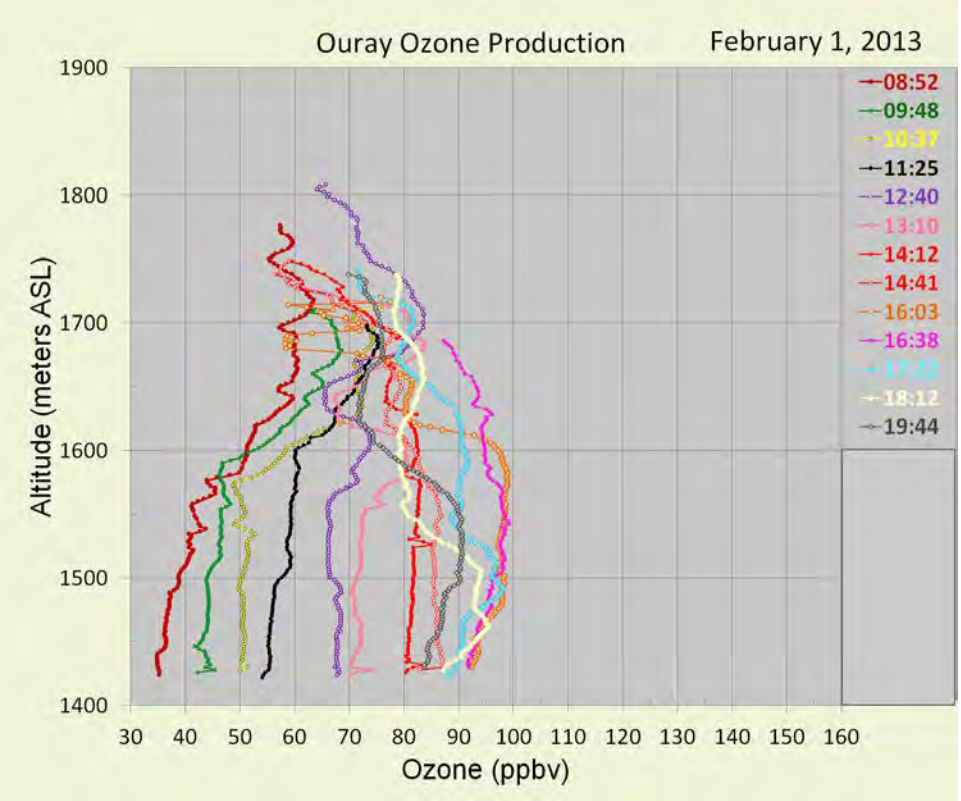


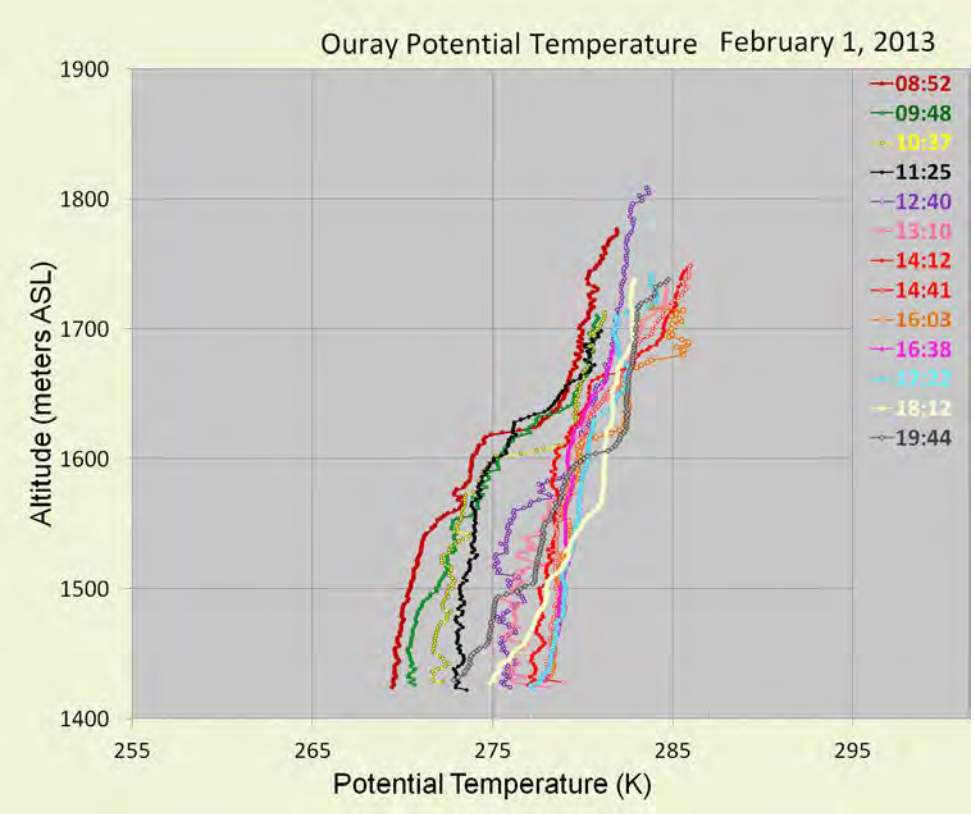


**Figure 8-21. (Upper) On February 1 ozone production substantially increased over the previous day reaching 100 ppb in the 13:10 profile then decreasing to 60 ppb after sunset. (Lower) The potential temperature plots show that the atmosphere was very stable with the inversion top maintained at just above 1600 m.**

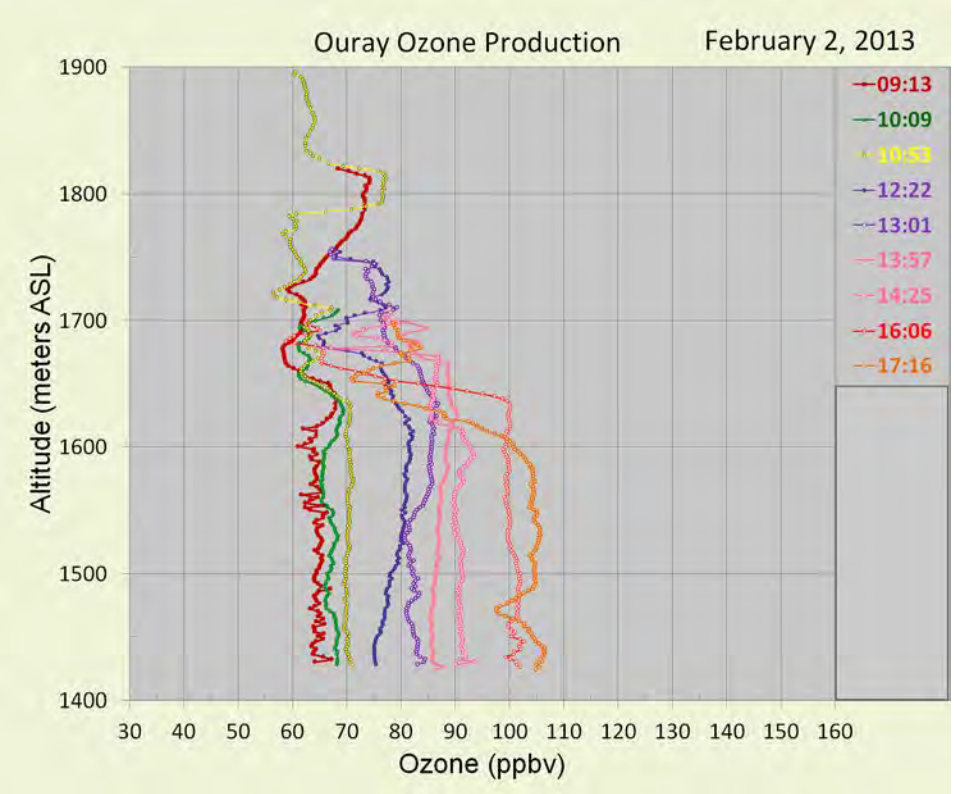


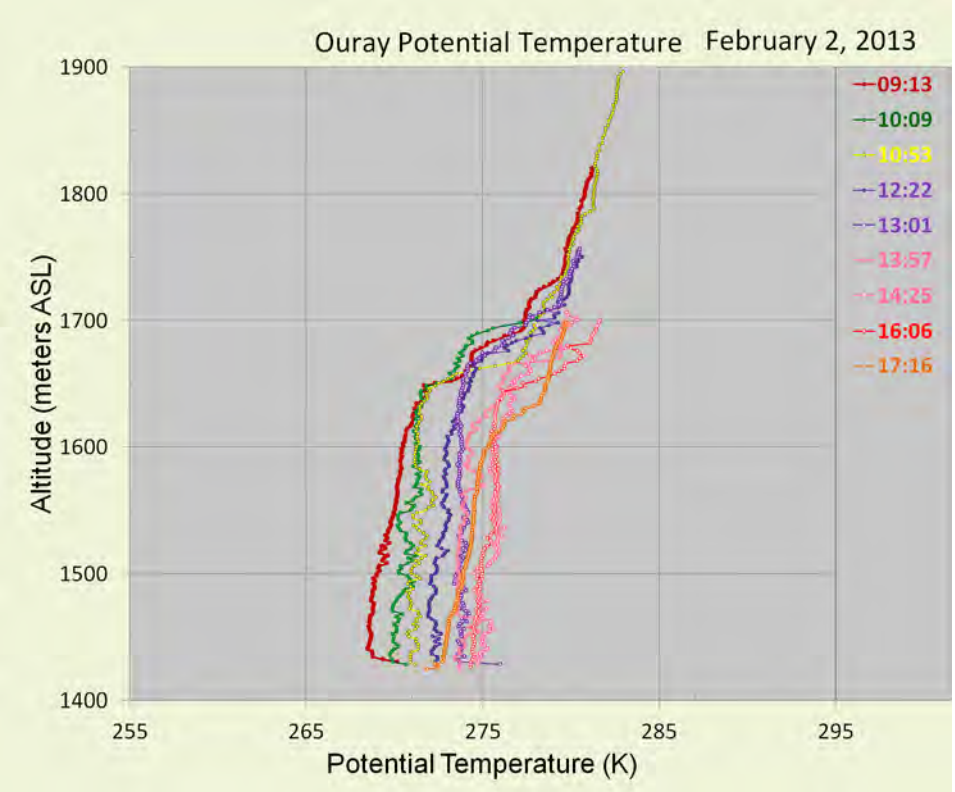


**Figure 8-22. (Upper) Ozone did not decrease as much over the night of February 1 as on previous nights and was in the range of 65 ppb in the morning of February 2, rising to 105 ppb by the 17:16 profile. (Lower) The air remained stable with the inversion top rising to 1650 m.**

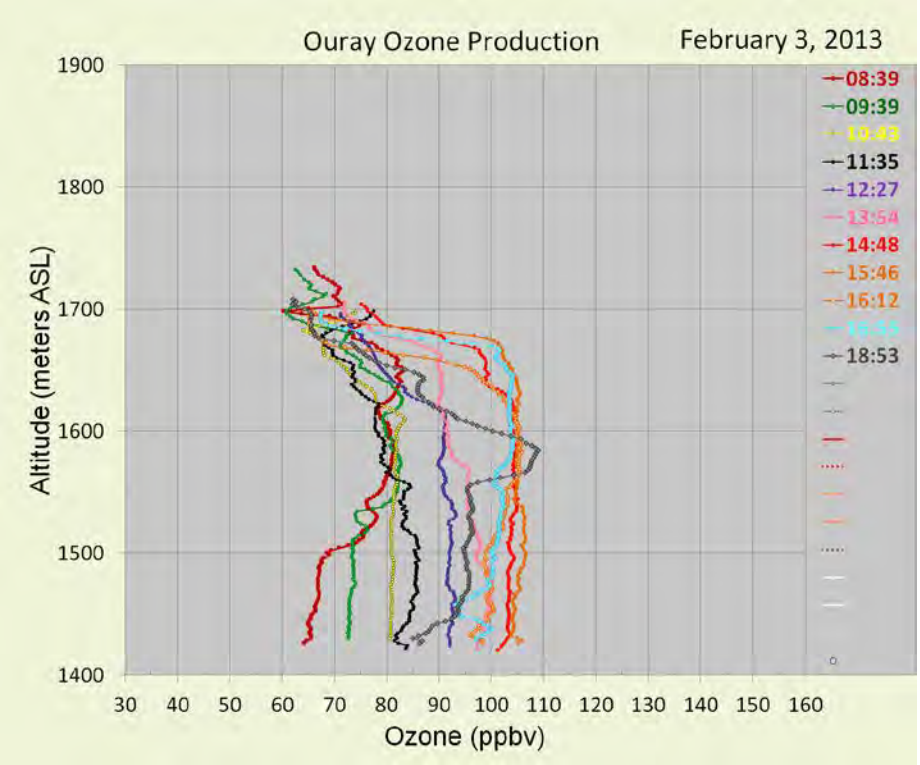


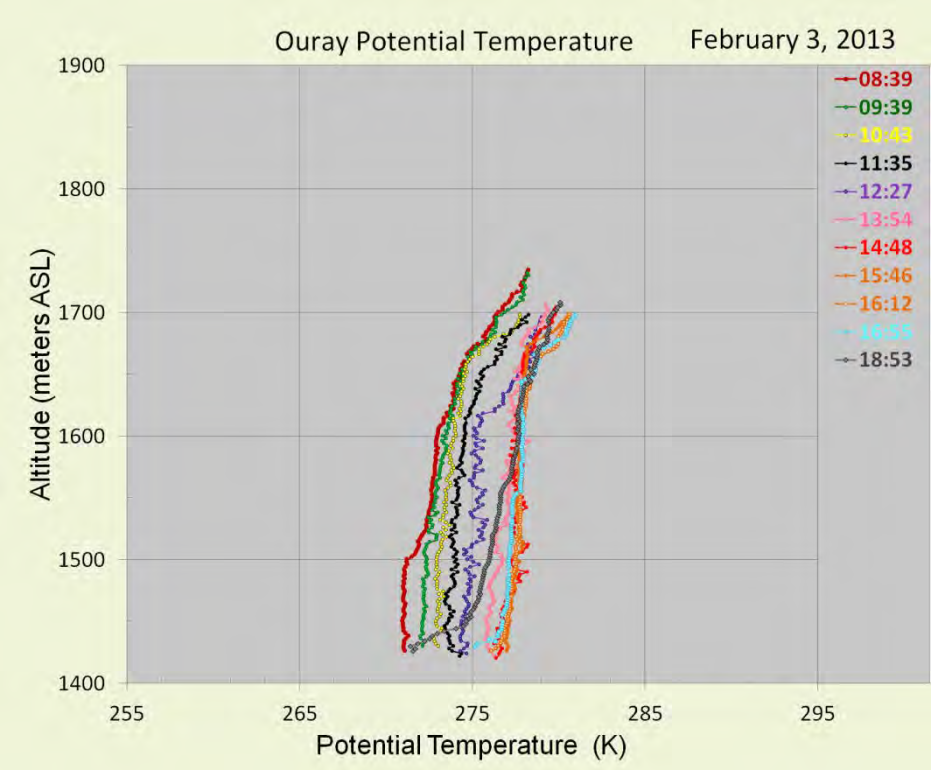


**Figure 8-23. (Upper) On February 3, ozone production was similar as on February 2, reaching 105 ppb in the 15:46 profile then decreasing to 85 ppb by 18:53. (Lower) The air remained relatively stable, but the sharp inversion at 1650 m observed on the prior day has somewhat weakened.**

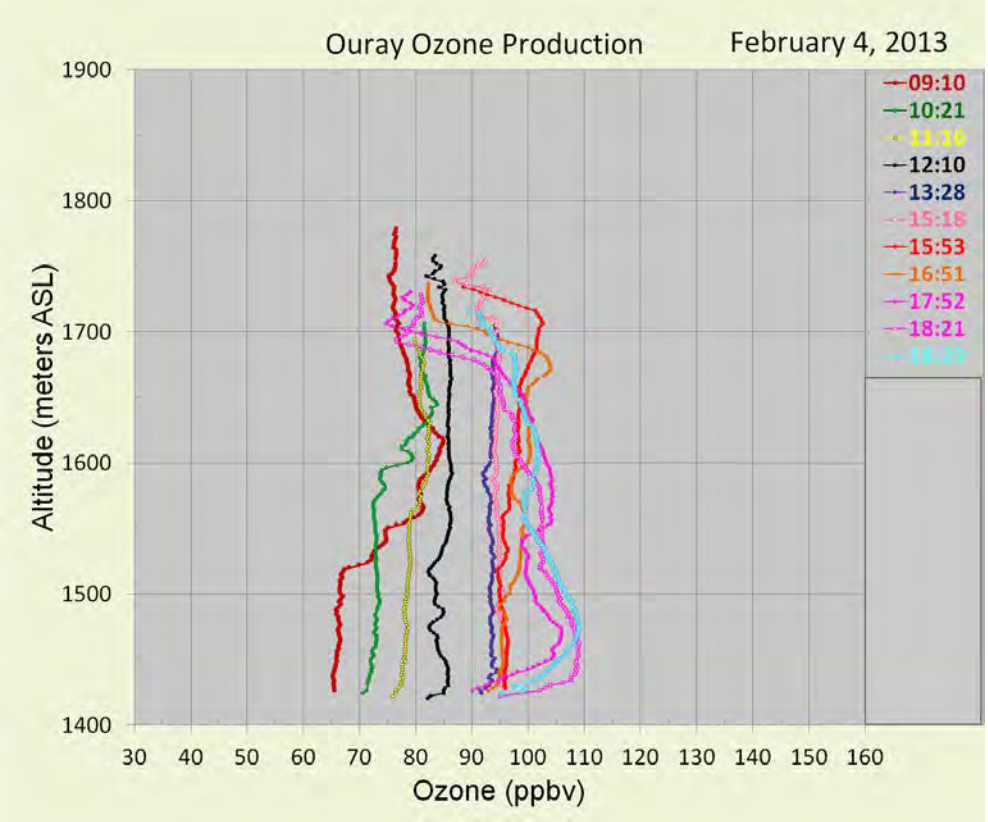


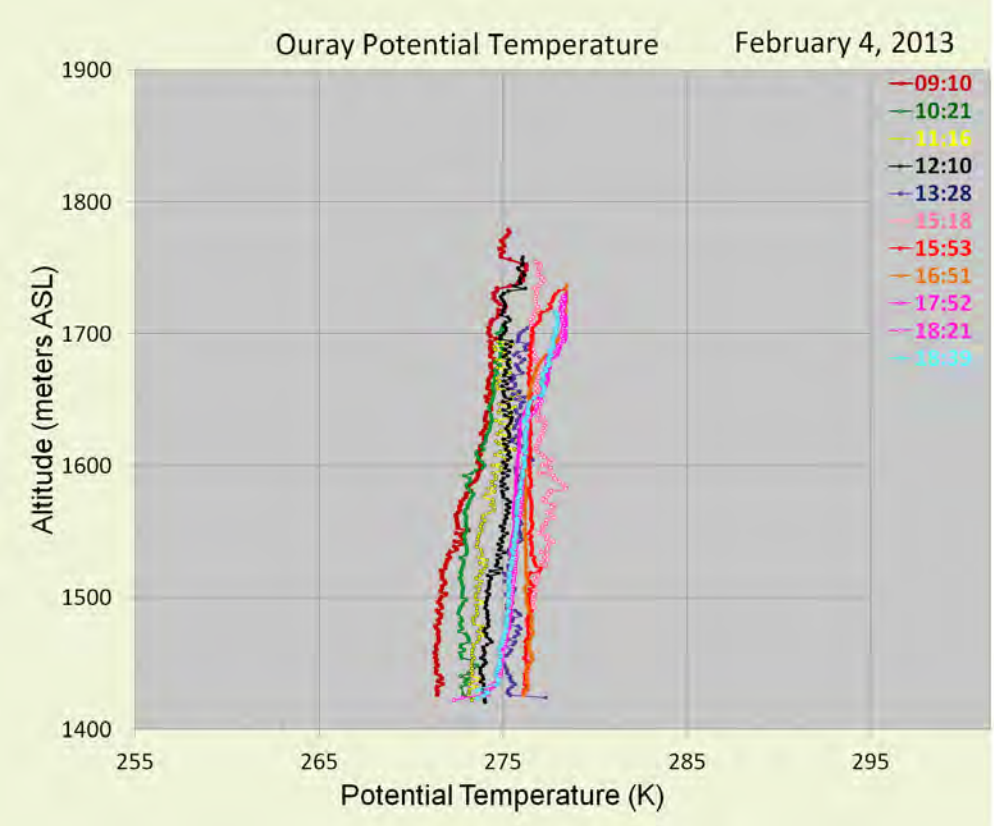


**Figure 8-24. (Upper) On February 4, ozone production was similar to that on February 3, but the peak of 110 ppb occurred later in the afternoon at 18:39. (Lower) The air column became better mixed and remained more uniform over the day than earlier in the ozone event.**

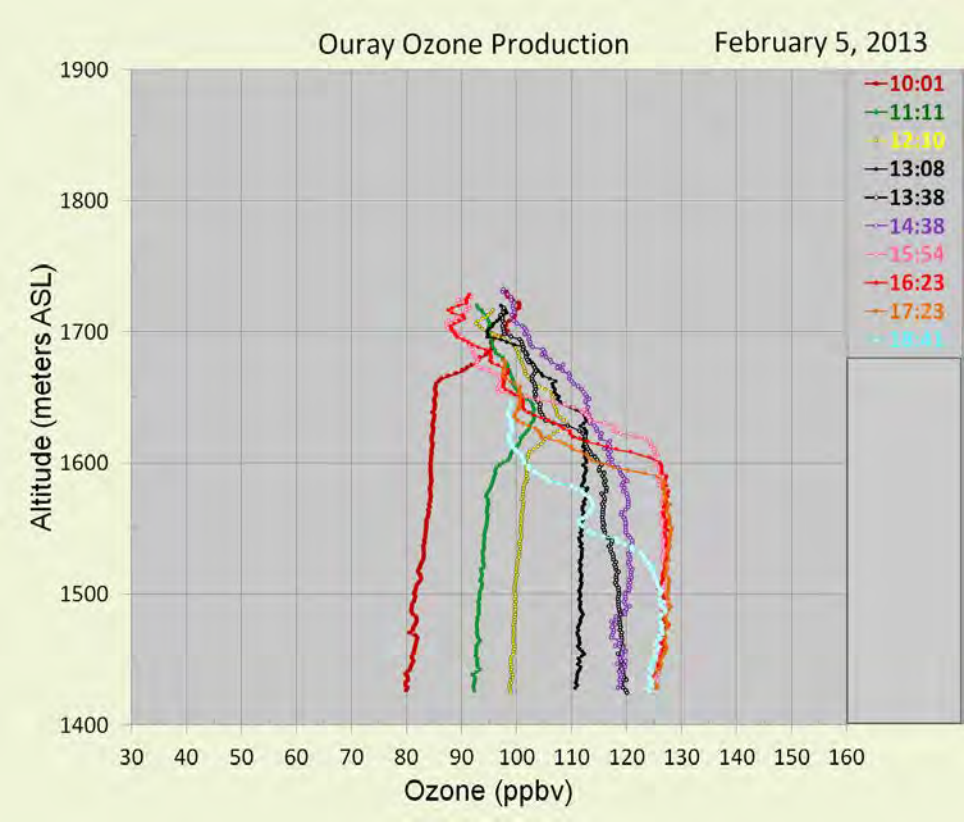


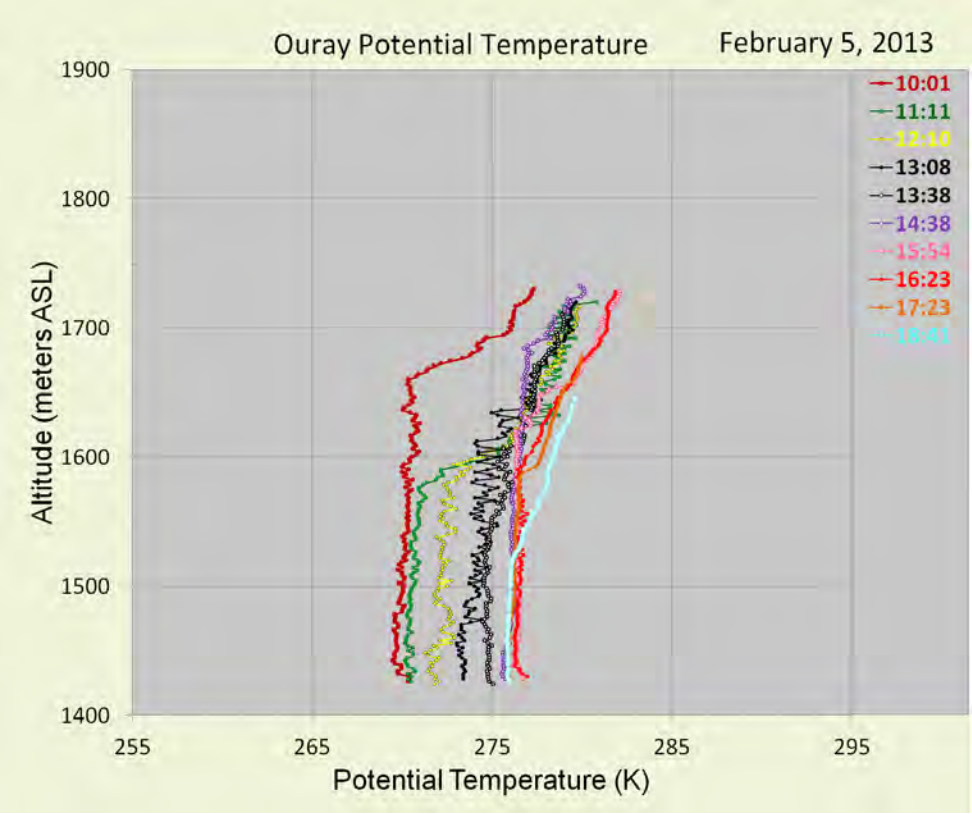


**Figure 8-25. (Upper) On February 5 ozone was 80+ ppb in mid-morning increasing to 127 ppb by 16:23 mst before beginning to erode at higher altitudes by 18:41. (Lower) The strong inversion at 1660 m observed in the 10:01 profile lost some of its strength as air warmed and mixed during the day.**

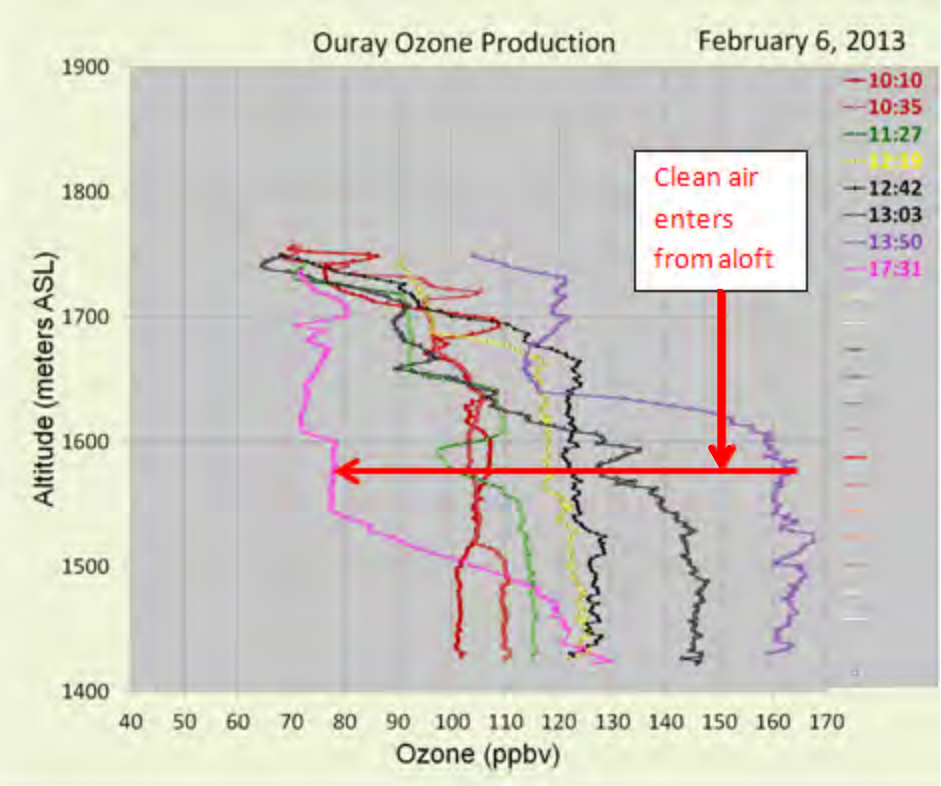


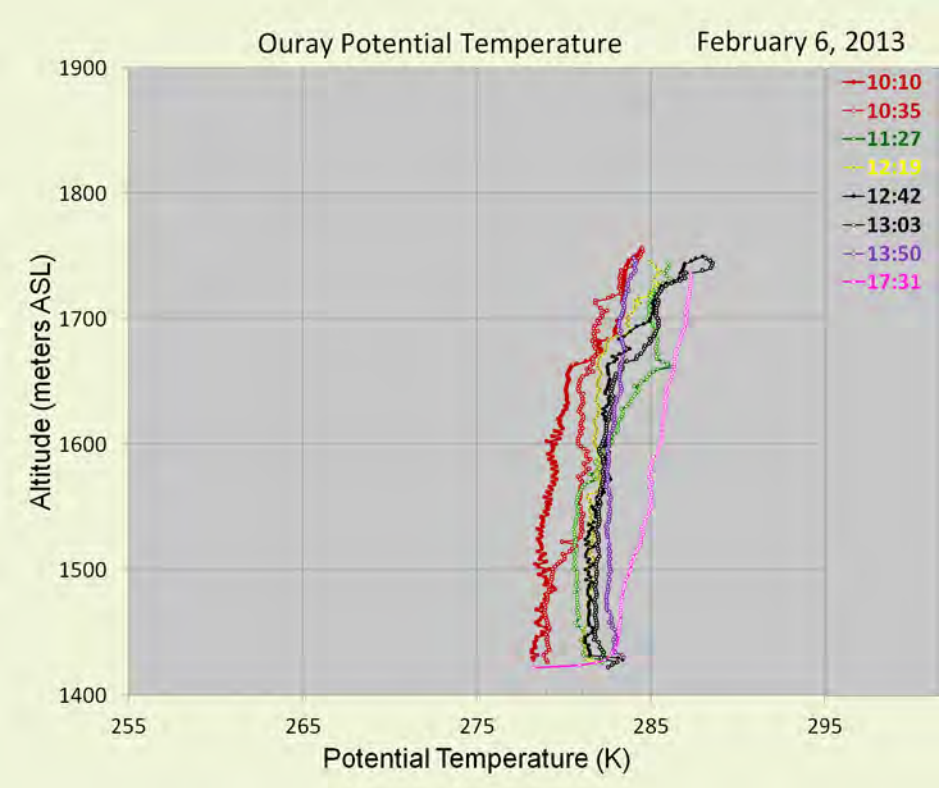


**Figure 8-26. (Upper) Ozone remained elevated throughout the night of February 5, with the 10:10 profile showing ozone in the 100+ ppb range. Ozone increased to 165 ppb by 13:50 before rapidly decreasing to the 72-78 ppb range above 15:50 m as clean air moved into the basin from aloft and the west. (Lower) Potential temperature showing the increase in potential temperature at 17:31 as fresh air, now began entering the basin.**

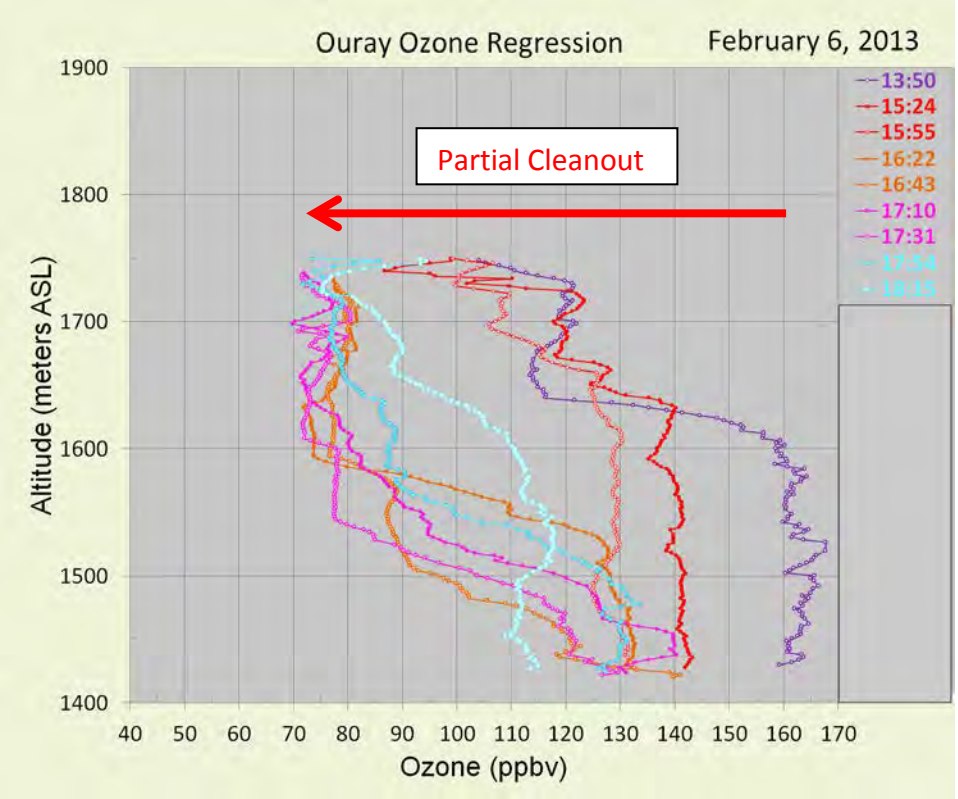


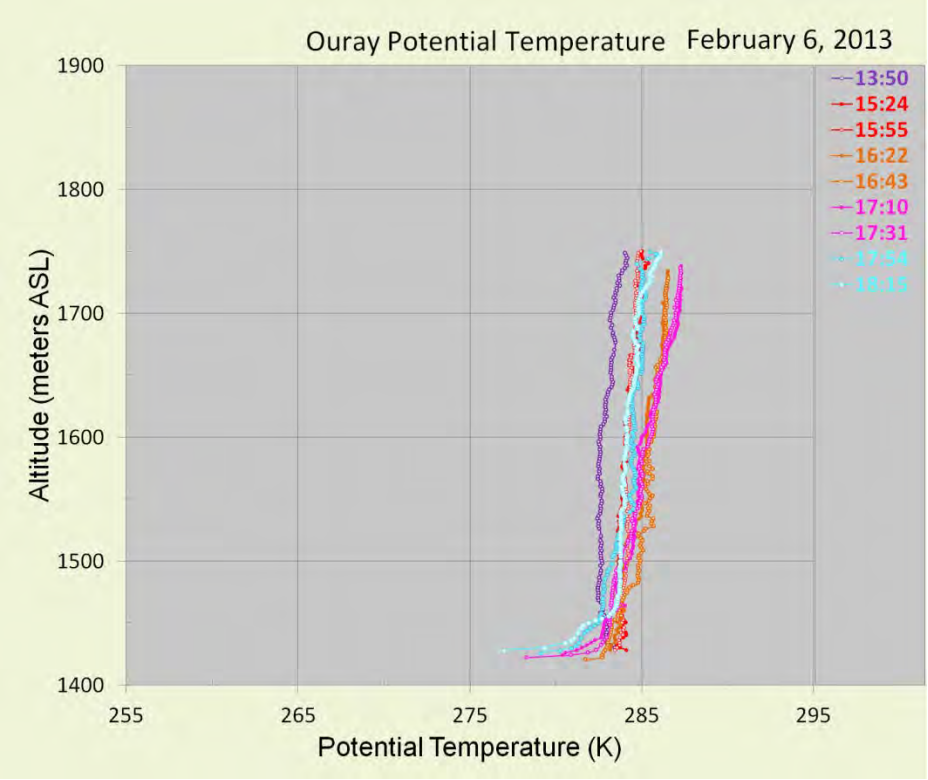


**Figure 8-27. (Upper) The profiles for February 6 show the intrusion of cleaner air from aloft from 13:50 to 17:31, then recovery of ozone in the 18:15 profile as ozone rich air sloshes around in the basin. (Lower) Potential temperature remained relatively consistent during the cleanout, but with a strong inversion beginning to develop within a few 10s of meters above the cold, snow covered surface.**

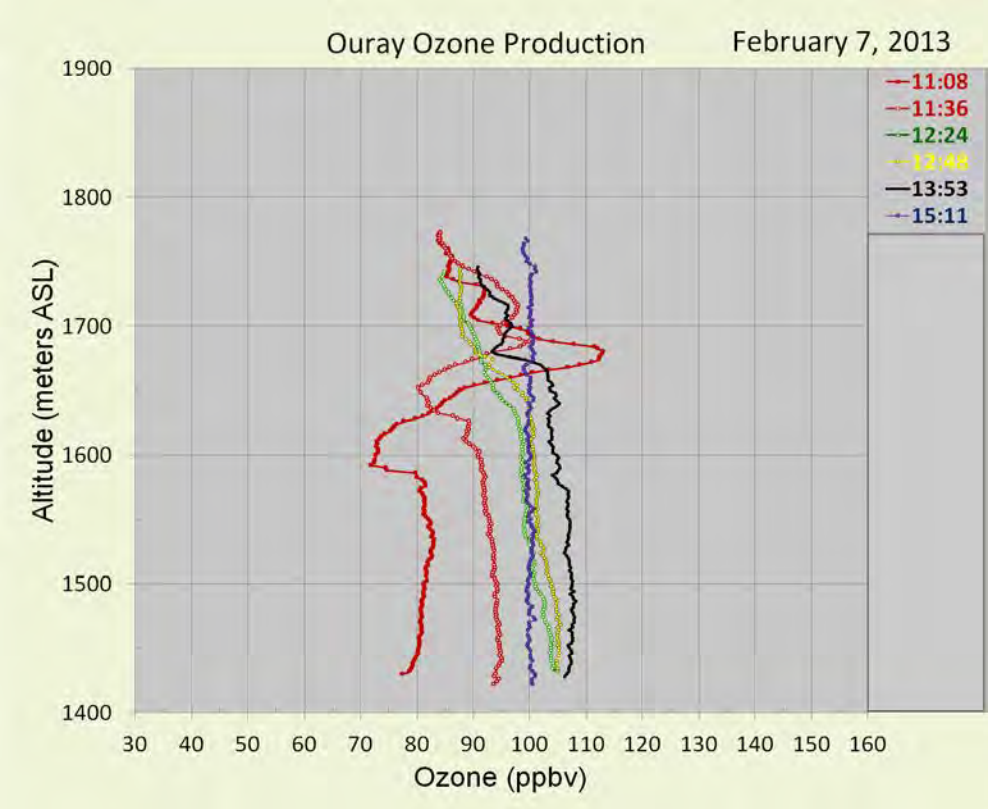


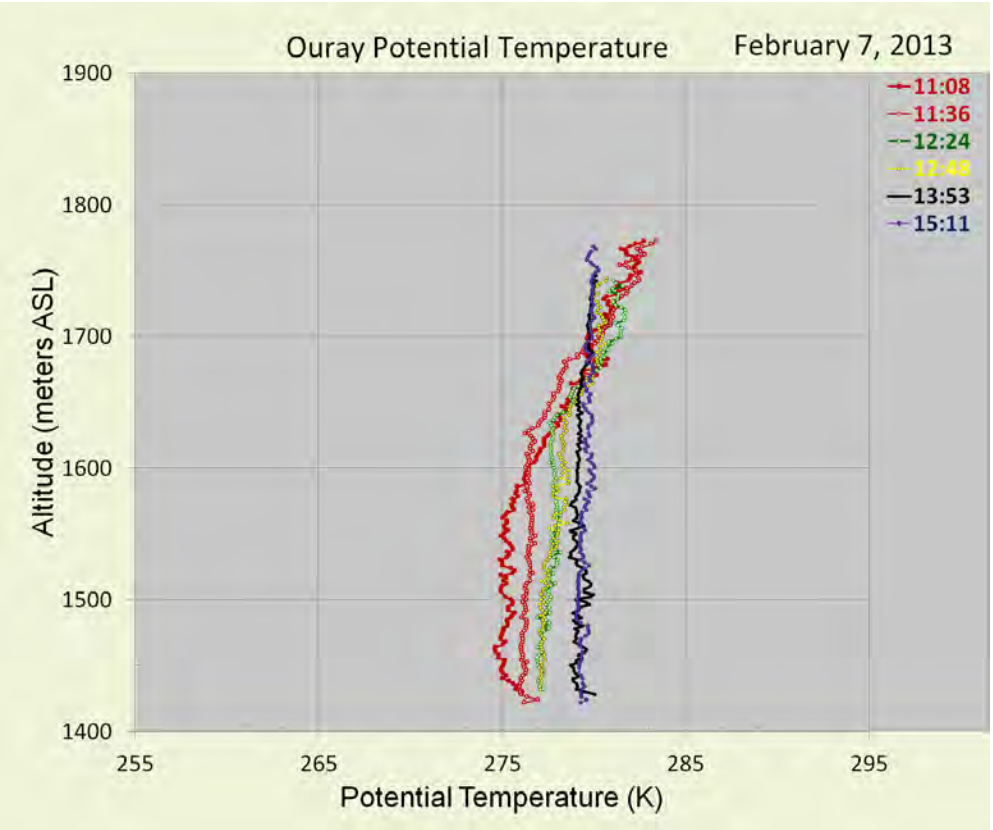


**Figure 8-28. (Upper) On February 7 ozone production began again as the prior day's cleanout of the basin was not complete. (Lower) Potential temperatures increased during the day as ozone production also increased.**

### 8.2.3 Free Flying Ozonesonde Profiles

To put the surface ozone and tethersonde measurements into perspective and to be assured that the high concentrations of ozone near the surface were not coming from descending stratospheric air, two free flying ozonesondes were released during the study period. In Figure 8-29 are presented profiles of ozone and temperature from the surface to 11 km on January 25 when surface ozone concentrations were 128 ppb. It is clear that stratospheric air was not contributing to the high surface concentrations. This is also the case for the high surface ozone event of February 7 shown in Figure 8-30. These two profiles were taken during the peaks of two respective high boundary layer ozone events and show that the stratospheric ozone was not coming down from above into the surface inversion. The surface layer ozone was produced at and near the surface. It is also clear that tropospheric air above the shallow, high ozone boundary layer is not the source of the exceptionally high ozone values in the boundary layer. The free troposphere ozone profile concentrations were similar in 2012 and 2013.

### 8.2.4 Mobile Surface Ozone Measurements

Each day of the study period, the NOAA crew measured ozone concentrations while driving from and returning to Vernal from tethersonde sites in the basin. On other days, mobile measurements were conducted east and south past Bonanza power plant and on one day through the basin and south up the mountain slope that carried the van above the temperature inversion and high ozone concentration layer. The configuration of the ozonesonde mounted on a NOAA van is presented in Figure 8-31. During the drives through the basin, the mobile van passed near the Red Wash and Ouray EPA and the Ouray Wildlife ozone monitors. Ozone measurements from the mobile ozonesonde and fixed sites are presented in Figure 8-33 where it may be observed that there was excellent agreement considering the difference in distance between the relative measurement sites and the fact the mobile van occasionally operated in excess of 60 mph when passing the fixed sites at distances of up to a mile.

Data from a drive around the basin during the February 6 ozone event is presented in Figure 8-32 for surface ozone concentrations plotted aganst elevation above sea level over time. From this figure it can be seen that ozone concentrations were in the 75 ppb range when leaving Vernal, rising to 115 ppb then decreasing to 90 ppb at Red Wash (point 3) as the elevation of the road was high enough (1720 m) that the van was beginning to poke through the top of the inversion layer. When the elevation of the road decreased, ozone concentrations increased to 120 ppb near Fantasy Canyon (point 5) and Horsepool (point 6). At Point 7, near the Ouray EPA site, surface ozone was 140 ppb. Driving up the south rim of the basin, ozone began to decrease at 1650 m as the van ascended through the base of the inversion layer, decreasing to backgrond ozone concentration of 50 ppb at 2000 m. The pattern was repeated in reverse on the descent. High ozone beneath the inversion and background concentrations above the inversion layer were consistently observed in the tethersonde and aircraft data. Graphs from the other days' drives are available at:
ftp://ftp.cmdl.noaa.gov/ozwv/ozone/Uintah_2013_Tether_OzoneSondes/ .

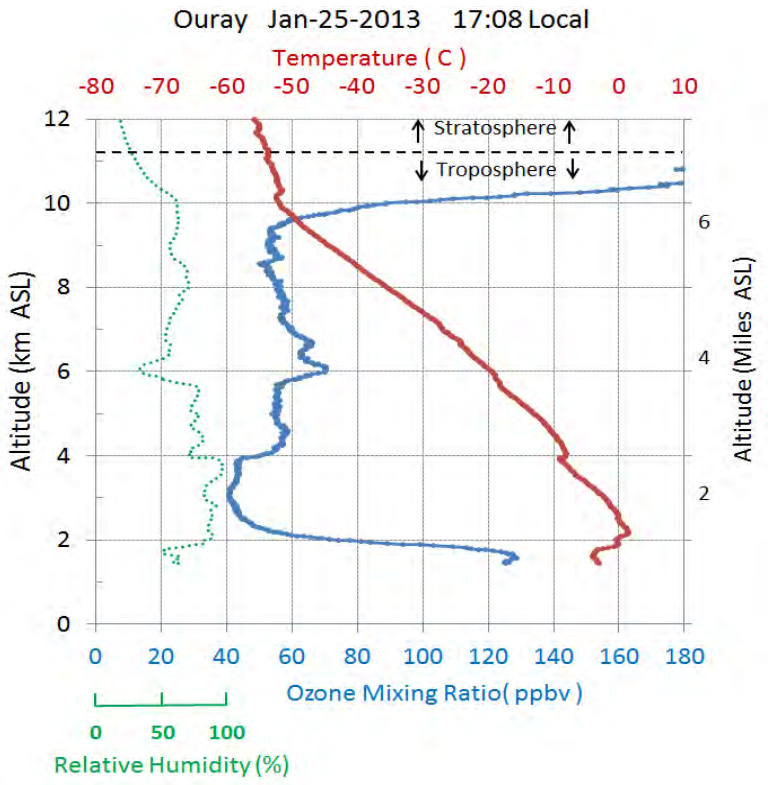


**Figure 8-29. Free flying ozonesonde released from the Ouray Wildlife Refuge when ozone in the boundary layer was in excess of 120 ppb, January 25, 2013. Note the shallow elevated ozone layer near the surface, background ozone concentrations from 3 km to 9.5 km and then stratospheric ozone concentrations exceeding 180 ppb above 10 km.**

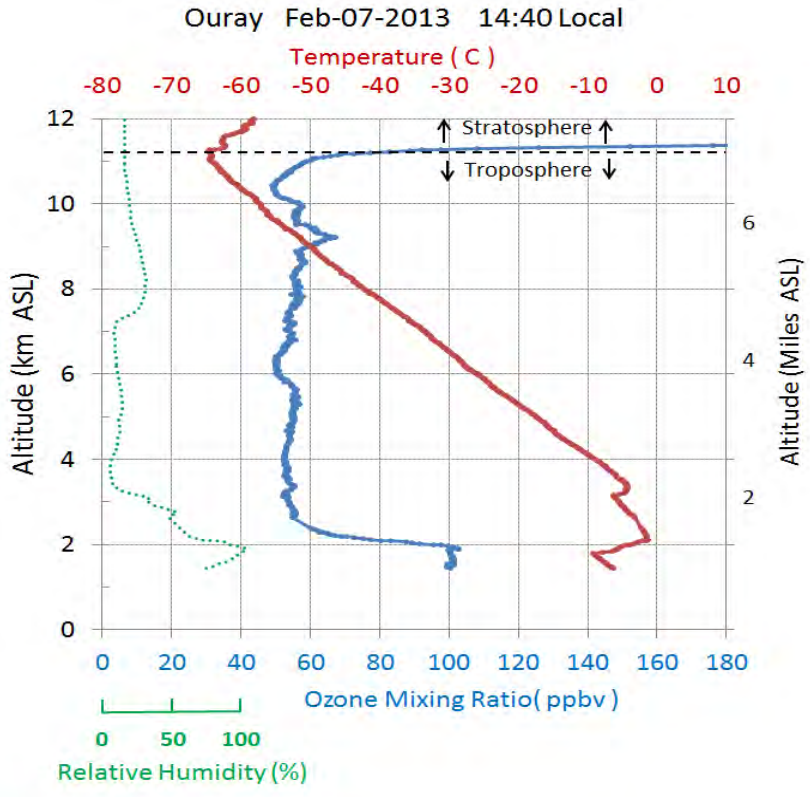


**Figure 8-30. Free flying ozonesonde released from the Ouray Wildlife Refuge when ozone in the boundary layer was 100 ppb, February 7, 2013. Note the shallow elevated ozone layer near the surface, background concentrations from 2 km to 11.5 km and then stratospheric ozone concentrations exceeding 180 ppb above that level.**


**Figure 8-31. Ozonesondes mounted in the window of a NOAA van used to measure ozone concentrations while driving around the Uinta Basin. This photo was taken during the 2012 study but a similar configuration was used in 2013.**

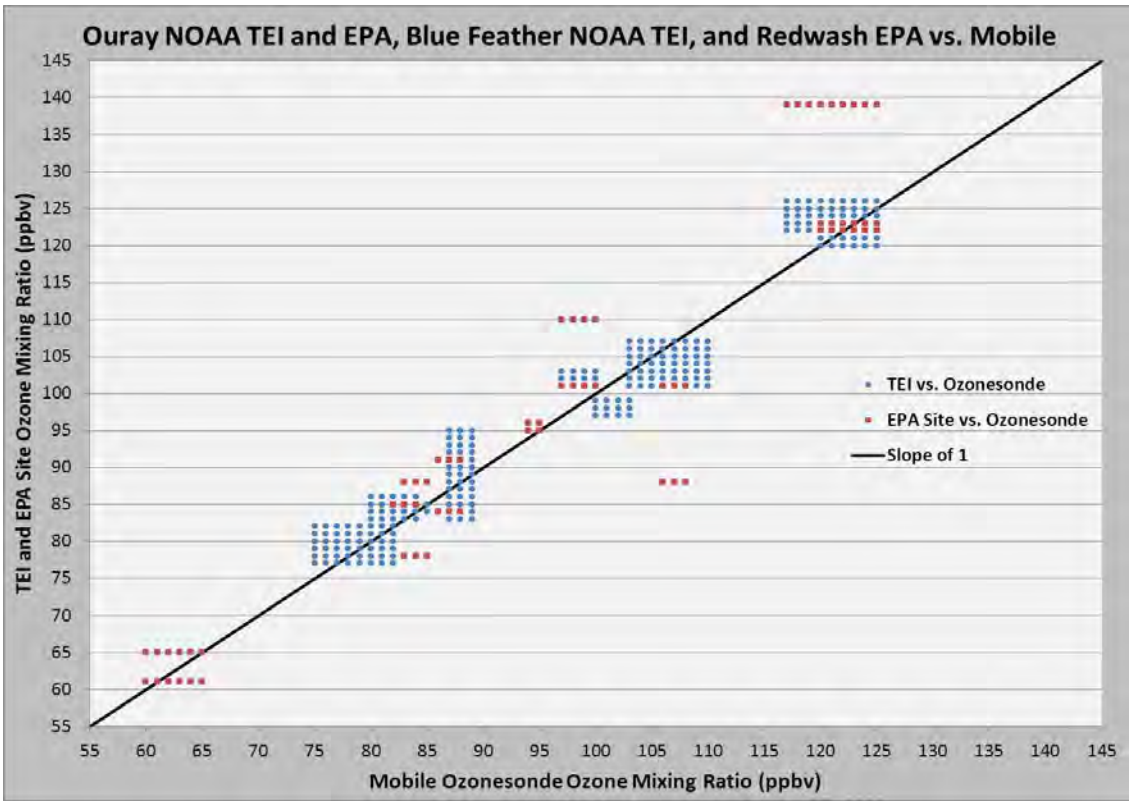


**Figure 8-32. Comparison between the mobile ozonesonde operated on the side of a NOAA van and fixed ozone measurements when the van passed near (up to a mile difference) the Red Wash and Ouray EPA ozone monitors and the NOAA monitor at the Ouray Wildlife Refuge. Considering the timing, difference in distance and the fact the mobile van occasionally operated in excess of 60 mph when passing the fixed sites, the agreement is excellent.**

# Mobile Ozone Measurements, Feb 6, 2013

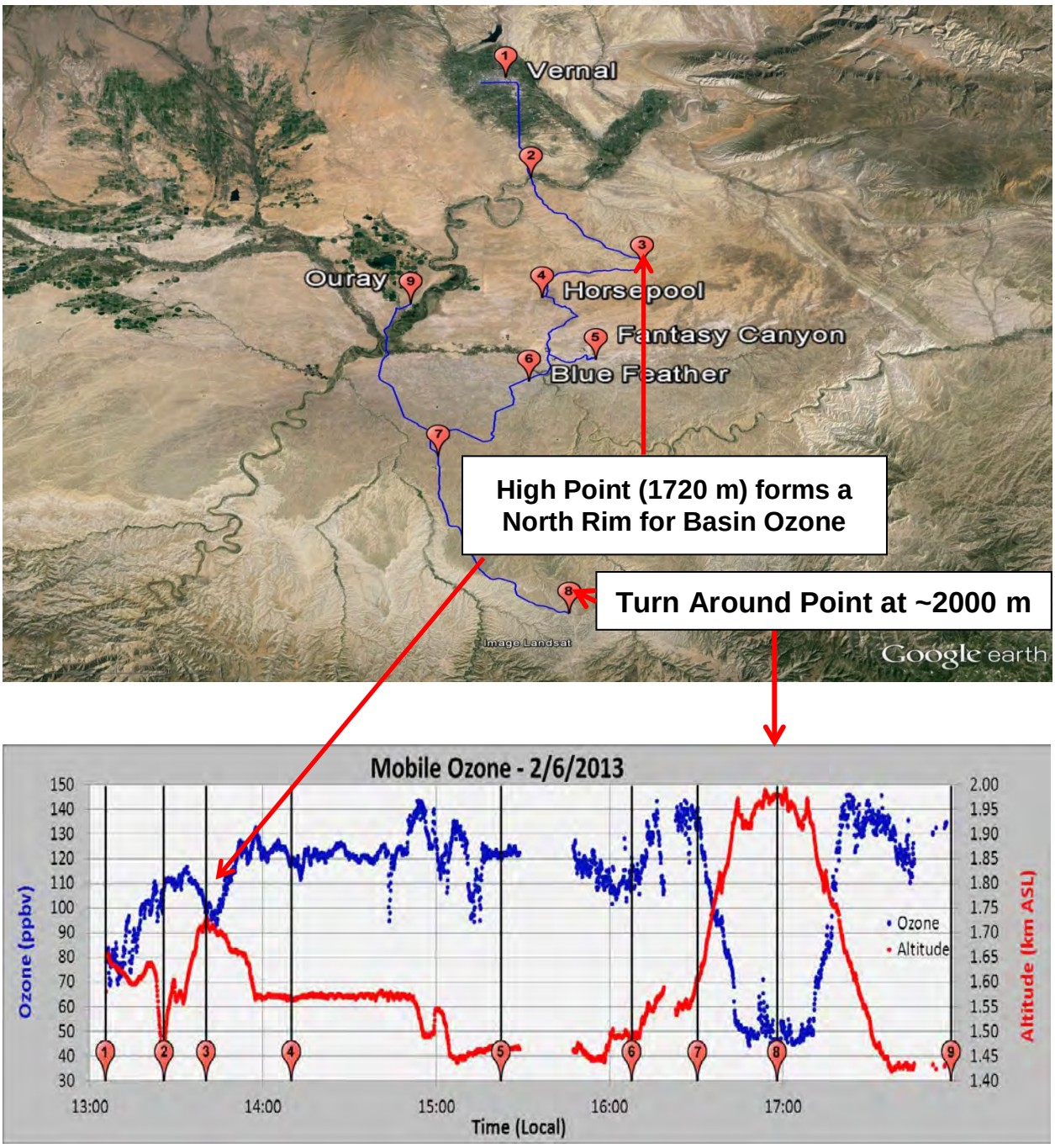


**Figure 8-33. Surface ozone concentrations plotted aganst altitude on a drive beginning in Vernal then through the eastern portion of the Uinta Basin, February 6, 2013. Note the the decrease in ozone (point 3) at 1720 m crossing the ridge near Red Wash, and the large ozone decrease as the van began to ascend through the inversion layer at 1720 m (Point 7) and the increase in ozone as the van descended back into the top of inversion layer after turning around at ~2,000 m (Point 8).**

### 8.2.5 Contour Plots of Ozone Structure during Ozone Production and Cleanout Events

Contour plots of ozone concentrations measured with tethersondes plotted by altitude and time are presented in Figures 8-34 through 8-40 for January 26 - February 6, 2013. On some days up to 22 separate tethersonde profiles were used to produce the contours. In Figure 34 may be seen the final day of a peak ozone event confined to a 150-200 m deep layer that topped out in the 1650-1700 m altitude. Figure 8-35 shows the middle stage of the subsequent cleanout produced by fresh air from the west mixing into the basin. Figure 8-36 shows that once the basin had been flushed out the incoming air contained background ozone concentrations. By January 31 (Figure 8-37), stagnation had redeveloped in the basin and local effluents from gas and oil operations began providing precursor gases for ozone formation. Ozone production continued through to February 6 (Figures 8-38, 8-39 and 8-40). On February 7 a partial cleanout of the basin began. The tethersonde operations were completed on the afternoon of February 7.

One of the most notable features of the ozone profile measurements is the vertical development of ozone production each day. Ozone production does not begin solely in a shallow layer next to the surface, but proceeds through the entire layer below the temperature inversion as indicated by the potential temperature profile (see Figures 8-18 - 8-24). As the inversion layer expands vertically with increasing temperature from solar heating, the ozone production layer grows vertically as well. This leads to nearly constant ozone mixing ratios in this thermally mixed layer. The mixing is, however, not so strong that the layer does not remain capped.

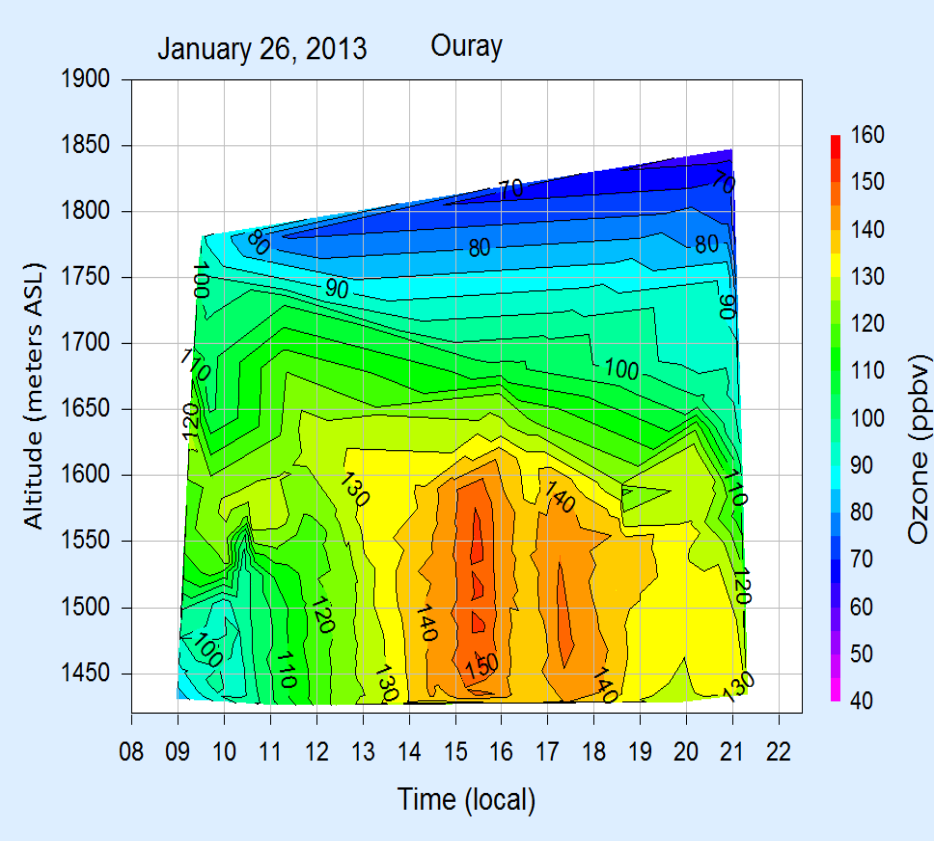


**Figure 8-34. Contour plot of ozone concentrations above the Ouray Wildlife Refuge in the first ozone event presented in Figure 8-9. Note that high concentrations of ozone occur in mid-afternoon and are concentrated between the surface and 1600 m altitude.**

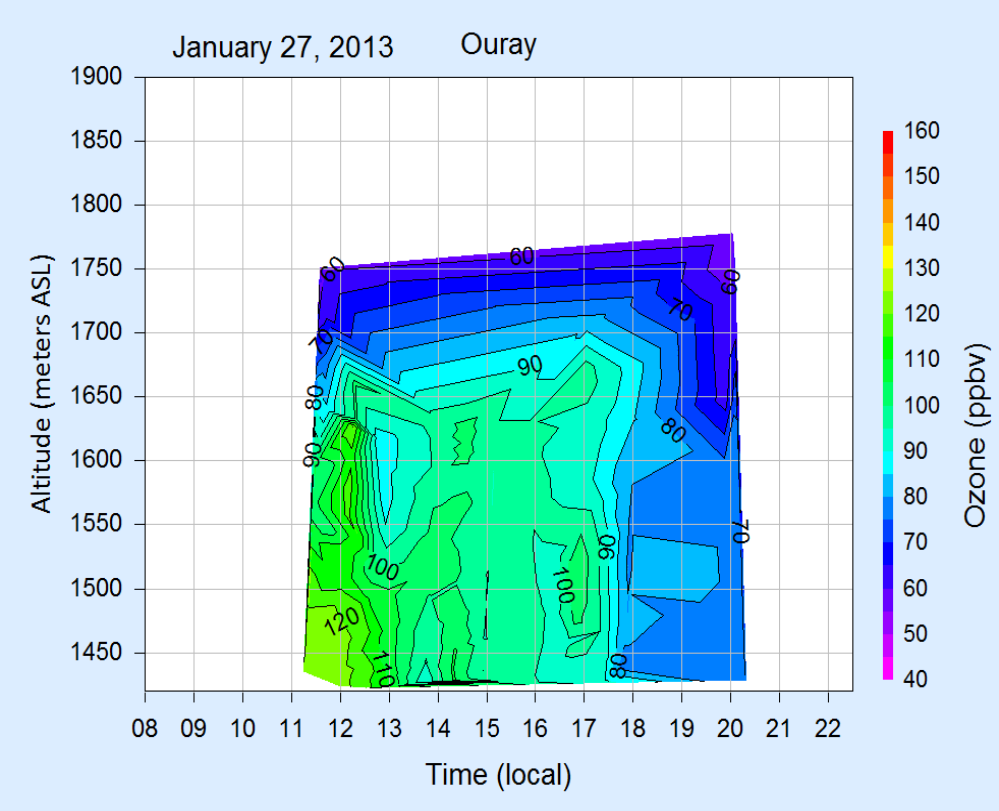


**Figure 8-35. Contour plot of ozone concentrations above the Ouray Wildlife Refuge showing the beginning of the basin-wide cleanout that began the evening of January 27.**

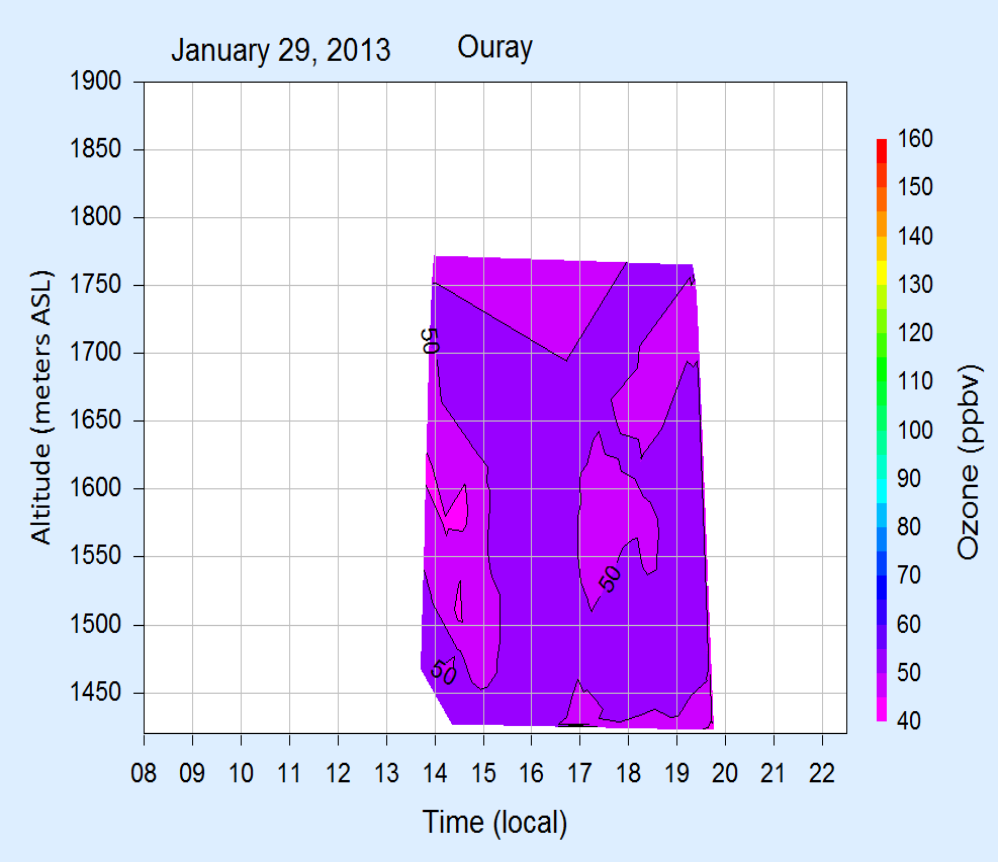


**Figure 8-36. Contour plot of ozone concentrations above the Ouray Wildlife Refuge the day the cleanout was essentially completed on January 29. Ozone concentrations of less than 50 ppb are considered background in this location and season.**

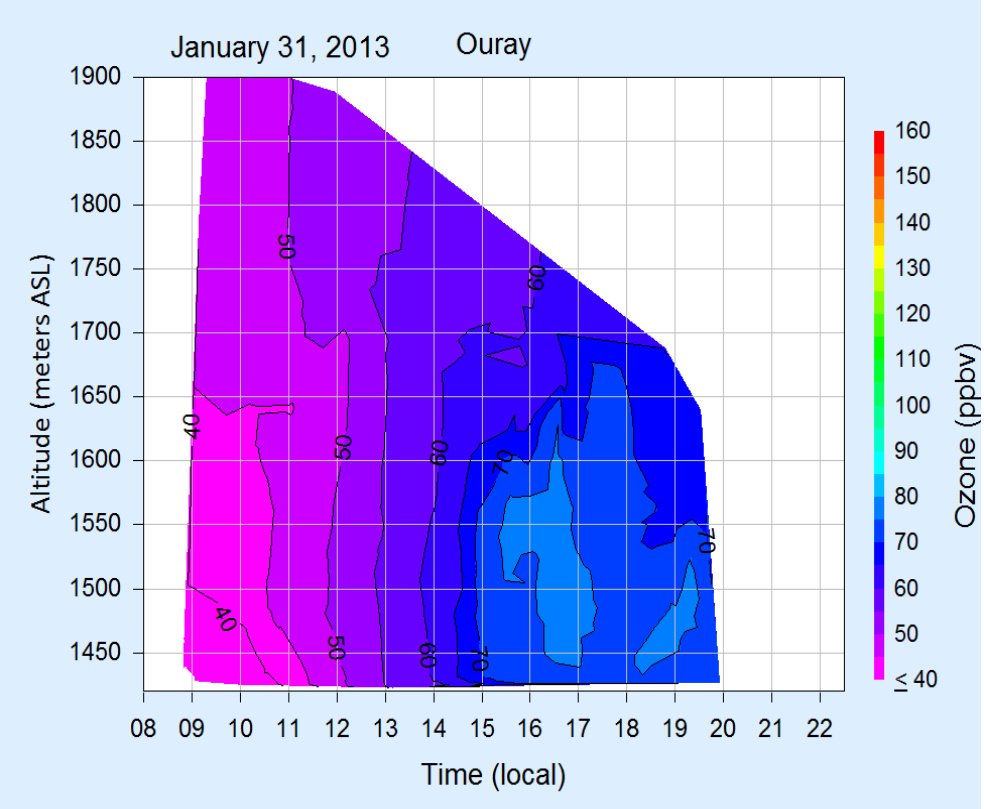


**Figure 8-37. Contour plot of ozone concentrations above the Ouray Wildlife Refuge showing the beginning of the next ozone event. This event was also the focus of the NOAA aircraft flights.**

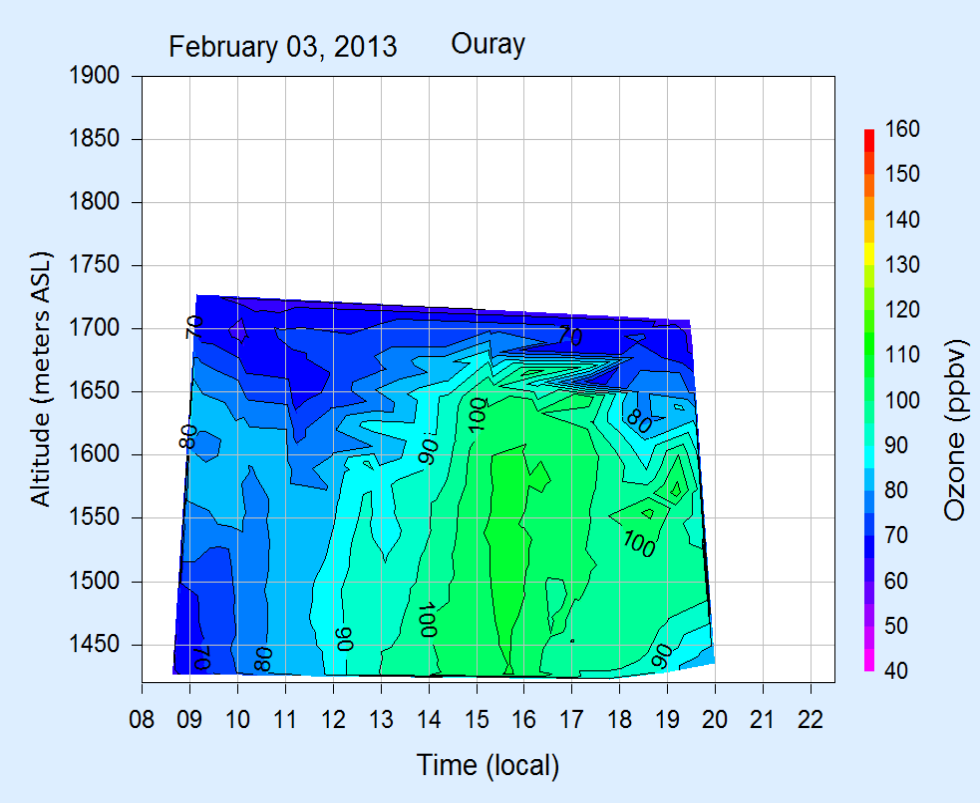


**Figure 8-38. Contour plot of ozone concentrations above the Ouray Wildlife Refuge showing the production of ozone now in excess of 100 ppb leading up to the peak on February 6.**

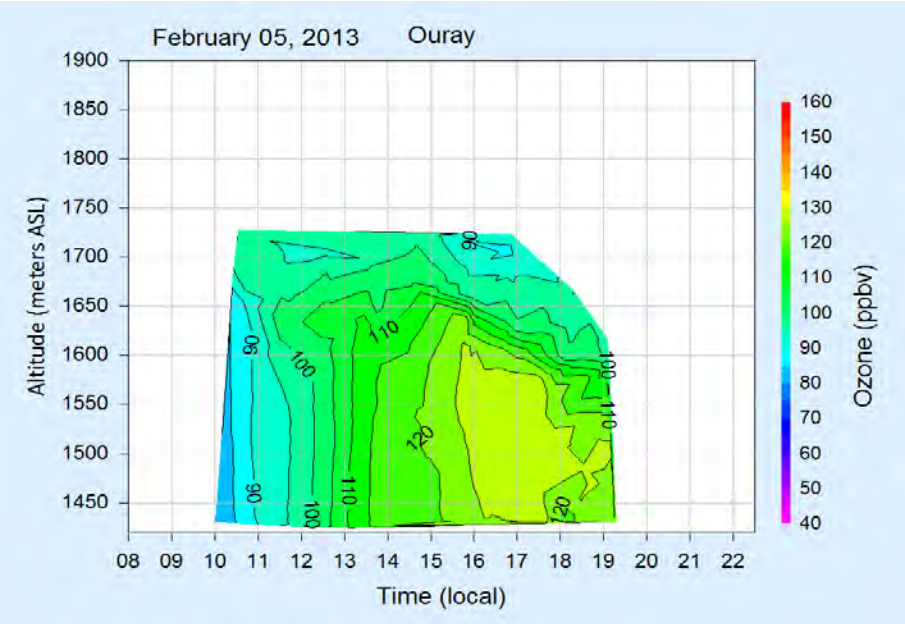


**Figure 8-39. Contour plot of ozone concentrations above the Ouray Wildlife Refuge the day prior to the peak of the basin wide ozone event. Note the high ozone concentrations in excess of 125 ppb in the late afternoon.**

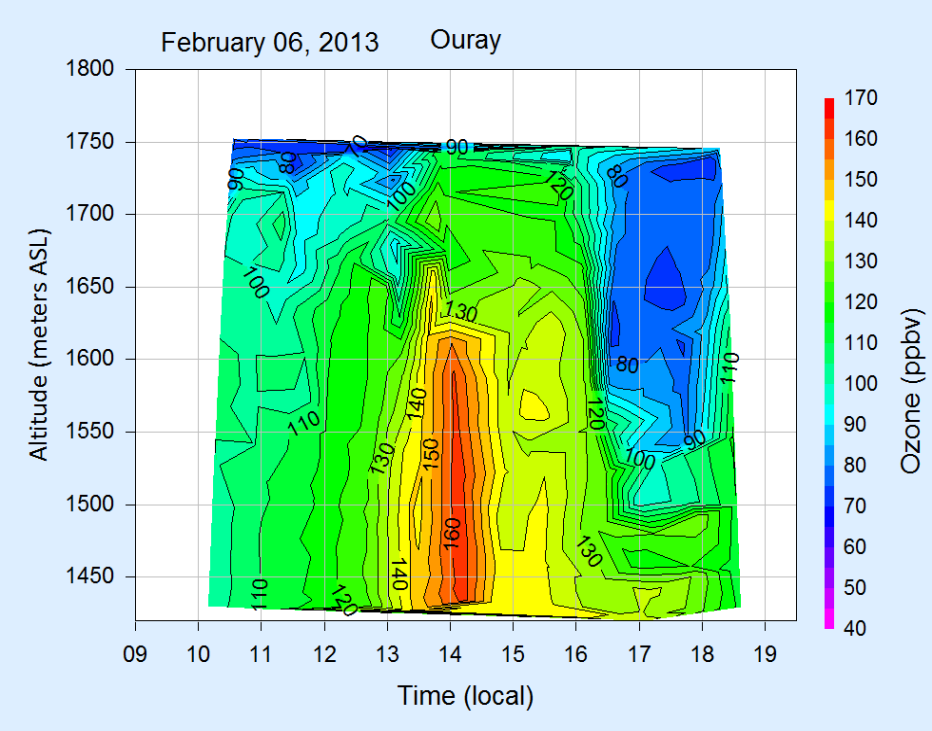


**Figure 8-40. Contour plot of ozone concentrations above the Ouray Wildlife Refuge at the peak of the basin wide ozone event. Later in the day air from the west began a partial basin cleanout as may be seen in the low ozone concentration air descending into the basin beginning around 1600 (blue area) down to 1550 m.**

### 8.2.6 Ozone Mixing Out of the Boundary Layer

Above the strong ozone production layer with a top at ~1650 m is a strong gradient layer that extends to ~1800 m (Figures 8-34 and 8-40) where tropospheric background ozone levels are encountered. This gradient layer suggests that some ozone (and likely other constituents) are mixed out of the ozone production layer into the overlaying troposphere even during the times with a capping inversion layer over the basin.

### 8.2.7 Contours of Two Ozone Production Events and the Intervening Cleanout.

A contour plot of ozone concentrations above Ouray January 24 - February 7 is presented in Figure 8-41. Two high ozone events (orange-red contours) and a cleanout separating the events (blue contours) are clearly seen.

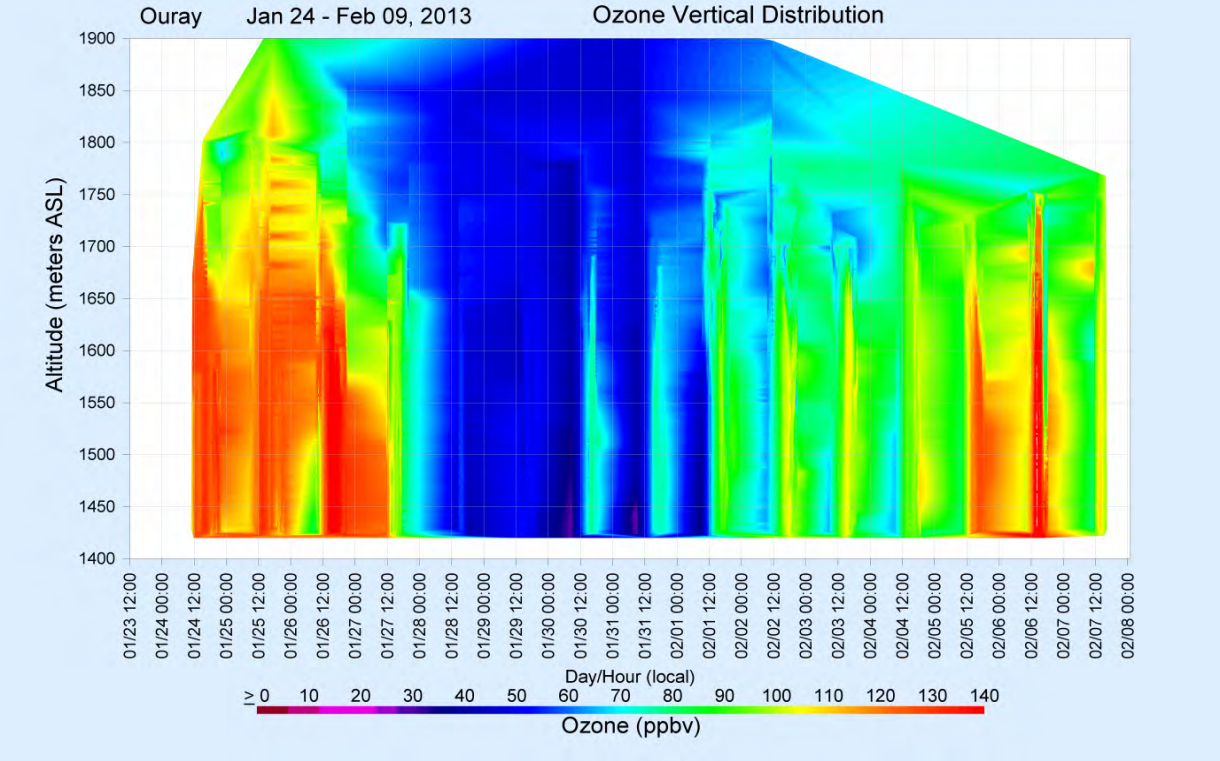


**Figure 8-41. Contour plot of ozone concentrations above the Ouray Wildlife Refuge January 24 - February 7 showing the ozone event ending January 27 and the cleanout that lasted from January 27 to the beginning of the new ozone production event in early February. That event peaked on February 6.**

## 8.3 Did the Bonanza Power Plant Contribute to Ozone Precursors in Winter 2013?

Bonanza power plant is located on the eastern edge of the Uinta gas field and questions as to the possibility of the plant contributing to ozone precursors (mostly $NO_x$) involved in the wintertime photochemical ozone production have been raised. During the 2013 Uintah ozone study, a wide variety of balloon borne, aircraft and remote sensing measurements were undertaken to address the question. In short, there is no evidence that the Bonanza power plant plume contributes significant amounts of precursors in the inversion layer and is therefore not likely a major driver of the wintertime high ozone events in the winter of 2013. The basis for this statement is presented below.

### 8.3.1 Aircraft Measurements in the Bonanza Power Plant Plume

Figure 8-42 is a photo of the Bonanza power plant plume and the water vapor condensate from the surface cooling ponds. The top of the power plant stack is at an elevation of 1715.8 m. Due to the relative warmth of the plume exhaust in winter, the plume generally rises an additional 2 to 3 stack heights before reaching neutral buoyancy at between 1900 and 2200 m. The inversion height in 2013 was in the 1600 to 1750 m range, well below the plume heights.

Figure 8-43 is a photo of the Bonanza power plant plume taken from the NOAA research aircraft on February 2, 2013 showing the top of the ozone rich surface layer and the power plant plume rising above the inversion. The plume eventually reaches neutral buoyancy at an altitude of about 1900 m. On this day that is 300 m above the top of the photochemical ozone production layer contained beneath the temperature inversion.

On February 2 and 5, 2013 the aircraft spent portions of the flights studying the altitude and dispersion of the power plant plume. Profiles were conducted near the plant, over Horsepool and westward across the basin as easterly winds carried the plume across the basin. In the aircraft section of this report, Figure 8-17, profile 4, shows the power plant plume to be centered at just less than 1900 m. Profiles through the plume on February 5 (aircraft section, Figure 8-19, profiles 1 and 3) also show the power plant plume at 1900 m.

**Figure 8-42. Bonanza power plant with buoyant exhaust plume and water vapor from the cooling ponds. The top of the stack is 1715.8 m and the plume generally rose an additional 2 to 3 stack heights before leveling out in the 1900 to 2200 m range. In the winter of 2013 the inversion top was generally between 1600 and 1750 m.**

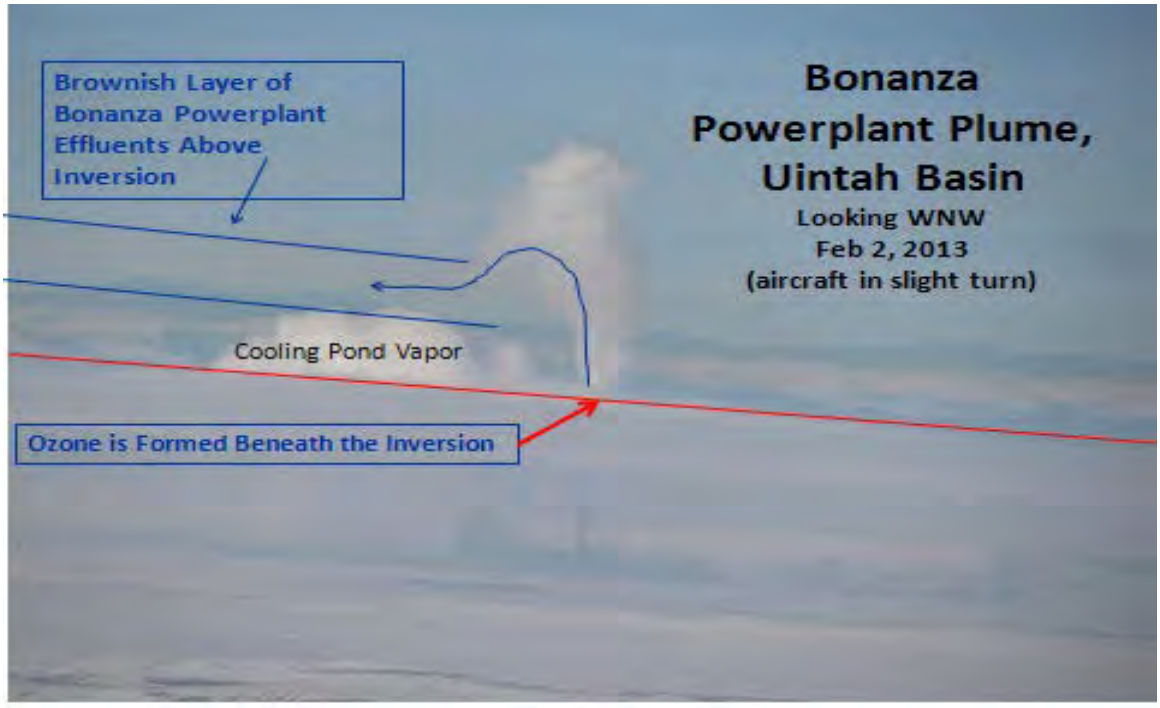


**Figure 8-43. Bonanza power plant plume rising well above the inversion layer at 1600 m before achieving neutral buoyancy and streaming westward out over the basin at 1900 m. Photograph by Colm Sweeney, airborne scientist, CIRES/NOAA.**

### 8.3.2 Horsepool Tethersonde Measurements of the Bonanza Power Plant Plume

The ozonesondes used in this study indicate low ozone concentrations in the presence of high sulfur dioxide ($SO_2$) concentrations observed in power plant plumes. In addition, when the ozonesondes are in power plant plumes, titration of the background ozone by $NO_x$ removes ozone. The net result of these two processes is zones of low or no ozone when the ozonesondes were in the Bonanza power plant plume. The tethersonde at Ouray was operated such that the maximum altitudes of the ascending profiles were determined by reaching the top of the enhanced ozone layer, at which point the tethersondes were put into descent mode. Thus, the tethersondes from the Ouray site was never high enough to enter the Bonanza power plant plume. On a few occasions, the Fantasy Canyon tethersonde was allowed to rise into the plume. The Horsepool tethersonde operated by the INSTAAR group was operated to much higher altitudes and regularly passed through the power plant plume when it was present over Horsepool. The Horsepool site is 17 km from the Bonanza power plant.

Figures 8-44 through 8-47 show representative measurements in the Bonanza power plant plume above the Horsepool site over a 12 day period. A composite ozone cross section with plumes annotated is presented in Figure 8-48 where it may be seen that Bonanza power plant plumes were at the 1900-2000 m level when over Horsepool except on the night of February 14 during the cleanout when the plume was probably pushed down 100-150 m by the fresh air descending into the basin.

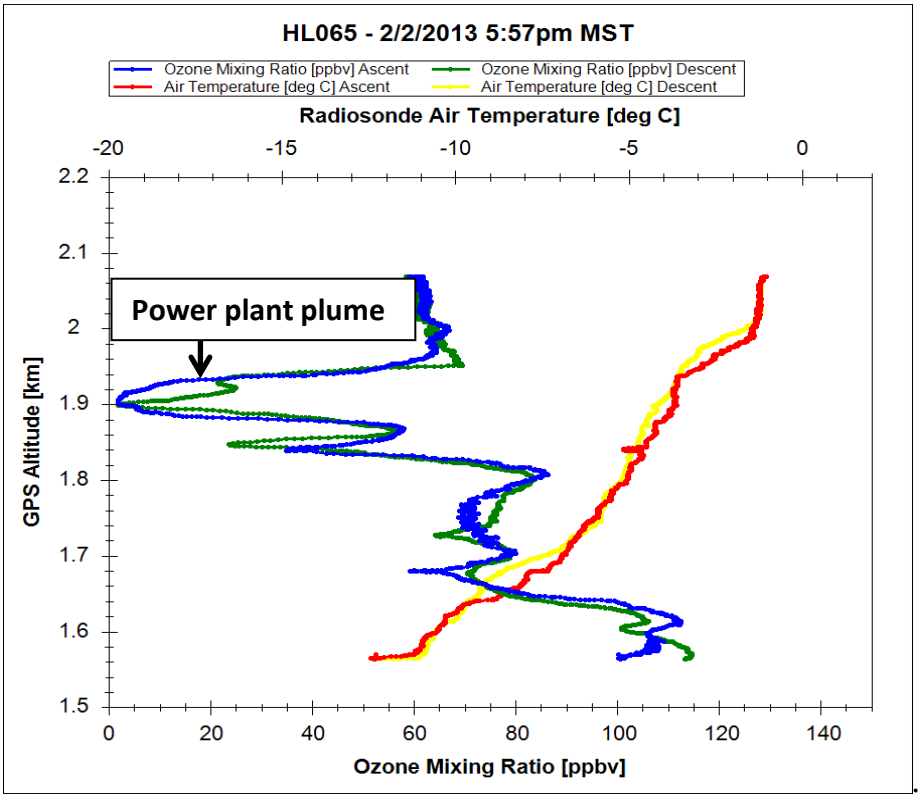


**Figure 8-44. Horsepool ozone and temperature profiles on February 2, 2013 showing the elevated ozone layer capped at 1620 m and the power plant plume at 1900 m. The time is the beginning of the balloon ascent that generally lasted from 30 to 45 minutes.**

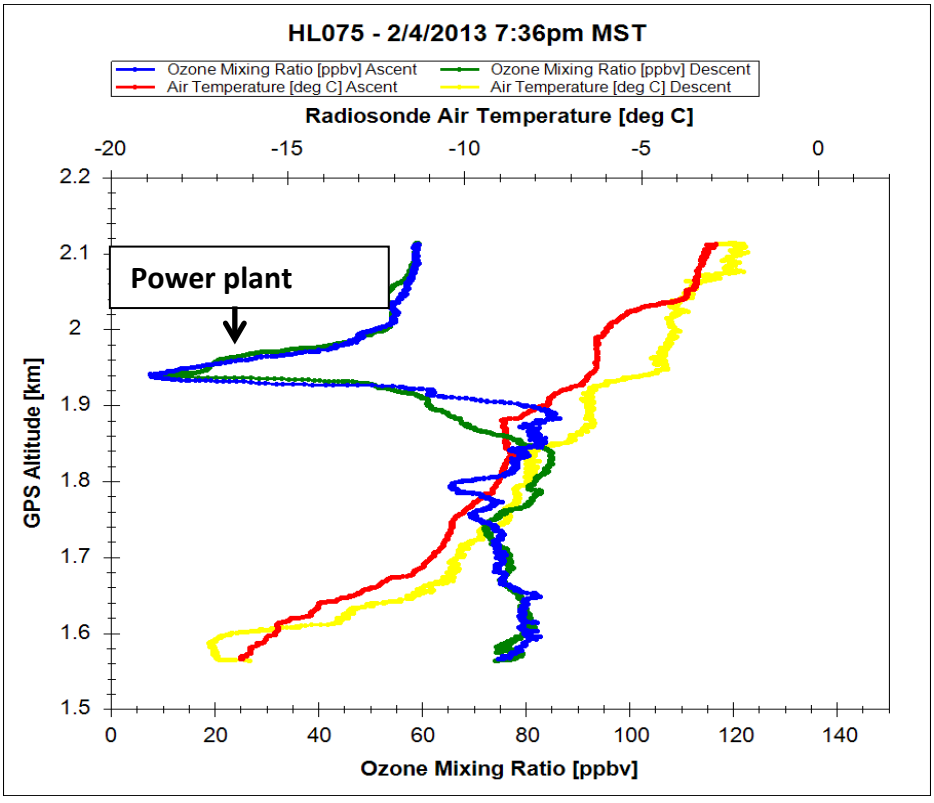


**Figure 8-45. Horsepool ozone and temperature profiles on February 4, 2013 showing a well-mixed ozone layer up to 1850 m and the Bonanza plume at 1940 m.**

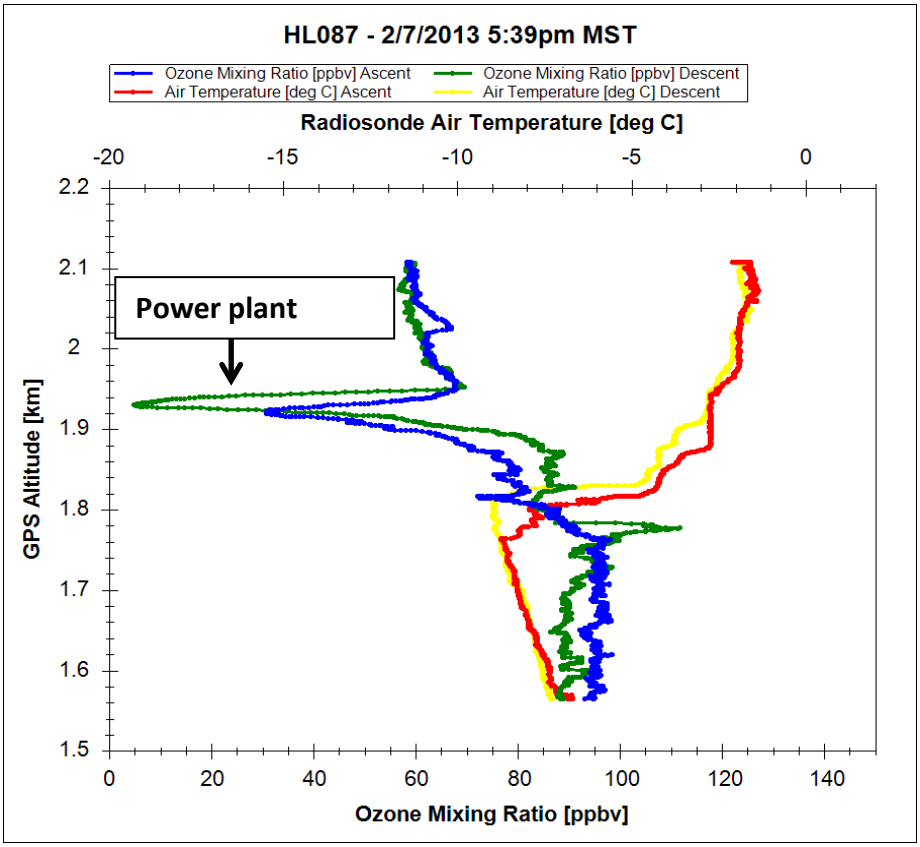


**Figure 8-46. Horsepool ozone and temperature profiles on February 7, 2013 showing the surface ozone layer capped at 1780 m and the Bonanza power plant plume centered at 1920 m.**

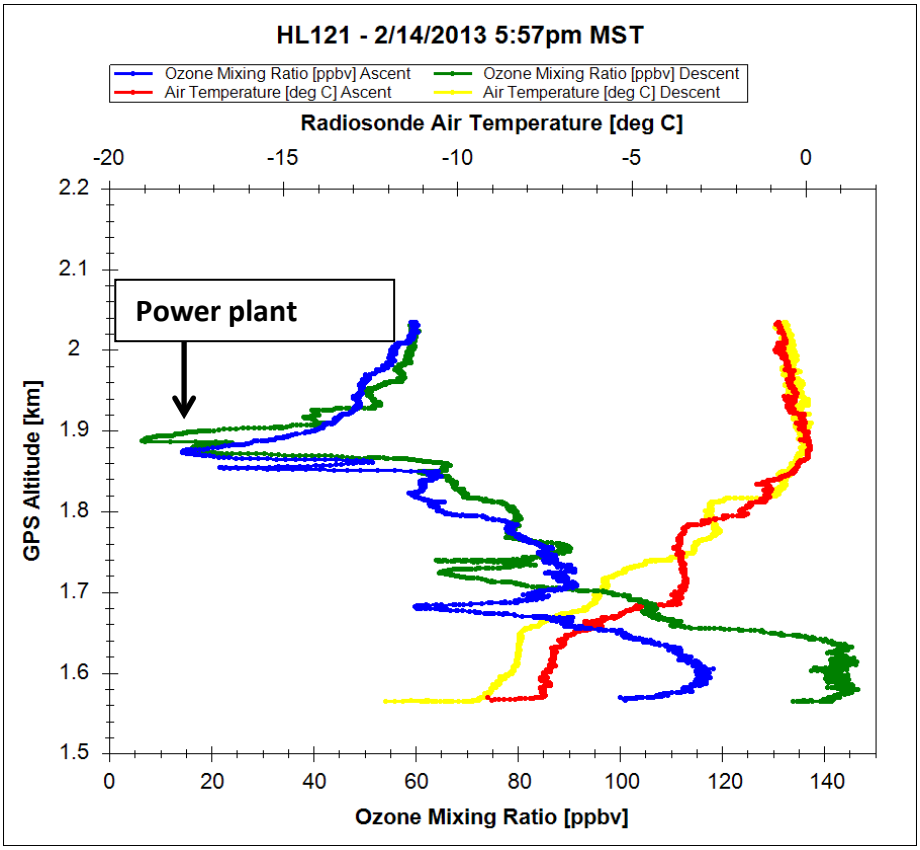


**Figure 8-47. Horsepool ozone and temperature profiles on February 14, 2013 showing a strong surface ozone layer capped at 1620 m and the power plant plume centered at 1860 m. This profile complements the data presented in Figure 48-9.**

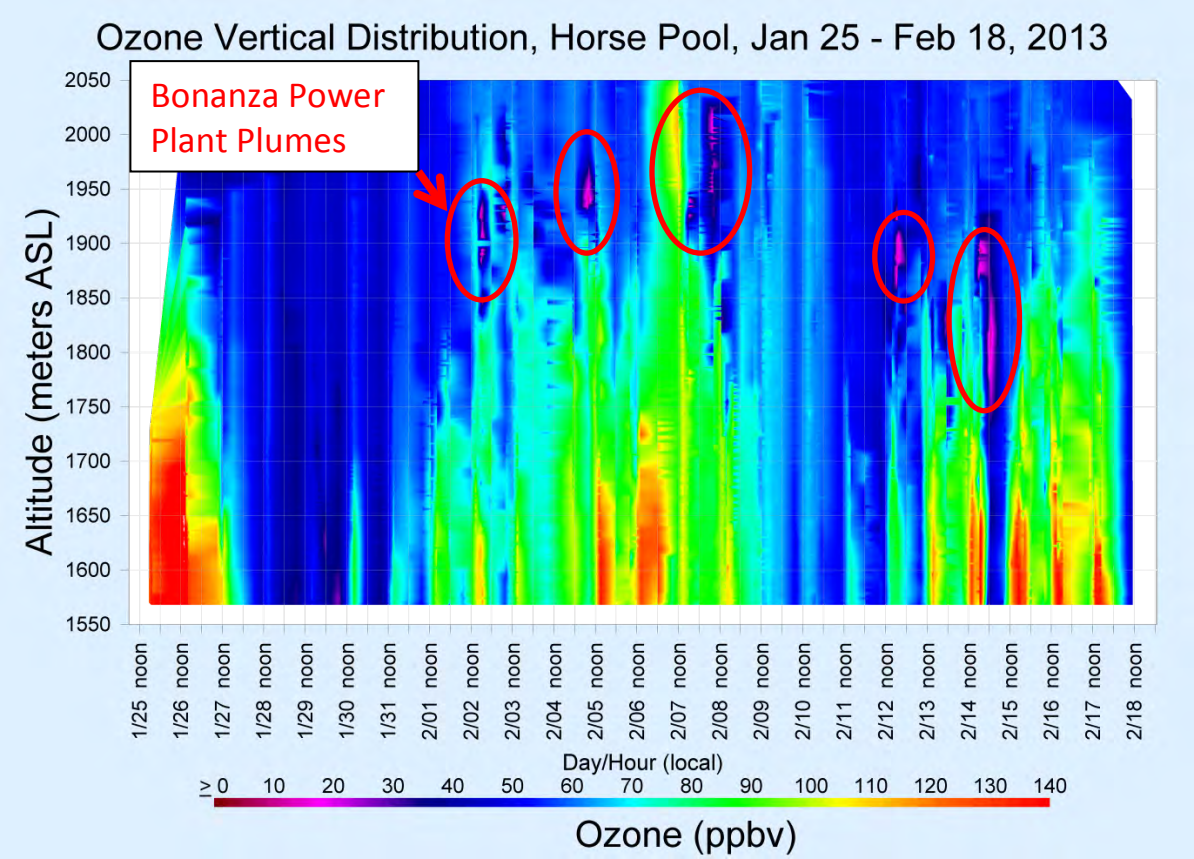


**Figure 8-48. Time-height cross section of ozone concentrations measured by tethersondes over Horsepool January 25 - February 18, 2013 with the Bonanza power plant plumes highlighted. The plume on the night of February 14 during the cleanout was probably pushed down to 1800 m by the fresh air descending into the basin.**

### 8.3.3 Tunable Optical Profiler for Aerosol and Ozone (TOPAZ) Lidar Measurements from Horsepool

During UBOS 2013, the NOAA TOPAZ lidar located at Horsepool occasionally observed ozone titration as the $NO_x$-rich plume from the nearby Bonanza power plant was advected over the Horsepool site. As an example, the data in Figure 8-49 shows a two-hour time-height cross section from near the surface up to 600 m agl (2100 m asl) on the evening of 14 February with the coincident profile of the ozone tethersonde data as presented in Figure 8-47. Both lidar and ozonesonde show the Bonanza plume at ~350 m agl (~1900m asl). Contrary to UBOS 2012, low ozone values were confined to the upper part of the cold-pool layer above the boundary layer. This suggests that power plant $NO_x$ was very likely not a significant part of the precursor mix that led to the high surface ozone values observed in 2013.

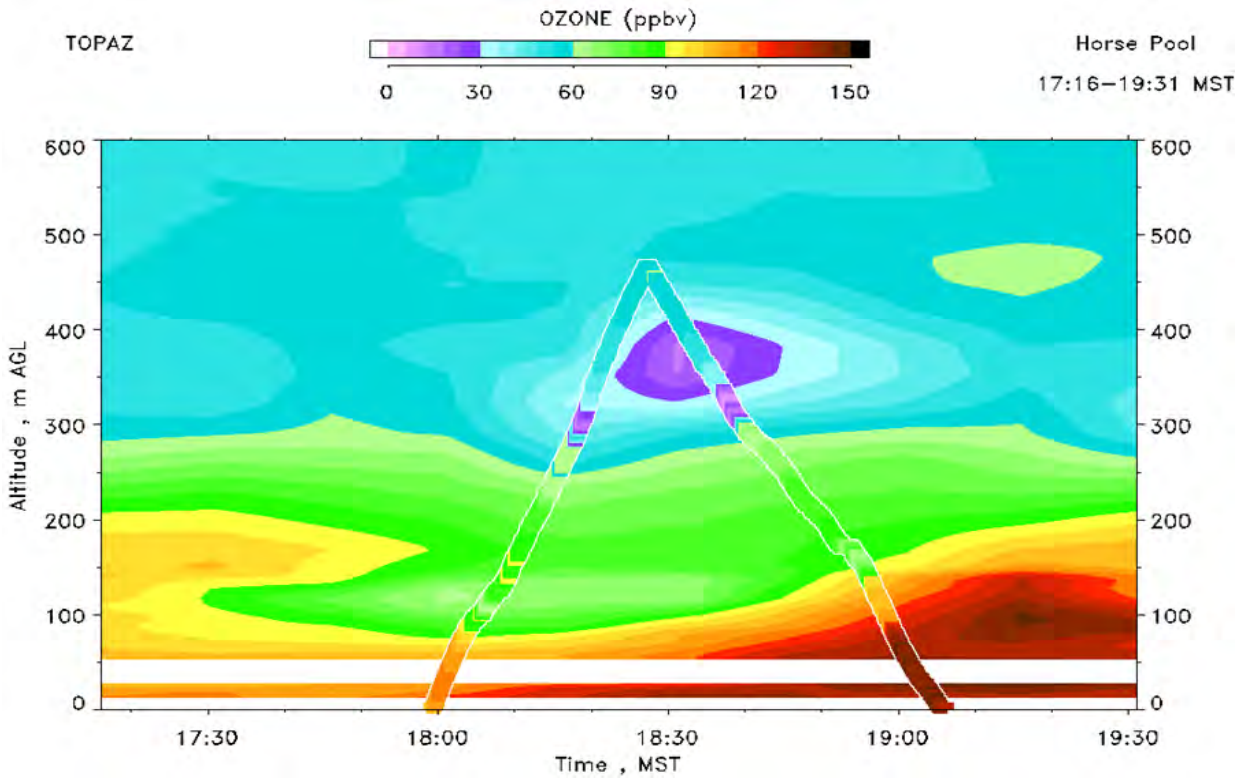


**Figure 8-49. TOPAZ time-height cross section of ozone from near the surface to 600 m AGL (2100 m ) for 17:16 – 19:31 MST on 14 February 2013 at Horsepool. The colored line shaped like an inverted "V" represents the ozone measurements from the collocated tethersonde data presented in Figure 8-47.**

### 8.3.4 Physical Boundaries to Ozone Production and Precursors in the Uinta Basin

Wintertime ozone production in the Uinta Basin, when there is snow cover on the ground, is confined to a relatively shallow boundary layer capped by a stable temperature inversion. In the winter of 2013 this inversion was level across the basin varying from 1600 to 1700 m. In Figure 8-50, the purple area falls approximately within the 1600 m contour within which ozone was always elevated in the 2013 events and the boundary between the turquoise and green shading approximates the 1700 m contour under which the photochemical ozone production occurred. As such, the precursors for the ozone production reactions have to also be beneath the 1700 m contour and for the most part beneath the 1600 m contour. From this figure it may also be suggested that both Dinosaur and Rangely, Colorado could occasionally be within the Uinta Basin ozone production zone when there are weak or elevated temperature inversions, or when west winds in the basin move precursors and ozone east.

In Figure 8-51 are plotted the oil and gas wells in the basin along with the elevation contours. From this figure it may be observed that many of the western oil wells are above the top of the inversion and thus may not be contributing precursor emissions to ozone production within the basin to as great an extent as wells located well below the inversion. Almost all gas wells (one of the ozone precursor sources) in Uintah County are beneath the 1700 m inversion level.

## Surface Elevation Contours in the Uinta Basin, Utah

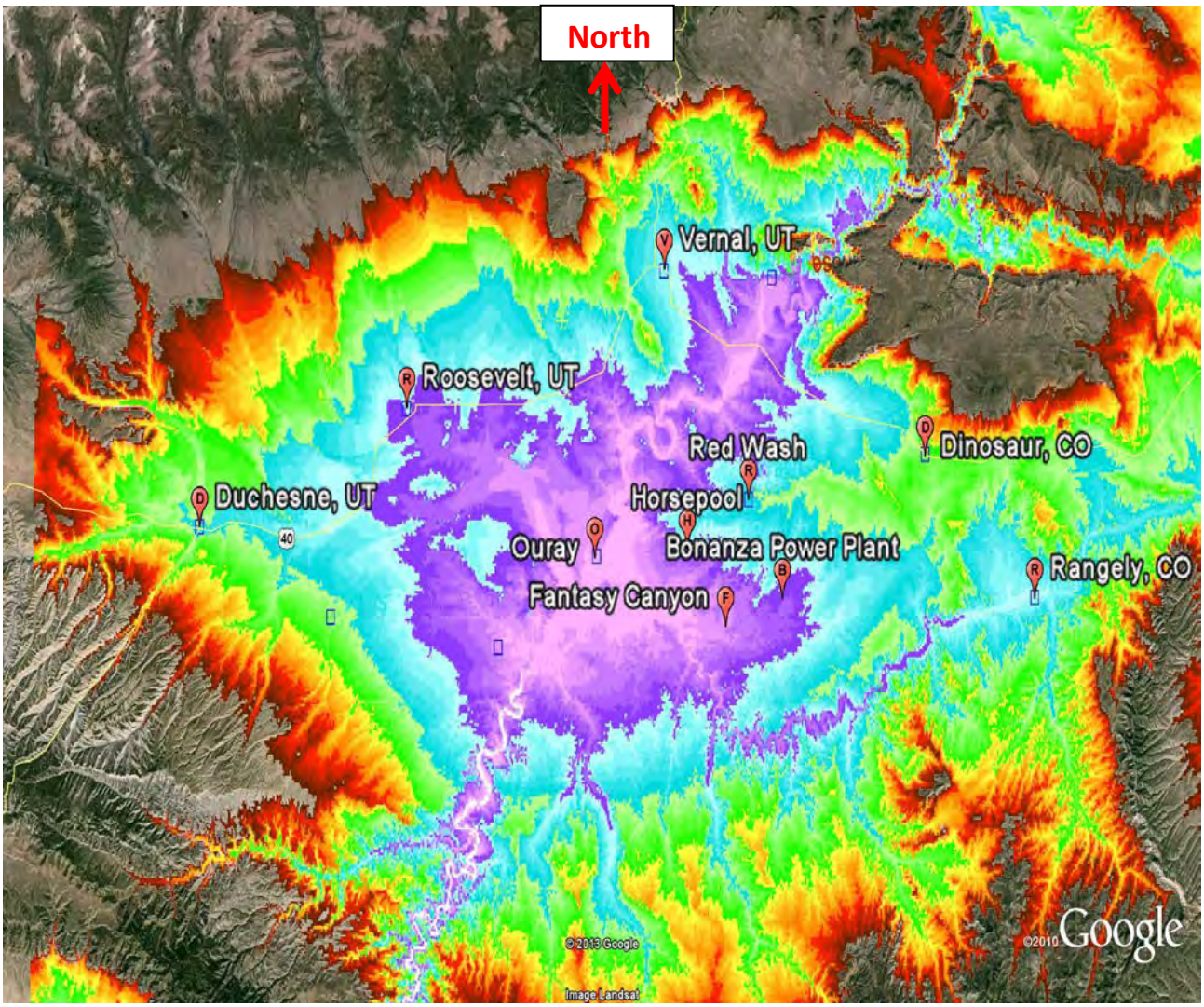


**Figure 8-50. Uinta Basin surface elevation contours where the purple hue delineates the lowest elevations in the basin bounded on the upper side by the ~1600 m contour. The boundary between the turquoise and green hues is the ~1700 m contour. Rapid, high concentration photochemical ozone production in the winter of 2013 occurred almost exclusively beneath the level of the 1700 m contour. The most frequent and intense ozone production occurred below 1600 m elevation. Rangely, Colorado is just within this zone as is Duchesne, Utah. The town of Dinosaur, Colorado near the Dinosaur National Monument is just on the edge of the high ozone production zone. Dinosaur could well experience elevated ozone under weak inversions or low altitude westerly winds.**

## Oil and Gas Wells and Surface Elevation Contours in the Uinta Basin, Utah

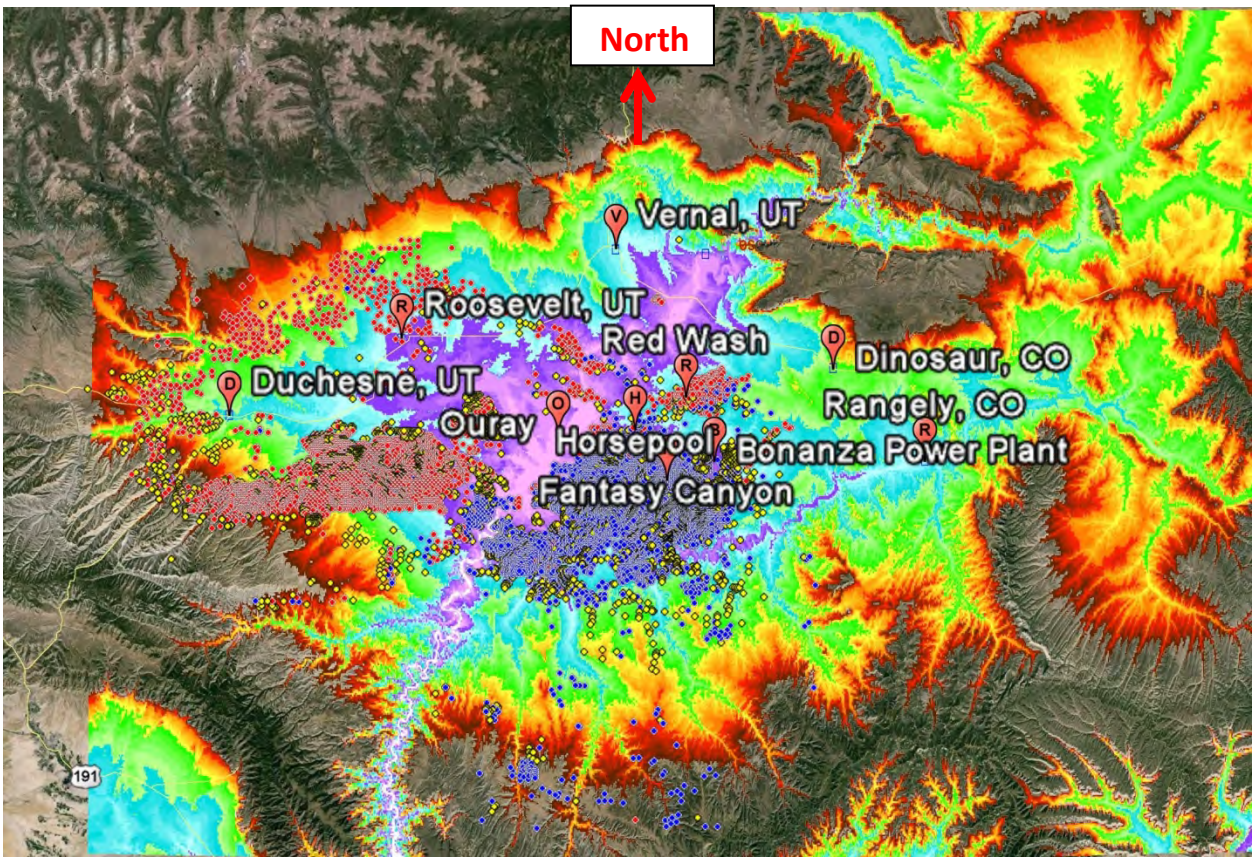


**Figure 8-51. Oil and gas wells plotted along with elevation contours. A large number of the western basin oil wells are at elevations above the 1600 -1700 m elevation of the temperature inversions and thus may not be significantly contributing precursor chemicals to the ozone production that occurs lower down in the Uinta Basin. This needs to be checked with mobile van measurements.**

## 8.4 Conclusions

A. The wintertime photochemical ozone production in the Uinta Basin requires snow on the ground, a shallow boundary layer, stagnation and a persistent temperature inversion capping the shallow ozone production layer. The snow helps to keep the surface cold reinforcing the production and maintenance of temperature inversion, reflects daytime solar radiation that enhances photochemical ozone production, and may be involved in snow chemistry as discussed in other sections of this report. The inversion layer traps gaseous effluents from the wells, pipelines, compressor stations and vehicle exhausts in a shallow layer where the rapid photochemical ozone production occurs.

B. During high ozone events, the tethersonde data show that air in the Uinta Basin below 1650-1700m is isolated from the rest of the atmosphere and emissions at the surface are trapped in this shallow layer (see sections 4 and 6, Aircraft and Horsepool balloon measurements respectively). The ozone precursors have to be coming from within the Uinta Basin below the 1700 m contour. There is some horizontal and vertical transport within the basin with some of the ozone mixing up through the inversion layer.

C. Within a few hours of a strong temperature inversion onset with a snow covered ground, ozone production begins during daylight hours and peaks around 2-3 hours after solar noon. This photochemical production can produce up to 60 ppb of ozone through a 250 m layer of the atmosphere within 4 hours. Once an ozone event is in progress, nighttime titration of ozone may only remove 10-20 ppb ozone. Thus, successive days build upon the elevated ozone levels of the previous day. Within 2-3 days of an ozone event, nighttime ozone concentrations can remain above 75 ppb and reach up to 160 ppb during the day.

D. Based on the tethersondes data from Horsepool and Fantasy Canyon, the Bonanza power plant plume was injected above the inversion layer and therefore was not a major source of ozone precursors in the shallow surface inversion layer during high ozone events in the winter of 2013.

E. The battery operated tethersonde system developed for the Uinta Basin ozone studies is an effective instrument for providing numerous continuous profiles of ozone, temperature and humidity semi-automatically from remote sites. A free flying ozonesonde costs about $1200 per launch and produces one profile. The tethersonde can produce more than 100 profiles (2 to 4 per hour) with high vertical resolution for about the same cost as one free flying ozonesonde.

## 8.5 Outreach and Education in 2012:

The tethered balloon ozonesonde system was set up for 3 different public relation events for the 2012 study. No similar public events were conducted during the 2013 study. In 2012, along with talks and slideshows, the balloons worked very well as a visual aid showing actual scientific measurements of ozone from the balloon tethersondes. Presentations were given during the Winter Ozone Study Kickoff Event at the Bingham Research Center press conference and two local schools: Uintah River High School in Fort Duchesne and Vernal Middle School.

**Figure 8-52. Presentation and balloon demonstration at Uintah River High School in Fort Duchesne, Utah.**

**Figure 8-53. Presentation and balloon demonstration at Vernal Middle School.**

## 8.6 Acknowledgements

A. The NOAA Global Monitoring Division greatly appreciated the permission, access to power, and the excellent physical facilities for operating an ozonesonde system for the 2013 study at the Ouray National Wildlife Refuge Site (Wildlife Refuge Rd., Ouray, UT). Thanks to Dan Schaad (Refuge Manager) and his capable and accommodating staff.
B. We thank the staff at the EDL Bingham Research Center for support during both campaigns and to Questar Resources for access to the Blue Feather Pipe Yard for operating an ozone monitor.
C. Funding for the campaigns came from NOAA, EPA and a consortium of industry resources represented by the Western Energy Alliance.

## 8.7 References

Deshler, T., et al., Atmospheric comparison of electrochemical cell ozonesondes from different manufacturers, and with different cathode solution strengths: The Balloon Experiment on Standards for Ozonesondes, *J Geophys Res-Atmos*, 113(D4), 2008.

Komhyr, W.D., Electrochemical concentration cells for gas analysis, *Ann. Geophys., 25*, 203-210, 1969.

Komhyr, W.D., R.A. Barnes, G.B. Brothers, J.A. Lathrop, and D.P. Opperman, Electrochemical concentration cell ozonesonde performance evaluation during STOIC 1989, *J. Geophys. Res*., 100, 9231-9244, 1995.

Martin, R., K. Moore, M. Mansfield, S. Hill, K. Harper, and H. Shorthill, Final Report: Uintah Basin Winter Ozone and Air Quality Study, December 2010 – March 2011., *Energy Dynamics Laboratory, Utah State University Research Foundation Report,* Document Ndo appumber EDL/11-039, June 14, 2011.

Morris, Gary A., Walter D. Komhyr, Jun Hirokawa, James Flynn, Barry Lefer, Nicholay Krotkov, Fong Ngan, A balloon sounding technique for measuring $SO_2$ plumes. *J. Atmos. Oceanic Technol*., 27, 1318–1330. doi: 10.1175/2010JTECHA1436.1, 2010.

Smit, H. G. J., et al., Assessment of the performance of ECC-ozonesondes under quasi-flight conditions in the environmental simulation chamber: Insights from the Juelich Ozone Sonde Intercomparison Experiment (JOSIE), *J Geophys Res-Atmos*, 112(D19), 2007.

**Contact:**

Bryan Johnson
U.S. Department of Commerce
NOAA/ESRL, 325 Broadway, R/GMD1
Ozone & Water Vapor Group
Boulder, CO 80305-3328
phone: (303) 497-6842
email: bryan.johnson@noaa.gov

2012 DATA FTP site: ftp://ftp.cmdl.noaa.gov/ozwv/ozone/Uintah/DATA_NOAA_Balloon
2013 DATA FTP site: ftp://ftp.cmdl.noaa.gov/ozwv/ozone/Uintah_2013_Tether_OzoneSondes/

# 9.0 EMISSION INVENTORY DEVELOPMENT ACTIVITIES

## 9.1 Uinta Basin Emissions Inventory

***Patrick Barickman***

***Utah Division of Air Quality***

### 9.1.1 Introduction

The emissions inventory in the Uinta Basin is dominated by development and production in the oil and gas sector which is illustrated in Table 9-2 in section 9.1.3 below. For this reason improvements in the oil and gas inventory will be of great benefit to all of the stakeholders involved in modeling and analyzing the effects of future development and regulatory policy. In addition to a specific inventory for oil and gas sources, estimates of emissions from other sectors of the counties such as large and small scale commercial and manufacturing, automobile and truck traffic, and household activities are also accounted for. Estimates for these activities come from the National Emissions Inventory (NEI) which is a detailed, publicly available, county-level inventory that is compiled every three years by each state and is maintained by the Environmental Protection Agency (EPA). The NEI is combined with the industry-specific oil and gas inventories currently being used by a variety of organizations for air quality modeling in the Uinta Basin. This section will focus on the current state of the oil and gas emissions inventory and the projects currently under way to improve those estimates.

### 9.1.2 WRAP Phase III – the Baseline Oil and Gas Inventory

In 2008 Western Regional Air Partnership (WRAP) undertook an effort to survey the oil and gas producers in the Intermountain West to create a comprehensive inventory of activity and equipment used in the region. From this effort emission factors were established for a set of activities used to create an annual emissions inventory for individual production basins for the year 2006.[1, 2] According to the WRAP technical memorandum on the development of the Phase III inventory[3],

> The companies that participated in the survey process by providing some survey responses for the Uinta Basin represented 71% of well ownership in the basin, 82% of gas production in the basin, and 78% of oil production in the basin. This represented a sufficiently large percentage of oil and gas activity in the basin that it was felt that the responses obtained from the participating companies would be representative of all oil and gas operations in the basin.

[1] WRAP. 2008. Joint Rocky Mountain Phase III Oil and Gas Emissions Inventory Project July 2008. http://www.wrapair.org/forums/ogwg/documents/Phase_III_Project_Overview.pdf
[2] WRAP. O&G Emissions Workgroup: Phase III Inventory. http://www.wrapair2.org/PhaseIII.aspx
[3] WRAP. 2009. Development of Baseline 2006 Emissions from Oil and Gas Activity in the Uinta Basin. http://www.wrapair.org/forums/ogwg/documents/2009-03_06_Baseline_Emissions_Uinta_Basin_Technical_Memo_03-25.pdf

It was, however, also noted in the memorandum that there was a considerable amount of extrapolation required to apply the results of surveys that were completed to sources of production that did not respond to the surveys.

### 9.1.3 Utah Division of Air Quality Oil and Gas Inventory for 2011

The WRAP Phase III inventory was used as the starting point for creating an updated 2011 oil and gas inventory for air quality modeling by the Utah Division of Air Quality (UDAQ). The Utah Division of Oil Gas and Mining (DOGM) database was used to create growth factors, based on production, to grow the inventory from 2006 to 2011. In addition the UDAQ database of permitted compressor stations was used for the portion of emissions related to permitted sites. A UDAQ memo from Kiera Harper describes the process that was used by UDAQ to update the WRAP Phase III inventory for the Uinta Basin and create an estimate for 2011.[4]

In addition to updating the inventory, UDAQ also used the location information in the DOGM database to create a set of spatial surrogates to distribute these emissions in the Basin. By concentrating the emissions based on production rather than by simple well location, a truer picture of the concentration of emissions in areas of intense development emerges. Figure 9-1 illustrates the location of gas producing wells in a 64 square kilometer region in Uintah County. Based on gas production in 2011 it is estimated that roughly one quarter of the emissions from natural gas production in the county come from that area. Table 9-1 shows the change in production between 2006 and 2011 in the Uinta Basin.

[4] Harper, Kiera. 2012. Memorandum: 2011 Uinta Basin Oil and Gas Emissions Estimates Technical Document. http://www.deq.utah.gov/locations/uintahbasin/docs/2013/aug/2011UintaBasinOilGasEmissionsEstimates.pdf

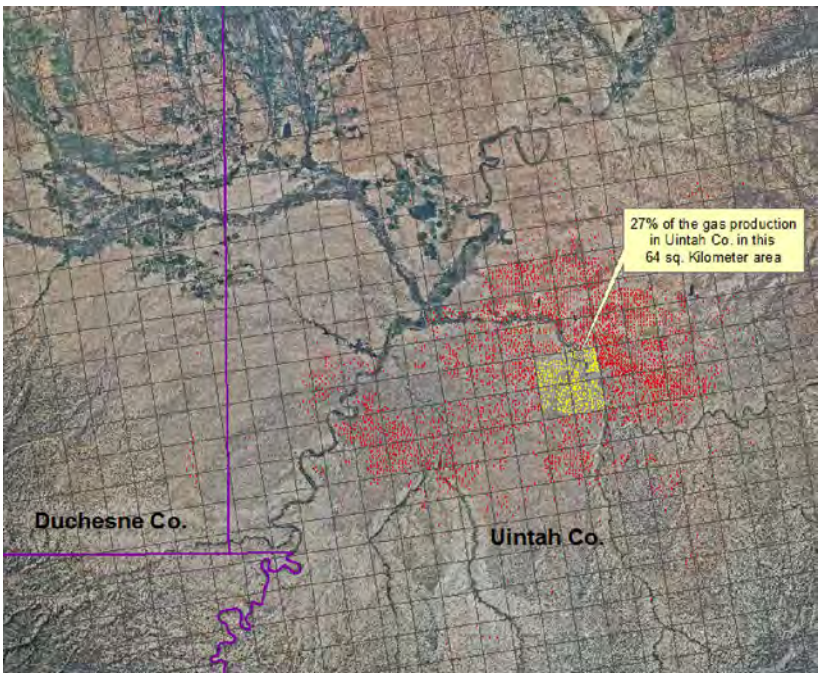


**Figure 9-1. Natural Gas Wells in the Uinta Basin in 2011 (production, and thus emissions, not necessarily distributed by well count; more production is concentrated in the yellow grid cells than is apparent from the actual number of wells).**

**Table 9-1. Production counts for oil, natural gas, produced water, gas well condensate, producing wells, and spuds for the years 2006 and 2011. (Harper[4]).**

| Year | County | Oil Prod. | Gas Prod. | Water Prod. | Gas Condensate | Well Count | Spuds |
|---|---|---|---|---|---|---|---|
| | | (BBLs) | (MCF) | (BBLs) | (BBLs) | | |
| 2006 | Uintah | 3396826 | 203511421 | 44736926 | 1560268 | 4029 | 685 |
| 2006 | Duchesne | 6265162 | 22530227 | 17973903 | 137752 | 1474 | 277 |
| 2011 | Uintah | 4688525 | 298697981 | 52853826 | 2320655 | 5852 | 524 |
| 2011 | Duchesne | 11633159 | 39338719 | 29748608 | 300575 | 2345 | 351 |

A complete emissions inventory for air quality modeling also includes estimates for all of the other sources of emissions in addition to the oil and gas sectors. These are incorporated using data from the NEI as mentioned above. The creation of this data set follows well established protocols for the distribution of emissions. Those that are not related to oil and gas get distributed by population, highway routes, industrial locations, land use for agriculture, etc.

Table 9-2 shows all of the major categories in the emissions inventory. Biogenic Volatile Organic Compounds (VOC) during the winter are estimated to be significantly less than during the summer in the Uinta Basin. Consequently one would not want to compare the annual VOC emissions in Table 9-2 without taking this seasonal difference into account. It is clear from the

table that the vast majority of ozone precursor emissions during the winter in Duchesne and Uintah counties come from the oil and gas sector.

**Table 9-2. UDAQ 2011 Emissions Inventory based on the Utah NEI submittal and updated WRAP Phase III inventory.**

| County | Source Tons/Year | $NO_x$ | $PM_{2.5}$ | SOx | VOC |
|---|---|---|---|---|---|
| **Duchesne** | Oil & Gas | 7,805 | | 125 | 34,787 |
| | All Other Activity | 3,220 | 382 | 18 | 1,864 |
| | Biogenic - Summer Only - Trees, Crops, Plants | 0 | | 0 | 22,390 |
| | | | | | |
| **Uintah** | Oil & Gas | 10,033 | | 209 | 76,502 |
| | All Other Activity | 1,728 | 978 | 20 | 1,921 |
| | Biogenic - Summer Only - Trees, Crops, Plants | 0 | 0 | 0 | 29,153 |
| | Bonanza Power Plant | 6,590 | 433 | 1,178 | 46 |

Figures 9-2 and 9-3 show the distribution of VOC and $NO_x$ emissions throughout the two-county area from the majority of sources in the emissions inventory. As noted in the section on produced water storage ponds, these emissions are not yet accounted for in the inventory.

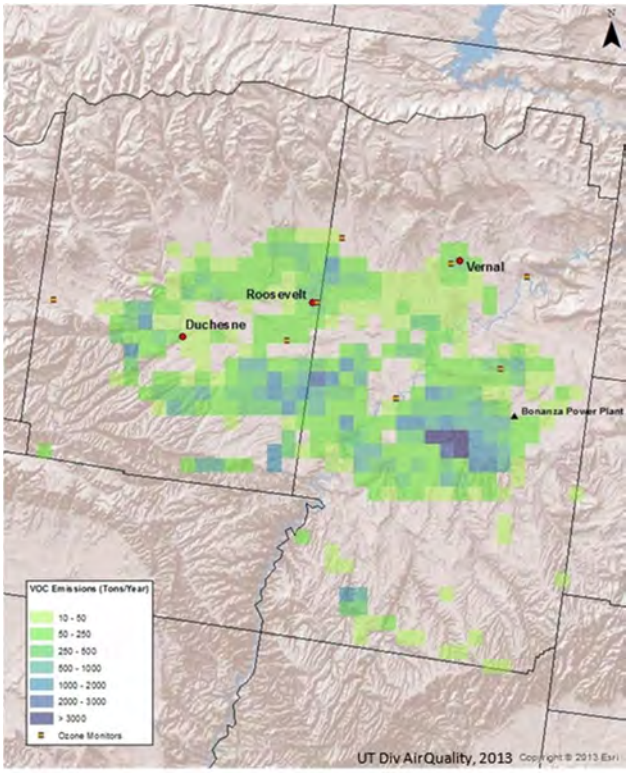


**Figure 9-2. 2011 VOC Inventory - All Emissions.**

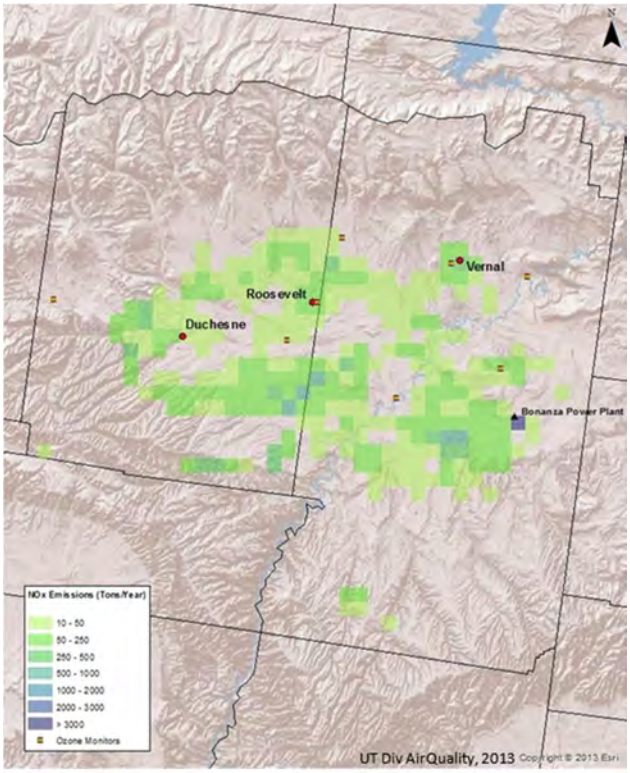


**Figure 9-3. 2011 NOx Inventory - All Emissions.**

More refinement to these emissions surrogates is possible since not all oil and gas emissions activity is directly related to production. By separating out the emissions activity that is not related to production but more appropriately associated with other industry processes, more accurate estimates of the emissions sources themselves as well as their location can be obtained. There is also room for improving the temporal distribution of emissions, whether it be by season or time of day. As noted in the following sections, work is currently underway on inventory improvements through the efforts of several different groups who are actively engaged in air quality modeling in the Basin.

### 9.1.4 BLM Utah Air Resource Management Strategy (ARMS)

The ARMS modeling project is an interagency program that will use a flexible modeling platform to analyze potential changes in air quality in the Uinta Basin. The emissions inventory that has been developed for this project is based on a 2010 base year with projected emissions scenarios out to the year 2021. The project contractor, AECOM, used the WRAP Phase III 2006 inventory as a starting point for oil and gas sector emissions. The WRAP inventory was then updated to 2010 with the use of operator surveys that were conducted by BLM in the Basin. This work also included an estimate for produced water ponds and oil and gas mobile sources which were not included in the WRAP Phase III inventory. This inventory represents a significant enhancement to the original WRAP inventory and the detailed technical support documentation of this effort was published by the ARMS Modeling Project in the Fall of 2013 (AECOM, 2013).

### 9.1.5 Inventory Improvement Projects Scheduled for 2014

During 2014 there are expectations for improvements to the oil and gas inventory for the Basin to increase the usefulness of the inventory for air quality modeling projects that will be undertaken in the next year. This includes ancillary studies that will compare data gathered during the 2012 and 2013 Uinta Basin field campaigns to the process and production-based inventories currently in use, improved emission factors, improved speciation profiles, and weighted reactivity indices.

#### 9.1.5.1 3-State and WestJump Air Quality Studies

The 3-State Air Quality Study and the West Wide Air Quality Modeling Study (WestJump) are multi-agency technical planning efforts to improve ozone modeling in the western US. The 3-State Study area of focus is primarily on the oil and gas regions of Southwest Wyoming, Northeast Utah, and Northwest Colorado. Both the 3-State Study and WestJump have participation from state and federal agencies as well as stakeholders from private industry. Specific projects focused on the Basin and scheduled to be undertaken during 2014 include the following (Tom Moore, Western States Air Resources Council, personal communication, 2014):

- Update of the WRAP Phase III inventory to 2011 base year
    - Obtain 2011 major and minor permitted source data from UDAQ for sources not on tribal land and from EPA for sources on tribal land.
    - Reconcile survey source emissions with minor permitted source emissions.
- Control analysis to account for changes to emission rates due to regulations
    - EPA Subpart OOOO
    - EPA New Source Performance Standards for spark-ignited engines
    - EPA offroad diesel Tier standards
    - State specific regulations
- VOC emissions inventory reactivity analysis
    - Augment the Speciation Tool database being developed for the study to estimate reactivity factors for each speciation profile in the database. Use these factors to conduct reactivity analysis by region, inventory sector, and source category.

#### 9.1.5.2 New Minor Source Permitting Requirements

The EPA established a new minor-source permitting rule for sources on Indian Country in 2011 with a deadline of March 13, 2013 for all sources affected by this rule to register with EPA. Since that deadline, the EPA regional office in Denver has been creating a database of source emissions information that has been submitted by companies with production on Indian Country. In addition to the EPA program the UDAQ permitting program for minor sources is currently undergoing review to improve oil and gas permitting.

When the EPA and UDAQ databases are compiled they can be integrated into the current inventories through careful cross reference to avoid any double-counting of emissions. Each of these programs will improve the ability of emissions modelers to add a great deal of granularity to location and activity information for many individual sources of ozone precursor emissions.

#### 9.1.5.3 Comparison of Estimates to Observations

In the majority of modeling studies it is not possible to compare the emissions estimates with measurements of pollutants in the air because of the expense of taking those measurements. With the exception of very large industrial sources, where continuous emissions monitors are required to track emissions, all inventories are created with the use of emission factors. These factors are used in combination with certain assumptions about the operating conditions and are based on industry-wide averages of operation and procedures.

Improvements in emission inventories always take place in an iterative process with a gradual buildup of confidence in the estimates as specific sectors are analyzed in detail. The data that was captured from the NOAA mobile laboratory and aircraft during the 2012 UBOS study provides location-specific observations of VOCs, methane, carbon monoxide, carbon dioxide, nitrogen monoxide and nitrogen dioxide. The analysis and application of these observed data to current estimates of VOC emissions from the oil and gas sector in the Basin can provide crucial information for evaluation of emissions estimates. Testing of emissions inventories with these data, along with the improvements noted above, will go a long way to improving the oil and gas inventory in the Basin during the coming year.

## 9.2 Wintertime Emissions of Hydrocarbons from Produced Water Evaporation Facilities

***Seth Lyman, Marc Mansfield, Howard Shorthill, Randy Anderson, Jordan Evans, Chad Mangum, and Tate Shorthill***

***Office of Commercialization and Regional Development, Utah State University, Vernal, Utah***

### 9.2.1 Introduction

Ozone concentrations exceeding EPA standards have been observed in the Uinta Basin during winter inversion conditions. Local sources that emit ozone precursors, including volatile organic compounds (VOC) and nitrogen oxides ($NO_X$), are largely responsible for the high ozone levels (Lyman and Shorthill, 2013), yet ozone precursor emissions from many of these sources, including upstream oil and gas production equipment and facilities, are inadequately characterized. The development of effective mitigation strategies for ozone pollution cannot proceed without a better understanding of these sources.

One source of VOC is the water that is brought to the surface during oil and gas production (Clark and Veil, 2009). In the Uinta Basin, this produced water is commonly disposed of via open-air evaporation, a technique involving the storage of produced water in shallow ponds where surface evaporation can take place, either passively or by active aeration (Clark and Veil,

2009). In 2012, more than five million barrels of produced water were evaporated from the 427 surface acres of produced water ponds in the Basin (http://oilgas.ogm.utah.gov/Data_Center/DataCenter.cfm). Locations, ownership, acreage, and status of each produced water pond in the Uinta Basin were compiled and verified by our group from data obtained from the Utah Division of Oil, Gas, and Mining; site visits; and aerial photos.

Since produced water ponds may be responsible for a significant percentage of ozone-forming emissions in the Uinta Basin, knowledge of the types and amounts of VOC emitted from these ponds is vital to the development of effective mitigation practices. Until this study, however, no measurements of produced water emissions had ever been conducted in the Basin. In 2009, the U.S. Environmental Protection Agency (EPA) released a report of measurements of VOC emissions from two different evaporation facilities in Western Colorado (Thoma, 2009), and while an important first step, the study only covered two small facilities for a few days during the summer, at best a difficult extrapolation to the winter conditions of the Uinta Basin.

To better understand emissions from produced water ponds during winter inversions in the Uinta Basin, a dynamic flux chamber was used to measure methane, methanol, and speciated nonmethane hydrocarbon (NMHC) emissions at three separate pond facilities during February and early March 2013. As a rule, VOC signifies only those hydrocarbons that are more reactive than ethane, but since ethane is known to be a major component of NMHC in local ambient air and likely contributes significantly to ozone production (Lyman and Shorthill, 2013), NMHC was an important measurement focus. Though much of the total pond surface area at the evaporation facilities was frozen during the study period, areas that regularly received water deliveries remained free of ice. Emissions were measured from both frozen and open pond surfaces, and total emissions were estimated from these and all facilities in the Basin during winter conditions.

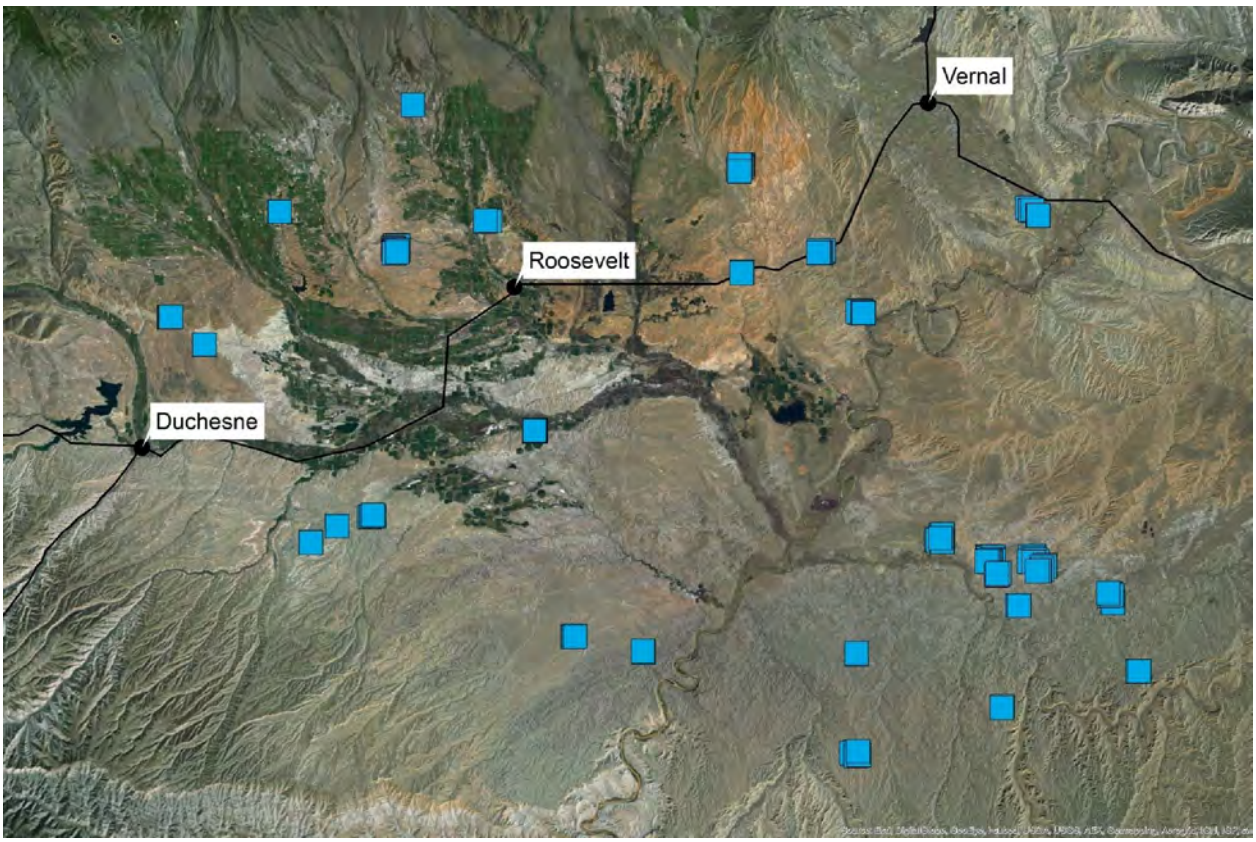


**Figure 9-4. Locations of produced water pond facilities in the Uinta Basin. Each pond is shown as a blue square.**

### 9.2.2 Methods

#### 9.2.2.1 Pond Facilities Descriptions

To protect the interests of produced water disposal facility operators, non-disclosure agreements were established as a precondition to access of pond facilities. The locations and operators of the sampled facilities, therefore, will not be given in this report. Three facilities in different parts of the Uinta Basin were sampled during this study, and their combined acreage comprised 17% of the total pond surface area in the Basin.

Water was trucked from well-site storage tanks to the disposal facilities and emptied into a skim tank where gravity separated the water from the residual oil (see Figure 9-5 for a diagram of a typical facility). During winter, well-site storage tanks were usually heated, so the produced water was warm when introduced into the skim tanks. The open skim tanks used by some facilities presented a pure oil surface directly to the atmosphere, and inclusion of this source in future studies would be valuable. As it separated from the oil, water drained from the bottom of the skim tank into an evaporation pond. During warm seasons, this water would then be distributed to other ponds at the facility where it could be sprayed into the air or cascaded down a lined dike to facilitate evaporation. During winter, transfer to other ponds was curtailed, and active evaporation methods did not occur.

During the winter 2012-13 study, all ponds that regularly received water from skim tanks remained at least partially unfrozen, while most of the ponds that did not regularly receive water from skim tanks remained frozen to some depth and covered with snow. Some ponds, however, were so saline that despite subfreezing air temperatures the water remained open. The salinity of produced water depends on the formation from which it was derived (Clark and Viel, 2009) and, when first extracted, typically is equivalent to that of seawater. Salinity increases, however, as evaporation takes place at the disposal facilities, with some ponds becoming hypersaline.

Some produced water facilities had a small pond (usually netted) downstream from the skim tank to catch additional residual oil, followed by a larger pond that received water from the small netted pond. Other facilities did not have this smaller intermediate pond. All facilities had oil storage tanks into which the skimmed oil was pumped.

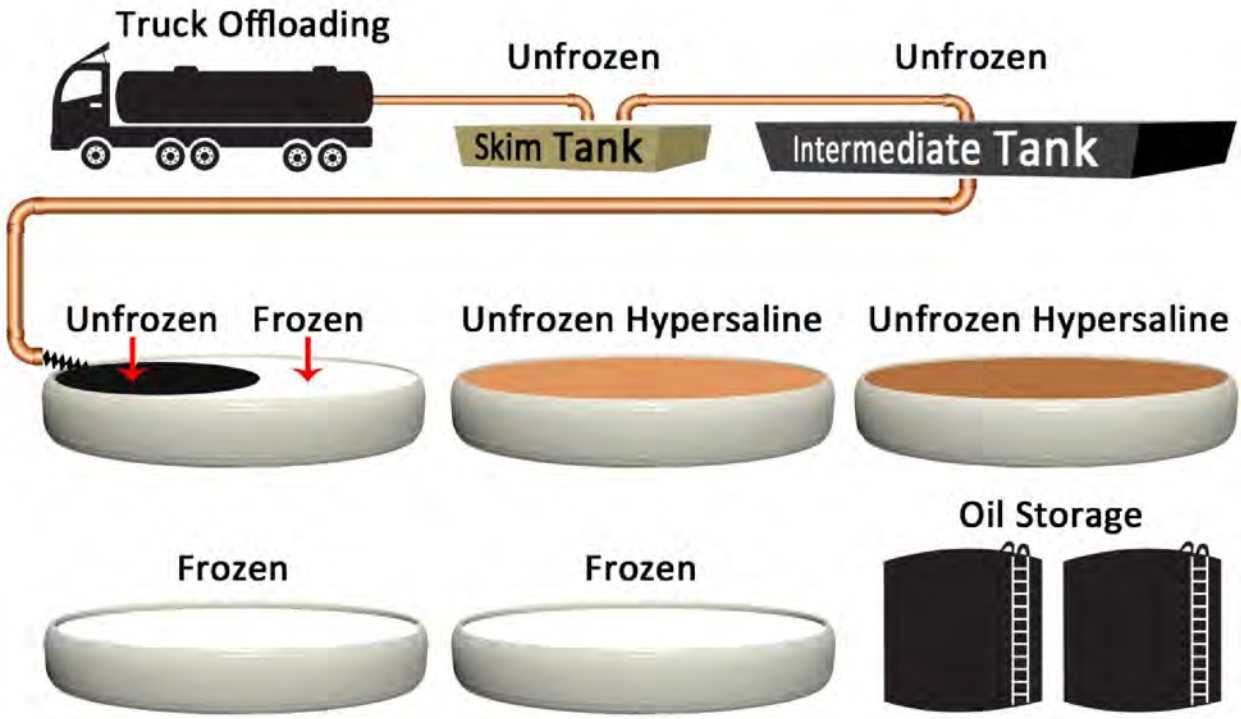


**Figure 9-5. Illustration of a typical Uinta Basin produced water facility sampled by our group during winter 2012-13.**

#### 9.2.2.2 Dynamic Flux Chamber Measurements

Emissions of methane, non-methane hydrocarbons, and methanol were sampled using a modified version of the EPA Emission Isolation Flux Chamber (Eklund, 1992) that currently is widely used for air toxics emissions. Dynamic flux chambers measure emissions (or deposition) as the difference in concentrations inside and outside the chamber, multiplied by the flow rate and divided by the surface area covered by the chamber. The chamber system utilized in this study connected to a laser-based methane and carbon dioxide analyzer (LGR Ultraportable Greenhouse Gas Analyzer) and stainless steel evacuated air sampling canisters, which were analyzed for C2-C12 hydrocarbons and methanol. C2-C12 hydrocarbons were analyzed by GC-FID according to EPA PAMS analysis protocols (EPA, 1998), and methanol was analyzed according to EPA TO-15 protocols (EPA, 1999).

The laser-based analyzer switched every two minutes between sampling air inside and outside the chamber, while a pair of evacuated canisters pulled air from inside and outside the chamber over a period of 30-45 minutes. A system of flow meters and pumps regulated air sampling, and the flow through the chamber was kept at 5 L $min^{-1}$. Concentrations, flows, and other information were logged with a Campbell Scientific CR1000 datalogger at five-second intervals. Figure 9-6 shows a photo of the chamber on a produced water pond.

Emissions were measured from a subset of ponds at each facility and from snow-covered ground near produced water ponds. Emissions were also measured from a clean, 1/8” thick Teflon surface to assess system contamination. Teflon surface emissions were measured periodically throughout the study to verify that the chamber system did not become contaminated over time. The chamber, tubing and wires, and foam floatation device were washed periodically with soap and water to remove oil and grease.

**Figure 9-6. USU dynamic flux chamber on a produced water pond.**

#### 9.2.2.3 Meteorological Measurements

Detailed meteorological data were collected during all emissions measurement periods. These included solar radiation; wind speed, direction, and turbulence; ambient temperature, pressure, and humidity; water temperature inside and outside the chamber; and air pressure and temperature inside the chamber.

#### 9.2.2.4 Water Samples

At each of the study's produced water facilities, water samples were collected from most ponds and analyzed for salinity, pH, methane, methanol, and a suite of other organic compounds. Samples were analyzed for methane by method RSK-175 (Kampbell and Vandegrift, 1998), for methanol by EPA Method 8015B (EPA, 1996a), and for other organics by EPA Method 8260B (EPA, 1996b). When ice was present, water was collected from under the ice.

### 9.2.3 Results and Discussion

#### 9.2.3.1 Water Chemistry

For simplicity, pond surfaces encountered during the study were classified as (1) frozen, (2) hypersaline, or (3) recently offloaded. These three types comprised all the pond surface area at sampled facilities. Frozen and hypersaline surfaces comprised about 90% of total pond surface area at the facilities sampled. Concentrations of organic compounds in hypersaline surfaces were below limits of detection, with the exception of methane, methanol, and octane (Table 9-3). These surfaces were several times more saline than other types. The recently offloaded

surface type tended to have the highest concentrations of most organic compounds, and water under frozen surfaces had either slightly lower or similar concentrations. Concentrations of methanol in some samples were more than two orders of magnitude higher than concentrations of other organic compounds and comprised as much as 0.5% of produced water.

**Table 9-3. Average concentrations of select organic compounds in, and chemical properties of, three produced water surface types encountered during the winter 2012-13 sampling season. N.D. means not detected.**

| | | Frozen | Hypersaline | Recently Offloaded |
|---|---|---|---|---|
| Methane | mg $L^{-1}$ | 0.4 | 0.02 | 0.7 |
| Methanol | mg $L^{-1}$ | 2690 | 6.3 | 2415 |
| Isopropyl alcohol | mg $L^{-1}$ | 6.3 | N.D. | 10.6 |
| n-Butyl alcohol | mg $L^{-1}$ | 5.3 | N.D. | 16.3 |
| tert-Butylbenzene | mg $L^{-1}$ | 0.0 | N.D. | 0.2 |
| Acetone | mg $L^{-1}$ | 1.5 | N.D. | 2.2 |
| Benzene | mg $L^{-1}$ | 4.7 | N.D. | 12.6 |
| Toluene | mg $L^{-1}$ | 7.3 | N.D. | 15.9 |
| Xylenes, Total | mg $L^{-1}$ | 4.4 | N.D. | 7.5 |
| Naphthalene | mg $L^{-1}$ | 0.1 | N.D. | 0.2 |
| Other aromatics | mg $L^{-1}$ | 1.2 | N.D. | 2.3 |
| n-Hexane | mg $L^{-1}$ | 0.3 | N.D. | 0.6 |
| Cyclohexane | mg $L^{-1}$ | 0.4 | N.D. | 1.1 |
| n-Octane | mg $L^{-1}$ | 0.7 | 0.1 | 2.3 |
| pH | -- | 8.8 | 8.6 | 8.4 |
| Conductivity | mS $cm^{-1}$ | 20 | 174 | 29 |
| Salinity | % NaCl sat. | 34 | 203 | 56 |

#### 9.2.3.2 Emissions from Different Pond Surface Types

Emissions from the Teflon surface were low, showing that the flux chamber system had consistent, low blanks (Figure 9-7). Emissions from hypersaline surfaces, frozen surfaces, and snow-covered ground were higher and more variable than emissions from the Teflon surface, but were not significantly different from one another ($p = 0.55$ to $0.90$). Emissions from the recently offloaded surface type were more than two orders of magnitude higher than emissions from the other surfaces.

The recently offloaded surface type had higher emissions of aromatics and lower emissions of methanol as a percentage of total emissions than other surface types (Figure 9-8). Even though the recently offloaded surface type made up only 10% of the pond surface area at sampled produced water facilities, it accounted for 99.2% of all emissions from the facilities studied.

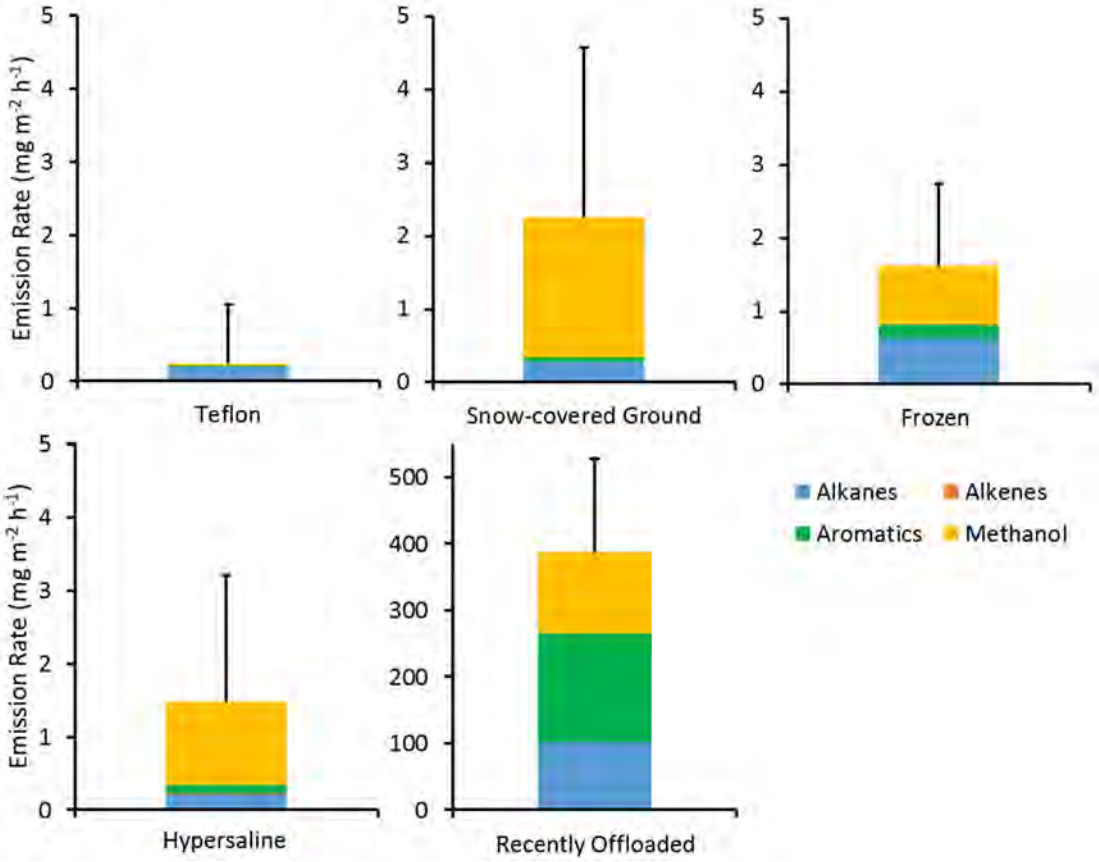


**Figure 9-7. Emissions from different surface types at produced water facilities. The top of the colored column is the average total emissions from four types of compounds, and the contribution of each type is delineated with a different color. The black line on top of the colored column is the 90% confidence interval for the average total emissions.**

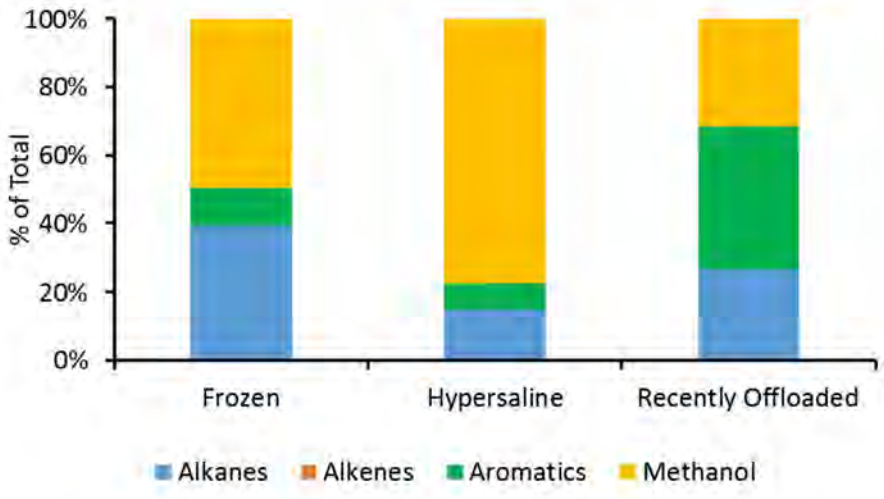


**Figure 9-8. Emissions of organic compounds from different surface types as a percentage of total emissions.**

### 9.2.3.3 Factors that Influenced Emission Rates

In many cases, organic compound concentrations in water were strongly correlated with emission rates of that compound. For example, the $R^2$ value for the correlation between toluene concentration in water and toluene emission flux was 0.91 (Figure 9-9). No significant correlation was observable for some other compounds, however. The average $R^2$ value for 14 compounds for which water concentrations and emission rates are both available was 0.48.

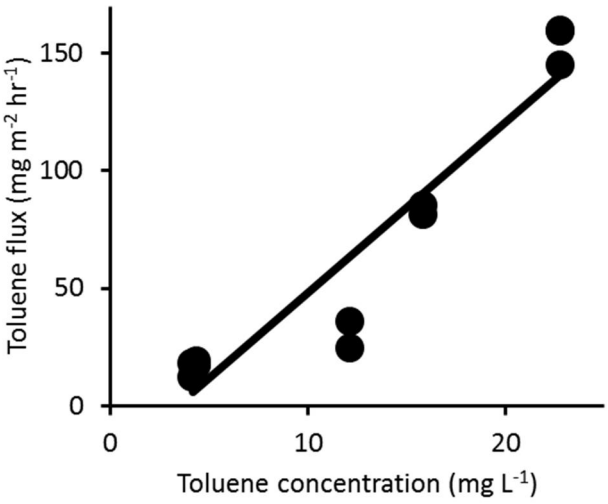


**Figure 9-9. Toluene concentration in unfrozen produced water versus toluene emission rate.**

Meteorology (most particularly, temperature) also influenced emission rates. Figure 9-10 shows a dramatic increase in emissions of organic compounds from a produced water pond as the layer of ice that had formed overnight melted. Emissions from ponds with ice cover were much lower than from open ponds with similar organic compound concentrations in water. Thus, the contribution of produced water pond emissions to ozone production in the Uinta Basin is likely to depend strongly on ice cover (which, in turn, depends on temperature).

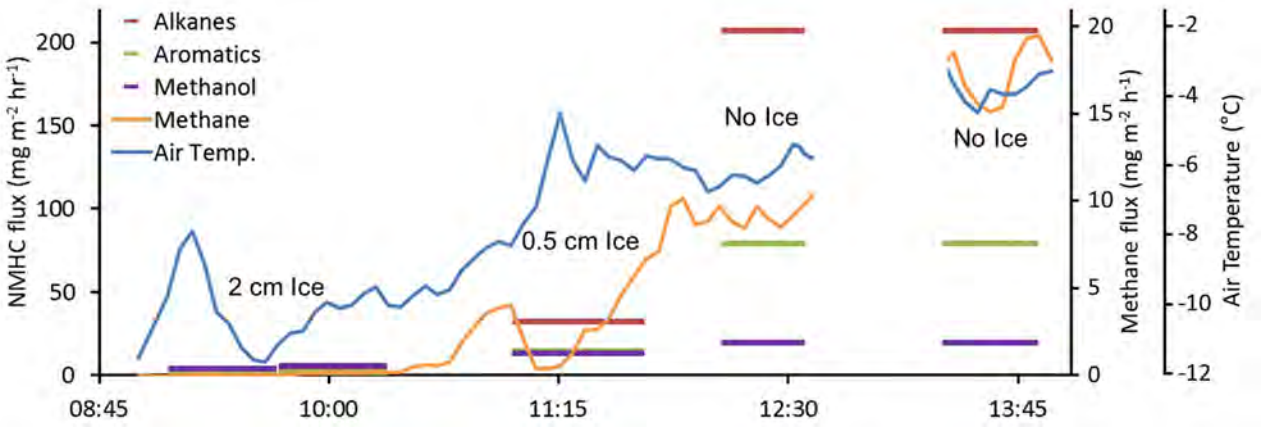


**Figure 9-10. Change in emission rate of alkanes, aromatics, methanol, and methane throughout the day as temperature warms and ice covering a produced water pond melts.**

### 9.2.3.4 Comparison to Basin-wide Emissions

To apply emissions data from this study to all produced water facilities in the Uinta Basin during the winter months, the following assumptions were made: (1) pond surface types follow a similar distribution, (2) produced water has a similar composition, and (3) observed emission rates are seasonally representative.

Table 9-4 shows estimated emissions from different surface types for the entire Uinta Basin, using the assumptions above. In Table 9-5, the emission rates from Table 9-4 are compared with total anthropogenic NMHC emissions from the 2011 Duchesne and Uintah County emissions inventory listed in Table 9-2 (biogenic emissions are near zero during the winter). Table 9-5 shows that emissions from produced water ponds are a small portion of total inventoried wintertime NMHC emissions, but since more than 50% of emissions from produced water are aromatic compounds (many highly reactive in terms of ozone production), this source may still contribute significantly to wintertime ozone.

Table 9-5 provides an estimate of wintertime methanol emissions from all produced water facilities in the Uinta Basin, but no estimate exists of methanol emissions for all sources in the Basin, so the significance of this source is unknown. A comprehensive emissions inventory for wintertime emissions of methanol and formaldehyde is needed (emissions of formaldehyde appear to be associated with methanol emissions in many cases; Roberts et al., 2013).

**Table 9-4. Estimated emission rate of organic compounds from all produced water facilities in the Uinta Basin, categorized by pond surface type. TNMHC is total nonmethane hydrocarbons and is the sum of alkanes, alkenes, and aromatics.**

| kg/h | Frozen | Hypersaline | Recently Offloaded |
|---|---|---|---|
| Alkanes | 0.61 | 0.21 | 98.7 |
| Alkenes | 0.002 | 0.001 | 0.000 |
| Aromatics | 0.17 | 0.11 | 155.3 |
| TNMHC | 0.78 | 0.32 | 254.0 |
| Methanol | 0.77 | 1.10 | 117.0 |

**Table 9-5. Wintertime produced water emissions in the Uinta Basin compared to total anthropogenic emissions from all sources (Table 9-2). TNMHC is total nonmethane hydrocarbons and is the sum of alkanes, alkenes, and aromatics.**

| | TNMHC | Methanol |
|---|---|---|
| kg/h from produced water | 255 | 119 |
| tons/month from produced water | 196 | 91 |
| Total tons/month from all sources for entire Basin | 9593 | -- |
| % of total emissions from ponds | 2.1% | -- |

#### 9.2.3.5 Uncertainties and Next Steps

During this single-season study, only a subset of total produced water facilities in the Uinta Basin was sampled. More study clearly is needed to better quantify emission rates and relationships between emissions, meteorology, and water chemistry. This study did not seek to quantify emissions from produced water storage tanks at well sites, from produced water loading and offloading areas, or from covered and uncovered skim tanks and oil storage tanks at produced water facilities. These additional produced water-related emission sources could substantially increase estimates of wintertime hydrocarbon emissions from produced water.

### 9.2.4 Summary

Produced water NMHC emissions are a small but meaningful percentage of total wintertime emissions in the Uinta Basin. Emissions from produced water are dependent on meteorology and water composition. More work is needed to refine current estimates of produced water emissions.

### 9.2.5 Acknowledgements

We gratefully acknowledge support from the Utah State and Institutional Trust Lands Administration (SITLA), the Uintah Impact Mitigation Special Service District (UIMSSD), the Utah Science, Technology, and Research Initiative (USTAR), and the United States Department of Energy (DOE).

### 9.2.6 References

AECOM (2013), *Utah State BLM Emissions Inventory Technical Support Document*. AECOM Fort Collins, CO, November [http://www.blm.gov/ut/st/en/prog/more/air_quality.html].

Clark, C.E., and J.A. Veil (2009), *Produced Water Volumes and Management Practices in the United States, ANL/EVS/R-09/1*, Argonne National Laboratory, Argonne, Illinois.

Eklund, B. (1992), Practical guidance for flux chamber measurements of fugitive volatile organic emission rates, *J. Air Waste Mgmt. Assoc., 42*, 1583-1591.

EPA (1996b), *Method 8015B: Nonhalogenated Organics Using GC/FID,* United States Environmental Protection Agency.

EPA (1996b), *Method 8260B: Volatile Organic Compounds by Gas Chromatography/Mass Spectrometry (GC/MS),* United States Environmental Protection Agency.

EPA (1998), *Technical Assistance Document for Sampling and Analysis of Ozone Precursors, EPA/600-R-98/161*, United States Environmental Protection Agency, Research Triangle Park, North Carolina.

EPA (1999), *Compendium of Methods for the Determination of Toxic Organic Compounds in Ambient Air, EPA/625/R-96/010b*, United States Environmental Protection Agency, Cincinnati, Ohio.

Kampbell, D.H., and S.A. Vandegrift (1998), Analysis of dissolved methane, ethane, and ethylene in ground water by a standard gas chromatographic technique, *J. Chromatographic Sci, 36*, 253-256.

Lyman, S., Mansfield, M., Shorthill, H., Anderson, R., Mangum, C., Evans, J., Shorthill, T., Horel, J., Crosman, E., Neeman, E., Christiansen, M., and O'Neil, T (2013), Distributed measurements of air quality and meteorology, in *Final Report: 2013 Uintah Basin Winter Ozone and Air Quality Study*, Environ, Novato, California.

Lyman, S., and H. Shorthill (Eds.) (2013), *Final Report: 2012 Uintah Basin Winter Ozone and Air Quality Study*, *CRD13-320.32*, Office of Commercialization and Regional Development, Utah State University, Logan, Utah.

Mansfield, M., D. Moss, C. Hall, E. Smith, and H. Shorthill (2013), Emissions inventory report, in *Final Report: 2012 Uintah Basin Winter Ozone and Air Quality Study*, *CRD13-320.32*, edited by S. Lyman and H. Shorthill, Office of Commercialization and Regional Development, Utah State University, Logan, Utah.

Roberts, J., E.J. Williams, S.B. Brown, L. Lee, R. Cohen, S. Murphy, J. Gilman, J. de Gouw, C. Warneke, C. Young, P. Edwards, R. McLaren, J. Kercher, J. Thornton, C. Tsai, J. Stutz, R. Zamora (2013), Intensive measurements at the Horsepool site, in *Final Report: 2012 Uintah Basin Winter Ozone and Air Quality Study*, *CRD13-320.32*, edited by S. Lyman and H. Shorthill, Office of Commercialization and Regional Development, Utah State University, Logan, Utah.

Thoma, E. (2009), *Measurement of Emissions from Produced Water Ponds: Upstream Oil and Gas Study #1: Final Report, EPA/600/R-09/132*, Office of Research and Development, U.S. Environmental Protection Agency, Cincinnati, Ohio.

# 10.0 NUMERICAL MODELING OF A THERMAL INVERSION IN THE UINTA BASIN, UTAH, JANUARY 26-30 2013

***Trang Tran, Marc Mansfield, Seth Lyman***

***Bingham Research Center, Utah State University, Vernal, Utah 84048***

WRF simulations have been performed to provide the meteorological conditions for photochemical grid calculations of the role of major emission sources (e.g., oil and gas extraction, the Bonanza power plant, vehicles) on winter ozone pollution in the Uinta Basin. The CAMx platform, which has been developed for studying ozone photochemistry (Yarwood et al., 2010; Emery et al. 2011; Shen et al., 2011) will be used as the chemistry model in our study. The high-ozone period occurring during January to March 2013 was selected as the study episode.

WRF model configurations were adapted from the report (AECOM, 2013) of the Utah Air Resource Management Strategy Modeling Project (Utah ARMS), performed by AECOM under contract with the Bureau of Land Management (BLM). Most of AECOM's winter-month setups were retained, although some changes were applied with the goal of improving both model performance and computational efficiency. (We increased vertical and horizontal resolutions, we employed one-way nesting, and we omitted sea surface temperature updating.) We examined model performance at different horizontal resolutions (1300 m versus 800 m) and will test different initial snow conditions to determine the optimum configurations for WRF simulations of winter inversions in the basin.

Primary evaluation of our WRF simulations was conducted using the episode of January 26-30, 2013 as a reference case (hereafter referred as REF). We focused on the capability of the model to simulate inversions and snow cover within the basin since they are the two major meteorological conditions triggering ozone pollution in the basin. In REF, 1-way nested domains were set at 36-12-4-1.3 km resolution with the finest domain extending from the Great Salt Lake in the northwest to the Uncompaghre Plateau in the southeast, covering much of eastern Utah and adjoining parts of Wyoming and Colorado (Fig. 10-1). The Pleim-Xiu scheme was selected for the LSM and no snow modification was applied for the initial condition. Other configurations can be found in AECOM (2013).

In general, WRF captured the timing and basic structure of the inversion at a number of observational sites within the basin (Roosevelt, Ouray, and Horsepool). The inversion conditions on a high ozone day, January 26, were reproduced (Fig. 10-2a,b). WRF also modeled the inversion breakup on January 28 that was caused by a storm (Fig. 10-2c,d). Snow depths within the basin were also represented reasonably in REF simulations. Within the basin, modeled snow depths ranged between 5 and 50 cm, which coincide with the 10-50 cm range of the NOAA snow analysis data for the basin (Fig. 10-3). Further evaluation of snow depths should be conducted for individual snow monitoring sites to strengthen this conclusion. WRF eventually overestimated wind speed in near-surface layer with large bias up to 4m/s.

Increasing grid resolution from 1300m to 800m did not improve model performance on simulating wind speed (Fig. 10.4) and other meteorological quantities at near-surface layer (e.g., temperature, sea-level pressure, precipitation; not shown).

For future work, besides doing further model evaluation of REF (e.g, skill-scores calculation), we will test the impact of modifying the snow initial conditions on model performance in simulating snow and albedo, which are important factors affecting ozone formation in the basin. Once these steps are finished, we will proceed with preparing emissions data and running CAMx to investigate ozone pollution in the Uinta Basin.

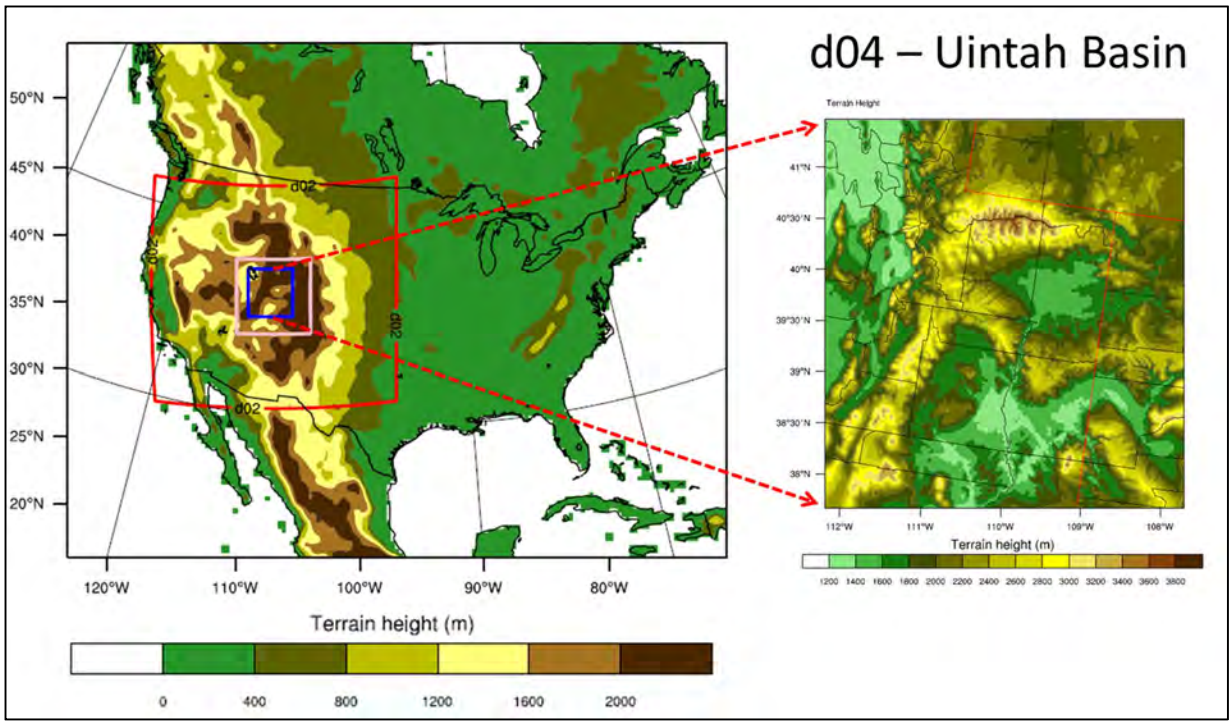


**Figure 10-1. Nested domains with horizontal resolution of 36, 12, 4 and 1.3 km, respectively (left). Domain 4 (right). The Uinta Basin is the low terrain centered at about 109.5°W longitude and 40°N latitude.**

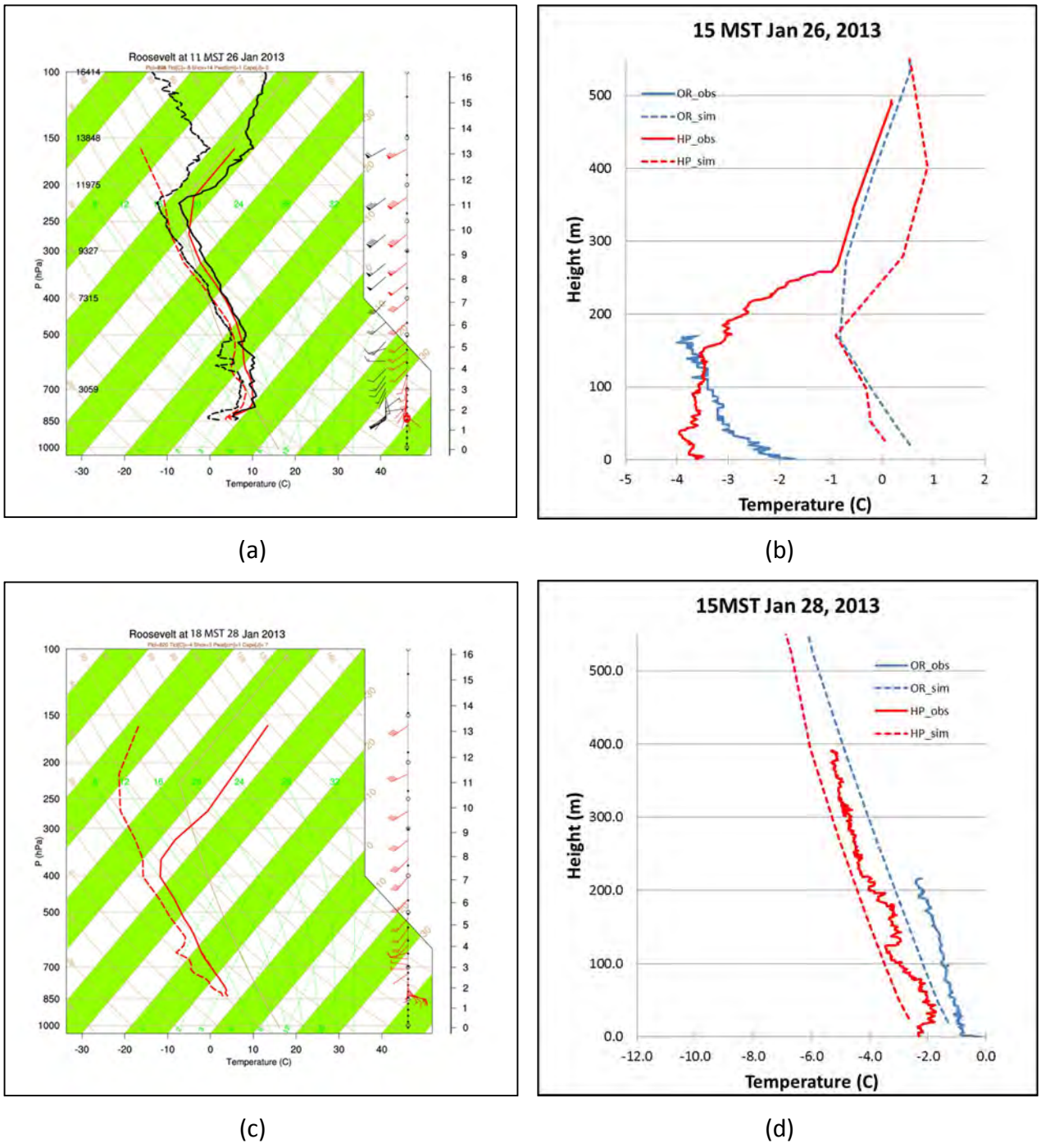


**Figure 10-2. Observed (black) and simulated (red) temperature vertical profiles at Roosevelt (a, c) and observed (solid) and simulated (dash) temperature vertical profiles at Ouray (blue) and HorsePool (red) (b,d). Observational data for Roosevelt and Ouray/Horsepool sites were collected from rawinsonde measurements conducted by the University of Utah and from ozonesonde measurements conducted by NOAA, respectively.**

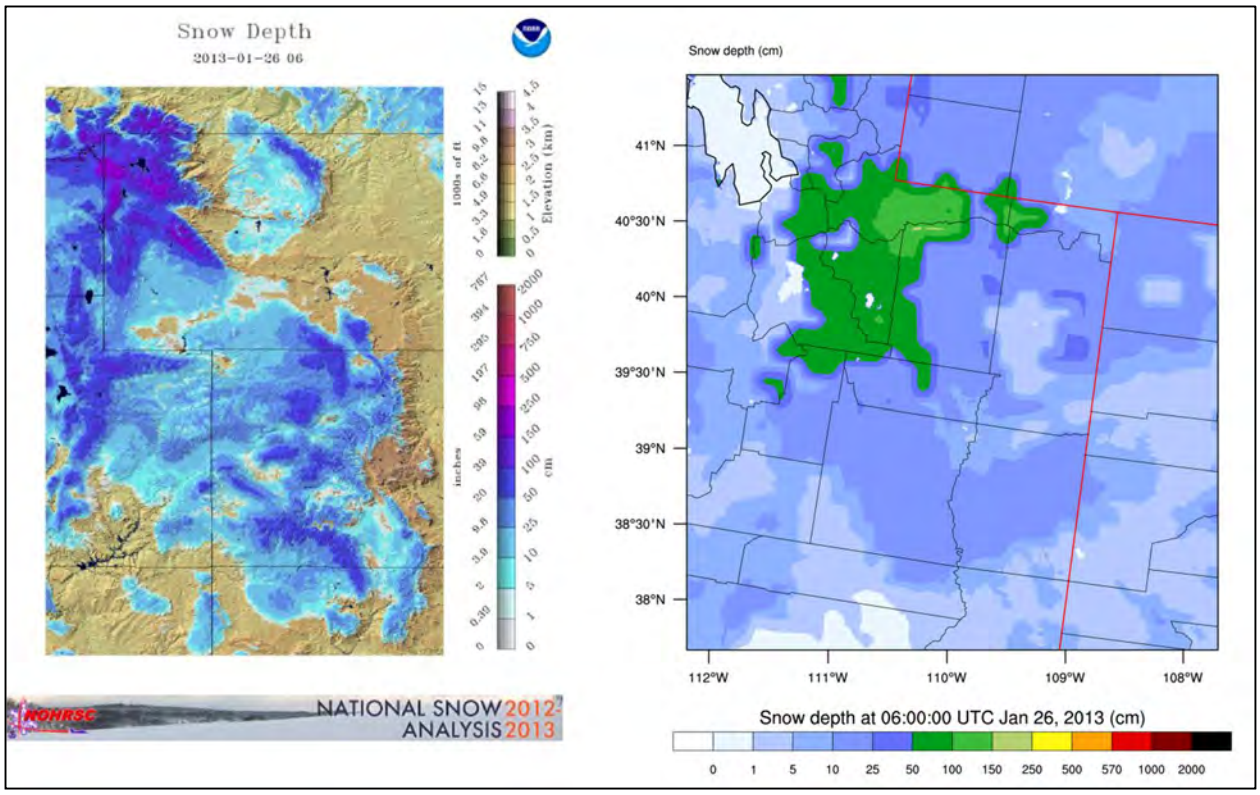


**Figure 10-3. Comparison of simulated (right) and NOAA analysis (left) snow depths.**

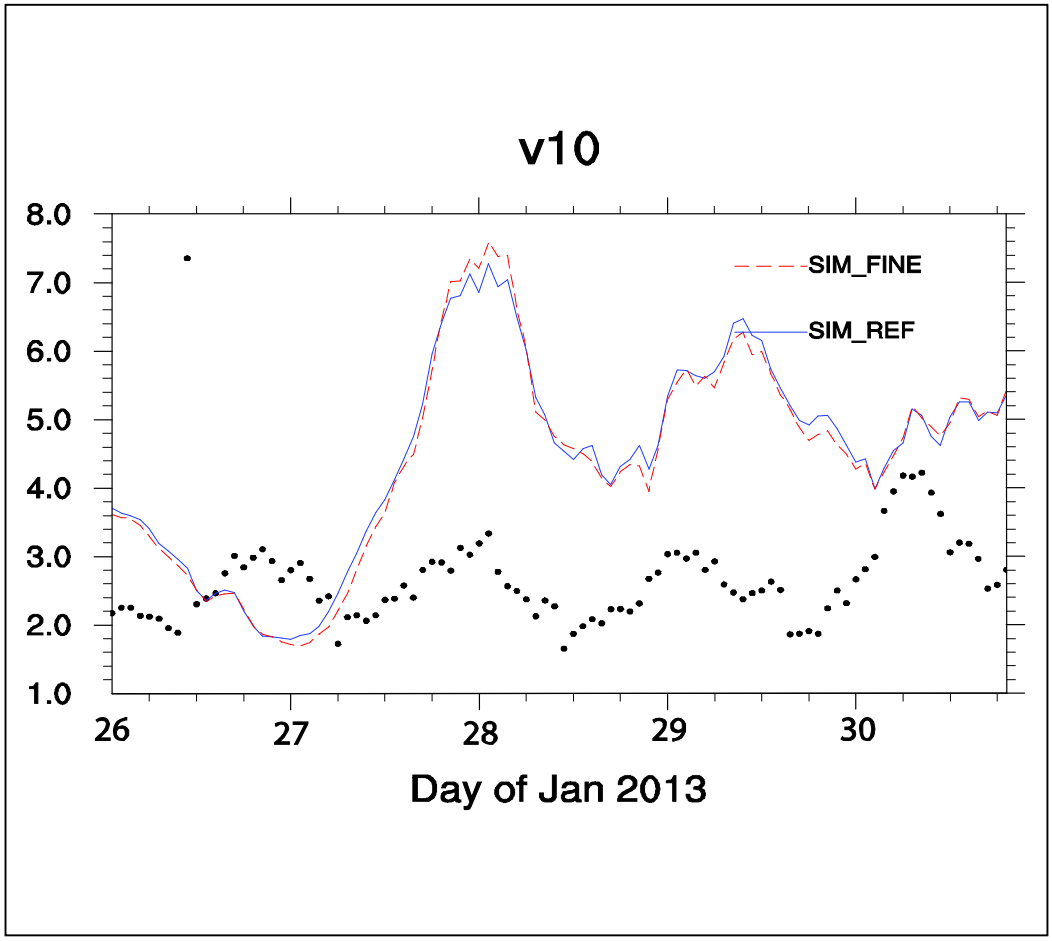


**Figure 10 4. Temporal evolution of hourly simulated (line) and observed (dot) near-surface wind speed (m/s) averaged over 61 monitoring sites within domain. Observational data were obtained from Western Regional Climate Center. SIM_REF and SIM_FINE stands for reference and fine resolution simulation, respectively.**

## 10.1 References

AECOM, 2013. Utah Air Resource Management Strategy Modeling Project: meteorological model performance evaluation. Report prepared for Bureau of Land Management – Utah State Office.

Emery, C., Jung, J., Downey, N., Johnson, J., Jumenez, M., Yarwood, G., Morris, R., 2011. Regional and global modeling estimates of policy relevant background ozone over the United States. Atm. Environ., doi:10.1016/j.atmosenv.2011.11.012

Shen, J., Wang, X.S., Li, J.P., Zhang, Y.H., 2011. Evaluation and intercomparison of ozone simulations by Models-3/CMAQ and CAMx over the Pearl River Delta. Sci. Chin., 11, 1789-1800.

Yarwood, G., Kemball-Cook, S., Koo, B., Johnson, J., 2010. Ozone transport analysis using back-trajectories and CAMx probing tools. 9th Annual CMAS conference, 2013.